



TECHNICAL UNIVERSITY OF CRETE  
SCHOOL OF PRODUCTION ENGINEERING AND MANAGEMENT

# **Rational design and development of nanostructured non-precious metal oxide catalysts for energy and environmental applications**

*Thesis submitted for the partial fulfillment of the requirements for the degree of  
Doctor of Philosophy (PhD)*

*by*

***Sofia Stefa***

*Supervisor: Professor Michalis Konsolakis*

Chania, Greece, September 2023



ΠΟΛΥΤΕΧΝΕΙΟ ΚΡΗΤΗΣ  
ΣΧΟΛΗ ΜΗΧΑΝΙΚΩΝ ΠΑΡΑΓΩΓΗΣ ΚΑΙ ΔΙΟΙΚΗΣΗΣ

# Ορθολογικός σχεδιασμός και ανάπτυξη νανοδομημένων καταλυτών μη-ευγενών μετάλλων για ενεργειακές και περιβαλλοντικές εφαρμογές

*Διδακτορική διατριβή  
Σοφία Στέφα*

*Επιβλέπων: Καθηγητής Μιχάλης Κονσολάκης*

Χανιά, Σεπτέμβριος 2023



### **Advisory Committee**

**Michalis Konsolakis** (Supervisor)

Professor, School of Production Engineering and Management

Technical University of Crete (TUC)

**Georgios E. Marnellos**

Professor, Department of Mechanical Engineering

University of Western Macedonia (UoWM)

**Spiros Papaefthimiou**

Professor, School of Production Engineering and Management

Technical University of Crete (TUC)

### **Thesis Examination Committee**

**Vassilios Binas**

Assistant Professor, School of Chemistry, Aristotle University of Thessaloniki(AUTH)

Researcher, Institute of Electronic Structure & Laser (IESL-FORTH)

**Dimitris Ipsakis**

Assistant Professor, School of Production Engineering and Management

Technical University of Crete (TUC)

**Vassilis N. Stathopoulos**

Professor, General Department

National and Kapodistrian University of Athens (NKUA)

**Nikolaos Kallithrakas-Kontos**

Professor, School of Mineral Resources Engineering

Technical University of Crete (TUC)



**Π Ρ Α Κ Τ Ι Κ Ο**  
**ΤΗΣ ΕΠΤΑΜΕΛΟΥΣ ΕΞΕΤΑΣΤΙΚΗΣ ΕΠΙΤΡΟΠΗΣ**  
**ΓΙΑ ΤΗΝ ΚΡΙΣΗ ΤΗΣ ΔΙΔΑΚΤΟΡΙΚΗΣ ΔΙΑΤΡΙΒΗΣ**

της **Στέφα Σοφίας**

ΔΙΠΛΩΜΑΤΟΥΧΟΥ/ΠΤΥΧΙΟΥΧΟΥ ΤΟΥ ΤΜΗΜΑΤΟΣ ΦΥΣΙΚΗΣ ΤΟΥ ΠΑΝΕΠΙΣΤΗΜΙΟΥ ΠΑΤΡΩΝ ΚΑΙ  
ΔΙΠΛΩΜΑΤΟΥΧΟΥ ΤΟΥ ΠΡΟΓΡΑΜΜΑΤΟΣ ΜΕΤΑΠΤΥΧΙΑΚΩΝ ΣΠΟΥΔΩΝ ΤΟΥ ΤΜΗΜΑΤΟΣ ΦΥΣΙΚΗΣ ΤΟΥ  
ΠΑΝΕΠΙΣΤΗΜΙΟΥ ΠΑΤΡΩΝ

Η εξεταστική επιτροπή που διορίσθηκε σύμφωνα με τις κείμενες διατάξεις και την απόφαση της Γενικής Συνέλευσης της Σχολής Μηχανικών Παραγωγής και Διοίκησης στη συνεδρίαση 22<sup>η</sup>/30.08.2023 για την κρίση της διδακτορικής διατριβής του/της **Στέφα Σοφίας** συνήλθε σε συνεδρίαση σήμερα την **Παρασκευή 22 Σεπτεμβρίου 2023** και παρακολούθησε την υποστήριξη της διατριβής με τίτλο:

**«Ορθολογικός σχεδιασμός και ανάπτυξη νανοδομημένων καταλυτών μη-ευγενών μετάλλων για ενεργειακές και περιβαλλοντικές εφαρμογές»**

**Αγγλικός τίτλος: «Rational design and development of nanostructured non-precious metal catalysts for energy and environmental applications»**

Μετά την ανάπτυξη της διατριβής, τα μέλη της εξεταστικής επιτροπής, έκαναν ερωτήσεις στην υποψήφια κα. Στέφα Σοφία τόσο γενικού περιεχομένου, όσο και σχετικές με το θέμα της διατριβής.

Στη συνέχεια, αποχώρησε η υποψήφια και ακολούθησε συζήτηση της επιτροπής.

Η επιτροπή, μετά από ψηφοφορία, έκρινε ότι η διατριβή της κας Στέφα Σοφία, είναι πρωτότυπη και αποτελεί ουσιαστική συμβολή στην επιστήμη, προτείνει δε προς τη Γενική Συνέλευση με ειδική σύνθεση της Σχολής, **ομόφωνα** να του απονεύσει τον τίτλο του Διδάκτορος.

**Η ΕΠΙΤΡΟΠΗ**

1. Κωνσολάκης Μιχάλης, Καθηγητής, Επιβλέπων, ΜΠΑ, Πολυτεχνείο Κρήτης

**Michail Konsolakis**  
Digitally signed by Michail Konsolakis  
Date: 2023.09.22 13:17:33 +03'00'

2. Μαρνέλλος Γεώργιος, Καθηγητής, Τμήμα Χημικών Μηχανικών, ΑΠΘ

**George Marnellos**  
Digitally signed by George Marnellos  
Date: 2023.09.22 14:29:08 +03'00'

3. Παπαεφθymiου Σπυριδων, Καθηγητής, ΜΠΑ, Πολυτεχνείο Κρήτης

**Digitally signed by Spyridon Papaefthymiou**  
Date: 2023.09.22 13:20:18 +03'00'

4. Μπίνας Βασίλης, Επίκουρος Καθηγητής, Τμήμα Χημείας, ΑΠΘ

**VASILEIOS BINAS**  
Digitally signed by VASILEIOS BINAS  
Date: 2023.09.22 14:38:53 +03'00'

5. Ιψάκης Δημήτριος, Επίκουρος Καθηγητής, ΜΠΑ, Πολυτεχνείο Κρήτης

**Dimitrios Ipsakis**  
Digitally signed by Dimitrios Ipsakis  
Date: 2023.09.22 13:23:32 +03'00'

6. Σταθόπουλος Βασίλης, Καθηγητής, Γενικό Τμήμα, ΕΚΠΑ

**Vasileios Stathopoulos**  
Digitally signed by Vasileios Stathopoulos  
Date: 2023.09.22 22:30:45 +03'00'

7. Καλλιθρακας-Κόντος Νικόλαος, Καθηγητής, ΜΗΧΟΠ, Πολυτεχνείο Κρήτης

**Nikolaos Kallithrakas-Kontos**  
Digitally signed by Nikolaos Kallithrakas-Kontos  
Date: 2023.09.26 10:26:23 +03'00'

The implementation of the doctoral thesis was co-financed by Greece and the European Union (European Social Fund-ESF) through the Operational Programme «Human Resources Development, Education and Lifelong Learning» in the context of the Act “Enhancing Human Resources Research Potential by undertaking a Doctoral Research” Sub-action 2: IKY Scholarship Programme for PhD candidates in the Greek Universities.



**Operational Programme  
Human Resources Development,  
Education and Lifelong Learning**  
Co-financed by Greece and the European Union



This research has been co-financed by the European Union and Greek national funds through the Operational Program Competitiveness, Entrepreneurship, and Innovation, under the call RESEARCH-CREATE-INNOVATE (project code: T1EDK-00094). Research project: NANOCO2.



**ΕΡΑνηΕΚ 2014-2020  
OPERATIONAL PROGRAMME  
COMPETITIVENESS  
ENTREPRENEURSHIP  
INNOVATION**



**Co-financed by Greece and the European Union**

This research has been co-financed by the European Union and Greek national funds through the Operational Program Competitiveness, Entrepreneurship and Innovation, under the call RESEARCH-CREATE-INNOVATE (project code: T1EDK-01894). Research project: LIGBIO-GASOFC.



**ΕΡΑνηΕΚ 2014-2020  
OPERATIONAL PROGRAMME  
COMPETITIVENESS  
ENTREPRENEURSHIP  
INNOVATION**



**Co-financed by Greece and the European Union**



The project has received funding from the LIFE Programme of the European Union under GA number LIFE19 ENV/GR/000100

This research was supported by LIFE VISIONS project (LIFE19 ENV/GR/000100) with the contribution of the LIFE Programme of the European Union. This work reflects only the authors' view and CINEA is not responsible for any use that may be made of the information it contains.

During the present thesis, the following laboratories collaborated on the basis of materials synthesis, characterization studies, and catalytic evaluation:

- Industrial, Energy and Environmental Systems Lab (IEESL), School of Production Engineering and Management, Technical University of Crete
- Institute of Electronic Structure and Laser (IESL), Foundation for Research and Technology-Hellas (FORTH)
- Chemical Process & Energy Resources Institute (CPERI), Centre for Research & Technology Hellas (CERTH)
- Department of Mechanical Engineering, University of Western Macedonia
- Laboratory of Chemistry and Materials Technology, General (Core) Department, National and Kapodistrian University of Athens.

In the framework of the two research projects mentioned above (LIGBIO-GASOFC and NANOCO<sub>2</sub>), the following doctoral theses have been conducted:

1. **"Synthesis and Characterization of Ceria-Based Nano-Structured Materials: Structure-Activity Relationships"** by Maria Lykaki.  
Supervisor: Associate Professor Michalis Konsolakis
2. **"Design and Evaluation of Advanced CeO<sub>2</sub>-Based Transition Metal Catalytic Composites for CO<sub>2</sub> Activation by Renewable H<sub>2</sub> toward Chemicals and Fuels"** by Georgios Varvoutis.  
Supervisor: Professor Georgios E. Marnellos

In this point, it should be mentioned that the aforementioned doctoral theses are interrelated and complementary to one another due to the collaborative nature and the scientific objectives of the research projects LIGBIO-GASOFC (project code: T1EDK-01894) and NANOCO<sub>2</sub> (project code: T1EDK-00094). In this regard, some characterization results obtained by Ph.D. Maria Lykaki and some catalytic results obtained by Ph.D. Georgios Varvoutis are cited in various chapters of the present thesis in a well-defined and distinctive manner.

## **Ευχαριστίες**

*Η υλοποίηση της παρούσας διδακτορικής διατριβής θα ήταν αδύνατη χωρίς την έμπρακτη συμβολή και στήριξη ορισμένων ατόμων, τους οποίους θα ήθελα να ευχαριστήσω ολόψυχα.*

*Αρχικά, θα ήθελα να ευχαριστήσω από καρδιάς και να εκφράσω την ευγνωμοσύνη μου στον επιβλέποντα Καθηγητή μου Μιχάλη Κονσολάκη για την αμέριστη συμπαράσταση, καθοδήγηση και εμπιστοσύνη που έδειξε στο πρόσωπο μου όλα αυτά τα χρόνια. Η αδιάκοπη καθοδήγηση του, οι πολύτιμες συμβουλές του και η συνεχής υποστήριξή του κατέστησαν δυνατή την πραγματοποίηση της παρούσας διδακτορικής διατριβής.*

*Επιπλέον, θα ήθελα να ευχαριστήσω ολόθερμα τον Επίκουρο Καθηγητή Βασίλειο Μπίνα για την συνεχή καθοδήγηση, την εμπιστοσύνη, την υπομονή και τη συμπαράσταση καθ' όλη την διάρκεια εκπόνησης της παρούσας διδακτορικής διατριβής, τόσο σε επιστημονικό όσο και σε προσωπικό επίπεδο. Η στήριξή του και η άψογη συνεργασία μας όλα αυτά τα χρόνια υπήρξαν καθοριστικοί παράγοντες για την υλοποίηση της παρούσας διατριβής.*

*Επίσης, θα ήθελα να ευχαριστήσω θερμά τον Καθηγητή Γεώργιο Μαρνέλλο για την επιστημονική καθοδήγηση και τη στήριξή του κατά τη διάρκεια της διδακτορικής διατριβής, καθώς επίσης τον Καθηγητή Σπύρο Παπαευθυμίου για τη συμβολή του στο πλαίσιο της παρούσας διδακτορικής διατριβής. Ευχαριστίες και σε όλα τα μέλη της επταμελούς εξεταστικής επιτροπής για την πρόθυμη συμμετοχή τους στην εξέταση της παρούσας διδακτορικής διατριβής.*

*Σε αυτό το σημείο, θα ήθελα να ευχαριστήσω τους ανθρώπους με τους οποίους συνεργάστηκα στους τομείς του χαρακτηρισμού υλικών και των καταλυτικών δοκιμών. Η συμβολή των ανθρώπων αυτών υπήρξε καθοριστική για την πραγματοποίηση της διδακτορικής αυτής διατριβής. Ευχαριστώ θερμά τον Καθηγητή Βασίλη Σταθόπουλο και τον Κύριο Ερευνητή Δρ. Παύλο Πανδή για την άψογη συνεργασία μας και τη σημαντική τους συμβολή στην υλοποίηση της παρούσας διδακτορικής διατριβής. Επίσης, βαθύτατες ευχαριστίες οφείλω στην Δρ. Μαρία Λυκάκη για την αμέριστη βοήθεια της στον τομέα της σύνθεσης και του χαρακτηρισμού υλικών και την άψογη συνεργασία όλα αυτά τα χρόνια. Επιπλέον, θα ήθελα να ευχαριστήσω τους διδάκτορες Γεώργιο Βαρβούτη και Θανάση Λαμπρόπουλο για την εξαιρετική συνεργασία και την καίρια συμβολή τους στα καταλυτικά πειράματα. Ένα μεγάλο ευχαριστώ στον Δρ. Μαρίνο Δημητρόπουλο για την σημαντική συμβολή του στον χαρακτηρισμό των υλικών αλλά και για τις πολύτιμες συζητήσεις μας.*

*Θερμές ευχαριστίες σε όλα τα μέλη του Εργαστηρίου Διάφανων και Ημιαγωγίμων Υλικών στο ΙΤΕ, Δρ. Εμμανουήλ Γκαγκαουδάκη, Δρ. Ευαγγελία Σκλήρη, Υπ. Δρ. Λείλα Ζουρίδη, Υπ. Δρ. Μιχάλη Χαραλαμπίκη, Υπ. Δρ. Αντωνία Λουφαρδάκη, Μαρία Ζωγραφάκη και Λένα Μάντζιου για τις*

*ουσιαστικές συζητήσεις που είχα μαζί τους στα διάφορα επιστημονικά θέματα της διατριβής όσο και για το φιλικό κλίμα που αναπτύχθηκε όλα αυτά τα χρόνια.*

*Τέλος, θα ήθελα να ευχαριστήσω ολόθερμα και να εκφράσω την ευγνωμοσύνη μου στον σύντροφό μου Γιάννη, τους γονείς μου Χαρίλαο και Δήμητρα, τον αδερφό μου Γιάννη και σε όλους τους φίλους για την ηθική στήριξη, την υπομονή, την αγάπη και την ενθάρρυνση τους καθ' όλη την πορεία της διδακτορικής μου διατριβής.*

*Σοφία Στέφα*

## Short abstract

The rational design and development of highly-active and cost-efficient catalysts for energy and environmental applications constitutes the main research pillar in the area of heterogeneous catalysis. In this perspective, the present thesis aims at the development of noble metal-free nanostructured ceria-based transition metal catalysts with innovative composition and architecture ( $M_xCe_{1-x}O_\delta$ , M: Ti, V, Cr, Mn, Fe, Co, Ni, Cu, Zn), which are characterized by low cost and optimal activity/stability. More specifically, the surface chemistry of the as-prepared catalysts and their catalytic activity was attempted to be fine-tuned through the advanced synthetic methods, the surface and/or structural promotion and the modification of metal-support interactions using promoting/reducing agents.

In the framework of the present thesis, the effect of the preparation method (hydrothermal, precipitation, and the Stöber method) of  $CeO_2/TiO_2$  mixed oxides on their physicochemical properties and CO oxidation performance was initially investigated. The catalyst prepared using the Stöber method exhibited optimal catalytic activity, which can be attributed to its enhanced reducing capability. Additionally, the effect of different Zn/Ce ratios on their physicochemical properties and CO oxidation performance of  $CeO_2/ZnO$  mixed oxides was examined. Using the hydrothermal method, a series of bare  $CeO_2$  and ZnO oxides, as well as  $CeO_2/ZnO$  mixed oxides with varying Zn/Ce atomic ratios (0.2, 0.4, 0.6), were prepared. The catalytic results demonstrate the improved performance of the mixed oxides compared to the bare catalysts, revealing synergistic interactions between  $CeO_2$  and ZnO.

In addition, the effect of the active phase nature on the physicochemical properties and catalytic activity for the  $CO_2$  hydrogenation reaction in ceria nanorods-based transition metal catalysts,  $M/CeO_2$  (M: Ti, V, Cr, Mn, Fe, Co, Ni, Cu) was explored. It was found that the  $CO_2$  conversion follows the order:  $Ni/CeO_2 > Co/CeO_2 > Cu/CeO_2 > Fe/CeO_2 > CeO_2 > Cr/CeO_2 > Mn/CeO_2 > Ti/CeO_2 > V/CeO_2$ . Based on the selectivity results, it was observed that bare ceria,  $Cu/CeO_2$ ,  $Fe/CeO_2$ ,  $Cr/CeO_2$ ,  $Mn/CeO_2$ ,  $Ti/CeO_2$ , and  $V/CeO_2$ , are selective towards CO production, while  $Co/CeO_2$  and  $Ni/CeO_2$  catalysts are particularly selective towards methane ( $CH_4$ ). Specifically, the combination of nickel with ceria significantly favors the  $CO_2$  methanation reaction.

Then, the role of Ni particle size in the  $CO_2$  hydrogenation reaction of  $Ni/CeO_2$ -nanorods catalysts was investigated. Specifically, catalysts were prepared with a Ni/Ce atomic ratio that varied between 0.10 and 1.50 and it was found that the increase of Ni loading had a significantly positive effect on the catalytic behavior with the best behavior being attributed to the sample with an atomic ratio of Ni/Ce=1.00, corresponding to an optimal Ni particle size  $\sim 20$  nm. Notably, all samples showed high  $CO_2$  methanation activity at temperatures lower than 300 °C and negligible CO production.

Furthermore, the phenomenon of promotion using ZnO was investigated by preparing CeO<sub>2</sub>/ZnO mixed oxides as supporting carries of Ni active phase. In contrast to the catalytic activity of Ni/CeO<sub>2</sub>, Ni/ZnO and Ni/CeO<sub>2</sub>-ZnO catalysts are selective towards CO production, suppressing the CO<sub>2</sub> methanation to a large extent, revealing the role of ZnO promoter in determining the reaction mechanism.

Aiming to develop a low-cost metal-free material that can be used either as a catalyst or as an active phase support, in the second part of the present thesis, graphitic carbon nitride (g-C<sub>3</sub>N<sub>4</sub>) was prepared and evaluated for the photocatalytic degradation of gases and liquids pollutants. Specifically, a comparative study was conducted on the physicochemical properties and adsorption capacity of bulk g-C<sub>3</sub>N<sub>4</sub> and g-C<sub>3</sub>N<sub>4</sub> nanosheets. The results revealed significantly improved physicochemical characteristics for the nanosheets, as well as enhanced adsorption capacity compared to the bulk structure of g-C<sub>3</sub>N<sub>4</sub>. Furthermore, both bulk g-C<sub>3</sub>N<sub>4</sub> and g-C<sub>3</sub>N<sub>4</sub> nanosheets were evaluated for their photocatalytic degradation of gaseous and liquid pollutants, and the g-C<sub>3</sub>N<sub>4</sub> nanosheets exhibited exceptional photocatalytic performance.

Collectively, the present thesis has unequivocally highlighted the important role of the preparation method and surface modification on the physicochemical properties, metal-support interactions and in turn, on the catalytic performance of as-prepared catalysts. More importantly, the fine-tuning of size, shape and electronic state can notably affect not only the reactivity of metal sites but also the interfacial activity offering a synergistic contribution towards the development of highly active composites. Through the proposed optimization approach extremely active and cost-efficient catalytic materials were obtained for CO oxidation, CO<sub>2</sub> hydrogenation and the photocatalytic degradation of gases and liquids pollutants, being among the most active reported so far in open literature.

## Σύντομη περίληψη

Ο ορθολογικός σχεδιασμός και η ανάπτυξη αποτελεσματικών και συνάμα οικονομικών καταλυτικών συστημάτων για ενεργειακές και περιβαλλοντικές εφαρμογές αποτελεί τον κύριο ερευνητικό πυλώνα στον τομέα της ετερογενούς κατάλυσης. Προς αυτή την κατεύθυνση, αντικείμενο μελέτης της παρούσας διδακτορικής διατριβής αποτελεί η σύνθεση καινοτόμων σε σύσταση και αρχιτεκτονική νανο-δομημένων καταλυτικών συστημάτων μικτών οξειδίων μετάλλων μετάπτωσης ( $M_xCe_{1-x}O_\delta$ , M: Ti, V, Cr, Mn, Fe, Co, Ni, Cu, Zn), απαλλαγμένων ευγενών μετάλλων, τα οποία χαρακτηρίζονται από χαμηλό κόστος και βέλτιστη δραστικότητα/σταθερότητα. Ιδιαίτερη σημασία επιδόθηκε στον ορθολογικό σχεδιασμό και στην ενίσχυση της δραστικότητας των προς ανάπτυξη υλικών μέσω της βέλτιστης τροποποίησης (fine-tuning) των χαρακτηριστικών δομής/μορφολογίας και χημικής κατάστασης. Αναλυτικότερα, η επιφανειακή χημεία των μικτών οξειδίων που θα αναπτυχθούν και κατ' επέκταση η καταλυτική τους συμπεριφορά επιχειρείται να ενισχυθεί/τροποποιηθεί κατάλληλα δια μέσου της εφαρμογής προηγμένων μεθόδων σύνθεσης, του φαινομένου της προώθησης και της τροποποίησης των αλληλεπιδράσεων μετάλλου-φορέα διαμέσου της χρήσης προωθητικών-αναγωγικών μέσων.

Επί τη βάση των ανωτέρω, στο πλαίσιο της παρούσας διδακτορικής διατριβής, μελετήθηκε αρχικά η επίδραση της μεθόδου παρασκευής (υδροθερμική μέθοδος ενός και δύο σταδίων, η καταβύθιση και η μέθοδος Stöber) των μικτών οξειδίων  $CeO_2/TiO_2$  στα φυσικοχημικά χαρακτηριστικά και στην καταλυτική δραστικότητα τους, επί την επιτέλεση της αντίδρασης οξείδωσης του CO. Ο καταλύτης που παρασκευάστηκε με τη μέθοδο Stöber παρουσίασε τη βέλτιστη καταλυτική δραστικότητα η οποία μπορεί να αποδοθεί στη βελτιωμένη αναγωγική ικανότητα του. Επιπλέον, διερευνήθηκε η επίδραση του διαφορετικού ποσοστού ZnO στις φυσικοχημικές ιδιότητες και στην καταλυτική απόδοση της οξείδωσης του CO των μικτών οξειδίων  $CeO_2/ZnO$ . Χρησιμοποιώντας την υδροθερμική μέθοδο, παρασκευάστηκε μια σειρά από καθαρά οξείδια  $CeO_2$  και ZnO, καθώς και μικτά οξείδια  $CeO_2/ZnO$  με διαφορετικές ατομικές αναλογίες Zn/Ce (0,2, 0,4, 0,6). Τα καταλυτικά αποτελέσματα δείχνουν βελτιωμένη απόδοση των μικτών οξειδίων σε σύγκριση με τα καθαρά υποστρώματα, αποκαλύπτοντας στις συνεργιστικές αλληλεπιδράσεις μεταξύ  $CeO_2$  και ZnO.

Στη συνέχεια, μελετήθηκε η επίδραση της φύσης της ενεργούς φάσης στις φυσικοχημικές ιδιότητες και στην καταλυτική συμπεριφορά, ως προς την αντίδραση υδρογόνωσης του  $CO_2$ , σε καταλύτες μετάλλων μετάπτωσης υποστηριγμένους σε νανοράβδους δημητριάς,  $M/CeO_2$  (M: Ti, V, Cr, Mn, Fe, Co, Ni, Cu). Βρέθηκε ότι η μετατροπή του  $CO_2$  ακολουθεί την εξής σειρά:  $Ni/CeO_2 > Co/CeO_2 > Cu/CeO_2 > Fe/CeO_2 > CeO_2 > Cr/CeO_2 > Mn/CeO_2 > Ti/CeO_2 > V/CeO_2$ . Επί τη βάση των αποτελεσμάτων εκλεκτικότητας, διαπιστώθηκε ότι οι καταλύτες καθαρής δημητριάς,  $Cu/CeO_2$ ,

Fe/CeO<sub>2</sub>, Cr/CeO<sub>2</sub>, Mn/CeO<sub>2</sub>, Ti/CeO<sub>2</sub> και V/CeO<sub>2</sub> είναι εκλεκτικοί ως προς την παραγωγή CO, ενώ οι καταλύτες Co/CeO<sub>2</sub> και Ni/CeO<sub>2</sub> είναι ιδιαίτερα εκλεκτικοί ως προς το μεθάνιο (CH<sub>4</sub>).

Έπειτα, δόθηκε έμφαση στο ρόλο του μεγέθους των σωματιδίων Ni στην αντίδραση υδρογόνωσης CO<sub>2</sub> των καταλυτών Ni/CeO<sub>2</sub>-nanorods. Συγκεκριμένα, παρασκευάστηκαν καταλύτες με ατομικό λόγο Ni/Ce που μεταβλήθηκε μεταξύ 0.10 και 1.50 και διαπιστώθηκε ότι η αύξηση του ποσοστού Ni είχε σημαντικά θετική επίδραση στην καταλυτική συμπεριφορά με τη βέλτιστη συμπεριφορά να αποδίδεται στο δείγμα με ατομικό λόγο Ni/Ce=1.00, ενώ το βέλτιστο μέγεθος σωματιδίων Ni για την επίτευξη της μέγιστης εγγενούς δραστηριότητας είναι ~ 20 nm. Σε κάθε περίπτωση, όλα τα δείγματα εμφάνισαν υψηλή ενεργότητα ως προς τη μεθανίωση του CO<sub>2</sub> σε θερμοκρασίες χαμηλότερες των 320 °C και πρακτικά μηδενική παραγωγή CO. Επιπλέον, διερευνήθηκε το φαινόμενο της προώθησης με χρήση ZnO με την παρασκευή μικτών οξειδίων CeO<sub>2</sub>/ZnO ως φορείς της ενεργής φάσης Ni. Σε αντίθεση με την καταλυτική δράση του Ni/CeO<sub>2</sub>, οι καταλύτες Ni/ZnO και Ni/CeO<sub>2</sub>-ZnO είναι εκλεκτικοί ως προς την παραγωγή CO, καταστέλλοντας σε μεγάλο βαθμό τη μεθανίωση του CO<sub>2</sub>, αποκαλύπτοντας το ρόλο του προωθητή ZnO ως προς τον καθορισμό του μηχανισμού της αντίδρασης.

Στοχεύοντας στην ανάπτυξη ενός χαμηλού κόστους υλικού, απαλλαγμένο από μέταλλα, το οποίο μπορεί να χρησιμοποιηθεί είτε ως καταλύτης είτε ως υποστηρικτής της ενεργού φάσης, παρασκευάστηκε το γραφιτικό νιτρίδιο του άνθρακα (g-C<sub>3</sub>N<sub>4</sub>) και αξιολογήθηκε ως προς την επιτέλεση της αντίδρασης της φωτοκαταλυτικής διάσπασης αέριων και υγρών ρύπων. Ειδικότερα, σε πρώτη φάση πραγματοποιήθηκε μια συγκριτική μελέτη ως προς τις φυσικοχημικές ιδιότητες και την ικανότητα προσρόφησης της bulk δομής g-C<sub>3</sub>N<sub>4</sub> και των νανο-φύλλων g-C<sub>3</sub>N<sub>4</sub>. Τα αποτελέσματα αποκάλυψαν εξαιρετικά βελτιωμένα φυσικοχημικά χαρακτηριστικά για τα νανο-φύλλα αλλά και βελτιωμένη προσροφητική ικανότητα σε σύγκριση με την bulk δομή g-C<sub>3</sub>N<sub>4</sub>. Επιπροσθέτως, οι δυο αυτές δομές g-C<sub>3</sub>N<sub>4</sub> αξιολογήθηκαν ως προς τη φωτοκαταλυτική διάσπαση αέριων και υγρών ρύπων, και τα νανο-φύλλα g-C<sub>3</sub>N<sub>4</sub> επέδειξαν εξαιρετική φωτοκαταλυτική απόδοση.

Συνοψίζοντας, η παρούσα διδακτορική διατριβή ανέδειξε αδιαμφισβήτητα το σημαντικό ρόλο της διαδικασίας παρασκευής του φορέα και της επιφανειακής ενίσχυσης στις φυσικοχημικές ιδιότητες, στις αλληλεπιδράσεις μετάλλου-φορέα και κατ' επέκταση στην καταλυτική απόδοση. Ειδικότερα, η κατάλληλη τροποποίηση του μεγέθους, του σχήματος και της ηλεκτρονιακής κατάστασης βρέθηκε να επηρεάζει σε σημαντικό βαθμό τόσο τη δραστηριότητα των μεταλλικών κέντρων όσο και τη διεπιφανειακή ενεργότητα συνεισφέροντας συνεργιστικά προς την ανάπτυξη ιδιαίτερα ενεργών υλικών. Η προτεινόμενη προσέγγιση βελτιστοποίησης οδήγησε σε εξαιρετικά ενεργά καταλυτικά υλικά χαμηλού κόστους για τις αντιδράσεις οξειδωσης του CO, υδρογόνωσης του CO<sub>2</sub> και

φωτοκαταλυτικής διάσπασης αέριων και υγρών ρύπων κατατάσσοντάς τα μεταξύ των πιο ενεργών υλικών αναφορικά με τη βιβλιογραφία.

## Extended Synopsis & Structure Thesis

Cerium dioxide ( $\text{CeO}_2$ ) or ceria has been studied in a variety of catalytic applications, either as a catalyst itself or as a support material, due to its unique properties such as high thermal stability, oxygen storage capacity (OSC), and oxygen mobility. Ceria exhibits two oxidation states ( $\text{Ce}^{3+}/\text{Ce}^{4+}$ ), and a facile shift between these two states, followed by the generation of surface/structural defects, e.g., oxygen vacancies, is responsible for its improved redox behavior.

The development of ceria-based materials at the nanoscale level is considered of particular importance, as the reduction in particle size leads to distinct physicochemical properties due to the electron interactions that occur between the nanoscale particles. In addition to size, recent studies have highlighted the significant influence of material morphology on physicochemical characteristics and activity. Furthermore, the incorporation of various transition metals into the ceria carrier can significantly induce modifications in the physicochemical properties through geometric and/or electronic interactions between the metal dopant and the support, with a significant impact on catalysis. Among these modifications, the following are mainly included:

- the formation of surface defects and oxygen vacancies,
- the creation of interfacial sites of high activity (interfacial reactivity),
- high reducibility,
- the electronic interactions between the interfacial sites.

The above-mentioned alterations resulting from the strong metal-support interactions are referred to as "synergy". However, the underlying causes of this phenomenon remain unclear due to the intricate nature of these interactions (geometrical and/or electronic type). The investigation of structure-activity relationships and the fundamental understanding of the phenomenon of "synergy" are crucial research areas in the field of catalysis.

In summary, the objective of the present thesis is the development of innovative composition and architecture of noble metal-free nanostructured ceria-based transition metal catalysts ( $\text{M}_x\text{Ce}_{1-x}\text{O}_\delta$ , M: Ti, V, Cr, Mn, Fe, Co, Ni, Cu), appropriately modified by aliovalent dopants (e.g.,  $\text{TiO}_2$ , ZnO, g- $\text{C}_3\text{N}_4$ ), which are characterized by low cost.

More specifically, the surface chemistry of the as-prepared catalysts and their catalytic activity was attempted to be enhanced (fine-tuning) appropriately through:

(a) the advanced synthetic methods (hydrothermal, precipitation, wet impregnation, Stöber) towards the development of nanomaterials with predefined morphology

(b) the appropriate adjustment of the catalysts' inherent properties through surface and/or structural promotion.

(c) the modification of metal-support interactions through the use of promoting/reducing agents (e.g. graphitic carbon nitride (g-C<sub>3</sub>N<sub>4</sub>)).

The impact of the aforementioned synthesis/modification parameters on the physicochemical characteristics of the as-synthesized materials was assessed using advanced techniques for texture and microstructure characterization, such as N<sub>2</sub> adsorption at -196 °C (BET method), temperature programmed (TPD/TPR), scanning/transmission electron microscopy (SEM/TEM), X-ray diffraction (XRD), Raman spectroscopy, UV-visible spectroscopy (UV-Vis), Infrared spectroscopy (IR), TGA thermogravimetric analysis, X-ray Photoelectron Spectroscopy (XPS), etc. Furthermore, the catalytic performance of the materials was examined for various applications such as CO oxidation, CO<sub>2</sub> hydrogenation for producing value-added products, and liquid- and gas-phase photocatalysis.

In light of the above aspects, the structure of this thesis is as follows:

- ❖ **Chapter 1** introduces the field of rational design and development of ceria-based catalysts, delving into the influence of preparation method, size, and shape on catalytic activity. Specifically, it includes a literature review of the effects of these factors on various energy and environmental catalytic applications such as CO oxidation, CO<sub>2</sub> hydrogenation to value-added products, and photocatalysis. Additionally, this chapter describes the impact of incorporating transition metal heteroatoms into the ceria lattice and the utilization of promoting/reducing agents (e.g., graphitic carbon nitride (g-C<sub>3</sub>N<sub>4</sub>)) on catalytic performance.
- ❖ **Chapter 2** provides a detailed description of the experimental part of this thesis, examining the material synthesis methods, characterization techniques, and catalytic reactions employed.
- ❖ **Chapter 3** presents the synthesis, characterization, and catalytic evaluation of CeO<sub>2</sub>/TiO<sub>2</sub> and CeO<sub>2</sub>/ZnO mixed oxides for the CO oxidation reaction. Specifically, the influence of the synthesis method of CeO<sub>2</sub>/TiO<sub>2</sub> mixed oxides on their physicochemical properties and catalytic activity was investigated. Four different synthesis methods were employed: hydrothermal one-step and two-step methods, precipitation, and the Stöber method. Among these, the catalyst prepared using the Stöber method exhibited optimal catalytic activity, which can be attributed to its enhanced reducing capability.

Additionally, CeO<sub>2</sub>/ZnO mixed oxides were synthesized, and the effect of different Zn/Ce ratios on their physicochemical properties and catalytic activity was investigated. Using the hydrothermal method, a series of bare CeO<sub>2</sub> and ZnO oxides, as well as CeO<sub>2</sub>/ZnO mixed oxides with varying Zn/Ce atomic ratios (0.2, 0.4, 0.6), were prepared. The catalytic results demonstrate the improved performance of the mixed oxides compared to the bare catalysts, revealing synergistic interactions between CeO<sub>2</sub> and ZnO.

The results of this chapter were published in the following scientific journals:

- ✓ **Sofia Stefa**, Maria Lykaki, Dimitrios Fragkoulis, Vasileios Binas, Vassilis N. Stathopoulos, and Michalis Konsolakis, "Effect of the Preparation Method on the Physicochemical Properties and the CO Oxidation Performance of Nanostructured CeO<sub>2</sub>/TiO<sub>2</sub> Oxides", *Processes* 8 (2020) 847. doi: 10.3390/pr8070847
- ✓ **Sofia Stefa**, Maria Lykaki, Vasillios Binas, Pavlos K. Pandis, Vassilis N. Stathopoulos and Michalis Konsolakis, "Hydrothermal Synthesis of ZnO–Doped Ceria Nanorods: Effect of ZnO Content on the Redox Properties and the CO Oxidation Performance", *Applied Sciences* 10 (2020) 7605. doi: 10.3390/app10217605

❖ **Chapter 4** presents the effect of the active phase nature on the physicochemical properties and catalytic activity for the CO<sub>2</sub> hydrogenation reaction in ceria-based transition metal catalysts, M/CeO<sub>2</sub> (M: Ti, V, Cr, Mn, Fe, Co, Ni, Cu). It was found that the CO<sub>2</sub> conversion follows the order: Ni/CeO<sub>2</sub> > Co/CeO<sub>2</sub> > Cu/CeO<sub>2</sub> > Fe/CeO<sub>2</sub> > CeO<sub>2</sub> > Cr/CeO<sub>2</sub> > Mn/CeO<sub>2</sub> > Ti/CeO<sub>2</sub> > V/CeO<sub>2</sub>. Based on the selectivity results, it was observed that bare ceria, Cu/CeO<sub>2</sub>, Fe/CeO<sub>2</sub>, Cr/CeO<sub>2</sub>, Mn/CeO<sub>2</sub>, Ti/CeO<sub>2</sub>, and V/CeO<sub>2</sub>, are selective towards CO production, while Co/CeO<sub>2</sub> and Ni/CeO<sub>2</sub> catalysts are particularly selective towards methane (CH<sub>4</sub>). Specifically, the combination of nickel with ceria significantly favors the CO<sub>2</sub> methanation reaction.

**Chapter 4** emphasizes the role of Ni particle size on the CO<sub>2</sub> hydrogenation performance of Ni/CeO<sub>2</sub>-nanorods catalysts. Furthermore, in **Chapter 4**, the phenomenon of promotion using ZnO was investigated by preparing CeO<sub>2</sub>/ZnO mixed oxides as supporting carries of Ni active phase. In contrast to the catalytic activity of Ni/CeO<sub>2</sub>, Ni/ZnO and Ni/CeO<sub>2</sub>-ZnO catalysts are selective towards CO production, suppressing the CO<sub>2</sub> methanation to a large extent, revealing the role of ZnO promoter in determining the reaction mechanism.

The results of this chapter were published in the following scientific journals:

- ✓ Michalis Konsolakis, Maria Lykaki, **Sofia Stefa**, Sónia A. C. Carabineiro, Georgios Varvoutis, Eleni Papista and Georgios E. Marnellos, "CO<sub>2</sub> Hydrogenation over Nanoceria-Supported Transition Metal Catalysts: Role of Ceria Morphology (Nanorods versus Nanocubes) and Active Phase Nature (Co versus Cu) ", *Nanomaterials* 9 (2019) 1739. doi: 10.3390/nano9121739
- ✓ Georgios Varvoutis, Maria Lykaki, **Sofia Stefa**, Eleni Papista, Sónia A.C. Carabineiro, Georgios E. Marnellos, and Michalis Konsolakis, "Remarkable efficiency of Ni supported on hydrothermally synthesized CeO<sub>2</sub> nanorods for low-temperature CO<sub>2</sub> hydrogenation to methane", *Catalysis Communications* 142 (2020) 106036. doi: 10.1016/j.catcom.2020.106036

- ✓ Georgios Varvoutis, Maria Lykaki, **Sofia Stefa**, Vassilios Binas, George E. Marnellos, and Michalis Konsolakis, "Deciphering the role of Ni particle size and nickel-ceria interfacial perimeter in the low-temperature CO<sub>2</sub> methanation reaction over remarkably active Ni/CeO<sub>2</sub> nanorods", *Applied Catalysis B: Environmental* 297 (2021) 120401. doi: 10.1016/j.apcatb.2021.120401
- ✓ Georgios Varvoutis, Stamatia A. Karakoulia, Maria Lykaki, **Sofia Stefa**, Vassilios Binas, George E. Marnellos, and Michalis Konsolakis, "Support-induced modifications on the CO<sub>2</sub> hydrogenation performance of Ni/CeO<sub>2</sub>: The effect of ZnO doping on CeO<sub>2</sub> nanorods", *Journal of CO<sub>2</sub> Utilization* 61 (2022) 102057. doi: 10.1016/j.jcou.2022.102057
- ❖ **Chapter 5** describes the synthesis, characterization, and catalytic activity of graphitic carbon nitride (g-C<sub>3</sub>N<sub>4</sub>) in liquid- and gas-phase photocatalysis. Specifically, a comparative study was conducted on the physicochemical properties and adsorption capacity of bulk g-C<sub>3</sub>N<sub>4</sub> and g-C<sub>3</sub>N<sub>4</sub> nanosheets. The results revealed significantly improved physicochemical characteristics for the nanosheets, as well as enhanced adsorption capacity compared to the bulk structure of g-C<sub>3</sub>N<sub>4</sub>. Furthermore, both bulk g-C<sub>3</sub>N<sub>4</sub> and g-C<sub>3</sub>N<sub>4</sub> nanosheets were evaluated for their photocatalytic degradation of gaseous and liquid pollutants, and the g-C<sub>3</sub>N<sub>4</sub> nanosheets exhibited exceptional photocatalytic performance.  
The results of this chapter were published in the following scientific journals:
  - ✓ **Sofia Stefa**, Maria Grinieziaki, Marinos Dimitropoulos, George Paterakis, Costas Galiotis, George Kiriakidis, Emmanuel Klontzas, Michalis Konsolakis, and Vassilios Binas, "Highly Porous Thin-Layer g-C<sub>3</sub>N<sub>4</sub> Nanosheets with Enhanced Adsorption Capacity", *ACS Applied Nano Materials* 6 (2023) 1732-1743. doi: 10.1021/acsnm.2c04632
  - ✓ **Sofia Stefa**, Maria Zografaki, Marinos Dimitropoulos, George Paterakis, Costas Galiotis, Palanivelu Sangeetha, George Kiriakidis, Michalis Konsolakis, and Vassilios Binas, "High surface area g-C<sub>3</sub>N<sub>4</sub> Nanosheets as superior Solar-Light Photocatalyst for the Degradation of Parabens", *Applied Physics A*, (2023) (accepted).
  - ✓ **Sofia Stefa**, Evangelia Skliri, Emmanouil Gagaoudakis, George Kiriakidis, Michalis Konsolakis, and Vassilios Binas, "Visible light photocatalytic oxidation of NO using g-C<sub>3</sub>N<sub>4</sub> nanosheets: Stability, kinetics, and effect of humidity", (2023) (submitted).
- ❖ **Chapter 6** provides a summary of the conclusions drawn from this thesis, while also presenting suggestions for future research regarding the rational design and development of highly active/selective catalytic systems for energy and environmental applications.

## Εκτεταμένη Σύνοψη & Δομή Εργασίας

Το οξείδιο του δημητρίου ( $\text{CeO}_2$ ) ή δημητρία έχει μελετηθεί σε πληθώρα καταλυτικών διεργασιών είτε ως καταλύτης αυτός καθαυτός είτε ως φορέας λόγω των μοναδικών του ιδιοτήτων, όπως η υψηλή θερμική σταθερότητα, η μεγάλη ικανότητα αποθήκευσης οξυγόνου (oxygen storage capacity, OSC) και κινητικότητα οξυγόνου. Το δημήτριο παρουσιάζει δύο οξειδωτικές καταστάσεις ( $\text{Ce}^{3+}/\text{Ce}^{4+}$ ) και η ευκολία εναλλαγής του μεταξύ αυτών των δύο οξειδωτικών καταστάσεων συνοδευόμενη από τη δημιουργία επιφανειακών ατελειών, όπως οι κενές θέσεις οξυγόνου (oxygen vacancies), θεωρούνται υπεύθυνες για τις βελτιωμένες οξειδοαναγωγικές του ιδιότητες.

Ιδιαίτερης σημασίας κρίνεται η ανάπτυξη υλικών με βάση το  $\text{CeO}_2$  σε επίπεδο νανο-κλίμακας, καθώς η μείωση του μεγέθους των σωματιδίων οδηγεί σε ξεχωριστές φυσικοχημικές ιδιότητες λόγω των ηλεκτρονιακών αλληλεπιδράσεων που αναπτύσσονται μεταξύ των νανο-σωματιδίων. Πέρα από τη σημασία του μεγέθους, πρόσφατες μελέτες έχουν αναδείξει τη σημαντική επίδραση της μορφολογίας των υλικών στα φυσικοχημικά χαρακτηριστικά και στη δραστηριότητα. Επιπλέον, η ενσωμάτωση έτερο-ατόμων μετάλλων μετάπτωσης στο πλέγμα του  $\text{CeO}_2$  επιφέρει σημαντικές φυσικοχημικές διαταραχές, μέσω γεωμετρικού ή/και ηλεκτρονιακού τύπου αλληλεπιδράσεις μετάλλου-φορέα, με σημαντικό αντίκτυπο στην κατάλυση. Ανάμεσα σε αυτές τις διαταραχές συμπεριλαμβάνονται κυρίως:

- η δημιουργία επιφανειακών ατελειών και κενών θέσεων οξυγόνου (oxygen vacancies),
- η δημιουργία διεπιφανειακών κέντρων υψηλής δραστηριότητας (interfacial reactivity),
- η υψηλή ικανότητα αναγωγής (reducibility),
- οι ηλεκτρονιακές αλληλεπιδράσεις μεταξύ των διεπιφανειακών κέντρων.

Οι προαναφερθείσες διαταραχές που δημιουργούνται από τις ισχυρές αλληλεπιδράσεις μετάλλου-φορέα, υπάγονται στο γενικό όρο "συνέργεια", χωρίς όμως να έχουν αποσαφηνιστεί τα βαθύτερα αίτια του φαινομένου λόγω της πολυπλοκότητας των αλληλεπιδράσεων (γεωμετρικού ή/και ηλεκτρονιακού τύπου). Η διερεύνηση των σχέσεων δομής-δραστηριότητας και η θεμελιώδης κατανόηση του φαινομένου της "συνέργειας" αποτελεί έναν από τους σημαντικότερους τομείς έρευνας στην κατάλυση.

Συνοψίζοντας, αντικείμενο μελέτης της παρούσας διδακτορικής διατριβής αποτελεί η σύνθεση καινοτόμων σε σύσταση και αρχιτεκτονική νανο-δομημένων καταλυτικών συστημάτων μικτών οξειδίων μετάλλων μετάπτωσης ( $\text{M}_x\text{Ce}_{1-x}\text{O}_8$ , M: Ti, V, Cr, Mn, Fe, Co, Ni, Cu), απαλλαγμένων ευγενών μετάλλων, τα οποία θα χαρακτηρίζονται από χαμηλό κόστος και υψηλή δραστηριότητα.

Αναλυτικότερα, η επιφανειακή χημεία των προς ανάπτυξη καταλυτών και κατ' επέκταση η καταλυτική τους συμπεριφορά επιχειρήθηκε να ενισχυθεί/τροποποιηθεί δια μέσου:

- (α) της εφαρμογής προηγμένων μεθόδων σύνθεσης (υδροθερμική, καταβύθιση, υγρός εμποτισμός) οι οποίες θα δύνανται να οδηγήσουν σε νανοϋλικά προκαθορισμένης μορφολογίας,
- (β) του φαινομένου της προώθησης μέσω της χρήσης επιφανειακών/δομικών ενισχυτών,
- (γ) της τροποποίησης των αλληλεπιδράσεων μετάλλου-φορέα διαμέσου της χρήσης προωθητικών-αναγωγικών μέσων (π.χ. graphitic carbon nitride (g-C<sub>3</sub>N<sub>4</sub>)).

Η επίδραση των ανωτέρω παραμέτρων σύνθεσης/τροποποίησης στα φυσικοχημικά χαρακτηριστικά των προς ανάπτυξη υλικών αποτιμήθηκε διαμέσου προηγμένων τεχνικών χαρακτηρισμού υφής και μικροδομής, οι οποίες περιλαμβάνουν μεταξύ άλλων τη φυσική ρόφηση BET, την θερμοπρογραμματιζόμενη εκρόφηση/αναγωγή (TPD/TPR), την ηλεκτρονική μικροσκοπία σάρωσης/διέλευσης (SEM/TEM), περίθλασης ακτίνων X (XRD), τη φασματοσκοπία Raman, την φασματοσκοπία ορατού-υπερύθρου (UV-Vis), την υπέρυθη φασματοσκοπία (IR), τη θερμοσταθμική ανάλυση TGA, κτλ. Επιπλέον, η καταλυτική συμπεριφορά των υλικών μελετήθηκε κατά την επιτέλεση της αντίδρασης οξείδωση του CO, της υδρογόνωσης του CO<sub>2</sub> καθώς και της φωτοκαταλυτικής διάσπασης αέριων και υγρών ρύπων, προκειμένου να ληφθεί γνώση επί των σχέσεων δομής-δραστικότητας (structure-activity relationships).

Επί τη βάση των παραπάνω, η διάρθρωση της παρούσας διδακτορικής διατριβής έχει ως κάτωθι:

- ❖ Το **Κεφάλαιο 1** αποτελεί μια εισαγωγή στο πεδίο του ορθολογικού σχεδιασμού και της ανάπτυξης καταλυτών βασισμένων στη δημητρία, εμβαθύνοντας στην επίδραση της μεθόδου παρασκευής, του μεγέθους και του σχήματος στην καταλυτική συμπεριφορά. Ειδικότερα, πραγματοποιείται βιβλιογραφική ανασκόπηση των επιδράσεων των προαναφερθέντων παραγόντων σε διάφορες ενεργειακές και περιβαλλοντικές καταλυτικές εφαρμογές, όπως η οξείδωση του μονοξειδίου του άνθρακα (CO), η υδρογόνωση του διοξειδίου του άνθρακα (CO<sub>2</sub>) προς προϊόντα υψηλής προστιθέμενης αξίας, και η φωτοκατάλυση. Επιπροσθέτως, στο συγκεκριμένο κεφάλαιο αναλύεται η επίδραση της ενσωμάτωσης έτερο-ατόμων μετάλλων μετάπτωσης στο πλέγμα της δημητρίας και της χρήσης προωθητικών-αναγωγικών μέσων (π.χ. graphitic carbon nitride (g-C<sub>3</sub>N<sub>4</sub>)) στην καταλυτική συμπεριφορά.
- ❖ Το **Κεφάλαιο 2** περιγράφει αναλυτικά το πειραματικό μέρος της εργασίας, αναλύοντας τις μεθόδους παρασκευής των υλικών, τις τεχνικές χαρακτηρισμού καθώς και τις καταλυτικές αντιδράσεις που μελετήθηκαν.
- ❖ Το **Κεφάλαιο 3** παρουσιάζει τη σύνθεση, το χαρακτηρισμό και την καταλυτική αξιολόγηση μικτών οξειδίων CeO<sub>2</sub>/TiO<sub>2</sub> και CeO<sub>2</sub>/ZnO ως προς την επιτέλεση της αντίδρασης της οξείδωσης του CO. Αναλυτικότερα, διερευνήθηκε η επίδραση της μεθόδου παρασκευής των μικτών οξειδίων CeO<sub>2</sub>/TiO<sub>2</sub> στα φυσικοχημικά χαρακτηριστικά και στην καταλυτική

δραστικότητα τους. Τέσσερις διαφορετικές μέθοδοι παρασκευής χρησιμοποιήθηκαν για τη σύνθεση  $\text{CeO}_2/\text{TiO}_2$ : υδροθερμική μέθοδος ενός και δύο σταδίων, η καταβύθιση και η μέθοδος Stöber. Μεταξύ αυτών, ο καταλύτης που παρασκευάστηκε με τη μέθοδο Stöber παρουσίασε τη βέλτιστη καταλυτική δραστηριότητα η οποία μπορεί να αποδοθεί στη βελτιωμένη αναγωγική ικανότητα του.

Επιπλέον, παρασκευάστηκαν μικτά οξειδία  $\text{CeO}_2/\text{ZnO}$  και διερευνήθηκε η επίδραση του διαφορετικού ποσοστού  $\text{ZnO}$  στις φυσικοχημικές ιδιότητες και στην καταλυτική δραστηριότητα τους. Χρησιμοποιώντας την υδροθερμική μέθοδο, παρασκευάστηκε μια σειρά από καθαρά οξειδία  $\text{CeO}_2$  και  $\text{ZnO}$ , καθώς και μικτά οξειδία  $\text{CeO}_2/\text{ZnO}$  με διαφορετικές ατομικές αναλογίες  $\text{Zn/Ce}$  (0.2, 0.4, 0.6). Τα καταλυτικά αποτελέσματα δείχνουν βελτιωμένη απόδοση των μικτών οξειδίων σε σύγκριση με τα καθαρά υποστρώματα, αποκαλύπτοντας στις συνεργιστικές αλληλεπιδράσεις μεταξύ  $\text{CeO}_2$  και  $\text{ZnO}$ .

Τα αποτελέσματα του κεφαλαίου αυτού δημοσιεύτηκαν στα ακόλουθα επιστημονικά περιοδικά:

- ✓ **Sofia Stefa**, Maria Lykaki, Dimitrios Fragkoulis, Vasileios Binas, Vassilis N. Stathopoulos, and Michalis Konsolakis, "Effect of the Preparation Method on the Physicochemical Properties and the CO Oxidation Performance of Nanostructured  $\text{CeO}_2/\text{TiO}_2$  Oxides", *Processes* 8 (2020) 847. doi: 10.3390/pr8070847
- ✓ **Sofia Stefa**, Maria Lykaki, Vasillios Binas, Pavlos K. Pandis, Vassilis N. Stathopoulos and Michalis Konsolakis, "Hydrothermal Synthesis of ZnO–Doped Ceria Nanorods: Effect of ZnO Content on the Redox Properties and the CO Oxidation Performance", *Applied Sciences* 10 (2020) 7605. doi: 10.3390/app10217605

- ❖ Το **Κεφάλαιο 4** παρουσιάζει την επίδραση της φύσης της ενεργούς φάσης στις φυσικοχημικές ιδιότητες και στην καταλυτική συμπεριφορά, κατά την αντίδραση υδρογόνωσης του  $\text{CO}_2$ , σε καταλύτες μετάλλων μετάπτωσης υποστηριγμένους στη δμητρία,  $\text{M/CeO}_2$  ( $\text{M}$ : Ti, V, Cr, Mn, Fe, Co, Ni, Cu). Βρέθηκε ότι η μετατροπή του  $\text{CO}_2$  ακολουθεί την εξής σειρά:  $\text{Ni/CeO}_2 > \text{Co/CeO}_2 > \text{Cu/CeO}_2 > \text{Fe/CeO}_2 > \text{CeO}_2 > \text{Cr/CeO}_2 > \text{Mn/CeO}_2 > \text{Ti/CeO}_2 > \text{V/CeO}_2$ . Επί τη βάση των αποτελεσμάτων εκλεκτικότητας, διαπιστώθηκε ότι οι καταλύτες καθαρής δμητρίας,  $\text{Cu/CeO}_2$ ,  $\text{Fe/CeO}_2$ ,  $\text{Cr/CeO}_2$ ,  $\text{Mn/CeO}_2$ ,  $\text{Ti/CeO}_2$  και  $\text{V/CeO}_2$  είναι εκλεκτικοί ως προς την παραγωγή CO, ενώ οι καταλύτες  $\text{Co/CeO}_2$  και  $\text{Ni/CeO}_2$  είναι ιδιαίτερα εκλεκτικοί ως προς το μεθάνιο ( $\text{CH}_4$ ).

Στο **Κεφάλαιο 4** δίνεται έμφαση στο ρόλο του μεγέθους των σωματιδίων Ni στην αντίδραση υδρογόνωσης  $\text{CO}_2$  των καταλυτών  $\text{Ni/CeO}_2$ -nanorods. Επιπλέον, στο **Κεφάλαιο 4**, διερευνήθηκε το φαινόμενο της προώθησης με χρήση  $\text{ZnO}$  με την παρασκευή μικτών οξειδίων  $\text{CeO}_2/\text{ZnO}$  ως φορείς της ενεργής φάσης Ni. Σε αντίθεση με την καταλυτική δράση του  $\text{Ni/CeO}_2$ , οι καταλύτες

Ni/ZnO και Ni/CeO<sub>2</sub>-ZnO είναι εκλεκτικοί ως προς την παραγωγή CO, καταστέλλοντας σε μεγάλο βαθμό τη μεθανίωση του CO<sub>2</sub>, αποκαλύπτοντας το ρόλο του προωθητή ZnO ως προς τον καθορισμό του μηχανισμού της αντίδρασης.

Τα αποτελέσματα του κεφαλαίου αυτού δημοσιεύτηκαν στα ακόλουθα επιστημονικά περιοδικά:

- ✓ Michalis Konsolakis, Maria Lykaki, **Sofia Stefa**, Sónia A. C. Carabineiro, Georgios Varvoutis, Eleni Papista and Georgios E. Marnellos, "CO<sub>2</sub> Hydrogenation over Nanoceria-Supported Transition Metal Catalysts: Role of Ceria Morphology (Nanorods versus Nanocubes) and Active Phase Nature (Co versus Cu)", *Nanomaterials* 9 (2019) 1739. doi: 10.3390/nano9121739
  - ✓ Georgios Varvoutis, Maria Lykaki, **Sofia Stefa**, Eleni Papista, Sónia A.C. Carabineiro, Georgios E. Marnellos, and Michalis Konsolakis, "Remarkable efficiency of Ni supported on hydrothermally synthesized CeO<sub>2</sub> nanorods for low-temperature CO<sub>2</sub> hydrogenation to methane", *Catalysis Communications* 142 (2020) 106036. doi: 10.1016/j.catcom.2020.106036
  - ✓ Georgios Varvoutis, Maria Lykaki, **Sofia Stefa**, Vassilios Binas, George E. Marnellos, and Michalis Konsolakis, "Deciphering the role of Ni particle size and nickel-ceria interfacial perimeter in the low-temperature CO<sub>2</sub> methanation reaction over remarkably active Ni/CeO<sub>2</sub> nanorods", *Applied Catalysis B: Environmental* 297 (2021) 120401. doi: 10.1016/j.apcatb.2021.120401
  - ✓ Georgios Varvoutis, Stamatia A. Karakoulia, Maria Lykaki, **Sofia Stefa**, Vassilios Binas, George E. Marnellos, and Michalis Konsolakis, "Support-induced modifications on the CO<sub>2</sub> hydrogenation performance of Ni/CeO<sub>2</sub>: The effect of ZnO doping on CeO<sub>2</sub> nanorods", *Journal of CO<sub>2</sub> Utilization* 61 (2022) 102057. doi: 10.1016/j.jcou.2022.102057
- ❖ Το **Κεφάλαιο 5** περιγράφει τη σύνθεση, το χαρακτηρισμό και την καταλυτική δραστηριότητα του γραφιτικού νιτριδίου του άνθρακα (g-C<sub>3</sub>N<sub>4</sub>) κατά την επιτέλεση της αντίδρασης της φωτοκαταλυτικής διάσπασης αέριων και υγρών ρύπων. Συγκεκριμένα, σε πρώτη φάση πραγματοποιήθηκε μια συγκριτική μελέτη ως προς τις φυσικοχημικές ιδιότητες και την ικανότητα προσρόφησης της bulk δομής g-C<sub>3</sub>N<sub>4</sub> και των νανο-φύλλων g-C<sub>3</sub>N<sub>4</sub>. Τα αποτελέσματα αποκάλυψαν εξαιρετικά βελτιωμένα φυσικοχημικά χαρακτηριστικά για τα νανο-φύλλα αλλά και βελτιωμένη προσροφητική ικανότητα σε σύγκριση με την bulk δομή g-C<sub>3</sub>N<sub>4</sub>. Επιπροσθέτως, η bulk δομή g-C<sub>3</sub>N<sub>4</sub> και τα νανο-φύλλα g-C<sub>3</sub>N<sub>4</sub> αξιολογήθηκαν ως προς τη φωτοκαταλυτική διάσπαση αέριων και υγρών ρύπων, και τα νανο-φύλλα g-C<sub>3</sub>N<sub>4</sub> επέδειξαν εξαιρετική φωτοκαταλυτική απόδοση.

Τα αποτελέσματα του κεφαλαίου αυτού δημοσιεύτηκαν στα ακόλουθα επιστημονικά περιοδικά:

- ✓ **Sofia Stefa**, Maria Grinieziaki, Marinos Dimitropoulos, George Paterakis, Costas Galiotis, George Kiriakidis, Emmanuel Klontzas, Michalis Konsolakis, and Vassilios Binas, "Highly Porous Thin-Layer g-C<sub>3</sub>N<sub>4</sub> Nanosheets with Enhanced Adsorption Capacity", ACS Applied Nano Materials 6 (2023) 1732-1743. doi: 10.1021/acsanm.2c04632
- ✓ **Sofia Stefa**, Maria Zografaki, Marinos Dimitropoulos, George Paterakis, Costas Galiotis, Palanivelu Sangeetha, George Kiriakidis, Michalis Konsolakis, and Vassilios Binas, "High surface area g-C<sub>3</sub>N<sub>4</sub> Nanosheets as superior Solar-Light Photocatalyst for the Degradation of Parabens", Applied Physics A, (2023) (accepted).
- ✓ **Sofia Stefa**, Evangelia Skliri, Emmanouil Gagaoudakis, George Kiriakidis, Michalis Konsolakis, and Vassilios Binas, "Visible light photocatalytic oxidation of NO using g-C<sub>3</sub>N<sub>4</sub> nanosheets: Stability, kinetics, and effect of humidity", (2023) (submitted).
- ❖ Το **Κεφάλαιο 6** αποτελεί σύνοψη των συμπερασμάτων της εκπονηθείσας διατριβής, και συγχρόνως, παρατίθενται προτάσεις για μελλοντική έρευνα ως προς τον ορθολογικό σχεδιασμό και την ανάπτυξη καταλυτικών συστημάτων υψηλής ενεργότητας/εκλεκτικότητας για ενεργειακές και περιβαλλοντικές εφαρμογές.

# Table of Contents

Short abstract.....	ix
Σύντομη περίληψη .....	xi
Extended Synopsis & Structure Thesis .....	xiv
Εκτεταμένη Σύνοψη & Δομή Εργασίας .....	xviii
<b>Chapter 1 .....</b>	<b>1</b>
<b>Rational design &amp; development of nanostructured non-precious metal catalysts.....</b>	<b>1</b>
Introduction.....	2
1.1. Nano-structured CeO <sub>2</sub> -based materials.....	4
1.1.1. Structure of CeO <sub>2</sub> .....	5
1.1.2. Synthesis of Cerium-based oxides.....	6
1.1.3. Fine-tuning of Cerium-based oxides .....	7
1.1.4. Applications of <i>Cerium-based Oxides</i> in Heterogeneous Catalysis.....	10
1.1.4.1. <i>CO Oxidation</i> .....	11
1.1.4.2. <i>CO<sub>2</sub> Hydrogenation</i> .....	12
1.2. Metal-free g-C <sub>3</sub> N <sub>4</sub> in Catalysis .....	14
1.2.1. Structure of g-C <sub>3</sub> N <sub>4</sub> .....	15
1.2.2. Bulk g-C <sub>3</sub> N <sub>4</sub> & g-C <sub>3</sub> N <sub>4</sub> Nanosheets.....	16
1.2.3. Adsorption properties of g-C <sub>3</sub> N <sub>4</sub> .....	19
1.2.4. Applications of g-C <sub>3</sub> N <sub>4</sub> in Catalysis .....	21
1.2.4.1. <i>Heterogeneous photocatalysis</i> .....	21
1.2.4.2. <i>Heterogeneous catalysis</i> .....	26
<b>Chapter 2 .....</b>	<b>50</b>
<b>Materials Synthesis and Characterization Studies .....</b>	<b>50</b>
2.1. Materials synthesis.....	51
2.1.1. Synthesis of Bare Ceria Nanorods .....	51

2.1.2. Synthesis of Ceria-Based Transition Metal Catalysts .....	51
2.1.3. Synthesis of Ceria-Titania Composites by Different Methods .....	53
2.1.4. Synthesis of CeO <sub>2</sub> /ZnO and Ni/CeO <sub>2</sub> -ZnO .....	56
2.1.5. Synthesis of ceria triangles (CeO <sub>2</sub> TR) and Ni/CeO <sub>2</sub> TR.....	57
2.1.6. Synthesis of Bulk g-C <sub>3</sub> N <sub>4</sub> and g-C <sub>3</sub> N <sub>4</sub> Nanosheets .....	57
2.1.7. Synthesis of g-C <sub>3</sub> N <sub>4</sub> -Based Transition Metal Catalysts .....	58
2.2 Characterization Techniques .....	60
2.2.1. Elemental Analysis (ICP).....	61
2.2.2. Textural and Structural Characterization (BET and XRD).....	61
2.2.3. Morphological and Topographical Characterization (TEM, SEM/EDS, AFM).....	62
2.2.4. Redox Characterization (H <sub>2</sub> -TPR) .....	64
2.2.5. Spectroscopic Characterization: XPS, Raman, FTIR, PL, and UV-Vis Spectroscopy .....	64
2.2.6. Thermogravimetric analysis (TGA).....	66
2.2.7. Zeta potential.....	66
2.3. Adsorption Experiments.....	66
2.4. Catalytic Evaluation Studies .....	68
2.4.1. CO Oxidation .....	68
2.4.2. CO <sub>2</sub> Hydrogenation .....	69
2.4.3. Photocatalysis.....	70
2.4.3.1. Photocatalytic Degradation of NO.....	70
2.4.3.2. Photocatalytic Degradation of Parabens .....	71
<b>Chapter 3 .....</b>	<b>77</b>
<b>Effect of TiO<sub>2</sub> and ZnO dopants on the physicochemical properties of ceria nanorods:</b>	
<b>Implications in CO Oxidation.....</b>	<b>77</b>
Introduction.....	78
3.1. Experimental .....	80
3.1.1. Materials Synthesis .....	80
3.1.2. Materials Characterization .....	80
3.2. Characterization studies of Ceria-Titania oxides .....	80
3.2.1. Textural/Structural Characterization .....	80

3.2.2. Morphological Characterization.....	83
3.2.3. Redox Properties (H <sub>2</sub> -TPR).....	85
3.3. Characterization studies of Ceria-Zinc oxides.....	87
3.3.1 Textural/Structural Characterization.....	87
3.3.2. Morphological Characterization.....	90
3.3.3. Redox Properties (H <sub>2</sub> -TPR).....	91
3.4. Implication in the CO oxidation reaction.....	93
3.4.1. CO Oxidation Performance of CeO <sub>2</sub> /TiO <sub>2</sub> .....	93
3.4.2. CO Oxidation Performance of CeO <sub>2</sub> /ZnO.....	96
3.5. Conclusions.....	100
<b>Chapter 4.....</b>	<b>115</b>
<b>Effect of Active Phase Nature and ZnO promotion on CO<sub>2</sub> hydrogenation performance of Ceria-based Catalysts.....</b>	<b>115</b>
Introduction.....	116
4.1. Experimental.....	119
4.1.1. Materials Synthesis.....	119
4.1.2. Materials Characterization.....	120
4.2. Characterization Studies of Ceria-Based Transition Metal Catalysts.....	120
4.2.1. Textural/Structural Characterization.....	120
4.2.2. Morphological Characterization.....	123
4.2.3. Redox Properties (H <sub>2</sub> -TPR).....	125
4.3. Characterization studies of Ni/CeO <sub>2</sub> -x.....	127
4.3.1. ICP-AES.....	127
4.3.2. Textural/Structural Characterization.....	127
4.3.3. Raman spectroscopy.....	130
4.3.4. Morphological Characterization.....	131
4.4. Characterization studies of CeO <sub>2</sub> /ZnO and Ni/CeO <sub>2</sub> -ZnO oxides.....	133
4.4.1 Textural/Structural Characterization.....	133
4.4.2. Morphological Characterization.....	137

4.4.3. Raman spectroscopy.....	139
4.4.4. Redox Properties (H <sub>2</sub> -TPR).....	141
4.5. Characterization studies of Bare Ceria Triangles (CeO <sub>2</sub> TR) and Ni/CeO <sub>2</sub> TR.....	143
4.5.1 Textural/Structural Characterization .....	143
4.5.2. Morphological Characterization.....	145
4.5.3. Raman spectroscopy.....	146
4.5.4. Surface Analysis (XPS).....	147
4.5.5. Redox Properties (H <sub>2</sub> -TPR).....	148
4.6. Implication in the CO <sub>2</sub> hydrogenation reaction .....	149
4.6.1. CO <sub>2</sub> Hydrogenation Performance of Bare Ceria Nanorods (CeO <sub>2</sub> NR) and Ceria-Based Transition Metal Catalysts .....	149
4.6.2. CO <sub>2</sub> Hydrogenation Performance of Ni/CeO <sub>2-x</sub> .....	152
4.6.3. CO <sub>2</sub> Hydrogenation Performance of CeO <sub>2</sub> /ZnO and Ni/CeO <sub>2</sub> -ZnO oxides .....	154
4.6.4. CO <sub>2</sub> Hydrogenation Performance of Bare Ceria Triangles (CeO <sub>2</sub> TR) and Ni/CeO <sub>2</sub> TR... ..	158
4.7. Conclusions.....	160
<b>Chapter 5 .....</b>	<b>178</b>
<b>Highly Porous Thin-Layer g-C<sub>3</sub>N<sub>4</sub> Nanosheets with Enhanced Adsorption Capacity and Photocatalytic Performance .....</b>	<b>178</b>
Introduction.....	179
5.1. Experimental.....	183
5.1.1. Materials Synthesis .....	183
5.1.2. Materials Characterization .....	183
5.2. Computational Study .....	183
5.3. Characterization studies of g-C <sub>3</sub> N <sub>4</sub> .....	184
5.3.1. Formation Mechanism of porous g-C <sub>3</sub> N <sub>4</sub> nanosheets .....	184
5.3.2. Textural/Structural Characterization .....	185
5.3.3. Morphological Characterization.....	188
5.3.4. Optical properties .....	191
5.4. Characterization Studies of g-C <sub>3</sub> N <sub>4</sub> -Based Transition Metal Catalysts .....	193

5.4.1. Structural Characterization.....	193
5.4.2 Morphological Characterization.....	195
5.4.3. Optical properties .....	195
5.5. Adsorption Studies .....	197
5.5.1. Effect of solution pH.....	198
5.5.2. Effect of various adsorption parameters.....	199
5.5.3. Adsorption kinetics and equilibrium modeling.....	201
5.5.4. Selective adsorption and separation of dyes .....	203
5.5.5. Regeneration and reusability of CNNs.....	206
5.5.6. Structure - adsorption relationships.....	207
5.6. Implication in Catalysis .....	209
5.6.1. Heterogeneous Catalysis - CO <sub>2</sub> hydrogenation reaction .....	209
5.6.2. Liquid-phase photocatalysis – Photocatalytic degradation of parabens.....	210
5.6.2.1. <i>Evaluation of catalyst activity</i> .....	210
5.6.2.2. <i>Effect of operating conditions</i> .....	213
5.6.2.3. <i>CNNs reusability and stability</i> .....	215
5.6.2.4. <i>Mechanism of parabens degradation over CNNs</i> .....	216
5.6.2.5. <i>Preliminary photocatalytic results of g-C<sub>3</sub>N<sub>4</sub>-Based Transition Metal Catalysts</i> .....	219
5.6.3. Gas-phase photocatalysis – Photocatalytic degradation of NO .....	219
5.6.3.1. <i>Evaluation of catalyst activity</i> .....	219
5.6.3.2. <i>CNNs reusability and stability</i> .....	224
5.6.3.3. <i>Effect of humidity on photocatalytic activity of CNNs</i> .....	225
5.6.3.4. <i>Determination of uptake coefficients</i> .....	227
5.7. Conclusions.....	229
<b>Chapter 6</b> .....	247
<b>General Conclusions &amp; Future Research Outlook</b> .....	247
General Conclusions .....	248
Future Research Outlook.....	249

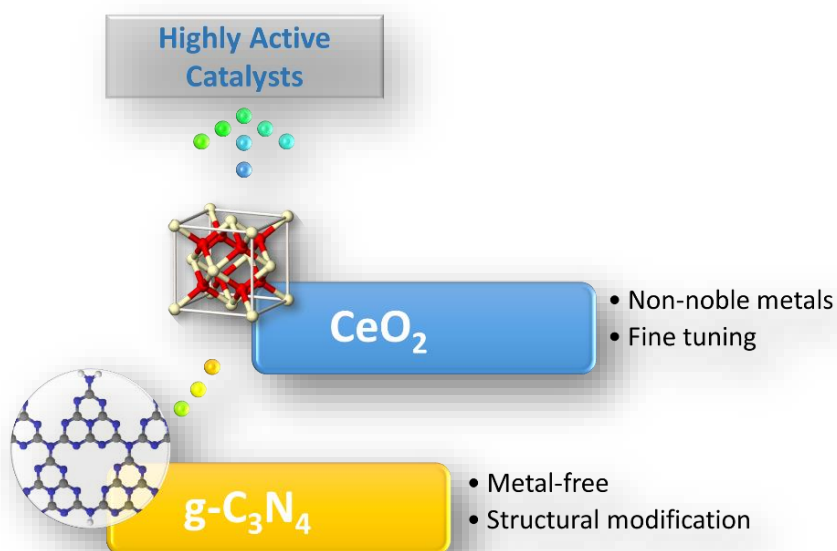


# Chapter 1

## Rational design & development of nanostructured non-precious metal catalysts

Chapter 1 focuses on providing recent advances in the rational design of non-precious metal oxides (MOs) catalysts, exemplified mainly by ceria- or carbon-based oxides. This includes a comprehensive optimization framework aimed at improving non-precious metal oxide sites and their environment through tailored

synthetic routes and promotion/modification pathways. Initially, the basic principles of size, shape, and electronic engineering are discussed. Evidently, fine-tuning has the potential to profoundly affect both the intrinsic reactivity of metal sites and the interfacial activity between metal and support. This, in turn, offers a path to develop materials of excellent activity and stability for practical applications in the field of energy and environment. Subsequently, the main implications of these adjustments in catalysis will be exemplified based on their energy catalytic applications, including CO oxidation and CO<sub>2</sub> hydrogenation reactions, as well as their environmental catalytic applications, such as photocatalysis.



## Introduction

Catalysis has gained significant and sustained attention from both the academic and industrial communities due to its vital role in numerous energy and environmental processes. These processes include a wide range of applications, such as the production of value-added fuels and chemicals, hydrocarbon processing, fuel cell technology, photocatalytic degradation, and the abatement of hazardous substances, among others. One of the primary research areas focused on the field of catalysis is centered around the development of cost-efficient catalysts with enhanced activity and durability. This pursuit forms a crucial pillar of catalysis research, aiming to find solutions that not only improve the efficiency of catalytic processes but also increase their longevity and effectiveness<sup>1-8</sup>.

Noble metals (NMs) play a crucial role in catalysis, enabling chemical bond activation and formation. However, their limited availability and high cost pose significant challenges. Therefore, current research aims to develop catalysts that combine low cost with high activity<sup>1-4,6,8-10</sup>. Consequently, research interest has been directed toward exploring the feasibility of enhancing the surface chemistry of earth-abundant yet relatively inactive materials to achieve performance similar to or even superior to that of noble metals (NMs). Encouragingly, recent advancements in nano-synthesis, surface/interface functionalization, and catalyst promotion support this possibility<sup>9,11-13</sup>.

Metal oxides, composed of earth-abundant transition metals (TMs), have gained significant interest as potential replacements for rare and costly NMs due to their unique characteristics, including enhanced redox properties and thermal stability<sup>2-4,8,10,14</sup>. Notably, the combination of different metal oxides (MOs) in precise proportions can yield mixed metal oxides (MMOs) with distinctive physicochemical properties, primarily attributed to interfacial phenomena. Transition metals based on MOs have received particular attention, owing to the special chemisorption ability of TMs, related to their partially filled d-shells<sup>12,13</sup>. Furthermore, certain reducible oxides (e.g., CeO<sub>2</sub>, ZnO, and TiO<sub>2</sub>) can serve as supporting carriers for TMs, leading to beneficial effects on intrinsic activity through unique metal-support interactions<sup>15-19</sup>.

Among various metal oxides (MOs), cerium oxide or ceria has emerged as a highly intriguing material for heterogeneous catalysis, primarily due to its exceptional redox properties resulting from the high oxygen mobility and rapid redox interplay between Ce<sup>3+</sup> and Ce<sup>4+</sup><sup>1,4,6,9-11,16,20</sup>. Beyond these physicochemical advantages, ceria possesses a distinct economic advantage compared to other MOs like ZrO<sub>2</sub>, ZnO, SiO<sub>2</sub>, and TiO<sub>2</sub>, making it a cost-effective choice for catalytic applications<sup>21</sup>. Moreover, the base middle-late 3d transition metals, such as Cu, and Ni, exhibit significantly lower costs, by about 3 to 4 orders of magnitude, compared to noble metals (NMs), further enhancing the

appeal of developing ceria-based transition metal catalysts from a financial perspective. The combination of reducible oxides, such as CeO<sub>2</sub>, with various transition metals (e.g., Fe, Co, Ni, Cu) opens possibilities for novel catalyst formulations with exceptional properties, arising from multifaceted electronic and geometric interactions among the different components<sup>15–19,22</sup>. Recent experimental and theoretical studies have extensively explored various interconnected phenomena at the metal-support interface, which significantly impact catalytic activity<sup>16,22–25</sup>. These phenomena include the following:

- Electronic perturbations linked to bonding interactions between TMs and ceria nanoparticles.
- Facilitation of oxygen vacancies' formation resulting in enhanced reducibility and oxygen exchange kinetics.
- The high intrinsic activity of interfacial sites.

The significant progress made in cutting-edge characterization techniques has shed light on the individual characteristics of catalyst counterparts, leading to a deeper understanding of their impact not only on their activity but also on the interactions between them, with profound implications for catalysis. Consequently, researchers have focused on adjusting the geometrical and electronic features of different catalyst components through well-designed synthetic and promotional approaches, resulting in the development of highly active materials<sup>11,15,16,24</sup>. Specifically, the surface chemistry of catalysts and their catalytic activity can be fine-tuned through the following strategies:

- (a) Advanced synthetic methods: Innovative approaches have been employed to develop nanomaterials with specific morphology, enabling precise control over their catalytic properties.
- (b) Adjustment of inherent properties: The characteristics of catalysts can be appropriately modified through surface and/or structural promotion, enhancing their catalytic performance.
- (c) Modification of metal-support interactions: Promoting and reducing agents, such as graphitic carbon nitride (g-C<sub>3</sub>N<sub>4</sub>), have been utilized to modify metal-support interactions, further enhancing the catalytic activity.

Another promising category of low-cost catalysts involves carbon-based materials, which can serve as catalysts themselves or as catalyst supports<sup>26–28</sup>. These carbon-based materials offer a range of advantages for catalytic applications, including high chemical stability, low corrosion capability, high thermal stability, hydrophobic character, and easy recovery from the reaction mixture<sup>26,27,29</sup>. Notably, certain carbon materials excel in industrial applications as adsorbents and are particularly valuable in fine chemical production, where their unique properties enable precise and selective catalysis<sup>29</sup>.

The catalytic activities of carbon materials are intricately linked to their defects, structures, and surface chemistry. Notably, carbon nanotubes (CNTs) and graphene, when incorporating defect sites

within their  $sp^2$ -bonded network, possess well-defined and controlled defects with essential catalytic functionalities and surface properties. Additionally, porous carbons characterized by large pores and high surface areas facilitate efficient mass transfer, allowing for a higher concentration of active sites per unit mass of carbon materials <sup>26</sup>. Moreover, graphitic carbon nitride (g-C<sub>3</sub>N<sub>4</sub>), a novel carbon counterpart, has gained increasing attention in sustainable environment and energy applications <sup>30</sup>. Thanks to its excellent thermal and chemical stability and tunable electronic structure, g-C<sub>3</sub>N<sub>4</sub> has found utility in various areas, including artificial photosynthesis, electrochemical oxygen reduction reaction (ORR), and base catalysis <sup>27,28,31</sup>.

Carbons serve as heterogeneous catalysts, offering flexibility in tailoring their physical properties, such as surface area and porosity, and chemical properties, including surface functional groups. The ongoing research focuses on developing synthesis methods that enable precise control over their surface chemistry and nanostructure, which is crucial for tailoring their catalytic performance. A comprehensive understanding of the reaction mechanisms involved in selective catalytic reactions, such as catalytic oxidation, hydrogenation, and dehydrogenation, plays a pivotal role in advancing chemical processes and catalyst design <sup>27,28</sup>.

It has become increasingly evident that by carefully adjusting the synthesis and modification parameters, highly active composites can be obtained with a comparable or even superior performance compared to composites based on noble metals (NMs). In this chapter, our focus is on providing a comprehensive and in-depth understanding of the key factors, including preparation methods, size, morphology, and the nature of the metal phase, that significantly influence the physicochemical characteristics and catalytic performance of bare CeO<sub>2</sub>, graphitic carbon nitride (g-C<sub>3</sub>N<sub>4</sub>), and their respective TMs/composites. Finally, the implications of these catalysts will be exemplified based on their energy catalytic applications, including CO oxidation and CO<sub>2</sub> hydrogenation reactions, as well as their environmental catalytic applications, such as photocatalysis.

### 1.1. Nano-structured CeO<sub>2</sub>-based materials

Cerium dioxide, commonly known as "ceria," has firmly established its role as one of the most promising materials for environment and energy, due to its exceptional redox properties driven by the high oxygen mobility and the rapid redox interplay between Ce<sup>3+</sup> and Ce<sup>4+</sup>. Up to now, ceria and ceria-based catalysts have been demonstrated to show great improvement of catalytic activity in various catalytic reactions (Figure 1.1), such as CO oxidation <sup>32-34</sup>, reforming reactions <sup>35,36</sup>, soot combustion <sup>37-39</sup>, water-gas shift reaction <sup>40-43</sup>, NO reduction <sup>44-46</sup>, CO<sub>2</sub> conversion <sup>47</sup>, solid-oxide fuel cells <sup>48</sup>, and photocatalytic degradation <sup>49</sup>.

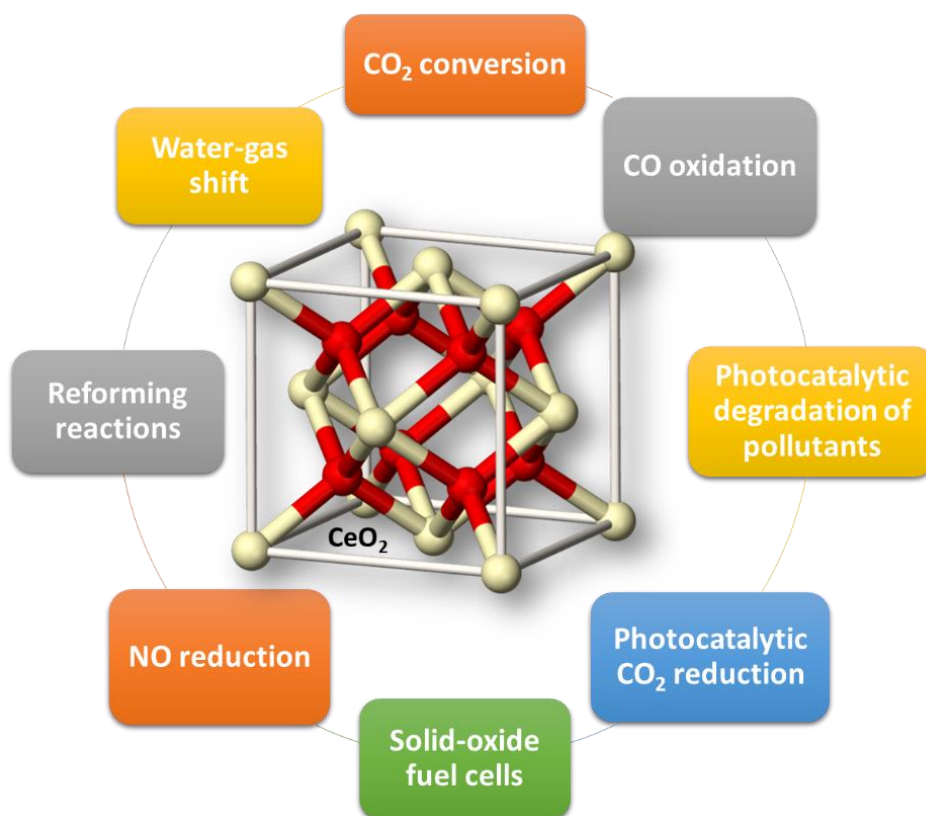


**Figure 1.1.** Main catalytic applications of CeO<sub>2</sub>-based catalysts.

### 1.1.1. Structure of CeO<sub>2</sub>

Cerium (IV) oxide, more commonly known as ceria (CeO<sub>2</sub>), typically assumes the fluorite phase, exhibiting a face-centered cubic lattice (fcc) structure. Each cerium cation finds coordination with eight oxygen anions. The electronic configuration of cerium makes it prone to reversible charge transfer between the Ce<sup>4+</sup> and Ce<sup>3+</sup> stages, as depicted in Figure 1.2 (a) <sup>50,51</sup>. As a result, the formation of Ce<sup>3+</sup> cations is usually accompanied by the presence of oxygen vacancies on the surface and in the bulk (Figure 1.2 (b)) <sup>50</sup>. The oxygen vacancy defects and Ce<sup>3+</sup> ions in ceria (designated as CeO<sub>2-x</sub>) significantly enhance oxygen gas adsorption and activation, as well as oxygen self-diffusion within the lattice of non-stoichiometric ceria. This phenomenon plays a pivotal role in enhancing the efficiency of the redox process and catalytic reactions. The creation of oxygen vacancies can be finely tuned through several factors, including thermal-treatment temperature and oxygen partial pressure, doping elements and content, synthesis methods, surface stress, and electrical field. On the basis of such unique surface properties of CeO<sub>2</sub>, researchers have explored and developed a series of cerium-based oxide catalysts.

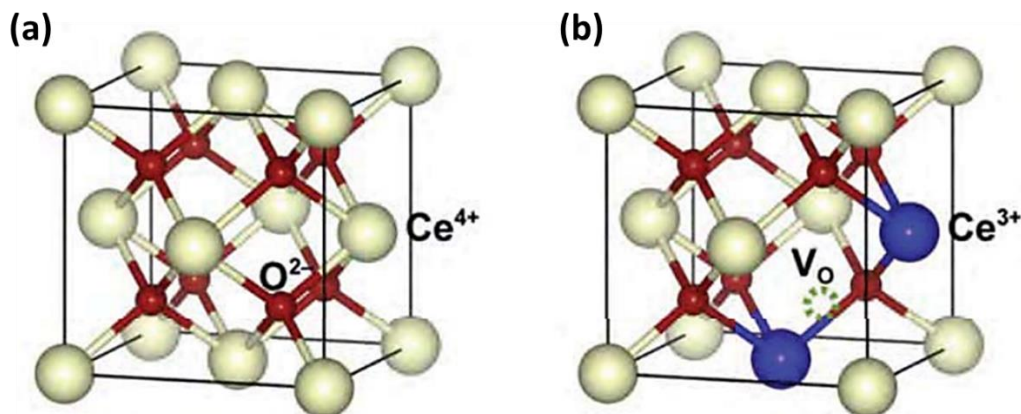


**Figure 1.2.** (a) Ideal crystal structure of CeO<sub>2</sub>; (b) Crystal structure of CeO<sub>2</sub> in the presence of one oxygen vacancy accompanied by two generated Ce<sup>3+</sup> species. Adapted from Reference <sup>50</sup>.

### 1.1.2. Synthesis of Cerium-based oxides

The performance of a catalyst is notably influenced by the specific synthesis or preparation methods employed <sup>52</sup>. Supported catalysts are typically prepared by loading the active metal component onto a carrier, employing either physical or chemical techniques. This strategic coupling allows the support to provide an effective surface and appropriate pore structure, facilitating the uniform dispersion of active components, and thereby enhancing the utilization rate of metal active components and the catalyst stability <sup>53</sup>. Furthermore, the support can occasionally yield additional active sites, leading to an overflow or potent interactions with the metal active components <sup>53</sup>.

In light of the aforementioned considerations, various strategies have emerged for developing highly dispersed supported metal catalysts, such as hydrothermal, impregnation, precipitation, and sol-gel (Figure 1.3). The hydrothermal and solvothermal method finds application in fabricating nanomaterials, offering advantages such as well-developed grains, small particle sizes, uniform distribution, and light particle agglomeration <sup>54</sup>. The impregnation method stands out as an economical and straightforward technique extensively employed in supported catalyst preparation. During impregnation, ultrasonic treatment can be employed to enhance modification effects, with the subsequent impregnated product being subject to pyrolysis to generate the desired catalyst <sup>55</sup>. The co-precipitation method involves the addition of a precipitant (typically NH<sub>3</sub>·H<sub>2</sub>O) to a solution containing soluble cerium and other metal salts. After several cycles of precipitation, washing, separation, drying, and subsequent calcination, nanoparticles are obtained <sup>56</sup>. However, due to the inherent variability in precipitation times, the resulting product particle sizes might exhibit non-uniformity. The sol-gel method offers a means of achieving homogeneous mixing between reactants. Its chemical process involves dispersing cerium and other metal salts within a solvent, followed by hydrolysis reactions that yield active monomers. These monomers polymerize to form a sol, which

then transforms into a gel with a distinct spatial structure. Ultimately, nanoparticles are generated through drying and heat treatment of the gel <sup>57</sup>.

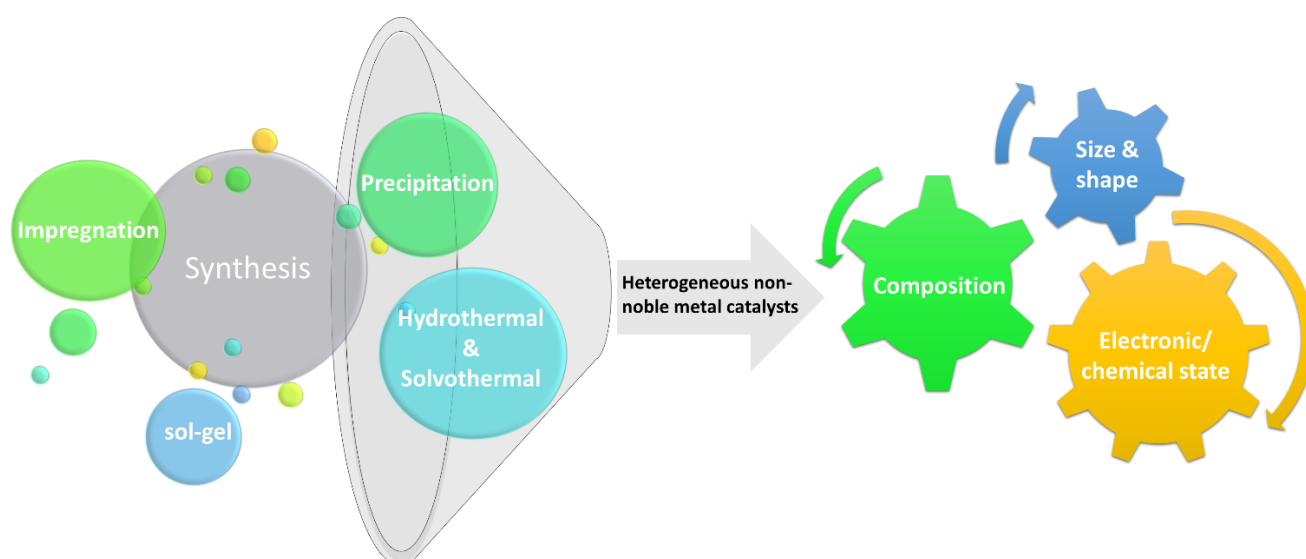


**Figure 1.3.** Illustration for synthetic methods and structural characteristics of heterogeneous non-noble metal catalysts.

### 1.1.3. Fine-tuning of Cerium-based oxides

Heterogeneous catalysis is a fundamental process where chemical reactions occur on the surface of a solid catalyst. This intricate phenomenon involves the adsorption and activation of reactants at specific active sites, the chemical transformation of adsorbed species, and product desorption. With advancements in both in-situ and ex-situ characterization techniques, it has become clear that the elementary steps of these reactions are intricately linked to various parameters. These parameters include factors such as particle size, shape, and electronic configuration, along with the interfacial interactions between these particles. Moreover, it has become clear that the behavior of these macroscopic catalytic systems emerges from interactions between reactants, intermediates, and products, and the finely tuned micro- and nanoscale environment of surface atoms, involving geometric arrangements, electronic confinement, and interfacial effects, among others. By manipulating these parameters, it becomes possible to finely tune the local surface structure and chemistry, yielding profound effects on catalytic performance. However, the interplay between structural and chemical influences poses a significant challenge in unraveling the fundamental origins of catalytic performance. Thus, it becomes paramount to establish reliable structure-property relationships, unveiling the distinctive role of each contributing factor. Such insights hold the potential to pave the way for a rational design approach, replacing the traditional trial-and-error methods by utilizing the fundamental knowledge at the nanoscale.

Supported catalysts are comprised of three pivotal components: metal particles, the supporting material, and their interface which provide many advantages for fine-tuning the geometric/electronic structure. Beyond the intrinsic properties of metal elements, the nano-effect of particles, and the interface effect exert substantial impacts on catalytic performance. Therefore, the composition of elements, geometry morphology, and surface/interface structure can be finely adjusted. This strategic manipulation involves modulating doping elements, particle sizes, and supporting materials, facilitating the development of high-performance supported catalysts.

**Size and Shape Effect.** The shape and size of metal particles play a vital role in determining the catalytic performance of supported catalysts. Fine-tuning these factors offers a pathway to uncovering the structure–property relationship<sup>58,59</sup>. When metal nanoparticles are loaded on support, they don't adopt perfect spherical shapes but form irregular polyhedrons with platforms, edges, corners, kinks, and perimeters<sup>60</sup>. This variation in atomic coordination at these spots leads to diverse adsorption strengths and configurations for reactants with distinct crystal planes exhibiting varied catalytic properties in most cases. However, regulating the morphology of these particles remains challenging due to current synthesis methods. As a result, the research focus has shifted to particle size, which is easier to control with precision. Manipulating particle size has a profound impact on catalytic performance by altering the geometric and electronic structure<sup>61</sup>. Investigations into the surface state have confirmed that the size domains of nanoparticles influence the exposed crystal planes and corresponding ratios of surface sites.

Reducing particle size (metal nanoparticles, metal clusters, and single-atom catalysts) prompts an increase in specific surface area. This optimizes contact between active components and reactants, consequently enhancing catalytic efficiency<sup>62</sup>. Surface atoms, under this scenario, exhibit higher coordination unsaturation, leading to an abundance of unsaturated coordination centers and a sharp rise in surface free energy. This not only transforms the catalyst's chemical properties but can also induce variations in the metal phase's lattice structure. As the nanoparticle/clusters' diameter decreases to a certain extent, the electron energy level close to the Fermi energy level splits into discrete energy levels, causing the quantization of strong electron energy<sup>63</sup>. This phenomenon, coupled with quantum confinement effects, results in particle isomerization. Furthermore, when particle size approaches or becomes smaller than the wavelength of de Broglie waves of conducting electrons, the periodic boundary conditions of nanomaterials are disrupted, leading to a notable reduction in surface electron density. This distinctive behavior underscores why the chemical and catalytic properties of nanomaterials deviate from those of conventional particles.

Nanostructured catalysts exhibit unique properties derived from nanoscale phenomena, mainly size effects as mentioned earlier, as well as shape effects. The latter encompasses altering catalytic

activity by exposing specific crystallographic facets in the reaction environment, a concept known as morphology-dependent nanocatalysis<sup>64-67</sup>. More specifically, the efficiency of the catalytic cycle and, consequently, the reaction efficiency, which depends on reactant adsorption/activation and product desorption processes, is heavily influenced by the surface planes of catalyst particles. In this context, the simultaneous manipulation of size and shape at the nanometer scale can determine the quantity and characteristics of exposed sites, thus influencing catalytic performance. This subject is a crucial issue in the realm of nanocatalysis, aiming to precisely steer specific chemical reactions by fine-tuning these parameters at the nanometer scale.

Thanks to recent advances in materials science, nanostructured catalysts with well-defined crystal facets can be fabricated by precisely controlling nanocrystal nucleation and growth rate<sup>65,68</sup>. The resulting crystal shapes emerge as a consequence of various synthesis factors, including temperature, pressure, concentration, and pH, among others. Numerous comprehensive reviews have delved into this subject<sup>10,68-71</sup>. Through these methods, diverse structures like nanospheres, nanocubes, nanowires, nanorods, and nanosheets can be synthesized with similar or different dimensions in all directions. Among metal oxides employed in heterogeneous catalysis, ceria has been subjected to extensive size and shape control investigations<sup>10,69-71</sup>.

**Promoter effect.** In addition to the modulation of local surface structures of MOs through size and shape effects, as previously discussed, the precise adjustment of electronic structures using suitable promoters presents an extra tool for modulation. Promoters play a pivotal role in heterogeneous catalysis, enabling the optimization of catalytic activity, selectivity, and stability by modifying the physicochemical properties of MOs. These promoters can be categorized into two main groups: structural promoters and electronic promoters. Structural promoters primarily involve the doping of supporting carriers to enhance their structural features, thereby stabilizing active phases. An example is the incorporation of rare earth dopants into three-way catalysts to enhance their characteristics<sup>4</sup>. In contrast, electronic promoters can bring about changes in catalyst surface chemistry either directly or indirectly. Directly, electrostatic interactions occur between reactant molecules and the local electric field generated by promoters. Indirectly, electronic promoters induce alterations in the metal Fermi level, impacting the chemisorption strength of reactants and intermediates, thereby significantly influencing catalysis. Particularly, the "promoter effect" is closely linked to modifications in the work function ( $\Phi$ ) of the catalyst surface following the introduction of a promoter. This adjustment is accompanied by a substantial modification of the catalyst's chemisorption properties. Alkali modifiers, primarily, drive electronic promotion over metal oxide catalysts. Numerous studies have shown that the addition of alkali can drastically enhance the activity and selectivity of various

catalytic systems, involving among others Pt-, Pd-, Rh-, Cu-, and Fe-based catalysts, applied in diverse energy and environmental-related reactions <sup>4,72-76</sup>.

In addition to the extensive use of alkalis and alkaline earths as promoters a plethora of other chemical substances can be employed to finely adjust the local surface chemistry and structure. This modulation consequently enhances the catalytic activity, selectivity, and long-term stability of the parent catalyst <sup>77</sup>. For instance, metal alloys, such as Au-Ni alloys employed as reforming catalysts <sup>78</sup> and Pt-Sn alloys for ethanol oxidation <sup>79</sup>, play a pivotal role in catalytic applications, achieving highly active and cost-effective catalytic formulations. The enhanced performance of bimetallic systems can be attributed to multiple mechanisms, involving structural factors (strain effects) and electronic factors (charge-transfer effects), which emerge due to interactions between the distinct components. The latter facet significantly alters the binding energy of adsorbates and the path of chemical reactions, leading to profound implications in catalytic processes <sup>80</sup>.

Likewise, chemical compounds with distinctive physicochemical characteristics, such as carbon-based materials, have recently gained notable interest as modifiers or supportive carriers <sup>28,81</sup>. Among these, various carbon materials including carbon nanotubes (CNTs), reduced graphene oxide (rGO), ordered mesoporous carbon (OMC), carbon nanofibers (CNFs), and graphitic carbon nitride (g-C<sub>3</sub>N<sub>4</sub>), have emerged as focal points in catalysis due to substantial advancements in controlled synthesis and a deeper comprehension of their properties. In general, nanocarbons (NCs) possess exceptional physical properties such as large surface area, specific morphology, and appropriate pore structure. Additionally, they exhibit notable chemical properties linked to their electronic structure and surface acidity/basicity. These distinctive traits are a direct result of their confined nanoscale structures <sup>28</sup>.

#### 1.1.4. Applications of *Cerium-based Oxides* in Heterogeneous Catalysis

In this section, the implications of the aforementioned fine-tuning engineering strategies in catalysis are shortly presented, on the basis of ceria-based transition metals. Specifically, it delves into the effect of size, shape, and electronic/chemical characteristics on the catalytic performance of TMs/CeO<sub>2</sub> oxides. These effects are elucidated through indicative oxidation and reduction reactions, such as CO oxidation and CO<sub>2</sub> hydrogenation to value-added products, which are also explored in the frame of the present thesis.

#### 1.1.4.1. CO Oxidation

CO oxidation reaction has been extensively studied in the field of heterogeneous catalysis due to its significant relevance to various energy and environmental processes such as the control of exhaust emissions from mobile and stationary sources, and fuel cell applications. Additionally, CO oxidation is commonly used as a model reaction to disclose structure–performance relationships. Ceria-based transition metal oxides have received considerable attention in CO oxidation studies due to their distinctive redox properties<sup>64</sup> and the peculiar metal–ceria synergistic interactions<sup>9,11,21,82,83</sup>. However, as previously mentioned, the distinct characteristics of both the active phase and ceria carrier (e.g., particle's size and shape) can exert a major impact on the redox properties, as well as the metal–support interactions, which can be consequently reflected on the catalytic activity.

In view of the above, numerous studies have investigated the impact of ceria shape (nanocubes, nanorods, and nanopolyhedra) on the CO oxidation activity of various transition metals supported on ceria nanoparticles<sup>64,84–91</sup>. Zhou et al.<sup>92</sup> initially investigated the CO oxidation performance of CeO<sub>2</sub> with different morphologies. They compared the catalytic activity of CeO<sub>2</sub> nanorods and irregular nanoparticles and found that the nanorods exposing {100} and {110} facets exhibited notable CO oxidation activity. This research established the correlation between the shape of CeO<sub>2</sub> and CO oxidation and paved the way for further studies on CO oxidation with different facets and morphologies of CeO<sub>2</sub><sup>64,88</sup>. Tana et al.<sup>93</sup> found that CeO<sub>2</sub> nanowires and nanorods, which expose active {110} and {100} facets, exhibited superior CO oxidation activity compared to nanoparticles featuring a stable {111} facet. Generally, the order of CO oxidation activity for distinct CeO<sub>2</sub> morphologies follows: nanorods > nanocubes > nanopolyhedrons. Moreover, the turnover frequency (TOF) for CO oxidation is the most pronounced on the {110} facets, followed by the {100} and {111} facets<sup>94</sup>. The high activity of the {110} and {100} facets is due to their low oxygen vacancy formation energy, a reduced surface oxygen coordination number, and an abundance of defect sites<sup>64,95,96</sup>. These characteristics facilitate the generation of reactive oxygen species on the {110} and {100} facets even at low temperatures<sup>64</sup>, thereby promoting CO oxidation at such conditions.

When different metals are loaded onto CeO<sub>2</sub>, the interaction between the metal and support can fine-tune the electronic structure of the metal–support interface. This adjustment facilitates the dispersion of metal particles on the CeO<sub>2</sub> surface, a phenomenon strongly influenced by the nature of the CeO<sub>2</sub> carrier, including its morphology and exposed facets<sup>97,98</sup>. The interaction between Cu and CeO<sub>2</sub> is particularly strong, resulting in high dispersion of Cu on the CeO<sub>2</sub> support and consequently, improved CO oxidation activity in Cu/CeO<sub>2</sub> catalysts. Lykaki et al.<sup>84</sup> synthesized various CeO<sub>2</sub> morphologies, such as nanorods, nanocubes, and nanopolyhedrons, as carriers for the Cu phase. Among these, the Cu/CeO<sub>2</sub> nanorod with {100} and {110} reactive planes displayed the most

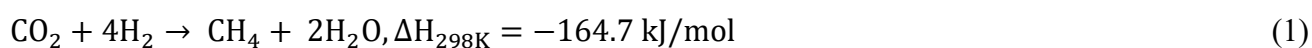
favorable CO oxidation activity. This result was attributed to the presence of weakly bonded oxygen species on the CeO<sub>2</sub> nanorod, enhancing catalyst reducibility and oxygen mobility. The strong interaction between CuO<sub>x</sub> species and the CeO<sub>2</sub> nanorod supports stabilized Cu<sup>+</sup> species, facilitating CO adsorption. Moreover, defects and oxygen vacancies on the CeO<sub>2</sub> nanorod surface contributed to the enhanced CO oxidation performance. Mock et al.<sup>89</sup> prepared the transition metals (Mn, Fe, Co, Ni, Cu) on CeO<sub>2</sub> nanorods that mainly exposed {111} facets. Among them, the Cu/CeO<sub>2</sub> catalyst exhibited the best CO oxidation activity. This good catalytic activity is mainly caused by the relatively rough {111} facets of CeO<sub>2</sub> nanorods, which contain a large number of defects and are more favorable for the adsorption of reaction gases, as well as the strong interaction between CuO and CeO<sub>2</sub>.

Additionally, the incorporation of transition metals into CeO<sub>2</sub> results in a reduction of the activation energy required for oxygen release. This process also induces the formation of defects or oxygen vacancies on the catalyst's surface. Additionally, it increases the ratio of Ce<sup>3+</sup>/Ce<sup>4+</sup> within the ceria lattice, thereby enhancing the catalyst's redox capacity. These modifications exert a significant influence on the catalytic reaction<sup>90,99</sup>. Both theoretical and experimental results support the idea that transition metal oxides and transition metal-doped oxides exhibit remarkable CO oxidation activity<sup>87,100</sup>. Transition metals such as Cu, Co, and Fe have been introduced as dopants in CeO<sub>2</sub>, resulting in improved catalytic performance. Park et al.<sup>91</sup> found that Cu-doped CeO<sub>2</sub> exhibited better catalytic activity than Ni- or Co-doped CeO<sub>2</sub>. Through characterization, they believed that the particle size and specific surface area were not the factors determining the catalytic activity. Wang et al.<sup>87</sup> synthesized a Co<sub>3</sub>O<sub>4</sub>-CeO<sub>2</sub> catalyst. DFT calculation showed that the charge transfer between Co<sub>3</sub>O<sub>4</sub> and CeO<sub>2</sub> through the interface changed the adsorption behavior of CO on the catalyst, weakened the O—O bond, and activated molecular oxygen. These conditions promoted the catalytic activity. Lee et al.<sup>85</sup> pointed out that the introduction of lower valence Mn and different oxidation states can enhance the reactivity of CeO<sub>2</sub> and promote the migration of oxygen atoms to the active site of the Mn—O bond through the CeO<sub>2</sub> lattice, thus playing the role of oxygen storage. Sahoo et al.<sup>86</sup> prepared 3% and 6% Fe-doped CeO<sub>2</sub> samples by microwave-assisted combustion. They found that with the increasing of the Fe content, the specific surface area of Fe-doped CeO<sub>2</sub> decreased, but exhibited better catalytic activity than the CeO<sub>2</sub> alone, among which 3% Fe-doped CeO<sub>2</sub> was the best, which is because the Fe doping increased the defect sites on the catalyst surface.

#### 1.1.4.2. CO<sub>2</sub> Hydrogenation

The unprecedented increase in atmospheric CO<sub>2</sub> levels, mainly due to human activities focused on fossil fuel combustion, has resulted in significant environmental impacts. Among various strategies

for mitigation, the conversion of carbon dioxide into value-added products using "green" hydrogen has gained considerable attention <sup>101–104</sup>. This process, known as CO<sub>2</sub> hydrogenation, has the potential to yield a wide range of chemical compounds, including methane, carbon monoxide, and methanol, as well as various hydrocarbons and oxygenates <sup>101,105,106</sup>. This particular approach can efficiently utilize both CO<sub>2</sub> emissions and "green" hydrogen, derived by the surplus power from non-intermittent Renewable Energy Sources (RES), providing, among others, CH<sub>4</sub> or CO through the reverse water–gas shift (rWGS) reaction (Eq. (1)) and Sabatier reaction (Eq. (2)), respectively:



While noble metal catalysts, such as Rh and Ru exhibit satisfactory hydrogenation activity, their scarcity and high cost are obstacles to wide applications <sup>107–110</sup>. Given this context, the research interest has focused on the rational design of NMs-free catalyst formulations. Particular emphasis was given to transition metals (e.g., Cu, Ni, Co, and Fe), due to their ability to chemisorb and consequently activate the CO<sub>2</sub> molecule <sup>111,112</sup>. Furthermore, cerium oxide was selected as the supporting carrier due to its exceptional redox/basic characteristics, in conjunction with the synergistic interactions that can be developed between TMs and CeO<sub>2</sub>. In line with the aforementioned fine-tuning aspects, the fine-tuning of the metal-support interface could lead to highly active and selective catalysts.

The effect of different morphology of CeO<sub>2</sub> support on the activity of CeO<sub>2</sub>-based catalysts for CO<sub>2</sub> hydrogenation has been studied extensively due to the highly tunable crystal texture <sup>113–116</sup>. Du et al. <sup>117</sup> conducted a comparative investigation between a commercially nano-CeO<sub>2</sub> (Aladdin, 20 nm, 99.5% metals basis)-supported Ni catalyst (~60%) and Ni/CeO<sub>2</sub>-nanoplates (Ni/CeO<sub>2</sub>-P). The latter demonstrated notably higher CO<sub>2</sub> conversion of 73% at 260 °C. This study indicated that the difference in catalytic activity between Ni/CeO<sub>2</sub> and Ni/CeO<sub>2</sub>-P was ascribed to the different shapes of the CeO<sub>2</sub> supports. Furthermore, Bian et al. <sup>118</sup> deposited Ni particles onto two distinct CeO<sub>2</sub> supports with varying shapes (nanorod and nanocube, referred to as NR and NC). These samples were then assessed for low-temperature methanation activity. Across the temperature range of 200–250 °C, Ni/CeO<sub>2</sub>-NR consistently exhibited higher CO<sub>2</sub> conversion than Ni/CeO<sub>2</sub>-NC. The increased activity was attributed to a greater concentration of oxygen vacancies resulting from the CeO<sub>2</sub>-NR structure. This variation in oxygen vacancy concentration directly impacted the formation of a crucial intermediate (formate).

Beyond tailoring specific morphologies, enhancing the structure of CeO<sub>2</sub>-based catalysts represents another approach to improving the catalyst's nature and activity. The support's structure not only influences the dispersion of the active metal but also profoundly alters the catalyst's reducibility and basicity<sup>119,120</sup>. Yang et al.<sup>121</sup> conducted a study involving Fe/CeO<sub>2</sub>-Al<sub>2</sub>O<sub>3</sub> catalysts, exploring the impact of selected transition metal promoters such as Cu, Ni, and Mo. Their findings showed substantially improved performance by both Ni and Cu in the monometallic Fe-catalyst. Moreover, these promoters exhibited distinct effects on selectivity. Specifically, while FeNi/CeO<sub>2</sub>-Al<sub>2</sub>O<sub>3</sub> favored CO<sub>2</sub> methanation, FeCu/CeO<sub>2</sub>-Al<sub>2</sub>O<sub>3</sub> exhibited full selectivity towards CO. Consequently, Cu-doped catalysts emerge as the preferred candidates for this reaction within the tested conditions. Furthermore, Varvoutis et al.<sup>122</sup> conducted the synthesis of CuO/CeO<sub>2</sub> composites through alkali promotion, exploring the impact of cesium doping (0-4 Cs atoms per nm<sup>2</sup>). The results highlighted that the incorporation of cesium acted as an inhibitor for CO<sub>2</sub> conversion, while simultaneously demonstrating a favorable influence on CO selectivity. Notably, the sample loaded with 2 Cs atoms per nm<sup>2</sup> exhibited equilibrium CO yields around 430 °C. These findings pave the way for the development of highly active and selective catalysts for the reverse water-gas shift (rWGS) reaction.

## 1.2. Metal-free g-C<sub>3</sub>N<sub>4</sub> in Catalysis

The variety of carbon polytypes, including fullerenes, nanotubes, graphite, graphene, nanodiamonds, and amorphous porous carbon, constitutes a rich class of solid materials characterized by their environmental friendliness and exceptional reusability<sup>27,28</sup>. Taking advantage of the unique physicochemical characteristics inherent in carbon-based materials, such as excellent thermal and chemical stability as well as adjustable surface peculiarities, positions them as versatile candidates for a plethora of applications ranging from catalysis, adsorption, and separation to electrochemistry<sup>27,29,31,123</sup>. In heterogeneous catalytic processes, carbon materials have emerged as catalyst supports due to their tailored porous architectures and surface reactivity. Their facile reducibility of metal oxides, resistance to corrosive agents, enduring stability at high temperatures (even above 750 °C), and low cost underline their appeal<sup>29</sup>. Recognizing that the pursuit of innovative chemical processes and catalysts is often driven by significant economic benefits, the search for new heterogeneous catalysts, potentially without or with reduced metal species, has gained much attention.

In recent years, research efforts into developing metal-free catalysts have been devoted to various carbon-based catalysts. Carbon materials themselves have demonstrated remarkable efficiencies across various catalytic processes, including chemical catalysis, photocatalysis, and electrocatalysis<sup>27-29,31,123</sup>. The catalytic activities of carbon materials are related to their defects, structures, and surface chemistry. For example, carbon nanotubes (CNTs) and graphene, which incorporate defect

sites in their  $sp^2$ -bonded network, provide precisely controlled defects with the necessary catalytic functionalities or surface properties. Furthermore, the inclusion of porous carbons with large pores and high surface areas can facilitate mass transfer, thus allowing an increased concentration of active sites per unit mass of carbon material <sup>124</sup>.

Graphitic carbon nitride materials ( $g\text{-C}_3\text{N}_4$ ) have gained significant attention in recent years due to their remarkable similarity to graphene. Unlike graphene,  $g\text{-C}_3\text{N}_4$  stands out as a medium-band gap semiconductor with excellent thermal and chemical stability and tunable electronic structure and has received increasing attention in the areas of sustainable environment and energy (Figure 1.4 (a)) <sup>125-128</sup>. In the last decade, there has been a remarkable research interest in tailored  $g\text{-C}_3\text{N}_4$ -based catalysts, targeting various applications. As illustrated in Figure 1.4 (b), the prevailing focus of these investigations mainly revolves around the elucidation of their photocatalytic performance, while it is worth noting that relatively few efforts have delved into the field of heterogeneous catalysis.

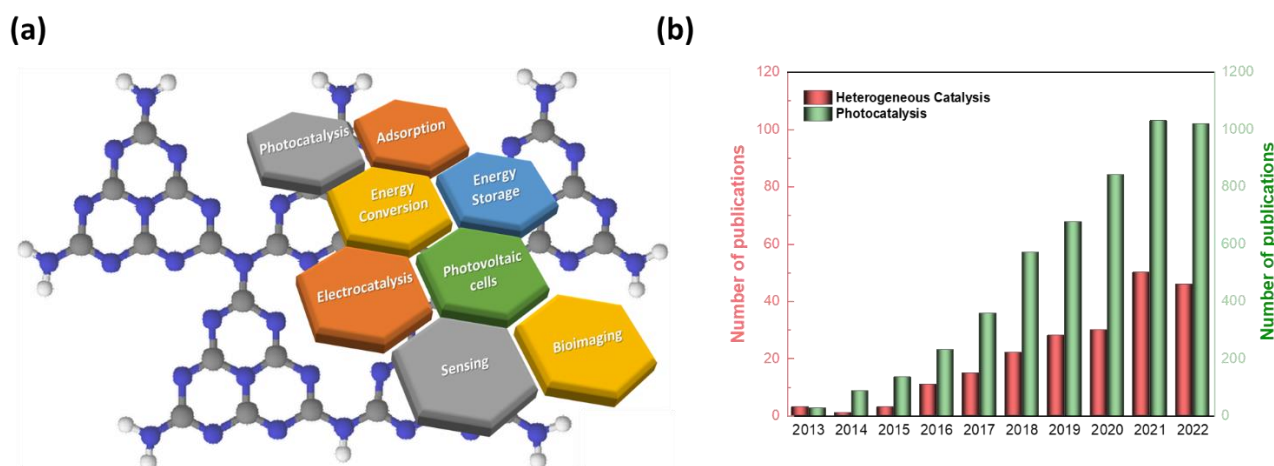


**Figure 1.4.** (a) Number of publications in the last decade obtained from a search of the Web of Science using the keywords "Carbon nitride catalysts for Photocatalysis", and "Carbon nitride catalysts for Heterogeneous catalysis"; (b) Multiple applications of graphitic carbon nitride.

### 1.2.1. Structure of $g\text{-C}_3\text{N}_4$

Graphitic carbon nitride can be formed through the polymerization of low-cost nitrogen-containing precursors. The first report of a  $\text{C}_3\text{N}_4$  polymer dates back to the 1830s. In the following decades, extensive research efforts were devoted to investigating the impact of various synthetic procedures on the reactivity and morphology of the resulting product. The intricate geometrical structure of  $g\text{-C}_3\text{N}_4$  includes two main units: tri-s-triazine ( $\text{C}_6\text{N}_7$ ) and s-triazine ( $\text{C}_3\text{N}_3$ ) rings, as depicted in Figure 1.5 (a) and (b), respectively <sup>125,129</sup>. Notably, tri-s-triazine has emerged as the most stable unit under ambient conditions <sup>130</sup>. Supporting this observation, density functional theory (DFT) calculations

focusing on these main units of g-C<sub>3</sub>N<sub>4</sub> have also shown that tri-s-triazine is the most stable thermodynamically<sup>131</sup>. Theoretically, it has been reported that a monolayer sheet of g-C<sub>3</sub>N<sub>4</sub> holds the potential to exhibit a surface area of up to approximately 2500 m<sup>2</sup> g<sup>-1</sup><sup>129,132</sup>. Moreover, the electronic structure of g-C<sub>3</sub>N<sub>4</sub> involves sp<sup>2</sup> hybridization of carbon and nitrogen atoms, forming a  $\pi$ -conjugated delocalized system<sup>129</sup>.

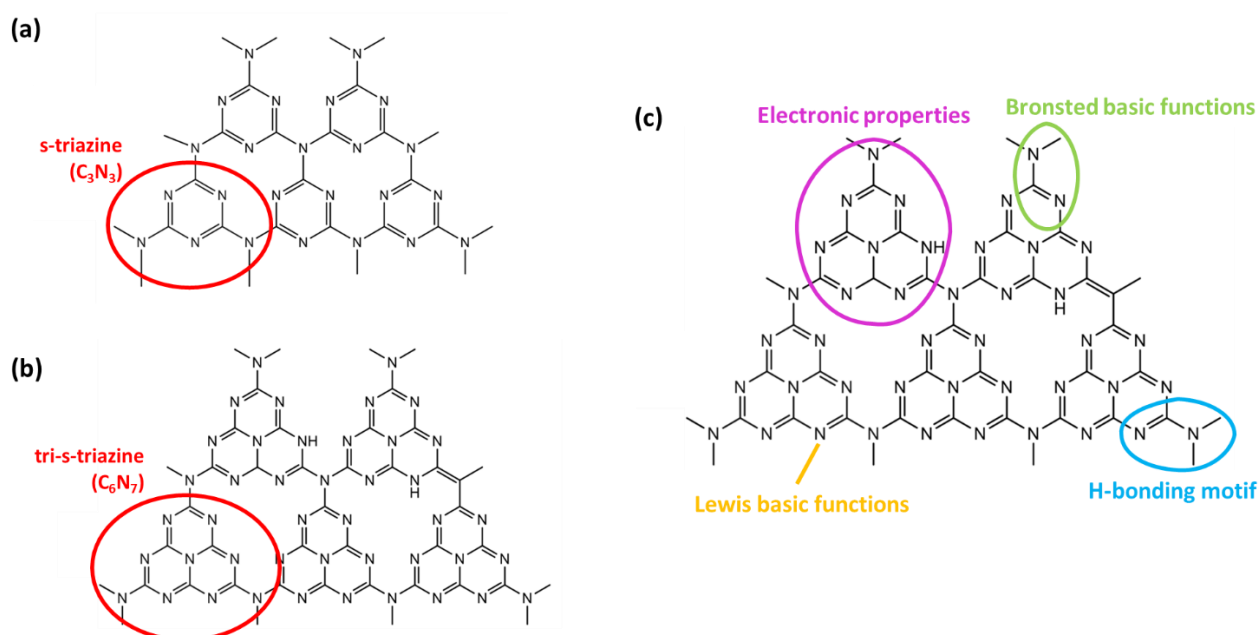


**Figure 1.5.** (a) s-Triazine and (b) tri-s-triazine-based structures of g-C<sub>3</sub>N<sub>4</sub>; (c) Multiple functionalities of g-C<sub>3</sub>N<sub>4</sub>.

### 1.2.2. Bulk g-C<sub>3</sub>N<sub>4</sub> & g-C<sub>3</sub>N<sub>4</sub> Nanosheets

g-C<sub>3</sub>N<sub>4</sub> has attracted great research interest in the field of catalytic and environmental remediation applications, due to its metal-free nature, catalytic, photocatalytic (bandgap energy of 2.7 eV, excellent visible light absorption), electronic properties, and physiochemical features. Additionally, g-C<sub>3</sub>N<sub>4</sub> is characterized by excellent thermal (up to 600 °C), chemical (in various solvents), and mechanical stability. Another major advantage is the facile preparation of g-C<sub>3</sub>N<sub>4</sub> high yield from low-cost and earth-abundant nitrogen-rich materials. This makes it feasible for large-scale catalytic applications<sup>126,129,133</sup>.

Bulk g-C<sub>3</sub>N<sub>4</sub> exhibits a three-dimensional structure similar to graphite. Conventionally, the synthesis of bulk g-C<sub>3</sub>N<sub>4</sub> involves the pyrolysis of nitrogen-rich precursors such as melamine, dicyandiamide, thiourea, or urea<sup>134,135</sup>. However, the intrinsic characteristics of bulk g-C<sub>3</sub>N<sub>4</sub>, characterized by a band gap of 2.7 eV, present some limitations, notably low specific surface area due to layer stacking during polycondensation, limited quantum yield due to limited or absent electronic transitions, and a

high recombination rate of photogenerated holes and electrons<sup>134–139</sup>. To overcome these challenges, various strategies have been employed to enhance its physicochemical properties and catalytic performance. These approaches include the exfoliation of bulk  $g\text{-C}_3\text{N}_4$  into nanosheets, nanotubes, and quantum dots, the introduction of doping elements into  $g\text{-C}_3\text{N}_4$ , and the incorporation of  $g\text{-C}_3\text{N}_4$  into other materials to create nanocomposites, as depicted in Figure 1.6 (a)<sup>128,137,138,140–143</sup>.

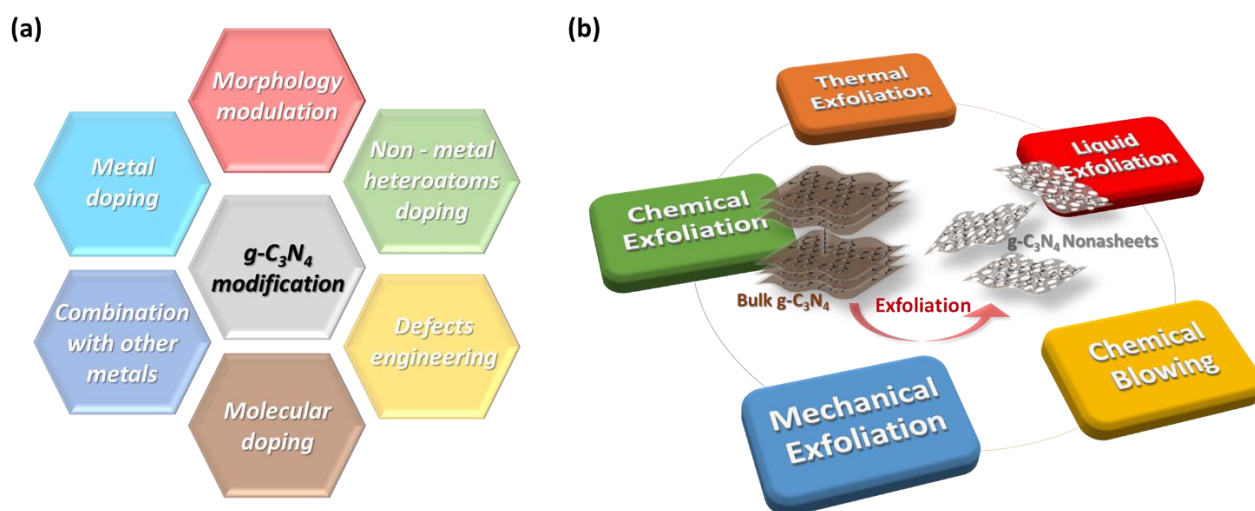


**Figure 1.6.** (a) Common modification methods of  $g\text{-C}_3\text{N}_4$  and (b) various exfoliation methods of bulk  $g\text{-C}_3\text{N}_4$ .

As previously highlighted, bulk  $g\text{-C}_3\text{N}_4$  consists of a layered and planar graphite-like structure. Nitrogen and carbon atoms are interconnected through covalent bonds, while weak van der Waals forces of attraction exist between the layers<sup>129</sup>. These layers can be separated into 2D nanosheets when sufficient energy is introduced to disrupt the van der Waals forces between the  $g\text{-C}_3\text{N}_4$  layers<sup>137,138</sup>. Therefore, the combination of strong covalent bonds between carbon and nitrogen atoms along with weak van der Waals forces between the layers in bulk  $g\text{-C}_3\text{N}_4$  allows for the potential exfoliation of these layers<sup>126,137,138,144</sup>.

Compared with bulk  $g\text{-C}_3\text{N}_4$ ,  $g\text{-C}_3\text{N}_4$  nanosheets possess a 2D sheet structure and abundant mesoporous structure, making them with promising features in several aspects:

- Larger specific surface area, facilitating the exposure of more active sites for trapping and activating reactants, and synchronously promoting mass transfer<sup>145</sup>.
- Abundant mesoporous structure, leading to multiple scattering effects, greatly enhancing the light-trapping ability of  $g\text{-C}_3\text{N}_4$ , thus extending the light absorption range<sup>146</sup>.

- Thinner thickness notably enhances the separation of photon-generated carriers, shortening their path to the material surface, decreasing their recombination rate, and enhancing their utilization rate <sup>147</sup>.

Thus, g-C<sub>3</sub>N<sub>4</sub> nanosheets demonstrate superior properties compared to bulk g-C<sub>3</sub>N<sub>4</sub>. This distinction is often used to explore the structure-activity relationship between structure and performance.

Various methods have been explored for the separation of bulk g-C<sub>3</sub>N<sub>4</sub> layers, including thermal exfoliation <sup>143,148–152</sup>, chemical exfoliation <sup>150,153–155</sup>, liquid ultrasonic exfoliation <sup>156–158</sup>, chemical blowing <sup>159,160</sup>, and mechanical exfoliation <sup>161</sup>, as illustrated in Figure 1.6 (b). However, some exfoliation processes, such as ultrasonically assisted solutions and chemical etching processes, require significant time consumption and use corrosive reagents such as hydrochloric acid and sulfuric acid, thus not following green principles <sup>129</sup>.

Thermal exfoliation exhibits several advantages, including cost-effectiveness, large surface area, absence of solvents, time efficiency, high efficiency, and introduction of beneficial structural defects into the resulting nanosheets <sup>143</sup>. Specifically, this method involves subjecting the g-C<sub>3</sub>N<sub>4</sub> bulk to heat, which disrupts the weak van der Waals forces that bind the layers together, leading to their separation <sup>143,162</sup>. Ideally, in this thermal process, the hydrogen attached to the tri-s-triazine or s-triazine units reacts with oxygen, creating a gas that escapes and forms pores within the bulk material, simultaneously causing sheet formations <sup>163</sup>. As a result, the obtained g-C<sub>3</sub>N<sub>4</sub> nanosheets exhibit high surface area and increased pore volumes, thus increasing the overall porosity. Challagulla et al. <sup>162</sup> employed both thermal and chemical etching approaches on bulk g-C<sub>3</sub>N<sub>4</sub> to form nanosheets for photocatalytic nitrobenzene reduction. For the thermal etching, bulk g-C<sub>3</sub>N<sub>4</sub> underwent exposure to a temperature of 500 °C for 2 h in an air environment. The resulting product exhibited a surface area of 216.3 m<sup>2</sup> g<sup>-1</sup>. Dong et al. <sup>148</sup> synthesized porous g-C<sub>3</sub>N<sub>4</sub> nanosheets via direct pyrolysis of thiourea followed by a thermal exfoliation. The g-C<sub>3</sub>N<sub>4</sub> nanosheet samples were applied for visible light photocatalytic removal of NO<sub>x</sub> in air. The performance of porous g-C<sub>3</sub>N<sub>4</sub> nanosheets was significantly enhanced with increased exfoliation temperature from 450 to 550 °C. The obtained sample with an exfoliation temperature of 550 °C exhibited the highest surface area of 151 m<sup>2</sup> g<sup>-1</sup> and the best photocatalytic performance. Similarly, Li et al. <sup>143</sup> prepared ultrathin g-C<sub>3</sub>N<sub>4</sub> nanosheets through thermal exfoliation of bulk g-C<sub>3</sub>N<sub>4</sub>. Particularly, a series of exfoliated g-C<sub>3</sub>N<sub>4</sub> were synthesized by adjusting the thermal exfoliation temperature and time. This work suggested that higher exfoliation temperature increased nitrogen vacancies and specific surface area while prolonged exfoliation time enhanced thermal exfoliation, forming more carbon vacancies and larger pore volume. Increasing the temperature and time also improved the exfoliation and photocatalytic ability of the resulting nanosheets.

### 1.2.3. Adsorption properties of g-C<sub>3</sub>N<sub>4</sub>

Adsorption constitutes a surface phenomenon that occurs between adsorbates and adsorbents. An effective adsorbent should possess a high specific surface area, optimal surface characteristics, and good stability to adsorb pollutants quickly and efficiently. These pollutants progressively adsorbed onto the surface of adsorbents until equilibrium is attained. Depending on the nature of the interaction between adsorbents and adsorbates, adsorption can be categorized into two types. Chemisorption involves a chemical reaction between the adsorbate and adsorbent, constituting an irreversible process. Physisorption, on the other hand, is governed by distinct interactive forces, such as van der Waals interactions<sup>164</sup> and hydrogen bonding<sup>165</sup>, manifesting as a reversible process. Consequently, adsorbents can be easily regenerated for subsequent use. The adsorption process is influenced by a range of factors, including temperature, contact time, the force between adsorbent and adsorbate, solution pH, coexisting impurities, concentration, and other pertinent parameters<sup>166,167</sup>.

Affordability, high efficiency, rapid adsorption rates, and the ability to target multiple pollutants simultaneously render adsorption a widely adopted and popular technique for pollutant degradation<sup>125,164,167</sup>. Various materials, such as activated carbons<sup>168</sup>, graphene-based materials<sup>169</sup>, carbon tubes<sup>170</sup>, chitosan<sup>171</sup>, clay substances<sup>172</sup>, and layered double hydroxides (LDHs)<sup>173</sup>, have been extensively explored as adsorbents for pollutant removal. Interestingly, modified g-C<sub>3</sub>N<sub>4</sub> also exhibits substantial adsorption capacity. Zhu et al.<sup>174</sup> investigated three distinct types of g-C<sub>3</sub>N<sub>4</sub> synthesized via the calcination of melamine, thiourea, or urea, each resulting in different microstructures during the fabrication process. The isoelectric points of these g-C<sub>3</sub>N<sub>4</sub> derivatives were determined by measuring their zeta potentials, revealing surface charge variations stemming from functional group interactions. Experimental findings revealed the facile adsorption of methylene blue (MB) by the prepared samples. Upon analyzing the adsorption kinetics and isotherms of MB on these samples, the urea-derivative g-C<sub>3</sub>N<sub>4</sub> demonstrated superior adsorption performance. This research underscores the exceptional adsorption capabilities of g-C<sub>3</sub>N<sub>4</sub>, attributed to its cost-effectiveness, environmental compatibility, high efficiency, and facile synthesis process. Additionally, Yousefi et al.<sup>175</sup> reported that exfoliation in the liquid phase by a combination of oxidation and sonication allows the preparation of g-C<sub>3</sub>N<sub>4</sub>-based materials with improved dispersibility in water, increased exposed surface, and abundance of surface functional groups. The obtained oxidized g-C<sub>3</sub>N<sub>4</sub> adsorbents exhibited high adsorption capacities which were remarkable towards organic dyes (~70-600 mg/g) and excellent in the case of the antibiotic tetracycline (895 mg/g) in an aqueous solution.

Various mechanisms governing the adsorption of pollutants onto the g-C<sub>3</sub>N<sub>4</sub> surface, including electrostatic interaction,  $\pi$ - $\pi$  interaction, and hydrogen bonding <sup>125,176</sup>, are depicted in Figure 1.7. Among these, electrostatic interaction emerges as the predominant pathway in the adsorption of dyes onto the g-C<sub>3</sub>N<sub>4</sub> surface. This mechanism occurs when either g-C<sub>3</sub>N<sub>4</sub> or its composites, along with the dye pollutants, have electric charges. In the context of pollutant removal, the nature of electrostatic interaction depends on the surface charges of the adsorbent and the pollutant. Key factors shaping this interaction are the pH of the medium and the point of zero charge (pH<sub>PZC</sub>) of the materials, significantly influencing their electrification and, consequently, the adsorption process. In particular, when the pH of the medium exceeds pH<sub>PZC</sub>, the surface of g-C<sub>3</sub>N<sub>4</sub> adopts a negative charge, facilitating interactions with positively charged pollutants or cationic dyes. Conversely, if the pH of the medium drops below the pH<sub>PZC</sub>, the adsorbent acquires a positive charge, thereby attracting negatively charged pollutants or anionic dyes <sup>177</sup>. In this context, Ren et al. <sup>167</sup> employed carbon-doped g-C<sub>3</sub>N<sub>4</sub> to remove MB dye pollutants in an aqueous solution. Their findings indicated that the adsorption process of MB occurred through a combination of electrostatic and  $\pi$ - $\pi$  interactions.

The  $\pi$ - $\pi$  interaction arises when aromatic pendant groups are present in both the composite and pollutant structures. The g-C<sub>3</sub>N<sub>4</sub> and its composites contain these aromatic groups within their structures, which are also commonly found in used dyes. This interaction facilitates bonding between two aromatic groups through non-covalent interactions. Importantly, the  $\pi$ - $\pi$  interaction serves as a prevalent adsorption mechanism in aromatic compounds containing  $\pi$  bonds <sup>178</sup>. Zhang et al. <sup>179</sup> synthesized a composite consisting of ZnO-layered double hydroxide and g-C<sub>3</sub>N<sub>4</sub> for adsorbing various dye pollutants under UV and visible light. Their study concluded that the adsorption process primarily occurs through  $\pi$ - $\pi$  interactions.

As previously mentioned, electrostatic interactions are the most common mechanisms in pollutant adsorption processes. A specific variant of this interaction involves hydrogen ions (H<sup>+</sup>), which occurs when the proton donor and acceptor groups of the process are present. Consequently, this weak hydrogen bonding can take place between the g-C<sub>3</sub>N<sub>4</sub> composite and pollutant molecules <sup>180</sup>. In a related study, Zhao et al. <sup>181</sup> synthesized a g-C<sub>3</sub>N<sub>4</sub>/Fe<sub>3</sub>O<sub>4</sub>/ZIF-8 nanocomposite with the capability of magnetic recycling for the adsorptive removal of the MG dye pollutant from aqueous solutions. These researchers highlighted that the primary adsorption mechanism in this process is closely associated with hydrogen bonding interactions.

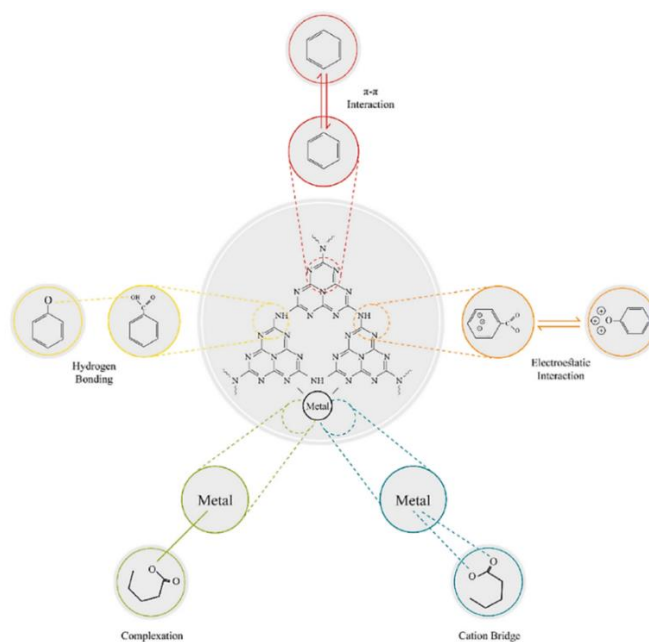


**Figure 1.7.** Possible adsorbate-adsorbent interactions on the g-C<sub>3</sub>N<sub>4</sub> surface. Adapted from Reference <sup>125</sup>.

In the case of photocatalysis, the adsorption of dyes on the surface of photocatalysts plays an important role in the efficiency of the photocatalytic degradation process of dyes. This adsorption phenomenon is related to the binding affinities and electrostatic interactions that occur between the catalyst surface and the dye molecules. The adsorption of dyes on the catalyst surface is considered a fundamental step in the photodegradation of these dyes. Both strong and weak adsorption of dyes results in reductions in the photocatalytic performance of the catalysts. While strong adsorption leads to the poisoning of catalysts, weak adsorption leads to the attachment of dyes to the catalyst surface for a photodegradation reaction. The high adsorption of dyes on the surface of the catalysts results in the surface being covered with dyes that block the access of photons to the surface of the catalyst. Therefore, strong adsorption reduces the photocatalytic efficiency. According to the Sabatier principle, the binding of the dye molecules to the surface of the catalysts should be neither strong nor weak for the best photocatalytic activity. The medium is beneficial due to the synergy between photocatalysis and adsorption for excellent photodegradation efficiency <sup>182–184</sup>.

## 1.2.4. Applications of g-C<sub>3</sub>N<sub>4</sub> in Catalysis

### 1.2.4.1. Heterogeneous photocatalysis

The process of photocatalytic reactions includes three main steps, as illustrated in Figure 1.8. Initially, semiconductors are excited by appropriate light irradiation with photon energy equal to or exceeding their band gap energy. This excitation triggers the movement of electrons (e<sup>-</sup>) from the

valence band (VB) to the conduction band (CB), resulting in the creation of holes ( $h^+$ ) in the VB <sup>185</sup>. Subsequently, these photoinduced  $e^-$  and  $h^+$  species migrate to the surface of the photocatalyst. Once at the surface, these electrons and holes react with target molecules adsorbed on the catalyst, leading to chemical reactions such as hydrogen evolution, CO<sub>2</sub> reduction, pollutant degradation, disinfection, and organic synthesis. It is important to note that the redox potentials of photocatalysts are determined by the relative positions of CB and VB <sup>186</sup>. However, a significant proportion of photogenerated  $e^-$  and  $h^+$  tends to recombine rather than participate in redox reactions. Only a minority of these species migrate to the catalyst surface for the actual redox processes. Although the fundamental principles of photocatalysis elucidated above are clear, the practical application of photocatalysis is hindered by its relatively low redox efficiency. This limitation can be attributed to the following factors:

- **Low light utilization efficiency.** When certain semiconductor materials are exposed to light of appropriate wavelengths and photon energies that match or exceed their band gap energy, electrons in their valence band (VB) can be excited. For example, within natural sunlight, only 5.7% consists of UV radiation ( $\lambda < 420$  nm), and an even smaller portion, 4.7%, falls into the UV range ( $\lambda < 387$  nm) capable of activating electrons in the valence band of TiO<sub>2</sub>. In contrast, the visible light range ( $420 \text{ nm} < \lambda < 760 \text{ nm}$ ) constitutes a significant 52.1% of natural sunlight <sup>186</sup>. This important section offers great potential for the design of photocatalysts that can respond to visible light. However, it is crucial to find a balance between achieving a broad light response and maintaining a high redox capacity of the catalyst.
- **Severe recombination of photoinduced  $e^-$  and  $h^+$ .** Photoinduced electrons and holes often face significant recombination challenges. While electrons exhibit rapid migration within the bulk or surface of a catalyst, they are likely to recombine with positively charged photoinduced holes <sup>187</sup>. For effective use in surface chemical reactions, only those electrons and holes that effectively interact with molecules on the catalyst surface prove valuable. Unfortunately, such useful photogenerated electrons and holes are relatively rare.
- **Low surface chemical reaction.** The photogenerated electrons and holes present on the catalyst surface face the challenge of exhibiting a low reaction rate, which is mainly attributed to the weak interaction between the photogenerated charge carriers and the target molecules <sup>188</sup>. Consequently, there is an urgent need to enhance the efficiency of surface chemical reactions for photocatalysts.

- **Insufficient stability of catalysts.** The physicochemical stability of catalysts can be compromised by various factors within the surrounding environment, such as pH levels and certain interfering ions, leading to a decrease in catalytic efficiency. Furthermore, many of these photocatalysts exist in the form of nanoparticles, posing challenges for efficient recovery and recycling when applied to pollutant degradation through photocatalysis <sup>189</sup>.

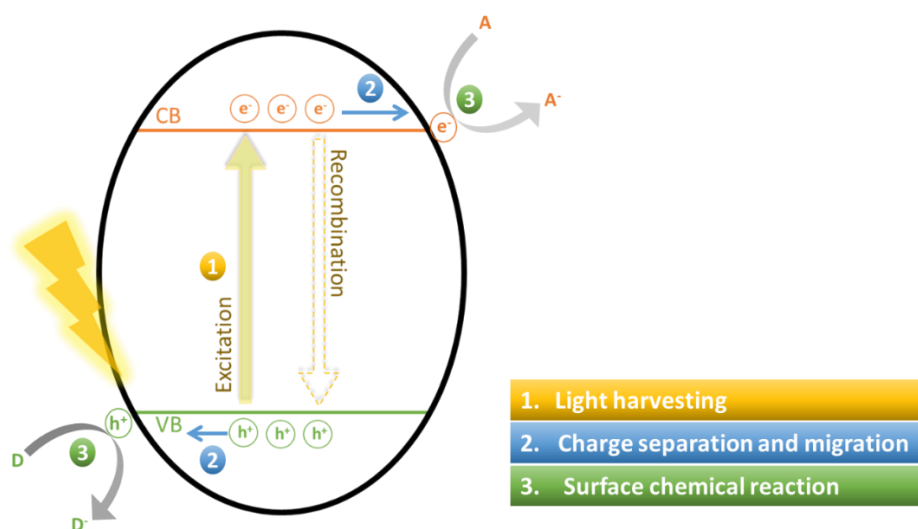


**Figure 1.8.** Schematic illustration of a typical semiconductor photocatalytic reaction.

Exploiting solar energy with remarkable efficiency, g-C<sub>3</sub>N<sub>4</sub> has found practical utility as a photocatalyst <sup>190</sup>. While bulk g-C<sub>3</sub>N<sub>4</sub> is limited to absorb exclusively blue light (about 450 nm) due to its relatively large band gap of about 2.7 eV, as well as surface confinement and fast charge recombination, innovative modifications have been made to improve. Notably, the graphitic carbon nitride nanosheets structure has attracted significant attention due to its expansive surface area and exceptional charge migration capabilities <sup>126</sup>. As demonstrated in Table 1.1, a variety of photocatalytic materials based on g-C<sub>3</sub>N<sub>4</sub> nanosheets have been applied in three main areas: the degradation of aqueous and gaseous pollutants, the splitting of water to produce H<sub>2</sub> and O<sub>2</sub>, and the photoreduction of CO<sub>2</sub>.

**Table 1.1.** Photocatalytic performance of some g-C<sub>3</sub>N<sub>4</sub> nanosheets-based materials.

Catalyst	g-C <sub>3</sub> N <sub>4</sub>		Specific surface area (m <sup>2</sup> g <sup>-1</sup> )	co-catalysts	Photocatalytic application	Photocatalytic activity
	Nanostructure	preparation method				
GS-CN <sup>191</sup>	Nanosheets	steam etching of bulk g-C <sub>3</sub> N <sub>4</sub>	66.3	3 wt % Pt	H <sub>2</sub> evolution Degradation of RhB and MO	0.658 mmol·g <sup>-1</sup> ·h <sup>-1</sup> 100% in 1 h
CN-Ex3/air <sup>192</sup>	Nanosheets	Pyrolysis	143	-	Degradation of Acid Orange 7	100% in 2 h
gCN <sup>193</sup>	Nanosheets	Pyrolysis	60.5	-	NO oxidation H <sub>2</sub> evolution	35.8% 764.8 μmol g <sup>-1</sup> h <sup>-1</sup>
R-CN-500 <sup>194</sup>	Nanosheets	Pyrolysis	143	-	NO oxidation	65.0%
SnO <sub>2</sub> -x/g-C <sub>3</sub> N <sub>4</sub> <sup>195</sup>	Nanosheets	Pyrolysis	-	SnO <sub>2</sub> -x	NO oxidation	40.8%
CeO <sub>2</sub> /g-C <sub>3</sub> N <sub>4</sub> <sup>196</sup>	Nanosheets	Pyrolysis	18.7	28.3 wt.% CeO <sub>2</sub>	Degradation of BPA	93.7% in 80 min
GCN-500 <sup>197</sup>	Nanosheets	Pyrolysis	111	-	Degradation of Parabens	100% in 20 min
CNPS-NH <sub>2</sub> <sup>152</sup>	Nanosheets	Pyrolysis	195.3	-	H <sub>2</sub> evolution	1233.5 μmol g <sup>-1</sup> h <sup>-1</sup>
g-CN-X <sup>198</sup>	Nanosheets	Pyrolysis	140.9	-	H <sub>2</sub> evolution CO <sub>2</sub> reduction	27.6 mmol g <sup>-1</sup> h <sup>-1</sup> 226.1 μmol g <sup>-1</sup> h <sup>-1</sup>
UCN-200 <sup>199</sup>	Nanosheets	Hydrothermal	128.5	-	H <sub>2</sub> evolution	1254.75 μmol g <sup>-1</sup> h <sup>-1</sup>
Co <sub>3</sub> O <sub>4</sub> /CNS <sup>200</sup>	Nanosheets	sulfur-mediated	-	3 wt% Co <sub>3</sub> O <sub>4</sub>	O <sub>2</sub> evolution	25.1 μmol g <sup>-1</sup> h <sup>-1</sup>

Photocatalytic removal of pollutants is one of the most important reactions in environmental catalysis. In this context, Fernandes et al.<sup>197</sup> turned their focus to the photocatalytic degradation of multiple parabens, using exfoliated g-C<sub>3</sub>N<sub>4</sub> under visible light exposure. Remarkably, within only 20 minutes of irradiation, they achieved complete degradation of each paraben, highlighting the effectiveness of g-C<sub>3</sub>N<sub>4</sub> as a photocatalyst for paraben removal. Furthermore, Long et al.<sup>191</sup> prepared porous few-layer nanosheets of g-C<sub>3</sub>N<sub>4</sub>, exhibiting an 18.3-fold increase in hydrogen evolution rate compared to pristine bulk g-C<sub>3</sub>N<sub>4</sub>. Notably, these nanosheets also displayed exceptional activity and stability for the photocatalytic degradation of RhB and MO. Alongside its ability to degrade aqueous pollutants, g-C<sub>3</sub>N<sub>4</sub> nanosheets extend its application to the photocatalytic removal of gaseous pollutants such as nitrogen monoxide (NO). Employing a hydrothermal pre-treatment-based approach, Huang et al.<sup>201</sup> succeeded in preparing high-quality thin-layered g-C<sub>3</sub>N<sub>4</sub>. This innovation

yielded significantly increased visible-light photocatalytic efficiency for NO removal, achieving a remarkable 5.5-fold improvement in efficiency over bulk g-C<sub>3</sub>N<sub>4</sub>. Similarly, Liu et al.<sup>202</sup> employed the co-pyrolysis of melamine and NH<sub>4</sub>HCO<sub>3</sub> to synthesize porous g-C<sub>3</sub>N<sub>4</sub> characterized by an enhanced specific surface area. This advancement led to a significantly improved photocatalytic performance for NO removal.

As one of the pivotal photocatalytic energy reactions, the utilization of g-C<sub>3</sub>N<sub>4</sub> nanosheet materials for photocatalytic water splitting to produce H<sub>2</sub> has gained extensive attention. The employment of solar energy to initiate water splitting, leading to H<sub>2</sub> generation through a photocatalyst, stands as an ideal solution to address the energy crisis and the greenhouse effect, presenting a pathway to offer environmentally friendly and sustainable energy<sup>152,198,199,201,203,204</sup>. Since the exploration of g-C<sub>3</sub>N<sub>4</sub> as a photocatalytic material, it has been demonstrated to possess the capability for water splitting to produce H<sub>2</sub>. Notably, the controlled nanostructure of g-C<sub>3</sub>N<sub>4</sub> nanosheets led to improved performance over bulk g-C<sub>3</sub>N<sub>4</sub>, although the improvement is not yet considered significant. However, the incorporation of a Pt cocatalyst has significantly increased the photocatalytic activity of H<sub>2</sub> evolution. Chen et al.<sup>199</sup> have produced ultra-thin g-C<sub>3</sub>N<sub>4</sub> nanosheets through the repolymerization of pristine, fluffy precursors. These ultra-thin g-C<sub>3</sub>N<sub>4</sub> nanosheets exhibit a large specific surface area (128.5 m<sup>2</sup> g<sup>-1</sup>) and demonstrate exceptional and stable photocatalytic hydrogen evolution performance (1254.75 μmol g<sup>-1</sup> h<sup>-1</sup>), a remarkable 21.9 times higher than that of pristine g-C<sub>3</sub>N<sub>4</sub>. However, in contrast to photocatalytic H<sub>2</sub> evolution, the exploration of photocatalytic O<sub>2</sub> evolution based on g-C<sub>3</sub>N<sub>4</sub> nanosheets has been relatively limited, serving as the lesser-attempted half-reaction within water splitting. The process of photocatalytic H<sub>2</sub>O oxidation to produce O<sub>2</sub> proves to be more intricate due to its involvement in a 4-electron reaction, which presents slower kinetics<sup>126,200,205</sup>. In this regard, Wang et al.<sup>200</sup> loaded Co<sub>3</sub>O<sub>4</sub> nanoparticles onto g-C<sub>3</sub>N<sub>4</sub> nanosheets, creating a Co<sub>3</sub>O<sub>4</sub>/CNS hybrid photocatalyst. The incorporation of this hybrid heterojunction facilitated efficient charge separation, effectively reduced the overpotential for water oxidation, and thereby achieving noteworthy photocatalytic O<sub>2</sub> evolution activity (25.1 μmol g<sup>-1</sup> h<sup>-1</sup>) under visible light, with a notable apparent quantum yield of 1.1% at 420 nm.

In addition, the photocatalytic reduction of CO<sub>2</sub> to produce chemical fuels and high-value compounds is of great importance. This process not only addresses the greenhouse effect and reduces environmental pressure, but also contributes to the production of renewable energy in response to the prevailing energy crisis<sup>126,198,205</sup>. In this pursuit, Hou et al.<sup>198</sup> have successfully synthesized graphitic carbon nitride (g-CN-X) nanosheets containing N-vacancy and C-doped defects. Remarkably, the optimized catalyst has shown an impressive hydrogen evolution rate of 27.6 mmol h<sup>-1</sup> g<sup>-1</sup>, surpassing the yield of bulk gCN by an impressive factor of 16.2. This increased activity is

accompanied by an apparent quantum yield of 9.1 % at 420 nm wavelength. Moreover, the optimized catalyst has exhibited a remarkable capability in the photoreduction of CO<sub>2</sub>, yielding a CO production rate of 226.1 μmol h<sup>-1</sup> g<sup>-1</sup>, a noteworthy increase of approximately 28.6 times when contrasted with the output from bulk g-CN (7.9 μmol h<sup>-1</sup> g<sup>-1</sup>).

#### 1.2.4.2. *Heterogeneous catalysis*

Based on the previous section, g-C<sub>3</sub>N<sub>4</sub> emerges as a promising and viable alternative for photocatalytic applications. Nonetheless, it is worth noting that surface terminations and defects play a pivotal role as the actual active sites in heterogeneous catalysis. These defects offer access to chemical modifications, which are advantageous for manipulating catalyst properties<sup>206</sup>. In addition, g-C<sub>3</sub>N<sub>4</sub> possesses several attractive features that make it suitable as both a metal-free catalyst and a sought-after catalyst support. Notably, its nitrogen-rich nature, combined with the incompletely condensed amino-functional groups, along with the tertiary and aromatic amines in its structure, gives it Lewis base catalyst properties<sup>207</sup>. This feature ensures the availability of abundant active sites for metal-free catalysis. Furthermore, the abundance of nitrogen also provides numerous anchoring sites for metal nanoparticles when g-C<sub>3</sub>N<sub>4</sub> is used as heterogeneous catalyst support<sup>30,208</sup>. Of utmost importance is its role as an organic polymer semiconductor capable of producing delocalized electron states, creating an interconnected relationship between the metal particles and g-C<sub>3</sub>N<sub>4</sub>. The work functions of most noble metals lie within the energy range between the conduction band and the valence band of g-C<sub>3</sub>N<sub>4</sub>. Metal particles with higher work function can give an elevated Schottky barrier, and thus enhanced charge separation at the interface of the metal-semiconductor heterojunction<sup>209</sup>. The enhanced charge separation has a great impact on the catalytic performance of the catalyst. In light of these considerations, g-C<sub>3</sub>N<sub>4</sub> would not only be just a metal carrier, but also an "active support" that promotes the catalytic activity or selectivity of the metal particles.

In this context, the incorporation of g-C<sub>3</sub>N<sub>4</sub> into the field of heterogeneous catalysis, either as a catalyst or as catalyst support, is emerging as a highly promising avenue for the development of efficient and sustainable catalytic processes. Bare g-C<sub>3</sub>N<sub>4</sub> possesses distinctive electrochemical and photoelectrochemical properties, attributed to its abundant surface attributes and structural merits<sup>127</sup>. However, these catalytic features inherent in g-C<sub>3</sub>N<sub>4</sub> are lacking in fully promoted catalytic processes. This deficiency stems from the limitations posed by the inferior surface area, low electrical conductivity, insufficient gas adsorption/activation/dissociation capacity, and inadequate visible light absorption properties exhibited by pristine g-C<sub>3</sub>N<sub>4</sub> nanostructures. Consequently, their practical viability in catalytic applications is hindered. In addition, oxygen-free g-C<sub>3</sub>N<sub>4</sub> fails to

facilitate gas activation, adsorption, or dissociation, necessitating the incorporation of additional metals, heteroatoms, and metal oxides into g-C<sub>3</sub>N<sub>4</sub>-based nanostructures. These incorporated elements serve as active sites that not only induce the adsorption and activation/decomposition of reactants but also allow the desorption of products during catalytic reactions. This is particularly important due to the challenges associated with the adsorption and activation of gaseous reactants at ambient atmospheric pressure and room temperature. In this regard, g-C<sub>3</sub>N<sub>4</sub>-based nanostructures take on the role of a support, engaging metals/oxides or non-metal atoms to fine-tune the reactant adsorption and activation/decomposition processes. This is accompanied by surface electron relocation to metal-free coordination along with tolerating the adsorption of intermediates during the reaction with the assistance of electron donation from C<sub>3</sub>N<sub>4</sub> to metals or non-metals<sup>210,211</sup>. These properties are predominantly shaped by factors such as preparation methods, porosity, defects, and doping, as previously mentioned<sup>134,212,213</sup>. Table 1.2 summarizes some of the catalytic materials based on g-C<sub>3</sub>N<sub>4</sub> nanosheets in various thermocatalytic reactions.

**Table 1.2.** Various thermocatalytic reactions over g-C<sub>3</sub>N<sub>4</sub> nanosheets.

Catalyst	g-C <sub>3</sub> N <sub>4</sub>		Specific surface area (m <sup>2</sup> g <sup>-1</sup> )	Catalytic application	Catalytic activity
	Nanostructure	Preparation method			
Ni-La/eg-C <sub>3</sub> N <sub>4</sub> <sup>214</sup>	Nanosheets	Pyrolysis	48	CO methanation CO <sub>2</sub> methanation	X <sub>CO</sub> = 72%, S <sub>CH<sub>4</sub></sub> = 89% X <sub>CO<sub>2</sub></sub> = 83%, S <sub>CH<sub>4</sub></sub> > 99%
Ni/g-C <sub>3</sub> N <sub>4</sub> <sup>215</sup>	Nanosheets	Pyrolysis	179	CO <sub>2</sub> methanation	X <sub>CO<sub>2</sub></sub> = 20%, S <sub>CH<sub>4</sub></sub> > 80%
Cu <sub>2</sub> O/g-C <sub>3</sub> N <sub>4</sub> <sup>216</sup>	Nanosheets	Pyrolysis	293	CO oxidation	X <sub>CO</sub> = 100% at 200°C
Co <sub>3</sub> O <sub>4</sub> /g-CN <sup>217</sup>	Nanosheets	Hydrothermal	10	CO oxidation	X <sub>CO</sub> = 100% at 200°C
Co <sub>3</sub> O <sub>4</sub> /mpg-CN <sup>217</sup>	Sponge-like		42		X <sub>CO</sub> = 100% at 160°C
Co <sub>3</sub> O <sub>4</sub> /g-CN <sup>218</sup>	Nanosheets	Pyrolysis	64	deN <sub>2</sub> O	X <sub>CO</sub> = 100% at 400°C
Ni/mpg-C <sub>3</sub> N <sub>4</sub> <sup>219</sup>	Nanosheets	Pyrolysis	48	CO methanation	X <sub>CO</sub> = 79.7%, S <sub>CH<sub>4</sub></sub> = 73.9%

Ahmad et al.<sup>214</sup> synthesized nickel catalysts on mesoporous g-C<sub>3</sub>N<sub>4</sub> sheets, studying the effect of air and nitrogen calcination for CO methanation. The results revealed that air calcination increased the catalyst surface area due to the creation of mesopores and the exfoliation of bulk g-C<sub>3</sub>N<sub>4</sub> to form thin sheets. In contrast, excessive Ni content in the catalyst decomposed the g-C<sub>3</sub>N<sub>4</sub> support during

calcination. 10% Ni/mpg-C<sub>3</sub>N<sub>4</sub> catalyst air-calcined displayed enhanced CO methanation due to increased active sites. Shi et al.<sup>216</sup> developed a Cu<sub>2</sub>O/g-C<sub>3</sub>N<sub>4</sub> composite via a simple impregnation method. They studied how different Cu<sub>2</sub>O loadings affected CO oxidation catalytic activity. At a 4:10 Cu<sub>2</sub>O to g-C<sub>3</sub>N<sub>4</sub> ratio, the composite demonstrated remarkable stability, maintaining 100% CO conversion for over 12 hours (200 °C). The strong performance was attributed to synergies between g-C<sub>3</sub>N<sub>4</sub> and Cu<sub>2</sub>O, improved dispersion, and smaller Cu<sub>2</sub>O particle size. Hu et al.<sup>218</sup> developed a Co<sub>3</sub>O<sub>4</sub>/g-C<sub>3</sub>N<sub>4</sub> nanosheets catalyst using impregnation synthesis and tested its performance in catalytic deN<sub>2</sub>O. They also prepared bare Co<sub>3</sub>O<sub>4</sub> and other Co<sub>3</sub>O<sub>4</sub> catalysts supported on activated carbon (AC) and  $\gamma$ -Al<sub>2</sub>O<sub>3</sub> for comparison. While g-C<sub>3</sub>N<sub>4</sub> effectively decomposed N<sub>2</sub>O, AC and  $\gamma$ -Al<sub>2</sub>O<sub>3</sub> were inactive. Co<sub>3</sub>O<sub>4</sub>/g-C<sub>3</sub>N<sub>4</sub> demonstrated superior catalytic activity compared to other catalysts, with significantly higher specific activity than bare Co<sub>3</sub>O<sub>4</sub>. Therefore, the literature suggests that g-C<sub>3</sub>N<sub>4</sub> sheets are promising as supports for various catalytic oxidation and hydrogenation reactions.

## References

- (1) Yang, W.; Wang, X.; Song, S.; Zhang, H. Syntheses and Applications of Noble-Metal-Free CeO<sub>2</sub>-Based Mixed-Oxide Nanocatalysts. *Chem* **2019**, *5* (7), 1743–1774. <https://doi.org/10.1016/j.chempr.2019.04.009>.
- (2) Su, X.; Yang, X.; Zhao, B.; Huang, Y. Designing of Highly Selective and High-Temperature Endurable RWGS Heterogeneous Catalysts: Recent Advances and the Future Directions. *J. Energy Chem.* **2017**, *26* (5), 854–867. <https://doi.org/10.1016/j.jechem.2017.07.006>.
- (3) Fang, Y.; Guo, Y. Copper-Based Non-Precious Metal Heterogeneous Catalysts for Environmental Remediation. *Cuihua Xuebao/Chinese J. Catal.* **2018**, *39* (4), 566–582. [https://doi.org/10.1016/S1872-2067\(17\)62996-6](https://doi.org/10.1016/S1872-2067(17)62996-6).
- (4) Montini, T.; Melchionna, M.; Monai, M.; Fornasiero, P. Fundamentals and Catalytic Applications of CeO<sub>2</sub>-Based Materials. *Chem. Rev.* **2016**, *116* (10), 5987–6041. <https://doi.org/10.1021/acs.chemrev.5b00603>.
- (5) Rodriguez, J. A.; Liu, P.; Graciani, J.; Senanayake, S. D.; Grinter, D. C.; Stacchiola, D.; Hrbek, J.; Fernández-Sanz, J. Inverse Oxide/Metal Catalysts in Fundamental Studies and Practical Applications: A Perspective of Recent Developments. *J. Phys. Chem. Lett.* **2016**, *7* (13), 2627–2639. <https://doi.org/10.1021/acs.jpcclett.6b00499>.
- (6) Melchionna, M.; Fornasiero, P. The Role of Ceria-Based Nanostructured Materials in Energy Applications. *Mater. Today* **2014**, *17* (7), 349–357. <https://doi.org/10.1016/j.mattod.2014.05.005>.
- (7) Yao, X.; Tang, C.; Gao, F.; Dong, L. Research Progress on the Catalytic Elimination of Atmospheric Molecular Contaminants over Supported Metal-Oxide Catalysts. *Catal. Sci. Technol.* **2014**, *4* (9), 2814–2829. <https://doi.org/10.1039/c4cy00397g>.
- (8) Yuan, C.; Wu, H. Bin; Xie, Y.; Lou, X. W. Mixed Transition-Metal Oxides: Design, Synthesis, and Energy-Related Applications. *Angew. Chemie - Int. Ed.* **2014**, *53* (6), 1488–1504. <https://doi.org/10.1002/anie.201303971>.
- (9) Konsolakis, M.; Lykaki, M. Facet-Dependent Reactivity of Ceria Nanoparticles Exemplified by CeO<sub>2</sub>-Based Transition Metal Catalysts: A Critical Review. *Catalysts* **2021**, *11* (4). <https://doi.org/10.3390/catal11040452>.
- (10) Tang, W.-X.; Gao, P.-X. Nanostructured Cerium Oxide: Preparation, Characterization, and Application in Energy and Environmental Catalysis. *MRS Commun.* **2016**, *6* (04), 311–329. <https://doi.org/10.1557/mrc.2016.52>.
- (11) Konsolakis, M.; Lykaki, M. Recent Advances on the Rational Design of Non-Precious Metal Oxide Catalysts Exemplified by CuO<sub>x</sub>/CeO<sub>2</sub> Binary System: Implications of Size, Shape and

- Electronic Effects on Intrinsic Reactivity and Metal-Support Interactions. *Catalysts* **2020**, *10* (2), 160. <https://doi.org/10.3390/catal10020160>.
- (12) Sapi, A.; Rajkumar, T.; Kiss, J.; Kukovecz, ..; Konya, Z.; Somorjai, G. A. Metallic Nanoparticles in Heterogeneous Catalysis. *Catal. Letters* **2021**, *151* (8), 2153–2175. <https://doi.org/10.1007/s10562-020-03477-5>.
- (13) Zhuang, G.; Chen, Y.; Zhuang, Z.; Yu, Y.; Yu, J. Oxygen Vacancies in Metal Oxides: Recent Progress towards Advanced Catalyst Design. *Sci. China Mater.* **2020**, *63* (11), 2089–2118. <https://doi.org/10.1007/s40843-020-1305-6>.
- (14) Konsolakis, M.; Sgourakis, M.; Carabineiro, S. A. C. Surface and Redox Properties of Cobalt–Cerium Binary Oxides: On the Effect of Co Content and Pretreatment Conditions. *Appl. Surf. Sci.* **2015**, *341*, 48–54. <https://doi.org/10.1016/j.apsusc.2015.02.188>.
- (15) Cargnello, M.; Doan-Nguyen, V. V. T.; Gordon, T. R.; Diaz, R. E.; Stach, E. A.; Gorte, R. J.; Fornasiero, P.; Murray, C. B. Control of Metal Nanocrystal Size Reveals Metal-Support Interface Role for Cerium Catalysts. *Science* (80-. ). **2013**, *341* (6147), 771–773. <https://doi.org/10.1126/science.1240148>.
- (16) Konsolakis, M. The Role of Copper–Cerium Interactions in Catalysis Science: Recent Theoretical and Experimental Advances. *Appl. Catal. B Environ.* **2016**, *198*, 49–66. <https://doi.org/10.1016/j.apcatb.2016.05.037>.
- (17) Dong, L.; Yao, X.; Chen, Y. Interactions among Supported Copper-Based Catalyst Components and Their Effects on Performance: A Review. *Cuihua Xuebao/Chinese J. Catal.* **2013**, *34* (5), 851–864. [https://doi.org/10.1016/s1872-2067\(12\)60592-0](https://doi.org/10.1016/s1872-2067(12)60592-0).
- (18) Capdevila-Cortada, M.; Vile, G.; Teschner, D.; Perez-Ramerez, J.; Lopez, N. Reactivity Descriptors for Cerium in Catalysis. *Appl. Catal. B Environ.* **2016**, *197*, 299–312. <https://doi.org/10.1016/j.apcatb.2016.02.035>.
- (19) Senanayake, S. D.; Rodriguez, J. A.; Stacchiola, D. Electronic Metal-Support Interactions and the Production of Hydrogen through the Water-Gas Shift Reaction and Ethanol Steam Reforming: Fundamental Studies with Well-Defined Model Catalysts. *Top. Catal.* **2013**, *56* (15–17), 1488–1498. <https://doi.org/10.1007/s11244-013-0148-5>.
- (20) Rodriguez, J. A.; Grinter, D. C.; Liu, Z.; Palomino, R. M.; Senanayake, S. D. Cerium-Based Model Catalysts: Fundamental Studies on the Importance of the Metal-Cerium Interface in CO Oxidation, the Water-Gas Shift, CO<sub>2</sub> Hydrogenation, and Methane and Alcohol Reforming. *Chem. Soc. Rev.* **2017**, *46* (7), 1824–1841. <https://doi.org/10.1039/c6cs00863a>.
- (21) Razmgar, K.; Altarawneh, M.; Oluwoye, I.; Senanayake, G. Cerium-Based Catalysts for Selective Hydrogenation Reactions: A Critical Review. *Catal. Surv. from Asia* **2021**, *25* (1),

27–47. <https://doi.org/10.1007/s10563-020-09319-z>.

- (22) Puigdollers, A. R.; Schlexer, P.; Tosoni, S.; Pacchioni, G. Increasing Oxide Reducibility: The Role of Metal/Oxide Interfaces in the Formation of Oxygen Vacancies. *ACS Catal.* **2017**, *7* (10), 6493–6513. <https://doi.org/10.1021/acscatal.7b01913>.
- (23) Di Sarli, V.; Landi, G.; Di Benedetto, A.; Lisi, L. Synergy Between Ceria and Metals (Ag or Cu) in Catalytic Diesel Particulate Filters: Effect of the Metal Content and of the Preparation Method on the Regeneration Performance. *Top. Catal.* **2021**, *64* (3–4), 256–269. <https://doi.org/10.1007/s11244-020-01384-y>.
- (24) Hermes, E. D.; Jenness, G. R.; Schmidt, J. R. Decoupling the Electronic, Geometric and Interfacial Contributions to Support Effects in Heterogeneous Catalysis. *Mol. Simul.* **2015**, *41* (1–3), 123–133. <https://doi.org/10.1080/08927022.2014.926549>.
- (25) Uzunoglu, A.; Zhang, H.; Andreescu, S.; Stanciu, L. A. CeO<sub>2</sub>–MO<sub>x</sub> (M: Zr, Ti, Cu) Mixed Metal Oxides with Enhanced Oxygen Storage Capacity. *J. Mater. Sci.* **2015**, *50* (10), 3750–3762. <https://doi.org/10.1007/s10853-015-8939-7>.
- (26) Veerakumar, P.; Thanasekaran, P.; Subburaj, T.; Lin, K.-C. A Metal-Free Carbon-Based Catalyst: An Overview and Directions for Future Research. *C* **2018**, *4* (4), 54. <https://doi.org/10.3390/c4040054>.
- (27) Liu, L.; Zhu, Y. P.; Su, M.; Yuan, Z. Y. Metal-Free Carbonaceous Materials as Promising Heterogeneous Catalysts. *ChemCatChem* **2015**, *7* (18), 2765–2787. <https://doi.org/10.1002/cctc.201500350>.
- (28) Liang, Y. N.; Oh, W. Da; Li, Y.; Hu, X. Nanocarbons as Platforms for Developing Novel Catalytic Composites: Overview and Prospects. *Appl. Catal. A Gen.* **2018**, *562* (May), 94–105. <https://doi.org/10.1016/j.apcata.2018.05.021>.
- (29) Pérez-Mayoral, E.; Calvino-Casilda, V.; Soriano, E. Metal-Supported Carbon-Based Materials: Opportunities and Challenges in the Synthesis of Valuable Products. *Catal. Sci. Technol.* **2016**, *6* (5), 1265–1291. <https://doi.org/10.1039/c5cy01437a>.
- (30) Gong, Y.; Li, M.; Li, H.; Wang, Y. Graphitic Carbon Nitride Polymers: Promising Catalysts or Catalyst Supports for Heterogeneous Oxidation and Hydrogenation. *Green Chem.* **2015**, *17* (2), 715–736. <https://doi.org/10.1039/c4gc01847h>.
- (31) Pérez-Mayoral, E.; Matos, I.; Bernardo, M.; Ventura, M.; Fonseca, I. M. Carbon-Based Materials for the Development of Highly Dispersed Metal Catalysts: Towards Highly Performant Catalysts for Fine Chemical Synthesis. *Catalysts* **2020**, *10* (12), 1–24. <https://doi.org/10.3390/catal10121407>.
- (32) Shen, Z.; Xing, X.; Wang, S.; Zheng, Z.; Lv, M. Low Temperature CO Oxidation from

- Sintering Flue Gas on CuO-CeO<sub>2</sub>/AC-Fe Catalyst. *Catal. Today* **2023**, No. December, 113988. <https://doi.org/10.1016/j.cattod.2022.12.019>.
- (33) Xiao, M.; Zhang, X.; Yang, Y.; Cui, X.; Chen, T.; Wang, Y. M (M = Mn, Co, Cu)-CeO<sub>2</sub> Catalysts to Enhance Their CO Catalytic Oxidation at a Low Temperature: Synergistic Effects of the Interaction between Ce<sup>3+</sup>-Mx+-Ce<sup>4+</sup> and the Oxygen Vacancy Defects. *Fuel* **2022**, 323 (April), 124379. <https://doi.org/10.1016/j.fuel.2022.124379>.
- (34) Martínez-Munuera, J. C.; Serrano-Martínez, V. M.; Giménez-Mañogil, J.; Yeste, M. P.; García-García, A. Unraveling the Nature of Active Sites onto Copper/Ceria-Zirconia Catalysts for Low Temperature CO Oxidation. *Catal. Today* **2022**, 384–386 (April 2021), 246–256. <https://doi.org/10.1016/j.cattod.2021.03.026>.
- (35) Hou, T.; Yu, B.; Zhang, S.; Xu, T.; Wang, D.; Cai, W. Hydrogen Production from Ethanol Steam Reforming over Rh/CeO<sub>2</sub> Catalyst. *Catal. Commun.* **2015**, 58, 137–140. <https://doi.org/10.1016/j.catcom.2014.09.020>.
- (36) da Silva, A. M.; de Souza, K. R.; Jacobs, G.; Graham, U. M.; Davis, B. H.; Mattos, L. V.; Noronha, F. B. Steam and CO<sub>2</sub> Reforming of Ethanol over Rh/CeO<sub>2</sub> Catalyst. *Appl. Catal. B Environ.* **2011**, 102 (1–2), 94–109. <https://doi.org/10.1016/j.apcatb.2010.11.030>.
- (37) Kumar, P. A.; Tanwar, M. D.; Russo, N.; Pirone, R.; Fino, D. Synthesis and Catalytic Properties of CeO<sub>2</sub> and Co/CeO<sub>2</sub> Nanofibres for Diesel Soot Combustion. *Catal. Today* **2012**, 184 (1), 279–287. <https://doi.org/10.1016/j.cattod.2011.12.025>.
- (38) Aneggi, E.; Wiater, D.; de Leitenburg, C.; Llorca, J.; Trovarelli, A. Shape-Dependent Activity of Ceria in Soot Combustion. *ACS Catal.* **2014**, 4 (1), 172–181. <https://doi.org/10.1021/cs400850r>.
- (39) Muroyama, H.; Hano, S.; Matsui, T.; Eguchi, K. Catalytic Soot Combustion over CeO<sub>2</sub>-Based Oxides. *Catal. Today* **2010**, 153 (3–4), 133–135. <https://doi.org/10.1016/j.cattod.2010.02.015>.
- (40) López Cámara, A.; Cortés Corberán, V.; Martínez-Arias, A.; Barrio, L.; Si, R.; Hanson, J. C.; Rodríguez, J. A. Novel Manganese-Promoted Inverse CeO<sub>2</sub>/CuO Catalyst: In Situ Characterization and Activity for the Water-Gas Shift Reaction. *Catal. Today* **2020**, 339 (January 2019), 24–31. <https://doi.org/10.1016/j.cattod.2019.01.014>.
- (41) Ronda-Lloret, M.; Rico-Francés, S.; Sepúlveda-Escribano, A.; Ramos-Fernandez, E. V. CuO<sub>x</sub>/CeO<sub>2</sub> Catalyst Derived from Metal Organic Framework for Reverse Water-Gas Shift Reaction. *Appl. Catal. A Gen.* **2018**, 562 (May), 28–36. <https://doi.org/10.1016/j.apcata.2018.05.024>.
- (42) Damaskinos, C. M.; Vasiliades, M. A.; Stathopoulos, V. N.; Efstathiou, A. M. The Effect of CeO<sub>2</sub> Preparation Method on the Carbon Pathways in the Dry Reforming of Methane on

- Ni/CeO<sub>2</sub> Studied by Transient Techniques. *Catalysts* **2019**, *9* (7), 621. <https://doi.org/10.3390/catal9070621>.
- (43) Chen, C.; Zhan, Y.; Zhou, J.; Li, D.; Zhang, Y.; Lin, X.; Jiang, L.; Zheng, Q. Cu/CeO<sub>2</sub> Catalyst for Water-Gas Shift Reaction: Effect of CeO<sub>2</sub> Pretreatment. *ChemPhysChem* **2018**, *19* (12), 1448–1455. <https://doi.org/10.1002/cphc.201800122>.
- (44) Akter, N.; Zhang, S.; Lee, J.; Kim, D. H.; Boscoboinik, J. A.; Kim, T. Selective Catalytic Reduction of NO by Ammonia and NO Oxidation Over CoO<sub>x</sub>/CeO<sub>2</sub> Catalysts. *Mol. Catal.* **2020**, *482* (July 2019), 110664. <https://doi.org/10.1016/j.mcat.2019.110664>.
- (45) Zhang, S.; Lee, J.; Kim, D. H.; Kim, T. NO Reduction by CO over CoO<sub>x</sub>/CeO<sub>2</sub> Catalysts: Effect of Support Calcination Temperature on Activity. *Mol. Catal.* **2020**, *482* (November 2019), 110703. <https://doi.org/10.1016/j.mcat.2019.110703>.
- (46) Zhang, S.; Li, Y.; Huang, J.; Lee, J.; Kim, D. H.; Frenkel, A. I.; Kim, T. Effects of Molecular and Electronic Structures in CoO<sub>x</sub>/CeO<sub>2</sub> Catalysts on NO Reduction by CO. *J. Phys. Chem. C* **2019**, *123* (12), 7166–7177. <https://doi.org/10.1021/acs.jpcc.8b12442>.
- (47) Chang, K.; Zhang, H.; Cheng, M.; Lu, Q. Application of Ceria in CO<sub>2</sub> Conversion Catalysis. *ACS Catal.* **2020**, *10* (1), 613–631. <https://doi.org/10.1021/acscatal.9b03935>.
- (48) Raza, R.; Zhu, B.; Rafique, A.; Naqvi, M. R.; Lund, P. Functional Ceria-Based Nanocomposites for Advanced Low-Temperature (300–600 °C) Solid Oxide Fuel Cell: A Comprehensive Review. *Mater. Today Energy* **2020**, *15*. <https://doi.org/10.1016/j.mtener.2019.100373>.
- (49) Ma, R.; Zhang, S.; Wen, T.; Gu, P.; Li, L.; Zhao, G.; Niu, F.; Huang, Q.; Tang, Z.; Wang, X. A Critical Review on Visible-Light-Response CeO<sub>2</sub>-Based Photocatalysts with Enhanced Photooxidation of Organic Pollutants. *Catal. Today* **2019**, *335* (October 2018), 20–30. <https://doi.org/10.1016/j.cattod.2018.11.016>.
- (50) Ma, Y.; Gao, W.; Zhang, Z.; Zhang, S.; Tian, Z.; Liu, Y.; Ho, J. C.; Qu, Y. Regulating the Surface of Nanoceria and Its Applications in Heterogeneous Catalysis. *Surf. Sci. Rep.* **2018**, *73* (1), 1–36. <https://doi.org/10.1016/j.surfrep.2018.02.001>.
- (51) Liu, L.; Corma, A. Metal Catalysts for Heterogeneous Catalysis: From Single Atoms to Nanoclusters and Nanoparticles. *Chem. Rev.* **2018**, *118* (10), 4981–5079. <https://doi.org/10.1021/acs.chemrev.7b00776>.
- (52) Mehrabadi, B. A. T.; Eskandari, S.; Khan, U.; White, R. D.; Regalbuto, J. R. *A Review of Preparation Methods for Supported Metal Catalysts*, 1st ed.; Elsevier Inc., 2017; Vol. 61. <https://doi.org/10.1016/bs.acat.2017.10.001>.
- (53) Jiang, Y.; Yang, H.; Gao, P.; Li, X.; Zhang, J.; Liu, H.; Wang, H.; Wei, W.; Sun, Y. Slurry

- Methanol Synthesis from CO<sub>2</sub> Hydrogenation over Micro-Spherical SiO<sub>2</sub> Support Cu/ZnO Catalysts. *J. CO<sub>2</sub> Util.* **2018**, *26* (July), 642–651. <https://doi.org/10.1016/j.jcou.2018.06.023>.
- (54) Reddy, K. P.; Kim, D.; Hong, S.; Kim, K.-J.; Ryoo, R.; Park, J. Y. Tuning CO<sub>2</sub> Hydrogenation Selectivity through Reaction-Driven Restructuring on Cu–Ni Bimetal Catalysts. *ACS Appl. Mater. Interfaces* **2023**, *15* (7), 9373–9381. <https://doi.org/10.1021/acsami.2c20832>.
- (55) Galhardo, T. S.; Braga, A. H.; Arpini, B. H.; Szanyi, J.; Gonçalves, R. V.; Zornio, B. F.; Miranda, C. R.; Rossi, L. M. Optimizing Active Sites for High CO Selectivity during CO<sub>2</sub> Hydrogenation over Supported Nickel Catalysts. *J. Am. Chem. Soc.* **2021**, *143* (11), 4268–4280. <https://doi.org/10.1021/jacs.0c12689>.
- (56) Zou, H.; Dong, X.; Lin, W. Selective CO Oxidation in Hydrogen-Rich Gas over CuO/CeO<sub>2</sub> Catalysts. *Appl. Surf. Sci.* **2006**, *253* (5), 2893–2898. <https://doi.org/10.1016/j.apsusc.2006.06.028>.
- (57) Yang, J.; Zhu, W.; Zhang, S.; Zhang, M.; Qu, W.; Li, H.; Zeng, Z.; Zhao, Y.; Zhang, J. Role of Flue Gas Components in Hg<sup>0</sup> Oxidation over La<sub>0.8</sub>Ce<sub>0.2</sub>MnO<sub>3</sub> Perovskite Catalyst in Coal Combustion Flue Gas. *Chem. Eng. J.* **2019**, *360* (July 2018), 1656–1666. <https://doi.org/10.1016/j.cej.2018.10.218>.
- (58) Xie, X.; Li, Y.; Liu, Z. Q.; Haruta, M.; Shen, W. Low-Temperature Oxidation of CO Catalysed by Co<sub>3</sub>O<sub>4</sub> Nanorods. *Nature* **2009**, *458* (7239), 746–749. <https://doi.org/10.1038/nature07877>.
- (59) Xia, Y.; Xiong, Y.; Lim, B.; Skrabalak, S. E. Shape-Controlled Synthesis of Metal Nanocrystals: Simple Chemistry Meets Complex Physics? *Angew. Chemie - Int. Ed.* **2009**, *48* (1), 60–103. <https://doi.org/10.1002/anie.200802248>.
- (60) Brodersen, S. H.; Grønberg, U.; Hvolbæk, B.; Schiøtz, J. Understanding the Catalytic Activity of Gold Nanoparticles through Multi-Scale Simulations. *J. Catal.* **2011**, *284* (1), 34–41. <https://doi.org/10.1016/j.jcat.2011.08.016>.
- (61) Zhang, L.; Zhou, M.; Wang, A.; Zhang, T. Selective Hydrogenation over Supported Metal Catalysts: From Nanoparticles to Single Atoms. *Chem. Rev.* **2020**, *120* (2), 683–733. <https://doi.org/10.1021/acs.chemrev.9b00230>.
- (62) Yang, Y.; Ren, Z.; Zhou, S.; Wei, M. Perspectives on Multifunctional Catalysts Derived from Layered Double Hydroxides toward Upgrading Reactions of Biomass Resources. *ACS Catal.* **2021**, *11*, 6440–6454. <https://doi.org/10.1021/acscatal.1c00699>.
- (63) Sichert, J. A.; Tong, Y.; Mutz, N.; Vollmer, M.; Fischer, S.; Milowska, K. Z.; García Cortadella, R.; Nickel, B.; Cardenas-Daw, C.; Stolarczyk, J. K.; Urban, A. S.; Feldmann, J. Quantum Size Effect in Organometal Halide Perovskite Nanoplatelets. *Nano Lett.* **2015**, *15*

- (10), 6521–6527. <https://doi.org/10.1021/acs.nanolett.5b02985>.
- (64) Trovarelli, A.; Llorca, J. Ceria Catalysts at Nanoscale: How Do Crystal Shapes Shape Catalysis? *ACS Catal.* **2017**, *7* (7), 4716–4735. <https://doi.org/10.1021/acscatal.7b01246>.
- (65) Li, Y.; Shen, W. *Morphology-Dependent Nanocatalysts: Rod-Shaped Oxides*; 2014; Vol. 43. <https://doi.org/10.1039/c3cs60296f>.
- (66) Cao, S.; Tao, F. F.; Tang, Y.; Li, Y.; Yu, J. Size- and Shape-Dependent Catalytic Performances of Oxidation and Reduction Reactions on Nanocatalysts. *Chem. Soc. Rev.* **2016**, *45* (17), 4747–4765. <https://doi.org/10.1039/c6cs00094k>.
- (67) Ta, N.; Liu, J.; Shen, W. Tuning the Shape of Ceria Nanomaterials for Catalytic Applications. *Cuihua Xuebao/Chinese J. Catal.* **2013**, *34* (5), 838–850. [https://doi.org/10.1016/s1872-2067\(12\)60573-7](https://doi.org/10.1016/s1872-2067(12)60573-7).
- (68) Zhou, K.; Li, Y. Catalysis Based on Nanocrystals with Well-Defined Facets. *Angew. Chemie - Int. Ed.* **2012**, *51* (3), 602–613. <https://doi.org/10.1002/anie.201102619>.
- (69) Wu, K.; Sun, L. D.; Yan, C. H. Recent Progress in Well-Controlled Synthesis of Ceria-Based Nanocatalysts towards Enhanced Catalytic Performance. *Adv. Energy Mater.* **2016**, *6* (17), 1–46. <https://doi.org/10.1002/aenm.201600501>.
- (70) Qiao, Z. A.; Wu, Z.; Dai, S. Shape-Controlled Ceria-Based Nanostructures for Catalysis Applications. *ChemSusChem* **2013**, *6* (10), 1821–1833. <https://doi.org/10.1002/cssc.201300428>.
- (71) Sun, C.; Xue, D. Size-Dependent Oxygen Storage Ability of Nano-Sized Ceria. *Phys. Chem. Chem. Phys.* **2013**, *15* (34), 14414–14419. <https://doi.org/10.1039/c3cp51959g>.
- (72) Stakheev, A. Y.; Kustov, L. M. Effects of the Support on the Morphology and Electronic Properties of Supported Metal Clusters: Modern Concepts and Progress in 1990s. *Appl. Catal. A Gen.* **1999**, *188* (1–2), 3–35. [https://doi.org/10.1016/S0926-860X\(99\)00232-X](https://doi.org/10.1016/S0926-860X(99)00232-X).
- (73) Lee, D. W.; Yoo, B. R. Advanced Metal Oxide (Supported) Catalysts: Synthesis and Applications. *J. Ind. Eng. Chem.* **2014**, *20* (6), 3947–3959. <https://doi.org/10.1016/j.jiec.2014.08.004>.
- (74) Konsolakis, M.; Aligizou, F.; Goula, G.; Yentekakis, I. V. N<sub>2</sub>O Decomposition over Doubly-Promoted Pt(K)/Al<sub>2</sub>O<sub>3</sub>-(CeO<sub>2</sub>-La<sub>2</sub>O<sub>3</sub>) Structured Catalysts: On the Combined Effects of Promotion and Feed Composition. *Chem. Eng. J.* **2013**, *230* (June), 286–295. <https://doi.org/10.1016/j.cej.2013.06.083>.
- (75) Yentekakis, I. .; Konsolakis, M.; Lambert, R. .; Macleod, N.; Nalbantian, L. Extraordinarily Effective Promotion by Sodium in Emission Control Catalysis: NO Reduction by Propene over Na-Promoted Pt/γ-Al<sub>2</sub>O<sub>3</sub>. *Appl. Catal. B Environ.* **1999**, *22* (2), 123–133.

[https://doi.org/10.1016/S0926-3373\(99\)00042-9](https://doi.org/10.1016/S0926-3373(99)00042-9).

- (76) Konsolakis, M.; Vrontaki, M.; Avgouropoulos, G.; Ioannides, T.; Yentekakis, I. V. Novel Doubly-Promoted Catalysts for the Lean NO<sub>x</sub> Reduction by H<sub>2</sub> + CO: Pd(K)/Al<sub>2</sub>O<sub>3</sub>-(TiO<sub>2</sub>). *Appl. Catal. B Environ.* **2006**, *68* (1–2), 59–67. <https://doi.org/10.1016/j.apcatb.2006.07.011>.
- (77) Cuenya, B. R. Synthesis and Catalytic Properties of Metal Nanoparticles: Size, Shape, Support, Composition, and Oxidation State Effects. *Thin Solid Films* **2010**, *518* (12), 3127–3150. <https://doi.org/10.1016/j.tsf.2010.01.018>.
- (78) Besenbacher, F.; Chorkendorff, I.; Clausen, B. S.; Hammer, B.; Molenbroek, A. M.; Nørskov, J. K.; Stensgaard, I. Design of a Surface Alloy Catalyst for Steam Reforming. *Science (80-. )*. **1998**, *279* (5358), 1913–1915. <https://doi.org/10.1126/science.279.5358.1913>.
- (79) Lamy, C.; Belgsir, E. M.; Léger, J. M. Electrocatalytic Oxidation of Aliphatic Alcohols: Application to the Direct Alcohol Fuel Cell (DAFC). *J. Appl. Electrochem.* **2001**, *31* (7), 799–809. <https://doi.org/10.1023/A:1017587310150>.
- (80) Pacchioni, G. Electronic Interactions and Charge Transfers of Metal Atoms and Clusters on Oxide Surfaces. *Phys. Chem. Chem. Phys.* **2013**, *15* (6), 1737. <https://doi.org/10.1039/c2cp43731g>.
- (81) Yang, F.; Deng, D.; Pan, X.; Fu, Q.; Bao, X. Understanding Nano Effects in Catalysis. *Natl. Sci. Rev.* **2015**, *2* (2), 183–201. <https://doi.org/10.1093/nsr/nwv024>.
- (82) Ren, Y.; Yang, Y.; Wei, M. Recent Advances on Heterogeneous Non-Noble Metal Catalysts toward Selective Hydrogenation Reactions. *ACS Catal.* **2023**, *13* (13), 8902–8924. <https://doi.org/10.1021/acscatal.3c01442>.
- (83) Xie, Y.; Wen, J.; Li, Z.; Chen, J.; Zhang, Q.; Ning, P.; Chen, Y.; Hao, J. Progress in Reaction Mechanisms and Catalyst Development of Ceria-Based Catalysts for Low-Temperature CO<sub>2</sub> Methanation. *Green Chem.* **2022**, *25* (1), 130–152. <https://doi.org/10.1039/d2gc03512j>.
- (84) Lykaki, M.; Pachatouridou, E.; Carabineiro, S. A. C.; Iliopoulou, E.; Andriopoulou, C.; Kallithrakas-Kontos, N.; Boghosian, S.; Konsolakis, M. Ceria Nanoparticles Shape Effects on the Structural Defects and Surface Chemistry: Implications in CO Oxidation by Cu/CeO<sub>2</sub> catalysts. *Appl. Catal. B Environ.* **2018**, *230* (February), 18–28. <https://doi.org/10.1016/j.apcatb.2018.02.035>.
- (85) Lee, K. J.; Kim, Y.; Lee, J. H.; Cho, S. J.; Kwak, J. H.; Moon, H. R. Facile Synthesis and Characterization of Nanostructured Transition Metal/Ceria Solid Solutions (TM<sub>x</sub>Ce<sub>1-x</sub>O<sub>2-δ</sub>, TM = Mn, Ni, Co, or Fe) for CO Oxidation. *Chem. Mater.* **2017**, *29* (7), 2874–2882. <https://doi.org/10.1021/acs.chemmater.6b05098>.
- (86) Sahoo, T. R.; Armandi, M.; Arletti, R.; Piumetti, M.; Bensaid, S.; Manzoli, M.; Panda, S. R.;

- Bonelli, B. Pure and Fe-Doped CeO<sub>2</sub> Nanoparticles Obtained by Microwave Assisted Combustion Synthesis: Physico-Chemical Properties Ruling Their Catalytic Activity towards CO Oxidation and Soot Combustion. *Appl. Catal. B Environ.* **2017**, *211* (August), 31–45. <https://doi.org/10.1016/j.apcatb.2017.04.032>.
- (87) Wang, C.; Wang, D.; Yang, Y.; Li, R.; Chen, C.; Chen, Q. Enhanced CO Oxidation on CeO<sub>2</sub>/Co<sub>3</sub>O<sub>4</sub> Nanojunctions Derived from Annealing of Metal Organic Frameworks. *Nanoscale* **2016**, *8* (47), 19761–19768. <https://doi.org/10.1039/c6nr07725k>.
- (88) Li, J.; Zhang, Z.; Gao, W.; Zhang, S.; Ma, Y.; Qu, Y. Pressure Regulations on the Surface Properties of CeO<sub>2</sub> Nanorods and Their Catalytic Activity for CO Oxidation and Nitrile Hydrolysis Reactions. *ACS Appl. Mater. Interfaces* **2016**, *8* (35), 22988–22996. <https://doi.org/10.1021/acsami.6b05343>.
- (89) Mock, S. A.; Sharp, S. E.; Stoner, T. R.; Radetic, M. J.; Zell, E. T.; Wang, R. CeO<sub>2</sub> Nanorods-Supported Transition Metal Catalysts for CO Oxidation. *J. Colloid Interface Sci.* **2016**, *466*, 261–267. <https://doi.org/10.1016/j.jcis.2015.12.026>.
- (90) Jampaiah, D.; Venkataswamy, P.; Coyle, V. E.; Reddy, B. M.; Bhargava, S. K. Low-Temperature CO Oxidation over Manganese, Cobalt, and Nickel Doped CeO<sub>2</sub> Nanorods. *RSC Adv.* **2016**, *6* (84), 80541–80548. <https://doi.org/10.1039/c6ra13577c>.
- (91) Park, Y.; Kim, S. K.; Pradhan, D.; Sohn, Y. Surface Treatment Effects on CO Oxidation Reactions over Co, Cu, and Ni-Doped and Codoped CeO<sub>2</sub> Catalysts. *Chem. Eng. J.* **2014**, *250*, 25–34. <https://doi.org/10.1016/j.cej.2014.03.070>.
- (92) Zhou, K.; Wang, X.; Sun, X.; Peng, Q.; Li, Y. Enhanced Catalytic Activity of Ceria Nanorods from Well-Defined Reactive Crystal Planes. *J. Catal.* **2005**, *229* (1), 206–212. <https://doi.org/10.1016/j.jcat.2004.11.004>.
- (93) Tana; Zhang, M.; Li, J.; Li, H.; Li, Y.; Shen, W. Morphology-Dependent Redox and Catalytic Properties of CeO<sub>2</sub> Nanostructures: Nanowires, Nanorods and Nanoparticles. *Catal. Today* **2010**, *148* (1–2), 179–183. <https://doi.org/10.1016/j.cattod.2009.02.016>.
- (94) Wu, Z.; Li, M.; Overbury, S. H. On the Structure Dependence of CO Oxidation over CeO<sub>2</sub> Nanocrystals with Well-Defined Surface Planes. *J. Catal.* **2012**, *285* (1), 61–73. <https://doi.org/10.1016/j.jcat.2011.09.011>.
- (95) Agarwal, S.; Zhu, X.; Hensen, E. J. M.; Lefferts, L.; Mojet, B. L. Defect Chemistry of Ceria Nanorods. *J. Phys. Chem. C* **2014**, *118* (8), 4131–4142. <https://doi.org/10.1021/jp409989y>.
- (96) Wu, Z.; Li, M.; Howe, J.; Meyer, H. M.; Overbury, S. H. Probing Defect Sites on CeO<sub>2</sub> Nanocrystals with Well-Defined Surface Planes by Raman Spectroscopy and O<sub>2</sub> Adsorption. *Langmuir* **2010**, *26* (21), 16595–16606. <https://doi.org/10.1021/la101723w>.

- (97) Huang, X. S.; Sun, H.; Wang, L. C.; Liu, Y. M.; Fan, K. N.; Cao, Y. Morphology Effects of Nanoscale Ceria on the Activity of Au/CeO<sub>2</sub> Catalysts for Low-Temperature CO Oxidation. *Appl. Catal. B Environ.* **2009**, *90* (1–2), 224–232. <https://doi.org/10.1016/j.apcatb.2009.03.015>.
- (98) Silvestre-Albero, J.; Rodríguez-Reinoso, F.; Sepúlveda-Escribano, A. Improved Metal-Support Interaction in Pt/CeO<sub>2</sub>-SiO<sub>2</sub> Catalysts after Zinc Addition. *J. Catal.* **2002**, *210* (1), 127–136. <https://doi.org/10.1006/jcat.2002.3670>.
- (99) Aryanpour, M.; Khetan, A.; Pitsch, H. Activity Descriptor for Catalytic Reactions on Doped Cerium Oxide. *ACS Catal.* **2013**, *3* (6), 1253–1262. <https://doi.org/10.1021/cs400034c>.
- (100) Ren, Y.; Ma, Z.; Qian, L.; Dai, S.; He, H.; Bruce, P. G. Ordered Crystalline Mesoporous Oxides as Catalysts for CO Oxidation. *Catal. Letters* **2009**, *131* (1–2), 146–154. <https://doi.org/10.1007/s10562-009-9931-0>.
- (101) Atspha, T. A.; Yoon, T.; Seongho, P.; Lee, C. J. A Review on the Catalytic Conversion of CO<sub>2</sub> using H<sub>2</sub> for Synthesis of CO, Methanol, and Hydrocarbons. *J. CO<sub>2</sub> Util.* **2021**, *44* (December 2020), 101413. <https://doi.org/10.1016/j.jcou.2020.101413>.
- (102) Hoekman, S. K.; Broch, A.; Robbins, C.; Purcell, R. CO<sub>2</sub> Recycling by Reaction with Renewably-Generated Hydrogen. *Int. J. Greenh. Gas Control* **2010**, *4* (1), 44–50. <https://doi.org/10.1016/j.ijggc.2009.09.012>.
- (103) Yang, N.; Wang, R. Sustainable Technologies for the Reclamation of Greenhouse Gas CO<sub>2</sub>. *J. Clean. Prod.* **2015**, *103*, 784–792. <https://doi.org/10.1016/j.jclepro.2014.10.025>.
- (104) Hepburn, C.; Adlen, E.; Beddington, J.; Carter, E. A.; Fuss, S.; Mac Dowell, N.; Minx, J. C.; Smith, P.; Williams, C. K. The Technological and Economic Prospects for CO<sub>2</sub> Utilization and Removal. *Nature* **2019**, *575* (7781), 87–97. <https://doi.org/10.1038/s41586-019-1681-6>.
- (105) Rafiee, A.; Rajab Khalilpour, K.; Milani, D.; Panahi, M. Trends in CO<sub>2</sub> Conversion and Utilization: A Review from Process Systems Perspective. *J. Environ. Chem. Eng.* **2018**, *6* (5), 5771–5794. <https://doi.org/10.1016/j.jece.2018.08.065>.
- (106) Kamkeng, A. D. N.; Wang, M.; Hu, J.; Du, W.; Qian, F. Transformation Technologies for CO<sub>2</sub> Utilisation: Current Status, Challenges and Future Prospects. *Chem. Eng. J.* **2021**, *409* (December 2020), 128138. <https://doi.org/10.1016/j.cej.2020.128138>.
- (107) Kacimi, S.; Barbier, J.; Taha, R.; Duprez, D. Oxygen Storage Capacity of Promoted Rh/CeC<sub>2</sub> Catalysts. Exceptional Behavior of RhCu/CeO<sub>2</sub>. *Catal. Letters* **1993**, *22* (4), 343–350. <https://doi.org/10.1007/BF00807243>.
- (108) Tada, S.; Ochieng, O. J.; Kikuchi, R.; Haneda, T.; Kameyama, H. Promotion of CO<sub>2</sub> Methanation Activity and CH<sub>4</sub> Selectivity at Low Temperatures over Ru/CeO<sub>2</sub>/Al<sub>2</sub>O<sub>3</sub>

- Catalysts. *Int. J. Hydrogen Energy* **2014**, *39* (19), 10090–10100. <https://doi.org/10.1016/j.ijhydene.2014.04.133>.
- (109) Martin, N. M.; Velin, P.; Skoglundh, M.; Bauer, M.; Carlsson, P. A. Catalytic Hydrogenation of CO<sub>2</sub> to Methane over Supported Pd, Rh and Ni Catalysts. *Catal. Sci. Technol.* **2017**, *7* (5), 1086–1094. <https://doi.org/10.1039/c6cy02536f>.
- (110) Karelavic, A.; Ruiz, P. CO<sub>2</sub> Hydrogenation at Low Temperature over Rh/ $\gamma$ -Al<sub>2</sub>O<sub>3</sub> Catalysts: Effect of the Metal Particle Size on Catalytic Performances and Reaction Mechanism. *Appl. Catal. B Environ.* **2012**, *113–114*, 237–249. <https://doi.org/10.1016/j.apcatb.2011.11.043>.
- (111) Varvoutis, G.; Lykaki, M.; Stefa, S.; Papista, E.; Carabineiro, S. A. C.; Marnellos, G. E.; Konsolakis, M. Remarkable Efficiency of Ni Supported on Hydrothermally Synthesized CeO<sub>2</sub> Nanorods for Low-Temperature CO<sub>2</sub> Hydrogenation to Methane. *Catal. Commun.* **2020**, *142* (March), 106036. <https://doi.org/10.1016/j.catcom.2020.106036>.
- (112) Konsolakis, M.; Lykaki, M.; Stefa, S.; Carabineiro, S. A. C.; Varvoutis, G.; Papista, E.; Marnellos, G. E. CO<sub>2</sub> Hydrogenation over Nanoceria-Supported Transition Metal Catalysts: Role of Ceria Morphology (Nanorods versus Nanocubes) and Active Phase Nature (Co versus Cu). *Nanomaterials* **2019**, *9* (12), 1739. <https://doi.org/10.3390/nano9121739>.
- (113) Jiang, F.; Wang, S.; Liu, B.; Liu, J.; Wang, L.; Xiao, Y.; Xu, Y.; Liu, X. Insights into the Influence of CeO<sub>2</sub> Crystal Facet on CO<sub>2</sub> Hydrogenation to Methanol over Pd/CeO<sub>2</sub> Catalysts. *ACS Catal.* **2020**, *10* (19), 11493–11509. <https://doi.org/10.1021/acscatal.0c03324>.
- (114) Fan, L.; Zhang, J.; Ma, K.; Zhang, Y.; Hu, Y. M.; Kong, L.; Jia, A. ping; Zhang, Z.; Huang, W.; Lu, J. Q. Ceria Morphology-Dependent Pd-CeO<sub>2</sub> Interaction and Catalysis in CO<sub>2</sub> Hydrogenation into Formate. *J. Catal.* **2021**, *397*, 116–127. <https://doi.org/10.1016/j.jcat.2021.03.025>.
- (115) Yang, B.; Wang, Y.; Li, L.; Gao, B.; Zhang, L.; Guo, L. Probing the Morphological Effects of ReO: X/CeO<sub>2</sub> catalysts on the CO<sub>2</sub> hydrogenation Reaction. *Catal. Sci. Technol.* **2022**, *12* (4), 1159–1172. <https://doi.org/10.1039/d1cy02096j>.
- (116) Khobragade, R.; Roškarič, M.; Žerjav, G.; Košiček, M.; Zavašnik, J.; Van de Velde, N.; Jerman, I.; Tušar, N. N.; Pintar, A. Exploring the Effect of Morphology and Surface Properties of Nanoshaped Pd/CeO<sub>2</sub> Catalysts on CO<sub>2</sub> Hydrogenation to Methanol. *Appl. Catal. A Gen.* **2021**, *627* (July). <https://doi.org/10.1016/j.apcata.2021.118394>.
- (117) Du, Y.; Qin, C.; Xu, Y.; Xu, D.; Bai, J.; Ma, G.; Ding, M. Ni Nanoparticles Dispersed on Oxygen Vacancies-Rich CeO<sub>2</sub> Nanoplates for Enhanced Low-Temperature CO<sub>2</sub> Methanation Performance. *Chem. Eng. J.* **2021**, *418* (March). <https://doi.org/10.1016/j.cej.2021.129402>.
- (118) Bian, Z.; Chan, Y. M.; Yu, Y.; Kawi, S. Morphology Dependence of Catalytic Properties of

- Ni/CeO<sub>2</sub> for CO<sub>2</sub> Methanation: A Kinetic and Mechanism Study. *Catal. Today* **2020**, *347* (April 2018), 31–38. <https://doi.org/10.1016/j.cattod.2018.04.067>.
- (119) Shen, L.; Xu, J.; Zhu, M.; Han, Y. F. Essential Role of the Support for Nickel-Based CO<sub>2</sub> Methanation Catalysts. *ACS Catal.* **2020**, *10* (24), 14581–14591. <https://doi.org/10.1021/acscatal.0c03471>.
- (120) Vrijburg, W. L.; Van Helden, J. W. A.; Parastaev, A.; Groeneveld, E.; Pidko, E. A.; Hensen, E. J. M. Ceria-Zirconia Encapsulated Ni Nanoparticles for CO<sub>2</sub> Methanation. *Catal. Sci. Technol.* **2019**, *9* (18), 5001–5010. <https://doi.org/10.1039/c9cy01428d>.
- (121) Yang, L.; Pastor-Pérez, L.; Villora-Pico, J. J.; Gu, S.; Sepúlveda-Escribano, A.; Reina, T. R. CO<sub>2</sub> Valorisation via Reverse Water-Gas Shift Reaction Using Promoted Fe/CeO<sub>2</sub>-Al<sub>2</sub>O<sub>3</sub> Catalysts: Showcasing the Potential of Advanced Catalysts to Explore New Processes Design. *Appl. Catal. A Gen.* **2020**, *593* (November 2019). <https://doi.org/10.1016/j.apcata.2020.117442>.
- (122) Varvoutis, G.; Lykaki, M.; Papista, E.; Carabineiro, S. nia A. C.; Psarras, A. C.; Marnellos, G. E.; Konsolakis, M. Effect of Alkali (Cs) Doping on the Surface Chemistry and CO<sub>2</sub> hydrogenation Performance of CuO/CeO<sub>2</sub> catalysts. *J. CO<sub>2</sub> Util.* **2021**, *44* (December 2020). <https://doi.org/10.1016/j.jcou.2020.101408>.
- (123) Wu, J.; Sharifi, T.; Gao, Y.; Zhang, T.; Ajayan, P. M. Emerging Carbon-Based Heterogeneous Catalysts for Electrochemical Reduction of Carbon Dioxide into Value-Added Chemicals. *Adv. Mater.* **2019**, *31* (13), 1–24. <https://doi.org/10.1002/adma.201804257>.
- (124) Su, C.; Loh, K. P. Carbocatalysts: Graphene Oxide and Its Derivatives. *Acc. Chem. Res.* **2013**, *46* (10), 2275–2285. <https://doi.org/10.1021/ar300118v>.
- (125) Ahmadi, A.; Hajilou, M.; Zavari, S.; Yaghmaei, S. A Comparative Review on Adsorption and Photocatalytic Degradation of Classified Dyes with Metal/Non-Metal-Based Modification of Graphitic Carbon Nitride Nanocomposites: Synthesis, Mechanism, and Affecting Parameters. *J. Clean. Prod.* **2023**, *382* (November 2022), 134967. <https://doi.org/10.1016/j.jclepro.2022.134967>.
- (126) Chen, L.; Maigbay, M. A.; Li, M.; Qiu, X. Synthesis and Modification Strategies of G-C<sub>3</sub>N<sub>4</sub> Nanosheets for Photocatalytic Applications. *Adv. Powder Mater.* **2023**, No. June, 100150. <https://doi.org/10.1016/j.apmate.2023.100150>.
- (127) Samanta, S.; Srivastava, R. Catalytic Conversion of CO<sub>2</sub> to Chemicals and Fuels: The Collective Thermocatalytic/Photocatalytic/Electrocatalytic Approach with Graphitic Carbon Nitride. *Mater. Adv.* **2020**, *1* (6), 1506–1545. <https://doi.org/10.1039/d0ma00293c>.
- (128) Wudil, Y. S.; Ahmad, U. F.; Gondal, M. A.; Al-Osta, M. A.; Almohammed, A.; Sa'id, R. S.;

- Hrahsheh, F.; Haruna, K.; Mohamed, M. J. S. Tuning of Graphitic Carbon Nitride (g-C<sub>3</sub>N<sub>4</sub>) for Photocatalysis: A Critical Review. *Arab. J. Chem.* **2023**, *16* (3). <https://doi.org/10.1016/j.arabjc.2023.104542>.
- (129) Rono, N.; Kibet, J. K.; Martincigh, B. S.; Nyamori, V. O. A Review of the Current Status of Graphitic Carbon Nitride. *Crit. Rev. Solid State Mater. Sci.* **2021**, *46* (3), 189–217. <https://doi.org/10.1080/10408436.2019.1709414>.
- (130) Kroke, E.; Schwarz, M.; Horath-Bordon, E.; Kroll, P.; Noll, B.; Norman, A. D. Tri-s-Triazine Derivatives. Part I. From Trichloro-Tri-s-Triazine to Graphitic C<sub>3</sub>N<sub>4</sub> Structures. *New J. Chem.* **2002**, *26* (5), 508–512. <https://doi.org/10.1039/b111062b>.
- (131) Sun, S. P.; Gu, S.; Sun, J. H.; Xia, F. F.; Chen, G. H. First Principles Investigation of the Electronic Properties of Graphitic Carbon Nitride with Different Building Block and Sheet Staggered Arrangement. *J. Alloys Compd.* **2018**, *735*, 131–139. <https://doi.org/10.1016/j.jallcom.2017.11.061>.
- (132) Cao, S.; Yu, J. G-C<sub>3</sub>N<sub>4</sub>-Based Photocatalysts for Hydrogen Generation. *J. Phys. Chem. Lett.* **2014**, *5* (12), 2101–2107. <https://doi.org/10.1021/jz500546b>.
- (133) Eid, K.; Gamal, A.; Abdullah, A. M. Graphitic Carbon Nitride-Based Nanostructures as Emergent Catalysts for Carbon Monoxide (CO) Oxidation. *Green Chem.* **2023**, *25* (4), 1276–1310. <https://doi.org/10.1039/d2gc02748h>.
- (134) Ong, W. J.; Tan, L. L.; Ng, Y. H.; Yong, S. T.; Chai, S. P. Graphitic Carbon Nitride (g-C<sub>3</sub>N<sub>4</sub>)-Based Photocatalysts for Artificial Photosynthesis and Environmental Remediation: Are We a Step Closer to Achieving Sustainability? *Chem. Rev.* **2016**, *116* (12), 7159–7329. <https://doi.org/10.1021/acs.chemrev.6b00075>.
- (135) Cao, S.; Low, J.; Yu, J.; Jaroniec, M. Polymeric Photocatalysts Based on Graphitic Carbon Nitride. *Adv. Mater.* **2015**, *27* (13), 2150–2176. <https://doi.org/10.1002/adma.201500033>.
- (136) Ismael, M. A Review on Graphitic Carbon Nitride (g-C<sub>3</sub>N<sub>4</sub>) Based Nanocomposites: Synthesis, Categories, and Their Application in Photocatalysis. *J. Alloys Compd.* **2020**, *846*, 156446. <https://doi.org/10.1016/j.jallcom.2020.156446>.
- (137) Wang, S.; Zhang, J.; Li, B.; Sun, H.; Wang, S.; Duan, X. Morphology-Dependent Photocatalysis of Graphitic Carbon Nitride for Sustainable Remediation of Aqueous Pollutants: A Mini Review. *J. Environ. Chem. Eng.* **2022**, *10* (3), 107438. <https://doi.org/10.1016/j.jece.2022.107438>.
- (138) Tian, N.; Huang, H.; Du, X.; Dong, F.; Zhang, Y. Rational Nanostructure Design of Graphitic Carbon Nitride for Photocatalytic Applications. *J. Mater. Chem. A* **2019**, *7* (19), 11584–11612. <https://doi.org/10.1039/c9ta01819k>.

- (139) Niu, P.; Zhang, L.; Liu, G.; Cheng, H. M. Graphene-like Carbon Nitride Nanosheets for Improved Photocatalytic Activities. *Adv. Funct. Mater.* **2012**, *22* (22), 4763–4770. <https://doi.org/10.1002/adfm.201200922>.
- (140) Patnaik, S.; Sahoo, D. P.; Parida, K. Recent Advances in Anion Doped G-C<sub>3</sub>N<sub>4</sub> Photocatalysts: A Review. *Carbon N. Y.* **2021**, *172*, 682–711. <https://doi.org/10.1016/j.carbon.2020.10.073>.
- (141) Yu, X.; Ng, S.; Putri, L. K.; Tan, L.; Mohamed, A. R.; Ong, W. Point-Defect Engineering: Leveraging Imperfections in Graphitic Carbon Nitride (G-C<sub>3</sub>N<sub>4</sub>) Photocatalysts toward Artificial Photosynthesis. *Small* **2021**, *2006851*, 2006851. <https://doi.org/10.1002/sml.202006851>.
- (142) Jiang, L.; Yuan, X.; Pan, Y.; Liang, J.; Zeng, G.; Wu, Z.; Wang, H. Doping of Graphitic Carbon Nitride for Photocatalysis: A Review. *Appl. Catal. B Environ.* **2017**, *217*, 388–406. <https://doi.org/10.1016/j.apcatb.2017.06.003>.
- (143) Li, Y.; Wang, M.-Q.; Bao, S.-J.; Lu, S.; Xu, M.; Long, D.; Pu, S. Tuning and Thermal Exfoliation Graphene-like Carbon Nitride Nanosheets for Superior Photocatalytic Activity. *Ceram. Int.* **2016**, *42* (16), 18521–18528. <https://doi.org/10.1016/j.ceramint.2016.08.190>.
- (144) Xie, K.; Fang, J.; Li, L.; Deng, J.; Chen, F. Progress of Graphite Carbon Nitride with Different Dimensions in the Photocatalytic Degradation of Dyes: A Review. *J. Alloys Compd.* **2022**, *901*. <https://doi.org/10.1016/j.jallcom.2021.163589>.
- (145) Panneri, S.; Ganguly, P.; Mohan, M.; Nair, B. N.; Mohamed, A. A. P.; Warriar, K. G.; Hareesh, U. S. Photoregenerable, Bifunctional Granules of Carbon-Doped g-C<sub>3</sub>N<sub>4</sub> as Adsorptive Photocatalyst for the Efficient Removal of Tetracycline Antibiotic. *ACS Sustain. Chem. Eng.* **2017**, *5* (2), 1610–1618. <https://doi.org/10.1021/acssuschemeng.6b02383>.
- (146) Huang, Y.; Li, D.; Feng, S.; Jia, Y.; Guo, S.; Wu, X.; Chen, M.; Shi, W. Pt Atoms/Clusters on Ni-Phytate-Sensitized Carbon Nitride for Enhanced NIR-Light-Driven Overall Water Splitting beyond 800 Nm. *Angew. Chemie - Int. Ed.* **2022**, *61* (45). <https://doi.org/10.1002/anie.202212234>.
- (147) Wang, G.; Chen, Z.; Wang, T.; Wang, D.; Mao, J. P and Cu Dual Sites on Graphitic Carbon Nitride for Photocatalytic CO<sub>2</sub> Reduction to Hydrocarbon Fuels with High C<sub>2</sub>H<sub>6</sub> Evolution. *Angew. Chemie - Int. Ed.* **2022**, *61* (40). <https://doi.org/10.1002/anie.202210789>.
- (148) Dong, F.; Li, Y.; Wang, Z.; Ho, W.-K. Enhanced Visible Light Photocatalytic Activity and Oxidation Ability of Porous Graphene-like g-C<sub>3</sub>N<sub>4</sub> Nanosheets via Thermal Exfoliation. *Appl. Surf. Sci.* **2015**, *358*, 393–403. <https://doi.org/10.1016/j.apsusc.2015.04.034>.
- (149) Niu, P.; Zhang, L.; Liu, G.; Cheng, H.-M. Graphene-Like Carbon Nitride Nanosheets for

- Improved Photocatalytic Activities. *Adv. Funct. Mater.* **2012**, *22* (22), 4763–4770. <https://doi.org/10.1002/adfm.201200922>.
- (150) Papailias, I.; Todorova, N.; Giannakopoulou, T.; Ioannidis, N.; Boukos, N.; Athanasekou, C. P.; Dimotikali, D.; Trapalis, C. Chemical vs Thermal Exfoliation of G-C<sub>3</sub>N<sub>4</sub> for NO<sub>x</sub> Removal under Visible Light Irradiation. *Appl. Catal. B Environ.* **2018**, *239* (May), 16–26. <https://doi.org/10.1016/j.apcatb.2018.07.078>.
- (151) Qiu, P.; Chen, H.; Xu, C.; Zhou, N.; Jiang, F.; Wang, X.; Fu, Y. Fabrication of an Exfoliated Graphitic Carbon Nitride as a Highly Active Visible Light Photocatalyst. *J. Mater. Chem. A* **2015**, *3* (48), 24237–24244. <https://doi.org/10.1039/C5TA08406G>.
- (152) Meng, N.; Ren, J.; Liu, Y.; Huang, Y.; Petit, T.; Zhang, B. Engineering Oxygen-Containing and Amino Groups into Two-Dimensional Atomically-Thin Porous Polymeric Carbon Nitrogen for Enhanced Photocatalytic Hydrogen Production. *Energy Environ. Sci.* **2018**, *11* (3), 566–571. <https://doi.org/10.1039/C7EE03592F>.
- (153) Xu, J.; Zhang, L.; Shi, R.; Zhu, Y. Chemical Exfoliation of Graphitic Carbon Nitride for Efficient Heterogeneous Photocatalysis. *J. Mater. Chem. A* **2013**, *1* (46), 14766. <https://doi.org/10.1039/c3ta13188b>.
- (154) Li, H.-J.; Sun, B.-W.; Sui, L.; Qian, D.-J.; Chen, M. Preparation of Water-Dispersible Porous g-C<sub>3</sub>N<sub>4</sub> with Improved Photocatalytic Activity by Chemical Oxidation. *Phys. Chem. Chem. Phys.* **2015**, *17* (5), 3309–3315. <https://doi.org/10.1039/C4CP05020G>.
- (155) Zhang, X.; Liao, H.; Liu, X.; Shang, R.; Zhou, Y.; Zhou, Y. Graphitic Carbon Nitride Nanosheets Made by Different Methods as Electrode Material for Supercapacitors. *Ionics (Kiel)*. **2020**, *26* (7), 3599–3607. <https://doi.org/10.1007/s11581-020-03458-z>.
- (156) Wang, S. G-C<sub>3</sub>N<sub>4</sub> Nanosheets as “on-off-on” Selective Fluorescence Biosensor to Detect Ascorbic Acid via Redox Reaction. *J. Alloys Compd.* **2019**, *770*, 952–958. <https://doi.org/10.1016/j.jallcom.2018.08.182>.
- (157) Yuan, Y.-J.; Shen, Z.; Wu, S.; Su, Y.; Pei, L.; Ji, Z.; Ding, M.; Bai, W.; Chen, Y.; Yu, Z.-T.; Zou, Z. Liquid Exfoliation of G-C<sub>3</sub>N<sub>4</sub> Nanosheets to Construct 2D-2D MoS<sub>2</sub>/g-C<sub>3</sub>N<sub>4</sub> Photocatalyst for Enhanced Photocatalytic H<sub>2</sub> Production Activity. *Appl. Catal. B Environ.* **2019**, *246* (November 2018), 120–128. <https://doi.org/10.1016/j.apcatb.2019.01.043>.
- (158) Hatamie, A.; Jalilian, P.; Rezvani, E.; Kakavand, A.; Simchi, A. Fast and Ultra-Sensitive Voltammetric Detection of Lead Ions by Two-Dimensional Graphitic Carbon Nitride (g-C<sub>3</sub>N<sub>4</sub>) Nanolayers as Glassy Carbon Electrode Modifier. *Measurement* **2019**, *134*, 679–687. <https://doi.org/10.1016/j.measurement.2018.10.082>.
- (159) Yan, J.; Han, X.; Zheng, X.; Qian, J.; Liu, J.; Dong, X.; Xi, F. One-Step Template/Chemical

- Blowing Route to Synthesize Flake-like Porous Carbon Nitride Photocatalyst. *Mater. Res. Bull.* **2017**, *94*, 423–427. <https://doi.org/10.1016/j.materresbull.2017.06.022>.
- (160) Ye, B.; Han, X.; Yan, M.; Zhang, H.; Xi, F.; Dong, X.; Liu, J. Fabrication of Metal-Free Two Dimensional/Two Dimensional Homo Junction Photocatalyst Using Various Carbon Nitride Nanosheets as Building Blocks. *J. Colloid Interface Sci.* **2017**, *507*, 209–216. <https://doi.org/10.1016/j.jcis.2017.08.002>.
- (161) Zhu, K.; Wang, W.; Meng, A.; Zhao, M.; Wang, J.; Zhao, M.; Zhang, D.; Jia, Y.; Xu, C.; Li, Z. Mechanically Exfoliated G-C<sub>3</sub>N<sub>4</sub> Thin Nanosheets by Ball Milling as High Performance Photocatalysts. *RSC Adv.* **2015**, *5* (69), 56239–56243. <https://doi.org/10.1039/c5ra09040g>.
- (162) Challagulla, S.; Payra, S.; Chakraborty, C.; Roy, S. Determination of Band Edges and Their Influences on Photocatalytic Reduction of Nitrobenzene by Bulk and Exfoliated G-C<sub>3</sub>N<sub>4</sub>. *Phys. Chem. Chem. Phys.* **2019**, *21* (6), 3174–3183. <https://doi.org/10.1039/c8cp06855k>.
- (163) Lei, G.; Cao, Y.; Zhao, W.; Dai, Z.; Shen, L.; Xiao, Y.; Jiang, L. Exfoliation of Graphitic Carbon Nitride for Enhanced Oxidative Desulfurization: A Facile and General Strategy. *ACS Sustain. Chem. Eng.* **2019**, *7* (5), 4941–4950. <https://doi.org/10.1021/acssuschemeng.8b05553>.
- (164) He, Q.; Liang, J. J.; Chen, L. X.; Chen, S. L.; Zheng, H. L.; Liu, H. X.; Zhang, H. J. Removal of the Environmental Pollutant Carbamazepine Using Molecular Imprinted Adsorbents: Molecular Simulation, Adsorption Properties, and Mechanisms. *Water Res.* **2020**, *168*, 115164. <https://doi.org/10.1016/j.watres.2019.115164>.
- (165) Yu, F.; Bai, X.; Liang, M.; Ma, J. Recent Progress on Metal-Organic Framework-Derived Porous Carbon and Its Composite for Pollutant Adsorption from Liquid Phase. *Chem. Eng. J.* **2021**, *405* (June 2020), 126960. <https://doi.org/10.1016/j.cej.2020.126960>.
- (166) Ghorai, S.; Sarkar, A.; Raoufi, M.; Panda, A. B.; Schönherr, H.; Pal, S. Enhanced Removal of Methylene Blue and Methyl Violet Dyes from Aqueous Solution Using a Nanocomposite of Hydrolyzed Polyacrylamide Grafted Xanthan Gum and Incorporated Nanosilica. *ACS Appl. Mater. Interfaces* **2014**, *6* (7), 4766–4777. <https://doi.org/10.1021/am4055657>.
- (167) Ren, B.; Xu, Y.; Zhang, L.; Liu, Z. Carbon-Doped Graphitic Carbon Nitride as Environment-Benign Adsorbent for Methylene Blue Adsorption: Kinetics, Isotherm and Thermodynamics Study. *J. Taiwan Inst. Chem. Eng.* **2018**, *88*, 114–120. <https://doi.org/10.1016/j.jtice.2018.03.041>.
- (168) Medhat, A.; El-Maghrabi, H. H.; Abdelghany, A.; Abdel Menem, N. M.; Raynaud, P.; Moustafa, Y. M.; Elsayed, M. A.; Nada, A. A. Efficiently Activated Carbons from Corn Cob for Methylene Blue Adsorption. *Appl. Surf. Sci. Adv.* **2021**, *3* (December 2020), 100037. <https://doi.org/10.1016/j.apsadv.2020.100037>.

- (169) Li, M. fang; Liu, Y. guo; Zeng, G. ming; Liu, N.; Liu, S. bo. Graphene and Graphene-Based Nanocomposites Used for Antibiotics Removal in Water Treatment: A Review. *Chemosphere* **2019**, *226*, 360–380. <https://doi.org/10.1016/j.chemosphere.2019.03.117>.
- (170) Peng, J.; He, Y.; Zhou, C.; Su, S.; Lai, B. The Carbon Nanotubes-Based Materials and Their Applications for Organic Pollutant Removal: A Critical Review. *Chinese Chem. Lett.* **2021**, *32* (5), 1626–1636. <https://doi.org/10.1016/j.ccllet.2020.10.026>.
- (171) Cheung, W. H.; Szeto, Y. S.; McKay, G. Enhancing the Adsorption Capacities of Acid Dyes by Chitosan Nano Particles. *Bioresour. Technol.* **2009**, *100* (3), 1143–1148. <https://doi.org/10.1016/j.biortech.2008.07.071>.
- (172) Han, H.; Rafiq, M. K.; Zhou, T.; Xu, R.; Mašek, O.; Li, X. A Critical Review of Clay-Based Composites with Enhanced Adsorption Performance for Metal and Organic Pollutants. *J. Hazard. Mater.* **2019**, *369* (February), 780–796. <https://doi.org/10.1016/j.jhazmat.2019.02.003>.
- (173) Feng, X.; Long, R.; Wang, L.; Liu, C.; Bai, Z.; Liu, X. A Review on Heavy Metal Ions Adsorption from Water by Layered Double Hydroxide and Its Composites. *Sep. Purif. Technol.* **2022**, *284* (November 2021), 120099. <https://doi.org/10.1016/j.seppur.2021.120099>.
- (174) Zhu, B.; Xia, P.; Ho, W.; Yu, J. Isoelectric Point and Adsorption Activity of Porous G-C<sub>3</sub>N<sub>4</sub>. *Appl. Surf. Sci.* **2015**, *344*, 188–195. <https://doi.org/10.1016/j.apsusc.2015.03.086>.
- (175) Yousefi, M.; Villar-Rodil, S.; Paredes, J. I.; Moshfegh, A. Z. Oxidized Graphitic Carbon Nitride Nanosheets as an Effective Adsorbent for Organic Dyes and Tetracycline for Water Remediation. *J. Alloys Compd.* **2019**, *809*. <https://doi.org/10.1016/j.jallcom.2019.151783>.
- (176) Yu, Y.; Huang, H. Coupled Adsorption and Photocatalysis of G-C<sub>3</sub>N<sub>4</sub> Based Composites: Material Synthesis, Mechanism, and Environmental Applications. *Chem. Eng. J.* **2023**, *453* (P1), 139755. <https://doi.org/10.1016/j.cej.2022.139755>.
- (177) Ambaye, T. G.; Vaccari, M.; van Hullebusch, E. D.; Amrane, A.; Rtimi, S. Mechanisms and Adsorption Capacities of Biochar for the Removal of Organic and Inorganic Pollutants from Industrial Wastewater. *Int. J. Environ. Sci. Technol.* **2021**, *18* (10), 3273–3294. <https://doi.org/10.1007/s13762-020-03060-w>.
- (178) Khan, I.; Saeed, K.; Ali, N.; Khan, I.; Zhang, B.; Sadiq, M. Heterogeneous Photodegradation of Industrial Dyes: An Insight to Different Mechanisms and Rate Affecting Parameters. *J. Environ. Chem. Eng.* **2020**, *8* (5). <https://doi.org/10.1016/j.jece.2020.104364>.
- (179) Zhang, L.; Li, L.; Sun, X.; Liu, P.; Yang, D.; Zhao, X. ZnO-Layered Double Hydroxide@graphitic Carbon Nitride Composite for Consecutive Adsorption and Photodegradation of Dyes under UV and Visible Lights. *Materials (Basel)*. **2016**, *9* (11).

<https://doi.org/10.3390/ma9110927>.

- (180) Lai, K. C.; Lee, L. Y.; Hiew, B. Y. Z.; Thangalazhy-Gopakumar, S.; Gan, S. Environmental Application of Three-Dimensional Graphene Materials as Adsorbents for Dyes and Heavy Metals: Review on Ice-Templating Method and Adsorption Mechanisms. *J. Environ. Sci. (China)* **2019**, *79*, 174–199. <https://doi.org/10.1016/j.jes.2018.11.023>.
- (181) Zhao, L.; Lv, W.; Hou, J.; Li, Y.; Duan, J.; Ai, S. Synthesis of Magnetically Recyclable G-C<sub>3</sub>N<sub>4</sub>/Fe<sub>3</sub>O<sub>4</sub>/ZIF-8 Nanocomposites for Excellent Adsorption of Malachite Green. *Microchem. J.* **2020**, *152* (November 2019), 104425. <https://doi.org/10.1016/j.microc.2019.104425>.
- (182) Nguyen-Phan, T. D.; Pham, V. H.; Shin, E. W.; Pham, H. D.; Kim, S.; Chung, J. S.; Kim, E. J.; Hur, S. H. The Role of Graphene Oxide Content on the Adsorption-Enhanced Photocatalysis of Titanium Dioxide/Graphene Oxide Composites. *Chem. Eng. J.* **2011**, *170* (1), 226–232. <https://doi.org/10.1016/j.cej.2011.03.060>.
- (183) Anwer, H.; Park, J. W. Synthesis and Characterization of a Heterojunction RGO/ZrO<sub>2</sub>/Ag<sub>3</sub>PO<sub>4</sub> Nanocomposite for Degradation of Organic Contaminants. *J. Hazard. Mater.* **2018**, *358* (February), 416–426. <https://doi.org/10.1016/j.jhazmat.2018.07.019>.
- (184) Ajmal, A.; Majeed, I.; Malik, R. N.; Idriss, H.; Nadeem, M. A. Principles and Mechanisms of Photocatalytic Dye Degradation on TiO<sub>2</sub> Based Photocatalysts: A Comparative Overview. *RSC Adv.* **2014**, *4* (70), 37003–37026. <https://doi.org/10.1039/c4ra06658h>.
- (185) Gao, C.; Low, J.; Long, R.; Kong, T.; Zhu, J.; Xiong, Y. Heterogeneous Single-Atom Photocatalysts: Fundamentals and Applications. *Chem. Rev.* **2020**, *120* (21), 12175–12216. <https://doi.org/10.1021/acs.chemrev.9b00840>.
- (186) Wang, J.; Lin, S.; Tian, N.; Ma, T.; Zhang, Y.; Huang, H. Nanostructured Metal Sulfides: Classification, Modification Strategy, and Solar-Driven CO<sub>2</sub> Reduction Application. *Adv. Funct. Mater.* **2021**, *31* (9), 2008008. <https://doi.org/10.1002/adfm.202008008>.
- (187) Linsebigler, A. L.; Lu, G.; Yates, J. T. Photocatalysis on TiO<sub>2</sub> Surfaces: Principles, Mechanisms, and Selected Results. *Chem. Rev.* **1995**, *95* (3), 735–758. <https://doi.org/10.1021/cr00035a013>.
- (188) Yu, Y.; Wu, K.; Xu, W.; Chen, D.; Fang, J.; Zhu, X.; Sun, J.; Liang, Y.; Hu, X.; Li, R.; Fang, Z. Adsorption-Photocatalysis Synergistic Removal of Contaminants under Antibiotic and Cr(VI) Coexistence Environment Using Non-Metal g-C<sub>3</sub>N<sub>4</sub> Based Nanomaterial Obtained by Supramolecular Self-Assembly Method. *J. Hazard. Mater.* **2021**, *404* (PA), 124171. <https://doi.org/10.1016/j.jhazmat.2020.124171>.
- (189) Huang, Y.; Wang, P.; Wang, Z.; Rao, Y.; Cao, J. Ji; Pu, S.; Ho, W.; Lee, S. C. Protonated G-C<sub>3</sub>N<sub>4</sub>/Ti<sup>3+</sup> Self-Doped TiO<sub>2</sub> Nanocomposite Films: Room-Temperature Preparation,

- Hydrophilicity, and Application for Photocatalytic NO<sub>x</sub> Removal. *Appl. Catal. B Environ.* **2019**, *240* (September 2018), 122–131. <https://doi.org/10.1016/j.apcatb.2018.08.078>.
- (190) Wang, Q.; Li, Y.; Huang, F.; Song, S.; Ai, G.; Xin, X.; Zhao, B.; Zheng, Y.; Zhang, Z. Recent Advances in G-C<sub>3</sub>N<sub>4</sub>-Based Materials and Their Application in Energy and Environmental Sustainability. *Molecules* **2023**, *28* (1). <https://doi.org/10.3390/molecules28010432>.
- (191) Long, B.; Yan, G.; He, H.; Meng, S. Porous and Few-Layer Carbon Nitride Nanosheets via Surface Steam Etching for Enhanced Photodegradation Activity. *ACS Appl. Nano Mater* **2022**, *5*, 7798–7810. <https://doi.org/10.1021/acsanm.2c00820>.
- (192) Praus, P.; Smýkalová, A.; Foniok, K.; Matějka, V.; Kormunda, M.; Smetana, B.; Cvejn, D. The Presence and Effect of Oxygen in Graphitic Carbon Nitride Synthesized in Air and Nitrogen Atmosphere. *Appl. Surf. Sci.* **2020**, *529* (May). <https://doi.org/10.1016/j.apsusc.2020.147086>.
- (193) Wu, X.; Cheng, J.; Li, X.; Li, Y.; Lv, K. Enhanced Visible Photocatalytic Oxidation of NO by Repeated Calcination of G-C<sub>3</sub>N<sub>4</sub>. *Appl. Surf. Sci.* **2019**, *465* (June 2018), 1037–1046. <https://doi.org/10.1016/j.apsusc.2018.09.165>.
- (194) Li, Y.; Sun, Y.; Ho, W.; Zhang, Y.; Huang, H.; Cai, Q.; Dong, F. Highly Enhanced Visible-Light Photocatalytic NO<sub>x</sub> purification and Conversion Pathway on Self-Structurally Modified g-C<sub>3</sub>N<sub>4</sub> nanosheets. *Sci. Bull.* **2018**, *63* (10), 609–620. <https://doi.org/10.1016/j.scib.2018.04.009>.
- (195) Van Viet, P.; Nguyen, T.-D.; Bui, D.-P.; Thi, C. M. Combining SnO<sub>2-x</sub> and g-C<sub>3</sub>N<sub>4</sub> Nanosheets toward S-Scheme Heterojunction for High Selectivity into Green Products of NO Degradation Reaction under Visible Light. *J. Mater.* **2021**, No. xxxx. <https://doi.org/10.1016/j.jmat.2021.06.006>.
- (196) Ma, R.; Zhang, S.; Li, L.; Gu, P.; Wen, T.; Khan, A.; Li, S.; Li, B.; Wang, S.; Wang, X. Enhanced Visible-Light-Induced Photoactivity of Type-II CeO<sub>2</sub>/g-C<sub>3</sub>N<sub>4</sub> Nanosheet toward Organic Pollutants Degradation. *ACS Sustain. Chem. Eng.* **2019**, *7* (10), 9699–9708. <https://doi.org/10.1021/acssuschemeng.9b01477>.
- (197) Fernandes, R. A.; Sampaio, M. J.; Dražić, G.; Faria, J. L.; Silva, C. G. Efficient Removal of Parabens from Real Water Matrices by a Metal-Free Carbon Nitride Photocatalyst. *Sci. Total Environ.* **2020**, *716*. <https://doi.org/10.1016/j.scitotenv.2019.135346>.
- (198) Hou, J.; Yang, M.; Dou, Q.; Chen, Q.; Wang, X.; Hu, C.; Paul, R. Defect Engineering in Polymeric Carbon Nitride with Accordion Structure for Efficient Photocatalytic CO<sub>2</sub> Reduction and H<sub>2</sub> Production. *Chem. Eng. J.* **2022**, *450* (P4), 138425. <https://doi.org/10.1016/j.cej.2022.138425>.

- (199) Chen, L.; Liang, X.; Wang, H.; Xiao, Q.; Qiu, X. Ultra-Thin Carbon Nitride Nanosheets for Efficient Photocatalytic Hydrogen Evolution. *Chem. Eng. J.* **2022**, *442* (P2), 136115. <https://doi.org/10.1016/j.cej.2022.136115>.
- (200) J. Zhang, M. Grzelczak, Y. Hou, K. Maeda, K. Domen, X. Fu, M. Antonietti, X. W. Photocatalytic Oxidation of Water by Polymeric Carbon Nitride Nanohybrids Made of Sustainable Elements. *Chem. Sci.* **2012**, *3*, 443. <https://doi.org/10.1039/c1sc00644d>.
- (201) Huang, H.; Xiao, K.; Tian, N.; Dong, F.; Zhang, T.; Du, X.; Zhang, Y. Template-Free Precursor-Surface-Etching Route to Porous, Thin g-C<sub>3</sub>N<sub>4</sub> Nanosheets for Enhancing Photocatalytic Reduction and Oxidation Activity. *J. Mater. Chem. A* **2017**, *5* (33), 17452–17463. <https://doi.org/10.1039/C7TA04639A>.
- (202) Liu, C.; Zhang, Y.; Dong, F.; Du, X.; Huang, H. Easily and Synchronously Ameliorating Charge Separation and Band Energy Level in Porous G-C<sub>3</sub>N<sub>4</sub> for Boosting Photooxidation and Photoreduction Ability. *J. Phys. Chem. C* **2016**, *120* (19), 10381–10389. <https://doi.org/10.1021/acs.jpcc.6b01705>.
- (203) Ruan, D.; Kim, S.; Fujitsuka, M.; Majima, T. Defects Rich G-C<sub>3</sub>N<sub>4</sub> with Mesoporous Structure for Efficient Photocatalytic H<sub>2</sub> Production under Visible Light Irradiation. *Appl. Catal. B Environ.* **2018**, *238*, 638–646. <https://doi.org/10.1016/j.apcatb.2018.07.028>.
- (204) Wu, X.; Wang, X.; Wang, F.; Yu, H. Soluble G-C<sub>3</sub>N<sub>4</sub> Nanosheets: Facile Synthesis and Application in Photocatalytic Hydrogen Evolution. *Appl. Catal. B Environ.* **2019**, *247* (January), 70–77. <https://doi.org/10.1016/j.apcatb.2019.01.088>.
- (205) Masih, D.; Ma, Y.; Rohani, S. Environmental Graphitic C<sub>3</sub>N<sub>4</sub> Based Noble-Metal-Free Photocatalyst Systems: A Review. *Appl. Catal. B, Environ.* **2017**, *206*, 556–588. <https://doi.org/10.1016/j.apcatb.2017.01.061>.
- (206) Wang, Y.; Wang, X.; Antonietti, M. Polymeric Graphitic Carbon Nitride as a Heterogeneous Organocatalyst: From Photochemistry to Multipurpose Catalysis to Sustainable Chemistry. *Angew. Chemie Int. Ed.* **2012**, *51* (1), 68–89. <https://doi.org/10.1002/anie.201101182>.
- (207) Jin, X.; Balasubramanian, V. V.; Selvan, S. T.; Sawant, D. P.; Chari, M. A.; Lu, G. Q.; Vinu, A. Highly Ordered Mesoporous Carbon Nitride Nanoparticles with High Nitrogen Content: A Metal-Free Basic Catalyst. *Angew. Chemie - Int. Ed.* **2009**, *48* (42), 7884–7887. <https://doi.org/10.1002/anie.200903674>.
- (208) Wang, Y.; Yao, J.; Li, H.; Su, D.; Antonietti, M. Highly Selective Hydrogenation of Phenol and Derivatives over a Pd@carbon Nitride Catalyst in Aqueous Media. *J. Am. Chem. Soc.* **2011**, *133* (8), 2362–2365. <https://doi.org/10.1021/ja109856y>.
- (209) Li, X. H.; Antonietti, M. Metal Nanoparticles at Mesoporous N-Doped Carbons and Carbon

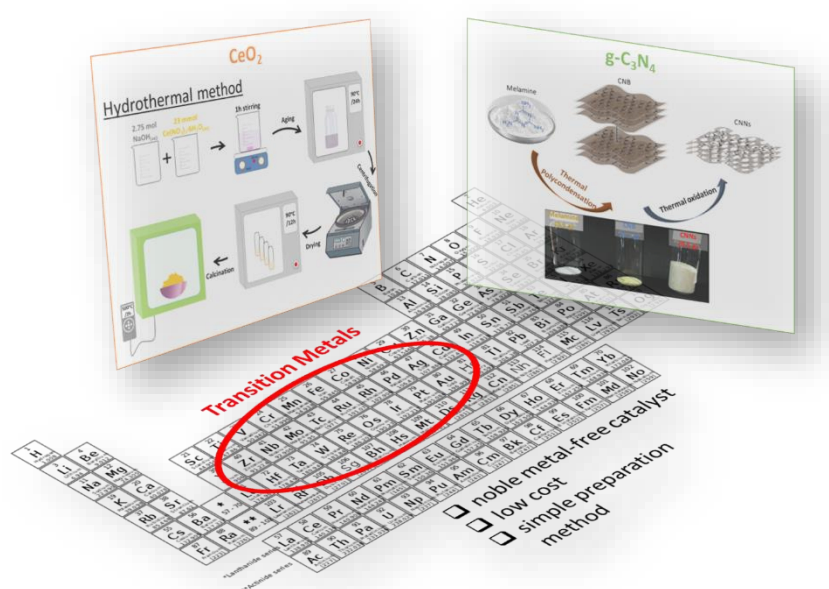
- Nitrides: Functional Mott–Schottky Heterojunctions for Catalysis. *Chem. Soc. Rev.* **2013**, *42* (16), 6593–6604. <https://doi.org/10.1039/c3cs60067j>.
- (210) Zhu, J.; Xiao, P.; Li, H.; Carabineiro, S. A. C. Graphitic Carbon Nitride: Synthesis, Properties, and Applications in Catalysis. *ACS Appl. Mater. Interfaces* **2014**, *6* (19), 16449–16465. <https://doi.org/10.1021/am502925j>.
- (211) Miller, T. S.; Jorge, A. B.; Suter, T. M.; Sella, A.; Corà, F.; McMillan, P. F. Carbon Nitrides: Synthesis and Characterization of a New Class of Functional Materials. *Phys. Chem. Chem. Phys.* **2017**, *19* (24), 15613–15638. <https://doi.org/10.1039/c7cp02711g>.
- (212) Zhao, G.; Huang, X.; Wang, X.; Wang, X. Progress in Catalyst Exploration for Heterogeneous CO<sub>2</sub> Reduction and Utilization: A Critical Review. *J. Mater. Chem. A* **2017**, *5* (41), 21625–21649. <https://doi.org/10.1039/c7ta07290b>.
- (213) Wen, J.; Xie, J.; Chen, X.; Li, X. A Review on G-C<sub>3</sub>N<sub>4</sub>-Based Photocatalysts. *Appl. Surf. Sci.* **2017**, *391* (August), 72–123. <https://doi.org/10.1016/j.apsusc.2016.07.030>.
- (214) Ahmad, K. N.; Wan Isahak, W. N. R.; Rosli, M. I.; Yusop, M. R.; Kassim, M. B.; Yarmo, M. A. Rare Earth Metal Doped Nickel Catalysts Supported on Exfoliated Graphitic Carbon Nitride for Highly Selective CO and CO<sub>2</sub> Methanation. *Appl. Surf. Sci.* **2022**, *571* (September 2021), 151321. <https://doi.org/10.1016/j.apsusc.2021.151321>.
- (215) Yu, Y.; Chan, Y. M.; Bian, Z.; Song, F.; Wang, J.; Zhong, Q.; Kawi, S. Enhanced Performance and Selectivity of CO<sub>2</sub> Methanation over G-C<sub>3</sub>N<sub>4</sub> Assisted Synthesis of Ni–CeO<sub>2</sub> Catalyst: Kinetics and DRIFTS Studies. *Int. J. Hydrogen Energy* **2018**, *43* (32), 15191–15204. <https://doi.org/10.1016/j.ijhydene.2018.06.090>.
- (216) Shi, Y.; Hu, X.; Zhao, J.; Zhou, X.; Zhu, B.; Zhang, S.; Huang, W. CO Oxidation over Cu<sub>2</sub>O Deposited on 2D Continuous Lamellar G-C<sub>3</sub>N<sub>4</sub>. *New J. Chem.* **2015**, *39* (8), 6642–6648. <https://doi.org/10.1039/c5nj00621j>.
- (217) Yang, H.; Lv, K.; Zhu, J.; Li, Q.; Tang, D.; Ho, W.; Li, M.; Carabineiro, S. A. C. Effect of Mesoporous G-C<sub>3</sub>N<sub>4</sub> Substrate on Catalytic Oxidation of CO over Co<sub>3</sub>O<sub>4</sub>. *Appl. Surf. Sci.* **2017**, *401*, 333–340. <https://doi.org/10.1016/j.apsusc.2016.12.238>.
- (218) Hu, X.; Wang, Y.; Wu, R.; Zhao, Y. Graphitic Carbon Nitride-Supported Cobalt Oxides as a Potential Catalyst for Decomposition of N<sub>2</sub>O. *Appl. Surf. Sci.* **2021**, *538* (April 2020), 148157. <https://doi.org/10.1016/j.apsusc.2020.148157>.
- (219) Ahmad, K. N.; Anuar, S. A.; Wan Isahak, W. N. R.; Rosli, M. I.; Yarmo, M. A. Influences of Calcination Atmosphere on Nickel Catalyst Supported on Mesoporous Graphitic Carbon Nitride Thin Sheets for CO Methanation. *ACS Appl. Mater. Interfaces* **2020**, *12* (6), 7102–7113. <https://doi.org/10.1021/acsami.9b18984>.

# Chapter 2

## Materials Synthesis and Characterization Studies

In **Chapter 2**, synthetic procedures, characterization techniques as well as catalytic reactions used in this thesis are described. More specifically, material synthesis of bare  $\text{CeO}_2$  nanoparticles, bare g- $\text{C}_3\text{N}_4$  as well as ceria- or g- $\text{C}_3\text{N}_4$ -based transition metal catalysts are presented in this chapter. A thorough characterization study of these materials was carried out by various techniques, revealing their

textural, structural, morphological, and redox features and their catalytic evaluation was performed on a variety of energy and environmental catalytic reactions, such as the oxidation of carbon monoxide (CO), the hydrogenation of carbon dioxide ( $\text{CO}_2$ ) to methane ( $\text{CH}_4$ ) and carbon monoxide (CO) and liquid or gas phase photocatalysis.



## 2.1. Materials synthesis

The catalytic materials were prepared at two separate laboratories: the Energy & Environmental Systems Lab (IEESL) of the School of Production Engineering and Management at the Technical University of Crete, and the Transparent Conductive Materials and Devices (TCMD) laboratory of the Institute of Electronic Structure and Laser (IESL) at the Foundation for Research and Technology Hellas (FORTH). A summary of all the materials developed in this thesis can be found in Table 2.1.

### 2.1.1. Synthesis of Bare Ceria Nanorods

Bare Ceria Nanorods ( $\text{CeO}_2$  NR) were prepared through the hydrothermal method<sup>1</sup>. In particular, 2.75 mol NaOH (purity  $\geq 98\%$ , Sigma-Aldrich) was initially dissolved in 75 mL of double-deionized water. Then, 175 mL of an aqueous solution containing 23 mmol  $\text{Ce}(\text{NO}_3)_3 \cdot 6\text{H}_2\text{O}$  (purity  $\geq 99.0\%$ , Fluka) (0.13 M) was added to the above solution under vigorous stirring until a milky slurry was formed. The mixture was left for additional stirring for 1 h. Then, the final slurry was transferred into a Teflon bottle and aged at 90 °C for 24 h. The resulting precipitate was dried at 90 °C for 12 h, followed by calcination at 500 °C for 2 h under air flow (heating ramp 5 °C/min). The hydrothermal synthesis of ceria nanorods is presented in Figure 2.1.

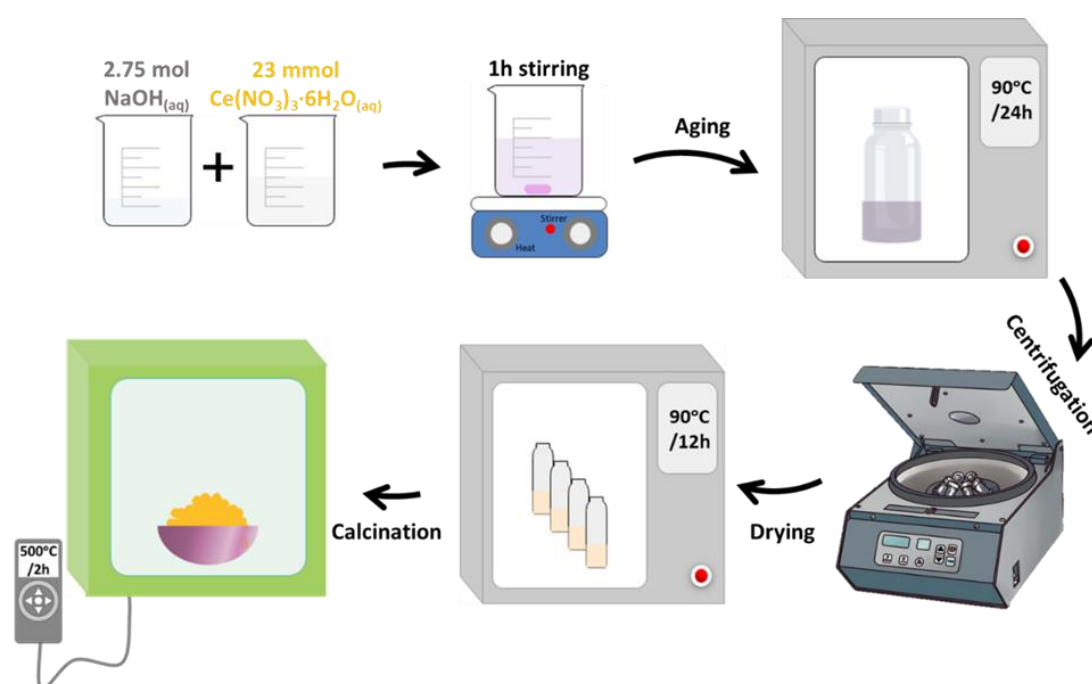


**Figure 2.1.** Hydrothermal synthesis of bare ceria nanorods ( $\text{CeO}_2$  NR).

### 2.1.2. Synthesis of Ceria-Based Transition Metal Catalysts

After the synthesis of bare  $\text{CeO}_2$  NR, the addition of different transition metals was performed by the wet impregnation method<sup>2-6</sup>. In particular, a variety of transition metals such as titanium (Ti),

vanadium (V), chromium (Cr), manganese (Mn), iron (Fe), cobalt (Co), nickel (Ni), and copper (Cu) were added in the aforementioned ceria supports via the wet impregnation method and the as-prepared catalysts were named as M/CeO<sub>2</sub> NR, where M: Ti, V, Cr, Mn, Fe, Co, Ni, Cu. Specifically, aqueous solutions of the metal precursors, i.e., tetrabutyl titanate (TBOT), NH<sub>4</sub>VO<sub>3</sub>, Cr(NO<sub>3</sub>)<sub>3</sub>·9H<sub>2</sub>O, Mn(NO<sub>3</sub>)<sub>2</sub>·4H<sub>2</sub>O, Fe(NO<sub>3</sub>)<sub>3</sub>·9H<sub>2</sub>O, Co(NO<sub>3</sub>)<sub>2</sub>·6H<sub>2</sub>O, Ni(NO<sub>3</sub>)<sub>2</sub>·6H<sub>2</sub>O, and Cu(NO<sub>3</sub>)<sub>2</sub>·2.5H<sub>2</sub>O were used to obtain a M/(M+Ce) atomic ratio of 0.2, corresponding to a metal loading between 7.5 and 8.5 wt.% M. Subsequently, the resulting suspensions were heated under stirring until water evaporation, dried at 90 °C for 12 h, and finally calcined at 500 °C for 2 h under air flow (heating ramp 5 °C/min). The synthetic process is shown in Figure 2.2.

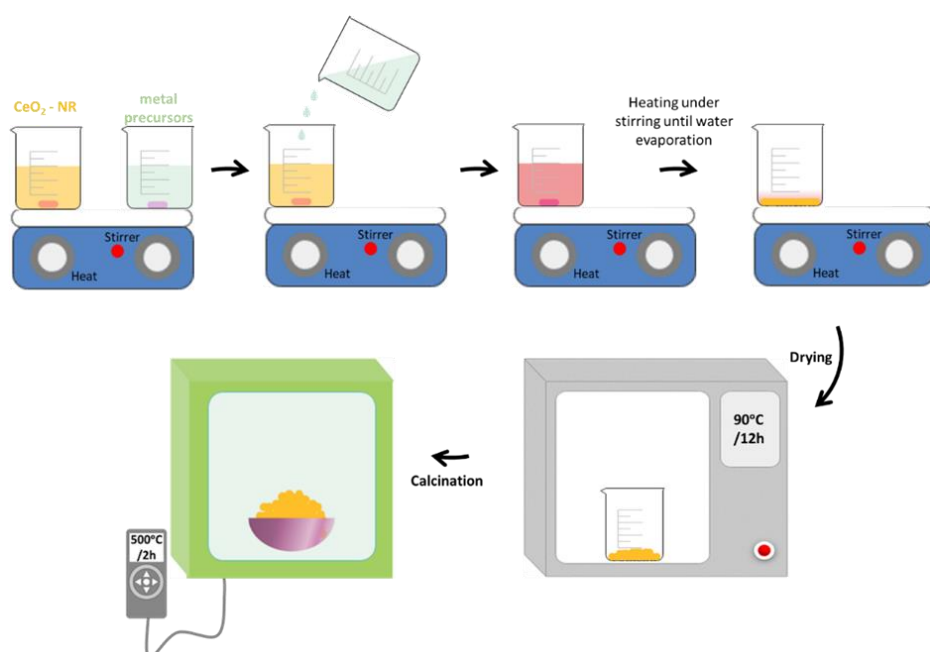


**Figure 2.2.** Synthesis of ceria-based transition metal catalysts M/CeO<sub>2</sub> NR (M: Ti, V, Cr, Mn, Fe, Co, Ni, Cu) via the wet impregnation method.

In the case of Ni/CeO<sub>2</sub> NR, a series of Ni/CeO<sub>2</sub> NR with varying metal loading was prepared using the wet impregnation method. Different Ni/Ce atomic ratios of 0.10, 0.25, 0.50, 1.00, and 1.50 were employed, corresponding to a Ni mass loading between 3-34 wt.%. The preparation process involved the addition of appropriate amounts of Ni(NO<sub>3</sub>)<sub>2</sub>·6H<sub>2</sub>O (Sigma Aldrich, purity > 98.5%) and CeO<sub>2</sub> NR to an aqueous solution, which were then mixed under stirring until water evaporation. The resulting slurry was dried overnight at 90 °C and subsequently calcined at 500 °C for 2 h in static air, using a heating ramp of 5 °C/min to eliminate residual nitrate species. The samples were further reduced at 400 °C for 1 h under a pure H<sub>2</sub> flow, followed by flushing with He until reaching room temperature to prevent re-oxidation. The resulting samples were labeled as Ni/CeO<sub>2</sub>-x, with x

representing the nominal atomic ratio of Ni/Ce. All samples were subsequently characterized after reduction.

### 2.1.3. Synthesis of Ceria-Titania Composites by Different Methods

A series of  $\text{CeO}_2/\text{TiO}_2$  mixed oxides with a Ce/Ti atomic ratio of 4 was synthesized by various methods, namely, precipitation, hydrothermal in one and two steps, and Stöber<sup>7</sup>.

**Ceria-titania by precipitation** ( $\text{CeO}_2/\text{TiO}_2\text{-P}$ ) was prepared as follows: initially, 10.4 mmol  $\text{Ce}(\text{NO}_3)_3 \cdot 6\text{H}_2\text{O}$  and 2.6 mmol  $\text{TiOSO}_4$  were dissolved in double deionized water (0.50 M) to achieve complete dissolution of the precursors. Then,  $\text{NH}_3$  (25 vol.%) was added at room temperature (RT) to the solution under constant stirring until pH reached the value of 10. After 3 h of stirring the resulting precipitate was centrifuged and washed with double deionized water and EtOH. The precipitate was treated at 90 °C for 12 h and 500 °C for 2 h under air flow (heating rate 5 °C  $\text{min}^{-1}$ ). The precipitation synthesis of  $\text{CeO}_2/\text{TiO}_2\text{-P}$  is presented in Figure 2.3.

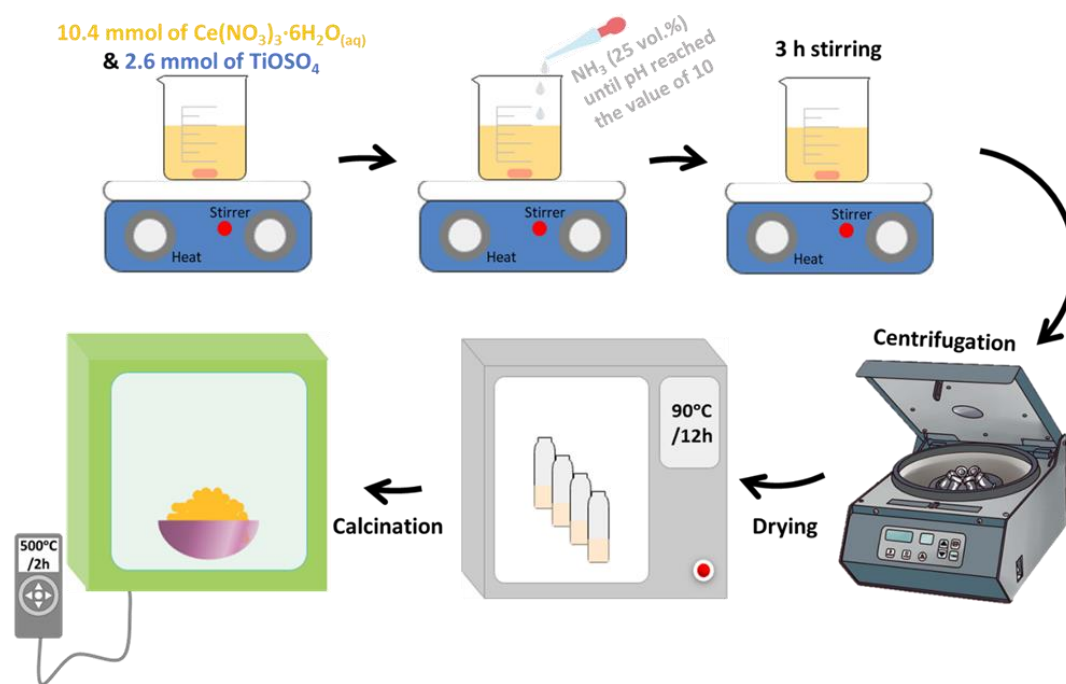


**Figure 2.3.** Precipitation synthesis of Ceria-titania ( $\text{CeO}_2/\text{TiO}_2\text{-P}$ ).

**Ceria-titania by one-step hydrothermal** ( $\text{CeO}_2/\text{TiO}_2\text{-H1}$ ) was prepared as follows: initially, 3.0 mol NaOH was added in 75 mL of water. An aqueous solution of 175 mL containing 20 mmol of  $\text{Ce}(\text{NO}_3)_3 \cdot 6\text{H}_2\text{O}$  and 5.0 mmol of  $\text{TiOSO}_4$  (0.14 M) was then added under vigorous stirring in the above solution until a milky slurry was formed. The mixture was left for 1 h of additional stirring and the final slurry was placed in a Teflon vial and aged for 24 h at 90 °C. The materials were thoroughly washed with double deionized water until pH 7, followed by EtOH washing to avoid

nanoparticle agglomeration. Finally, the precipitate was dried for 12 h at 90 °C and calcined at 500 °C for 2 h under air (heating rate 5 °C min<sup>-1</sup>). The one-step hydrothermal synthesis of CeO<sub>2</sub>/TiO<sub>2</sub>-H1 is presented in Figure 2.4.

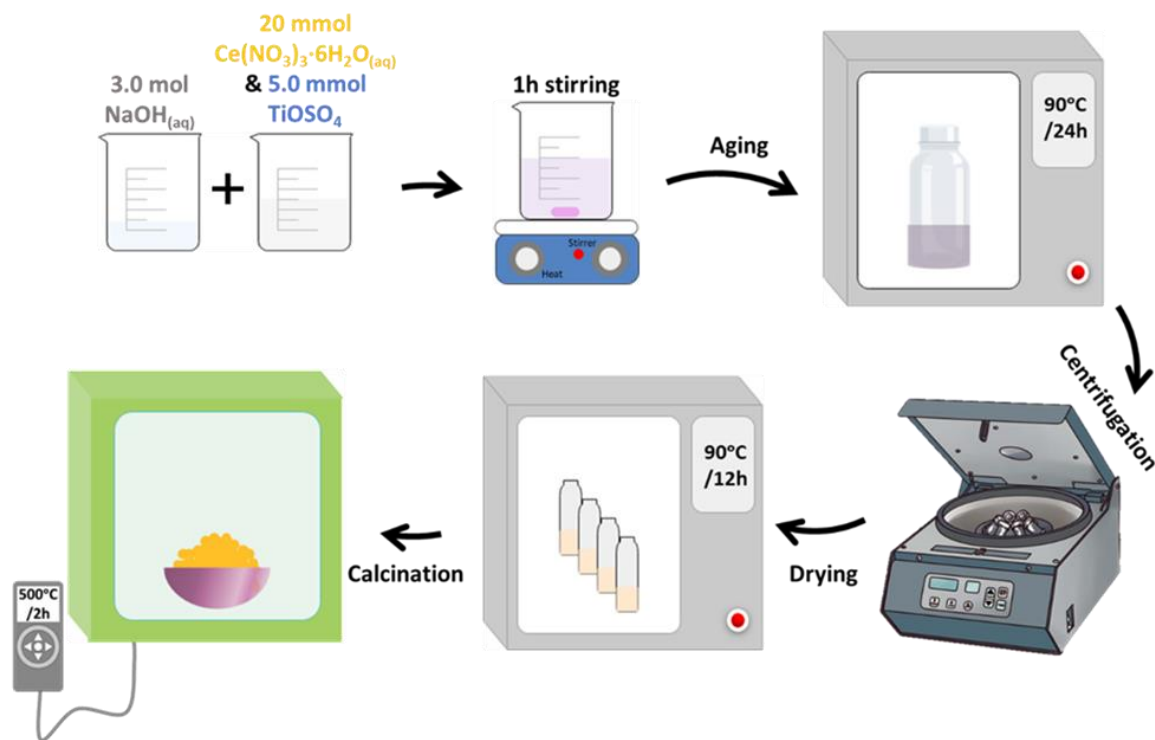


**Figure 2.4.** One-step hydrothermal synthesis of Ceria-titania (CeO<sub>2</sub>/TiO<sub>2</sub>-H1).

**Ceria-titania by two-step hydrothermal synthesis** (CeO<sub>2</sub>/TiO<sub>2</sub>-H2) was prepared as follows: bare ceria nanorods (CeO<sub>2</sub> NRs) were initially prepared by the hydrothermal method, as mentioned above in the one-step hydrothermal method, with the variation of utilizing 25 mmol Ce(NO<sub>3</sub>)<sub>3</sub>·6H<sub>2</sub>O instead of 20 mmol and the absence of TiOSO<sub>4</sub>. Then, CeO<sub>2</sub>/TiO<sub>2</sub> nanorods were prepared by a wet-chemical method. Typically, 0.15 g of bare ceria nanorods was dispersed into 200 mL of double-deionized water under vigorous stirring and 0.035 g TiOSO<sub>4</sub> was dissolved into 1.1 mL of double-deionized water and added into the aforementioned suspension at room temperature. The mixture was left for additional stirring for 3 h and aged at room temperature for 2–3 h. The precipitate was dried for 12 h at 90 °C, followed by calcination at 500 °C for 2 h under air (heating rate 5 °C min<sup>-1</sup>). The two-step hydrothermal synthesis of CeO<sub>2</sub>/TiO<sub>2</sub>-H2 is presented in Figure 2.5.

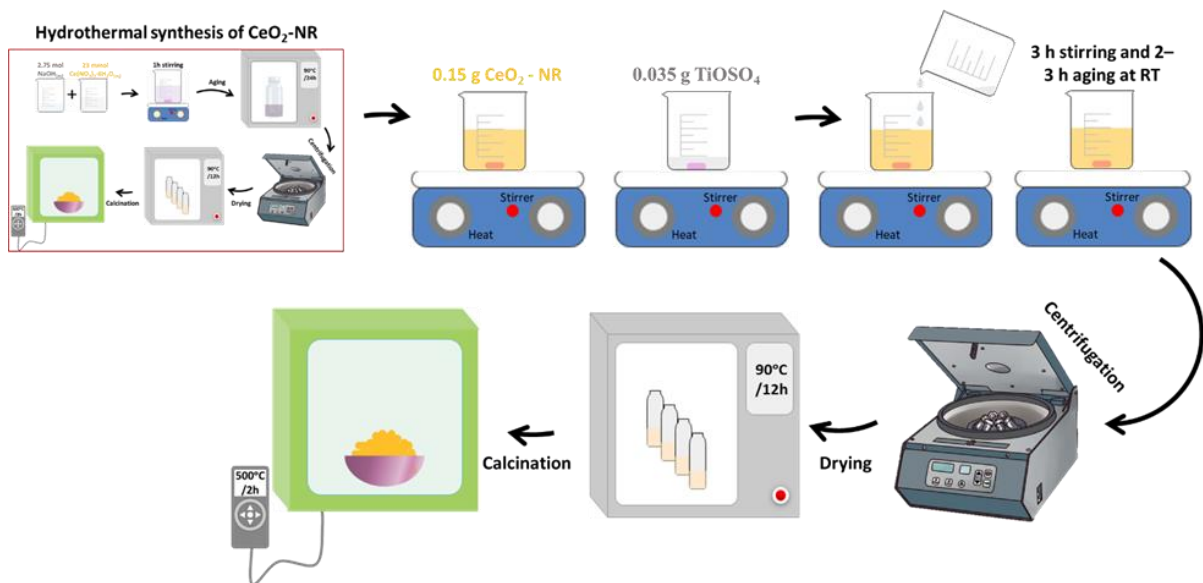


**Figure 2.5.** Two-step hydrothermal synthesis of Ceria-titania ( $\text{CeO}_2/\text{TiO}_2\text{-H2}$ ).

*Ceria-titania by the Stöber method* ( $\text{CeO}_2/\text{TiO}_2\text{-S}$ ) was prepared as follows: bare ceria nanorods were initially synthesized by the hydrothermal method as previously described. 0.25 g of bare ceria nanorods were dispersed in 334 mL of absolute ethanol and mixed with 1 mL concentrated ammonia solution (28 wt.%) under ultrasonication for 20 min. Then, 0.125 mL TBOT was added dropwise, and the solution was left stirring at 45 °C for 24 h. The resulting precipitate was recovered by centrifugation and washed with double-deionized water and ethanol. The precipitate was dried for 12 h at 90 °C, followed by calcination at 500 °C for 2 h under air (heating rate 5 °C  $\text{min}^{-1}$ ). The Stöber method of  $\text{CeO}_2/\text{TiO}_2\text{-S}$  is presented in Figure 2.6.

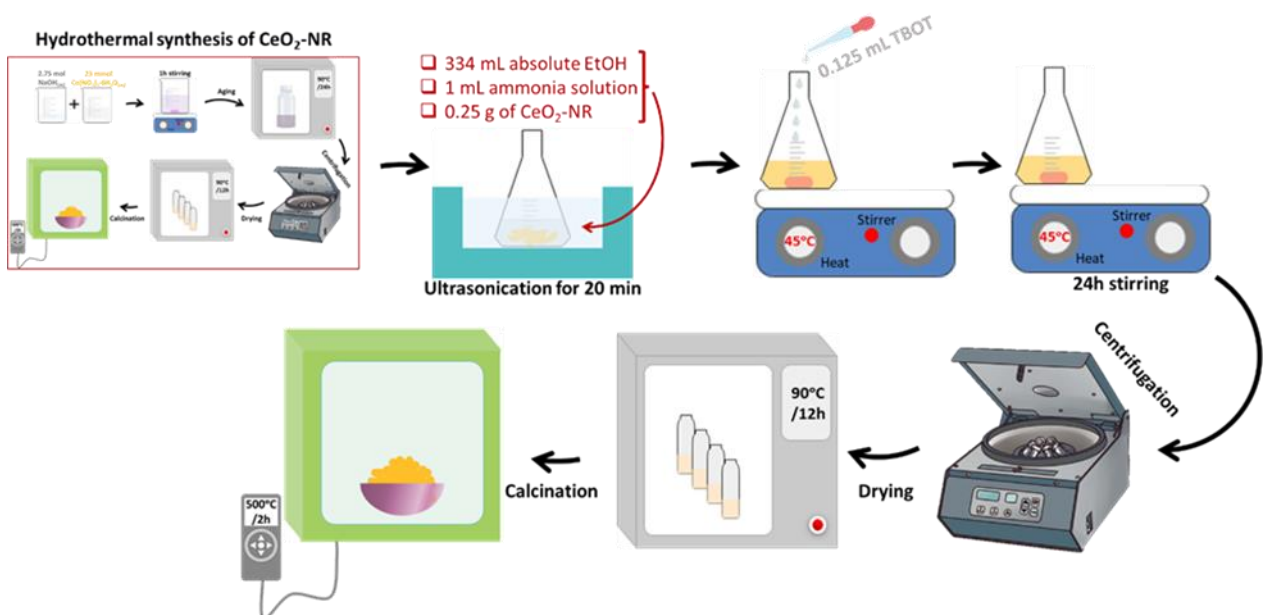


**Figure 2.6.** Stöber method of Ceria-titania ( $\text{CeO}_2/\text{TiO}_2\text{-S}$ ).

#### 2.1.4. Synthesis of CeO<sub>2</sub>/ZnO and Ni/CeO<sub>2</sub>-ZnO

Bare ceria nanorods were initially synthesized using the hydrothermal method, as detailed in subsection 2.1.1. To prepare CeO<sub>2</sub>/ZnO mixed oxides with different Zn:Ce ratios (0.2, 0.4, 0.6), a modified hydrothermal method was employed<sup>8</sup>. Specifically, 0.38 g of HO<sub>2</sub>CCO<sub>2</sub>H, 0.64 g of Zn(CH<sub>3</sub>COO)<sub>2</sub>·2H<sub>2</sub>O, and a specific quantity of CeO<sub>2</sub> nanorods (2.42 g, 1.21 g, and 0.81 g for Zn/Ce = 0.2, 0.4, and 0.6, respectively) were dispersed in 40 mL of double deionized water under stirring for 20 minutes. The resulting suspension was then transferred into a plastic bottle and aged at 70 °C for 1 h. The precipitate was recovered through centrifugation, washed with double deionized water and ethanol, dried at room temperature overnight, and finally calcined at 500 °C for 2 h under air flow, with a heating ramp of 5 °C min<sup>-1</sup>. Additionally, a pure zinc oxide sample was prepared using the same method for comparison purposes. The resulting materials were labeled as CeO<sub>2</sub>/ZnO-x, where x represents the Zn:Ce atomic ratio. The preparation procedure of CeO<sub>2</sub>/ZnO is presented in Figure 2.7.

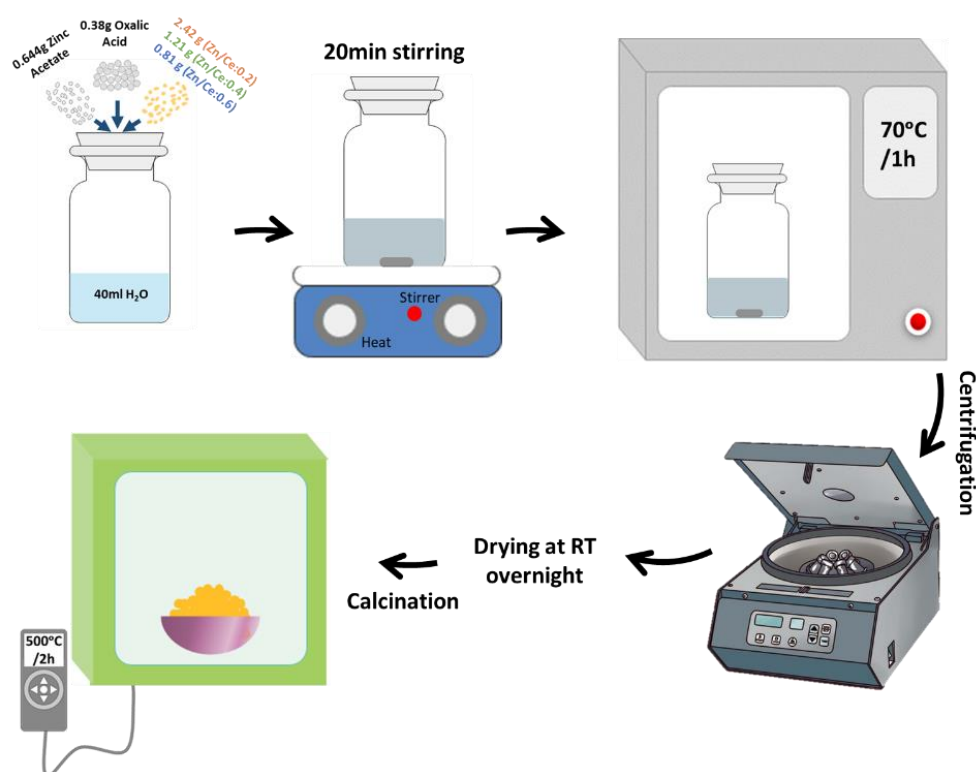


**Figure 2.7.** Preparation method of Ceria-Zinc (CeO<sub>2</sub>/ZnO).

Regarding the Ni-containing samples, nickel was introduced using a typical wet impregnation method, as detailed in subsection 2.1.2. The nominal Ni loading remained consistent at approximately 8 wt.%, and the resulting samples were labeled as Ni/CeO<sub>2</sub>, Ni/ZnO, and Ni/CeO<sub>2</sub>-ZnO-x, based on the respective underlying support materials employed<sup>9</sup>.

### 2.1.5. Synthesis of ceria triangles ( $\text{CeO}_2$ TR) and Ni/ $\text{CeO}_2$ TR

Cerium oxide triangles ( $\text{CeO}_2$  TR) were synthesized using the solvothermal method. In a typical experiment, 3.17 g of  $\text{Ce}(\text{CH}_3\text{CO}_2)_3 \cdot x\text{H}_2\text{O}$  and 3 g of urea were dissolved in 30 ml of ethylene glycol (EG) with vigorous stirring for 1 h. The resulting solution was then transferred into a Teflon-lined stainless-steel autoclave and heated at 220 °C for 24 h. Afterward, the precipitate obtained was dried at room temperature and calcined at 400 °C for 2 h under an air flow, using a heating ramp of 5 °C  $\text{min}^{-1}$ , to obtain the final product. The preparation process of  $\text{CeO}_2$  TR is presented in Figure 2.8.

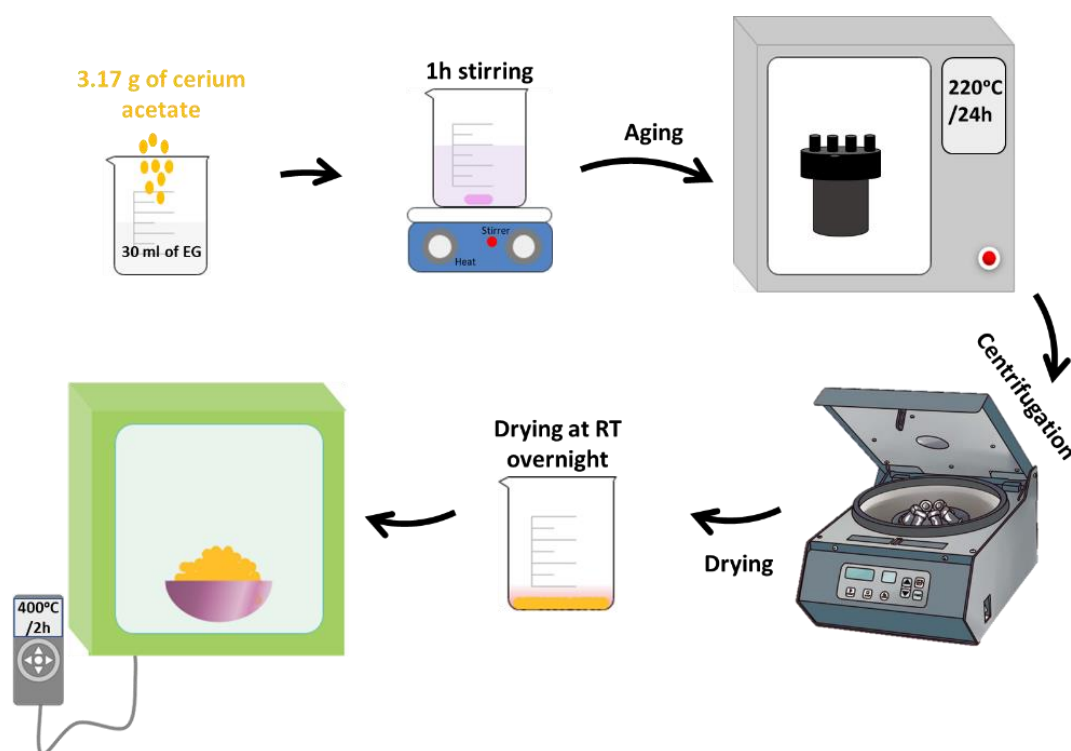


**Figure 2.8.** Solvothermal synthesis of bare ceria triangles ( $\text{CeO}_2$  TR).

In order to synthesize the Ni/ $\text{CeO}_2$  TR sample, the wet impregnation method was employed (Figure 2.2.), with the nominal Ni loading maintained at approximately 8 wt.%.

### 2.1.6. Synthesis of Bulk $\text{g-C}_3\text{N}_4$ and $\text{g-C}_3\text{N}_4$ Nanosheets

The **bulk  $\text{g-C}_3\text{N}_4$**  (denoted as CNB) was synthesized through the thermal polycondensation of melamine<sup>10</sup>. In a typical synthesis, 50 g of melamine was placed in an alumina crucible with a cover inside a muffle furnace and heated at 510 °C for 2 h, followed by an additional 2 hour-heating at 530 °C, while maintaining a constant air flow (heating rate: 2 °C  $\text{min}^{-1}$ ). After the process, a dark yellow solid was obtained, which was subsequently milled and collected for further use.

**$\text{g-C}_3\text{N}_4$  nanosheets** (denoted as CNNs) were synthesized by direct thermal exfoliation of CNB. For this, 5 g of CNB was placed in an open ceramic container and heated at 580 °C for 2 h, using a ramp

rate of  $2\text{ }^{\circ}\text{C min}^{-1}$  in a muffle furnace. The resulting sample exhibited a pale-yellow color. The preparation process of bulk  $\text{g-C}_3\text{N}_4$  and  $\text{g-C}_3\text{N}_4$  nanosheets is presented in Figure 2.9.

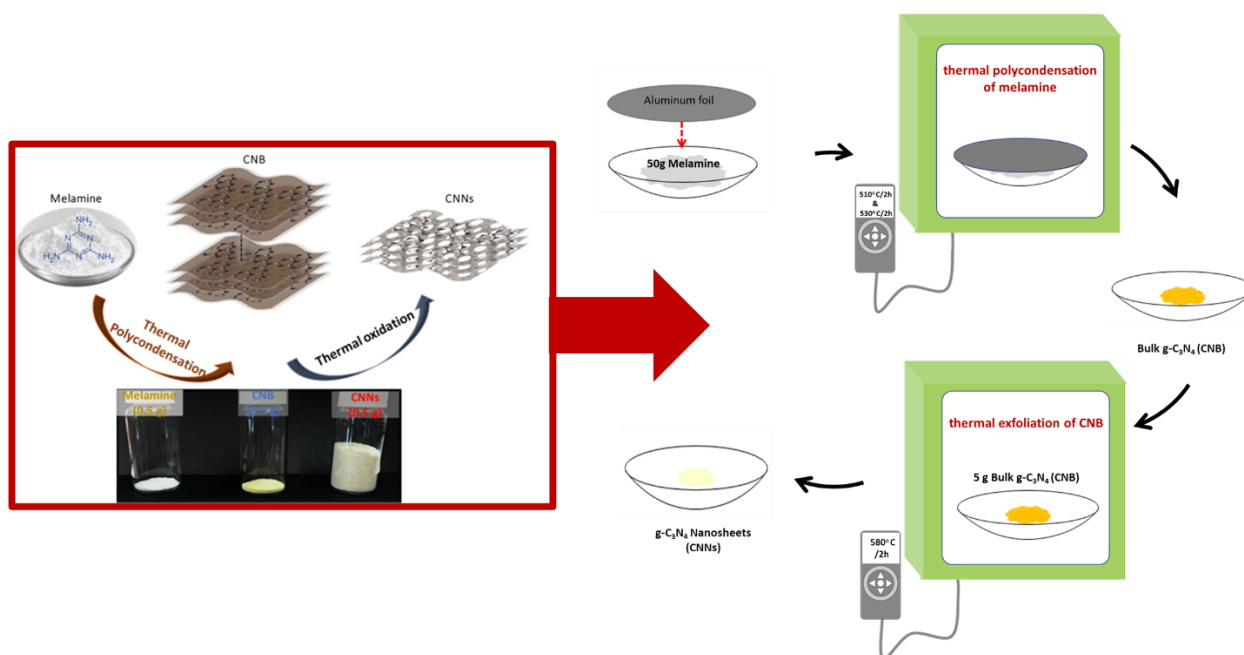


**Figure 2.9.** The preparation process of Bulk  $\text{g-C}_3\text{N}_4$  and  $\text{g-C}_3\text{N}_4$  Nanosheets.

### 2.1.7. Synthesis of $\text{g-C}_3\text{N}_4$ -Based Transition Metal Catalysts

After synthesizing bulk  $\text{g-C}_3\text{N}_4$ , different transition metals were added using the impregnation method. Specifically, titanium (Ti), vanadium (V), chromium (Cr), manganese (Mn), iron (Fe), cobalt (Co), nickel (Ni), copper (Cu), and zinc (Zn) were incorporated into the bulk  $\text{g-C}_3\text{N}_4$  via impregnation. The resulting catalysts were labeled as  $\text{M/g-C}_3\text{N}_4$ , where M represents Ti, V, Cr, Mn, Fe, Co, Ni, Cu, or Zn. Metal precursor, including Titanium IV oxysulfate ( $\text{TiOSO}_4 \cdot 2\text{H}_2\text{O}$ ), Vanadium (V) oxytripropoxide (VOTP), Chromium(III) acetate hydroxide ( $\text{Cr}_3(\text{OH})_2(\text{OOCCH}_3)_7$ ), Manganese (II) acetate tetrahydrate ( $\text{CH}_3\text{COO})_2\text{Mn} \cdot 4\text{H}_2\text{O}$ ), Iron(II) sulfate heptahydrate ( $\text{Fe}_2(\text{SO}_4)_3 \cdot x\text{H}_2\text{O}$ ), Cobalt(II) acetate tetrahydrate ( $\text{CH}_3\text{COO})_2\text{Co} \cdot 4\text{H}_2\text{O}$ ), Nickel(II) acetate tetrahydrate ( $\text{Ni}(\text{OCOCH}_3)_2 \cdot 4\text{H}_2\text{O}$ ), Copper(II) acetate hydrate ( $\text{Cu}(\text{CO}_2\text{CH}_3)_2 \cdot x\text{H}_2\text{O}$ ) and Zinc acetate dihydrate ( $\text{Zn}(\text{CH}_3\text{COO})_2 \cdot 2\text{H}_2\text{O}$ ) were utilized to achieve a metal loading of 1 wt.% M.

The synthesis of the  $\text{M/g-C}_3\text{N}_4$  catalysts followed the procedure outlined below: First, 500 mg of bulk  $\text{g-C}_3\text{N}_4$  was dispersed in methanol under ultrasonication for 20 min and then an appropriate amount of each metal precursor was added into the above solution. The mixture was stirred until the solvent evaporated. The resulting product was dried overnight at room temperature followed by milling and heating at  $400\text{ }^{\circ}\text{C}$  for 1 h under air flow (heating ramp of  $2\text{ }^{\circ}\text{C min}^{-1}$ ). A visual representation of the synthetic process of  $\text{M/g-C}_3\text{N}_4$  is presented in Figure 2.10.

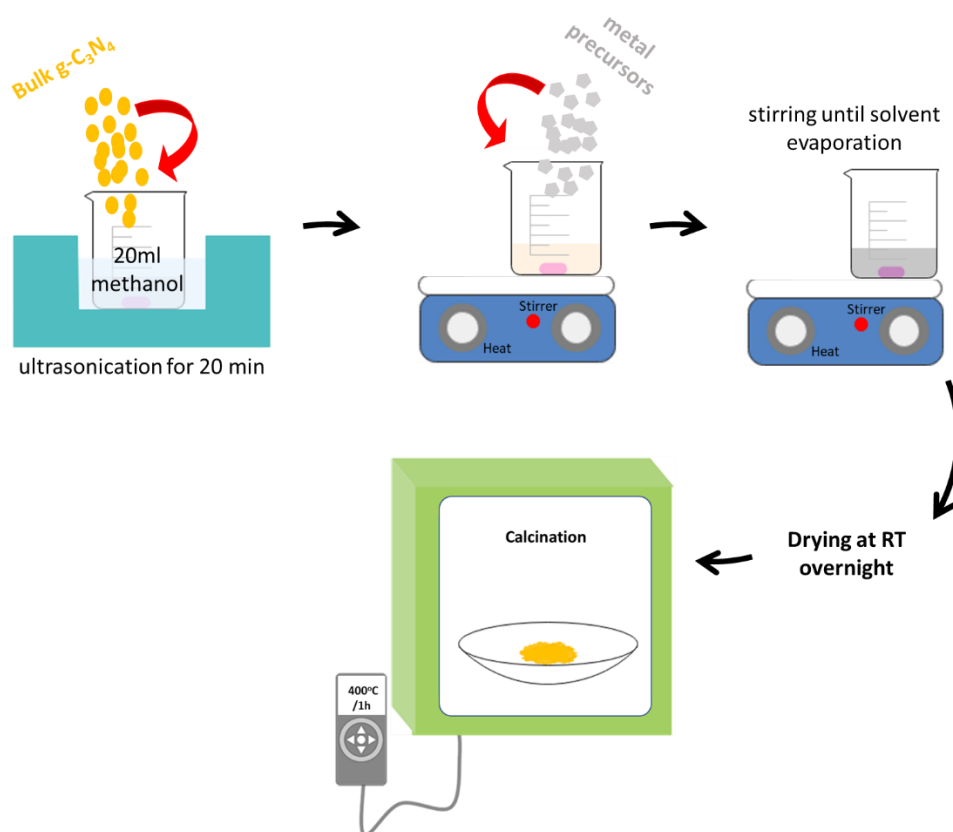


**Figure 2.10.** The preparation process of M/g- $\text{C}_3\text{N}_4$ .

**Table 2.1.** The catalytic materials synthesized in the present thesis along with the characterization techniques used and the targeted reactions.

Material	Preparation method	metal loading wt. %	Characterization	Catalytic reaction
CeO <sub>2</sub> NR	hydrothermal	-	BET, XRD, SEM/EDS, TEM, RAMAN, TPR	CO + O <sub>2</sub> , CO <sub>2</sub> + H <sub>2</sub>
CeO <sub>2</sub> TR	solvothermal	-	BET, XRD, SEM/EDS, XPS, Raman, TPR	CO <sub>2</sub> + H <sub>2</sub>
CNB	thermal polycondensation	-	BET, XRD, TGA, SEM/EDS, TEM, AFM, UV-Vis, PL, FTIR, zeta potential	Photocatalysis, Adsorption
CNNs	thermal exfoliation	-		Photocatalysis, Adsorption
<b>Ceria-based metal catalysts</b>				
M/CeO <sub>2</sub> NR (M: Ti, V, Cr, Mn, Fe, Co, Ni, Cu)	Wet impregnation	~8	BET, XRD, SEM/EDS, TEM, TPR	CO <sub>2</sub> + H <sub>2</sub>
Ni/CeO <sub>2-x</sub> (x = Ni/Ce = 0.10, 0.25, 0.50, 1.00, 1.50)	Wet impregnation	~3-34	BET, XRD, SEM/EDS, TEM, Raman	CO <sub>2</sub> + H <sub>2</sub>
CeO <sub>2</sub> /TiO <sub>2</sub>	precipitation, hydrothermal in one and two steps, Stöber		BET, XRD, SEM/EDS, TEM, TPR	CO + O <sub>2</sub>
CeO <sub>2</sub> /ZnO	hydrothermal in two steps		BET, XRD, SEM/EDS, TEM, Raman, TPR	CO + O <sub>2</sub> , CO <sub>2</sub> + H <sub>2</sub>
Ni/CeO <sub>2</sub> -ZnO	Wet impregnation	8	BET, XRD, SEM/EDS, TEM, Raman, TPR	CO <sub>2</sub> + H <sub>2</sub>
Ni/CeO <sub>2</sub> TR	Wet impregnation	8	BET, XRD, SEM/EDS, XPS, Raman, TPR	CO <sub>2</sub> + H <sub>2</sub>
<b>g-C<sub>3</sub>N<sub>4</sub>-based metal catalysts</b>				
M/g-C <sub>3</sub> N <sub>4</sub> (M: Ti, V, Cr, Mn, Fe, Co, Ni, Cu, Zn)	Wet impregnation	1	XRD, SEM/EDS, TEM, UV-Vis	Photocatalysis

## 2.2 Characterization Techniques

The physicochemical properties of the as-prepared materials were comprehensively characterized using a range of techniques. The actual metal content was determined using Inductively Coupled Plasma (ICP) analysis. To gain insight into the textural properties, N<sub>2</sub> adsorption-desorption at -196

°C (BET method) was employed. The structural properties were examined using X-ray Diffraction (XRD), while Transmission Electron Microscopy (TEM) was utilized to study the morphological features. Elemental mapping was carried out using Scanning Electron Microscopy-Energy Dispersive X-ray Spectroscopy (SEM-EDS). The redox properties were determined using Temperature Programmed Reduction with H<sub>2</sub> as a reducing agent (H<sub>2</sub>-TPR). Surface characteristics were defined through X-ray Photoelectron Spectroscopy (XPS), and the structural defects of the as-prepared samples were analyzed using Raman spectroscopy.

These characterizations were performed at the following institutions: the Institute of Electronic Structure and Laser (IESL-FORTH), the Technical University of Crete, the Chemical Process & Energy Resources Institute (CPERI) of the Centre for Research & Technology Hellas (CERTH), the Laboratory of Chemistry and Materials Technology at the National and Kapodistrian University of Athens, and the Department of Chemical Engineering at the University of Patras. Detailed descriptions of the procedures followed for each characterization technique are presented in the subsequent sub-sections.

#### 2.2.1. Elemental Analysis (ICP)

Elemental analysis of various metals in indicative samples was performed by means of Inductively Coupled Plasma Atomic Emission Spectroscopy (ICP-AES) in a Perkin-Elmer Optima 4300DVm apparatus at CPERI/CERTH.

#### 2.2.2. Textural and Structural Characterization (BET and XRD)

**N<sub>2</sub> physisorption (BET method):** The textural characteristics of the catalysts were assessed using N<sub>2</sub> adsorption-desorption isotherms at the boiling point of nitrogen (−196 °C). The specific surface areas (m<sup>2</sup>/g) were determined using the well-established Brunauer-Emmett-Teller (BET) method, which involved measuring the relative pressures in the range of 0.05-0.30. The specific pore volume (cm<sup>3</sup>/g) was calculated based on the highest relative pressure, while the average pore size (nm) was determined using the Barrett-Joyner-Halenda (BJH) method. Before each experiment, the samples underwent a vacuum degassing process at temperatures ranging from 250 to 300 °C for 3–5 hours, depending on the specific materials used. N<sub>2</sub> physisorption experiments were conducted at CPERI/CERTH. At CPERI/CERTH, a Micromeritics Tristar 3000 (Micromeritics, Norcross, GA, USA) instrument was utilized.

**X-Ray Diffractometry (XRD):** The structural properties of the samples were analyzed using powder X-ray diffraction (XRD) on a Rigaku diffractometer (model RINT 2000, Tokyo, Japan). X-rays were generated by a 12 kW rotating anode generator with a Cu anode, equipped with a secondary pyrolytic graphite monochromator. Cu K $\alpha$  radiation with a wavelength ( $\lambda$ ) of 0.154 nm was employed. XRD

measurements were conducted in a  $\theta/2\theta$  configuration, scanning from  $10^\circ$  to  $80^\circ$  with a step size of  $0.05^\circ \text{ min}^{-1}$ .

Scherrer's equation (Eq. 1) was employed to determine the primary particle size of a given crystal phase based on the most intense diffraction peak of each pattern <sup>2,7</sup>:

$$D_{XRD} = \frac{0.9\lambda}{\beta_{hkl}\cos\theta} \quad (1)$$

where  $\beta_{hkl}$  is the full width at half maximum and  $\theta$  is the Bragg diffraction angle.

The microstrain ( $\varepsilon$ ) of crystal is an assessment of lattice stress available in the materials due to lattice elongation, distortion, or contraction, which can be determined according to the broadening degree of XRD diffraction peak <sup>11</sup>.

$$\varepsilon = \frac{\beta_{hkl}}{4\tan\theta} \quad (2)$$

where  $\beta_{hkl}$  is the full width at half maximum and  $\theta$  is the Bragg diffraction angle.

### 2.2.3. Morphological and Topographical Characterization (TEM, SEM/EDS, AFM)

**Transmission Electron Microscopy (TEM):** Transmission Electron Microscopy (TEM) imaging was conducted using a JEM-2100 instrument from JEOL (Tokyo, Japan) equipped with a LaB<sub>6</sub> filament. The TEM operated at an acceleration voltage of 200 kV. To prepare the materials for TEM observation, they were dispersed in an ultrasonic bath to ensure uniform distribution. A 400 mesh formvar/carbon copper grid (Agar Scientific, Essex, UK) was then dipped into the solution containing the dispersed materials. This grid served as the substrate for the TEM analysis. Characterization of the size and distribution of metal and oxide particles was performed by analyzing representative TEM images using the ImageJ software. The TEM images provided high-resolution details of the sample, allowing for precise measurement and analysis of the particles' characteristics. The particle size of Ni was further evaluated by comparing the number of average diameters ( $d_n$ ) with the calculated values for the surface average diameter ( $d_s$ ) and volume average diameter ( $d_v$ ) (Chapter 4, Sub-section 4.3.4) <sup>3,12</sup>. The complete particle size distribution data obtained from TEM analysis for each sample were used for these calculations. The expressions used for the calculations are as follows:

$$d_n = \frac{\sum_i n_i d_i}{\sum_i n_i} \quad (3)$$

$$d_s = \frac{\sum_i n_i d_i^3}{\sum_i n_i d_i^2} \quad (4)$$

$$d_v = \frac{\sum_i n_i d_i^4}{\sum_i n_i d_i^3} \quad (5)$$

$D_{Ni}$  (%) is the Ni dispersion calculated by TEM analysis, according to Eq. (6) <sup>12</sup> assuming hemispherical particle shape, where  $V_M$  is the bulk atomic volume ( $1.09 \times 10^{-23}$  cm<sup>3</sup>) and  $A_M$  is the atomic area ( $6.51 \times 10^{-16}$  cm<sup>2</sup>) of a Ni atom:

$$D_{Ni}(\%) = 6 \times 10^9 \frac{V_{Ni}}{A_{Ni}} \frac{1}{d_s} \quad (6)$$

**Scanning Electron Microscopy - Energy Dispersive Spectroscopy (SEM-EDS):** The surface morphology of the samples was examined using Scanning Electron Microscopy (SEM) with a JEOL JSM-6390LV instrument from JEOL Ltd. (Akishima, Tokyo, Japan). The SEM operated at 20 keV and was equipped with an energy-dispersive X-ray spectrometry (EDS) system for elemental analysis. To prepare the samples for SEM observation, the powders were placed on double-sided adhesive tape and coated with a thin layer of gold (Au) using a sputtering process. The gold coating, approximately 10 nm in thickness, helped enhance the conductivity and improve imaging quality. The specimens were observed under two different detection modes: secondary electrons (SE) and backscattered electrons (BSE).

**Atomic Force Microscopy (AFM):** AFM measurements were carried out using a Bruker Dimension Icon instrument under ambient conditions. For obtaining topographic images, silicon nitride ScanAsyst-Air probes with a tip radius (R) of 2 nm, spring constant (k) of 0.4 N/m, and resonance frequency (f) of 70 kHz were utilized. To ensure better visualization of the finer features of the sample, the applied forces were kept as low as possible during the measurements. This approach helped minimize any potential sample deformation or damage while maintaining a high-resolution imaging capability. AFM measurements and analysis were conducted collaboratively at the Department of Chemical Engineering at the University of Patras and FORTH/ICE-HT.

#### 2.2.4. Redox Characterization (H<sub>2</sub>-TPR)

The redox properties of the as-prepared samples were evaluated through temperature-programmed reduction (H<sub>2</sub>-TPR), carried out in three separate laboratories: the Energy & Environmental Systems Lab (IEESL) of the School of Production Engineering and Management at the Technical University of Crete, the Laboratory of Chemistry and Materials Technology at the National and Kapodistrian University of Athens, and the Chemical Process & Energy Resources Institute, Centre for Research & Technology Hellas (CPERI/CERTH).

In a typical experiment, a 100 mg sample was placed in a quartz fixed-bed reactor and heated to 800 °C at a rate of 10-20 K min<sup>-1</sup> using a 5% H<sub>2</sub>/He. Prior to the TPR experiments, the samples underwent a pre-treatment process. They were subjected to a temperature of up to 500 °C for 30 min under a gas mixture of 20 vol.% O<sub>2</sub> in He with a flow rate of 20-50 cm<sup>3</sup> min<sup>-1</sup>. Subsequently, the samples were cooled down to 200 °C while maintaining the same gas mixture, and then further cooled to room temperature under pure He flow. To quantify the H<sub>2</sub> uptake from the samples, a known quantity of CuO standard sample was used as a reference. The H<sub>2</sub> uptake (mmol H<sub>2</sub> g<sup>-1</sup>), which corresponds to the H<sub>2</sub> consumed by reducible oxygen species, was determined by integrating the area under the TPR peaks. The Oxygen Storage Capacity (OSC), measured in μmol O<sub>2</sub> g<sup>-1</sup>, was calculated as half of the H<sub>2</sub> uptake value.

#### 2.2.5. Spectroscopic Characterization: XPS, Raman, FTIR, PL, and UV-Vis Spectroscopy

**X-ray photoelectron spectroscopy (XPS):** X-ray photoelectron spectroscopy (XPS) analysis was conducted on the as-prepared samples using a SPECS FlexMod XPS instrument equipped with a 1D-DLD upgraded Detector and an XR-50 Dual Anode X-ray source. To prepare the samples for analysis, they were pressed into pellets with approximately 1 mm thickness. These pellets were then securely attached to the sample holder using small pieces of double-sided carbon tape. The XPS analysis was performed using a monochromatic Al K $\alpha$  X-ray source operating at 15 kV, with an energy of 1486.7 eV. The data acquisition was carried out using SpecsLAB Prodigy software, while the data analysis was performed using CASAXPS software. To correct the effects of electric charging during the analysis, the carbon peak C 1s (285 eV) was used as a reference. The electric charge correction was applied to ensure an accurate and reliable interpretation of the XPS spectra. The peak spectra obtained from the analysis were fitted using CasaXPS software. A Gaussian–Lorentzian peak shape was utilized for peak fitting, and the background subtraction was performed using the Shirley (or Linear) type background subtraction method.

**Raman spectroscopy:** Raman measurements were performed using a Nicolet Almega XR Raman spectrometer. The excitation source employed was a 473 nm blue laser, selected for its ability to

induce Raman scattering in the sample. The Raman spectrometer was operated at room temperature, and the laser power was set to 15 mW. The excitation beam was focused onto the sample through a confocal microscope equipped with a 50x objective lens.

**Fourier Transform Infrared (FTIR) spectroscopy:** The attenuated total reflectance–Fourier transform infrared (ATR–FTIR) spectra were acquired using a Thermo-Electron Nicolet 6700 FT-IR optical spectrometer equipped with a DTGS KBr detector. The spectra were recorded at a high resolution of 2 cm<sup>-1</sup>, allowing for a detailed analysis of the sample's infra-red absorption characteristics.

**UV-Visible (UV-Vis) spectroscopy:** The UV-Vis/Near-IR diffuse reflectance spectra of the g-C<sub>3</sub>N<sub>4</sub>-based catalysts in powder form were acquired using a Perkin Elmer LAMBDA 950 spectrophotometer. These spectra were recorded over a wavelength range of 250–2500 nm, with BaSO<sub>4</sub> employed as the reference standard. The adoption of Diffuse Reflectance Spectroscopy (DRS) enabled the characterization of the sample's optical properties.

To analyze the collected DRS data and derive the absorption coefficient, a transformation based on the Kubelka-Munk function <sup>13</sup> (Eq. (7)) was employed:

$$F(R_{\infty}) = \frac{K(\lambda)}{S(\lambda)} = \frac{(1-R_{\infty})^2}{2R_{\infty}} \quad (7)$$

where K: absorption coefficient, S: scattering coefficient, and  $R_{\infty} = R/R_{ref}$ : reflectance.

The optical band gap energies of the samples were determined by plotting the Kubelka–Munk function as a function of incident energy (hv) (Eq. (8)) <sup>14</sup>.

$$(ahv)^{1/n} = B(hv - E_g) \quad (8)$$

where  $\alpha$ : absorption coefficient, hv: incident photon energy,  $E_g$ : band gap energy, B: a constant related to the effective masses of charge carriers associated with valance and conduction bands, and n: a factor controlled by the kind of optical transition caused by absorbed photons (n = 1/2 for direct transition, n = 2 for indirect transition).

To estimate the band gap energy ( $E_g$ ), the F(R) values were assumed to be proportional to the optical absorption coefficients. The estimation of  $E_g$  was carried out by plotting  $(F(R)*hv)^{1/n}$  against hv, following the Tauc plot method <sup>13,14</sup>. For this analysis, an indirect band gap transition of g-C<sub>3</sub>N<sub>4</sub> was considered. The reflectance spectra were transformed to dependencies of  $(F(R)*hv)^{1/2}$  on hv, which facilitates the determination of the optical band gap energy ( $E_g$ ) using the Tauc plot method.

**Photoluminescence (PL) spectroscopy:** Photoluminescence spectra were acquired using an advanced fluorescence spectrophotometer manufactured by Agilent Technologies. The instrument was equipped with a high-performance Xenon lamp, which served as the excitation source for the measurements. To initiate photoluminescence, the sample was excited with light at a specific wavelength of 325 nm. This excitation wavelength was carefully selected to optimize the emission response and capture the fluorescence signals of interest. These measurements were conducted collaboratively at the Department of Chemical Engineering at the University of Patras and FORTH/ICE-HT.

#### 2.2.6. Thermogravimetric analysis (TGA)

Thermal analysis of the samples was conducted using a thermogravimetric analyzer (SDT, Q600). The analysis was performed under a synthetic air flow of  $100 \text{ mL min}^{-1}$  to simulate atmospheric conditions. The programmed heating profile involved ramping the temperature from room temperature ( $25 \text{ }^\circ\text{C}$ ) up to  $750 \text{ }^\circ\text{C}$  at a constant heating rate of  $2 \text{ }^\circ\text{C min}^{-1}$ . For each measurement, a mass of 10 mg of the powder sample was used.

#### 2.2.7. Zeta potential

The zeta potential measurements were conducted using a Zetasizer Nano-ZS90 instrument manufactured by Malvern, UK. The zeta potential is a key parameter that characterizes the surface charge and stability of colloidal particles in a solution. To perform the measurements, 10 mg of each powder sample was dispersed in 200 mL of an aqueous solution containing  $\text{KNO}_3$ . The dispersion process was facilitated by applying ultrasonication for 30 minutes. This ensured the homogenous dispersion of the particles in the solution. The pH of the suspension was then adjusted to different values ranging from 2 to 11. This was achieved by carefully adding either 0.1 M  $\text{HNO}_3$  or KOH solutions to the suspension, allowing for precise control of the pH.

### 2.3. Adsorption Experiments

Adsorption experiments were conducted using two types of adsorbents, namely, bulk  $\text{g-C}_3\text{N}_4$  (CNB) and  $\text{g-C}_3\text{N}_4$  nanosheets (CNNs). In a typical experiment, 25 mg of the sample was dispersed in 20 mL of a dye solution with concentrations ranging from 10 to 200 ppm. The mixture was then stirred at a specific temperature between 274 K and 300 K for a defined period until adsorption equilibrium was achieved. The pH of the solution was adjusted using either 0.1 M HCl or 0.1 M NaOH. Subsequently, the solution was centrifuged to separate and remove the  $\text{g-C}_3\text{N}_4$  particles. The absorbance values of the resulting dye solution were measured using a UV-visible spectrophotometer (Cary 50, Agilent Technologies), and the equilibrium concentrations were determined by referencing

an external standard calibration. The equilibrium adsorption amount was calculated using the following equation:

$$Q_e = \frac{(C_0 - C_e)V}{m} \quad (9)$$

where  $Q_e$  (mg/g) is the equilibrium adsorption amount,  $C_0$  (mg/L) is the initial concentration of the dye solution,  $C_e$  (mg/L) is the equilibrium concentration of the dye solution, and  $V$  and  $m$  are the volume (L) and mass (g) of dye solution, respectively.

To investigate the adsorption kinetics, pseudo-first-order, and pseudo-second-order kinetic models were studied<sup>15-17</sup>.

Pseudo-first-order model:  $\ln(Q_e - Q_t) = \ln Q_e - k_1 t$  (10)

Pseudo-second-order model:  $\frac{t}{Q_t} = \frac{1}{k_2 Q_e^2} + \frac{t}{Q_e}$  (11)

where  $Q_e$ ,  $Q_t$  (mg/g) are the amounts of dye adsorbed at equilibrium and  $t$  (time), respectively;  $k_1$  ( $\text{min}^{-1}$ ) is the pseudo-first-order rate constant;  $k_2$  ( $\text{g mg}^{-1} \text{min}^{-1}$ ) is the pseudo-second-order rate constant.

The experimental equilibrium data were fitted by Langmuir and Freundlich isotherm models to gain an understanding of the sorption process<sup>15,17,18</sup>. The expression of each model is the following:

Langmuir model:  $q_e = \frac{q_m K_L C_e}{1 + K_L C_e}$  (12)

Freundlich model:  $q_e = K_f C_e^{1/n}$  (13)

where  $Q_m$  is the maximum adsorption capacity (mg/g);  $K_L$  is the Langmuir adsorption constant (L/mg);  $C_e$  is the dye concentration at equilibrium (mg/L);  $K_f$  and  $n$  are Freundlich constants.

To investigate the adsorption selectivity of CNNs, selective adsorption experiments were conducted using cationic dyes, anionic dyes, as well as three groups of dye mixtures. In a typical procedure, 25 mg of CNNs was added to 20 mL of a dye solution with a concentration of 10 ppm and was stirred at room temperature for 24 h. For the regeneration of CNNs, desorption experiments were performed.

Specifically, CNNs that had adsorbed methylene blue were placed in an eluent containing 0.1 M HCl. The suspension was then subjected to sonication for 1 h. Subsequently, the CNNs were collected and separated by centrifugation, washed with water, and dried overnight at 60 °C.

## 2.4. Catalytic Evaluation Studies

The present thesis investigates the performance of the catalytic materials in a range of reactions, including CO oxidation, CO<sub>2</sub> hydrogenation to CH<sub>4</sub> and CO, and photocatalysis. These investigations were carried out at the Industrial, Energy, and Environmental Systems Lab (IEESL) in the School of Production Engineering and Management at the Technical University of Crete. Collaboratively, this research involved the Institute of Electronic Structure and Laser (IESL-FORTH), the Chemical Process & Energy Resources Institute (CPERI) of the Centre for Research & Technology Hellas (CERTH), the University of Western Macedonia, and the National and Kapodistrian University of Athens. The subsequent subsections provide comprehensive details regarding the experimental procedures employed during these catalytic studies.

### 2.4.1. CO Oxidation

Catalytic tests were carried out to investigate the performance of bare ceria, ceria-titania, and ceria-zinc oxide catalysts for CO oxidation. The experiments were conducted in a quartz fixed-bed tubular microreactor with a diameter of 12.95 mm, operating at atmospheric pressure and containing 100 mg of catalyst. To create a controlled and homogeneous environment, a feed gas mixture consisting of 0.2 vol.% CO and 1 vol.% O<sub>2</sub> in He was passed through the reactor at a total flow rate of 80 mL min<sup>-1</sup>, regulated by Mass Flow controllers and mixed in a dedicated chamber.

The temperature of the catalyst was measured using a K-Type thermocouple located in the catalyst bed. The Gas Hour Space Velocity (GHSV) of the feed stream was set to 40,000 h<sup>-1</sup>. Prior to the catalytic experiments, all samples were treated by heating them up to 480 °C at a rate of 10 degrees/min using a flow of 20 vol.% O<sub>2</sub> in He at a rate of 20 cm<sup>3</sup>/min. After reaching 480 °C, the samples were maintained at this temperature for 30 minutes before being cooled down to 25 °C at the same rate. To remove any physisorbed species, a final purge was performed using He flow.

During the catalytic evaluation, measurements were taken at 20-degree intervals up to 500 °C. The effluent gas was analyzed for CO and CO<sub>2</sub> using gas chromatography (GC) equipped with two channels containing separated thermal conductivity (TCD) detectors, injectors, and capillary columns (Molecular Sieve 5X and PoraPlot Q). The CO conversion ( $X_{CO}$ , %) was determined using Eq. 14

6-8.

$$X_{\text{CO}}(\%) = \frac{[\text{CO}]_{\text{in}} - [\text{CO}]_{\text{out}}}{[\text{CO}]_{\text{in}}} \times 100 \quad [14]$$

where  $[\text{CO}]_{\text{in}}$  and  $[\text{CO}]_{\text{out}}$  are the CO concentration (ppm) in the inlet and outlet gas streams, respectively.

To obtain a better understanding of the intrinsic activity of the ceria samples, kinetic measurements were also performed under differential conditions ( $X_{\text{CO}} < 15\%$ ,  $T = 200$  °C,  $W/F = 0.075$  g s cm<sup>-3</sup>). The specific reaction rate of CO consumption in terms of the catalyst's mass (mol g<sup>-1</sup> s<sup>-1</sup>) or surface area (mol m<sup>-2</sup> s<sup>-1</sup>) were calculated using Eq. [15] and [16], respectively.

$$r_{\text{CO}}(\text{nmol} \cdot \text{m}^{-2} \cdot \text{s}^{-1}) = \frac{X_{\text{CO}} \cdot [\text{CO}]_{\text{in}} \cdot F \left( \frac{\text{cm}^3}{\text{min}} \right)}{100 \cdot 60 \left( \frac{\text{s}}{\text{min}} \right) \cdot V_m \left( \frac{\text{cm}^3}{\text{mol}} \right)} \cdot 10^9 \quad [15]$$

$$r_{\text{CO}}(\text{nmol} \cdot \text{m}^{-2} \cdot \text{s}^{-1}) = \frac{X_{\text{CO}} \cdot [\text{CO}]_{\text{in}} \cdot F \left( \frac{\text{cm}^3}{\text{min}} \right)}{100 \cdot 60 \left( \frac{\text{s}}{\text{min}} \right) \cdot V_m \left( \frac{\text{cm}^3}{\text{mol}} \right) \cdot S_{\text{BET}} \left( \frac{\text{m}^2}{\text{g}} \right)} \cdot 10^9 \quad [16]$$

where  $F$  (cm<sup>3</sup>/min) is the total flow rate,  $V_m$  (cm<sup>3</sup>/mol) is the gas molar volume at STP conditions (298 K and 1 bar),  $m_{\text{cat}}$  (g) is the mass of catalyst and  $S_{\text{BET}}$  (m<sup>2</sup>/g) is the surface area.

#### 2.4.2. CO<sub>2</sub> Hydrogenation

To assess the performance of various catalysts in the CO<sub>2</sub> hydrogenation reaction, catalytic tests were conducted. Specifically, the catalysts studied included bare ceria, M/CeO<sub>2</sub> (M: Ti, V, Cr, Mn, Fe, Co, Ni, Cu), CeO<sub>2</sub>/ZnO, and Ni/CeO<sub>2</sub>-ZnO. The CO<sub>2</sub> hydrogenation experiments were conducted using a fixed-bed quartz U-shaped reactor with an inner diameter of 1 cm. A temperature controller and a K-type thermocouple were placed in the middle of the catalytic bed, within an electric furnace. In each experiment, the reactor was filled with a 200 mg catalyst that was diluted with 200 mg of inert SiO<sub>2</sub>. Prior to the tests, the catalysts were reduced in situ at a temperature of 400 °C for an hour using a pure H<sub>2</sub> flow of 50 cm<sup>3</sup>/min. This was followed by flushing with He at a rate of 10 cm<sup>3</sup>/min. The catalytic tests were conducted at atmospheric pressure over a temperature range of 200–500 °C with intervals of 20–25 °C and a heating rate of 1 °C min<sup>-1</sup>. The total flow rate of the feed gas mixture was 100 cm<sup>3</sup>/min, corresponding to a Gas Hourly Space Velocity (GHSV) of 20,000 mL g<sup>-1</sup> h<sup>-1</sup>. The gas feed was a mixture of H<sub>2</sub> and CO<sub>2</sub> in a molar ratio of 9. The thermodynamic equilibrium calculations were derived from the mathematical model RGibbs in the Aspen Plus software®.

Carbon dioxide conversion,  $X_{CO_2}$ , and product selectivities,  $S_{CO}$  and  $S_{CH_4}$ , were calculated as follows (Eqs. 17-19)<sup>3,4,9</sup>:

$$X_{CO_2}(\%) = \frac{([CO_2]_{in} \cdot F_{in}) - ([CO_2]_{out} \cdot F_{out})}{[CO_2]_{in} \cdot F_{in}} \times 100 \quad (17)$$

$$S_{CO}(\%) = \frac{[CO]_{out}}{[CO]_{out} + [CH_4]_{out}} \times 100 \quad (18)$$

$$S_{CH_4}(\%) = \frac{[CH_4]_{out}}{[CO]_{out} + [CH_4]_{out}} \times 100 \quad (19)$$

where  $[i]_{in}$  and  $[i]_{out}$  represent the concentrations of reactants ( $i = CO_2$ ) or products ( $i = CO$  or  $CH_4$ ) at the inlet and outlet of the reactor, respectively.  $F_{in}$  and  $F_{out}$  are the total flow rates ( $cm^3/min$ ) at the inlet and outlet of the reactor, respectively.

### 2.4.3. Photocatalysis

Photocatalytic tests were conducted to assess the activity of different photocatalysts, including bulk g- $C_3N_4$ , g- $C_3N_4$  nanosheets, and M/g- $C_3N_4$ , where M represents Ti, V, Cr, Mn, Fe, Co, Ni, Cu, or Zn. Specifically, the photocatalytic degradation of NO was examined using bulk g- $C_3N_4$ , g- $C_3N_4$  nanosheets, while the degradation of Parabens was investigated using bulk g- $C_3N_4$ , g- $C_3N_4$  nanosheets, and M/g- $C_3N_4$ .

#### 2.4.3.1. Photocatalytic Degradation of NO

The photocatalytic activity of the samples was assessed by removing approximately 600 ppb of NO in a continuous flow reactor operating at ambient temperature. A 10 W visible LED light source (4000K) was placed vertically outside the reactor. To prepare the photocatalyst, 0.2 g of the material was combined with 10 ml of methanol and subjected to ultrasonication for 20 min. Subsequently, the resulting suspension was coated onto a glass substrate with an area of  $64 \text{ cm}^2$ . To remove the solvent from the coated substrate, it was preheated at  $60 \text{ }^\circ\text{C}$ . Within the reactor, a mass flow controller was employed to maintain a constant gas flow rate of  $1.5 \text{ L/min}$ . The NO gas used in the experiments was obtained from a compressed gas cylinder containing NO at a concentration of 10 ppm, with the remaining balance composed of nitrogen ( $N_2$ ). The experimental photocatalytic set-up for the photocatalytic degradation of NO is presented in Figure 2.11. The relative humidity of the system was adjusted between 10% and 60% by directing zero air streams through a gas washing bottle. Once

the adsorption-desorption equilibrium was achieved, the LED lamp was switched on to initiate the photocatalytic reaction.

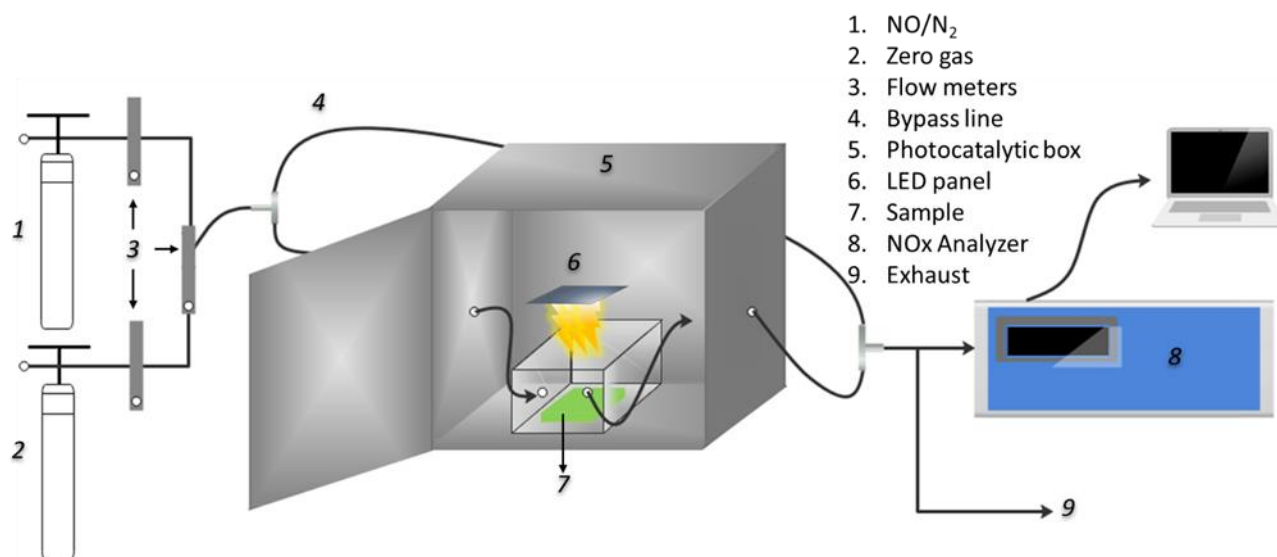


**Figure 2.11.** Experimental photocatalytic set-up for the photocatalytic degradation of NO.

The NO and NO<sub>2</sub> concentrations were continuously measured using a NOx analyzer (Thermo Environmental Instruments, Model 42i). The removal ratio of NO ( $\eta$ ) was calculated as follows:

$$\eta (\%) = (1 - C/C_0) \times 100 \quad (20)$$

where  $C$  and  $C_0$  are the NO concentrations in the outlet stream and feed stream, respectively.

The photocatalytic oxidation rate of NO is defined by Eq. (21), where  $F$  (m<sup>3</sup>/s) is the flow rate,  $A$  (m<sup>2</sup>) is the illuminated photocatalyst area and  $C_0$ ,  $C$  ( $\mu\text{g}/\text{m}^3$ ) is the inlet and outlet NO concentrations, respectively.

$$r\left(\frac{\text{mg}}{\text{m}^2\text{s}}\right) = (C_0 - C)F/A \quad (21)$$

#### 2.4.3.2. Photocatalytic Degradation of Parabens

The photocatalytic degradation of single parabens or a mixture of them was investigated using CNB and CNNs as catalysts. The experiments were conducted on a solar simulator (Mega Lab, model

MegCeraX10) equipped with a 300 W xenon lamp and an Air Mass 1.5 Global Filter, which simulated solar irradiation (> 280 nm).

In a typical experiment, a reaction vessel was loaded with 100 mL of an aqueous solution containing 10 mg/L of MP, EP, PP, or a mixture of these parabens (10 mg/L for each paraben). The solution was maintained at ambient temperature and continuously stirred. To achieve adsorption-desorption equilibrium, 50 mg of the as-prepared photocatalyst was added to the reaction solution, followed by stirring in the dark for 30 minutes. After this period, samples were collected at specified time intervals and filtered using a 0.45 µm diameter glass microfiber Whatman syringe filter. The absorbance of the collected samples was measured using UV–Vis spectroscopy (Cary 50, Agilent Technologies), with the main absorption peak of each paraben occurring at a wavelength of 255 nm. This measurement allowed for monitoring the degradation of the parabens over time. To evaluate the influence of other processes, such as photolysis, on the degradation of MP, EP, and PP, control experiments without catalysts were performed. The experimental photocatalytic set-up for the photocatalytic degradation of parabens is presented in Figure 2.12.

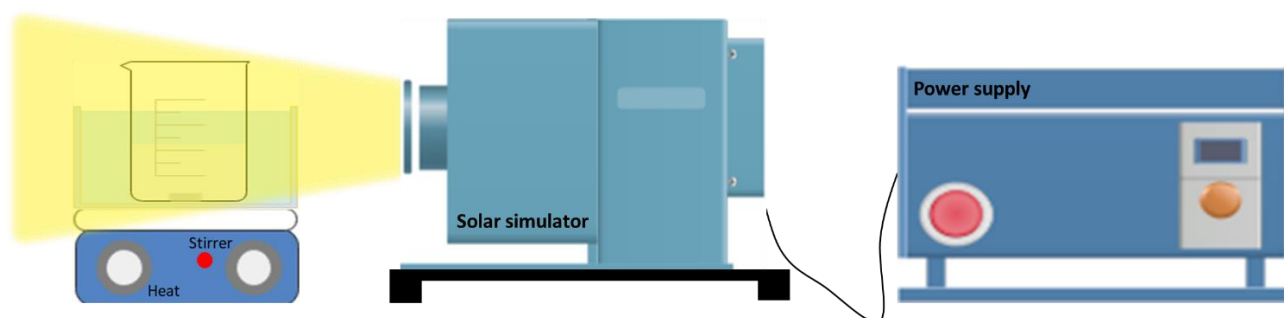


**Figure 2.12.** Experimental photocatalytic set-up for the photocatalytic degradation of Parabens.

The removal ratio of parabens ( $\eta$ ) was calculated using Eq. (22). Additionally, the reaction rate for each system was determined, and the decay in the concentration of paraben over irradiation time was found to follow a pseudo-first-order kinetic rate, as described by Eq. (22)<sup>13,14</sup>:

$$\text{rate} = -\frac{d(\text{Paraben})}{dt} = k \quad \text{or} \quad \ln\left(\frac{[\text{Paraben}]_0}{[\text{Paraben}]}\right) = k \times t \quad (22)$$

where  $[\text{Paraben}]_0$  and  $[\text{Paraben}]$  denote the Paraben concentration at time zero and  $t$ , respectively,  $t$  is the treatment time, and  $k$  is the apparent (observed) pseudo-first-order kinetic constant ( $\text{time}^{-1}$ ).

Furthermore, the study explored the impact of catalyst concentration (ranging from 0.1 to 0.75 g/L), initial paraben concentration (ranging from 0.001 to 0.02 g/L), and the type of irradiation using CNNs as the photocatalyst and MP as the model pollutant. For experiments conducted under visible irradiation, a filter with a 420 nm cut-off was utilized.

Moreover, the reactive species involved in the photocatalytic process were identified by introducing different scavengers. Specifically, 10 mM isopropyl alcohol (IPA) and disodium ethylenediaminetetraacetate dihydrate (EDTA- $\text{Na}_2$ ) were employed as scavengers for  $\bullet\text{OH}$  and  $\text{h}^+$  species, respectively. Additionally, to suppress the presence of  $\bullet\text{O}_2^-$ , a photocatalytic experiment was performed under a nitrogen atmosphere.

To assess the reusability of CNNs, three cycles of photocatalytic reactions were conducted. After each cycle, the MP solution containing CNNs was subjected to centrifugation, followed by washing the precipitate with water. This process was repeated by conducting another round of centrifugation and allowing the photocatalyst to dry overnight, thereby isolating the photocatalyst for subsequent usage.

## References

- (1) Lykaki, M.; Pachatouridou, E.; Iliopoulou, E.; Carabineiro, S. A. C.; Konsolakis, M. Impact of the Synthesis Parameters on the Solid State Properties and the CO Oxidation Performance of Ceria Nanoparticles. *RSC Adv.* **2017**, *7* (10), 6160–6169. <https://doi.org/10.1039/C6RA26712B>.
- (2) Lykaki, M.; Stefa, S.; Carabineiro, S. A. C.; Soria, M. A.; Madeira, L. M.; Konsolakis, M. Shape Effects of Ceria Nanoparticles on the Water-Gas Shift Performance of  $\text{CuO}_x/\text{CeO}_2$  Catalysts. *Catalysts* **2021**, *11* (6), 1–17. <https://doi.org/10.3390/catal11060753>.
- (3) Varvoutis, G.; Lykaki, M.; Stefa, S.; Binas, V.; Marnellos, G. E.; Konsolakis, M. Deciphering the Role of Ni Particle Size and Nickel-Ceria Interfacial Perimeter in the Low-Temperature  $\text{CO}_2$  Methanation Reaction over Remarkably Active Ni/ $\text{CeO}_2$  Nanorods. *Appl. Catal. B Environ.* **2021**, *297* (May), 120401. <https://doi.org/10.1016/j.apcatb.2021.120401>.
- (4) Varvoutis, G.; Lykaki, M.; Stefa, S.; Papista, E.; Carabineiro, S. A. C.; Marnellos, G. E.; Konsolakis, M. Remarkable Efficiency of Ni Supported on Hydrothermally Synthesized  $\text{CeO}_2$  Nanorods for Low-Temperature  $\text{CO}_2$  Hydrogenation to Methane. *Catal. Commun.* **2020**, *142* (March), 106036. <https://doi.org/10.1016/j.catcom.2020.106036>.
- (5) Konsolakis, M.; Lykaki, M.; Stefa, S.; Carabineiro, S. A. C.; Varvoutis, G.; Papista, E.; Marnellos, G. E.  $\text{CO}_2$  Hydrogenation over Nanoceria-Supported Transition Metal Catalysts: Role of Ceria Morphology (Nanorods versus Nanocubes) and Active Phase Nature (Co versus Cu). *Nanomaterials* **2019**, *9* (12), 1739. <https://doi.org/10.3390/nano9121739>.
- (6) Lykaki, M.; Stefa, S.; Carabineiro, S.; Pandis, P.; Stathopoulos, V.; Konsolakis, M. Facet-Dependent Reactivity of  $\text{Fe}_2\text{O}_3/\text{CeO}_2$  Nanocomposites: Effect of Ceria Morphology on CO Oxidation. *Catalysts* **2019**, *9* (4), 371. <https://doi.org/10.3390/catal9040371>.
- (7) Stefa, S.; Lykaki, M.; Frangkoulis, D.; Binas, V.; Pandis, P. K.; Stathopoulos, V. N.; Konsolakis, M. Effect of the Preparation Method on the Physicochemical Properties and the CO Oxidation Performance of Nanostructured  $\text{CeO}_2/\text{TiO}_2$  Oxides. *Processes* **2020**, *8* (7), 847. <https://doi.org/10.3390/pr8070847>.
- (8) Stefa, S.; Lykaki, M.; Binas, V.; Pandis, P. K.; Stathopoulos, V. N.; Konsolakis, M. Hydrothermal Synthesis of ZnO-Doped Ceria Nanorods: Effect of ZnO Content on the Redox Properties and the CO Oxidation Performance. *Appl. Sci.* **2020**, *10* (21), 7605. <https://doi.org/10.3390/app10217605>.

- (9) Varvoutis, G.; Karakoulia, S. A.; Lykaki, M.; Stefa, S.; Binas, V.; Marnellos, G. E.; Konsolakis, M. Support-Induced Modifications on the CO<sub>2</sub> Hydrogenation Performance of Ni/CeO<sub>2</sub>: The Effect of ZnO Doping on CeO<sub>2</sub> Nanorods. *J. CO<sub>2</sub> Util.* **2022**, *61* (April), 102057. <https://doi.org/10.1016/j.jcou.2022.102057>.
- (10) Stefa, S.; Grinieziaki, M.; Dimitropoulos, M.; Paterakis, G.; Galiotis, C.; Kiriakidis, G.; Klontzas, E.; Konsolakis, M.; Binas, V. Highly Porous Thin-Layer g-C<sub>3</sub>N<sub>4</sub> Nanosheets with Enhanced Adsorption Capacity. *ACS Appl. Nano Mater.* **2023**, *6* (3), 1732–1743. <https://doi.org/10.1021/acsanm.2c04632>.
- (11) Nithiyavathi, R.; John Sundaram, S.; Theophil Anand, G.; Raj Kumar, D.; Dhayal Raj, A.; Al Farraj, D. A.; Aljowaie, R. M.; AbdelGawwad, M. R.; Samson, Y.; Kaviyarasu, K. Gum Mediated Synthesis and Characterization of CuO Nanoparticles towards Infectious Disease-Causing Antimicrobial Resistance Microbial Pathogens. *J. Infect. Public Health* **2021**, *14* (12), 1893–1902. <https://doi.org/10.1016/j.jiph.2021.10.022>.
- (12) Kesavan, J. K.; Luisetto, I.; Tuti, S.; Meneghini, C.; Iucci, G.; Battocchio, C.; Mobilio, S.; Casciardi, S.; Sisto, R. Nickel Supported on YSZ: The Effect of Ni Particle Size on the Catalytic Activity for CO<sub>2</sub> Methanation. *J. CO<sub>2</sub> Util.* **2018**, *23* (September 2017), 200–211. <https://doi.org/10.1016/j.jcou.2017.11.015>.
- (13) Arvaniti, O. S.; Petala, A.; Zalaora, A. A.; Mantzavinos, D.; Frontistis, Z. Solar Light-Induced Photocatalytic Degradation of Methylparaben by g-C<sub>3</sub>N<sub>4</sub> in Different Water Matrices. *J. Chem. Technol. Biotechnol.* **2020**, *95* (11), 2811–2821. <https://doi.org/10.1002/jctb.6564>.
- (14) Faka, V.; Grinieziaki, M.; Kiriakidis, G.; Grilla, E.; Mantzavinos, D.; Mao, S.; Shen, S.; Frontistis, Z.; Binas, V. Solar Light Induced Photocatalytic Degradation of Sulfamethoxazole by ZnWO<sub>4</sub>/CNNs Nanocomposites. *J. Photochem. Photobiol. A Chem.* **2022**, *432* (June), 114108. <https://doi.org/10.1016/j.jphotochem.2022.114108>.
- (15) Qin, J.; Qiu, F.; Rong, X.; Yan, J.; Zhao, H.; Yang, D. Adsorption Behavior of Crystal Violet from Aqueous Solutions with Chitosan-Graphite Oxide Modified Polyurethane as an Adsorbent. *J. Appl. Polym. Sci.* **2015**, *132* (17), 1–10. <https://doi.org/10.1002/app.41828>.
- (16) Calimli, M. H.; Nas, M. S.; Burhan, H.; Mustafaov, S. D.; Demirbas, Ö.; Sen, F. Preparation, Characterization and Adsorption Kinetics of Methylene Blue Dye in Reduced-Graphene Oxide Supported Nano-adsorbents. *J. Mol. Liq.* **2020**, *309*, 113171. <https://doi.org/10.1016/j.molliq.2020.113171>.

- (17) Sonawane, G. H.; Shrivastava, V. S. Removal of Hazardous Dye from Synthetic Textile Dyeing and Printing Effluents by *Archis Hypogaea* L. Shell: A Low Cost Agro Waste Material. *Desalin. Water Treat.* **2011**, *29* (1–3), 29–38. <https://doi.org/10.5004/dwt.2011.1813>.
- (18) Ghorai, S.; Sarkar, A.; Raoufi, M.; Panda, A. B.; Schönherr, H.; Pal, S. Enhanced Removal of Methylene Blue and Methyl Violet Dyes from Aqueous Solution Using a Nanocomposite of Hydrolyzed Polyacrylamide Grafted Xanthan Gum and Incorporated Nanosilica. *ACS Appl. Mater. Interfaces* **2014**, *6* (7), 4766–4777. <https://doi.org/10.1021/am4055657>.

# Chapter 3

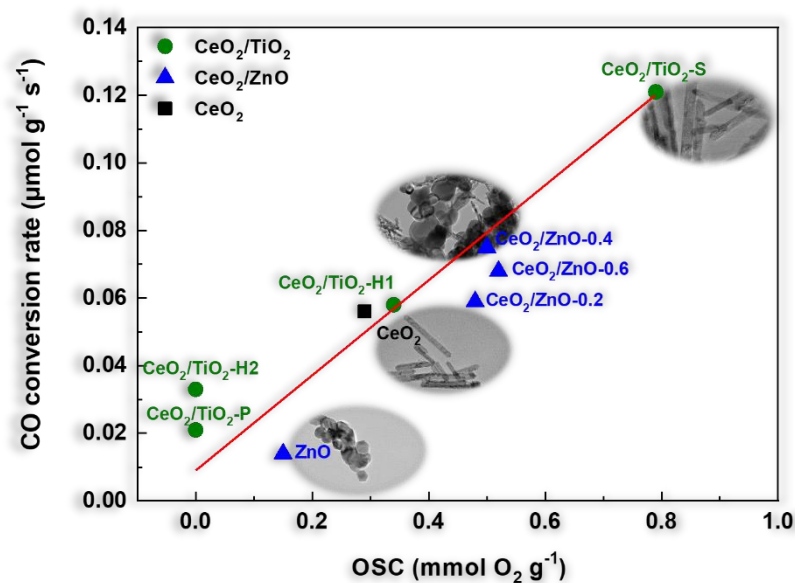
## Effect of TiO<sub>2</sub> and ZnO dopants on the physicochemical properties of ceria nanorods: Implications in CO Oxidation

Chapter 3 focuses on the synthesis, characterization, and catalytic evaluation of TiO<sub>2</sub>- and ZnO-doped ceria nanorods. The chapter is divided into two parts, each focusing on a specific mixed oxide system.

In the first part, the impact of various synthesis methods on the physicochemical properties and CO oxidation performance of bare ceria and ceria-titania catalysts is explored. Four different preparation methods were employed for the synthesis of ceria-titania nanomaterials: the one- and two-stage hydrothermal methods, precipitation, and Stöber. Among these methods, Stöber exhibited the highest CO oxidation performance.

The second part of the chapter focuses on investigating the influence of ZnO content on the physicochemical properties of CeO<sub>2</sub>/ZnO mixed oxides. Using the hydrothermal method, a series of bare CeO<sub>2</sub> and ZnO oxides, as well as CeO<sub>2</sub>/ZnO mixed oxides with varying Zn/Ce atomic ratios (0.2, 0.4, 0.6), were prepared. The catalytic results demonstrate the superior performance of the mixed oxides as compared to the individual components.

Additionally, the chapter explores the relationship between the catalytic activity and the oxygen storage capacity (OSC) of both CeO<sub>2</sub>/TiO<sub>2</sub> and CeO<sub>2</sub>/ZnO systems. The investigation confirms the significance of OSC as a crucial activity descriptor for reactions following a redox-type mechanism.



## Introduction

Ceria ( $\text{CeO}_2$ ) is a metal oxide with great potential for catalytic applications, including CO oxidation<sup>1-3</sup>, NO reduction<sup>4-6</sup>, water-gas shift reaction<sup>7-10</sup>, reforming reactions<sup>11,12</sup>, and soot combustion<sup>13-15</sup>.  $\text{CeO}_2$  has gained significant attention in heterogeneous catalysis due to its exceptional features, such as its high oxygen storage capacity (OSC) and thermal stability<sup>16-18</sup>. The ease with which it can shift between its two oxidation states ( $\text{Ce}^{3+}/\text{Ce}^{4+}$ ) and produce surface and structural defects, like oxygen vacancies, is responsible for its improved redox behavior<sup>18-22</sup>. Moreover, the development of ceria particles at the nanoscale is crucial because smaller particles possess distinctive physicochemical properties that are absent in larger particles. These properties include high specific surface area, tunable pore size, abundant defects, and adjustable surface chemistry<sup>13,23-25</sup>.

Ceria-based metal oxides have attracted significant attention in heterogeneous catalysis as either supporting carriers or catalysts on their own, mainly due to their distinct surface and structural features that are significantly different from those of parent oxide<sup>2,7,16,17,26-35</sup>. The synergistic interaction between these components often results in unique physicochemical properties that have a substantial effect on catalytic activity. Among mixed oxides, transition metal-based oxide catalysts are particularly important due to their peculiar chemisorption properties. Introducing various transition metals into the ceria carrier can cause significant physicochemical changes through the geometric and/or electronic interactions between the different components<sup>16,36-40</sup>.

The incorporation of titanium oxide ( $\text{TiO}_2$ ) into the ceria lattice can have a significant impact on its physicochemical and redox properties, and consequently, on its catalytic performance. While  $\text{TiO}_2$  is commonly used as a semiconductor photocatalyst, its photocatalytic performance is limited by its wide band gap (3.0-3.2 eV) and the easy recombination of electron-hole pairs<sup>40,41</sup>. In this context, the combination of  $\text{TiO}_2$  with ceria is considered a promising approach due to ceria's narrow band gap and reversible redox couple ( $\text{Ce}^{3+}/\text{Ce}^{4+}$ )<sup>41</sup>.  $\text{CeO}_2/\text{TiO}_2$  mixed oxides have been studied for various applications, including the removal of volatile organic compounds (VOCs), the photocatalytic degradation of organic pollutants, the partial oxidation of methane, the steam reforming of ethanol, and the oxidation of CO, among others<sup>41-51</sup>.

Various methods have been employed to synthesize ceria-titania mixed oxides, including hydrothermal<sup>41,42,44,52-56</sup>, co-precipitation<sup>44,57-60</sup>, sol-gel<sup>45,61-63</sup>, microemulsion<sup>64</sup>, and incipient wetness impregnation<sup>65-67</sup>. The preparation method plays a significant role in the morphology and surface properties of  $\text{CeO}_2/\text{TiO}_2$  composites, resulting in different nanostructures such as core-shell spheres, nanoparticles or nanorods, and flower-like heterostructures<sup>44,54 52,56,68</sup>. For instance, Li et al.<sup>44</sup> prepared ceria-titania nanorods and nanoparticles through the hydrothermal and co-precipitation

methods, respectively, as noble metal supports, with the CeO<sub>2</sub>/TiO<sub>2</sub> support of nanorod-like morphology exhibiting excellent CO oxidation performance. Additionally, CeO<sub>2</sub>/TiO<sub>2</sub> catalysts were prepared using three synthetic methods (impregnation, co-precipitation, and single-step sol-gel), with the sol-gel method yielding the most active catalyst for the selective catalytic reduction of NO with NH<sub>3</sub>, due to the high surface area of the composites, their excellent reducibility, and the strong interaction between ceria and titania<sup>62</sup>.

Zinc oxide (ZnO) is a wide and direct band gap semiconductor among various transition metal oxides. It has gained popularity in multiple fields due to its environmental sustainability and low cost<sup>69-71</sup>. Though zinc is not considered a critical raw material and has no direct impact on environmental resources, it is abundantly available in the steel industry as one of the main products recovered from metal scrap recycling processes<sup>72</sup>. In view of this fact, the potential of a cost-effective metal that can further enhance the catalytic performance of CeO<sub>2</sub> is crucial from both environmental and economic perspectives.

Although CeO<sub>2</sub>-ZnO composites have been widely used in photocatalysis<sup>73-77</sup>, only a few studies have been conducted on their catalytic applications. Xie et al.<sup>78</sup> have reported on the improved CO oxidation activity of CeO<sub>2</sub>-ZnO composites, which is attributed to the synergistic interaction between commercial CeO<sub>2</sub> powders and ZnO hollow microspheres. Similarly, the enhanced CO oxidation performance of three-dimensional ordered macroporous CeO<sub>2</sub>-ZnO was attributed to the synergistic interaction between ZnO and CeO<sub>2</sub><sup>79</sup>.

The oxidation of CO is a well-established probe reaction in various catalytic systems that is used to gain insight into the structure-property relationships<sup>80-83</sup>. The employment of such a reaction can provide valuable information and feedback on the catalytic behavior of ceria-titania and ceria-zinc composites, which have potential applications as catalysts or supporting carriers in various energy and environmental applications.

In view of the above aspects, this chapter aims to investigate the impact of TiO<sub>2</sub> and ZnO as modifiers for ceria nanorods, to further adjust their surface/redox properties. The first part focuses on the effect of various synthesis methods, such as one- and two-stage hydrothermal methods, precipitation, and Stöber, on the physicochemical properties and the CO oxidation performance of CeO<sub>2</sub>/TiO<sub>2</sub> mixed oxides. The second part focuses on the effect of ZnO content on the physicochemical properties of CeO<sub>2</sub>/ZnO mixed oxides. The materials, including pure CeO<sub>2</sub> and ZnO, as well as CeO<sub>2</sub>/ZnO mixed oxides with varying Zn:Ce atomic ratios (0.2, 0.4, 0.6), were prepared through the hydrothermal method. The resulting materials were thoroughly characterized using techniques such as N<sub>2</sub> physisorption, XRD, SEM/EDS, TEM, and H<sub>2</sub>-TPR to reveal the relationship between materials' structure and activity (see chapter 2.2). Subsequently, the catalytic

performance of the materials was evaluated in the CO oxidation reaction, serving as a probe reaction to elucidate the structure-property relationships.

### 3.1. Experimental

#### 3.1.1. Materials Synthesis

All the chemical compounds used in this chapter were of analytical grade.  $\text{TiOSO}_4$  (purity  $\geq 29\%$ , Sigma-Aldrich, St. Louis, MO, USA), tetrabutyl titanate (TBOT, purity  $\geq 97\%$ , Sigma-Aldrich, St. Louis, MO, USA),  $\text{Zn}(\text{CH}_3\text{COO})_2 \cdot 2\text{H}_2\text{O}$  (purity  $\geq 99\%$ , Sigma-Aldrich, St. Louis, MO, USA), and  $\text{Ce}(\text{NO}_3)_3 \cdot 6\text{H}_2\text{O}$  ( $\geq 99.0\%$ , Fluka, Bucharest, Romania) were employed as precursors for the synthesis of ceria-titania and ceria-zinc samples.  $\text{HO}_2\text{CCO}_2\text{H}$  (purity  $\geq 99\%$ , Sigma-Aldrich, St. Louis, MO, USA), NaOH (purity  $\geq 98\%$ , Honeywell Fluka, Seelze, Germany),  $\text{NH}_3$  (25 vol.%, Sigma-Aldrich, St. Louis, MO, USA), and absolute EtOH ( $\geq 99.8\%$ , ACROS Organics, Geel, Belgium) were also used during preparation.

The catalysts prepared in this chapter ( $\text{CeO}_2$ ,  $\text{CeO}_2/\text{TiO}_2\text{-P}$ ,  $\text{CeO}_2/\text{TiO}_2\text{-H1}$ ,  $\text{CeO}_2/\text{TiO}_2\text{-H2}$ ,  $\text{CeO}_2/\text{TiO}_2\text{-S}$ ,  $\text{CeO}_2/\text{ZnO}\text{-0.2}$ ,  $\text{CeO}_2/\text{ZnO}\text{-0.4}$ ,  $\text{CeO}_2/\text{ZnO}\text{-0.6}$ , ZnO) were synthesized by the methods described in Chapter 2 in section 2.1 (Materials Synthesis). Also, Table 2.1 in Chapter 2 presents all the materials developed in this study.

#### 3.1.2. Materials Characterization

The textural characteristics of as-prepared catalysts were determined by the  $\text{N}_2$  adsorption-desorption isotherms at  $-196^\circ\text{C}$ . The crystalline structure of samples was determined by X-ray diffraction (XRD). Scherrer's equation was employed to determine the average crystallite size of samples. Morphological characterization was carried out by Scanning/Transmission Electron Microscopy (SEM/TEM) analyses. The size distribution of ceria particles and HRTEM analysis were performed from TEM images using ImageJ software. The redox properties of the samples were assessed by temperature-programmed reduction under  $\text{H}_2$  ( $\text{H}_2\text{-TPR}$ ). The characterization techniques are fully described in Chapter 2 in section 2.2 (Characterization Techniques).

### 3.2. Characterization studies of Ceria-Titania oxides

#### 3.2.1. Textural/Structural Characterization

Table 3.1 displays the primary textural and structural features of bare  $\text{CeO}_2$  and  $\text{CeO}_2/\text{TiO}_2$  samples. Among them,  $\text{CeO}_2/\text{TiO}_2\text{-H1}$  exhibits the highest BET surface area ( $100.9 \text{ m}^2 \text{ g}^{-1}$ ) as it is prepared using a one-step hydrothermal method, followed by bare  $\text{CeO}_2$  ( $73.9 \text{ m}^2 \text{ g}^{-1}$ ),  $\text{CeO}_2/\text{TiO}_2\text{-S}$  ( $72.0 \text{ m}^2 \text{ g}^{-1}$ ),  $\text{CeO}_2/\text{TiO}_2\text{-H2}$  ( $63.2 \text{ m}^2 \text{ g}^{-1}$ ) and  $\text{CeO}_2/\text{TiO}_2\text{-P}$  ( $41.5 \text{ m}^2 \text{ g}^{-1}$ ). Notably, there is an increase in the surface area observed in the  $\text{CeO}_2/\text{TiO}_2\text{-H1}$  sample in comparison to bare  $\text{CeO}_2$ . However,

CeO<sub>2</sub>/TiO<sub>2</sub>-S, CeO<sub>2</sub>/TiO<sub>2</sub>-H2, and CeO<sub>2</sub>/TiO<sub>2</sub>-P samples demonstrate a decrease in the BET surface area. Obviously, the preparation method plays a significant role in determining the textural and structural characteristics of the samples, which will be further elaborated below.

**Table 3.1.** Textural and structural properties of CeO<sub>2</sub> and CeO<sub>2</sub>/TiO<sub>2</sub> samples.

Sample	BET Analysis				XRD Analysis			
	BET Surface Area (m <sup>2</sup> g <sup>-1</sup> )	Pore Volume (cm <sup>3</sup> /g)	Average Pore Size (nm)	d <sub>(111)</sub> -spacing (nm)	Lattice Parameter (nm) a = b = c	Unit Cell Volume (nm) <sup>3</sup>	Average crystallite diameter CeO <sub>2</sub> , D <sub>XRD</sub> (nm)	$\epsilon \times 10^{-3}$
CeO <sub>2</sub>	73.9	0.48	24.2	0.314	0.5441	0.1610	13.0	13.0312
CeO <sub>2</sub> /TiO <sub>2</sub> -P	41.5	0.13	9.3	0.313	0.5413	0.1586	12.2	11.5455
CeO <sub>2</sub> /TiO <sub>2</sub> -H1	100.9	0.41	15.0	0.313	0.5419	0.1591	9.4	14.9806
CeO <sub>2</sub> /TiO <sub>2</sub> -H2	63.2	0.48	24.1	0.313	0.5421	0.1593	13.5	10.4426
CeO <sub>2</sub> /TiO <sub>2</sub> -S	72.0	0.58	32.0	0.313	0.5422	0.1594	11.8	12.1387

Figure 3.1 (a) displays the adsorption-desorption isotherms of the as-synthesized samples, whereas Figure 3.1 (b) illustrates the corresponding BJH pore size distribution (PSD). The maximum pore sizes in all the samples are greater than 3 nm, indicating the presence of mesopores, which is supported by type IV adsorption-desorption isotherms (Figure 3.1 (a)). The CeO<sub>2</sub>/TiO<sub>2</sub>-S sample possesses the largest pore size (32.0 nm), followed by CeO<sub>2</sub> (24.2 nm), CeO<sub>2</sub>/TiO<sub>2</sub>-H2 (24.1 nm), CeO<sub>2</sub>/TiO<sub>2</sub>-H1 (15.0 nm) and CeO<sub>2</sub>/TiO<sub>2</sub>-P (9.3 nm). Furthermore, the PSD of the CeO<sub>2</sub>/TiO<sub>2</sub>-S sample is broader than that of the other samples.

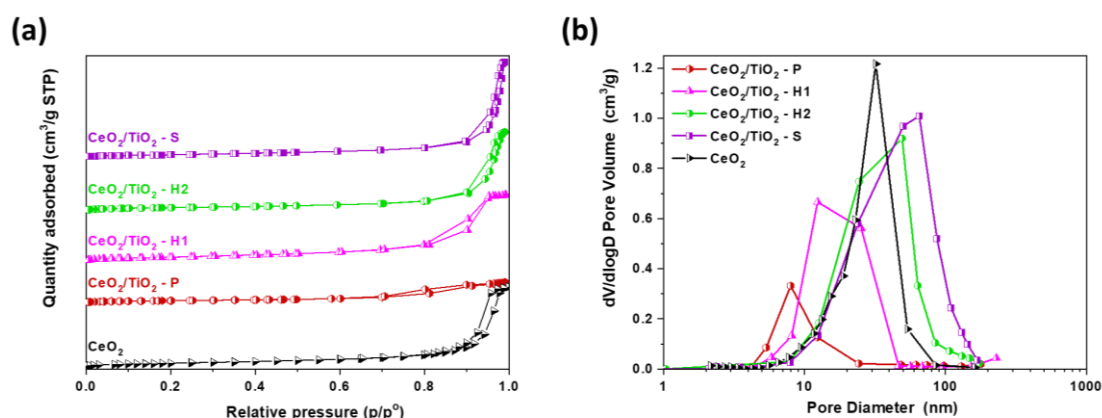


**Figure 3.1.** (a) BJH desorption pore size distribution; (b) adsorption-desorption isotherms of bare CeO<sub>2</sub> and CeO<sub>2</sub>/TiO<sub>2</sub> samples. Adapted from Reference <sup>84</sup>.

In Figure 3.2, the X-ray diffraction (XRD) patterns for all samples are displayed, and the main peaks observed at planes (111), (200), (220), (311), (222), (400), (331), and (420) correspond to the face-centered cubic fluorite structure of ceria (Fm3m symmetry, no. 225) <sup>85-87</sup>. The TiO<sub>2</sub> phase is difficult

to detect in all samples except for CeO<sub>2</sub>/TiO<sub>2</sub>-S, which shows a small peak at 2θ value ~25° corresponding to the anatase (TiO<sub>2</sub>) phase<sup>88–91</sup>, likely due to the low loading of TiO<sub>2</sub> combined with its high dispersion.

To further investigate how the preparation method affects the structural characteristics of CeO<sub>2</sub>/TiO<sub>2</sub> samples, the d<sub>111</sub>-spacing, lattice parameter, unit cell volume, and crystalline size for the (111) diffraction peak of ceria were calculated and summarized in Table 3.1. A slight shift in the position of diffraction peaks was observed in Figure 3.2 (b), which suggests a contraction in the lattice parameters and unit cell volume of ceria. This phenomenon can be attributed to the successful incorporation of Ti<sup>4+</sup> into the lattice of CeO<sub>2</sub>, which has a smaller ionic radius than ceria<sup>92,93</sup>. Additionally, the primary crystallite size of ceria was calculated using the Scherrer equation. Bare CeO<sub>2</sub> shows a crystallite size of 13.0 nm, while CeO<sub>2</sub>/TiO<sub>2</sub>-H1, CeO<sub>2</sub>/TiO<sub>2</sub>-S, CeO<sub>2</sub>/TiO<sub>2</sub>-P, and CeO<sub>2</sub>/TiO<sub>2</sub>-H2 samples exhibit crystallite sizes of 9.4, 11.8, 12.2 and 13.5 nm, respectively. Apart from the sample prepared by the two-step hydrothermal method (CeO<sub>2</sub>/TiO<sub>2</sub>-H2), all the other ceria–titania samples exhibit a small reduction in the crystallite size of ceria. These slight differences in the crystallite size and morphology of ceria may be ascribed to various parameters, such as the extent of calcination and the interaction between heteroatoms, on the growth rate of ceria nanoparticles<sup>94–96</sup>. Furthermore, CeO<sub>2</sub>/TiO<sub>2</sub>-H1 exhibited the highest microstrain, followed by CeO<sub>2</sub>, CeO<sub>2</sub>/TiO<sub>2</sub>-S, CeO<sub>2</sub>/TiO<sub>2</sub>-P, and CeO<sub>2</sub>/TiO<sub>2</sub>-H2, as shown in Table 3.1. Microstrain is a well-known measurement of lattice stress due to lattice distortion, elongation, or contraction<sup>92,93,97</sup>. Consequently, the variation in microstrain indicates a similar trend in the concentration of oxygen vacancies.

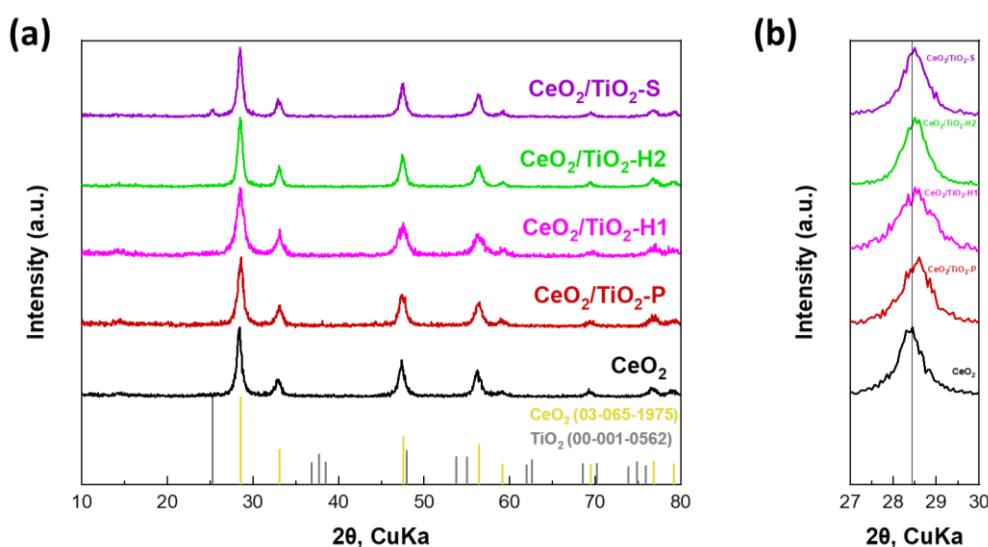


**Figure 3.2.** (a) XRD patterns of CeO<sub>2</sub> and CeO<sub>2</sub>/TiO<sub>2</sub> samples; (b) the (111) diffraction peak of CeO<sub>2</sub>.

### 3.2.2. Morphological Characterization

Transmission electron microscopy analysis was employed to investigate the morphological features of ceria-titania nanostructures. Figure 3.3 (a) presents the TEM image of bare ceria nanorods, along with the particle size distribution (PSD) histograms for the diameter (Figure 3.3 (b)) and length (Figure 3.3 (c)) of nanorods. The bare ceria sample exhibits a rod-like shape with a diameter ranging from 10 to 25 nm and a length ranging from 50 to 300 nm. To enhance the clarity of the results, the PSD histograms provide a visual representation of the distribution of particle sizes.

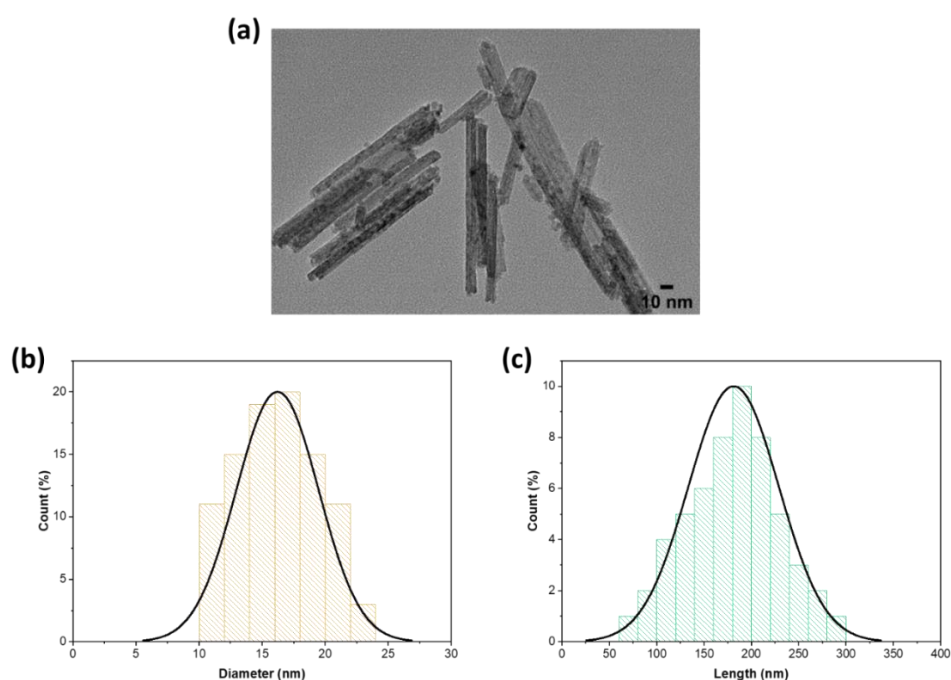


**Figure 3.3.** (a) TEM image of CeO<sub>2</sub>; Particle Size Distribution (PSD) histograms for the diameter (b) and length (c) of CeO<sub>2</sub>.

TEM images of CeO<sub>2</sub>/TiO<sub>2</sub>-P samples with irregular shapes are presented in Figures 3.4 (a) and (b). Conversely, CeO<sub>2</sub>/TiO<sub>2</sub>-H1 mixed oxides synthesized by the hydrothermal method exhibit a rod-like morphology, as depicted in Figures 3.4 (c) and (d). Specifically, the CeO<sub>2</sub>/TiO<sub>2</sub>-H1 sample displays smaller-sized nanorods, ranging from 25 to 100 nm, as compared to bare CeO<sub>2</sub>. No separated TiO<sub>2</sub> particles are observed, and HRTEM analysis in Figure 3.4 (d) indicates a uniform distribution of TiO<sub>2</sub> within the CeO<sub>2</sub> host structure. The lattice spacing of 0.36 nm corresponds to the TiO<sub>2</sub> (101) crystal plane, and the lattice spacings of 0.31 nm correspond to the CeO<sub>2</sub> (111) crystal plane, respectively<sup>25,33,41,43,50,98–101</sup>. The CeO<sub>2</sub>/TiO<sub>2</sub>-H2 sample (Figure 3.4 (e) and (f)) also exhibits a rod-like morphology but with distinct TiO<sub>2</sub> nanoparticles in contact with nanorods. This is confirmed by HRTEM analysis in Figure 3.4 (f). The CeO<sub>2</sub>/TiO<sub>2</sub>-S sample in Figure 3.4 (g) also shows a rod-like morphology, with no separated TiO<sub>2</sub> particles detected. HRTEM results in Figure 3.4 (h) show a

uniform distribution of TiO<sub>2</sub> around ceria nanorods, with lattice spacings of 0.36 nm corresponding to the TiO<sub>2</sub> (101) crystal plane, and lattice spacings of 0.31 and 0.19 nm corresponding to the CeO<sub>2</sub> (111) and (220) crystal planes, respectively<sup>25,33,41,43,50,98-101</sup>. Thus, it can be concluded that the CeO<sub>2</sub>/TiO<sub>2</sub>-S sample achieves a uniform distribution of TiO<sub>2</sub> around ceria nanorods.

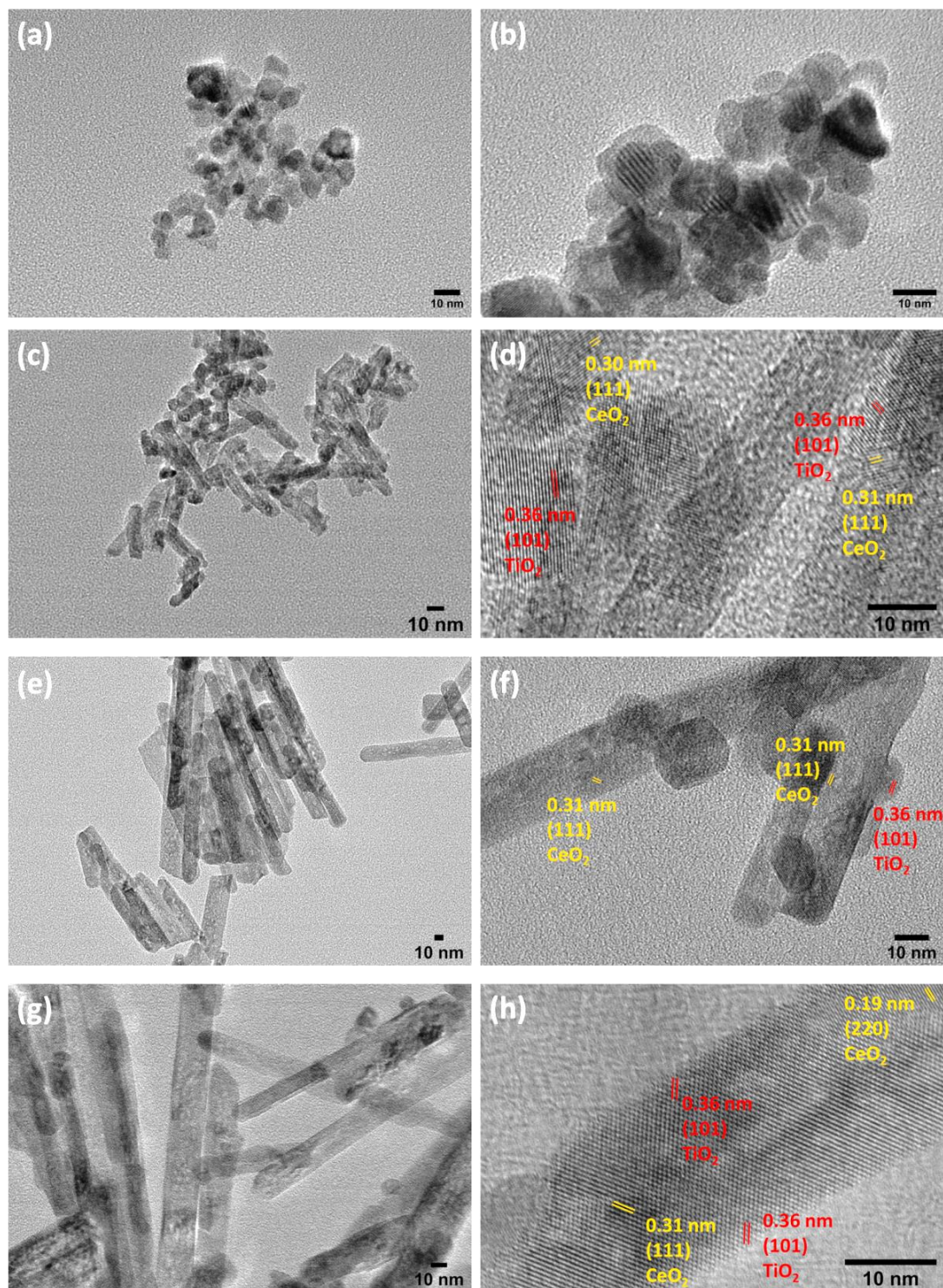


**Figure 3.4.** TEM images of the samples: (a), (b) CeO<sub>2</sub>/TiO<sub>2</sub>-P; (c), (d) CeO<sub>2</sub>/TiO<sub>2</sub>-H1; (e), (f) CeO<sub>2</sub>/TiO<sub>2</sub>-H2; (g), (h) CeO<sub>2</sub>/TiO<sub>2</sub>-S.

Elemental mapping of the CeO<sub>2</sub>/TiO<sub>2</sub> samples was carried out using SEM/EDS analysis, as depicted in Figure 3.5. Figures 3.5 (a), (e), (i), and (m) show SEM images of the mixed oxides of ceria-titania, while Figures 3.5 (b-d), (f-h), (j-l), and (n-p) display the corresponding elemental mapping images. The results of the SEM/EDS analysis demonstrate a homogeneous distribution of Ce, Ti, and O elements within the mixed oxides of ceria-titania.

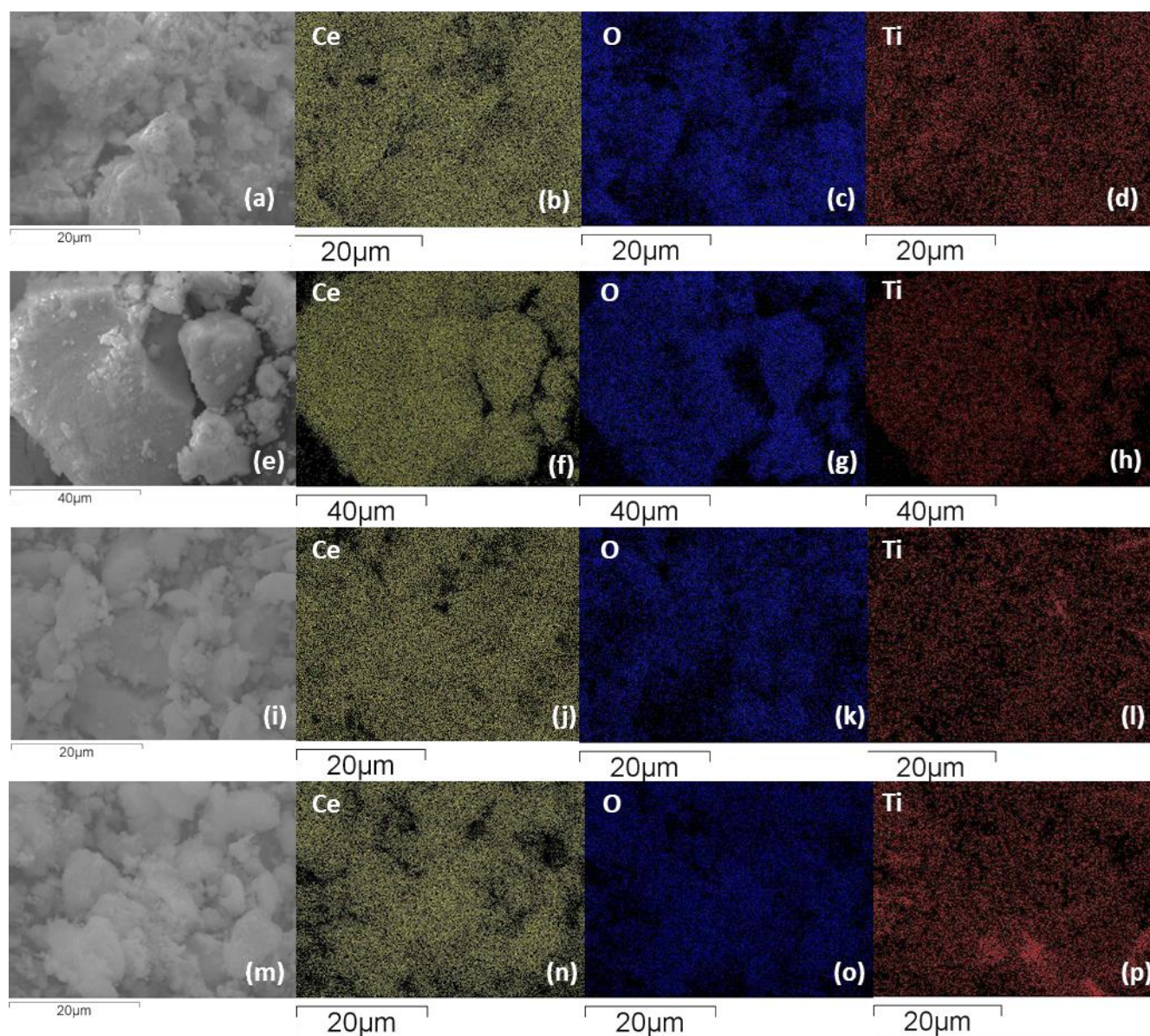


**Figure 3.5.** SEM and elemental mapping images of the samples: (a–d) CeO<sub>2</sub>/TiO<sub>2</sub>-P; (e–h) CeO<sub>2</sub>/TiO<sub>2</sub>-H1; (i–l) CeO<sub>2</sub>/TiO<sub>2</sub>-H2; (m–p) CeO<sub>2</sub>/TiO<sub>2</sub>-S.

### 3.2.3. Redox Properties (H<sub>2</sub>-TPR)

H<sub>2</sub>-TPR results can be used to identify and quantify the active oxygen sites in catalysts involved in reactions that proceed via a surface reduction step, such as CO oxidation. Figure 3.6 illustrates the reduction profiles of the samples in a temperature range of 100–800 °C. The CeO<sub>2</sub>/TiO<sub>2</sub>-S,

CeO<sub>2</sub>/TiO<sub>2</sub>-H1, and CeO<sub>2</sub> samples exhibit a peak in the low-temperature range of 500–700 °C, which is attributed to weakly bound surface oxygen species and differs from bulk oxygen that is reduced at higher temperatures (around 750 °C). In contrast, CeO<sub>2</sub>/TiO<sub>2</sub>-P and CeO<sub>2</sub>/TiO<sub>2</sub>-H2 samples do not display any reduction peaks in the investigated temperature range, indicating their inferior reducibility, which is consistent with their poor catalytic performance, as will be discussed below. Moreover, the addition of TiO<sub>2</sub> to CeO<sub>2</sub> leads to a shift in TPR peaks to higher temperatures as compared to bare CeO<sub>2</sub>, as shown in Table 3.2. This shift suggests that TiO<sub>2</sub> incorporation inhibits the detachment of surface oxygen species during the reduction process.

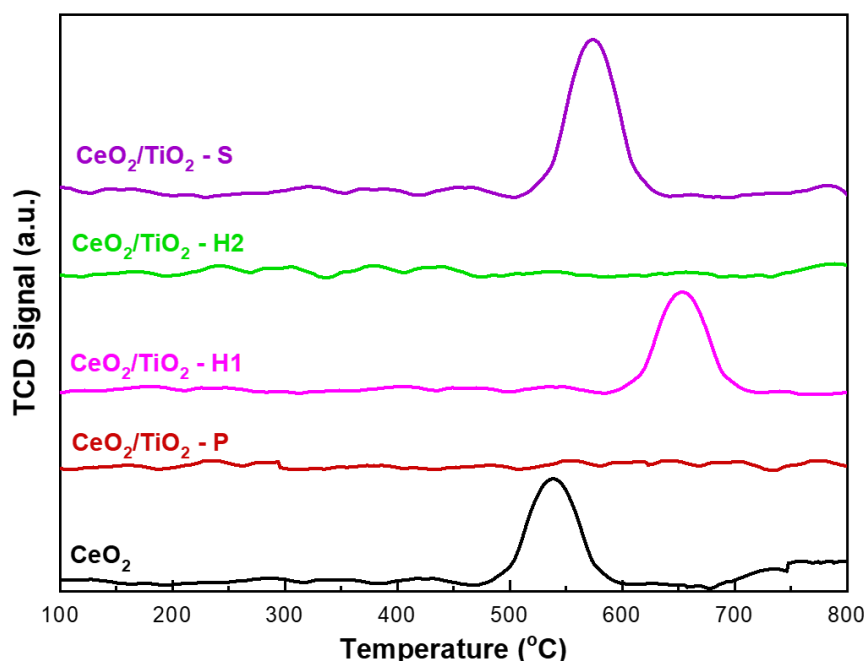


**Figure 3.6.** H<sub>2</sub>-TPR profiles of CeO<sub>2</sub> and CeO<sub>2</sub>/TiO<sub>2</sub> samples. Adapted from Reference <sup>84</sup>.

Regarding H<sub>2</sub> uptake, significant differences were observed, corresponding to main TPR peaks (Table 3.2). CeO<sub>2</sub>/TiO<sub>2</sub>-S displayed the highest value (1.58 mmol H<sub>2</sub> g<sup>-1</sup>), followed by CeO<sub>2</sub>/TiO<sub>2</sub>-H1 (0.68 mmol H<sub>2</sub> g<sup>-1</sup>) and CeO<sub>2</sub> (0.58 mmol H<sub>2</sub> g<sup>-1</sup>), resulting in OSC values of 0.79, 0.34, and 0.29 mmol O<sub>2</sub> g<sup>-1</sup>, respectively. The TiO<sub>2</sub> incorporation into CeO<sub>2</sub> via the Stöber method results in almost a three-fold increase in the population of reducible/active oxygen species, which are expected to determine the oxygen exchange kinetics and, in turn, the CO oxidation process via a Mars-van Krevelen mechanism. The differences in reducibility can be mainly attributed to the extent of ceria-titania interactions, demonstrating the importance of the preparation method on the intrinsic characteristics of mixed oxides. Furthermore, a close relationship exists between the catalytic activity and OSC, as discussed below, which supports the above arguments.

**Table 3.2.** Redox properties of CeO<sub>2</sub> and CeO<sub>2</sub>/TiO<sub>2</sub> samples.

Sample	Oxygen Storage Capacity (mmol O <sub>2</sub> g <sup>-1</sup> )	Temperature of Peak Maximum (°C)
CeO <sub>2</sub>	0.29	545
CeO <sub>2</sub> /TiO <sub>2</sub> -P	-	-
CeO <sub>2</sub> /TiO <sub>2</sub> -H1	0.34	654
CeO <sub>2</sub> /TiO <sub>2</sub> -H2	-	-
CeO <sub>2</sub> /TiO <sub>2</sub> -S	0.79	573

### 3.3. Characterization studies of Ceria-Zinc oxides

#### 3.3.1 Textural/Structural Characterization

The textural properties of CeO<sub>2</sub>/ZnO samples, including surface area, pore volume, and pore size, were determined using nitrogen adsorption-desorption (BET) analysis, and the results are summarized in Table 3.3. CeO<sub>2</sub> nanorods showed the highest BET surface area (79.3 m<sup>2</sup>/g), while ZnO exhibited the lowest (7.05 m<sup>2</sup>/g). The samples ranked in between were CeO<sub>2</sub>/ZnO-0.2 (76.2 m<sup>2</sup>/g), CeO<sub>2</sub>/ZnO-0.4 (62.2 m<sup>2</sup>/g), and CeO<sub>2</sub>/ZnO-0.6 (56.1 m<sup>2</sup>/g). Notably, the addition of ZnO caused a gradual decrease in BET surface area. This trend is in line with the gradual increase in pore size observed as ZnO content increases, as discussed below.

**Table 3.3.** Textural characteristics of bare CeO<sub>2</sub>, ZnO, and the CeO<sub>2</sub>/ZnO samples.

Sample	BET Analysis		
	BET Surface Area (m <sup>2</sup> /g)	Pore Volume (cm <sup>3</sup> /g)	Average Pore Size (nm)
CeO <sub>2</sub>	79.3	0.48	24.2
CeO <sub>2</sub> /ZnO-0.2	76.2	0.67	34.4
CeO <sub>2</sub> /ZnO-0.4	62.2	0.65	40.6
CeO <sub>2</sub> /ZnO-0.6	56.1	0.91	55.9
ZnO	7.1	0.58	23.0

In Figure 3.7 (a) and (b), the adsorption-desorption isotherms and the Barrett-Joyner-Halenda (BJH) desorption pore size distribution (PSD) of the as-prepared samples are presented. All samples exhibit a mesoporous pore size distribution, which is supported by the presence of type IV isotherms in Figure 3.7 (a). The addition of ZnO to the samples leads to an increase in both pore volume and average pore size, as shown in Table 3.3 and Figure 3.7 (b). CeO<sub>2</sub>/ZnO-0.6 has the largest pore size

(55.9 nm) among the samples, followed by CeO<sub>2</sub>/ZnO-0.4 (40.6 nm), CeO<sub>2</sub>/ZnO-0.2 (34.4 nm), CeO<sub>2</sub> (24.2 nm), and ZnO (23.0 nm).

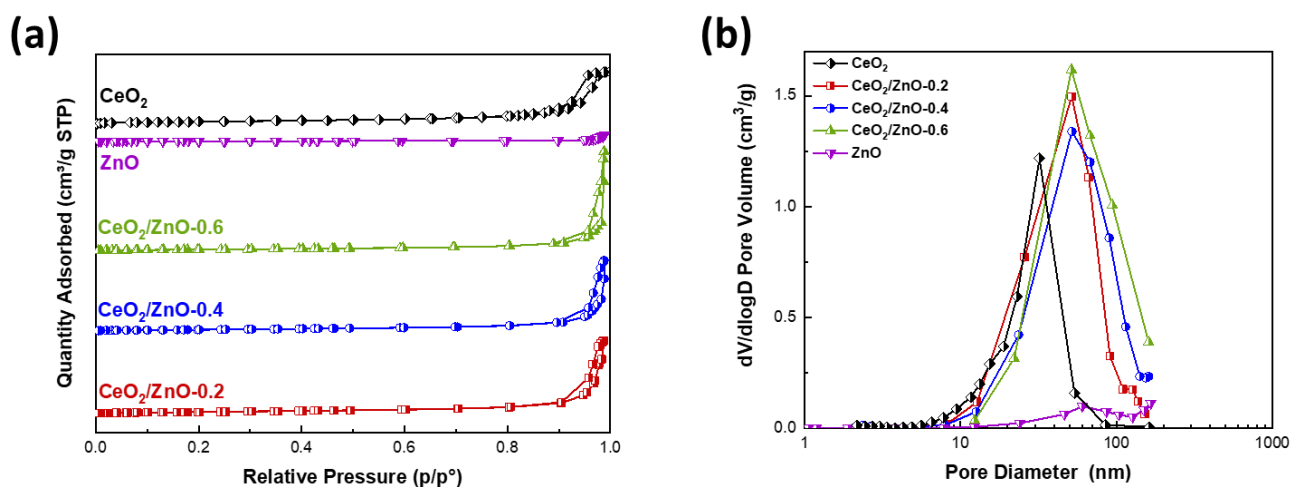


**Figure 3.7.** (a) N<sub>2</sub> adsorption-desorption isotherms and (b) pore size distribution of bare CeO<sub>2</sub>, ZnO, and the CeO<sub>2</sub>/ZnO samples. Adapted from Reference <sup>102</sup>.

Figure 3.8 displays the X-ray diffraction (XRD) patterns of CeO<sub>2</sub>, ZnO, and CeO<sub>2</sub>/ZnO (Zn:Ce = 0.2, 0.4, 0.6) mixed oxide phases. The XRD peaks of pure CeO<sub>2</sub> appear at  $2\theta = 28.5^\circ$ ,  $33.1^\circ$ ,  $47.5^\circ$ , and  $56.3^\circ$ , corresponding to (111), (200), (220), and (311) planes, respectively, indicating its face-centered cubic fluorite structure (Fm3m symmetry, no. 225) (JCPDS card: 01-081-0792) <sup>86,87</sup>. Similarly, the typical hexagonal wurtzite structure (P63mc symmetry, no. 186) (JCPDS card: 01-079-0208) is observed for pure ZnO with strong peaks at  $2\theta = 31.7^\circ$ ,  $34.4^\circ$ , and  $36.2^\circ$ , corresponding to (100), (002), and (101) lattice planes, respectively <sup>69,87</sup>. The XRD patterns of CeO<sub>2</sub>/ZnO samples indicate the formation of mixed oxides with finely dispersed phases of parent oxides, perfectly matching the indexed CeO<sub>2</sub> cubic and ZnO hexagonal structures. The ZnO reflections at (100), (002), and (101) increased with increasing ZnO content, while the XRD profile of CeO<sub>2</sub> remained unchanged. The sharp diffraction peaks in the XRD patterns suggest well-crystallized as-synthesized catalysts.

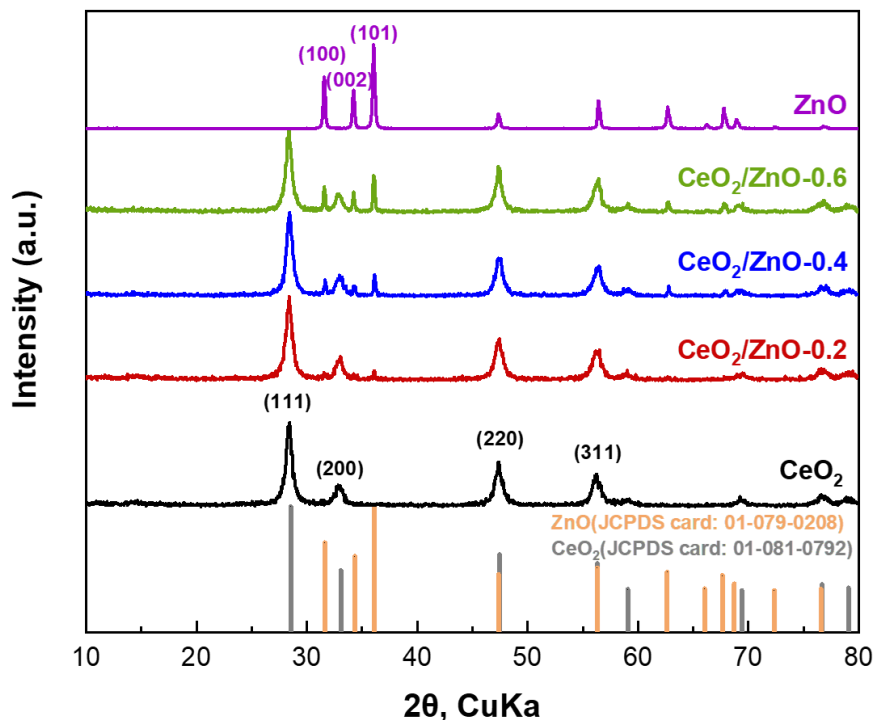


**Figure 3.8.** XRD patterns of CeO<sub>2</sub>, ZnO, and the CeO<sub>2</sub>/ZnO samples.

The average crystallite size of the samples was calculated using the Scherrer equation and is presented in Table 3.4. Pure ZnO exhibited a larger crystallite size (34.5 nm) than bare CeO<sub>2</sub> (13.0 nm). In CeO<sub>2</sub>/ZnO samples, the addition of ZnO led to a slight decrease in the crystallite size of CeO<sub>2</sub>, while the crystallite size of ZnO increased. The lattice parameters of mixed oxides remained unaffected, indicating well-dispersed phases of the constituent oxides (Table 3.4).

**Table 3.4.** Structural characteristics of CeO<sub>2</sub>, ZnO, and the CeO<sub>2</sub>/ZnO samples.

**XRD Analysis**

Samples	Phase detected	Average crystallite size, D <sub>XRD</sub> (nm)		Lattice Parameter (nm)
		CeO <sub>2</sub>	ZnO	
CeO <sub>2</sub>	Cerium(IV) oxide	13.0	-	a = b = c = 0.543
	Cerium(IV) oxide	12.1	44.4	a = b = c = 0.544
CeO <sub>2</sub> /ZnO-0.2	Zincite			a = b = 0.327, c = 0.523
	Cerium(IV) oxide	11.9	44.6	a = b = c = 0.543
CeO <sub>2</sub> /ZnO-0.4	Zincite			a = b = 0.326, c = 0.523
	Cerium(IV) oxide	11.6	39.3	a = b = c = 0.544
CeO <sub>2</sub> /ZnO-0.6	Zincite			a = b = 0.327, c = 0.523
	ZnO	-	34.5	a = b = 0.327, c = 0.523

### 3.3.2. Morphological Characterization

The morphology of  $\text{CeO}_2$ ,  $\text{ZnO}$ , and  $\text{CeO}_2/\text{ZnO}$  mixed oxides was analyzed using SEM and TEM techniques. Figure 3.9 illustrates the SEM and TEM images of bare  $\text{CeO}_2$  and  $\text{ZnO}$ . In particular, the images of pure  $\text{ZnO}$  (Figure 3.9 (a), (b)) reveal an irregular morphology, ranging from 50–100 nm in size, while bare  $\text{CeO}_2$  (Figure 3.9 (c), (d)) shows a distinct rod-like morphology, ranging from 50–200 nm in length (see sub-section 3.2.2).

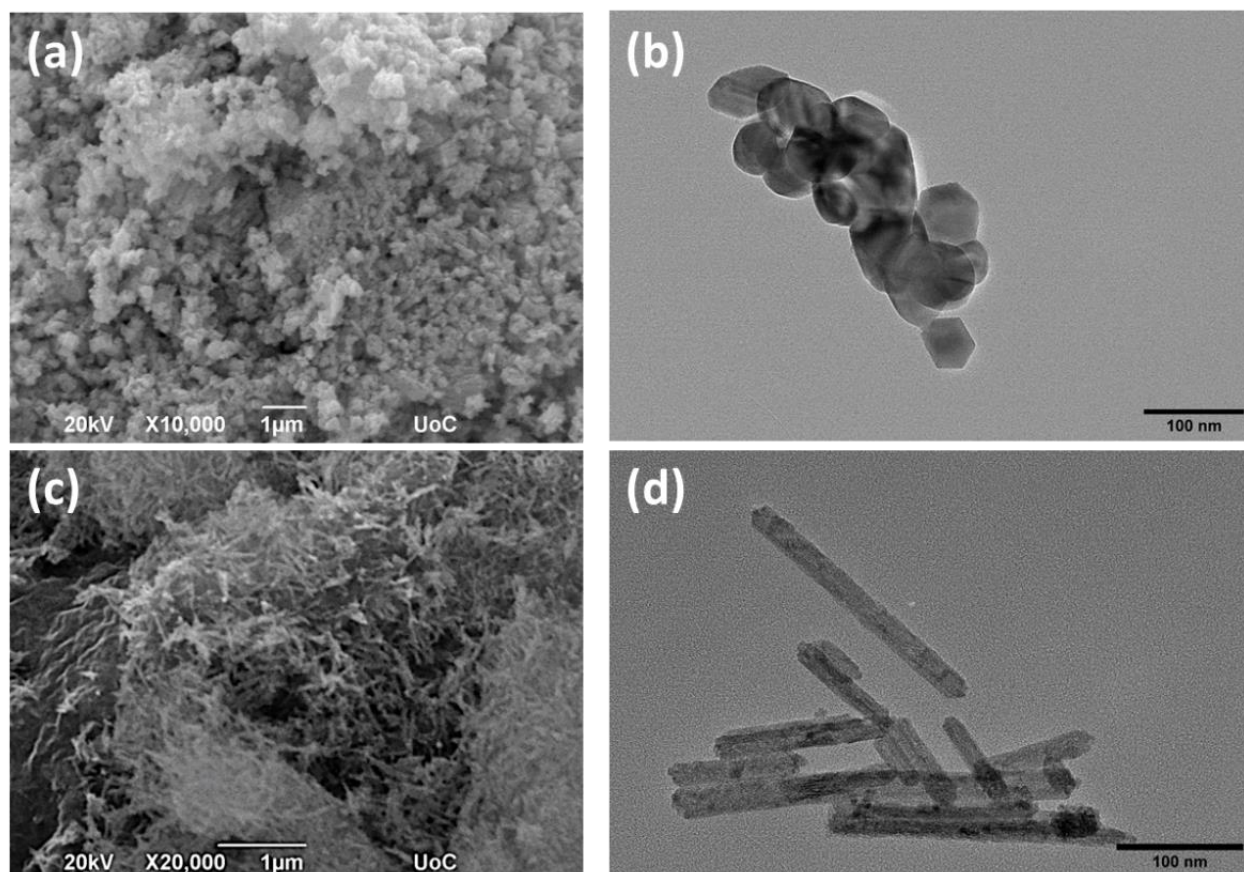


**Figure 3.9.** SEM and TEM images of (a), (b)  $\text{ZnO}$  and (c), (d)  $\text{CeO}_2$ , respectively.

The TEM images of the  $\text{CeO}_2/\text{ZnO}$  mixed oxides are presented in Figure 3.10 (a)-(c). It is revealed that the mixed oxides display the rod-like morphology of  $\text{CeO}_2$  nanorods, while separated  $\text{ZnO}$  particles with irregular morphology are also detected. These observations are consistent with the XRD results, which suggest the formation of distinct oxide phases. Additionally, scanning electron microscopy analysis coupled with energy-dispersive X-ray spectrometry (SEM/EDS) was conducted to perform elemental analysis on the  $\text{CeO}_2/\text{ZnO}$ -0.2 sample. Figure 3.10 (d) shows the corresponding SEM image along with the elemental analysis. The SEM/EDS analysis indicates a Zn:Ce atomic ratio of approximately 0.19, which is in good agreement with the nominal Zn/Ce ratio. This suggests a uniform distribution of  $\text{CeO}_2$  and  $\text{ZnO}$  phases throughout the entire material.

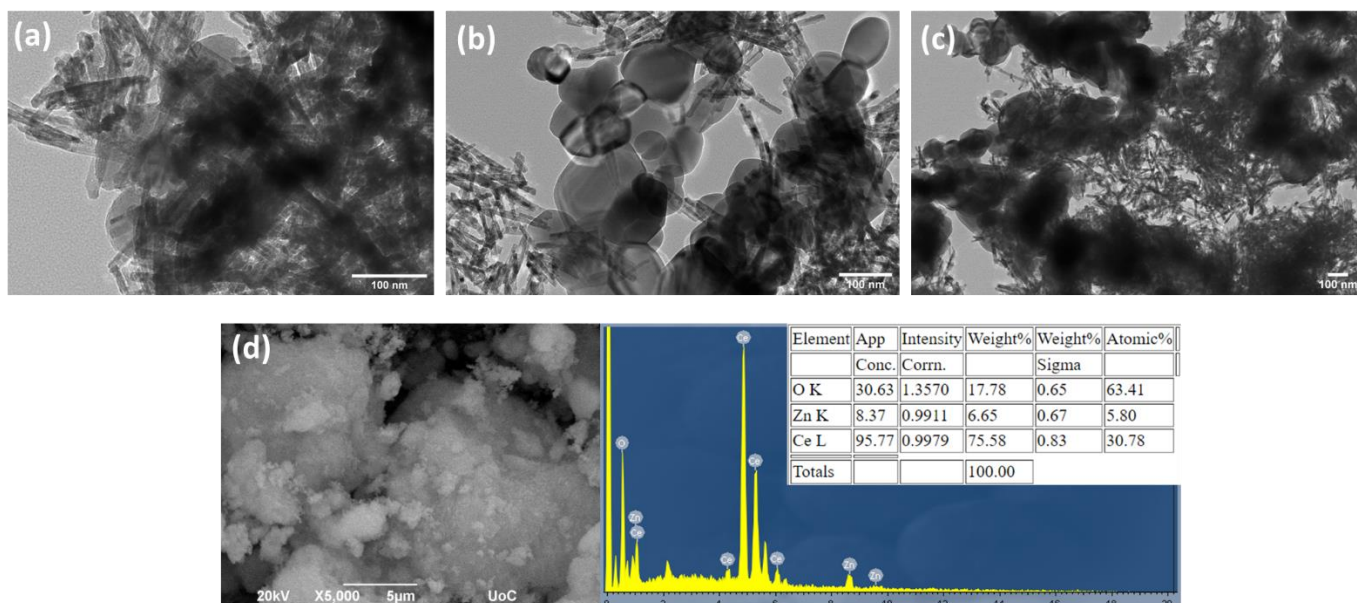


**Figure 3.10.** TEM images of (a) CeO<sub>2</sub>/ZnO–0.2, (b) CeO<sub>2</sub>/ZnO–0.4, and (c) CeO<sub>2</sub>/ZnO–0.6; (d) SEM/EDS analysis of the CeO<sub>2</sub>/ZnO–0.2 sample.

### 3.3.3. Redox Properties (H<sub>2</sub>-TPR)

The quantity and quality of active oxygen sites in catalysts can be determined through H<sub>2</sub>-TPR experiments, which is crucial for redox-type reactions such as CO oxidation. Figure 3.11 illustrates the reduction profiles of bare and mixed oxides in the 100–800 °C temperature range. The CeO<sub>2</sub> sample displays a peak (peak C) at 500–700 °C, which is attributed to loosely bound surface species, in contrast to the bulk oxygen that is reduced at temperatures exceeding 700 °C<sup>3,103–105</sup>. The pure ZnO sample, on the other hand, exhibits two broad peaks (peak A and peak B) in the 150–300 °C and 410–530 °C regions, which correspond to the reduction of hydroxyl species associated with ZnO and the surface oxygen reduction from ZnO, respectively<sup>106</sup>. Furthermore, the reduction of Zn<sup>2+</sup> to Zn<sup>0</sup> has been reported at 465 °C in pristine ZnO<sup>107</sup>. The TPR profiles of CeO<sub>2</sub>/ZnO samples demonstrate distinct peaks from both CeO<sub>2</sub> and ZnO phases. Interestingly, unlike CeO<sub>2</sub>/TiO<sub>2</sub> mixed oxides (see sub-section 3.2.3), the addition of ZnO to CeO<sub>2</sub> does not shift TPR peaks, implying that ZnO and CeO<sub>2</sub> in the mixed oxides are structurally independent. This finding is consistent with the XRD and TEM results, which show distinct ZnO nanoparticles near CeO<sub>2</sub> nanorods without any Zn incorporation into the nanostructure of CeO<sub>2</sub> nanorods.

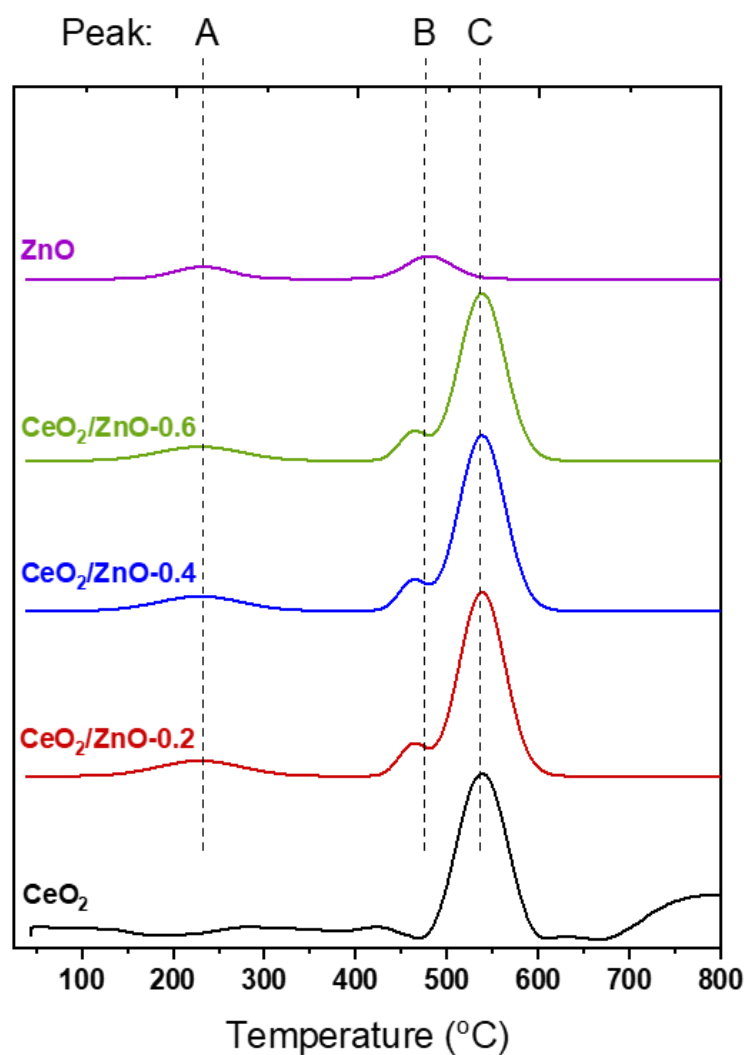


**Figure 3.11.** H<sub>2</sub>-TPR profiles of CeO<sub>2</sub> and the CeO<sub>2</sub>/ZnO samples. Adapted from Reference <sup>102</sup>.

To gain greater insight into the effect of ZnO on the reducibility of CeO<sub>2</sub>/ZnO oxides, the H<sub>2</sub> uptake in the temperature range of 50-700 °C was estimated by quantifying the TPR peaks (Table 3.5). Interestingly, ZnO addition leads to an increase in H<sub>2</sub> uptake in the CeO<sub>2</sub>/ZnO samples, suggesting an easier detachment of surface oxygen species. It is also worth noticing the increase of H<sub>2</sub> uptake related to ceria reduction (peak C), despite the gradual decrease of ceria content. This indicates that ceria capping oxygen is easily reduced with an increase in ZnO content. All mixed oxides exhibit a total H<sub>2</sub> consumption of ca. 1.0 mmol H<sub>2</sub>/g, as compared to 0.59 and 0.31 mmol H<sub>2</sub>/g of bare CeO<sub>2</sub> and ZnO, respectively.

In terms of oxygen storage capacity (OSC), the trend is as follows: CeO<sub>2</sub>/ZnO-0.6 (0.52 mmol O<sub>2</sub>/g) > CeO<sub>2</sub>/ZnO-0.4 (0.50 mmol O<sub>2</sub>/g) > CeO<sub>2</sub>/ZnO-0.2 (0.48 mmol O<sub>2</sub>/g) > CeO<sub>2</sub> (0.29 mmol O<sub>2</sub>/g) > ZnO (0.15 mmol O<sub>2</sub>/g). This order aligns relatively well with the catalytic activity (discussed below), highlighting the critical role of reducibility. The abundance of reducible oxygen species is expected

to influence oxygen mobility and, consequently, the CO oxidation process, as will be discussed further below. Overall, this data sheds light on how ZnO impacts the reducibility of CeO<sub>2</sub>/ZnO oxides and its potential implications for the CO oxidation process.

**Table 3.5.** Redox features of CeO<sub>2</sub> and CeO<sub>2</sub>/ZnO samples.

Sample	H <sub>2</sub> Uptake (mmol H <sub>2</sub> /g) and OSC (mmol O <sub>2</sub> /g)				
	Peak A	Peak B	Peak C	H <sub>2</sub> Uptake (mmol H <sub>2</sub> /g)	OSC (mmol O <sub>2</sub> /g)
<b>CeO<sub>2</sub></b>	-	-	0.59	0.59	0.29
<b>CeO<sub>2</sub>/ZnO-0.2</b>	0.15	0.21	0.61	0.97	0.48
<b>CeO<sub>2</sub>/ZnO-0.4</b>	0.15	0.23	0.63	1.01	0.50
<b>CeO<sub>2</sub>/ZnO-0.6</b>	0.16	0.25	0.63	1.04	0.52
<b>ZnO</b>	0.14	0.17	-	0.31	0.15

### 3.4. Implication in the CO oxidation reaction

#### 3.4.1. CO Oxidation Performance of CeO<sub>2</sub>/TiO<sub>2</sub>

To gain insight into the effect of the different preparation methods on the catalytic performance of the CeO<sub>2</sub>/TiO<sub>2</sub> samples, their CO oxidation performance was investigated. Figure 3.12 depicts the CO conversion at various temperatures for CeO<sub>2</sub> and CeO<sub>2</sub>/TiO<sub>2</sub> samples, with a commercially available TiO<sub>2</sub> sample from Evonik Industries used as a reference material. The results indicate that the preparation method strongly influences the nanostructure of the samples, which is consistent with previous findings<sup>2</sup>. Among the samples tested, the CeO<sub>2</sub>/TiO<sub>2</sub>-S sample prepared using the Stöber method exhibited the best CO conversion performance, as demonstrated in Figure 3.12. The CeO<sub>2</sub> and CeO<sub>2</sub>/TiO<sub>2</sub>-H1 samples showed similar catalytic behavior, but both required approximately 30 degrees higher temperatures than the CeO<sub>2</sub>/TiO<sub>2</sub>-S sample. On the other hand, mixed oxides of ceria-titania prepared by precipitation and two-step hydrothermal methods exhibited negligible CO conversion performance, namely ~8% and 22% at 500 °C, respectively, indicating the key role of the synthesis procedure. Finally, the bare TiO<sub>2</sub> sample was found to be inactive within the range of temperatures investigated.

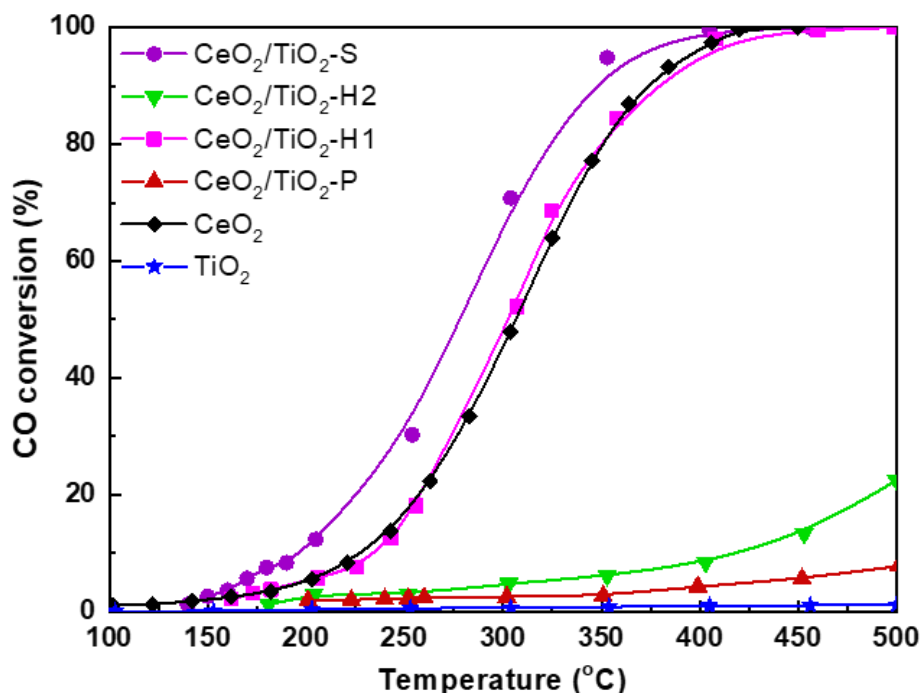


**Figure 3.12.** Conversion of CO with temperature for CeO<sub>2</sub>, TiO<sub>2</sub>, and CeO<sub>2</sub>/TiO<sub>2</sub> samples. Reaction conditions: 0.2 vol.% CO, 1 vol.% O<sub>2</sub>, GHSV = 40,000 h<sup>-1</sup>. Adapted from Reference <sup>84</sup>.

To fully comprehend the impact of the preparation procedure and catalyst composition (bare or mixed oxides) on the intrinsic reactivity, the different textural properties among the as-prepared samples (Table 3.1) should be considered. The specific activity of the catalysts was therefore calculated in terms of catalyst surface area ( $\mu\text{mol m}^{-2} \text{s}^{-1}$ ) and mass ( $\mu\text{mol g}^{-1} \text{s}^{-1}$ ) under differential reaction conditions with  $X_{\text{CO}} < 15\%$ ,  $T = 200 \text{ }^\circ\text{C}$ , and  $\text{GHSV} = 40,000 \text{ h}^{-1}$ , which helps to reveal the relationship between CO oxidation activity and textural properties. The results are summarized in Table 3.6 and clearly show that CeO<sub>2</sub>/TiO<sub>2</sub>-S demonstrates by far the optimum catalytic performance, in terms of conversion as well as of specific activity, indicating its superiority. Additionally, a stable conversion performance (ca. 99% CO conversion) was achieved at 400 °C in short-term (12 h) stability experiments.

**Table 3.6.** Conversion of CO and specific rates of CeO<sub>2</sub> and CeO<sub>2</sub>/TiO<sub>2</sub> samples at 200 °C. Reaction conditions: 0.2 vol.% CO and 1 vol.% O<sub>2</sub> in He.

Sample	CO Conversion (%)	Specific Rate	
		r ( $\mu\text{mol g}^{-1} \text{s}^{-1}$ )	r ( $\times 100$ ) ( $\mu\text{mol m}^{-2} \text{s}^{-1}$ )
CeO <sub>2</sub>	5.1	0.056	0.075
CeO <sub>2</sub> /TiO <sub>2</sub> -P	1.9	0.021	0.050
CeO <sub>2</sub> /TiO <sub>2</sub> -H1	5.3	0.058	0.057
CeO <sub>2</sub> /TiO <sub>2</sub> -H2	3.0	0.033	0.052
CeO <sub>2</sub> /TiO <sub>2</sub> -S	11.1	0.121	0.168

The results of this chapter can be interpreted by a Mars-van Krevelen, redox-type mechanism, which mainly involves CO chemisorption towards the formation of  $\text{Ce}^{\delta+}\text{-CO}$  species,  $\text{O}_2$  activation on the oxygen vacancies of ceria, and active oxygen species formation<sup>108,109</sup>. The reaction occurs between chemisorbed CO and adjacent active oxygen, followed by regeneration of active sites and replenishment of oxygen vacancies by gas phase oxygen participated in sequential catalytic cycles<sup>108,109</sup>.

The above mechanism clearly explains the crucial role of redox properties during the CO oxidation process over  $\text{CeO}_2$ -based oxides. The  $\text{CeO}_2/\text{TiO}_2\text{-S}$  sample showed superior oxidation performance compared to the other samples, thanks to its high oxygen storage capacity (Table 3.2), which is linked to improved oxygen exchange kinetics and reducibility. In a recent study, it was shown that  $\text{CeO}_2$  composites with rod-like morphology have improved redox properties due to their abundance of defects and oxygen vacancies, leading to better catalytic performance. This was demonstrated by both in-situ and ex-situ techniques<sup>29</sup>. These structure-activity relationships are supported by the linear relationship between the specific reaction rate ( $\mu\text{mol g}^{-1} \text{s}^{-1}$ ) and the redox properties (OSC,  $\text{mmol O}_2 \text{g}^{-1}$ ), as shown in Figure 3.13.

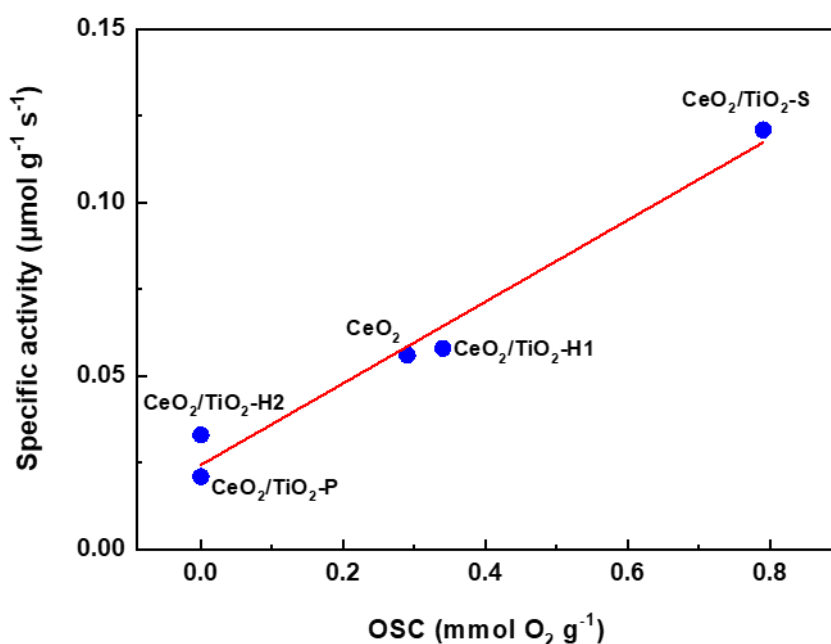


**Figure 3.13.** Relationship of the specific activity and the oxygen storage capacity of as-prepared samples. Adapted from Reference<sup>84</sup>.

Taking into account the aforementioned factors, the superior performance of the  $\text{CeO}_2/\text{TiO}_2\text{-S}$  catalyst can be attributed to the abundance of weakly bound oxygen species, which results in greater oxygen storage capacity and reducibility, as identified by  $\text{H}_2\text{-TPR}$ . This can be ascribed to the

beneficial role of the Stöber method towards achieving highly homogenized composites with rod-like morphology, in which no distinct separation between ceria and titania phases was observed. Hence, it can be argued that the Stöber method may promote a synergistic interaction between ceria and titania, facilitating the formation of oxygen vacancies and promoting the redox interplay between the interfacial sites, leading to a higher concentration of active oxygen species. In line with the above discussion, it has been revealed using DFT calculations that the formation of oxygen vacancies and  $\text{Ce}^{3+}$  sites is energetically favored at the ceria–titania interface <sup>110</sup>.

Although bare titania is not catalytically active in CO oxidation, the combination of titania with  $\text{CeO}_2$  could result in highly active  $\text{CeO}_2/\text{TiO}_2$  mixed oxides through a synergistic interaction (Figure 3.12). However, the synthesis method strongly affects the performance of the mixed oxides. For instance, the hydrothermal method, whether conducted in one or two steps, does not improve, but may even worsen the catalytic activity as compared to bare ceria, whereas the Stöber method does indeed enhance the catalytic performance. Specifically, the addition of titania into ceria nanorods through the hydrothermal method ( $\text{CeO}_2/\text{TiO}_2\text{-H1}$ ) clearly enhanced the textural properties (surface area), without improving the catalytic performance. This can be explained by taking into account the distinctive shift of the TPR peak to a higher temperature (Figure 3.6, Table 3.2), indicating a harder partial  $\text{Ce}^{4+} \rightarrow \text{Ce}^{3+}$  reduction and detachment of O atoms, i.e., lower reducibility and an increase in oxygen vacancy formation energy. The hydrothermal method has no significant effect on the concentration of reducible oxygen species, as shown by the similar OSC values between  $\text{CeO}_2$  and  $\text{CeO}_2/\text{TiO}_2\text{-H1}$  (Table 3.2). In contrast, although the Stöber method slightly inhibits surface oxygen reduction (shift of TPR peak to higher temperature), it drastically increases the population of active oxygen species, resulting in a three-fold increase in OSC as compared to that provided by the hydrothermal method. In summary,  $\text{CeO}_2/\text{TiO}_2\text{-S}$  samples exhibit superior catalytic performance in comparison to bare  $\text{CeO}_2$ , highlighting the beneficial effect of the synthesis method and the incorporation of a second oxide phase. These materials could serve as supporting carriers for various transition metals, facilitating the transition to a noble metal-free catalysis.

#### 3.4.2. CO Oxidation Performance of $\text{CeO}_2/\text{ZnO}$

Figure 3.14 illustrates the conversion profiles of CO over temperature for bare ZnO,  $\text{CeO}_2$ , and  $\text{CeO}_2/\text{ZnO}$  mixed oxides. The results clearly indicate that all mixed oxides exhibit superior performance as compared to the bare materials. Among the mixed oxides, there is a similar level of performance, with  $\text{CeO}_2/\text{ZnO}\text{-0.4}$  showing a slightly better performance. To better understand the influence of the preparation method and the synergistic interaction between the different counterparts, the catalytic performance of a mechanical mixture ( $\text{CeO}_2+\text{ZnO}\text{-0.4}$ ) with the same

composition as the optimum sample (CeO<sub>2</sub>/ZnO-0.4) was explored in parallel. The results show that the bare ceria nanorods (CeO<sub>2</sub>) exhibit a catalytic profile shifted ca. 30 °C towards higher temperatures as compared to the optimum CeO<sub>2</sub>/ZnO-0.4 sample. On the other hand, ZnO is significantly less active, with a profile located ca. 170 °C higher. Most importantly, the conversion profile of the mechanical mixture (CeO<sub>2</sub>+ZnO-0.4) is shifted approximately 100 °C towards higher temperatures as compared to that of CeO<sub>2</sub>/ZnO-0.4. This observation highlights the beneficial interaction between CeO<sub>2</sub> and ZnO, which is induced by the preparation method employed (see experimental section).

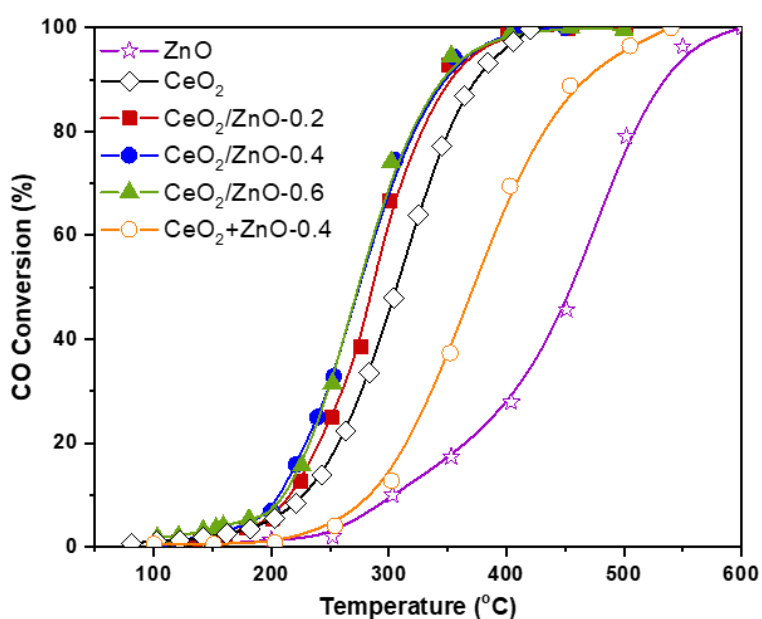


**Figure 3.14.** CO conversion profiles of CeO<sub>2</sub>, ZnO, and CeO<sub>2</sub>/ZnO samples. Adapted from Reference <sup>102</sup>.

To gain a deeper understanding in the intrinsic activity of the investigated samples, the specific activity was estimated, both in terms of catalyst mass ( $\mu\text{mol g}^{-1} \text{s}^{-1}$ ) and surface area ( $\mu\text{mol m}^{-2} \text{s}^{-1}$ ), as shown in Table 3.7. The results clearly indicate that the CeO<sub>2</sub>/ZnO-0.4 sample exhibits the highest performance in both conversion and mass-normalized specific activity, highlighting its superior reactivity. However, it should be noted that in terms of area-normalized activity, bare ceria and mixed oxides demonstrate lower activity as compared to bare ZnO. This can be attributed to the low surface area of ZnO ( $7.1 \text{ m}^2/\text{g}$ ), which is approximately one order of magnitude lower than that of bare CeO<sub>2</sub> and CeO<sub>2</sub>/ZnO mixed oxides. Therefore, based on these findings, the enhanced catalytic performance of CeO<sub>2</sub>/ZnO mixed oxides can be attributed to a compromise between redox and surface properties. Furthermore, the optimum CeO<sub>2</sub>/ZnO-0.4 sample exhibits an apparent

activation energy ( $E_a$ ) of 32.1 kJ/mol, which is significantly lower than that of bare ceria (44.2 kJ/mol), ZnO (42.1 kJ/mol), and the mechanical mixture of CeO<sub>2</sub>+ZnO-0.4 (43.2 kJ/mol). These results reveal a lower energy barrier for CO oxidation over the hydrothermally prepared mixed oxides in comparison to the individual ones and the mechanical mixture, thereby demonstrating the beneficial synergistic interactions induced by the synthesis procedure.

**Table 3.7.** Conversion of CO and specific rates of CeO<sub>2</sub> and CeO<sub>2</sub>/ZnO samples at 200 °C. Reaction conditions: 0.2 vol.% CO and 1 vol.% O<sub>2</sub> in He.

Sample	CO Conversion (%)	Specific Rate	
		r (μmol g <sup>-1</sup> s <sup>-1</sup> )	r (×100) (μmol m <sup>-2</sup> s <sup>-1</sup> )
CeO <sub>2</sub>	5.1	0.056	0.070
CeO <sub>2</sub> /ZnO-0.2	5.4	0.059	0.077
CeO <sub>2</sub> /ZnO-0.4	6.9	0.075	0.121
CeO <sub>2</sub> /ZnO-0.6	6.2	0.068	0.121
ZnO	1.3	0.014	0.201

The CO oxidation process investigated can be supported by a redox-type (Mars–van Krevelen) mechanism. This mechanism specifically involves CO chemisorption on Ce<sup>δ+</sup> active sites, followed by oxygen activation on oxygen vacancies<sup>1,29,111</sup>. CO oxidation takes place between the Ce<sup>δ+</sup>–CO and adjacent oxygen species, followed by the regeneration of active sites and the reoccupation of oxygen vacancies through gas-phase oxygen, as also described in sub-section 3.4.1.

Considering the mechanistic aspects discussed above, the catalyst's redox properties play a crucial and evident role in its performance. Notably, the catalyst's high oxygen storage capacity, as demonstrated in Table 3.5, along with the improved reducibility and oxygen exchange kinetics, significantly contribute to its enhanced oxidation performance. Any modifications in the structure or composition of ceria that affect the ceria-oxygen or ceria-oxygen-metal bond can facilitate the activation of O<sub>2</sub>, leading to CO oxidation. Recent findings have highlighted the fundamental importance of CeO<sub>2</sub> nanorods' increased reducibility, which is attributed to an abundance of oxygen vacancies, in achieving superior catalytic performance<sup>29</sup>. Furthermore, as discussed in sub-section 3.4.1, the incorporation of a transition metal element, even if catalytically inactive (e.g., Ti), into the structure of ceria nanorods can influence the coordination environment of oxygen species, thereby impacting the oxygen storage capacity (OSC) and the overall catalytic performance.

These arguments regarding the essential role of reducibility are strongly supported by the direct relationship between the redox properties (OSC, mmol O<sub>2</sub> g<sup>-1</sup>) and the normalized reaction rate

( $\mu\text{mol g}^{-1} \text{s}^{-1}$ ), as depicted in Figure 3.15. It is noteworthy that the significance of oxygen storage capacity (OSC) as an activity indicator is further highlighted in this chapter by incorporating relevant data from sub-section 3.4.1, in which bare  $\text{CeO}_2$  and  $\text{CeO}_2/\text{TiO}_2$  oxides were investigated, as presented in Figure 3.15. This inclusion is particularly important in advancing the development of cost-effective and highly efficient metal oxides by appropriately manipulating their redox characteristics.

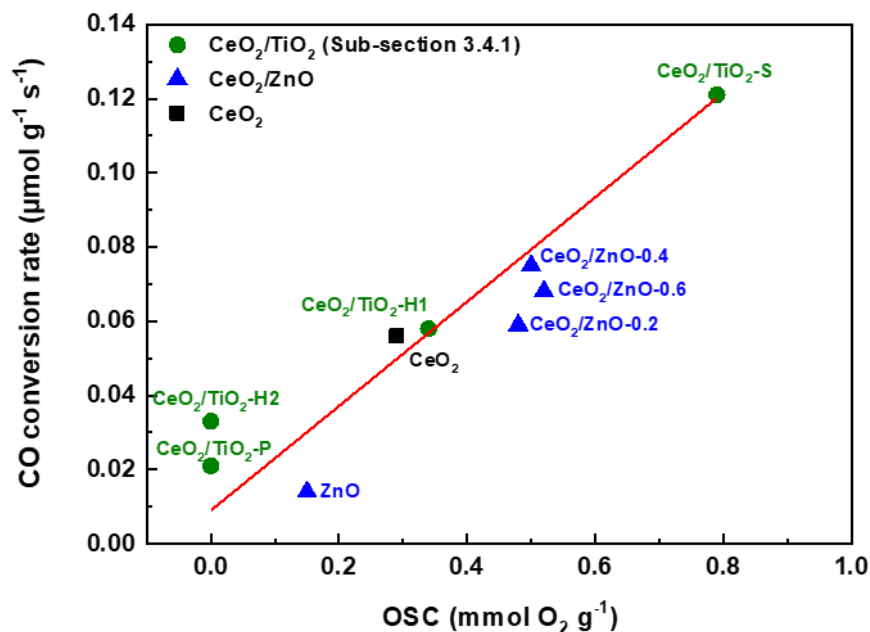


**Figure 3.15.** Correlation of specific activity with oxygen storage capacity (OSC). Scientific data are also included. Specific rates were obtained at 200 °C under the reaction conditions: 0.2 vol.% CO and 1 vol.%  $\text{O}_2$  in He. The line simply represents the general trend of the data. The designation of the samples inside the figure refers to the  $\text{CeO}_2/\text{TiO}_2$  samples from sub-section 3.4.1. Adapted from Reference <sup>102</sup>.

Regarding the present findings, it is evident that while bare ZnO exhibits significantly lower catalytic activity as compared to  $\text{CeO}_2$  (Figure 3.14), their combination leads to a synergistic effect in the formation of  $\text{CeO}_2/\text{ZnO}$  mixed oxides with improved activity. This synergistic interaction was observed in  $\text{TiO}_2$ -doped  $\text{CeO}_2$  systems, where the doping element was incorporated into the nanostructure, resulting in the formation of active Ce-O-Ti sites. Notably, in this chapter, ZnO is not integrated into the structure of  $\text{CeO}_2$  nanorods. As evident from TEM images (Figure 3.10), ZnO nanoparticles are in close interaction with nanorods but clearly as separate particles. This is also supported by the XRD results (Figure 3.8), which indicate distinct oxide phases without the formation of a solid solution. Consequently, the enhanced catalytic activity of  $\text{CeO}_2/\text{ZnO}$  mixed oxides, attributed to the presence of active oxygen species and the facile reduction of surface oxygen,

can be ascribed to the facilitation of ceria capping oxygen reduction by adjacent ZnO nanoparticles. This, in turn, leads to higher oxygen storage capacity (Figure 3.11 and Table 3.5). Therefore, although ZnO is not incorporated into the ceria nanorod structure, it significantly contributes to the reduction of surface oxygen, most likely through the interfacial ZnO-CeO<sub>2</sub> sites. This combination, along with the abundance and lower cost of zinc as compared to cerium oxide, constitutes an intriguing aspect in terms of catalyst design.

### 3.5. Conclusions

In Chapter 3, the synthesis, characterization, and catalytic evaluation of TiO<sub>2</sub>- and ZnO-doped ceria nanorods are investigated.

Ceria-titania mixed oxides were prepared by the hydrothermal, Stöber, and precipitation methods. The CO oxidation was used as a probe reaction to reveal possible structure-property relationships. The following order, in terms of CO conversion, was obtained: CeO<sub>2</sub>/TiO<sub>2</sub>-S > CeO<sub>2</sub>/TiO<sub>2</sub>-H1 > CeO<sub>2</sub> > CeO<sub>2</sub>/TiO<sub>2</sub>-H2 > CeO<sub>2</sub>/TiO<sub>2</sub>-P > TiO<sub>2</sub>. A characterization study by various complementary techniques revealed the significant effect of the synthesis procedure on the textural, morphological, and redox features. Despite the inferior textural properties of the mixed oxides synthesized by the Stöber method, they exhibit the best catalytic performance, which can be ascribed to their improved reducibility, associated with their relative abundance in loosely bound oxygen species and high oxygen storage capacity. The Stöber method leads to rod-shaped ceria nanoparticles uniformly decorated by titania, which can be considered responsible for synergistic ceria-titania interactions towards an increased population of highly reducible active sites.

CeO<sub>2</sub>/ZnO mixed oxides were synthesized via a two-step hydrothermal method, and a comprehensive characterization study was conducted to examine their texture, structure, morphology, and redox properties. In order to understand the relationship between structure and activity, CO oxidation was once more used as a probe reaction. The results showed the following order in terms of both CO conversion and specific activity: CeO<sub>2</sub>/ZnO-0.4 > CeO<sub>2</sub>/ZnO-0.6 > CeO<sub>2</sub>/ZnO-0.2 > CeO<sub>2</sub> > ZnO. Interestingly, despite the appearance of the distinct ZnO and CeO<sub>2</sub> phases in the mixed oxides and the low reactivity of pure ZnO, the mixed oxides exhibited improved catalytic performance as compared to the individual oxides. This enhancement in catalytic performance can be attributed to the synergistic interactions between CeO<sub>2</sub> and ZnO, which led to enhanced oxygen mobility and reducibility. Notably, a strong correlation was found between the catalytic activity and the oxygen storage capacity (OSC), which is in agreement with the findings of ceria-titania catalysts and highlights the importance of OSC as a key activity descriptor for reactions involving a redox-type mechanism.

Overall, this chapter emphasizes the significance of the rational design of noble metal-free mixed oxides towards the development of highly active materials that could be used as catalysts or supporting carriers in various environmental and energy applications.

## References

- (1) Wu, Z.; Li, M.; Overbury, S. H. On the Structure Dependence of CO Oxidation over CeO<sub>2</sub> Nanocrystals with Well-Defined Surface Planes. *J. Catal.* **2012**, *285* (1), 61–73. <https://doi.org/10.1016/j.jcat.2011.09.011>.
- (2) Lykaki, M.; Stefa, S.; Carabineiro, S.; Pandis, P.; Stathopoulos, V.; Konsolakis, M. Facet-Dependent Reactivity of Fe<sub>2</sub>O<sub>3</sub>/CeO<sub>2</sub> Nanocomposites: Effect of Ceria Morphology on CO Oxidation. *Catalysts* **2019**, *9* (4), 371. <https://doi.org/10.3390/catal9040371>.
- (3) Lykaki, M.; Pachatouridou, E.; Iliopoulou, E.; Carabineiro, S. A. C.; Konsolakis, M. Impact of the Synthesis Parameters on the Solid State Properties and the CO Oxidation Performance of Ceria Nanoparticles. *RSC Adv.* **2017**, *7* (10), 6160–6169. <https://doi.org/10.1039/C6RA26712B>.
- (4) Zhang, S.; Li, Y.; Huang, J.; Lee, J.; Kim, D. H.; Frenkel, A. I.; Kim, T. Effects of Molecular and Electronic Structures in CoO<sub>x</sub>/CeO<sub>2</sub> Catalysts on NO Reduction by CO. *J. Phys. Chem. C* **2019**, *123* (12), 7166–7177. <https://doi.org/10.1021/acs.jpcc.8b12442>.
- (5) Zhang, S.; Lee, J.; Kim, D. H.; Kim, T. NO Reduction by CO over CoO<sub>x</sub>/CeO<sub>2</sub> Catalysts: Effect of Support Calcination Temperature on Activity. *Mol. Catal.* **2020**, *482* (November 2019), 110703. <https://doi.org/10.1016/j.mcat.2019.110703>.
- (6) Akter, N.; Zhang, S.; Lee, J.; Kim, D. H.; Boscoboinik, J. A.; Kim, T. Selective Catalytic Reduction of NO by Ammonia and NO Oxidation Over CoO<sub>x</sub>/CeO<sub>2</sub> Catalysts. *Mol. Catal.* **2020**, *482* (July 2019), 110664. <https://doi.org/10.1016/j.mcat.2019.110664>.
- (7) Damaskinos, C. M.; Vasiliades, M. A.; Stathopoulos, V. N.; Efstathiou, A. M. The Effect of CeO<sub>2</sub> Preparation Method on the Carbon Pathways in the Dry Reforming of Methane on Ni/CeO<sub>2</sub> Studied by Transient Techniques. *Catalysts* **2019**, *9* (7), 621. <https://doi.org/10.3390/catal9070621>.
- (8) López Cámara, A.; Cortés Corberán, V.; Martínez-Arias, A.; Barrio, L.; Si, R.; Hanson, J. C.; Rodríguez, J. A. Novel Manganese-Promoted Inverse CeO<sub>2</sub>/CuO Catalyst: In Situ Characterization and Activity for the Water-Gas Shift Reaction. *Catal. Today* **2020**, *339* (January 2019), 24–31. <https://doi.org/10.1016/j.cattod.2019.01.014>.
- (9) Chen, C.; Zhan, Y.; Zhou, J.; Li, D.; Zhang, Y.; Lin, X.; Jiang, L.; Zheng, Q. Cu/CeO<sub>2</sub> Catalyst for Water-Gas Shift Reaction: Effect of CeO<sub>2</sub> Pretreatment. *ChemPhysChem* **2018**,

19 (12), 1448–1455. <https://doi.org/10.1002/cphc.201800122>.

- (10) Ronda-Lloret, M.; Rico-Francés, S.; Sepúlveda-Escribano, A.; Ramos-Fernandez, E. V. CuO<sub>x</sub>/CeO<sub>2</sub> Catalyst Derived from Metal Organic Framework for Reverse Water-Gas Shift Reaction. *Appl. Catal. A Gen.* **2018**, *562* (May), 28–36. <https://doi.org/10.1016/j.apcata.2018.05.024>.
- (11) da Silva, A. M.; de Souza, K. R.; Jacobs, G.; Graham, U. M.; Davis, B. H.; Mattos, L. V.; Noronha, F. B. Steam and CO<sub>2</sub> Reforming of Ethanol over Rh/CeO<sub>2</sub> Catalyst. *Appl. Catal. B Environ.* **2011**, *102* (1–2), 94–109. <https://doi.org/10.1016/j.apcatb.2010.11.030>.
- (12) Hou, T.; Yu, B.; Zhang, S.; Xu, T.; Wang, D.; Cai, W. Hydrogen Production from Ethanol Steam Reforming over Rh/CeO<sub>2</sub> Catalyst. *Catal. Commun.* **2015**, *58*, 137–140. <https://doi.org/10.1016/j.catcom.2014.09.020>.
- (13) Aneggi, E.; Wiater, D.; de Leitenburg, C.; Llorca, J.; Trovarelli, A. Shape-Dependent Activity of Ceria in Soot Combustion. *ACS Catal.* **2014**, *4* (1), 172–181. <https://doi.org/10.1021/cs400850r>.
- (14) Muroyama, H.; Hano, S.; Matsui, T.; Eguchi, K. Catalytic Soot Combustion over CeO<sub>2</sub>-Based Oxides. *Catal. Today* **2010**, *153* (3–4), 133–135. <https://doi.org/10.1016/j.cattod.2010.02.015>.
- (15) Kumar, P. A.; Tanwar, M. D.; Russo, N.; Pirone, R.; Fino, D. Synthesis and Catalytic Properties of CeO<sub>2</sub> and Co/CeO<sub>2</sub> Nanofibres for Diesel Soot Combustion. *Catal. Today* **2012**, *184* (1), 279–287. <https://doi.org/10.1016/j.cattod.2011.12.025>.
- (16) Konsolakis, M. The Role of Copper–Ceria Interactions in Catalysis Science: Recent Theoretical and Experimental Advances. *Appl. Catal. B Environ.* **2016**, *198*, 49–66. <https://doi.org/10.1016/j.apcatb.2016.05.037>.
- (17) Konsolakis, M.; Lykaki, M. Recent Advances on the Rational Design of Non-Precious Metal Oxide Catalysts Exemplified by CuO<sub>x</sub>/CeO<sub>2</sub> Binary System: Implications of Size, Shape and Electronic Effects on Intrinsic Reactivity and Metal-Support Interactions. *Catalysts* **2020**, *10* (2), 160. <https://doi.org/10.3390/catal10020160>.
- (18) Montini, T.; Melchionna, M.; Monai, M.; Fornasiero, P. Fundamentals and Catalytic Applications of CeO<sub>2</sub>-Based Materials. *Chem. Rev.* **2016**, *116* (10), 5987–6041. <https://doi.org/10.1021/acs.chemrev.5b00603>.
- (19) Cortés Corberán, V.; Rives, V.; Stathopoulos, V. Recent Applications of Nanometal Oxide

Catalysts in Oxidation Reactions. In *Advanced Nanomaterials for Catalysis and Energy*; Elsevier, 2019; pp 227–293. <https://doi.org/10.1016/B978-0-12-814807-5.00007-3>.

- (20) Melchionna, M.; Fornasiero, P. The Role of Ceria-Based Nanostructured Materials in Energy Applications. *Mater. Today* **2014**, *17* (7), 349–357. <https://doi.org/10.1016/j.mattod.2014.05.005>.
- (21) Paier, J.; Penschke, C.; Sauer, J. Oxygen Defects and Surface Chemistry of Ceria: Quantum Chemical Studies Compared to Experiment. *Chem. Rev.* **2013**, *113* (6), 3949–3985. <https://doi.org/10.1021/cr3004949>.
- (22) Tang, W.-X.; Gao, P.-X. Nanostructured Cerium Oxide: Preparation, Characterization, and Application in Energy and Environmental Catalysis. *MRS Commun.* **2016**, *6* (04), 311–329. <https://doi.org/10.1557/mrc.2016.52>.
- (23) Sun, C.; Xue, D. Size-Dependent Oxygen Storage Ability of Nano-Sized Ceria. *Phys. Chem. Chem. Phys.* **2013**, *15* (34), 14414–14419. <https://doi.org/10.1039/c3cp51959g>.
- (24) Qiao, Z. A.; Wu, Z.; Dai, S. Shape-Controlled Ceria-Based Nanostructures for Catalysis Applications. *ChemSusChem* **2013**, *6* (10), 1821–1833. <https://doi.org/10.1002/cssc.201300428>.
- (25) Zhang, D.; Du, X.; Shi, L.; Gao, R. Shape-Controlled Synthesis and Catalytic Application of Ceria Nanomaterials. *Dalt. Trans.* **2012**, *41* (48), 14455–14475. <https://doi.org/10.1039/c2dt31759a>.
- (26) Zhu, W.; Tang, K.; Li, J.; Liu, W.; Niu, X.; Zhao, G.; Ma, X.; Liu, Z.; Wei, H.; Yang, Y. The Effect of Copper Species in Copper-Ceria Catalysts: Structure Evolution and Enhanced Performance in CO Oxidation. *RSC Adv.* **2016**, *6* (52), 46966–46971. <https://doi.org/10.1039/c6ra08204a>.
- (27) Zhu, H.; Chen, Y.; Wang, Z.; Liu, W.; Wang, L. Catalytic Oxidation of CO over Mesoporous Copper-Doped Ceria Catalysts: Via a Facile CTAB-Assisted Synthesis. *RSC Adv.* **2018**, *8* (27), 14888–14897. <https://doi.org/10.1039/c8ra02327a>.
- (28) Konsolakis, M.; Lykaki, M.; Stefa, S.; Carabineiro, S. A. C.; Varvoutis, G.; Papista, E.; Marnellos, G. E. CO<sub>2</sub> Hydrogenation over Nanoceria-Supported Transition Metal Catalysts: Role of Ceria Morphology (Nanorods versus Nanocubes) and Active Phase Nature (Co versus Cu). *Nanomaterials* **2019**, *9* (12), 1739. <https://doi.org/10.3390/nano9121739>.

- (29) Lykaki, M.; Pachatouridou, E.; Carabineiro, S. A. C.; Iliopoulou, E.; Andriopoulou, C.; Kallithrakas-Kontos, N.; Boghosian, S.; Konsolakis, M. Ceria Nanoparticles Shape Effects on the Structural Defects and Surface Chemistry: Implications in CO Oxidation by Cu/CeO<sub>2</sub> catalysts. *Appl. Catal. B Environ.* **2018**, *230* (February), 18–28. <https://doi.org/10.1016/j.apcatb.2018.02.035>.
- (30) Gu, Z.; Li, K.; Qing, S.; Zhu, X.; Wei, Y.; Li, Y.; Wang, H. Enhanced Reducibility and Redox Stability of Fe<sub>2</sub>O<sub>3</sub> in the Presence of CeO<sub>2</sub> Nanoparticles. *RSC Adv.* **2014**, *4* (88), 47191–47199. <https://doi.org/10.1039/c4ra06715k>.
- (31) Konsolakis, M. Recent Advances on Nitrous Oxide (N<sub>2</sub>O) Decomposition over Non-Noble-Metal Oxide Catalysts: Catalytic Performance, Mechanistic Considerations, and Surface Chemistry Aspects. *ACS Catal.* **2015**, *5* (11), 6397–6421. <https://doi.org/10.1021/acscatal.5b01605>.
- (32) Konsolakis, M.; Sgourakis, M.; Carabineiro, S. A. C. Surface and Redox Properties of Cobalt–Ceria Binary Oxides: On the Effect of Co Content and Pretreatment Conditions. *Appl. Surf. Sci.* **2015**, *341*, 48–54. <https://doi.org/10.1016/j.apsusc.2015.02.188>.
- (33) Zou, W.; Ge, C.; Lu, M.; Wu, S.; Wang, Y.; Sun, J.; Pu, Y.; Tang, C.; Gao, F.; Dong, L. Engineering the NiO/CeO<sub>2</sub> Interface to Enhance the Catalytic Performance for CO Oxidation. *RSC Adv.* **2015**, *5* (119), 98335–98343. <https://doi.org/10.1039/C5RA20466F>.
- (34) Konsolakis, M.; Ioakimidis, Z.; Kraia, T.; Marnellos, G. Hydrogen Production by Ethanol Steam Reforming (ESR) over CeO<sub>2</sub> Supported Transition Metal (Fe, Co, Ni, Cu) Catalysts: Insight into the Structure-Activity Relationship. *Catalysts* **2016**, *6* (3), 39. <https://doi.org/10.3390/catal6030039>.
- (35) Li, L.; Han, W.; Tang, Z.; Zhang, J.; Lu, G. Hard-Template Synthesis of Three-Dimensional Mesoporous Cu-Ce Based Catalysts with Tunable Architectures and Their Application in the CO Catalytic Oxidation. *RSC Adv.* **2016**, *6* (69), 64247–64257. <https://doi.org/10.1039/c6ra12384h>.
- (36) Chen, L.; Weng, D.; Si, Z.; Wu, X. Synergistic Effect between Ceria and Tungsten Oxide on WO<sub>3</sub>–CeO<sub>2</sub>–TiO<sub>2</sub> Catalysts for NH<sub>3</sub>-SCR Reaction. *Prog. Nat. Sci. Mater. Int.* **2012**, *22* (4), 265–272. <https://doi.org/10.1016/j.pnsc.2012.07.004>.
- (37) Qiu, N.; Zhang, J.; Wu, Z. Peculiar Surface-Interface Properties of Nanocrystalline Ceria-

- Cobalt Oxides with Enhanced Oxygen Storage Capacity. *Phys. Chem. Chem. Phys.* **2014**, *16* (41), 22659–22664. <https://doi.org/10.1039/c4cp03390f>.
- (38) Konsolakis, M.; Carabineiro, S. A. C.; Papista, E.; Marnellos, G. E.; Tavares, P. B.; Moreira, J. A.; Romaguera-Barcelay, Y.; Figueiredo, J. L. Effect of Preparation Method on the Solid State Properties and the DeN<sub>2</sub>O Performance of CuO–CeO<sub>2</sub> Oxides. *Catal. Sci. Technol.* **2015**, *5* (7), 3714–3727. <https://doi.org/10.1039/C5CY00343A>.
- (39) Devaiah, D.; Thrimurthulu, G.; Smirniotis, P. G.; Reddy, B. M. Nanocrystalline Alumina-Supported Ceria-Praseodymia Solid Solutions: Structural Characteristics and Catalytic CO Oxidation. *RSC Adv.* **2016**, *6* (50), 44826–44837. <https://doi.org/10.1039/c6ra06679h>.
- (40) Wu, K.; Sun, L.-D.; Yan, C.-H. Recent Progress in Well-Controlled Synthesis of Ceria-Based Nanocatalysts towards Enhanced Catalytic Performance. *Adv. Energy Mater.* **2016**, *6* (17), 1600501. <https://doi.org/10.1002/aenm.201600501>.
- (41) Chen, F.; Ho, P.; Ran, R.; Chen, W.; Si, Z.; Wu, X.; Weng, D.; Huang, Z.; Lee, C. Synergistic Effect of CeO<sub>2</sub> Modified TiO<sub>2</sub> Photocatalyst on the Enhancement of Visible Light Photocatalytic Performance. *J. Alloys Compd.* **2017**, *714*, 560–566. <https://doi.org/10.1016/j.jallcom.2017.04.138>.
- (42) Vieira, G. B.; José, H. J.; Peterson, M.; Baldissarelli, V. Z.; Alvarez, P.; de Fátima Peralta Muniz Moreira, R. CeO<sub>2</sub>/TiO<sub>2</sub> Nanostructures Enhance Adsorption and Photocatalytic Degradation of Organic Compounds in Aqueous Suspension. *J. Photochem. Photobiol. A Chem.* **2018**, *353*, 325–336. <https://doi.org/10.1016/j.jphotochem.2017.11.045>.
- (43) Ding, J.; Zhong, Q.; Zhang, S. A New Insight into Catalytic Ozonation with Nanosized Ce–Ti Oxides for NO<sub>x</sub> Removal: Confirmation of Ce–O–Ti for Active Sites. *Ind. Eng. Chem. Res.* **2015**, *54* (7), 2012–2022. <https://doi.org/10.1021/ie504100b>.
- (44) Li, S.; Zhu, H.; Qin, Z.; Wang, G.; Zhang, Y.; Wu, Z.; Li, Z.; Chen, G.; Dong, W.; Wu, Z.; Zheng, L.; Zhang, J.; Hu, T.; Wang, J. Morphologic Effects of Nano CeO<sub>2</sub>-TiO<sub>2</sub> on the Performance of Au/CeO<sub>2</sub>-TiO<sub>2</sub> Catalysts in Low-Temperature CO Oxidation. *Appl. Catal. B Environ.* **2014**, *144*, 498–506. <https://doi.org/10.1016/j.apcatb.2013.07.049>.
- (45) Deng, W.; Dai, Q.; Lao, Y.; Shi, B.; Wang, X. Low Temperature Catalytic Combustion of 1,2-Dichlorobenzene over CeO<sub>2</sub>-TiO<sub>2</sub> Mixed Oxide Catalysts. *Appl. Catal. B Environ.* **2016**, *181*, 848–861. <https://doi.org/10.1016/j.apcatb.2015.07.053> 0926-3373/©.

- (46) Yang, X.; Kattel, S.; Senanayake, S. D.; Boscoboinik, J. A.; Nie, X.; Graciani, J.; Rodriguez, J. A.; Liu, P.; Stacchiola, D. J.; Chen, J. G. Low Pressure CO<sub>2</sub> Hydrogenation to Methanol over Gold Nanoparticles Activated on a CeO<sub>x</sub>/TiO<sub>2</sub> Interface. *J. Am. Chem. Soc.* **2015**, *137* (32), 10104–10107. <https://doi.org/10.1021/jacs.5b06150>.
- (47) Qu, X.; Xie, D.; Gao, L.; Du, F. Synthesis and Photocatalytic Activity of TiO<sub>2</sub>/CeO<sub>2</sub> Core-Shell Nanotubes. *Mater. Sci. Semicond. Process.* **2014**, *26* (1), 657–662. <https://doi.org/10.1016/j.mssp.2014.04.009>.
- (48) Lamallem, M.; Ayadi, H. El; Gennequin, C.; Cousin, R.; Siffert, S.; Aïssi, F.; Aboukaïs, A. Effect of the Preparation Method on Au/Ce-Ti-O Catalysts Activity for VOCs Oxidation. *Catal. Today* **2008**, *137* (2–4), 367–372. <https://doi.org/10.1016/j.cattod.2007.12.141>.
- (49) Chang, K.; Wang, T.; Chen, J. G. Hydrogenation of CO<sub>2</sub> to Methanol over CuCeTiO<sub>x</sub> Catalysts. *Appl. Catal. B Environ.* **2017**, *206*, 704–711. <https://doi.org/10.1016/j.apcatb.2017.01.076>.
- (50) Li, P.; Xin, Y.; Li, Q.; Wang, Z.; Zhang, Z.; Zheng, L. Ce–Ti Amorphous Oxides for Selective Catalytic Reduction of NO with NH<sub>3</sub>: Confirmation of Ce–O–Ti Active Sites. *Environ. Sci. Technol.* **2012**, *46* (17), 9600–9605. <https://doi.org/10.1021/es301661r>.
- (51) Ameen, S.; Shaheer Akhtar, M.; Seo, H.-K.; Shin, H.-S. Solution-Processed CeO<sub>2</sub>/TiO<sub>2</sub> Nanocomposite as Potent Visible Light Photocatalyst for the Degradation of Bromophenol Dye. *Chem. Eng. J.* **2014**, *247*, 193–198. <https://doi.org/10.1016/j.cej.2014.02.104>.
- (52) Chen, Y.-J.; Xiao, G.; Wang, T.-S.; Zhang, F.; Ma, Y.; Gao, P.; Zhu, C.-L.; Zhang, E.; Xu, Z.; Li, Q. Synthesis and Enhanced Gas Sensing Properties of Crystalline CeO<sub>2</sub>/TiO<sub>2</sub> Core/Shell Nanorods. *Sensors Actuators B Chem.* **2011**, *156* (2), 867–874. <https://doi.org/10.1016/j.snb.2011.02.057>.
- (53) Wang, Y.; Zhao, J.; Wang, T.; Li, Y.; Li, X.; Yin, J.; Wang, C. CO<sub>2</sub> Photoreduction with H<sub>2</sub>O Vapor on Highly Dispersed CeO<sub>2</sub>/TiO<sub>2</sub> Catalysts: Surface Species and Their Reactivity. *J. Catal.* **2016**, *337*, 293–302. <https://doi.org/10.1016/j.jcat.2015.12.030>.
- (54) Fan, Z.; Meng, F.; Gong, J.; Li, H.; Hu, Y.; Liu, D. Enhanced Photocatalytic Activity of Hierarchical Flower-like CeO<sub>2</sub>/TiO<sub>2</sub> Heterostructures. *Mater. Lett.* **2016**, *175*, 36–39. <https://doi.org/10.1016/j.matlet.2016.03.136>.
- (55) Tian, J.; Sang, Y.; Zhao, Z.; Zhou, W.; Wang, D.; Kang, X.; Liu, H.; Wang, J.; Chen, S.; Cai,

- H.; Huang, H. Enhanced Photocatalytic Performances of CeO<sub>2</sub>/TiO<sub>2</sub> Nanobelt Heterostructures. *Small* **2013**, *9* (22), 3864–3872. <https://doi.org/10.1002/sml.201202346>.
- (56) Samadi, S.; Asadi Cordshooli, G.; Yousefi, M.; Kalateh, K.; Zakaria, S. A. CeO<sub>2</sub>/TiO<sub>2</sub> Core/Shell Nanoparticles as Quantitative Gas Sensor at Room Temperature. *Sens. Rev.* **2018**, *38* (4), 458–466. <https://doi.org/10.1108/SR-05-2017-0093>.
- (57) Miah, A. T.; Malakar, B.; Saikia, P. Gold over Ceria–Titania Mixed Oxides: Solar Light Induced Catalytic Activity for Nitrophenol Reduction. *Catal. Letters* **2016**, *146* (2), 291–303. <https://doi.org/10.1007/s10562-015-1644-y>.
- (58) Gao, X.; Du, X.; Cui, L.; Fu, Y.; Luo, Z.; Cen, K. A Ce–Cu–Ti Oxide Catalyst for the Selective Catalytic Reduction of NO with NH<sub>3</sub>. *Catal. Commun.* **2010**, *12* (4), 255–258. <https://doi.org/10.1016/j.catcom.2010.09.029>.
- (59) Du, X.; Wang, X.; Chen, Y.; Gao, X.; Zhang, L. Supported Metal Sulfates on Ce–TiO<sub>x</sub> as Catalysts for NH<sub>3</sub>–SCR of NO: High Resistances to SO<sub>2</sub> and Potassium. *J. Ind. Eng. Chem.* **2016**, *36*, 271–278. <https://doi.org/10.1016/j.jiec.2016.02.013>.
- (60) Li, S.; Zhu, H.; Qin, Z.; Wang, G.; Zhang, Y.; Wu, Z.; Li, Z.; Chen, G.; Dong, W.; Wu, Z.; Zheng, L.; Zhang, J.; Hu, T.; Wang, J. Morphologic Effects of Nano CeO<sub>2</sub>–TiO<sub>2</sub> on the Performance of Au/CeO<sub>2</sub>–TiO<sub>2</sub> Catalysts in Low-Temperature CO Oxidation. *Appl. Catal. B Environ.* **2014**, *144*, 498–506. <https://doi.org/10.1016/j.apcatb.2013.07.049>.
- (61) Shi, Z.; Yang, P.; Tao, F.; Zhou, R. New Insight into the Structure of CeO<sub>2</sub> –TiO<sub>2</sub> Mixed Oxides and Their Excellent Catalytic Performances for 1,2-Dichloroethane Oxidation. *Chem. Eng. J.* **2016**, *295*, 99–108. <https://doi.org/10.1016/j.cej.2016.03.032>.
- (62) Gao, X.; Jiang, Y.; Fu, Y.; Zhong, Y.; Luo, Z.; Cen, K. Preparation and Characterization of CeO<sub>2</sub>/TiO<sub>2</sub> Catalysts for Selective Catalytic Reduction of NO with NH<sub>3</sub>. *Catal. Commun.* **2010**, *11* (5), 465–469. <https://doi.org/10.1016/j.catcom.2009.11.024>.
- (63) Gao, X.; Jiang, Y.; Zhong, Y.; Luo, Z.; Cen, K. The Activity and Characterization of CeO<sub>2</sub>-TiO<sub>2</sub> Catalysts Prepared by the Sol–Gel Method for Selective Catalytic Reduction of NO with NH<sub>3</sub>. *J. Hazard. Mater.* **2010**, *174* (1–3), 734–739. <https://doi.org/10.1016/j.jhazmat.2009.09.112>.
- (64) Muñoz-Batista, M. J.; Fernández-García, M.; Kubacka, A. Promotion of CeO<sub>2</sub>–TiO<sub>2</sub> Photoactivity by g-C<sub>3</sub>N<sub>4</sub>: Ultraviolet and Visible Light Elimination of Toluene. *Appl. Catal. B*

*Environ.* **2015**, *164*, 261–270. <https://doi.org/10.1016/j.apcatb.2014.09.037>.

- (65) Yao, X.; Zhao, R.; Chen, L.; Du, J.; Tao, C.; Yang, F.; Dong, L. Selective Catalytic Reduction of NO<sub>x</sub> by NH<sub>3</sub> over CeO<sub>2</sub> Supported on TiO<sub>2</sub>: Comparison of Anatase, Brookite, and Rutile. *Appl. Catal. B Environ.* **2017**, *208* (x), 82–93. <https://doi.org/10.1016/j.apcatb.2017.02.060>.
- (66) Huang, K.; Lin, L.; Yang, K.; Dai, W.; Chen, X.; Fu, X. Applied Catalysis B : Environmental Promotion Effect of Ultraviolet Light on NO + CO Reaction over Pt /TiO<sub>2</sub> and Pt/CeO<sub>2</sub>–TiO<sub>2</sub> Catalysts. **2015**, *179*, 395–406.
- (67) Yao, X.; Zhao, R.; Chen, L.; Du, J.; Tao, C.; Yang, F.; Dong, L. Selective Catalytic Reduction of NO<sub>x</sub> by NH<sub>3</sub> over CeO<sub>2</sub> Supported on TiO<sub>2</sub> : Comparison of Anatase, Brookite, and Rutile. *Appl. Catal. B Environ.* **2017**, *208* (x), 82–93. <https://doi.org/10.1016/j.apcatb.2017.02.060>.
- (68) Fang, Q.; Liang, X. CeO<sub>2</sub>–Al<sub>2</sub>O<sub>3</sub>, CeO<sub>2</sub>–SiO<sub>2</sub>, CeO<sub>2</sub>–TiO<sub>2</sub> Core-Shell Spheres: Formation Mechanisms and UV Absorption. *RSC Adv.* **2012**, *2* (12), 5370. <https://doi.org/10.1039/c2ra01331b>.
- (69) Sajjad, M.; Ullah, I.; Khan, M. I.; Khan, J.; Khan, M. Y.; Qureshi, M. T. Structural and Optical Properties of Pure and Copper Doped Zinc Oxide Nanoparticles. *Results Phys.* **2018**, *9* (February), 1301–1309. <https://doi.org/10.1016/j.rinp.2018.04.010>.
- (70) Wang, J.; Chen, R.; Xiang, L.; Komarneni, S. Synthesis, Properties and Applications of ZnO Nanomaterials with Oxygen Vacancies: A Review. *Ceram. Int.* **2018**, *44* (7), 7357–7377. <https://doi.org/10.1016/j.ceramint.2018.02.013>.
- (71) Lee, C.-G.; Na, K.-H.; Kim, W.-T.; Park, D.-C.; Yang, W.-H.; Choi, W.-Y. TiO<sub>2</sub>/ZnO Nanofibers Prepared by Electrospinning and Their Photocatalytic Degradation of Methylene Blue Compared with TiO<sub>2</sub> Nanofibers. *Appl. Sci.* **2019**, *9* (16), 3404. <https://doi.org/10.3390/app9163404>.
- (72) Stathopoulos, V. N.; Papandreou, A.; Kanellopoulou, D.; Stournaras, C. J. Structural Ceramics Containing Electric Arc Furnace Dust. *J. Hazard. Mater.* **2013**, *262*, 91–99. <https://doi.org/10.1016/j.jhazmat.2013.08.028>.
- (73) Lima, J. F. de; Martins, R. F.; Neri, C. R.; Serra, O. A. ZnO:CeO<sub>2</sub>-Based Nanopowders with Low Catalytic Activity as UV Absorbers. *Appl. Surf. Sci.* **2009**, *255* (22), 9006–9009. <https://doi.org/10.1016/j.apsusc.2009.06.071>.
- (74) Ma, T.-Y.; Yuan, Z.-Y.; Cao, J.-L. Hydrangea-Like Meso-/Macroporous ZnO-CeO<sub>2</sub> Binary

Oxide Materials: Synthesis, Photocatalysis and CO Oxidation. *Eur. J. Inorg. Chem.* **2010**, *2010* (5), 716–724. <https://doi.org/10.1002/ejic.200900991>.

- (75) Liu, I.-T.; Hon, M.-H.; Teoh, L. G. The Preparation, Characterization and Photocatalytic Activity of Radical-Shaped CeO<sub>2</sub>/ZnO Microstructures. *Ceram. Int.* **2014**, *40* (3), 4019–4024. <https://doi.org/10.1016/j.ceramint.2013.08.053>.
- (76) Lv, Z.; Zhong, Q.; Ou, M. Utilizing Peroxide as Precursor for the Synthesis of CeO<sub>2</sub>/ZnO Composite Oxide with Enhanced Photocatalytic Activity. *Appl. Surf. Sci.* **2016**, *376*, 91–96. <https://doi.org/10.1016/j.apsusc.2016.01.280>.
- (77) Rodwihok, C.; Wongratanaphisan, D.; Van Tam, T.; Choi, W. M.; Hur, S. H.; Chung, J. S. Cerium-Oxide-Nanoparticle-Decorated Zinc Oxide with Enhanced Photocatalytic Degradation of Methyl Orange. *Appl. Sci.* **2020**, *10* (5). <https://doi.org/10.3390/app10051697>.
- (78) Xie, Q.; Zhao, Y.; Guo, H.; Lu, A.; Zhang, X.; Wang, L.; Chen, M.-S.; Peng, D. Facile Preparation of Well-Dispersed CeO<sub>2</sub>-ZnO Composite Hollow Microspheres with Enhanced Catalytic Activity for CO Oxidation. *ACS Appl. Mater. Interfaces* **2014**, *6* (1), 421–428. <https://doi.org/10.1021/am404487b>.
- (79) Mu, G.; Liu, C.; Wei, Q.; Huang, Y. Three Dimensionally Ordered Macroporous CeO<sub>2</sub>-ZnO Catalysts for Enhanced CO Oxidation. *Mater. Lett.* **2016**, *181*, 161–164. <https://doi.org/10.1016/j.matlet.2016.05.147>.
- (80) Mock, S. A.; Sharp, S. E.; Stoner, T. R.; Radetic, M. J.; Zell, E. T.; Wang, R. CeO<sub>2</sub> Nanorods-Supported Transition Metal Catalysts for CO Oxidation. *J. Colloid Interface Sci.* **2016**, *466*, 261–267. <https://doi.org/10.1016/j.jcis.2015.12.026>.
- (81) Piumetti, M.; Andana, T.; Bensaid, S.; Russo, N.; Fino, D.; Pirone, R. Study on the CO Oxidation over Ceria-Based Nanocatalysts. *Nanoscale Res. Lett.* **2016**, *11* (1), 165. <https://doi.org/10.1186/s11671-016-1375-z>.
- (82) Soler, L.; Casanovas, A.; Urrich, A.; Angurell, I.; Llorca, J. CO Oxidation and COPrOx over Preformed Au Nanoparticles Supported over Nanoshaped CeO<sub>2</sub>. *Appl. Catal. B Environ.* **2016**, *197*, 47–55. <https://doi.org/10.1016/j.apcatb.2016.02.025>.
- (83) Elias, J. S.; Risch, M.; Giordano, L.; Mansour, A. N.; Shao-Horn, Y. Structure, Bonding, and Catalytic Activity of Monodisperse, Transition-Metal-Substituted CeO<sub>2</sub> Nanoparticles. *J. Am. Chem. Soc.* **2014**, *136* (49), 17193–17200. <https://doi.org/10.1021/ja509214d>.

- (84) Stefa, S.; Lykaki, M.; Fragkoulis, D.; Binas, V.; Pandis, P. K.; Stathopoulos, V. N.; Konsolakis, M. Effect of the Preparation Method on the Physicochemical Properties and the CO Oxidation Performance of Nanostructured CeO<sub>2</sub>/TiO<sub>2</sub> Oxides. *Processes* **2020**, *8* (7), 847. <https://doi.org/10.3390/pr8070847>.
- (85) Ali, M. M.; Mahdi, H. S.; Parveen, A.; Azam, A. Optical Properties of Cerium Oxide (CeO<sub>2</sub>) Nanoparticles Synthesized by Hydroxide Mediated Method. In *AIP Conference Proceedings*; 2018; Vol. 1953, p 030044. <https://doi.org/10.1063/1.5032379>.
- (86) Sebastiammal, S. S.; Shally, V.; Priyadharshini, M.; Jayam, S. G. Structural and Optical Properties of Cerium Oxide Nanoparticles. *Int. J. Eng. Trends Technol.* **2017**, *49* (4), 503–508.
- (87) Babitha, K. K.; Sreedevi, A.; Priyanka, K. P.; Sabu, B.; Varghese, T. Structural Characterization and Optical Studies of CeO<sub>2</sub> Nanoparticles Synthesized by Chemical Precipitation. *Indian J. Pure Appl. Phys.* **2015**, *53* (9), 596–603.
- (88) Lu, X.; Li, X.; Qian, J.; Miao, N.; Yao, C.; Chen, Z. Synthesis and Characterization of CeO<sub>2</sub>/TiO<sub>2</sub> Nanotube Arrays and Enhanced Photocatalytic Oxidative Desulfurization Performance. *J. Alloys Compd.* **2016**, *661*, 363–371. <https://doi.org/10.1016/j.jallcom.2015.11.148>.
- (89) Abdullah, H.; Khan, M. R.; Pudukudy, M.; Yaakob, Z.; Ismail, N. A. CeO<sub>2</sub>-TiO<sub>2</sub> as a Visible Light Active Catalyst for the Photoreduction of CO<sub>2</sub> to Methanol. *J. Rare Earths* **2015**, *33* (11), 1155–1161. [https://doi.org/10.1016/S1002-0721\(14\)60540-8](https://doi.org/10.1016/S1002-0721(14)60540-8).
- (90) Zhao, H.; Dong, Y.; Jiang, P.; Wang, G.; Zhang, J. Highly Dispersed CeO<sub>2</sub> on TiO<sub>2</sub> Nanotube: A Synergistic Nanocomposite with Superior Peroxidase-like Activity. *ACS Appl. Mater. Interfaces* **2015**, *7* (12), 6451–6461. <https://doi.org/10.1021/acsami.5b00023>.
- (91) Fang, J.; Bao, H.; He, B.; Wang, F.; Si, D.; Jiang, Z.; Pan, Z.; Wei, S.; Huang, W. Interfacial and Surface Structures of CeO<sub>2</sub> –TiO<sub>2</sub> Mixed Oxides. *J. Phys. Chem. C* **2007**, *111* (51), 19078–19085. <https://doi.org/10.1021/jp076627m>.
- (92) Ren, Z.; Peng, F.; Chen, B.; Mei, D.; Li, J. ScienceDirect A Combined Experimental and Computational Study of Water-Gas Shift Reaction over Rod-Shaped Catalysts. *Int. J. Hydrogen Energy* **2017**, *42* (51), 30086–30097. <https://doi.org/10.1016/j.ijhydene.2017.10.047>.

- (93) Wang, N.; Qian, W.; Chu, W.; Wei, F. Crystal-Plane Effect of Nanoscale CeO<sub>2</sub> on the Catalytic Performance of Ni/CeO<sub>2</sub> Catalysts for Methane Dry Reforming. *Catal. Sci. Technol.* **2016**, *6* (10), 3594–3605. <https://doi.org/10.1039/C5CY01790D>.
- (94) Castanet, U.; Feral-Martin, C.; Demourgues, A.; Neale, R. L.; Sayle, D. C.; Caddeo, F.; Flitcroft, J. M.; Caygill, R.; Pointon, B. J.; Molinari, M.; Majimel, J. Controlling the {111}/{110} Surface Ratio of Cuboidal Ceria Nanoparticles. *ACS Appl. Mater. Interfaces* **2019**, *11* (12), 11384–11390. <https://doi.org/10.1021/acsami.8b21667>.
- (95) Bepalko, Y.; Kuznetsova, T.; Kriger, T.; Chesalov, Y.; Lapina, O.; Ishchenko, A.; Larina, T.; Sadykov, V.; Stathopoulos, V. La<sub>2</sub>Zr<sub>2</sub>O<sub>7</sub>/LaAlO<sub>3</sub> Composite Prepared by Mixing Precipitated Precursors: Evolution of Its Structure under Sintering. *Mater. Chem. Phys.* **2020**, *251* (April), 123093. <https://doi.org/10.1016/j.matchemphys.2020.123093>.
- (96) Ansari, A. A.; Labis, J.; Alam, M.; Ramay, S. M.; Ahmad, N.; Mahmood, A. Physicochemical and Redox Characteristics of Fe Ion-Doped CeO<sub>2</sub> Nanoparticles. *J. Chinese Chem. Soc.* **2015**, *62* (10), 925–932. <https://doi.org/10.1002/jccs.201500195>.
- (97) Liu, S.; Liao, X.; Zhang, Q.; Zhang, Y.; Wang, H.; Zhao, Y. Crystal-Plane and Shape Influences of Nanoscale CeO<sub>2</sub> on the Activity of Ni/CeO<sub>2</sub> Catalysts for Maleic Anhydride Hydrogenation. *Nanomaterials* **2022**, *12* (5), 762. <https://doi.org/10.3390/nano12050762>.
- (98) Chen, Y.-J.; Xiao, G.; Wang, T.-S.; Zhang, F.; Ma, Y.; Gao, P.; Zhu, C.-L.; Zhang, E.; Xu, Z.; Li, Q. Synthesis and Enhanced Gas Sensing Properties of Crystalline CeO<sub>2</sub>/TiO<sub>2</sub> Core/Shell Nanorods. *Sensors Actuators B Chem.* **2011**, *156* (2), 867–874. <https://doi.org/10.1016/j.snb.2011.02.057>.
- (99) Wang, J.; Li, Z.; Zhang, S.; Yan, S.; Cao, B.; Wang, Z.; Fu, Y. Enhanced NH<sub>3</sub> Gas-Sensing Performance of Silica Modified CeO<sub>2</sub> Nanostructure Based Sensors. *Sensors Actuators B Chem.* **2018**, *255*, 862–870. <https://doi.org/10.1016/j.snb.2017.08.149>.
- (100) Tang, W. X.; Gao, P. X. Nanostructured Cerium Oxide: Preparation, Characterization, and Application in Energy and Environmental Catalysis. *MRS Commun.* **2016**, *6* (4), 311–329. <https://doi.org/10.1557/mrc.2016.52>.
- (101) Phokha, S.; Pinitsoontorn, S.; Maensiri, S. Structure and Magnetic Properties of Monodisperse Fe<sup>3+</sup>-Doped CeO<sub>2</sub> Nanospheres. *Nano-Micro Lett.* **2013**, *5* (4), 223–233. <https://doi.org/10.5101/nml.v5i4.p223-233>.

- (102) Stefa, S.; Lykaki, M.; Binas, V.; Pandis, P. K.; Stathopoulos, V. N.; Konsolakis, M. Hydrothermal Synthesis of ZnO–Doped Ceria Nanorods: Effect of ZnO Content on the Redox Properties and the CO Oxidation Performance. *Appl. Sci.* **2020**, *10* (21), 7605. <https://doi.org/10.3390/app10217605>.
- (103) Yu, S.-W.; Huang, H.-H.; Tang, C.-W.; Wang, C.-B. The Effect of Accessible Oxygen over  $\text{Co}_3\text{O}_4$ – $\text{CeO}_2$  Catalysts on the Steam Reforming of Ethanol. *Int. J. Hydrogen Energy* **2014**, *39* (35), 20700–20711. <https://doi.org/10.1016/j.ijhydene.2014.07.139>.
- (104) Luo, J.; Meng, M.; Li, X.; Li, X.; Zha, Y.; Hu, T.; Xie, Y.; Zhang, J. Mesoporous  $\text{Co}_3\text{O}_4$ – $\text{CeO}_2$  and  $\text{Pd}/\text{Co}_3\text{O}_4$ – $\text{CeO}_2$  Catalysts: Synthesis, Characterization and Mechanistic Study of Their Catalytic Properties for Low-Temperature CO Oxidation. *J. Catal.* **2008**, *254* (2), 310–324. <https://doi.org/10.1016/j.jcat.2008.01.007>.
- (105) Liu, J.; Zhao, Z.; Wang, J.; Xu, C.; Duan, A.; Jiang, G.; Yang, Q. The Highly Active Catalysts of Nanometric  $\text{CeO}_2$ -Supported Cobalt Oxides for Soot Combustion. *Appl. Catal. B Environ.* **2008**, *84* (1–2), 185–195. <https://doi.org/10.1016/j.apcatb.2008.03.017>.
- (106) Subramanian, V.; Potdar, H. S.; Jeong, D.-W.; Shim, J.-O.; Jang, W.-J.; Roh, H.-S.; Jung, U. H.; Yoon, W. L. Synthesis of a Novel Nano-Sized Pt/ZnO Catalyst for Water Gas Shift Reaction in Medium Temperature Application. *Catal. Letters* **2012**, *142* (9), 1075–1081. <https://doi.org/10.1007/s10562-012-0868-3>.
- (107) Khan, A.; Smirniotis, P. G. Relationship between Temperature-Programmed Reduction Profile and Activity of Modified Ferrite-Based Catalysts for WGS Reaction. *J. Mol. Catal. A Chem.* **2008**, *280* (1–2), 43–51. <https://doi.org/10.1016/j.molcata.2007.10.022>.
- (108) Mukherjee, D.; Rao, B. G.; Reddy, B. M. CO and Soot Oxidation Activity of Doped Ceria: Influence of Dopants. *Appl. Catal. B Environ.* **2016**, *197*, 105–115. <https://doi.org/10.1016/j.apcatb.2016.03.042>.
- (109) Wu, Z.; Li, M.; Overbury, S. H. On the Structure Dependence of CO Oxidation over  $\text{CeO}_2$  Nanocrystals with Well-Defined Surface Planes. *J. Catal.* **2012**, *285* (1), 61–73. <https://doi.org/10.1016/j.jcat.2011.09.011>.
- (110) Johnston-Peck, A. C.; Senanayake, S. D.; Plata, J. J.; Kundu, S.; Xu, W.; Barrio, L.; Graciani, J.; Sanz, J. F.; Navarro, R. M.; Fierro, J. L. G.; Stach, E. A.; Rodriguez, J. A. Nature of the Mixed-Oxide Interface in Ceria-Titania Catalysts: Clusters, Chains, and Nanoparticles. *J.*

*Phys. Chem. C* **2013**, *117* (28), 14463–14471. <https://doi.org/10.1021/jp3125268>.

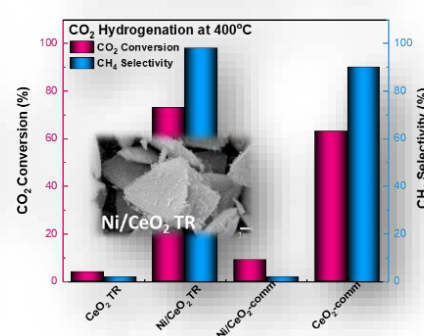
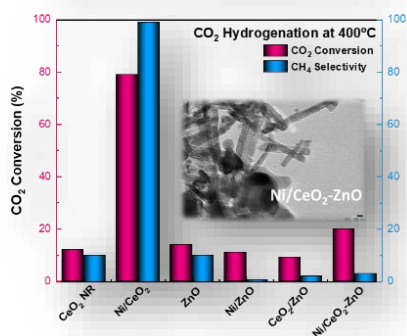
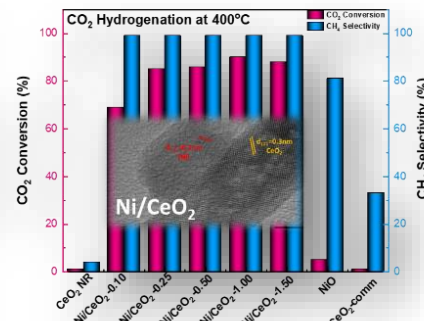
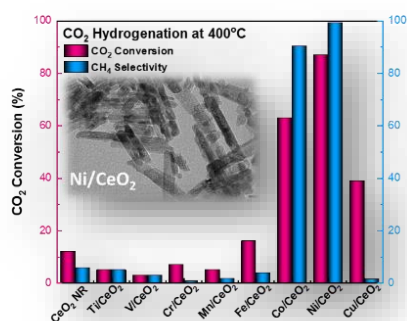
- (111) Mukherjee, D.; Rao, B. G.; Reddy, B. M. CO and Soot Oxidation Activity of Doped Ceria: Influence of Dopants. *Appl. Catal. B Environ.* **2016**, *197*, 105–115. <https://doi.org/10.1016/j.apcatb.2016.03.042>.

# Chapter 4

## Effect of Active Phase Nature and ZnO promotion on CO<sub>2</sub> hydrogenation performance of Ceria-based Catalysts

Chapter 4 delves into the investigation of the non-noble metal phase nature and ZnO promotion effects on the physicochemical properties and CO<sub>2</sub> hydrogenation performance of ceria-based nano-catalysts. The study initially examines the different metal phases' influence on catalytic activity, highlighting the significant enhancement of

CO<sub>2</sub> methanation with the combination of nickel and ceria. Subsequently, the research focuses on Ni/CeO<sub>2</sub>-nanorod catalysts, exploring the role of Ni particle size and the impact of ZnO promotion on the reaction mechanism. Notably, Ni/ZnO and Ni/CeO<sub>2</sub>-ZnO catalysts exhibit selective CO production while effectively suppressing CO<sub>2</sub> methanation compared to Ni/CeO<sub>2</sub> catalysts. Additionally, a preliminary study investigates the use of CeO<sub>2</sub> triangles as supporting carriers for the Ni active phase in CO<sub>2</sub> hydrogenation, comparing the results with those of a nickel catalyst supported on commercial CeO<sub>2</sub>. These findings provide valuable insights for the development of efficient catalysts for CO<sub>2</sub> hydrogenation.



## Introduction

The scientific community widely accepts that the continuous increase in CO<sub>2</sub> emissions in the Earth's atmosphere since the beginning of industrialization is the primary cause of the planet's temperature rise over the past two centuries <sup>1</sup>. According to the latest report from the Intergovernmental Panel on Climate Change (IPCC) on the impacts of global warming, global temperatures are projected to rise by 1.5 °C by the year 2040, compared to pre-industrial levels <sup>2,3</sup>. To address this environmental issue, mitigation efforts can be categorized into three main approaches: (i) complete or partial replacement of carbon-based fuels with renewable energy sources (RESs), (ii) implementation of carbon dioxide capture and storage (CCS) technology, and (iii) the chemical conversion and utilization of CO<sub>2</sub> to produce value-added chemicals and fuels <sup>4</sup>.

The third approach has garnered significant attention in recent decades, particularly concerning CO<sub>2</sub> hydrogenation, as it offers a wide range of potential products <sup>5</sup>. This method presents an effective means of valorizing CO<sub>2</sub> emissions and efficiently storing surplus power from non-intermittent renewable energy sources (such as solar and wind) in the form of "green" hydrogen. It can be achieved by either the mildly endothermic reverse water-gas shift (rWGS) reaction (Eq. 1), which yields CO, or the highly exothermic methanation reaction, commonly known as the "Sabatier reaction" (Eq. 2), which produces CH<sub>4</sub> <sup>6</sup>.



In addition to the aforementioned products, CO<sub>2</sub> hydrogenation can yield other valuable products such as methanol <sup>7-10</sup>, dimethyl ether <sup>11</sup>, formic acid <sup>12</sup>, and hydrocarbons <sup>13</sup>.

Among these products, carbon monoxide holds significant value as a feedstock in the C1 chemical industry. Carbon monoxide can be further upgraded through the well-established Fischer-Tropsch synthesis, enabling the production of various liquid synthetic hydrocarbons and chemicals <sup>14,15</sup>. Furthermore, the process of carbon dioxide methanation offers an effective means of converting a less manageable energy vector, such as gaseous hydrogen, into a high-energy source like methane. This is particularly advantageous due to methane's volumetric energy density, which is three times higher than that of hydrogen <sup>16</sup>.

In terms of the overall sustainability of the proposed process, it is essential to highlight that the CO<sub>2</sub> hydrogenation concept is based on the utilization of "green" H<sub>2</sub>, which is derived from the surplus energy generated by renewable energy sources (RESs) and the concentrated CO<sub>2</sub> emissions as

feedstock. To maximize its efficiency, the CO<sub>2</sub> hydrogenation process can be strategically located near sources of highly concentrated CO<sub>2</sub> emissions, such as effluent streams from the steel industry or CO<sub>2</sub> capture plants. By employing highly active and cost-effective catalysts, significant amounts of CO<sub>2</sub> can be potentially mitigated while simultaneously producing value-added products like CH<sub>4</sub> or CO, which can serve as fuels or feedstock in the chemical industry. Regarding the use of renewable hydrogen, it can be fully utilized in the hydrogenation process or partially converted into the electricity required for the reaction. Additionally, excess hydrogen can be directly injected into the gas grid or used to power vehicles equipped with fuel cells. Numerous comprehensive studies have been conducted to evaluate the sustainability aspects of the CO<sub>2</sub> hydrogenation process, providing further information for interested readers <sup>17–21</sup>.

While CO<sub>2</sub> hydrogenation can be a promising way to reduce the environmental carbon footprint, there are several limitations to consider when implementing technologies based on Eqs. 1 or 2. The first limitation arises from the activation of carbon dioxide itself, as it is a fully oxidized and thermodynamically stable compound that is not energetically favorable to reduce <sup>22</sup>. Consequently, strong reductants such as H<sub>2</sub> or electrochemical-assisted reduction processes are necessary to drive the reaction <sup>23,24</sup>. In addition to the energy requirements, CO<sub>2</sub> hydrogenation also faces kinetic and equilibrium limitations, necessitating the promotion of reaction rates <sup>25</sup>. To overcome these challenges, extensive research has explored various catalytic systems, and the literature contains several reviews summarizing the catalysts investigated for rWGS <sup>2,26,27</sup> and CO<sub>2</sub> methanation <sup>28–30</sup> reactions. Among the extensively studied catalytic systems are composites consisting of metals supported on reducible metal oxides (e.g., CeO<sub>2</sub>, ZrO<sub>2</sub>) or their combinations. These systems function as bi-functional catalysts, with the oxide supports primarily providing oxygen vacancies for CO<sub>2</sub> activation, while the metal active sites facilitate the dissociation of molecular hydrogen, known as the hydrogen spillover process <sup>26,31</sup>.

Among the investigated oxide materials, CeO<sub>2</sub> has garnered significant attention as a supporting carrier due to its exceptional oxygen mobility and unique redox properties, as cerium can rapidly change between its two oxidation states (Ce<sup>3+</sup> and Ce<sup>4+</sup>) <sup>32,33</sup>. Furthermore, ceria is a basic oxide that facilitates strong interaction and adsorption of CO<sub>2</sub> <sup>34</sup>. In addition to the remarkable redox properties of bare ceria, extensive research has focused on the development of cost-effective and highly efficient catalytic composites based on ceria. The incorporation of various non-noble transition metals (TMs), such as Cu, Co, Ni, and Fe, with ceria has been shown to enhance catalytic activity and/or selectivity through unique synergistic interactions between the metal and the support <sup>35–37</sup>. Precious metals like Ru <sup>38</sup>, Rh <sup>39</sup>, and Pd <sup>40</sup> have demonstrated good catalytic activity; however, their high cost and limited availability make them less preferable from a techno-economic standpoint.

Therefore, the utilization of TM-based catalysts is more favorable, as these metals can achieve comparable activity to noble metal catalysts at a significantly lower cost <sup>41,42</sup>. In line with this perspective, our research group has been dedicated to developing inexpensive TM-based catalytic composites, with a particular focus on 3d metals, namely Ti, V, Cr, Mn, Fe, Co, Ni, and Cu. These metals have demonstrated the ability to adsorb and activate CO<sub>2</sub> through charge transfer from the metal phase to the CO<sub>2</sub> molecule <sup>43</sup>. Density Functional Theory (DFT) calculations have confirmed the spontaneous chemisorption of CO<sub>2</sub> and favorable thermodynamic properties for Cu, Co, Ni, and Fe, with Cu, however, exhibiting a weaker interaction <sup>43</sup>.

Furthermore, among transition metal-based catalysts, Ni-based catalysts hold a particular interest in CO<sub>2</sub> methanation. This is attributed to the presence of mobile d-orbital valence electrons in Ni atoms, making them conducive to catalytic activity. Ni-based catalysts offer a combination of cost-effectiveness, high CO<sub>2</sub> conversion at low temperatures, and remarkable selectivity towards methane production by effectively suppressing CO formation <sup>44-53</sup>. Recent reviews have highlighted the advancements in active nickel-based catalysts for low-temperature CO<sub>2</sub> methanation <sup>54,55</sup>. Several characteristics are known to influence the methanation activity of these catalysts. The nature and morphology of the support play a significant role <sup>52,55-61</sup>, as well as the synthesis methods and protocols employed <sup>52,62-65</sup>. The presence of a second metallic phase has also been found to impact catalytic performance <sup>66-72</sup> and nickel content <sup>67,73-75</sup> are recognized factors affecting the methanation activity of these catalysts. The understanding and optimization of these characteristics contribute to the development of highly efficient Ni-based catalysts for CO<sub>2</sub> methanation.

Moreover, the catalytic properties of transition metal (TM)--based composites can be further enhanced through appropriate fine-tuning. One effective approach involves the structural promotion of the catalyst, aiming to modify various characteristics such as oxygen storage capacity and surface basicity <sup>76-78</sup>. However, it is important to note that the effects of promotion are not always beneficial. High concentrations of promoters can lead to defect interactions <sup>79</sup> or vacancy traps <sup>80</sup>, which ultimately reduce the mobility of lattice oxygen. In essence, when two or more metal species are combined on a support surface, a complex and multifunctional system is formed, exhibiting intriguing properties arising from the synergy between each oxide and metallic phase. These systems can display unique characteristics that impact catalytic activity in terms of both reactant conversion and product distribution <sup>81-84</sup>. For instance, in the case of CO<sub>2</sub> hydrogenation, the addition of an appropriate promoter has been shown to induce significant shifts in product distribution <sup>85-88</sup>, even for Ni-based catalysts. Ni-based catalysts are widely recognized for their exceptional activity in the CO<sub>2</sub>-to-CH<sub>4</sub> conversion pathway <sup>89-91</sup>. However, the factors determining the main product and the

preferred reaction pathway have not been unequivocally elucidated. Many questions regarding the promoter-induced changes in catalytic characteristics of materials remain unanswered.

In light of the above, this chapter aims to investigate the impact of non-noble metal phase nature and ZnO promotion on the physicochemical properties and CO<sub>2</sub> hydrogenation performance of ceria-based nanocatalysts. Initially, the study explores the influence of different active metal phases on the physicochemical properties and catalytic activity of ceria-based transition metal catalysts (M/CeO<sub>2</sub>, where M represents Ti, V, Cr, Mn, Fe, Co, Ni, Cu) for CO<sub>2</sub> hydrogenation. The results reveal that bare ceria, Cu/CeO<sub>2</sub>, Fe/CeO<sub>2</sub>, Cr/CeO<sub>2</sub>, Mn/CeO<sub>2</sub>, Ti/CeO<sub>2</sub>, and V/CeO<sub>2</sub> catalysts exhibit selectivity towards CO production, while Co/CeO<sub>2</sub> and Ni/CeO<sub>2</sub> catalysts show a strong preference for methane (CH<sub>4</sub>) formation. Particularly, the combination of nickel with ceria significantly enhances the CO<sub>2</sub> methanation reaction. Subsequently, the research focuses on investigating the role of Ni particle size in the CO<sub>2</sub> hydrogenation performance of Ni/CeO<sub>2</sub>-nanorod catalysts. Furthermore, the study explores the effect of ZnO promotion by preparing CeO<sub>2</sub>/ZnO mixed oxides as supporting carriers for the Ni active phase. In contrast to the catalytic activity observed for Ni/CeO<sub>2</sub> catalysts, Ni/ZnO and Ni/CeO<sub>2</sub>-ZnO catalysts exhibit selectivity towards CO production while significantly suppressing CO<sub>2</sub> methanation. These findings underscore the influential role of the ZnO promoter in determining the reaction mechanism. Additionally, a preliminary study is conducted using CeO<sub>2</sub> triangles as supporting carriers for the Ni active phase in CO<sub>2</sub> hydrogenation. The obtained results are compared with those obtained from a nickel catalyst supported on commercial CeO<sub>2</sub>.

## 4.1. Experimental

### 4.1.1. Materials Synthesis

All the chemical compounds used in this chapter were of analytical grade.

Ce(NO<sub>3</sub>)<sub>3</sub>·6H<sub>2</sub>O (purity ≥ 99.0%, Fluka), tetrabutyl titanate (TBOT), NH<sub>4</sub>VO<sub>3</sub>, Cr(NO<sub>3</sub>)<sub>3</sub>·9H<sub>2</sub>O, Mn(NO<sub>3</sub>)<sub>2</sub>·4H<sub>2</sub>O, Fe(NO<sub>3</sub>)<sub>3</sub>·9H<sub>2</sub>O (≥ 98%, Sigma-Aldrich), Co(NO<sub>3</sub>)<sub>2</sub>·6H<sub>2</sub>O (≥ 98%, Sigma-Aldrich), Ni(NO<sub>3</sub>)<sub>2</sub>·6H<sub>2</sub>O (purity ≥ 98%, Sigma-Aldrich), and Cu(NO<sub>3</sub>)<sub>2</sub>·2.5H<sub>2</sub>O (Fluka) were employed as precursors for the synthesis of bare ceria nanorods as well as of ceria-based transition metal catalysts (M/CeO<sub>2</sub>, M: Ti, V, Cr, Mn, Fe, Co, Ni, Cu). Also, NaOH (purity ≥ 98%, Honeywell Fluka), absolute EtOH (purity ≥ 99.8%, ACROS Organics), and double-deionized water were used during materials synthesis.

Zn(CH<sub>3</sub>COO)<sub>2</sub>·2H<sub>2</sub>O (purity ≥ 99%, Sigma-Aldrich), Ce(NO<sub>3</sub>)<sub>3</sub>·6H<sub>2</sub>O (purity ≥ 99.0%, Fluka) and Ni(NO<sub>3</sub>)<sub>2</sub>·6H<sub>2</sub>O (purity ≥ 98%, Sigma-Aldrich) were employed as precursors for the synthesis of CeO<sub>2</sub>/ZnO and Ni/CeO<sub>2</sub>-ZnO samples. HO<sub>2</sub>CCO<sub>2</sub>H (purity ≥ 99%, Sigma-Aldrich), NaOH (purity ≥

98%, Honeywell Fluka), and absolute EtOH (purity  $\geq$  99.8%, ACROS Organics) were also used during preparation.

$\text{Ce}(\text{CH}_3\text{CO}_2)_3 \cdot x\text{H}_2\text{O}$  (purity  $\geq$  99.9%, Sigma–Aldrich) and  $\text{Ni}(\text{NO}_3)_2 \cdot 6\text{H}_2\text{O}$  (purity  $\geq$  98%, Sigma–Aldrich) were used as precursors for the synthesis of bare ceria triangles as well as of Ni/CeO<sub>2</sub> TR. Also, urea (purity  $\geq$  99.5%, Sigma–Aldrich), ethylene glycol (EG, purity  $\geq$  99.5%, Merck), absolute EtOH (purity  $\geq$  99.8%, ACROS Organics), and double deionized water were utilized during materials preparation.

The catalysts prepared in this chapter (CeO<sub>2</sub> NR, M/CeO<sub>2</sub>, ZnO, CeO<sub>2</sub>/ZnO-x, Ni/CeO<sub>2</sub>-ZnO-x, Ni/ZnO, CeO<sub>2</sub> TR, Ni/CeO<sub>2</sub> TR) were synthesized by the methods described in Chapter 2 in section 2.1 (Materials Synthesis). Also, Table 2.1 in Chapter 2 presents all the materials developed in this study.

#### 4.1.2. Materials Characterization

The N<sub>2</sub> adsorption-desorption isotherms at  $-196$  °C were used to determine the textural properties of the catalysts. X-ray diffraction (XRD) was employed to identify the crystalline structure of the samples. The average crystallite size of the samples was determined using Scherrer's equation (refer to Eq. 1 in Chapter 2). Scanning/Transmission Electron Microscopy (SEM/TEM) analyses were conducted to examine the morphology of the catalysts. To analyze the size distribution of ceria particles and perform HRTEM analysis, TEM images were processed using ImageJ software. X-ray photoelectron spectroscopy (XPS) analyses were conducted to determine the surface composition and chemical state of each element. The redox properties of the samples were evaluated through temperature-programmed reduction under H<sub>2</sub> (H<sub>2</sub>-TPR). A comprehensive description of these characterization techniques can be found in Chapter 2, specifically in Section 2.4 (Characterization Techniques).

### 4.2. Characterization Studies of Ceria-Based Transition Metal Catalysts

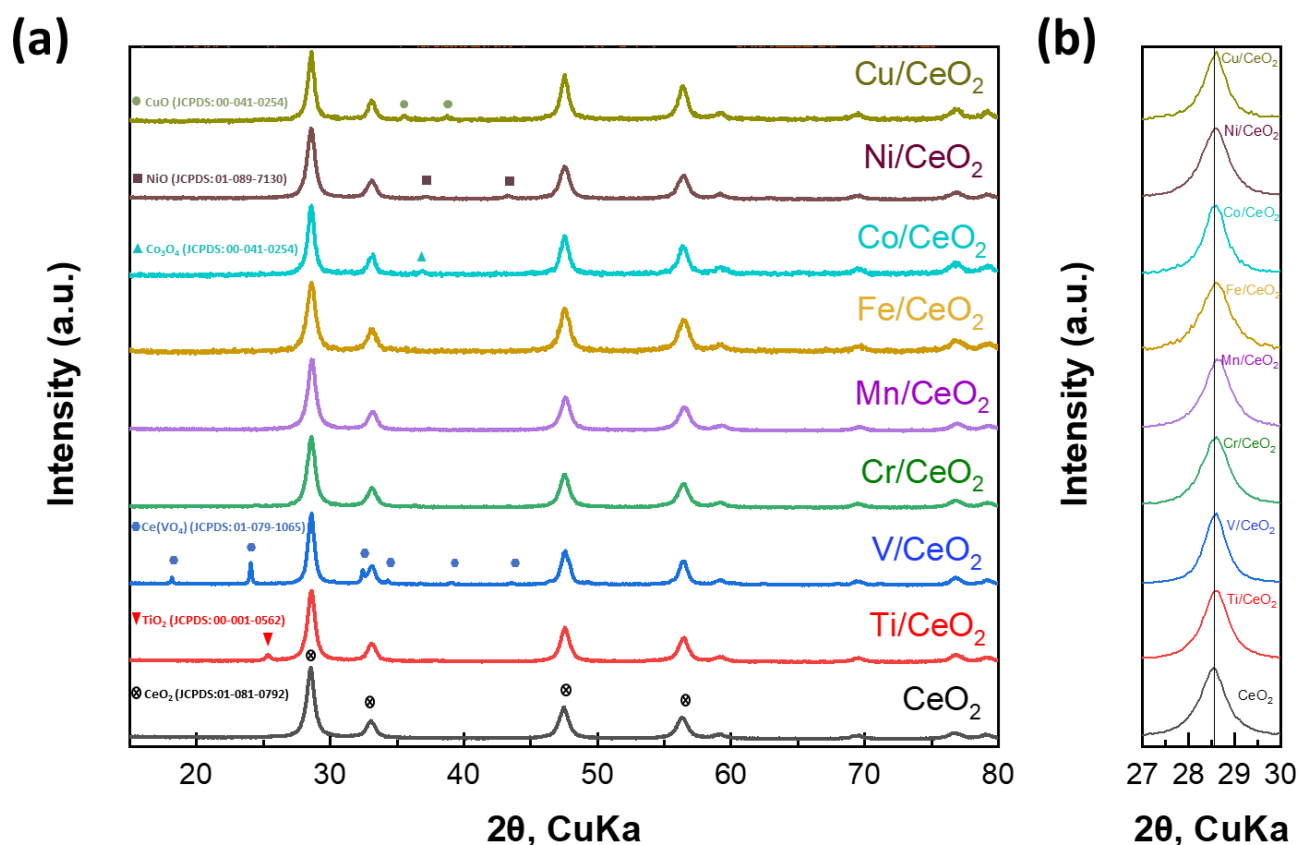
#### 4.2.1. Textural/Structural Characterization

Table 4.1 presents an overview of the key textural and structural properties of both bare CeO<sub>2</sub> and TM/CeO<sub>2</sub> samples. Bare CeO<sub>2</sub> demonstrates a BET surface area of 79.3 m<sup>2</sup>/g. However, upon incorporating transition metals into the ceria support, a slight decrease in the BET area was observed.

**Table 4.1.** Textural and structural properties of CeO<sub>2</sub> NR and M/CeO<sub>2</sub> (M: Ti, V, Cr, Mn, Fe, Co, Ni, Cu) samples.

Sample	EDS analysis		S <sub>BET</sub> (m <sup>2</sup> /g)	XRD analysis		TEM analysis
	Atomic ratio	M loading		Average Crystallite Size (nm)		M <sub>x</sub> O <sub>y</sub> particle size (nm)
	M/Ce	(wt.%)		CeO <sub>2</sub>	M <sub>x</sub> O <sub>y</sub>	
CeO <sub>2</sub> NR	-	-	79.3	11.0	-	-
Ti/CeO <sub>2</sub>	0.24	6.3	-	11.5	20	16.3
V/CeO <sub>2</sub>	0.28	7.6	-	13.6	45	27.5
Cr/CeO <sub>2</sub>	0.26	7.2	-	11.2	-	10.1
Mn/CeO <sub>2</sub>	0.22	6.5	-	10.9	-	15.0
Fe/CeO <sub>2</sub>	0.21	6.3	68.6	10.6	-	11.2
Co/CeO <sub>2</sub>	0.26	8.1	71.9	13.2	16	14.8
Ni/CeO <sub>2</sub>	0.25	7.8	72.1	10.6	14	9.7
Cu/CeO <sub>2</sub>	0.25	8.6	75.4	13.9	17	15.8

Figure 4.1 illustrates the XRD patterns obtained for bare CeO<sub>2</sub> NR and M/CeO<sub>2</sub> (M: Ti, V, Cr, Mn, Fe, Co, Ni, Cu) samples. The primary diffraction peaks of bare CeO<sub>2</sub> NR can be attributed to the (111), (200), (220), (311), (222), (400), (331), and (420) planes, indicating a face-centered cubic (FCC) fluorite structure of ceria with Fm3m symmetry (no. 225)<sup>92</sup>. For the Ti/CeO<sub>2</sub>, Co/CeO<sub>2</sub>, Ni/CeO<sub>2</sub>, and Cu/CeO<sub>2</sub> samples, smaller peaks corresponding to their respective oxides were detected. These observations suggest the presence of TiO<sub>2</sub>, Co<sub>3</sub>O<sub>4</sub>, NiO, and CuO in the Ti/CeO<sub>2</sub>, Co/CeO<sub>2</sub>, Ni/CeO<sub>2</sub>, and Cu/CeO<sub>2</sub> samples, respectively, with no other crystal phases detected besides ceria. Conversely, the Mn/CeO<sub>2</sub>, Fe/CeO<sub>2</sub>, and Cr/CeO<sub>2</sub> samples exhibited no distinct diffraction peaks, except for the ceria crystal phase. This can be attributed to the low metal loading and high dispersion of these metals within the CeO<sub>2</sub> support. In the case of V/CeO<sub>2</sub>, in addition to the characteristic peaks of ceria, a series of XRD peaks were observed at 2θ values around 18.2°, 24.0°, 32.4°, 34.2°, 39.0°, 43.5°, 46.4°, 47.9°, 49.2°, 55.5°, and 60.2°<sup>93</sup>. These peaks correspond to the (101), (200), (112), (220), (301), (103), (321), (312), (400), (420), and (332) planes of Ce(VO<sub>4</sub>). Hence, it can be inferred that the impregnation method resulted in the formation of a mixed crystal phase in the V/CeO<sub>2</sub> sample, consisting of CeO<sub>2</sub> and Ce(VO<sub>4</sub>).



**Figure 4.1.** (a) XRD patterns of CeO<sub>2</sub> NR and M/CeO<sub>2</sub> (M: Ti, V, Cr, Mn, Fe, Co, Ni, Cu) samples; (b) the (111) diffraction peak of CeO<sub>2</sub>.

The average crystallite sizes of the CeO<sub>2</sub> and M<sub>x</sub>O<sub>y</sub> phases in bare ceria nanorods and M/CeO<sub>2</sub> samples were calculated using the Scherrer equation and are summarized in Table 4.1. The results indicate that the crystallite size of the ceria particles remains relatively unchanged upon the incorporation of transition metals, suggesting that the structural properties of ceria remain unaffected by the addition of metals. Regarding the average crystallite sizes of the active metal phases, Ce(VO<sub>4</sub>) exhibits the largest average size of 45 nm, followed by TiO<sub>2</sub> with a size of 20 nm. Furthermore, CuO, Co<sub>3</sub>O<sub>4</sub>, and NiO exhibit sizes of 17 nm, 16 nm, and 14 nm, respectively.

Table 4.2 provides a summary of various characteristics of ceria, including d<sub>111</sub>-spacing, lattice parameter, unit cell volume, crystalline size, and microstrain ( $\epsilon$ ) for the (111) diffraction peak. The results reveal a slight decrease in the lattice parameters and unit cell volume of ceria, which is evident from a slight shift in the position of the diffraction peaks, as depicted in Figure 4.1 (b). This contraction of the ceria lattice can be attributed to the incorporation of transition metal ions with smaller ionic radii into the ceria lattice, in comparison to the ion radius of ceria ( $r_{Ce^{+4}} > r_{TM}$ )<sup>94-96</sup>.

**Table 4.2.** The  $d_{111}$ -spacing, lattice parameter, unit cell volume, crystalline size, and microstrain ( $\epsilon$ ) for (111) diffraction peak of ceria.

Samples	$d_{111}$ -spacing (nm)	Lattice parameter (nm)	Unit cell volume (nm <sup>3</sup> )	Crystalline size (nm)	$\epsilon \times 10^{-3}$
CeO <sub>2</sub> NR	0.3130	0.5416	0.1589	11.0	15.3964
Ti/CeO <sub>2</sub>	0.3122	0.5408	0.1581	11.5	12.2632
V/CeO <sub>2</sub>	0.3123	0.5409	0.1582	13.6	10.3124
Cr/CeO <sub>2</sub>	0.3123	0.5409	0.1582	11.2	12.6005
Mn/CeO <sub>2</sub>	0.3118	0.5401	0.1575	10.9	12.8525
Fe/CeO <sub>2</sub>	0.3120	0.5405	0.1579	10.6	13.2889
Co/CeO <sub>2</sub>	0.3122	0.5407	0.1581	13.2	10.6033
Ni/CeO <sub>2</sub>	0.3122	0.5408	0.1581	10.6	13.2392
Cu/CeO <sub>2</sub>	0.3122	0.5407	0.1581	13.9	10.1159
Zn/CeO <sub>2</sub>	0.3141	0.5440	0.1610	11.5	12.2586

#### 4.2.2. Morphological Characterization

Elemental analysis was performed using a scanning electron microscope (SEM) in combination with energy-dispersive X-ray spectrometry (EDS) on the M/CeO<sub>2</sub> (M: Ti, V, Cr, Mn, Fe, Co, Ni, Cu) samples. The results of the SEM analysis, including the atomic ratio of M/Ce and M loading (%), are presented in Table 4.1. The obtained atomic ratio of M/Ce is in close agreement with the nominal atomic ratio. This indicates the successful synthesis of the desired composition. Furthermore, Figure 4.2 shows the SEM images of all M/CeO<sub>2</sub> samples. From the SEM/EDS analysis, it was observed that the CeO<sub>2</sub> and metal phases were uniformly distributed throughout the samples. This suggests a homogeneous dispersion of the components, which is crucial for achieving the desired properties and catalytic performance of the material.

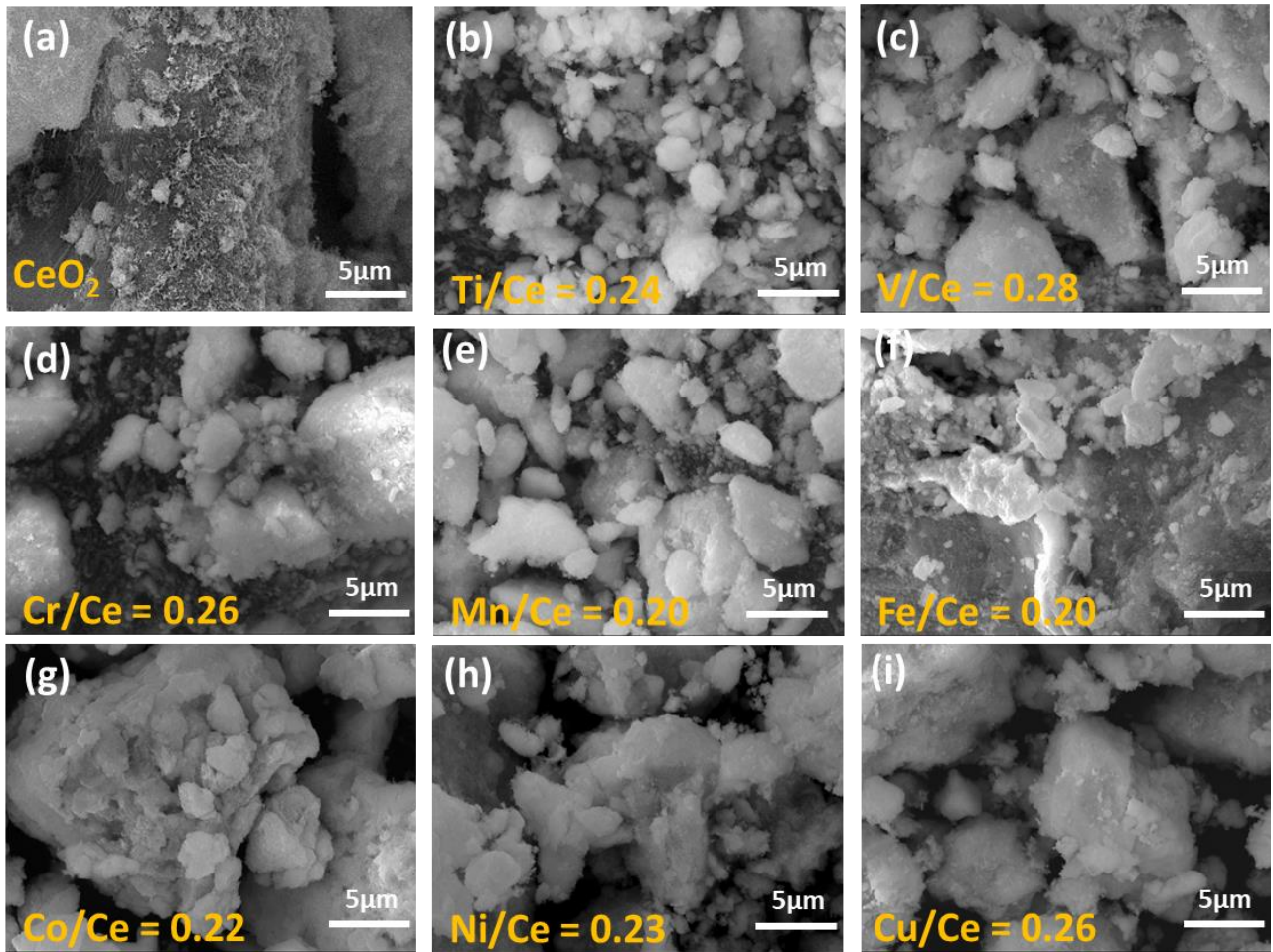


**Figure 4.2.** SEM/EDS analysis of  $\text{CeO}_2$  and  $\text{M/CeO}_2$  (M: Ti, V, Cr, Mn, Fe, Co, Ni, Cu) sample.

The morphological characteristics of the samples were investigated using transmission electron microscopy (TEM). TEM analysis, as shown in Figure 4.3, revealed that the nanorod-like morphology of the  $\text{CeO}_2$  support was maintained even after the incorporation of transition metals. Additionally, isolated particles of  $\text{M}_x\text{O}_y$  with an irregular shape were detected in all  $\text{M/CeO}_2$  samples. The particle size of the  $\text{M}_x\text{O}_y$  particles varied depending on the specific metal incorporated into the  $\text{CeO}_2$  lattice. Moreover, the particle size of  $\text{M}_x\text{O}_y$  (M: Ti, V, Cr, Mn, Fe, Co, Ni, Cu) was determined through TEM analysis. Figure 4.3 and Table 4.1 illustrate the particle size distribution obtained for all samples, providing insights into the range of particle sizes observed. These results are consistent with the crystallographic information obtained from X-ray diffraction (XRD) analysis, as shown in Table 4.1. The TEM analysis not only confirmed the nanorod-like morphology of the  $\text{CeO}_2$  support but also highlighted the presence of isolated  $\text{M}_x\text{O}_y$  particles with an irregular shape in all  $\text{M/CeO}_2$  samples. The determination of particle size distribution through TEM analysis provided further insights into the characteristics of the  $\text{M}_x\text{O}_y$  particles, complementing the XRD results.

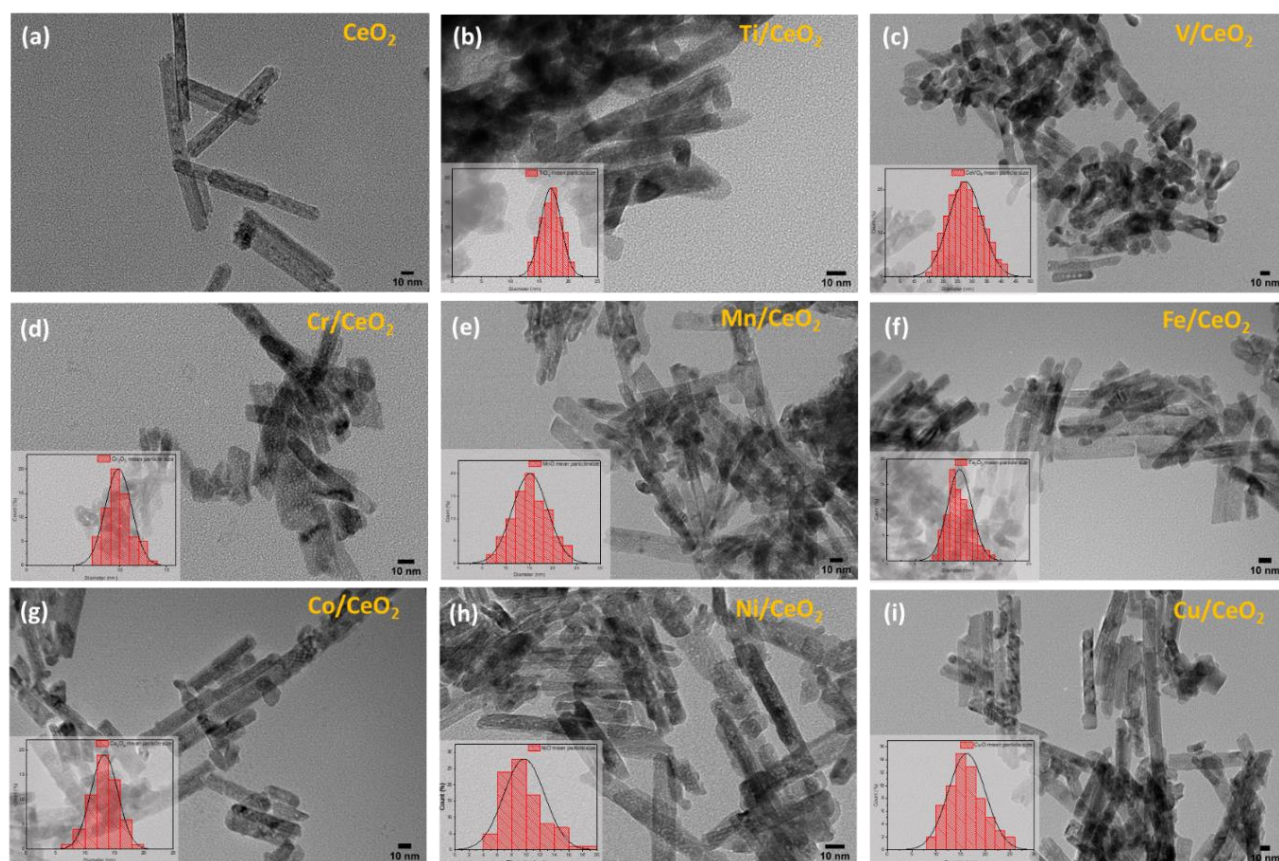


**Figure 4.3.** TEM images and Particle Size Distribution (PSD) histograms for the metal diameter of  $\text{CeO}_2$  and  $\text{M/CeO}_2$  (M: Ti, V, Cr, Mn, Fe, Co, Ni, Cu).

#### 4.2.3. Redox Properties ( $\text{H}_2$ -TPR)

The  $\text{H}_2$ -TPR profiles of the samples were analyzed, including bare ceria ( $\text{CeO}_2$  NR) and ceria-based transition metal catalysts ( $\text{M/CeO}_2$ , M: Fe, Co, Cu, Ni) with rod-like nanomorphology. Figure 4.4 presents the  $\text{H}_2$ -TPR profiles for the different samples.  $\text{CeO}_2$  NR displays two broad reduction peaks centered at  $545^\circ\text{C}$  and  $788^\circ\text{C}$ , which correspond to the reduction of surface oxygen ( $\text{O}_s$ ) and bulk oxygen ( $\text{O}_b$ ) of ceria, respectively<sup>97</sup>. In the case of  $\text{Fe/CeO}_2$ , four reduction peaks are observed. The peaks at  $465^\circ\text{C}$  and  $759^\circ\text{C}$  are attributed to the reduction of ceria surface oxygen and bulk oxygen, respectively. The peaks at  $390^\circ\text{C}$  and  $588^\circ\text{C}$  correspond to the reduction of iron species, specifically  $\text{Fe}_2\text{O}_3$  to  $\text{Fe}_3\text{O}_4$  and  $\text{Fe}_3\text{O}_4$  to  $\text{Fe}^0$ <sup>98</sup>. For the  $\text{Co/CeO}_2$  sample, two main reduction peaks are observed at  $318^\circ\text{C}$  and  $388^\circ\text{C}$ , corresponding to the stepwise reduction of  $\text{Co}_3\text{O}_4$  to  $\text{CoO}$  and  $\text{CoO}$  to metallic Co, respectively<sup>99</sup>. In the case of  $\text{Cu/CeO}_2$ , the low-temperature peak at  $181^\circ\text{C}$  is attributed to the reduction of finely dispersed  $\text{CuO}_x$  species strongly interacting with the ceria surface<sup>100</sup>, while the peak at  $217^\circ\text{C}$  is ascribed to the formation of larger CuO clusters on the ceria surface<sup>101</sup>. Nickel-ceria nanorods exhibit two main peaks at  $288^\circ\text{C}$  and  $353^\circ\text{C}$ . The low-temperature peak is associated with the reduction of adsorbed oxygen species, leading to the formation of a Ni-O-Ce structure. The

peak at higher temperatures is attributed to the reduction of the well-dispersed NiO phase, which interacts strongly with the ceria support<sup>102</sup>. All M/CeO<sub>2</sub> samples display a high-temperature peak in the range of 747–793 °C, attributed to the reduction of ceria sub-surface oxygen. As shown in Figure 4.4, the incorporation of the metal phase into the rod-shaped ceria catalyst promotes the reduction of ceria surface oxygen. Except for Fe/CeO<sub>2</sub>, all M/CeO<sub>2</sub> samples exhibit main reduction peaks at significantly lower temperatures than bare ceria nanorods, indicating complete reduction at temperatures approximately below 500 °C.

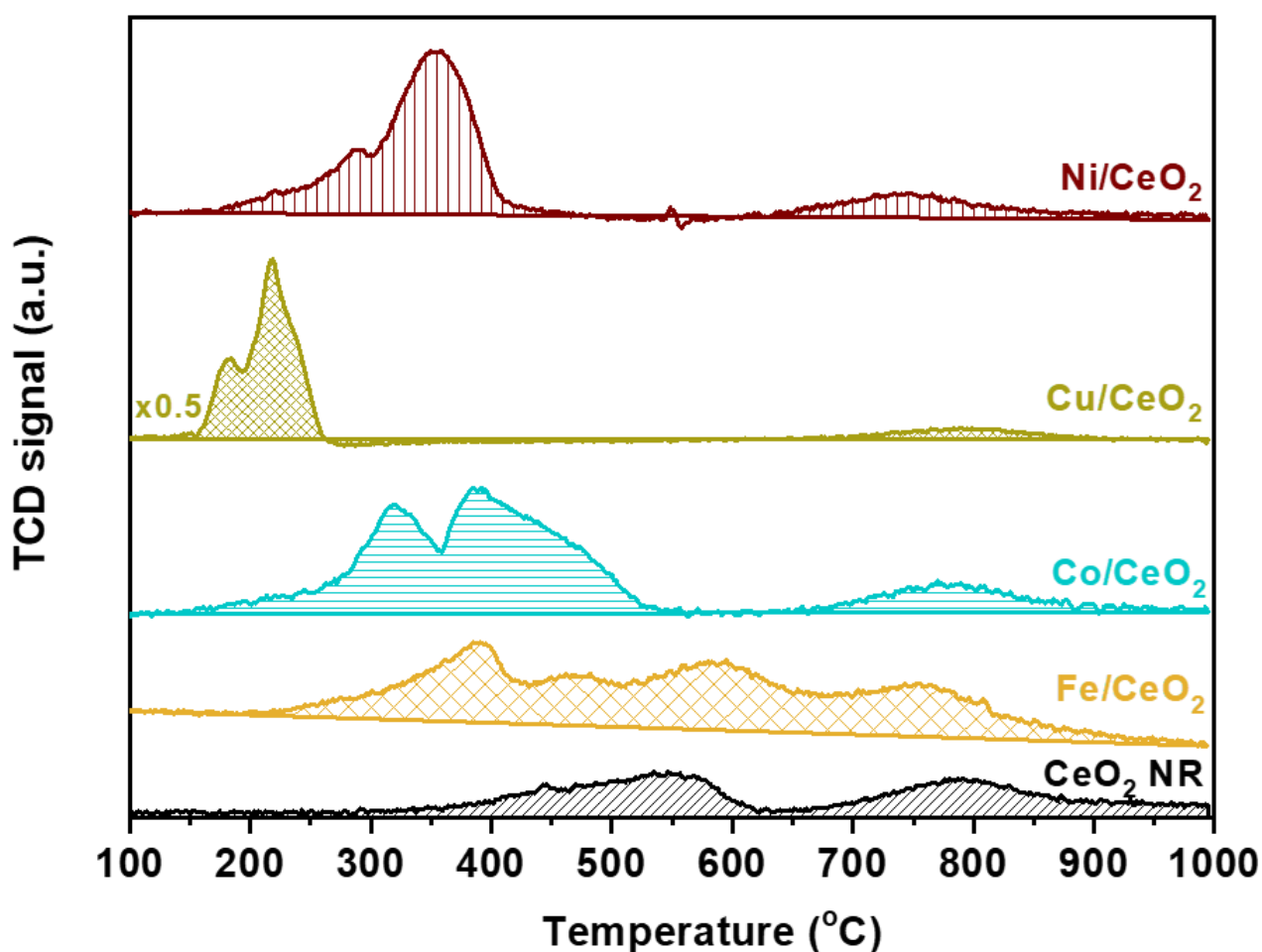


**Figure 4.4.** H<sub>2</sub>-TPR profiles of CeO<sub>2</sub> NR and M/CeO<sub>2</sub> (M: Fe, Co, Ni, Cu) samples.

Furthermore, as presented in Table 4.3, it is observed that hydrogen consumption exceeds the theoretical amount for all M/CeO<sub>2</sub> samples, except for the Fe/CeO<sub>2</sub> sample. This finding indicates that the incorporation of the metallic phase greatly enhances the reducibility of ceria nanorods. The observed synergistic metal-support interactions contribute to this enhanced reducibility.

**Table 4.3.** Redox properties of CeO<sub>2</sub> NR and M/CeO<sub>2</sub> (M: Fe, Co, Ni, Cu) samples.

Sample	H <sub>2</sub> consumption (mmol H <sub>2</sub> g <sup>-1</sup> ) <sup>1</sup>	Theoretical H <sub>2</sub> consumption (mmol H <sub>2</sub> g <sup>-1</sup> ) <sup>2</sup>	Peak temperature (°C)			
CeO <sub>2</sub> NR	0.6	-	545	788		
Fe/CeO <sub>2</sub>	1.6	1.9	390	465	588	759
Cu/CeO <sub>2</sub>	1.8	1.3	181	217	793	
Ni/CeO <sub>2</sub>	1.8	1.3	288	353	747	
Co/CeO <sub>2</sub>	2.4	1.7	318	388	789	

<sup>1</sup>Estimated by the area of the corresponding TPR peaks, which is calibrated against a known amount of CuO standard sample.

<sup>2</sup>Calculated as the amount of H<sub>2</sub> required for the complete reduction of fully oxidized M<sub>x</sub>O<sub>y</sub> to M<sup>0</sup> on the basis of the metal nominal loading.

### 4.3. Characterization studies of Ni/CeO<sub>2</sub>-x

#### 4.3.1. ICP-AES

The nickel content of the samples was quantified using inductively coupled plasma atomic emission spectroscopy (ICP-AES), and the measured values are presented in Table 4.4. Notably, the actual nickel values closely align with the nominal Ni loading, indicating the successful incorporation of the desired amount of nickel into the ceria support.

**Table 4.4.** Textural characteristics of bare CeO<sub>2</sub> NR and the as-prepared Ni/CeO<sub>2</sub>-x samples.

Sample	Ni loading (wt.%)		BET Analysis	
	Nominal	Actual	BET Surface Area (m <sup>2</sup> /g)	Average Pore Size (nm)
CeO <sub>2</sub> NR	-	-	79.3	24.2
Ni/CeO <sub>2</sub> -0.10	3.30	3.57	76.9	17.1
Ni/CeO <sub>2</sub> -0.25	7.86	7.97	72.0	18.3
Ni/CeO <sub>2</sub> -0.50	14.57	13.80	65.3	14.4
Ni/CeO <sub>2</sub> -1.00	25.43	23.45	56.5	14.3
Ni/CeO <sub>2</sub> -1.50	33.84	32.46	51.3	15.8

<sup>a</sup>Determined by ICP-AES.

#### 4.3.2. Textural/Structural Characterization

The main textural characteristics of the bare CeO<sub>2</sub> NR and as-prepared Ni/CeO<sub>2</sub>-x samples are presented in Table 4.4. Upon the addition of nickel, the BET surface area of the support exhibits a

consistent decrease. For instance, the surface area decreases from 79.3 m<sup>2</sup>/g for CeO<sub>2</sub> NR to 51.3 m<sup>2</sup>/g for Ni/CeO<sub>2</sub>-1.50. However, this reduction in surface area does not indicate significant pore blockage, as evidenced by the pore size measurements. The bare CeO<sub>2</sub> NR exhibits a pore size of 24.2 nm, whereas the average pore diameter of the Ni/CeO<sub>2</sub>-x catalysts ranges between 14.3 and 18.3 nm.

The crystal structure of the as-prepared Ni/CeO<sub>2</sub>-x samples was investigated using X-ray diffraction (XRD), and the corresponding diffractograms are depicted in Figure 4.5. The primary diffraction peaks observed at 2θ = 28.5°, 33.1°, 47.5°, and 56.3° correspond to the (111), (200), (220), and (311) crystal planes, respectively, and can be attributed to the FCC fluorite structure of ceria (Fm3m symmetry, no. 225, Reference code: 00-043-1002)<sup>92</sup>. Furthermore, the XRD peaks detected at 2θ = 44.5° and 51.8° correspond to the (111) and (200) crystal planes, respectively, and are associated with the characteristic cubic structure of metallic nickel (Ni<sup>0</sup>) (Fm3m symmetry, no. 225, Reference code: 01-070-1849)<sup>75</sup>. Importantly, no peaks indicative of NiO were observed, confirming the complete reduction of nickel species during the synthesis procedure. The intensities of the Ni<sup>0</sup> peaks exhibit an increasing trend with the increase in Ni loading, while they are below the detection limit for the Ni/CeO<sub>2</sub>-0.10 and Ni/CeO<sub>2</sub>-0.25 samples. This observation can be attributed to either a relatively high dispersion of nickel species over the ceria support, the formation of a solid solution between cerium (Ce) and nickel (Ni), or the amorphous nature of the nickel particles<sup>103</sup>, as further discussed below.

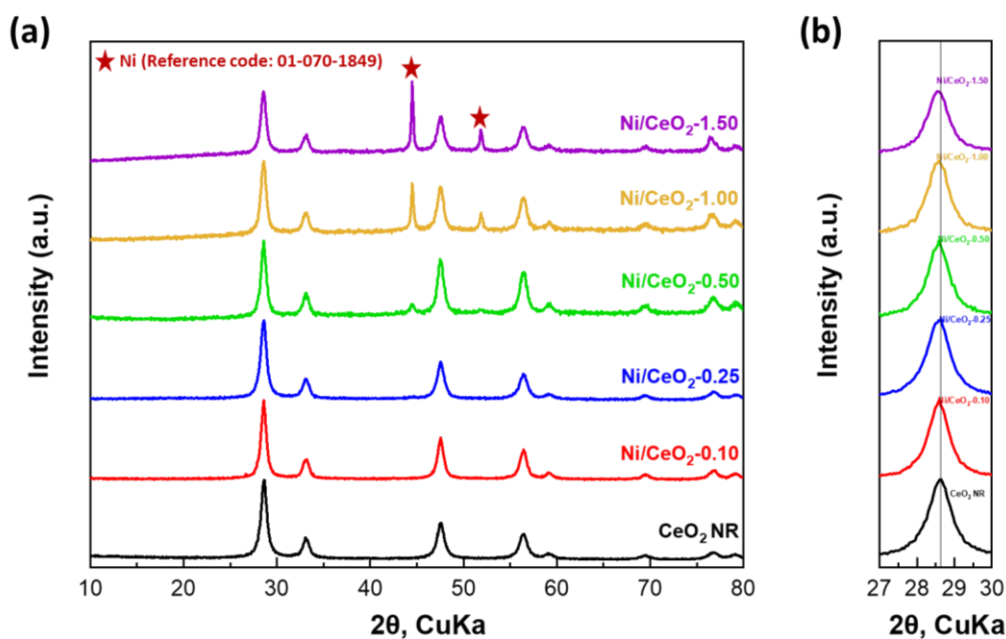


**Figure 4.5.** (a) XRD patterns of CeO<sub>2</sub> NR and Ni/CeO<sub>2</sub>-x samples; (b) the (111) diffraction peak of CeO<sub>2</sub>.

The quantitative results obtained from the XRD analysis, including ceria (111) and nickel (111) crystallite size, lattice parameter, unit cell volume, and microstrain ( $\epsilon$ ) for the ceria (111) diffraction peak, are summarized in Table 4.5. The ceria crystallite size decreases upon the addition of nickel, although no significant change is observed in the CeO<sub>2</sub> crystallite size among the Ni/CeO<sub>2</sub>-x samples, except for Ni/CeO<sub>2</sub>-0.25, where a size of 10.3 nm is measured compared to an average value of approximately 11.3 nm for the other four Ni/CeO<sub>2</sub>-x samples. In contrast, the crystallite size of nickel exhibits a significant increase with higher Ni loading. Specifically, the Ni crystallite size measures 15.4 nm, 26.6 nm, and 31.4 nm for Ni/CeO<sub>2</sub>-0.50, Ni/CeO<sub>2</sub>-1.00, and Ni/CeO<sub>2</sub>-1.50, respectively. However, for the Ni/CeO<sub>2</sub>-0.10 and Ni/CeO<sub>2</sub>-0.25 samples, meaningful results could not be obtained due to the absence of detectable Ni<sup>0</sup> peaks in their respective diffractograms. Nevertheless, it is worth noting that the obtained values generally align with those measured by TEM (further discussed below).

Moreover, the lattice parameter, unit cell volume, and microstrain ( $\epsilon$ ) calculated from the most intense planar reflection of CeO<sub>2</sub> (111) for all Ni/CeO<sub>2</sub>-x samples are lower compared to bare CeO<sub>2</sub> NR. Interestingly, the reduction in these values is particularly pronounced in the case of Ni/CeO<sub>2</sub>-0.10, followed by a slight lattice expansion with further increases in nickel content. This behavior is also reflected in the shift of the diffraction angle, as shown in Figure 4.5 (b). This intriguing phenomenon is likely a direct consequence of the solubility limit for Ce  $\leftrightarrow$  Ni exchange within the range of 10-12 mol.% (or 3.7-4.5 wt.%) of Ni<sup>104</sup>. The observed overall contraction of the CeO<sub>2</sub> lattice can be attributed to the partial substitution of larger Ce<sup>4+</sup> ions ( $r_{Ce^{4+}} = 94$  pm) with smaller Ni<sup>2+</sup> ions ( $r_{Ni^{2+}} = 72$  pm), forming a Ni<sub>x</sub>Ce<sub>1-x</sub>O<sub>2- $\delta$</sub>  solid solution<sup>105</sup>. Subsequently, with the addition of more Ni, the solubility limit is exceeded, and the excess Ni ions give rise to interstitial defects, which are known to slightly increase the lattice parameter<sup>102,106</sup>.

**Table 4.5.** Structural and morphological characteristics of bare CeO<sub>2</sub> NR and the as-prepared Ni/CeO<sub>2</sub>-x samples.

Sample	XRD Analysis				TEM Analysis			
	CeO <sub>2</sub> (111)			$\epsilon \times 10^{-3}$	Average crystallite diameter, D <sub>XRD</sub> (nm)		Ni particle size, d <sub>n</sub> (nm)	D <sub>Ni</sub> (%)
	d <sub>(111)</sub> -spacing (nm)	Lattice Parameter (nm) a = b = c	Unit Cell Volume (nm) <sup>3</sup>		CeO <sub>2</sub> (111)	Ni (111)		
CeO <sub>2</sub> NR	0.313	0.5416	0.1589	15.3964	11.0	-	-	-
Ni/CeO <sub>2</sub> -0.10	0.312	0.5406	0.1580	12.3182	11.4	<i>n.d.</i>	9.7 ± 2.9	10.4
Ni/CeO <sub>2</sub> -0.25	0.312	0.5408	0.1582	13.5785	10.3	<i>n.d.</i>	10.4 ± 2.8	9.7
Ni/CeO <sub>2</sub> -0.50	0.312	0.5407	0.1581	12.1960	11.5	15.4	14.4 ± 3.0	7.1
Ni/CeO <sub>2</sub> -1.00	0.312	0.5408	0.1582	12.5401	11.2	26.6	20.3 ± 4.3	5.0
Ni/CeO <sub>2</sub> -1.50	0.312	0.5409	0.1583	12.4598	11.3	31.4	24.6 ± 8.1	4.1

### 4.3.3. Raman spectroscopy

The surface structure and oxygen vacancy density of the as-synthesized CeO<sub>2</sub> NR and Ni/CeO<sub>2</sub>-x samples were analyzed using visible Raman spectroscopy (Figure 4.6). The Raman spectra revealed distinct features for all samples. In all Ni/CeO<sub>2</sub>-x samples, a main peak was observed at approximately 463 cm<sup>-1</sup>, accompanied by a secondary wide peak around 598 cm<sup>-1</sup> (Figure 4.6 (a)). On the other hand, CeO<sub>2</sub> NR predominantly exhibited a peak at ~463 cm<sup>-1</sup>. Additionally, a peak at approximately 630 cm<sup>-1</sup> was specifically identified in the NiCe-0.25 sample, which can be attributed to the Ni-O-Ce interaction<sup>107</sup>. This peak has also been observed in other studies involving Ni/CeO<sub>2</sub> samples with similar nickel content<sup>53,102</sup>. The Raman shifts at around 463 cm<sup>-1</sup> and 598 cm<sup>-1</sup> are associated with the F<sub>2g</sub> symmetry mode and the defect-induced mode (D band), respectively<sup>108,109</sup>. The F<sub>2g</sub> symmetry mode corresponds to the Fm3m cubic fluorite structure of ceria and represents the dominant Raman-active mode. The occurrence of the D band indicates structural perturbations in the CeO<sub>2</sub> lattice, which are linked to localized defects and oxygen vacancies induced by the addition of nickel<sup>92,110</sup>. No peaks related to the NiO phase were detected in the 1080-1180 cm<sup>-1</sup> region for any of the Ni/CeO<sub>2</sub>-x samples, consistent with the XRD findings (Figure 4.5)<sup>111</sup>. The peak at ~463 cm<sup>-1</sup> exhibited increased width and decreased intensity with higher nickel addition. Additionally, the F<sub>2g</sub> vibration peak showed a red shift in all Ni/CeO<sub>2</sub>-x samples, except for the sample with the lowest loading (Ni/CeO<sub>2</sub>-0.10)<sup>103</sup>. This red shift indicates an increase in lattice distortion upon nickel addition and a concurrent decrease in the symmetry of the Ce-O bond. It suggests a stronger interaction at the interphase between nickel and ceria, suggesting the substitution of Ce<sup>4+</sup> with Ni ions and the eventual formation of Ni-O-Ce. These findings align with the XRD results (as mentioned earlier) and corroborate relevant literature studies<sup>102,109,112</sup>.

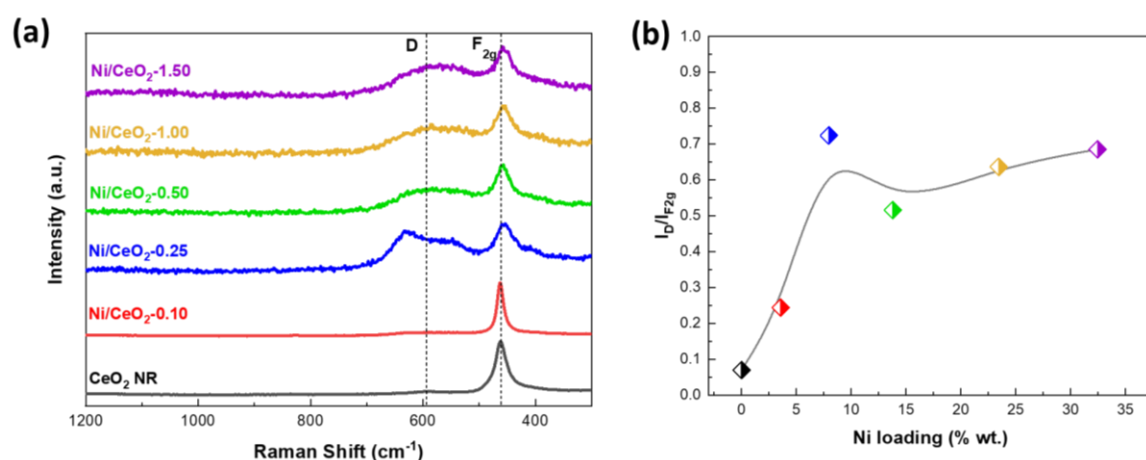


**Figure 4.6.** (a) Raman spectra for bare CeO<sub>2</sub> NR and Ni/CeO<sub>2</sub>-x samples; (b) I<sub>D</sub>/I<sub>F<sub>2g</sub></sub> ratio for bare CeO<sub>2</sub> NR and Ni/CeO<sub>2</sub>-x samples.

Furthermore, the assessment of oxygen vacancy density in the ceria-based catalytic composites can be achieved by analyzing the ratio of the intensities of the D and  $F_{2g}$  bands<sup>102,113</sup>, denoted as  $I_D/I_{F_{2g}}$ . In Figure 4.6 (a), the corresponding  $I_D/I_{F_{2g}}$  values for the as-synthesized  $CeO_2$  NR and  $Ni/CeO_2-x$  samples are presented as a function of the nickel loading (Table 4.4). As anticipated, the  $I_D/I_{F_{2g}}$  value for bare  $CeO_2$  NR is relatively low, approximately 0.07, since for  $CeO_2$  nanocrystals this ratio tends to be much higher in the UV rather than in the visible Raman spectra<sup>113</sup>. However, with the introduction of nickel, the  $I_D/I_{F_{2g}}$  ratio significantly increases, particularly for samples with lower nickel loadings such as  $Ni/CeO_2-0.10$  and  $Ni/CeO_2-0.25$ <sup>113</sup>. This notable increase indicates that nickel plays a crucial role in facilitating ceria reduction. Interestingly, a further increase in the nickel content only causes a slight variation in the intensity ratio, ranging from approximately 0.6 to 0.7. This suggests that the concentration of oxygen vacancies is not greatly influenced by higher levels of nickel incorporation. These findings align with results reported in relevant studies investigating nickel-ceria catalysts, providing further support for the observed effects<sup>102,110,114</sup>.

#### 4.3.4. Morphological Characterization

The morphology of the samples was evaluated using TEM analysis, and representative images are presented in Figure 4.7. Notably, the nanorod-like morphology of the  $CeO_2$  support remained unchanged upon the addition of nickel, regardless of the Ni content. Additionally, isolated sphere-like Ni particles were observed, as clearly shown in Figure 4.7 (f), which displays a representative HRTEM image of the sample with intermediate Ni loading,  $Ni/CeO_2-0.50$ . The well-defined lattice fringes of both Ni and  $CeO_2$  indicated the crystalline nature of the sample. The observed lattice spacings for the Ni and  $CeO_2$  phases were measured as 0.2 nm and 0.3 nm, respectively. This confirmed the presence of  $Ni^0$  particles exposing (111) planes that encounter  $CeO_2$  (111), providing further validation for the XRD results (Figure 4.5). Moreover, the image revealed that the Ni cluster was partially submerged within the nanorod support, exhibiting a quasi-spherical shape.

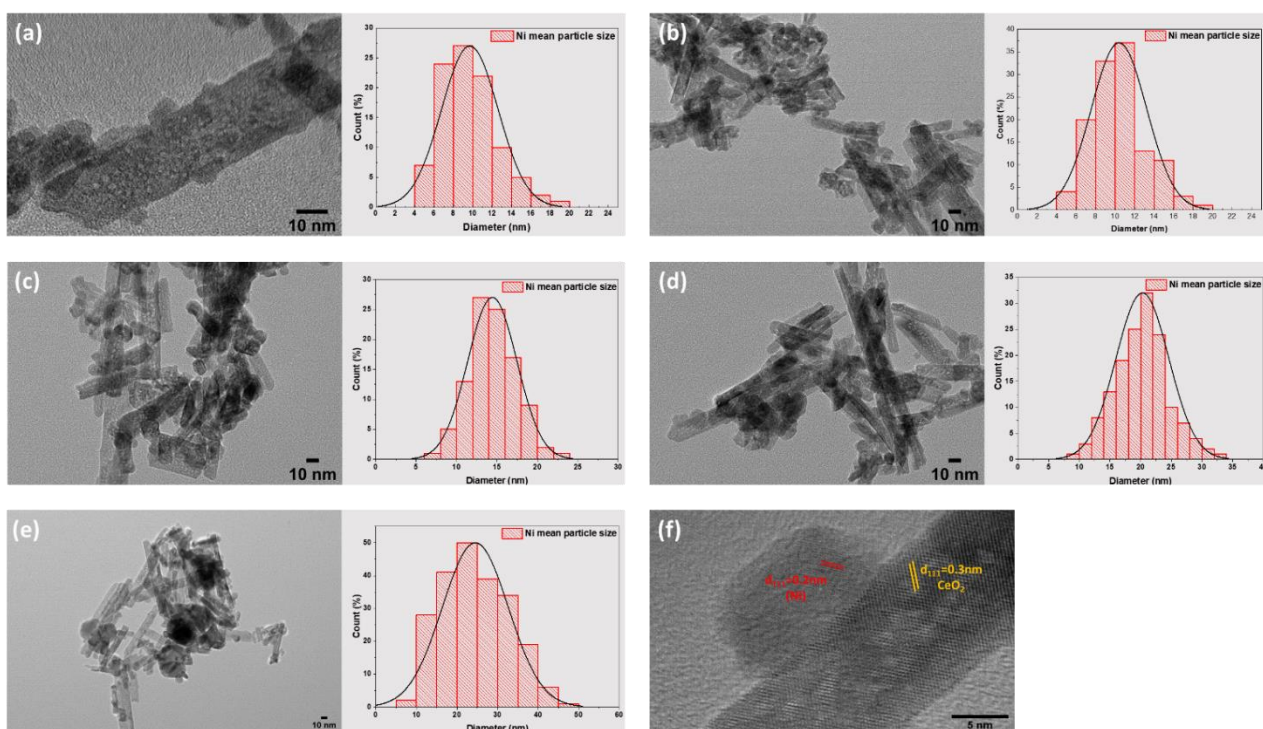


**Figure 4.7.** Representative TEM images and Ni particle distribution of Ni/CeO<sub>2-x</sub> samples, (a) Ni/CeO<sub>2</sub>-0.10, (b) Ni/CeO<sub>2</sub>-0.25, (c) Ni/CeO<sub>2</sub>-0.50, (d) Ni/CeO<sub>2</sub>-1.00 and (e) Ni/CeO<sub>2</sub>-1.50. In (f), the HRTEM image of Ni/CeO<sub>2</sub>-0.50 is shown.

The determination of the average Ni particle size ( $d_n$ ) and dispersion ( $D$ ) was carried out for all samples using a reliable method known for its accuracy in measuring particle size<sup>115</sup>. Although the high electron density of CeO<sub>2</sub> presents challenges in analyzing size distributions through TEM analysis in some cases<sup>35</sup>, Ni particle size distribution (PSD) could be successfully acquired for Ni/CeO<sub>2-x</sub> samples. The results are depicted in Figure 4.7 and summarized in Table 4.5. The average size of Ni particles ranges between 10-25 nm, exhibiting a consistent trend relative to the nickel loading. To account for the broadness of the PSD observed in the Ni/CeO<sub>2-x</sub> samples, not only the number average (arithmetic diameter,  $d_n$ ) but also the surface-weighted ( $d_s$ ) and volume-weighted ( $d_v$ ) diameters were calculated. Additional details can be found in Section 2.2 (Characterization Techniques). Figure 4.8 illustrates that all three diameters follow the same trend, although Ni/CeO<sub>2</sub>-1.50 shows a more pronounced variability. This suggests a slight agglomeration of Ni particles in this sample, which could explain the relatively higher particle size value obtained by XRD analysis (Table 4.5). Taking this into consideration,  $d_n$  was used in the subsequent calculations regarding the particle size of Ni and reaction rates (see below).

As anticipated from geometric considerations, the increase of the Ni crystallite size correlates with a reduction in the dispersion of the metallic phase. This is evident from the measured values of 10.4% for Ni/CeO<sub>2</sub>-0.10 and 4.1% for Ni/CeO<sub>2</sub>-1.50. These findings are consistent with similar results

reported in previous studies concerning Ni-ceria composites<sup>52,116,117</sup>. To provide a visual representation of these observations, Figure 4.8 illustrates the average Ni particle size and dispersion plotted against the actual Ni content of the samples, allowing for a comparative analysis of the aforementioned trends.

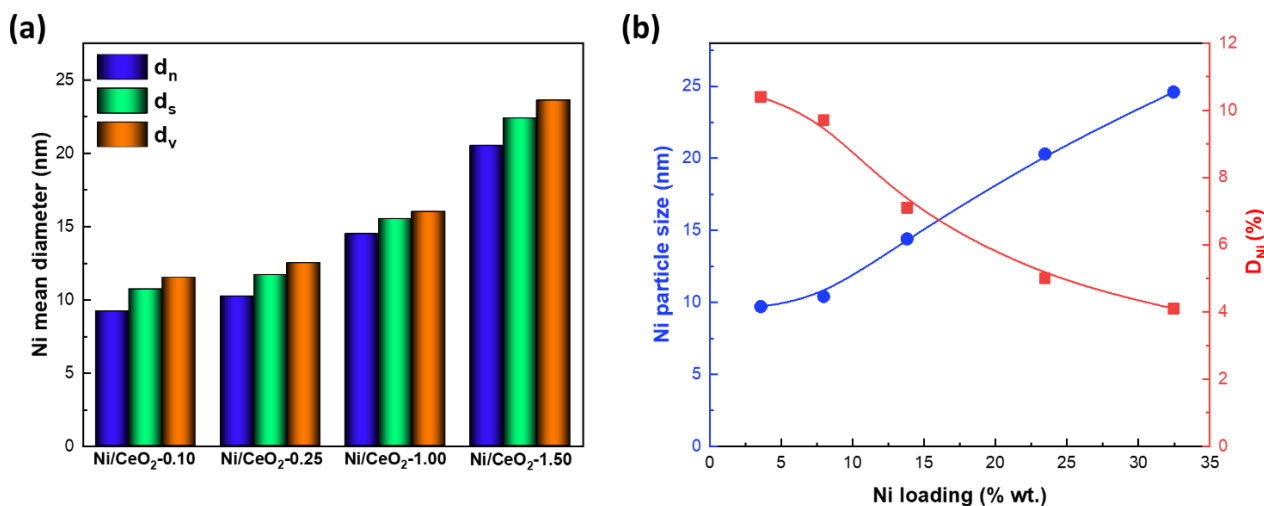


**Figure 4.8.** (a) Calculated values for the arithmetic ( $d_n$ ), surface ( $d_s$ ) and volume ( $d_v$ ) mean diameter for Ni particles obtained by TEM analysis for all Ni/CeO<sub>2</sub>-x samples; (b) Relationship between Ni particle size and dispersion (measured by TEM) and Ni loading (determined by ICP-AES) for the as-prepared Ni/CeO<sub>2</sub>-x samples.

#### 4.4. Characterization studies of CeO<sub>2</sub>/ZnO and Ni/CeO<sub>2</sub>-ZnO oxides

##### 4.4.1 Textural/Structural Characterization

To gain a deeper understanding of the impact of ZnO on the CO<sub>2</sub> hydrogenation performance of Ni-based catalysts, a comprehensive characterization study was conducted. Initially, the textural properties were assessed through N<sub>2</sub> adsorption-desorption experiments, and the results are summarized in Table 4.6. The BET surface area values of the bare supports were determined to be 7.1 m<sup>2</sup>/g for ZnO and 79.3 m<sup>2</sup>/g for CeO<sub>2</sub> NR, while the mixed oxide, CeO<sub>2</sub>/ZnO, exhibited an intermediate value of 62.2 m<sup>2</sup>/g. Importantly, the introduction of nickel did not cause significant changes in the surface area of the supports. Additionally, the Ni-containing samples followed the same order as the bare supports in terms of surface area. Regarding the pore size of the samples, both CeO<sub>2</sub> NR and ZnO displayed similar values ranging from 23 to 24 nm. In contrast, the mixed oxide CeO<sub>2</sub>/ZnO exhibited a substantially higher pore size of 40.6 nm. Upon the addition of Ni, the pore size decreased for Ni/CeO<sub>2</sub> and Ni/CeO<sub>2</sub>-ZnO, while it increased for Ni/ZnO. The observed trends in pore size were inversely correlated with the BET surface area, meaning that Ni/CeO<sub>2</sub> had the smallest pore size (18.3 nm), followed by Ni/CeO<sub>2</sub>-ZnO (26.8 nm), and Ni/ZnO (43.6 nm). These

findings regarding the textural properties are further discussed in conjunction with the corresponding structural characteristics, which will be elaborated upon subsequently.

**Table 4.6.** Textural and structural properties of CeO<sub>2</sub>/ZnO and Ni/CeO<sub>2</sub>-ZnO.

Sample	BET Analysis		XRD Analysis				
	BET Surface Area (m <sup>2</sup> /g)	Average Pore Size (nm)	Lattice Parameter (nm)		Average crystallite diameter, D <sub>XRD</sub> (nm)		
			CeO <sub>2</sub> (111)	ZnO (101)	CeO <sub>2</sub> (111)	ZnO (101)	NiO (200)
CeO <sub>2</sub> NR	79.3	24.2	a = b = c = 0.5430	-	11.0	-	-
ZnO	7.1	23.0	-	a = b = 0.3272, c = 0.5233	-	34.7	-
CeO <sub>2</sub> /ZnO	62.2	40.6	a = b = c = 0.5430	a = b = 0.3262, c = 0.5225	11.5	44.0	-
Ni/ZnO	10.3	43.6	-	a = b = 0.3248, c = 0.5206	-	37.6	19.1
Ni/CeO <sub>2</sub>	72.0	18.3	a = b = c = 0.5410	-	10.6	-	14.4
Ni/CeO <sub>2</sub> -ZnO	61.1	26.8	a = b = c = 0.5404	a = b = 0.3248, c = 0.5197	10.8	36.5	20.8

The crystallographic properties of the samples were analyzed using X-ray diffraction (XRD), and the corresponding diffractograms are presented in Figure 4.9. For bare CeO<sub>2</sub>, characteristic peaks were observed at  $2\theta = 28.5^\circ$ ,  $33.1^\circ$ ,  $47.5^\circ$ , and  $56.3^\circ$ , which can be attributed to the (111), (200), (220), and (311) crystallographic planes, respectively<sup>92</sup>. These peaks are consistent with the face-centered cubic fluorite structure of ceria (Fm3m symmetry, no. 225, JCPDS card: 01-081-0792). Similarly, the XRD patterns of pure ZnO exhibited the typical hexagonal wurtzite structure (P63mc symmetry, no. 186) (JCPDS card: 01-079-0208). The main peaks observed at  $2\theta = 31.7^\circ$ ,  $34.4^\circ$ , and  $36.2^\circ$  can be attributed to the (100), (002), and (101) lattice planes, respectively<sup>118,119</sup>. In the case of the mixed oxide CeO<sub>2</sub>/ZnO, the XRD analysis revealed prominent reflection planes that perfectly matched those indexed for both cubic CeO<sub>2</sub> and hexagonal ZnO structures. This observation indicates the formation of a mixed oxide consisting of finely dispersed phases of the parent oxides. Additionally, upon the introduction of NiO, XRD peaks were detected at  $2\theta = 37.2^\circ$  and  $43.3^\circ$ , corresponding to the (101) and (012) crystal planes, respectively<sup>120</sup>. These peaks are associated with the characteristic cubic structure of nickel oxide (NiO) (Fm3m symmetry, no. 225, Reference code: 01-089-7130).

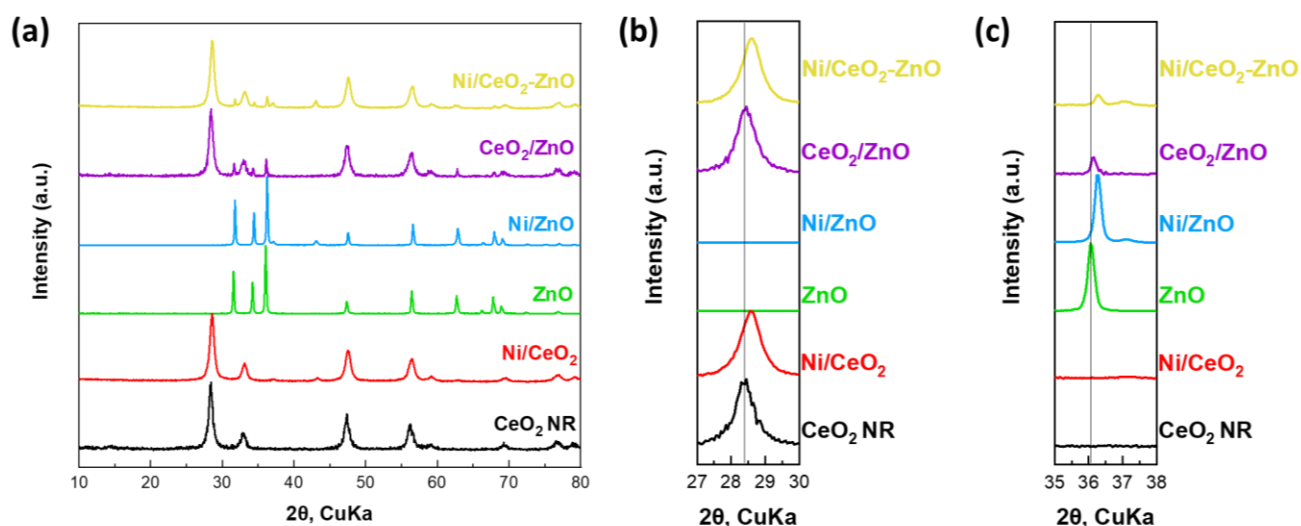


**Figure 4.9.** (a) XRD patterns of as-prepared samples; (b) the (111) diffraction peak of CeO<sub>2</sub>; (c) the (101) diffraction peak of ZnO.

The average crystallite size and lattice parameter values of the samples were determined using the Scherrer equation, and the results are summarized in Table 4.6. For the bare CeO<sub>2</sub>, the calculated crystallite size was found to be 11.0 nm. In contrast, the crystallite size of ZnO showed a significant increase, nearly three times larger at 34.7 nm. Upon incorporating ZnO into the CeO<sub>2</sub>/ZnO mixed oxide, the crystallite size of ceria exhibited a slight increase, while the crystallite size of ZnO experienced a more pronounced increase. Furthermore, with the impregnation of nickel, the crystallite sizes of ceria decreased slightly, indicating a subtle effect of nickel on the crystallite size of ceria. The NiO crystallite sizes were estimated based on the (200) planar reflection and followed the order: Ni/CeO<sub>2</sub> (14.4 nm) < Ni/ZnO (19.1 nm) < Ni/CeO<sub>2</sub>-ZnO (20.8 nm). This trend in NiO crystallite sizes corresponds to the trend observed for the crystallite sizes of the bare supports, suggesting that it is a direct outcome of the interactions between nickel and the respective supporting materials<sup>57</sup>.

Furthermore, the lattice parameters of CeO<sub>2</sub> (111) and ZnO (101) in the CeO<sub>2</sub>/ZnO sample remained practically unaffected compared to bare CeO<sub>2</sub> NR and ZnO, indicating a good dispersion of the different constituent oxide phases. However, a noticeable lattice contraction was observed in all Ni-based samples, as evidenced by the simultaneous decrease in the lattice parameters of ceria and zinc oxide phases<sup>105,108</sup>. This suggests the formation of a solid solution upon the addition of nickel into the bare supports. This lattice contraction can be clearly observed in the diffractograms near the most intense peaks of CeO<sub>2</sub> and ZnO, specifically at  $2\theta = 28.5^\circ$  and  $36.2^\circ$ , respectively (Figure 4.9 (b) and (c)). A distinct shift of the diffraction angle towards slightly higher values is apparent, indicating the overall lattice contraction of the parent oxides in all cases. These findings provide evidence for the

formation of a solid solution between the nickel, ceria, and zinc oxide phases, indicating a strong interaction and integration of these components within the catalyst structure. The lattice contraction observed suggests structural modifications and intimate mixing at the atomic level, potentially influencing the catalytic performance of the Ni-based samples<sup>104</sup>.

Moreover, in the XRD analysis of the Ni-based samples after the reaction (Figure 4.10), no detectable NiO peaks were observed. This can be attributed to the extensive reduction of the initially oxidized nickel species under the CO<sub>2</sub> hydrogenation reaction conditions. The reduction process converts NiO to metallic nickel, which does not exhibit characteristic XRD peaks in the studied range. Additionally, a quantitative XRD analysis was performed on the used Ni/CeO<sub>2</sub>-ZnO catalyst (Table 4.7). The results revealed that the crystallite sizes and lattice parameters of ceria and zinc oxide remained nearly unchanged compared to the fresh sample. This indicates the absence of significant sintering or phase reconstruction during the reaction<sup>121,122</sup>.

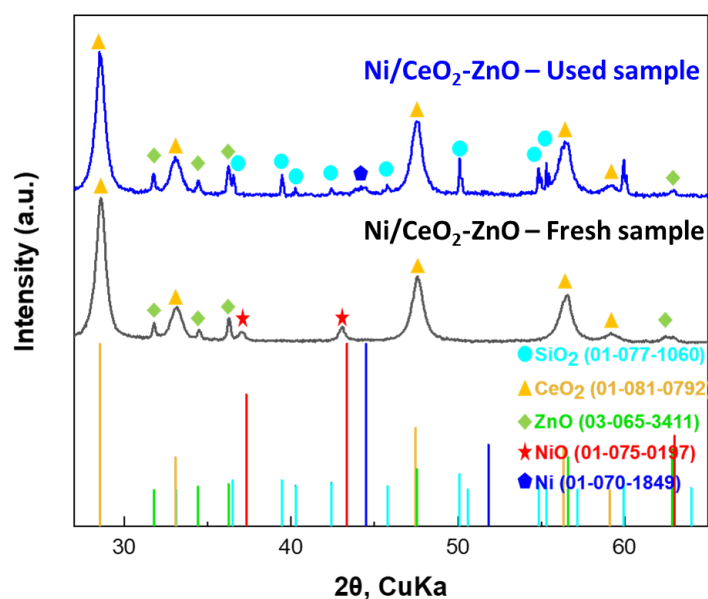


**Figure 4.10.** XRD plots for fresh and used Ni/CeO<sub>2</sub>-ZnO. SiO<sub>2</sub> peaks are present in all samples due to the physical mixing of fresh catalysts with silica glass before the reaction.

**Table 4.7.** Lattice parameters and crystallite sizes of fresh and used Ni/CeO<sub>2</sub>-ZnO.

Sample	Lattice parameter (nm)		Crystallite size (nm)	
	CeO <sub>2</sub> (111)	ZnO (101)	CeO <sub>2</sub> (111)	ZnO (101)
Ni/CeO <sub>2</sub> -ZnO - fresh	0.540	a = b = 0.325, c = 0.520	10.8	36.5
Ni/CeO <sub>2</sub> -ZnO - used	0.541	a = b = 0.325, c = 0.520	11.7	35.7

#### 4.4.2. Morphological Characterization

The morphological characteristics of the as-prepared samples were initially examined using scanning electron microscopy-energy-dispersive X-ray spectroscopy (SEM-EDS) (Figure 4.11). SEM images of the samples revealed no significant morphological alterations, indicating the structural stability of the catalysts during the reaction. EDX analysis was conducted to determine the surface nickel loading in the as-prepared samples. The results demonstrated that the surface nickel loading in the Ni/CeO<sub>2</sub> sample closely matched the nominal loading (approximately 8 wt.%). However, slightly lower but comparable values were obtained for Ni/ZnO and Ni/CeO<sub>2</sub>-ZnO (6.1% and 5.3%, respectively). This finding can be attributed to a combination of factors such as the low surface area of ZnO and the relatively larger size of nickel particles in the ZnO-containing samples. These observations are consistent with the XRD data (Table 4.6) and TEM analysis, which will be further discussed in the following section.

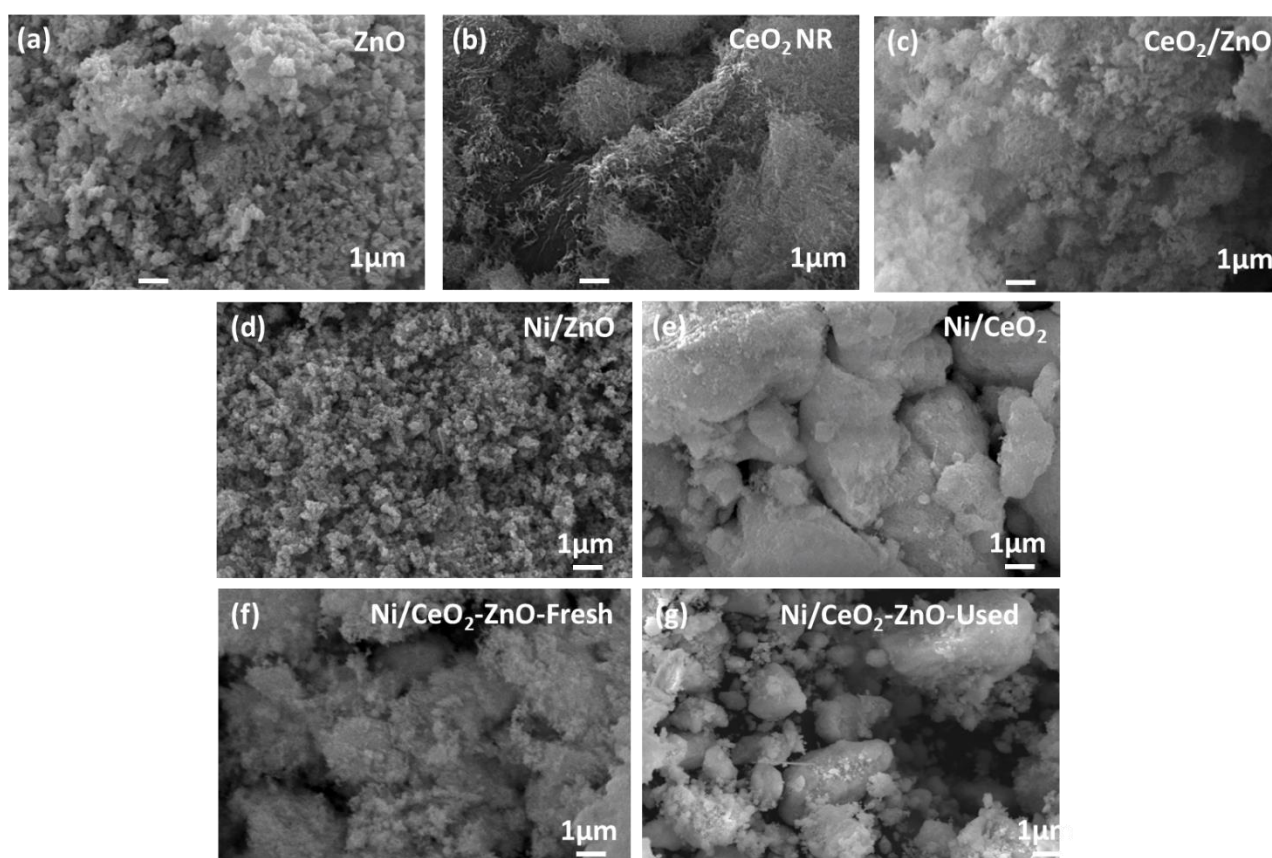


**Figure 4.11.** SEM images of the fresh and used samples.

Further insights into the morphology of the samples were obtained through transmission electron microscopy (TEM) analysis (Figure 4.12). Pure zinc oxide exhibits an irregular shape, with lengths ranging from 50 to 100 nm. On the other hand, bare ceria exhibits a rod-like morphology with

lengths ranging from 50 to 200 nm. The TEM analysis confirms the distinct morphologies of these individual oxides. In the case of the CeO<sub>2</sub>/ZnO sample, the TEM images demonstrate the presence of nanorods characteristic of ceria, indicating the preservation of the morphology of bare ceria. Additionally, irregularly-shaped, and isolated ZnO particles can also be observed in the mixed oxide structure. These findings align with the XRD results (Figure 4.9), further supporting the formation of distinct oxide phases within the CeO<sub>2</sub>/ZnO sample. When considering the Ni-based samples, it is evident that the addition of nickel does not induce significant modifications in the morphology of the parent oxide. The morphological features of bare ceria and pure zinc oxide are maintained in the Ni/CeO<sub>2</sub>, Ni/ZnO, and Ni/CeO<sub>2</sub>-ZnO samples, suggesting that the presence of nickel does not alter the original morphology of the individual oxide components.

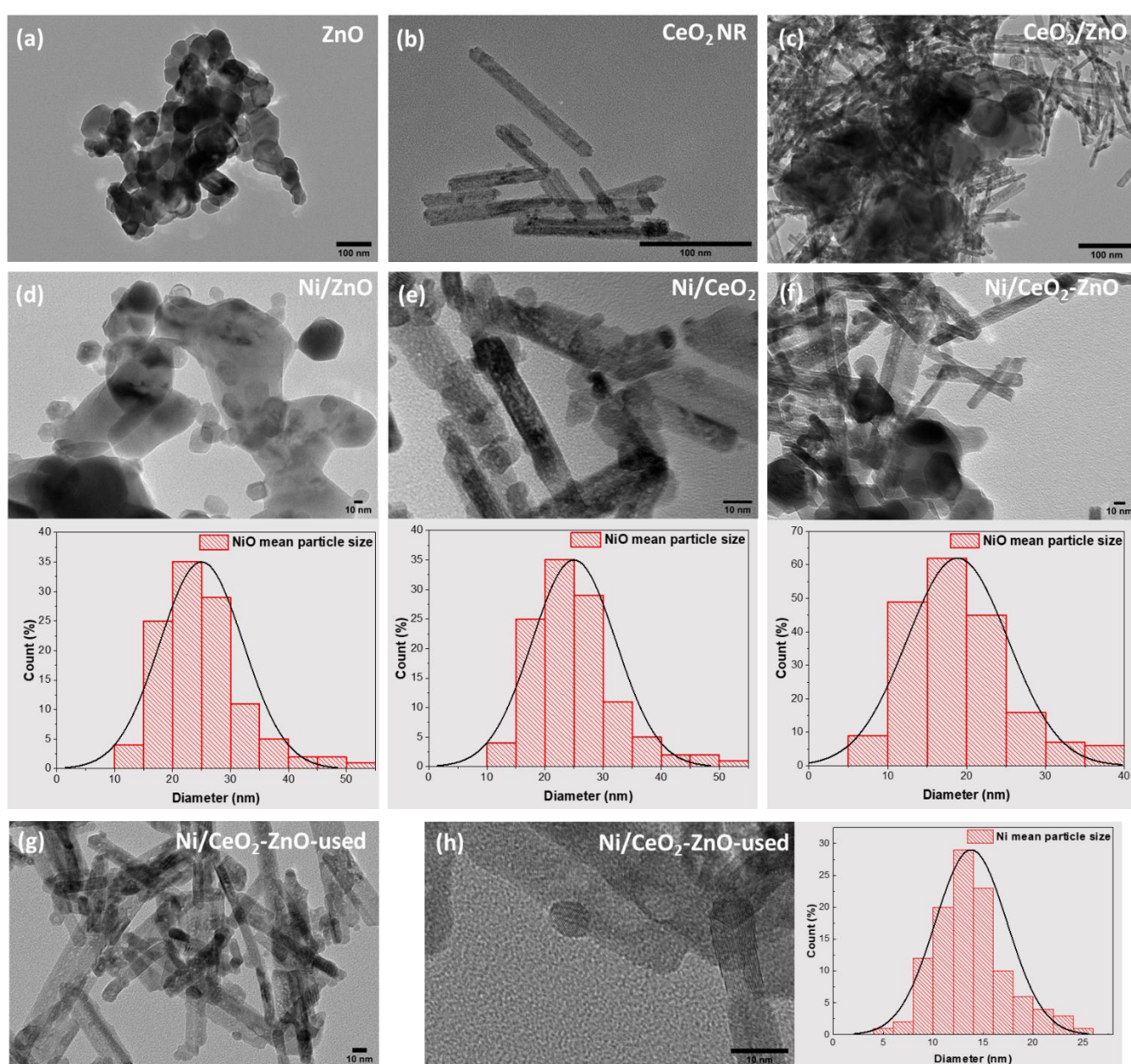


**Figure 4.12.** TEM images and histograms of the as-prepared samples.

In addition to the previous findings, high-resolution TEM (HRTEM) analysis was conducted to estimate the particle size of NiO in the samples. Since distinguishing between ZnO and NiO particles when both are deposited on ceria nanorods, the distinction was achieved by calculating the d-spacing values in indicative HRTEM images (Figure 4.13). The calculated d-spacing values matched the theoretical values specifically for NiO, providing validation that the measured particles indeed corresponded to the nickel oxide phase rather than ZnO.

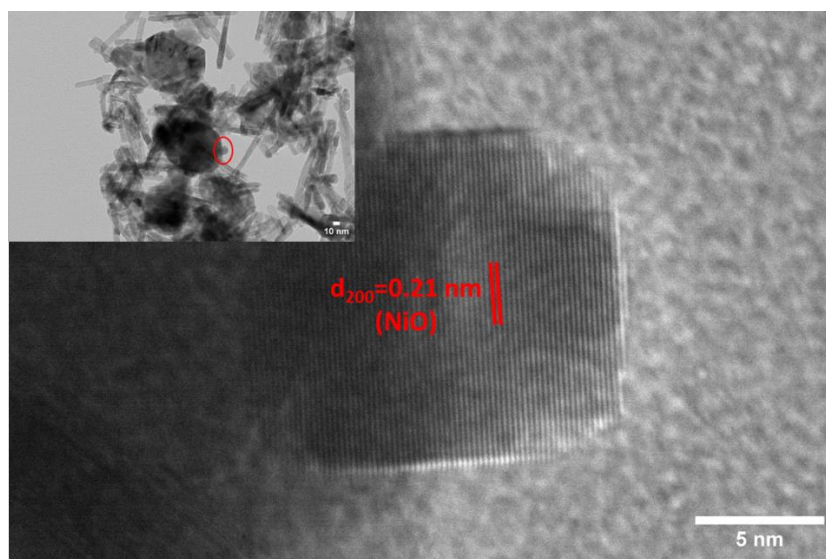


**Figure 4.13.** HRTEM images for the determination of the particle size of NiO in Ni/CeO<sub>2</sub>-ZnO sample.

To visualize the particle size distribution (PSD) of the NiO particles, histograms were constructed and presented in Figure 4.12. The PSD analysis revealed the following values for the NiO particle sizes: Ni/CeO<sub>2</sub> (9.7 nm) < Ni/CeO<sub>2</sub>-ZnO (19.1 nm) < Ni/ZnO (25.0 nm). These findings are in good agreement with the XRD values reported in Table 4.6. Moreover, a representative TEM image along with the respective PSD of the used Ni/CeO<sub>2</sub>-ZnO sample is displayed in Figure 4.12. The TEM image confirms that the nanorod morphology of ceria remains unchanged after the reaction. Importantly, no increase in the size of Ni particles was observed, indicating the absence of sintering or agglomeration under the reaction atmosphere.

#### 4.4.3. Raman spectroscopy

Figure 4.14 illustrates the Raman spectra of the bare supports as well as the Ni-based samples in the relevant spectral range of 300-800 cm<sup>-1</sup>. In the case of CeO<sub>2</sub> NR, a distinct peak is observed at approximately 460 cm<sup>-1</sup>, which is the most prominent peak. This peak corresponds to the optical Raman F<sub>2g</sub> mode of CeO<sub>2</sub> and is attributed to oxygen ions in CeO<sub>8</sub> moieties i.e., oxygen atoms

around  $\text{Ce}^{x+}$  in eightfold coordination (fluorite lattice) <sup>57,123,124</sup>. The Raman spectrum of pure ZnO exhibits a main Raman band at  $437\text{ cm}^{-1}$ , which corresponds to the high  $E_2$  phonon mode of bulk ZnO. Additionally, two smaller peaks are observed at approximately  $580$  and  $330\text{ cm}^{-1}$ , which are attributed to the acoustic overtone and  $E_1(\text{LO})$  modes, respectively <sup>125,126</sup>. As expected, the Raman spectrum of  $\text{CeO}_2/\text{ZnO}$  displays contributions from both pure ZnO and  $\text{CeO}_2$ . Importantly, upon the addition of ZnO into ceria, a red-shift and a decrease in the intensity of the  $F_{2g}$  peak are observed. This observation indicates a favorable dispersion of the two phases, suggesting good interaction and mixing between ZnO and  $\text{CeO}_2$  <sup>76,127</sup>.

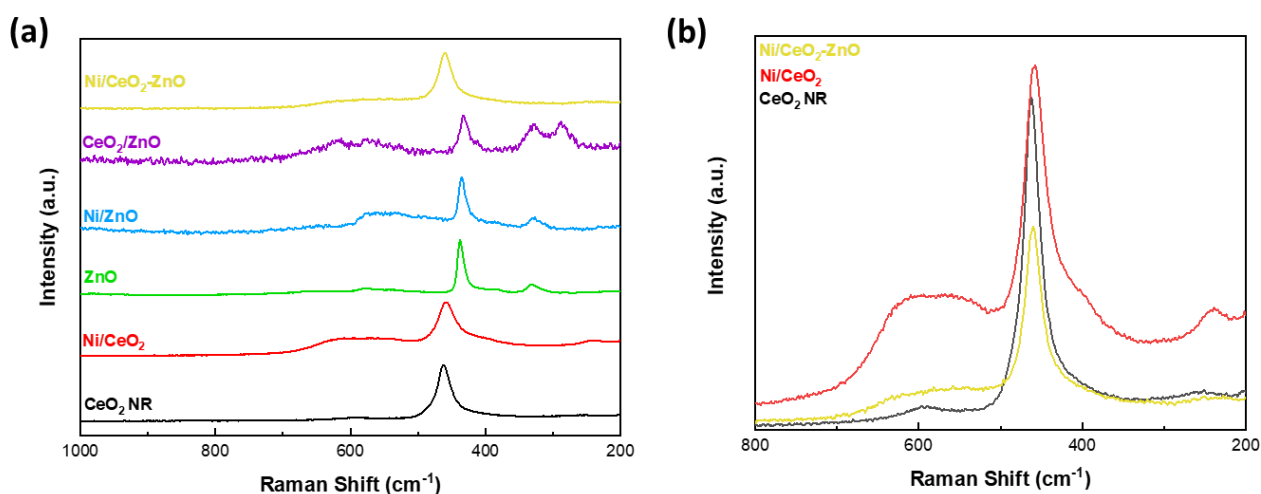


**Figure 4.14.** (a) Raman spectra for all samples; (b) Magnified spectra for  $\text{CeO}_2$  NR,  $\text{Ni}/\text{CeO}_2$ , and  $\text{Ni}/\text{CeO}_2\text{-ZnO}$  in the region  $200\text{--}800\text{ cm}^{-1}$ .

The incorporation of Ni induces significant changes in the Raman spectra of the bare supports. Notably, the peak intensities for the Ni-based samples follow the order:  $\text{Ni}/\text{CeO}_2 > \text{Ni}/\text{CeO}_2\text{-ZnO} > \text{Ni}/\text{ZnO}$ , indicating varying degrees of interaction between Ni and the support materials. In the case of  $\text{Ni}/\text{CeO}_2$ , a low-intensity secondary Raman band at around  $250\text{ cm}^{-1}$  is observed, which is attributed to the second-order  $A_{1g}$  mode of cerium oxide <sup>108,128</sup>. More importantly, a wide band between  $530$  to  $600\text{ cm}^{-1}$  is observed in the Raman spectra, and this feature is particularly pronounced in the case of  $\text{Ni}/\text{CeO}_2$  (Figure 4.14 (b)). Raman shifts in this region are commonly denoted as D or  $O_v$  bands and are associated with structure perturbations of the ceria lattice. These perturbations are related to the presence of punctual defects and oxygen vacancies, which are directly induced by the addition of the nickel phase, which leads to enhanced reducibility <sup>92,129</sup>.

Furthermore, a semi-quantitative assessment of the concentration of oxygen vacancies in ceria-based catalysts can be made by calculating the ratio of the intensities of the D and  $F_{2g}$  bands,  $I_D/I_{F_{2g}}$  (Table 4.8) <sup>102,113</sup>. The  $I_D/I_{F_{2g}}$  values for  $\text{CeO}_2$  NR,  $\text{Ni}/\text{CeO}_2\text{-ZnO}$ , and  $\text{Ni}/\text{CeO}_2$  were found to be 0.07, 0.21,

and 0.37, respectively. These values highlight the pronounced effect of the nickel-ceria synergy on the redox properties of Ni/CeO<sub>2</sub> compared to bare CeO<sub>2</sub> NR and Ni/CeO<sub>2</sub>-ZnO. The increase in the I<sub>D</sub>/I<sub>F<sub>2g</sub></sub> ratio indicates a higher concentration of oxygen vacancies and suggests enhanced redox activity in the Ni/CeO<sub>2</sub> catalyst. Additionally, the concentration of oxygen vacancies (referred to as N) can be estimated for all Ce-containing samples using an equivalent method described in Section 2.2 (Characterization Techniques)<sup>130</sup>. The calculated values for oxygen vacancy concentration in the bare supports were  $1.38 \times 10^{21} \text{ cm}^{-3}$  for CeO<sub>2</sub> NR and  $0.50 \times 10^{21} \text{ cm}^{-3}$  for Ni/ZnO. In contrast, for Ni/CeO<sub>2</sub> and Ni/CeO<sub>2</sub>-ZnO, the values were determined as  $2.27 \times 10^{21} \text{ cm}^{-3}$  and  $1.65 \times 10^{21} \text{ cm}^{-3}$ , respectively. These results provide further evidence of the combined beneficial effect of nickel and the inhibitory effect of zinc on the formation of oxygen vacancies in the as-synthesized samples. The observed red-shift of the F<sub>2g</sub> band in Ni/CeO<sub>2</sub>-ZnO and Ni/CeO<sub>2</sub> (Figure 4.14 (b)) can be attributed to lattice distortion induced by nickel and the resultant decrease in the Ce-O bond symmetry due to stronger interactions at the nickel-ceria interface, as well as the abundance of surface oxygen vacancies<sup>108</sup>. This finding aligns with the incorporation of nickel into the ceria lattice and the formation of a solid solution, as supported by the XRD analysis<sup>102,109,131</sup>.

**Table 4.8.** Redox properties of the Ni-based samples.

Sample	Raman Analysis		H <sub>2</sub> -TPR					
	I <sub>D</sub> /I <sub>F<sub>2g</sub></sub>	N (10 <sup>21</sup> × cm <sup>-1</sup> )	Peak Temperature (°C)			H <sub>2</sub> consumption (mmol H <sub>2</sub> /g <sub>cat</sub> ) <sup>a</sup>		
			α	β	γ	α	β	γ
Ni/ZnO	-	-	-	-	424	-	-	0.74
Ni/CeO <sub>2</sub>	0.37	2.27	176	303	-	0.29	1.43	-
Ni/CeO <sub>2</sub> -ZnO	0.21	1.65	264	-	451	0.26	-	0.88

<sup>a</sup>H<sub>2</sub> uptake was estimated by the quantification of the TPR peaks below 500 °C.

#### 4.4.4. Redox Properties (H<sub>2</sub>-TPR)

To gain further insights into the redox properties of the as-prepared samples, H<sub>2</sub>-TPR experiments were performed. Figure 4.15 (b) illustrates the reduction profiles of the Ni-based samples, while Table 4.8 presents the results from quantitative analysis. The addition of nickel into the bare supports has a significant positive impact on their overall reducibility, as evidenced by the larger reduction peaks and the shift towards lower temperatures compared to the corresponding bare support oxides (Figure 4.15 (a)). Notably, for Ni/CeO<sub>2</sub> and Ni/CeO<sub>2</sub>-ZnO, the onset reduction temperature is around 150 °C, whereas for Ni/ZnO, this temperature is significantly higher, at approximately 360 °C. This disparity demonstrates the beneficial effect of ceria in low-temperature reducibility. Specifically, in

the temperature range below 500 °C, Ni/CeO<sub>2</sub> exhibits two distinct reduction peaks. A low-temperature peak at 176 °C (peak  $\alpha$ ) and a prominent medium-temperature peak at 303 °C (peak  $\beta$ ) are observed. Similarly, Ni/CeO<sub>2</sub>-ZnO also shows peak  $\alpha$ , albeit at 264 °C, and a major high-temperature peak (peak  $\gamma$ ) at around 451 °C. In contrast, Ni/ZnO displays only a single high-temperature peak (peak  $\gamma$ ) at approximately 424 °C.

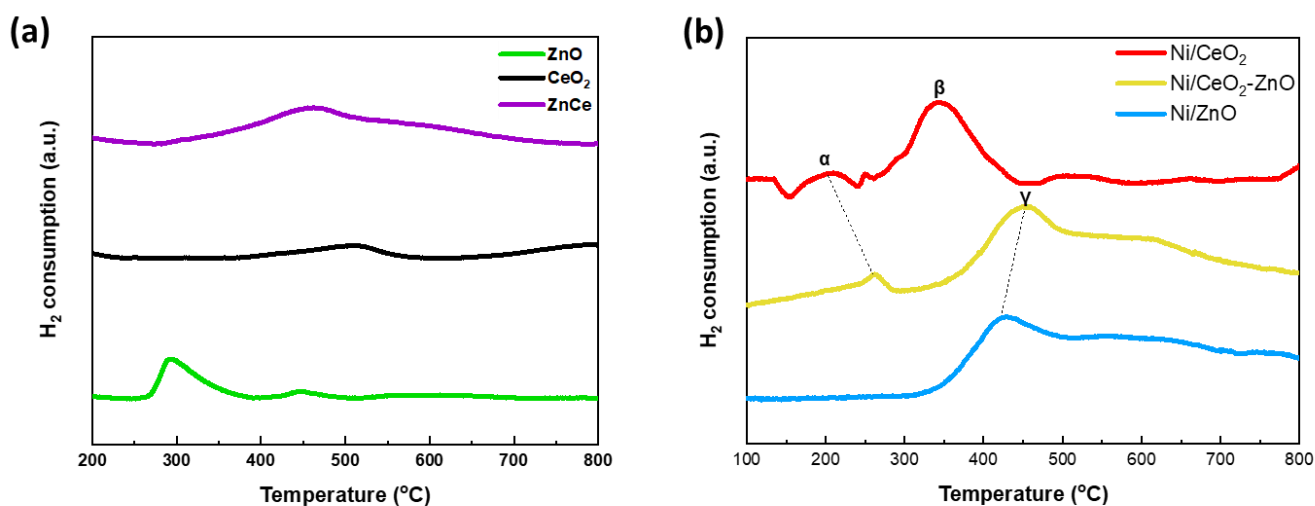


**Figure 4.15.** H<sub>2</sub>-TPR profiles of (a) bare supports; (b) Ni-based samples.

It is well-established that the reduction peaks of bare CeO<sub>2</sub> typically appear above 500 °C and are attributed to the successive removal of surface and bulk oxygen. Therefore, the low-temperature peaks observed in this study can be attributed to the reduction of various nickel species in the vicinity of the cerium oxide support<sup>92,132</sup>. Specifically, the first two peaks ( $\alpha$  and  $\beta$ ) are absent in the TPR profile of Ni/ZnO and are commonly associated with the reduction of nickel species, such as the general transition Ni<sup>2+</sup> → Ni<sup>0</sup>, and the partial reduction of the surface oxygen of CeO<sub>2</sub>, facilitated by the synergistic presence of nickel<sup>106,133</sup>. Peak  $\alpha$  can be attributed to various phenomena, including oxygen vacancies associated with the formation of the Ni-O-Ce structure, such as surface adsorbed O<sup>2-</sup>/O<sup>-</sup> species, or highly dispersive NiO. Peak  $\beta$ , on the other hand, is primarily ascribed to the reduction of NiO species that strongly interact with CeO<sub>2</sub><sup>95,113</sup>. It should be noted that the intensity of peak  $\alpha$  for Ni/CeO<sub>2</sub>-ZnO is lower compared to Ni/CeO<sub>2</sub>, suggesting differences in the reduction behavior between the two samples. Lastly, the broad reduction peak observed above 400 °C in Ni/ZnO and Ni/CeO<sub>2</sub>-ZnO (referred to as peak  $\gamma$ ) can be attributed to either free nickel oxide<sup>134</sup> or less reducible Ni<sup>2+</sup> species reacting with ZnO<sup>135,136</sup>.

To quantitatively analyze the H<sub>2</sub>-TPR results, the consumption of hydrogen for each peak was calculated (Table 4.8). As expected, the calculated H<sub>2</sub> consumption values attributed solely to peak  $\alpha$ ,

representing the reducibility of the samples in the low-temperature region ( $T < 500\text{ }^{\circ}\text{C}$ ), exhibit a monotonic decrease with increasing Zn content. This decrease indicates that the reduction of NiO in the Ni-ceria interface is predominantly a surface phenomenon, as supported by the results from Raman analysis<sup>108,137</sup>. Furthermore, the calculated hydrogen consumption for Ni/CeO<sub>2</sub> exceeds the theoretical amount required for the complete reduction of NiO to Ni (approximately 1.36 mmol H<sub>2</sub>/g<sub>cat</sub>). This result highlights the synergy between nickel and ceria, which facilitates the reduction of surface oxygen species in CeO<sub>2</sub>. However, the presence of ZnO significantly hampers this effect, as indicated by the total H<sub>2</sub> consumption values for Ni/ZnO and Ni/CeO<sub>2</sub>-ZnO, which are lower than the theoretical amount.

#### 4.5. Characterization studies of Bare Ceria Triangles (CeO<sub>2</sub> TR) and Ni/CeO<sub>2</sub> TR

##### 4.5.1 Textural/Structural Characterization

The main textural characteristics of the bare CeO<sub>2</sub> TR and Ni/CeO<sub>2</sub> TR are presented in Table 4.9. Bare CeO<sub>2</sub> TR demonstrates a BET surface area of 46.0 m<sup>2</sup>/g. However, upon incorporating Ni into the ceria support, a decrease in the BET area was observed.

**Table 4.9.** Textural characteristics of bare CeO<sub>2</sub> TR and Ni/CeO<sub>2</sub> TR.

Sample	EDS Analysis		BET Analysis
	Atomic ratio Ni/Ce	Ni loading (wt%)	BET Surface Area (m <sup>2</sup> /g)
CeO <sub>2</sub> TR	-	-	46.0
Ni/CeO <sub>2</sub> TR	0.26	8.1	28.3

The crystal structure analysis of the bare CeO<sub>2</sub> TR and Ni/CeO<sub>2</sub> TR samples was carried out using X-Ray Diffraction (XRD), and the corresponding XRD patterns are shown in Figure 4.16. For the bare CeO<sub>2</sub> TR sample, the XRD pattern revealed distinct peaks at  $2\theta = 28.5^{\circ}$ ,  $33.1^{\circ}$ ,  $47.5^{\circ}$ , and  $56.3^{\circ}$ , which can be attributed to the (111), (200), (220), and (311) crystal planes, respectively<sup>92</sup>. These peaks are indicative of the face-centered cubic fluorite structure of ceria (Fm3m symmetry, no. 225, Reference code: 00-043-1002). Upon the addition of NiO to the CeO<sub>2</sub> TR sample, the XRD pattern for the Ni/CeO<sub>2</sub> TR sample exhibited additional diffraction peaks. Specifically, at  $2\theta = 37.3^{\circ}$  and  $43.4^{\circ}$ , the observed peaks can be associated with the (111) and (200) crystal planes, respectively<sup>57,120</sup>. These peaks can be attributed to the typical cubic structure of NiO (Reference code: 01-075-0197). Therefore, the XRD analysis confirms that the Ni/CeO<sub>2</sub> TR sample exhibits a combination of

the face-centered cubic fluorite structure of ceria and the cubic structure of NiO, indicating the successful incorporation of nickel oxide into the ceria lattice.

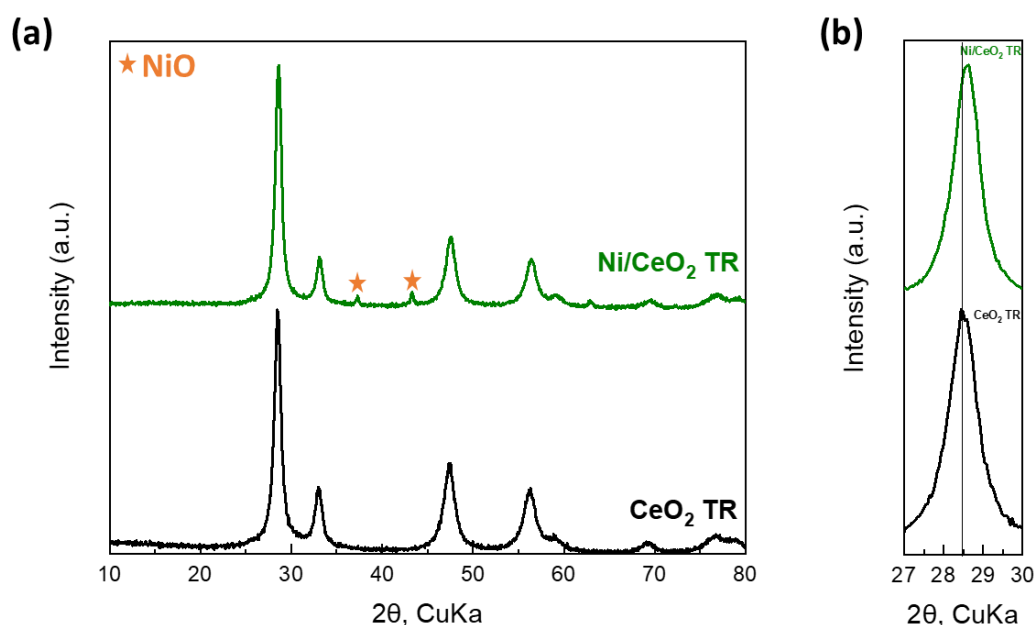


**Figure 4.16.** (a) XRD patterns of CeO<sub>2</sub> TR and Ni/CeO<sub>2</sub> TR; (b) the (111) diffraction peak of CeO<sub>2</sub>.

In addition to the XRD analysis, the average crystallite size ( $D_{\text{XRD}}$ ) of the as-obtained samples was determined using the Scherrer equation. The results are summarized in Table 4.10. The bare CeO<sub>2</sub> TR sample exhibited an average crystallite size of 9.1 nm. Upon the addition of NiO to the CeO<sub>2</sub> TR sample (Ni/CeO<sub>2</sub> TR), a small increase in the ceria crystallite size was observed, with a value of 9.9 nm, while the crystallite size of NiO was estimated to be ca. 28.0 nm. Furthermore, the d-spacing, lattice parameter, and unit cell volume were calculated based on the most intense planar reflection of CeO<sub>2</sub> (111) for the Ni/CeO<sub>2</sub> TR sample. It was found that these parameters were lower in the Ni/CeO<sub>2</sub> TR sample compared to the bare CeO<sub>2</sub> TR sample. This change in lattice parameters is also evident in the shift of the diffraction angle, as depicted in Figure 4.16 (b). The contraction of the ceria lattice in the Ni/CeO<sub>2</sub> TR sample can be attributed to the incorporation of nickel oxide, which has smaller ionic radii compared to cerium ions ( $r_{\text{Ce}^{+4}} > r_{\text{TM}}$ )<sup>94-96</sup>. The presence of these smaller ions in the ceria lattice causes a reduction in the interatomic distances and leads to a contraction of the lattice. This phenomenon is consistent with the observed changes in lattice parameters and the shift in the diffraction peaks.

**Table 4.10.** Structural, and morphological characteristics of bare CeO<sub>2</sub> TR and Ni/CeO<sub>2</sub> TR.

Sample	XRD Analysis			D <sub>XRD</sub> (nm)		TEM Analysis	Raman Analysis
	CeO <sub>2</sub> (111)		Unit Cell Volume (nm) <sup>3</sup>	CeO <sub>2</sub> (111)	NiO (200)	Ni particle size (nm)	I <sub>D</sub> /I <sub>F2g</sub>
	d <sub>(111)</sub> -spacing (nm)	Lattice Parameter (nm) a = b = c					
CeO <sub>2</sub> TR	0.313	0.5422	0.1594	9.1	-	-	0.024
Ni/CeO <sub>2</sub> TR	0.312	0.5406	0.1580	9.9	28.0	28.1 ± 6.0	0.63

#### 4.5.2. Morphological Characterization

The morphology of bare CeO<sub>2</sub> TR and Ni/CeO<sub>2</sub> TR was determined by SEM and TEM. More specifically, from SEM analysis, the CeO<sub>2</sub> TR sample exhibits a triangle-like morphology, as illustrated in Figure 4.17 (a). Ni/CeO<sub>2</sub> TR sample also displays a triangle-like morphology, while distinct NiO nanoparticles in contact with the triangle are detected (Figure 4.17 (b)). Additionally, the TEM images of bare ceria triangles and Ni/CeO<sub>2</sub> TR are depicted in Figure 4.17 (c) and (d), respectively. The triangle-like morphology of the CeO<sub>2</sub> is also confirmed through TEM analysis (Figure 4.17 (c)), while it remains unchanged with the incorporation of NiO (Figure 4.17 (d)). Moreover, separated NiO particles of sphere-like morphology are detected, as shown in Figure 4.17 (d). The mean particle size of NiO was estimated by TEM analysis and the results are presented in Figure 4.17 (d) and Table 4.10. From the particle size distribution (PSD) analysis, the NiO particle size was estimated at 28.1 nm, which is in full agreement with the XRD analysis (Table 4.10).

Field emission scanning electron microscopy analysis equipped with energy-dispersive X-ray spectrometry (EDS) was conducted to obtain the elemental mapping images of the Ni/CeO<sub>2</sub> TR sample (Figure 4.17 (e)). From FE-SEM/EDS analysis, it is evident that there is a uniform distribution of Ce and Ni in the Ni/CeO<sub>2</sub> TR sample. Additionally, the atomic ratio Ni/Ce and Ni loading (wt.%) were calculated by EDS analysis and the corresponding values are presented in Table 4.9. The calculated Ni/Ce and Ni loading values are 0.26 and 8.1 wt.%, respectively, which are consistent with the corresponding nominal values (0.25 Ni/Ce and 8 wt.% Ni). To further investigate the surface elemental composition of the Ni/CeO<sub>2</sub> TR sample, XPS analysis was also carried out, which is in good agreement with the aforementioned findings.

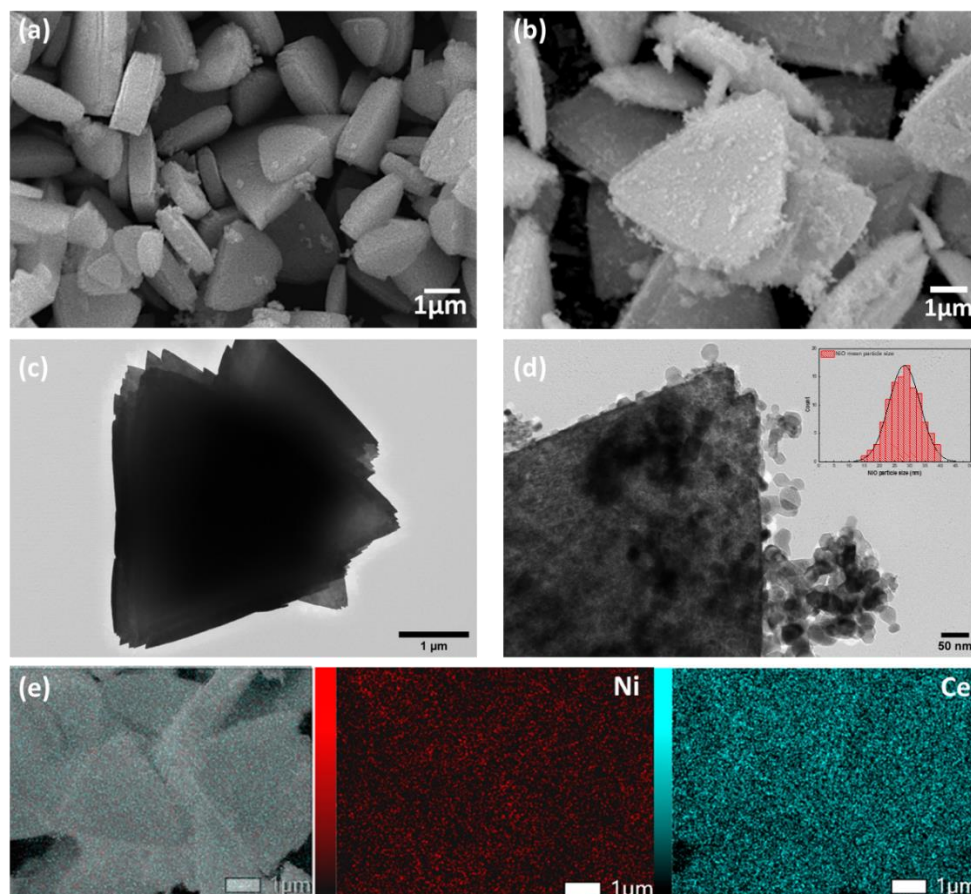


**Figure 4.17.** SEM images of the samples: (a) CeO<sub>2</sub> TR, (b) Ni/CeO<sub>2</sub> TR; TEM images of the samples: (c) CeO<sub>2</sub> TR, (d) Ni/CeO<sub>2</sub> TR; (e) SEM-EDS elemental mapping images of Ni/CeO<sub>2</sub> TR.

#### 4.5.3. Raman spectroscopy

Figure 4.18 depicts the Raman spectra of bare CeO<sub>2</sub> TR and Ni/CeO<sub>2</sub> TR samples. For bare CeO<sub>2</sub> TR support, the characteristic F<sub>2g</sub> mode at 457 cm<sup>-1</sup> is observed which is attributed to the Fm3m fluorite cubic ceria structure, and a weak band at ~250 cm<sup>-1</sup> which is ascribed to second-order transverse acoustic mode<sup>107</sup>. Moreover, a wide band in the 530 and 700 cm<sup>-1</sup> region, which is commonly called the defect-induced band (denoted as the "D" band), can be attributed to structural perturbations of the ceria cubic lattice<sup>107-109</sup>. With the addition of NiO into ceria, a small red shift of the F<sub>2g</sub> peak is observed, as well as a decrease in intensity, demonstrating the good dispersion of the two phases<sup>103</sup>. In addition, in the case of Ni/CeO<sub>2</sub> TR, the wide D band significantly exhibits increased intensity, which is related to punctual defects and oxygen vacancies due to the incorporation of NiO. Therefore, the I<sub>D</sub>/I<sub>F2g</sub> ratio is associated with the abundance of structural defects<sup>102,113</sup>. I<sub>D</sub>/I<sub>F2g</sub> values for both CeO<sub>2</sub> TR and Ni/CeO<sub>2</sub> TR were calculated and presented in Table 4.10. Particularly, the I<sub>D</sub>/I<sub>F2g</sub> ratio for bare CeO<sub>2</sub> TR is very low (0.024) while a significant increase in this ratio is observed for Ni/CeO<sub>2</sub> TR (0.630), revealing the remarkable impact of the nickel-ceria synergy on the redox properties of Ni/CeO<sub>2</sub> TR.

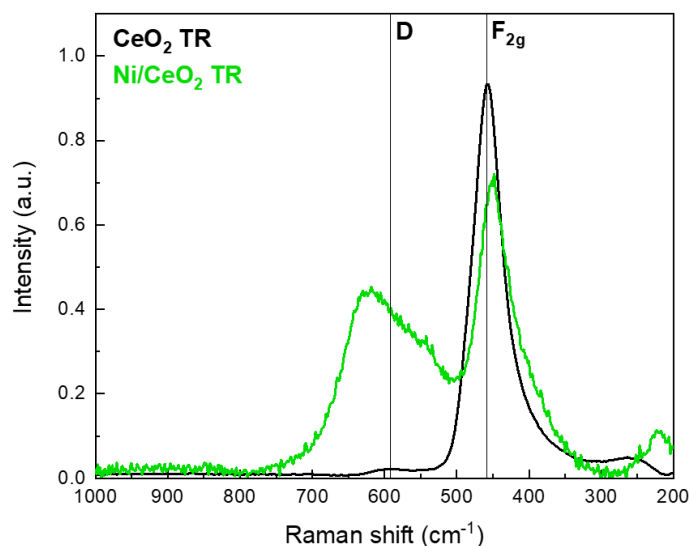


**Figure 4.18.** Raman spectra for bare CeO<sub>2</sub> TR and Ni/CeO<sub>2</sub> TR.

#### 4.5.4. Surface Analysis (XPS)

To further gain insight into the effect of the addition of NiO into ceria on the chemical composition and oxidation state of the samples, XPS analysis was carried out. Figure 4.19 (a) shows the Ce 3d XPS spectra of bare CeO<sub>2</sub> TR and Ni/CeO<sub>2</sub> TR samples. The Ce3d curves were deconvoluted into ten peaks. More specifically, the "u" peaks refer to the spin-orbit coupling 3d<sub>5/2</sub> while the "v" peaks correspond to the spin-orbit coupling 3d<sub>3/2</sub><sup>138–140</sup>. The v' (903.6 eV), v''' (898.9 eV), u' (885.5 eV), and u''' (881.0 eV) peaks are attributed to Ce<sup>3+</sup> and the v<sub>0</sub> (917.0 eV), v (907.9 eV), v'' (901.3 eV), u<sub>0</sub> (897.2 eV), u (888.9 eV), and u'' (882.9 eV) are ascribed to Ce<sup>4+</sup><sup>138,140</sup>.

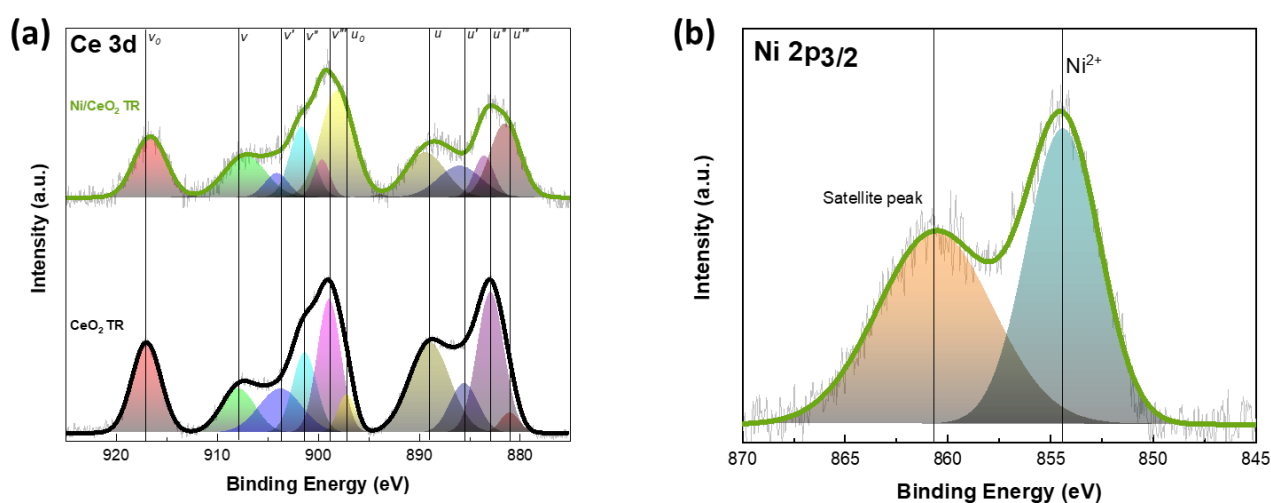


**Figure 4.19.** (a) XPS spectra of Ce 3d for bare CeO<sub>2</sub> TR and Ni/CeO<sub>2</sub> TR; (b) XPS spectrum of Ni 2p<sub>3/2</sub> for Ni/CeO<sub>2</sub> TR.

Additionally, Table 4.11 summarizes the results obtained from XPS analysis for both bare CeO<sub>2</sub> TR and Ni/CeO<sub>2</sub> TR. The ratio of Ce<sup>3+</sup> ions to the whole peak area in the Ce 3d region is calculated from the area ratio of the sum of the Ce<sup>3+</sup> species to that of the total cerium species. Bare CeO<sub>2</sub> exhibits a 25.6% amount of the Ce<sup>3+</sup> species while Ni/CeO<sub>2</sub> TR shows a higher population of Ce<sup>3+</sup> ions (44.8%) than the bare ceria sample. These findings indicate the presence of more oxygen vacancies, in the case of Ni/CeO<sub>2</sub> TR compared to that of support material which is in good agreement with the Raman analysis. The high-resolution spectrum of Ni 2p<sub>3/2</sub> is presented in Figure 4.19 (b). The presence of Ni<sup>2+</sup> was detected on the surface of the Ni/CeO<sub>2</sub> catalyst.

**Table 4.11.** XPS results of bare CeO<sub>2</sub> TR and Ni/CeO<sub>2</sub> TR samples.

Sample	Ce (%)	Ni (%)	O (%)	Ni/Ce	Ce <sup>3+</sup> (%)
CeO <sub>2</sub> TR	23.9	-	76.1	-	25.6
Ni/CeO <sub>2</sub> TR	55.3	15.1	29.6	0.27	44.8

#### 4.5.5. Redox Properties (H<sub>2</sub>-TPR)

TPR experiments were also conducted to investigate the redox properties of the as-prepared samples. Figure 4.20 presents the reduction profiles of bare CeO<sub>2</sub> TR and Ni/CeO<sub>2</sub> TR. Bare CeO<sub>2</sub> TR consists of two broad peaks centered at ca. 500 °C and 860 °C and can be ascribed to the reduction of surface oxygen (O<sub>s</sub>) and bulk oxygen (O<sub>b</sub>) of ceria, respectively<sup>141</sup>. The addition of nickel into the bare supports has a significant positive impact on their overall reducibility, as evidenced by the larger reduction peaks and the shift towards lower temperatures compared to the corresponding bare support oxides. Specifically, for Ni/CeO<sub>2</sub>, the reduction onset temperature is around 150 °C while in the temperature range below 500 °C, Ni/CeO<sub>2</sub> exhibits two distinct reduction peaks. A low-temperature peak at 271 °C and a prominent medium-temperature peak at 368 °C are observed.

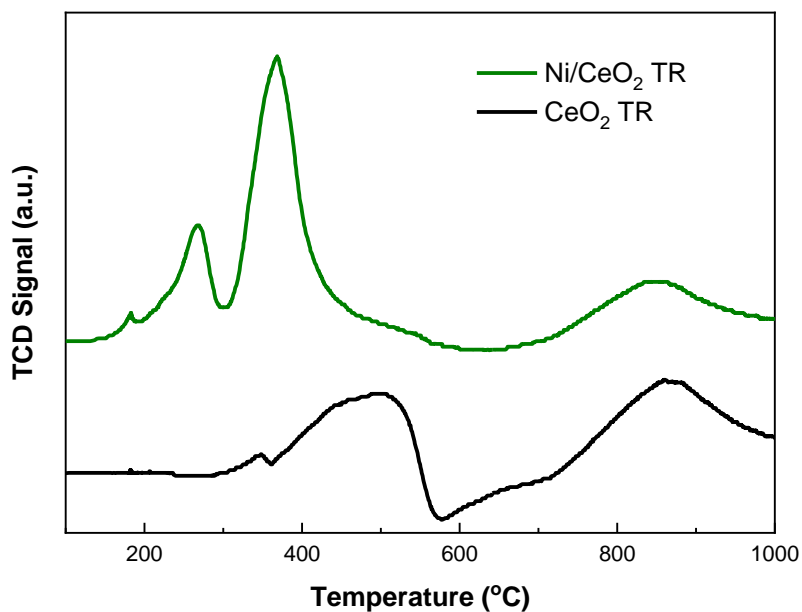


**Figure 4.20.** H<sub>2</sub>-TPR profiles of bare CeO<sub>2</sub> TR and Ni/CeO<sub>2</sub> TR.

## 4.6. Implication in the CO<sub>2</sub> hydrogenation reaction

### 4.6.1. CO<sub>2</sub> Hydrogenation Performance of Bare Ceria Nanorods (CeO<sub>2</sub> NR) and Ceria-Based Transition Metal Catalysts

A series of M/CeO<sub>2</sub> samples was synthesized, where M represents 3d transition metals including Ti, V, Cr, Mn, Fe, Co, Ni, and Cu. The catalytic performance of these samples in the CO<sub>2</sub> hydrogenation reaction was investigated over a temperature range of 200–500 °C. As a reference sample, a commercial CeO<sub>2</sub> sample (Fluka,  $S_{\text{BET}} = 15 \text{ m}^2 \text{ g}^{-1}$ ), denoted as CeO<sub>2</sub>-com, was also tested.

Figure 4.21 illustrates the CO<sub>2</sub> conversion of all samples compared to the thermodynamic equilibrium CO<sub>2</sub> conversion profiles for methanation and reverse water-gas shift (rWGS) reactions. The results reveal significant differences among the samples, primarily influenced by the nature of the metal. The order of CO<sub>2</sub> conversion is as follows: V/CeO<sub>2</sub> < Ti/CeO<sub>2</sub> < Mn/CeO<sub>2</sub> < Cr/CeO<sub>2</sub> < CeO<sub>2</sub> < Fe/CeO<sub>2</sub> < Cu/CeO<sub>2</sub> < Co/CeO<sub>2</sub> < Ni/CeO<sub>2</sub>, highlighting the pivotal role of the metal phase. Among the samples, Ni/CeO<sub>2</sub> exhibits the highest performance, achieving approximately 98% conversion at 300 °C. This indicates that the combination of nickel with ceria nanorods results in extremely active CO<sub>2</sub> methanation catalysts, which reach equilibrium at very low temperatures, around 300 °C. The superior catalytic activity of the nanoceria samples compared to CeO<sub>2</sub>-com clearly demonstrates the beneficial effect of the synthesis method.

Notably, CO<sub>2</sub> conversion initially increases and reaches a plateau for the highly selective Ni/CeO<sub>2</sub> and Co/CeO<sub>2</sub> catalysts, which promote the exothermic CO<sub>2</sub> methanation below 500 °C, in agreement with thermodynamic calculations. A different trend is observed for bare CeO<sub>2</sub>, V/CeO<sub>2</sub>, Ti/CeO<sub>2</sub>,

Mn/CeO<sub>2</sub>, Cr/CeO<sub>2</sub>, Fe/CeO<sub>2</sub>, and Cu/CeO<sub>2</sub> samples, where CO<sub>2</sub> conversion increases steadily but to a lesser extent, practically reaching equilibrium values for the rWGS reaction in the case of Cu/CeO<sub>2</sub>. The V/CeO<sub>2</sub>, Ti/CeO<sub>2</sub>, Mn/CeO<sub>2</sub>, and Cr/CeO<sub>2</sub> samples exhibit inferior catalytic activity compared to bare CeO<sub>2</sub> NR. However, no direct correlation can be established between the atomic number of the transition metal and CO<sub>2</sub> conversion. These findings indicate that the presence of an active metal phase with at least partially filled 3d orbitals (e.g., [Ar] 3d<sup>8</sup> 4s<sup>2</sup>) is necessary for adequate catalytic activity. Furthermore, the presence of multiple pairs of 3d electrons possibly leads to peculiar electronic phenomena attributed to the complex and strong metal-support interactions in the presence of CeO<sub>2</sub>. These phenomena cannot be solely attributed to the electron configuration of the metal phase.

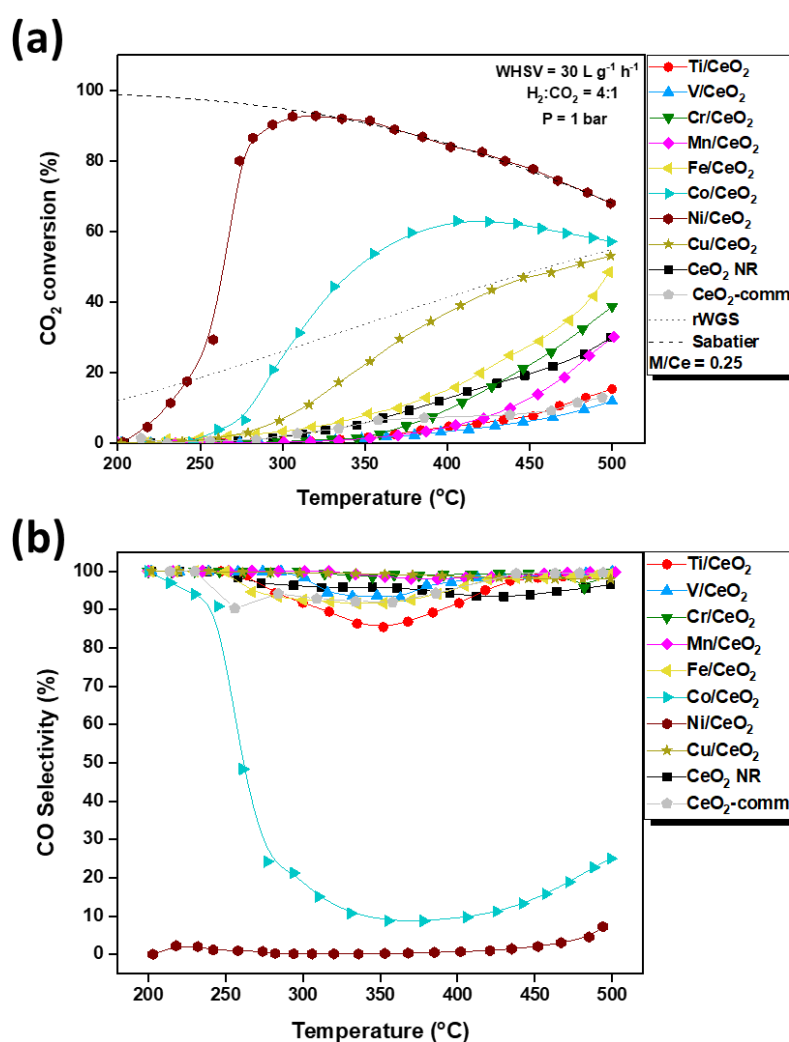


**Figure 4.21.** Catalytic evaluation of M/CeO<sub>2</sub> NR. (a) CO<sub>2</sub> conversion, (b) CO selectivity. Reaction conditions: WHSV = 30 L·g<sup>-1</sup>·h<sup>-1</sup>, H<sub>2</sub>:CO<sub>2</sub> = 4, P = 1 atm.

The impact of the metal phase's nature on the CO<sub>2</sub> hydrogenation performance is further evaluated by considering the selectivity towards CO, as depicted in Figure 4.21 (b). It is apparent that

commercial ceria, CeO<sub>2</sub> NR, Cu/CeO<sub>2</sub>, V/CeO<sub>2</sub>, Ti/CeO<sub>2</sub>, Mn/CeO<sub>2</sub>, and Cr/CeO<sub>2</sub> samples exhibit high selectivity towards CO (> 90%). Consequently, these samples are expected to have maximum CO<sub>2</sub> conversion values closer to the equilibrium of the reverse water-gas shift (rWGS) reaction, which is a less favorable reaction compared to CO<sub>2</sub> methanation, as shown by the dotted equilibrium curve in Figure 4.21 (a). Interestingly, Cu/CeO<sub>2</sub> reaches equilibrium conversion values at approximately 380 °C, which is lower than those reported for many rWGS catalysts. In contrast, the addition of cobalt and nickel into CeO<sub>2</sub> results in a completely different trend. The selectivity towards CH<sub>4</sub> for Co/CeO<sub>2</sub> samples is approximately 95% at temperatures above 400 °C. However, at temperatures below 400 °C, the selectivity towards CO is significant, but it decreases rapidly with higher temperatures. Remarkably, Ni/CeO<sub>2</sub> sample exhibit practically complete selectivity towards methane across the entire range of the investigated reaction temperatures, with only traces of CO being detected at any temperature.

The observed variations in activity and selectivity among the metal-based catalysts can be understood by considering the underlying mechanism of the CO<sub>2</sub> hydrogenation reaction, in conjunction with the characterization results obtained. The rate-determining step of the CO<sub>2</sub> methanation process is typically the dissociation of adsorbed CO, which occurs through two main pathways: direct CO adsorption dissociation and H-assisted CO adsorption dissociation. Group VIII metal-based catalysts, such as Co, are known to favor the first mechanism<sup>142,143</sup>. Liu et al.<sup>43</sup> demonstrated that Co exhibits more favorable thermodynamics and lower CO<sub>2</sub> decomposition barriers for CO<sub>2</sub> reduction compared to Cu. Similarly, a close correlation has been found between the CO<sub>2</sub> and H<sub>2</sub> adsorption capacity of Co/KIT-6 catalysts and their CO<sub>2</sub> conversion/selectivity performance<sup>144</sup>. A high H<sub>2</sub> adsorption capacity can provide many active H species for the further hydrogenation of intermediate species (such as HCOO<sup>-</sup>) to methane, thereby favoring methane formation. Conversely, a low H<sub>2</sub> adsorption and activation capacity promotes CO formation.

In contrast, a redox mechanism has been proposed in the literature for the reverse water-gas shift (rWGS) reaction over Cu-based catalysts<sup>24,145</sup>. According to this mechanism, Cu<sup>0</sup> atoms serve as active sites for the dissociation of CO<sub>2</sub>, and the resulting Cu<sub>2</sub>O is subsequently reduced by hydrogen to regenerate metallic Cu species. It has been suggested that hydrogen acts solely as a reducing agent in the rWGS reaction and does not directly participate in the formation of intermediate species<sup>146</sup>. The facile reduction of Cu/CeO<sub>2</sub> catalysts to reduced copper species at temperatures lower than approximately 300 °C, as evidenced by the H<sub>2</sub>-TPR results (Figure 4.4), could potentially support this redox mechanism. This may explain the high selectivity towards CO even at low temperatures.

The superior performance of Ni/CeO<sub>2</sub> catalysts can be attributed to the enhanced reducibility and oxygen mobility provided primarily by ceria nanorods, as previously reported<sup>92</sup>. This is consistent

with the abundance of reduced  $\text{Ce}^{3+}$  species, as observed in the  $\text{H}_2$ -TPR analyses (discussed above). Nickel exhibits the ability to readily dissociate molecular hydrogen into  $\text{H}_{(\text{ad})}$  atoms on the catalytic surface<sup>75</sup>. These  $\text{H}_{(\text{ad})}$  species can then migrate to the ceria support through an activated surface diffusion process, facilitating the hydrogenation of species formed upon  $\text{CO}_2$  adsorption, predominantly at the Ni-ceria interface, leading to methane formation<sup>147</sup>. Recent isotopic and in situ DRIFTS studies have further demonstrated that the higher methanation activity of Ni/ $\text{CeO}_2$  compared to Ni/ $\text{Al}_2\text{O}_3$  catalysts can be primarily attributed to the interactions between nickel and ceria, as well as the high oxygen mobility of ceria, which prevents the accumulation of water and carbon-containing species on the catalyst surface. Similarly, the increased methanation activity of  $\text{CeO}_2$ -based samples has been attributed to the high concentration of  $\text{Ce}^{3+}$  species, which promotes  $\text{CO}_2$  adsorption and the formation of formate active species, leading to higher coverage<sup>140,147</sup>. Furthermore, Ni/ $\text{CeO}_2$  catalysts have been found to exhibit greater activity for  $\text{CO}_2$  methanation compared to other lanthanide-supported nickel catalysts, primarily due to the strong interaction between nickel and ceria, along with the high  $\text{H}_2$  dissociation ability of reduced nickel sites<sup>56</sup>. Thus, based on the findings of these studies, the superior performance of Ni/ $\text{CeO}_2$  catalysts can be attributed to the synergistic interactions between nickel particles and ceria nanorods, which enhance the reducibility, particularly the high population of  $\text{Ce}^{3+}$  species under reaction conditions, ultimately leading to improved  $\text{CO}_2$  methanation performance.

#### 4.6.2. $\text{CO}_2$ Hydrogenation Performance of Ni/ $\text{CeO}_{2-x}$

The catalytic evaluation results of the Ni/ $\text{CeO}_{2-x}$  ( $x = \text{Ni}/\text{Ce} = 0.10, 0.25, 0.50, 1.00, \text{ and } 1.50$ ) in the  $\text{CO}_2$  hydrogenation reaction are presented in Figure 4.22 (a). To provide a basis for comparison, complementary experiments were conducted using the as-prepared bare  $\text{CeO}_2$  nanorods, as well as commercial NiO and  $\text{CeO}_2$  powders (Sigma Aldrich, > 99.5%), referred to as NiO-comm and  $\text{CeO}_2$ -comm, respectively. To ensure consistency, the commercial samples were also subjected to an in-situ reduction step under pure  $\text{H}_2$  flow at 400 °C for 1 h prior to the reaction.

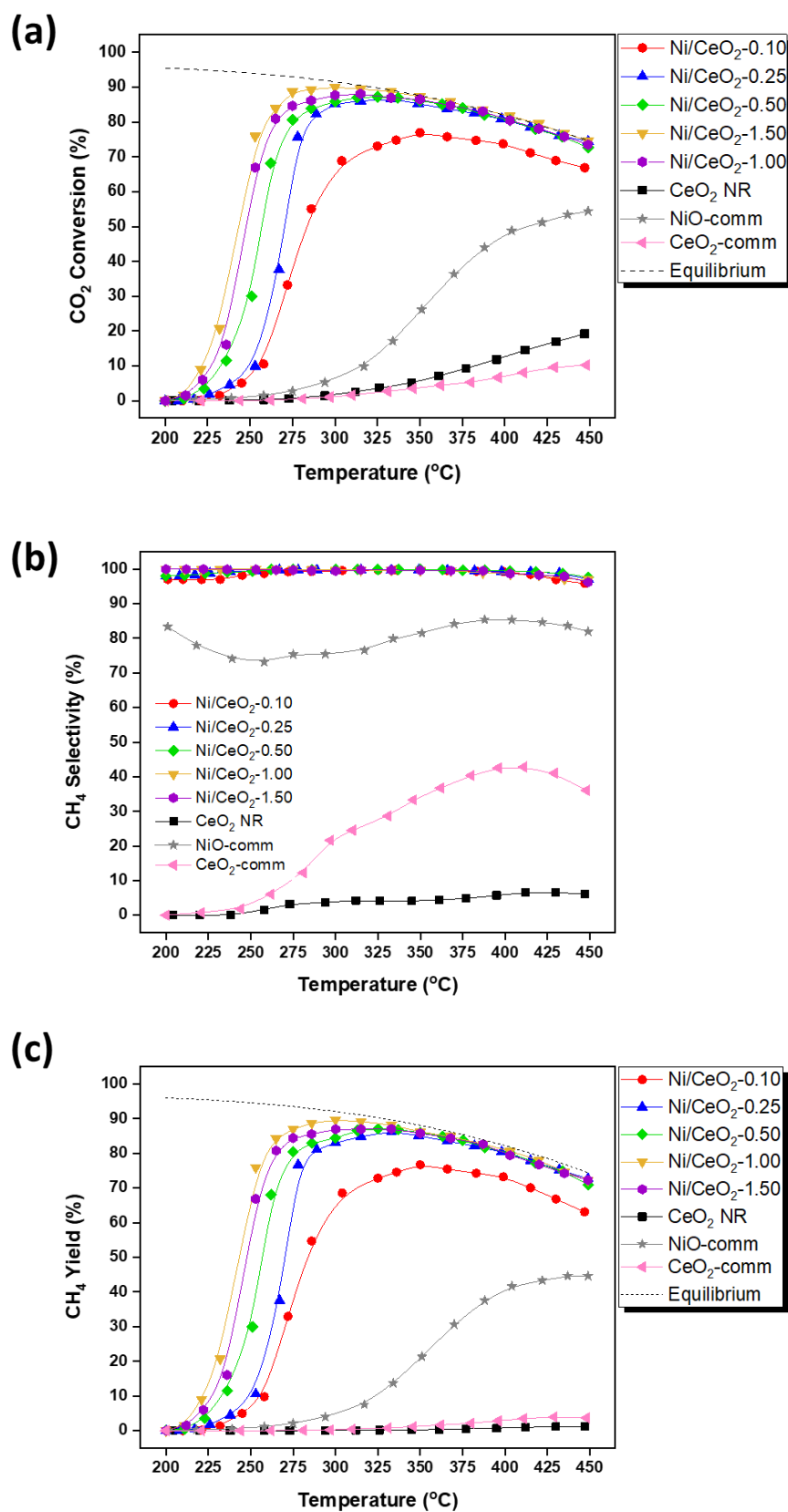


**Figure 4.22.** (a) CO<sub>2</sub> conversion, (b) CH<sub>4</sub> selectivity and (c) CH<sub>4</sub> yield values for all samples as a function of temperature. Reaction conditions: H<sub>2</sub>:CO<sub>2</sub> = 4, P=1 atm, WHSV = 30 L g<sup>-1</sup> h<sup>-1</sup>.

Clearly, increasing the reaction temperature enhances the conversion of CO<sub>2</sub> for all samples. Additionally, the beneficial effect of Ni addition to CeO<sub>2</sub> nanorods is evident, as it leads to a significant improvement in catalytic activity across all Ni/CeO<sub>2</sub>-x samples, even in the case of the catalyst with the lowest nickel loading, Ni/CeO<sub>2</sub>-0.10. The order of CO<sub>2</sub> conversion is as follows: Ni/CeO<sub>2</sub>-1.00 < Ni/CeO<sub>2</sub>-1.50 < Ni/CeO<sub>2</sub>-0.50 < Ni/CeO<sub>2</sub>-0.25 < Ni/CeO<sub>2</sub>-0.10 < NiO-comm < CeO<sub>2</sub>-NR < CeO<sub>2</sub>-comm. This suggests the existence of an optimum Ni loading for CO<sub>2</sub> conversion, which is determined to be 23.5 wt.% based on Table 4.4. Remarkably, the Ni/CeO<sub>2</sub>-1.00 sample exhibits a maximum CO<sub>2</sub> conversion of approximately 92% at a remarkably low temperature of 275 °C, indicating its exceptional low-temperature methanation activity. Notably, all Ni/CeO<sub>2</sub>-0.50, Ni/CeO<sub>2</sub>-1.00, and Ni/CeO<sub>2</sub>-1.50 samples outperform the Ni/CeO<sub>2</sub>-0.25 sample tested in our preliminary study, which showed maximum CO<sub>2</sub> conversion at around 300 °C (see above). This effect is particularly pronounced at temperatures below 275 °C, highlighting the superior intrinsic activity of these samples towards CO<sub>2</sub> methanation under kinetic conditions.

The selectivity of the samples towards CH<sub>4</sub> is shown in Figure 4.22 (b). Carbon monoxide (CO) was the only other product, although CO selectivity values are not shown for the sake of brevity. It is evident that all Ni/CeO<sub>2</sub>-x samples exhibit near-complete selectivity towards methane production, while NiO-comm shows intermediate CH<sub>4</sub> selectivity values ranging from 70% to 80%. Importantly, the bare ceria samples, CeO<sub>2</sub> NR and CeO<sub>2</sub>-comm, predominantly exhibit selectivity towards CO production via the reverse water-gas shift (rWGS) reaction. These results strongly indicate the presence of a synergistic effect between nickel and ceria nanoparticles, as well as the indispensability of the nickel phase up to an optimum Ni content for achieving efficient low-temperature CO<sub>2</sub> methanation activity. This is further illustrated by the corresponding CH<sub>4</sub> yield values shown in Figure 4.22 (c). Additionally, the observed catalytic trend for CeO<sub>2</sub> NR and Ni/CeO<sub>2</sub>-x aligns with the trend observed for the I<sub>D</sub>/I<sub>F2g</sub> ratio, as shown in Figure 4.6.

#### 4.6.3. CO<sub>2</sub> Hydrogenation Performance of CeO<sub>2</sub>/ZnO and Ni/CeO<sub>2</sub>-ZnO oxides

The catalytic performance of CeO<sub>2</sub>/ZnO-x and Ni/CeO<sub>2</sub>-ZnO-x (where x = Zn/Ce = 0.2, 0.4, 0.6) was evaluated in the CO<sub>2</sub> hydrogenation reaction. Initially, the influence of the Zn/Ce ratio was investigated for bare supports (CeO<sub>2</sub>/ZnO-x) as well as Ni-based samples (Ni/CeO<sub>2</sub>-ZnO-x) (Figure 4.23). It is worth noting that no significant variations were observed among the samples with different Zn/Ce ratios (0.2, 0.4, 0.6). Therefore, this discussion will primarily focus on the results obtained from the samples with a Zn/Ce ratio of 0.4. For simplicity, the sample Ni/CeO<sub>2</sub>-ZnO-0.4 will be subsequently referred to as Ni/CeO<sub>2</sub>-ZnO.

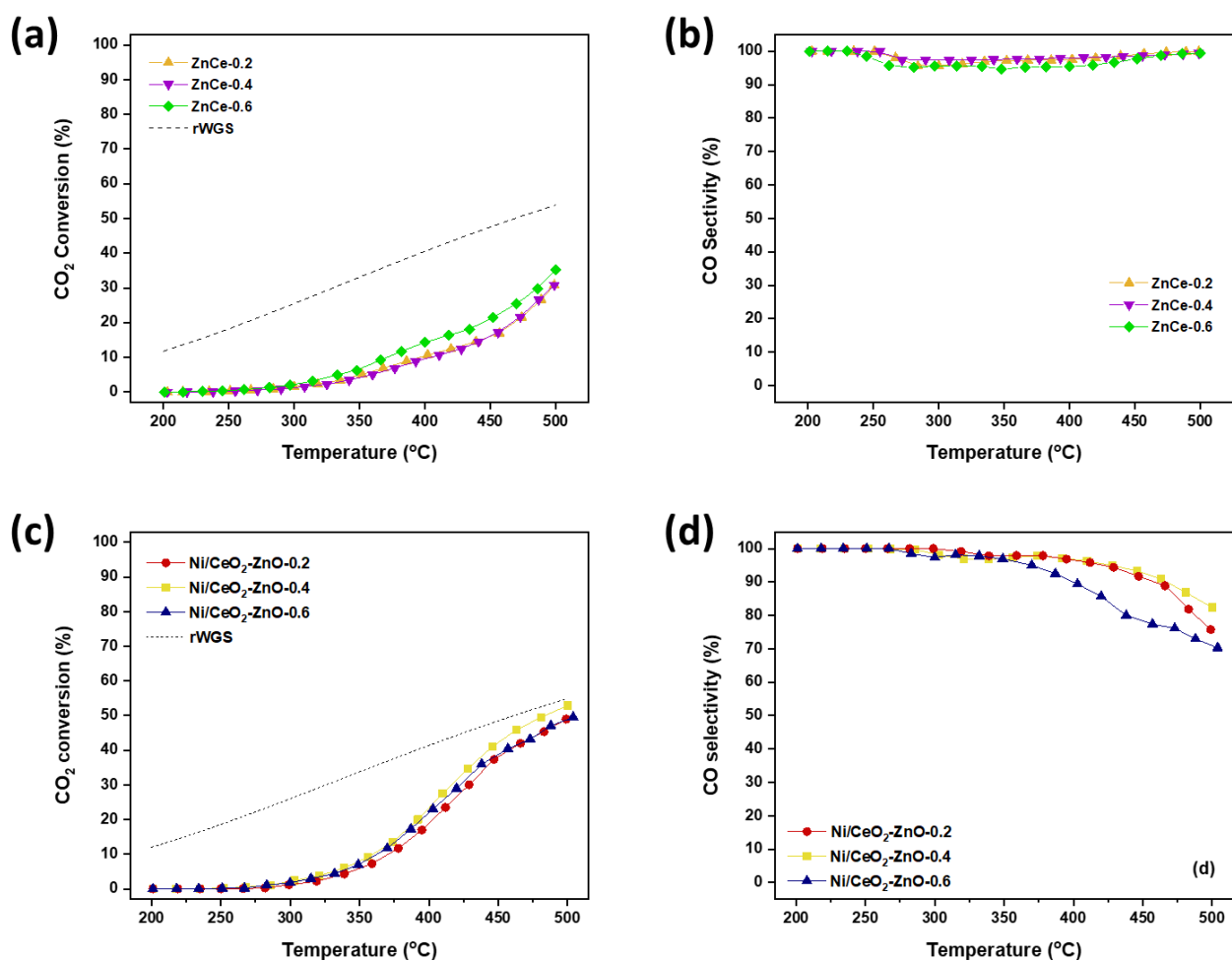


**Figure 4.23.** (a), (c) CO<sub>2</sub> conversion and (b), (d) CO selectivity values as a function of temperature for the as-prepared CeO<sub>2</sub>/ZnO-x and Ni/CeO<sub>2</sub>-ZnO-x samples. Reaction conditions: H<sub>2</sub>:CO<sub>2</sub> = 4, WHSV = 30 L·g<sup>-1</sup>·h<sup>-1</sup>, P = 1 atm.

Figure 4.24 (a) illustrates the comparison between bare supports and Ni-based samples in terms of CO<sub>2</sub> conversion values at different reaction temperatures. It is evident that higher reaction temperatures promote CO<sub>2</sub> conversion, and the values generally follow this order: CeO<sub>2</sub>/ZnO < Ni/ZnO < Ni/CeO<sub>2</sub>-ZnO << Ni/CeO<sub>2</sub>. This trend clearly highlights the beneficial effect of incorporating Ni into the oxide supports. However, the extent of this effect strongly depends on the nature of the supporting material. Notably, the addition of Ni to ceria nanorods significantly enhances CO<sub>2</sub> conversion to CH<sub>4</sub>, enabling the attainment of equilibrium predicted values for CO<sub>2</sub> methanation even at relatively low temperatures (approximately 300 °C). In complete contrast, incorporating Ni into either bare ZnO or CeO<sub>2</sub>/ZnO has a relatively minor impact on CO<sub>2</sub> conversion. This suggests that the presence of ZnO actually hampers CO<sub>2</sub> conversion, resulting in a detrimental effect.

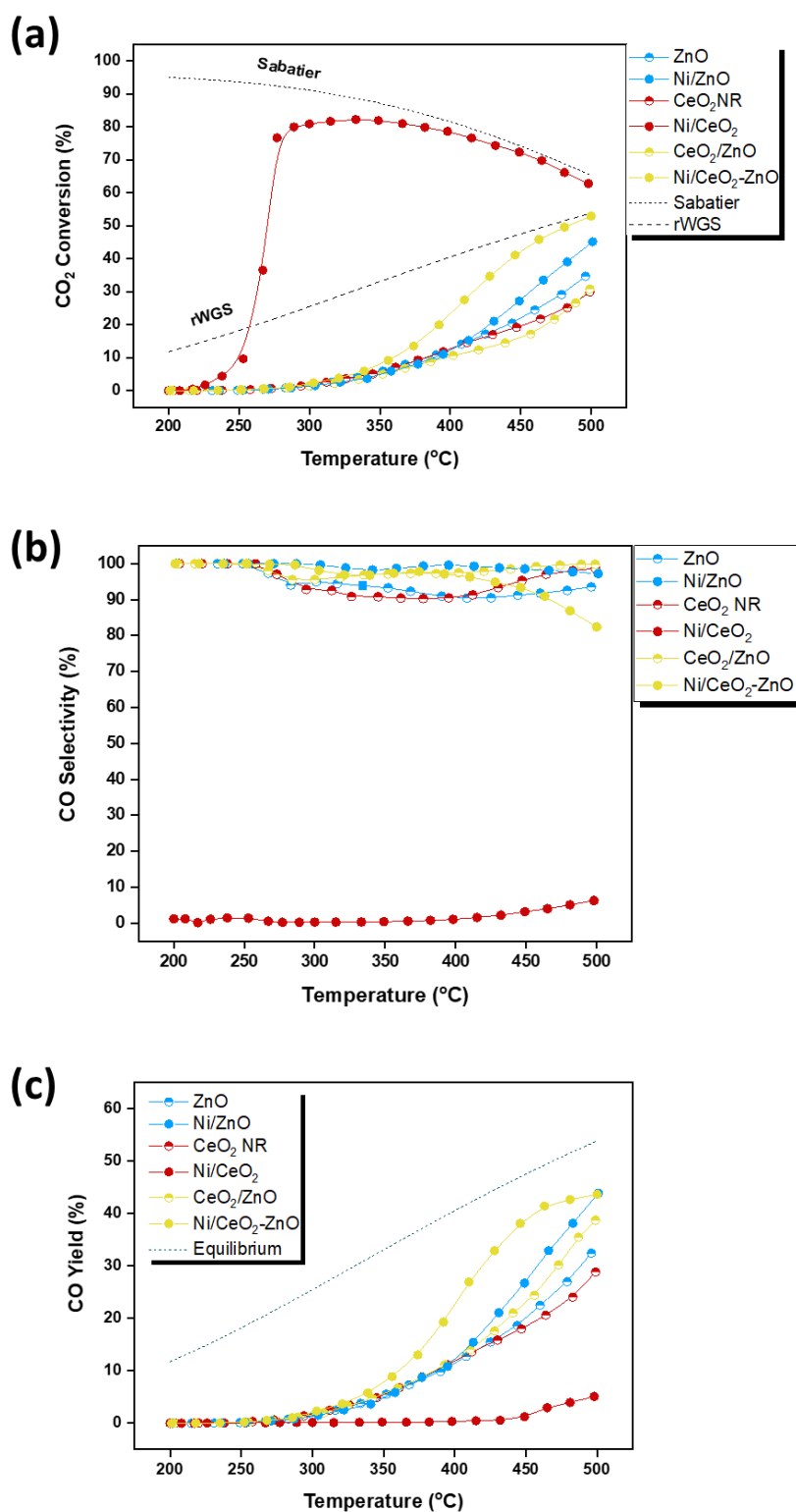


**Figure 4.24.** (a) CO<sub>2</sub> conversion, (b) CO selectivity and (c) CO yield values as a function of temperature. Reaction conditions:  $H_2:CO_2 = 4$ ,  $WHSV = 30 \text{ L}\cdot\text{g}^{-1}\cdot\text{h}^{-1}$ ,  $P = 1 \text{ atm}$ .

Significantly, all ZnO-containing samples exhibit a notable preference for the reverse water-gas shift (rWGS) reaction, as depicted in Figure 4.24 (b). This implies that the presence of ZnO, whether in the form of bare ZnO or mixed CeO<sub>2</sub>/ZnO, promotes the formation of CO at the expense of CH<sub>4</sub>,

without any other discernible by-products. Specifically, at a temperature of 400 °C, CO selectivity values were around 1% for Ni/CeO<sub>2</sub>, whereas they exceeded 90% for all other samples. This temperature range favors the exothermic Sabatier reaction over the slightly endothermic rWGS reaction from a thermodynamic perspective. To further highlight the favorable impact of ZnO on rWGS activity, it is enlightening to consider the corresponding CO yield values, as shown in Figure 4.24 (c). At 450 °C, Ni/CeO<sub>2</sub>-ZnO achieves a CO yield value that is approximately 90% of the thermodynamically predicted value. This intriguing finding contradicts the product distribution reported in the literature for the reaction of CO<sub>2</sub> hydrogenation over Ni-based catalysts with similar Ni loading values (approximately 8.0 wt.%)<sup>54</sup> to the ones employed in this study. The aforementioned catalytic performance was further confirmed by the comparable activity observed among the as-prepared Ni/CeO<sub>2</sub>-ZnO-x samples, as shown in Figure 4.23 (c) and (d).

The incorporation of ZnO into the ceria carrier has a profound impact on the activity and selectivity of Ni-based samples in CO<sub>2</sub> hydrogenation, as revealed by the presented findings. Notably, ZnO addition not only hinders CO<sub>2</sub> conversion but also promotes the reverse water-gas shift (rWGS) reaction, resulting in an increased generation of CO. Furthermore, extensive physicochemical characterizations have provided valuable insights into the changes induced by ZnO doping in the physicochemical properties of Ni-based samples. These changes include a decrease in the BET surface area, inhibition of reducibility as evidenced by the shift of H<sub>2</sub>-TPR peaks towards higher temperatures, and a decrease in the concentration of oxygen vacancies.

The impact of ZnO on key physicochemical properties and catalytic performance at 400 °C is summarized in Table 4.12. Firstly, in terms of redox properties, it is evident that the presence of ZnO leads to a significant decrease in the density of oxygen vacancies. This is supported by two semi-quantitative descriptors, namely the ratio I<sub>D</sub>/I<sub>F<sub>2g</sub></sub> and the values for N, as shown in Table 4.12. Additionally, the excellent redox properties exhibited by Ni/CeO<sub>2</sub> are further confirmed by H<sub>2</sub>-TPR experiments, where distinct peaks are observed at lower temperatures. It has been reported that the low-temperature peak observed in H<sub>2</sub>-TPR on nickel-ceria catalysts is attributed to the substitution of Ce<sup>4+</sup> by Ni<sup>2+</sup> within the CeO<sub>2</sub> lattice. This charge imbalance results in lattice distortion and the formation of a Ni-O-Ce solid solution, leading to the generation of reactive oxygen species that can be readily reduced at low temperatures<sup>131</sup>.

**Table 4.12.** Key redox properties, and catalytic activity results of Ni-based samples.

Sample	Redox Properties			Activity/Selectivity at 400 °C	
	$I_D/I_{F2g}$	N ( $10^{21} \times \text{cm}^{-1}$ )	H <sub>2</sub> consumption at T < 400 °C (mmol/g)	% CO <sub>2</sub> conversion	% CO selectivity
Ni/ZnO	-	-	0.01	10.9	99.6
Ni/CeO <sub>2</sub> -ZnO	0.21	1.65	0.26	28.1	96.0
Ni/CeO <sub>2</sub>	0.37	2.27	1.72	74.3	0.6

Furthermore, taking into account the pretreatment procedure where all samples were reduced at 400 °C, the specific consumption of H<sub>2</sub> at this temperature was calculated based on the deconvoluted H<sub>2</sub>-TPR profiles. For Ni/ZnO, negligible consumption values were observed as no peaks were present in this temperature range. Conversely, for Ni/CeO<sub>2</sub>-ZnO, the consumption values mainly corresponded to the low-temperature peak (peak  $\alpha$ ). It is noteworthy that the total consumption for Ni/CeO<sub>2</sub> encompassed contributions from both peak  $\alpha$  and peak  $\beta$ , resulting in a significantly higher low-temperature H<sub>2</sub> consumption that exceeded the theoretically expected amount for NiO reduction. Thus, with regards to the oxidation state of nickel in the as-prepared samples prior to CO<sub>2</sub> hydrogenation, the Ni/CeO<sub>2</sub> sample exhibited the highest population of reduced Ni<sup>0</sup> species, followed by Ni/CeO<sub>2</sub>-ZnO. In contrast, nickel in Ni/ZnO was predominantly present in its fully oxidized state, Ni<sup>2+</sup>, as confirmed by the absence of a detectable peak below 400 °C (Figure 4.15). Collectively, it can be deduced that the optimal catalytic surface for CO<sub>2</sub> conversion in the as-prepared samples lies at the interface between nickel and ceria. The addition of zinc, however, introduces an interface between nickel and ceria that exhibits an inferior capability for the activation and dissociation of both gas-phase CO<sub>2</sub> and H<sub>2</sub>, resulting in lower CO<sub>2</sub> (and consequently H<sub>2</sub>) conversion values. The detrimental effect of zinc can be attributed to the presence of agglomerated ZnO ensembles, which could physically obstruct the active catalytic sites responsible for CO<sub>2</sub> activation. Simultaneously, the addition of zinc impedes the dissociation of H<sub>2</sub> by providing an increased population of surface sites that are less easily reduced, or by inducing greater agglomeration of NiO entities.

#### 4.6.4. CO<sub>2</sub> Hydrogenation Performance of Bare Ceria Triangles (CeO<sub>2</sub> TR) and Ni/CeO<sub>2</sub> TR

The catalytic performance of bare CeO<sub>2</sub> TR (ceria-triangles) and Ni/CeO<sub>2</sub> TR catalysts was studied in the CO<sub>2</sub> hydrogenation reaction within a temperature range of 200–400 °C. Figure 4.25 (a) presents the CO<sub>2</sub> conversion profiles of both catalysts, comparing them to the thermodynamic equilibrium conversion profiles for methanation and reverse water-gas shift (rWGS) reactions. The results clearly demonstrate the superior methanation performance of the Ni/CeO<sub>2</sub> TR catalyst, indicating the advantageous effect of combining Ni metal with the ceria-triangles support.

Importantly, the supported Ni catalyst exhibited an onset methanation temperature of approximately 245 °C, while the bare CeO<sub>2</sub> TR showed negligible reactivity. Furthermore, it is noteworthy that the as-synthesized Ni/CeO<sub>2</sub> TR catalyst displayed complete selectivity towards methane at all investigated temperatures, in contrast to bare CeO<sub>2</sub> TR (Figure 4.25 (b)). This selectivity towards methane further emphasizes the advantageous characteristics of the Ni/CeO<sub>2</sub> TR catalyst, making it a promising candidate for efficient CO<sub>2</sub> conversion and methanation across a wide temperature range. To further highlight the enhanced catalytic performance of Ni/CeO<sub>2</sub> TR, a comparison was made with corresponding commercial samples, CeO<sub>2</sub>-comm and Ni/CeO<sub>2</sub>-comm, as shown in Figure 4.25. The comparison clearly demonstrates that Ni/CeO<sub>2</sub> TR is significantly more active and selective towards CH<sub>4</sub> compared to Ni/CeO<sub>2</sub>-comm, underscoring the crucial role of the ceria nanostructure. At 300 °C, CeO<sub>2</sub>-comm and Ni/CeO<sub>2</sub>-comm exhibit CH<sub>4</sub> selectivity values of 4% and 63%, respectively. In contrast, CeO<sub>2</sub> TR, and Ni/CeO<sub>2</sub> TR display selectivity values of 3% and 98.1%, respectively. These results provide clear evidence that the presence of the nickel active phase is indispensable for methane production. Notably, bare CeO<sub>2</sub> TR exhibits negligible methanation performance. However, when combined with Ni, the catalytic activity of CeO<sub>2</sub> TR is significantly promoted, leading to conversion and methane selectivity values close to 80% and 100%, respectively. In contrast, the corresponding modifications on the commercial Ni/CeO<sub>2</sub>-comm sample are noticeably less prominent.

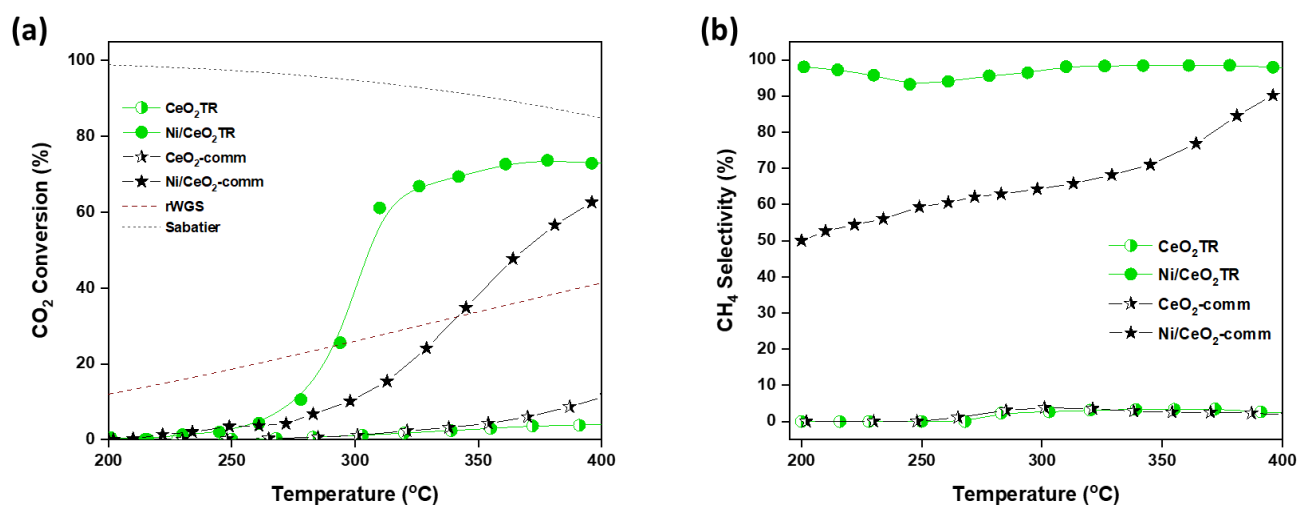


**Figure 4.25.** (a) CO<sub>2</sub> conversion (%) and (b) CH<sub>4</sub> selectivity (%) versus temperature profiles for CeO<sub>2</sub>-comm, Ni/CeO<sub>2</sub>-comm, CeO<sub>2</sub> TR and Ni/CeO<sub>2</sub> TR catalysts. Reaction conditions: WHSV = 30 L·g<sup>-1</sup>·h<sup>-1</sup>, H<sub>2</sub>:CO<sub>2</sub> = 4, P = 1 atm.

#### 4.7. Conclusions

In this chapter, an investigation was conducted to explore the physicochemical properties and CO<sub>2</sub> hydrogenation performance of ceria-based nano-catalysts, with a focus on the influence of non-noble metal phases and ZnO promotion. The results obtained in this study revealed a strong correlation between the metal phase and the CO<sub>2</sub> hydrogenation performance of nanoceria-based M/CeO<sub>2</sub> catalysts. Specifically, hydrothermally synthesized ceria nanorods exhibited better catalytic activity in the hydrogenation of CO<sub>2</sub> compared to commercial ceria. Moreover, the addition of different metals into the nanostructured ceria support demonstrated a significant enhancement in catalytic activity. The order of CO<sub>2</sub> conversion followed the sequence: V/CeO<sub>2</sub> < Ti/CeO<sub>2</sub> < Mn/CeO<sub>2</sub> < Cr/CeO<sub>2</sub> < CeO<sub>2</sub> < Fe/CeO<sub>2</sub> < Cu/CeO<sub>2</sub> < Co/CeO<sub>2</sub> < Ni/CeO<sub>2</sub>. It was observed that the nature of the metal entity incorporated into cerium oxide determined the main product of the reaction. Notably, the Co/CeO<sub>2</sub> and Ni/CeO<sub>2</sub> catalysts exhibited high selectivity towards CH<sub>4</sub>, with CO<sub>2</sub> conversion values close to equilibrium. Furthermore, the Cu/CeO<sub>2</sub> samples displayed remarkable CO selectivity, even under hydrogen excess conditions, approaching the equilibrium for the reverse water-gas shift (rWGS) reaction. Conversely, bare CeO<sub>2</sub>, Fe/CeO<sub>2</sub>, Cr/CeO<sub>2</sub>, Mn/CeO<sub>2</sub>, Ti/CeO<sub>2</sub>, and V/CeO<sub>2</sub> demonstrated inferior catalytic activity. Subsequently, the research focused on Ni/CeO<sub>2</sub>-nanorod catalysts to investigate the role of Ni particle size and the impact of ZnO promotion on the reaction mechanism. The results showed that Ni/ZnO and Ni/CeO<sub>2</sub>-ZnO catalysts facilitated selective CO production while effectively suppressing CO<sub>2</sub> methanation compared to Ni/CeO<sub>2</sub> catalysts. Additionally, a preliminary study explored the utilization of CeO<sub>2</sub> triangles as supporting carriers for the Ni active phase in CO<sub>2</sub> hydrogenation, comparing the results with those obtained using a nickel catalyst supported on commercial CeO<sub>2</sub>. Overall, these promising results pave the way for the application of these catalysts in large-scale processes, where renewable hydrogen generated from excess renewable energy sources can be efficiently and selectively used to convert CO<sub>2</sub> to CO or CH<sub>4</sub>.

## References

- (1) Olah, G. A.; Prakash, G. K. S.; Goepfert, A. Anthropogenic Chemical Carbon Cycle for a Sustainable Future. *J. Am. Chem. Soc.* **2011**, *133* (33), 12881–12898. <https://doi.org/10.1021/ja202642y>.
- (2) Wang, W.; Wang, S.; Ma, X.; Gong, J. Recent Advances in Catalytic Hydrogenation of Carbon Dioxide. *Chem. Soc. Rev.* **2011**, *40* (7), 3703. <https://doi.org/10.1039/c1cs15008a>.
- (3) Rodriguez, J. A.; Liu, P.; Stacchiola, D. J.; Senanayake, S. D.; White, M. G.; Chen, J. G. Hydrogenation of CO<sub>2</sub> to Methanol: Importance of Metal-Oxide and Metal-Carbide Interfaces in the Activation of CO<sub>2</sub>. *ACS Catal.* **2015**, *5* (11), 6696–6706. <https://doi.org/10.1021/acscatal.5b01755>.
- (4) Xiaoding, X.; Moulijn, J. A. Mitigation of CO<sub>2</sub> by Chemical Conversion: Plausible Chemical Reactions and Promising Products. *Energy and Fuels* **1996**, *10* (2), 305–325. <https://doi.org/10.1021/ef9501511>.
- (5) Centi, G.; Perathoner, S. Opportunities and Prospects in the Chemical Recycling of Carbon Dioxide to Fuels. *Catal. Today* **2009**, *148* (3–4), 191–205. <https://doi.org/10.1016/j.cattod.2009.07.075>.
- (6) Konsolakis, M.; Lykaki, M. Facet-Dependent Reactivity of Ceria Nanoparticles Exemplified by CeO<sub>2</sub>-Based Transition Metal Catalysts: A Critical Review. *Catalysts* **2021**, *11* (4). <https://doi.org/10.3390/catal11040452>.
- (7) Bahruji, H.; Bowker, M.; Hutchings, G.; Dimitratos, N.; Wells, P.; Gibson, E.; Jones, W.; Brookes, C.; Morgan, D.; Lalev, G. Pd/ZnO Catalysts for Direct CO<sub>2</sub> hydrogenation to Methanol. *J. Catal.* **2016**, *343*, 133–146. <https://doi.org/10.1016/j.jcat.2016.03.017>.
- (8) Li, M. M. J.; Zeng, Z.; Liao, F.; Hong, X.; Tsang, S. C. E. Enhanced CO<sub>2</sub> Hydrogenation to Methanol over CuZn Nanoalloy in Ga Modified Cu/ZnO Catalysts. *J. Catal.* **2016**, *343*, 157–167. <https://doi.org/10.1016/j.jcat.2016.03.020>.
- (9) Vourros, A.; Garagounis, I.; Kyriakou, V.; Carabineiro, S. A. C.; Maldonado-Hódar, F. J.; Marnellos, G. E.; Konsolakis, M. Carbon Dioxide Hydrogenation over Supported Au Nanoparticles: Effect of the Support. *J. CO<sub>2</sub> Util.* **2017**, *19* (April), 247–256. <https://doi.org/10.1016/j.jcou.2017.04.005>.
- (10) Senanayake, S. D.; Ramírez, P. J.; Waluyo, I.; Kundu, S.; Mudiyansele, K.; Liu, Z.; Liu, Z.;

- Axnanda, S.; Stacchiola, D. J.; Evans, J.; Rodriguez, J. A. Hydrogenation of CO<sub>2</sub> to Methanol on CeO<sub>x</sub>/Cu(111) and ZnO/Cu(111) Catalysts: Role of the Metal-Oxide Interface and Importance of Ce<sup>3+</sup> Sites. *J. Phys. Chem. C* **2016**, *120* (3), 1778–1784. <https://doi.org/10.1021/acs.jpcc.5b12012>.
- (11) Aguayo, A. T.; Ereña, J.; Sierra, I.; Olazar, M.; Bilbao, J. Deactivation and Regeneration of Hybrid Catalysts in the Single-Step Synthesis of Dimethyl Ether from Syngas and CO<sub>2</sub>. *Catal. Today* **2005**, *106* (1–4), 265–270. <https://doi.org/10.1016/j.cattod.2005.07.144>.
- (12) Zhang, Y.; Fei, J.; Yu, Y.; Zheng, X. Silica Immobilized Ruthenium Catalyst Used for Carbon Dioxide Hydrogenation to Formic Acid (I): The Effect of Functionalizing Group and Additive on the Catalyst Performance. *Catal. Commun.* **2004**, *5* (10), 643–646. <https://doi.org/10.1016/j.catcom.2004.08.001>.
- (13) Saeidi, S.; Amin, N. A. S.; Rahimpour, M. R. Hydrogenation of CO<sub>2</sub> to Value-Added Products - A Review and Potential Future Developments. *J. CO<sub>2</sub> Util.* **2014**, *5*, 66–81. <https://doi.org/10.1016/j.jcou.2013.12.005>.
- (14) Pastor-Pérez, L.; Baibars, F.; Le Sache, E.; Arellano-García, H.; Gu, S.; Reina, T. R. CO<sub>2</sub> Valorisation via Reverse Water-Gas Shift Reaction Using Advanced Cs Doped Fe-Cu/Al<sub>2</sub>O<sub>3</sub> Catalysts. *J. CO<sub>2</sub> Util.* **2017**, *21* (August), 423–428. <https://doi.org/10.1016/j.jcou.2017.08.009>.
- (15) Kaiser, P.; Unde, R. B.; Kern, C.; Jess, A. Production of Liquid Hydrocarbons with CO<sub>2</sub> as Carbon Source Based on Reverse Water-Gas Shift and Fischer-Tropsch Synthesis. *Chemie-Ingenieur-Technik* **2013**, *85* (4), 489–499. <https://doi.org/10.1002/cite.201200179>.
- (16) Tada, S.; Ochieng, O. J.; Kikuchi, R.; Haneda, T.; Kameyama, H. Promotion of CO<sub>2</sub> Methanation Activity and CH<sub>4</sub> Selectivity at Low Temperatures over Ru/CeO<sub>2</sub>/Al<sub>2</sub>O<sub>3</sub> Catalysts. *Int. J. Hydrogen Energy* **2014**, *39* (19), 10090–10100. <https://doi.org/10.1016/j.ijhydene.2014.04.133>.
- (17) van Leeuwen, C.; Mulder, M. Power-to-Gas in Electricity Markets Dominated by Renewables. *Appl. Energy* **2018**, *232* (October), 258–272. <https://doi.org/10.1016/j.apenergy.2018.09.217>.
- (18) Götz, M.; Lefebvre, J.; Mörs, F.; McDaniel Koch, A.; Graf, F.; Bajohr, S.; Reimert, R.; Kolb, T. Renewable Power-to-Gas: A Technological and Economic Review. *Renew. Energy* **2016**, *85*, 1371–1390. <https://doi.org/10.1016/j.renene.2015.07.066>.

- (19) Ghaib, K.; Ben-Fares, F. Z. Power-to-Methane: A State-of-the-Art Review. *Renew. Sustain. Energy Rev.* **2018**, *81* (August 2017), 433–446. <https://doi.org/10.1016/j.rser.2017.08.004>.
- (20) Mazza, A.; Bompard, E.; Chicco, G. Applications of Power to Gas Technologies in Emerging Electrical Systems. *Renew. Sustain. Energy Rev.* **2018**, *92* (May), 794–806. <https://doi.org/10.1016/j.rser.2018.04.072>.
- (21) Lewandowska-Bernat, A.; Desideri, U. Opportunities of Power-to-Gas Technology. *Energy Procedia* **2017**, *105*, 4569–4574. <https://doi.org/10.1016/j.egypro.2017.03.982>.
- (22) Zangeneh, F. T.; Sahebdehfar, S.; Ravanchi, M. T. Conversion of Carbon Dioxide to Valuable Petrochemicals: An Approach to Clean Development Mechanism. *J. Nat. Gas Chem.* **2011**, *20* (3), 219–231. [https://doi.org/10.1016/S1003-9953\(10\)60191-0](https://doi.org/10.1016/S1003-9953(10)60191-0).
- (23) Ma, J.; Sun, N.; Zhang, X.; Zhao, N.; Xiao, F.; Wei, W.; Sun, Y. A Short Review of Catalysis for CO<sub>2</sub> Conversion. *Catal. Today* **2009**, *148* (3–4), 221–231. <https://doi.org/10.1016/j.cattod.2009.08.015>.
- (24) Saeidi, S.; Najari, S.; Fazlollahi, F.; Nikoo, M. K.; Sefidkon, F.; Klemeš, J. J.; Baxter, L. L. Mechanisms and Kinetics of CO<sub>2</sub> Hydrogenation to Value-Added Products: A Detailed Review on Current Status and Future Trends. *Renew. Sustain. Energy Rev.* **2017**, *80* (September 2016), 1292–1311. <https://doi.org/10.1016/j.rser.2017.05.204>.
- (25) Centi, G.; Perathoner, S. *Heterogeneous Catalytic Reactions with CO<sub>2</sub>: Status and Perspectives*; Elsevier Masson SAS, 2004; Vol. 153. [https://doi.org/10.1016/s0167-2991\(04\)80212-x](https://doi.org/10.1016/s0167-2991(04)80212-x).
- (26) Boaro, M.; Colussi, S.; Trovarelli, A. Ceria-Based Materials in Hydrogenation and Reforming Reactions for CO<sub>2</sub> Valorization. *Front. Chem.* **2019**, *7* (February). <https://doi.org/10.3389/fchem.2019.00028>.
- (27) Porosoff, M. D.; Yan, B.; Chen, J. G. Catalytic Reduction of CO<sub>2</sub> by H<sub>2</sub> for Synthesis of CO, Methanol and Hydrocarbons: Challenges and Opportunities. *Energy Environ. Sci.* **2016**, *9* (1), 62–73. <https://doi.org/10.1039/C5EE02657A>.
- (28) Gao, J.; Liu, Q.; Gu, F.; Liu, B.; Zhong, Z.; Su, F. Recent Advances in Methanation Catalysts for the Production of Synthetic Natural Gas. *RSC Adv.* **2015**, *5* (29), 22759–22776. <https://doi.org/10.1039/c4ra16114a>.
- (29) Frontera, P.; Macario, A.; Ferraro, M.; Antonucci, P. L. Supported Catalysts for CO<sub>2</sub>

- Methanation: A Review. *Catalysts* **2017**, 7 (2), 1–28. <https://doi.org/10.3390/catal7020059>.
- (30) Ghaib, K.; Nitz, K.; Ben-Fares, F. Z. Chemical Methanation of CO<sub>2</sub>: A Review. *ChemBioEng Rev.* **2016**, 3 (6), 266–275. <https://doi.org/10.1002/cben.201600022>.
- (31) Winter, L. R.; Chen, R.; Chen, X.; Chang, K.; Liu, Z.; Senanayake, S. D.; Ebrahim, A. M.; Chen, J. G. Elucidating the Roles of Metallic Ni and Oxygen Vacancies in CO<sub>2</sub> Hydrogenation over Ni/CeO<sub>2</sub> Using Isotope Exchange and in Situ Measurements. *Appl. Catal. B Environ.* **2019**, 245 (December 2018), 360–366. <https://doi.org/10.1016/j.apcatb.2018.12.069>.
- (32) Montini, T.; Melchionna, M.; Monai, M.; Fornasiero, P. Fundamentals and Catalytic Applications of CeO<sub>2</sub>-Based Materials. *Chem. Rev.* **2016**, 116 (10), 5987–6041. <https://doi.org/10.1021/acs.chemrev.5b00603>.
- (33) Melchionna, M.; Fornasiero, P. The Role of Ceria-Based Nanostructured Materials in Energy Applications. *Mater. Today* **2014**, 17 (7), 349–357. <https://doi.org/10.1016/j.mattod.2014.05.005>.
- (34) Hemalatha, P.; Bhagiyalakshmi, M.; Ganesh, M.; Palanichamy, M.; Murugesan, V.; Jang, H. T. Role of Ceria in CO<sub>2</sub> Adsorption on NaZSM-5 Synthesized Using Rice Husk Ash. *J. Ind. Eng. Chem.* **2012**, 18 (1), 260–265. <https://doi.org/10.1016/j.jiec.2011.11.046>.
- (35) Cargnello, M.; Doan-Nguyen, V. V. T.; Gordon, T. R.; Diaz, R. E.; Stach, E. A.; Gorte, R. J.; Fornasiero, P.; Murray, C. B. Control of Metal Nanocrystal Size Reveals Metal-Support Interface Role for Ceria Catalysts. *Science (80-. )*. **2013**, 341 (6147), 771–773. <https://doi.org/10.1126/science.1240148>.
- (36) Konsolakis, M. The Role of Copper–Ceria Interactions in Catalysis Science: Recent Theoretical and Experimental Advances. *Appl. Catal. B Environ.* **2016**, 198, 49–66. <https://doi.org/10.1016/j.apcatb.2016.05.037>.
- (37) Cargnello, M.; Fornasiero, P.; Gorte, R. J. Opportunities for Tailoring Catalytic Properties Through Metal-Support Interactions. *Catal. Letters* **2012**, 142 (9), 1043–1048. <https://doi.org/10.1007/s10562-012-0883-4>.
- (38) Sharma, S.; Hu, Z.; Zhang, P.; McFarland, E. W.; Metiu, H. CO<sub>2</sub> Methanation on Ru-Doped Ceria. *J. Catal.* **2011**, 278 (2), 297–309. <https://doi.org/10.1016/j.jcat.2010.12.015>.
- (39) Beuls, A.; Swalus, C.; Jacquemin, M.; Heyen, G.; Karelavic, A.; Ruiz, P. Methanation of CO<sub>2</sub>:

- Further Insight into the Mechanism over Rh/ $\gamma$ -Al<sub>2</sub>O<sub>3</sub> Catalyst. *Appl. Catal. B Environ.* **2012**, *113–114*, 2–10. <https://doi.org/10.1016/j.apcatb.2011.02.033>.
- (40) Díez-Ramírez, J.; Valverde, J. L.; Sánchez, P.; Dorado, F. CO<sub>2</sub> Hydrogenation to Methanol at Atmospheric Pressure: Influence of the Preparation Method of Pd/ZnO Catalysts. *Catal. Letters* **2016**, *146* (2), 373–382. <https://doi.org/10.1007/s10562-015-1627-z>.
- (41) Spezzati, G.; Benavidez, A. D.; DeLaRiva, A. T.; Su, Y.; Hofmann, J. P.; Asahina, S.; Olivier, E. J.; Neethling, J. H.; Miller, J. T.; Datye, A. K.; Hensen, E. J. M. CO Oxidation by Pd Supported on CeO<sub>2</sub>(100) and CeO<sub>2</sub>(111) Facets. *Appl. Catal. B Environ.* **2019**, *243* (October 2018), 36–46. <https://doi.org/10.1016/j.apcatb.2018.10.015>.
- (42) Klankermayer, J.; Wesselbaum, S.; Beydoun, K.; Leitner, W. Selective Catalytic Synthesis Using the Combination of Carbon Dioxide and Hydrogen: Catalytic Chess at the Interface of Energy and Chemistry. *Angew. Chemie - Int. Ed.* **2016**, *55* (26), 7296–7343. <https://doi.org/10.1002/anie.201507458>.
- (43) Liu, C.; Cundari, T. R.; Wilson, A. K. CO<sub>2</sub> Reduction on Transition Metal (Fe, Co, Ni, and Cu) Surfaces: In Comparison with Homogeneous Catalysis. *J. Phys. Chem. C* **2012**, *116* (9), 5681–5688. <https://doi.org/10.1021/jp210480c>.
- (44) Tada, S.; Shimizu, T.; Kameyama, H.; Haneda, T.; Kikuchi, R. Ni/CeO<sub>2</sub> Catalysts with High CO<sub>2</sub> Methanation Activity and High CH<sub>4</sub> Selectivity at Low Temperatures. *Int. J. Hydrogen Energy* **2012**, *37* (7), 5527–5531. <https://doi.org/10.1016/j.ijhydene.2011.12.122>.
- (45) Nizio, M.; Benrabbah, R.; Krzak, M.; Debek, R.; Motak, M.; Cavadias, S.; Gálvez, M. E.; Da Costa, P. Low Temperature Hybrid Plasma-Catalytic Methanation over Ni-Ce-Zr Hydrotalcite-Derived Catalysts. *Catal. Commun.* **2016**, *83*, 14–17. <https://doi.org/10.1016/j.catcom.2016.04.023>.
- (46) Atzori, L.; Cutrufello, M. G.; Meloni, D.; Cannas, C.; Gazzoli, D.; Monaci, R.; Sini, M. F.; Rombi, E. Highly Active NiO-CeO<sub>2</sub> Catalysts for Synthetic Natural Gas Production by CO<sub>2</sub> Methanation. *Catal. Today* **2018**, *299* (November 2016), 183–192. <https://doi.org/10.1016/j.cattod.2017.05.065>.
- (47) Vita, A.; Italiano, C.; Pino, L.; Frontera, P.; Ferraro, M.; Antonucci, V. Activity and Stability of Powder and Monolith-Coated Ni/GDC Catalysts for CO<sub>2</sub> Methanation. *Appl. Catal. B Environ.* **2018**, *226* (October 2017), 384–395. <https://doi.org/10.1016/j.apcatb.2017.12.078>.

- (48) Ye, R. P.; Li, Q.; Gong, W.; Wang, T.; Razink, J. J.; Lin, L.; Qin, Y. Y.; Zhou, Z.; Adidharma, H.; Tang, J.; Russell, A. G.; Fan, M.; Yao, Y. G. High-Performance of Nanostructured Ni/CeO<sub>2</sub> Catalyst on CO<sub>2</sub> Methanation. *Appl. Catal. B Environ.* **2020**, *268* (March 2019), 118474. <https://doi.org/10.1016/j.apcatb.2019.118474>.
- (49) Vissanu, M.; Nopadol, P.; Nat, P.; Xineng, G.; Chunshan, L.; Thirasak, R. Low Temperature Methanation of CO<sub>2</sub> on High Ni Content Ni-Ce-ZrO<sub>2</sub> Catalysts Prepared via One-Pot Hydrothermal Synthesis. *Catalysts* **2020**, *10* (1), 1–10.
- (50) Podrojková, N.; Sans, V.; Oriňak, A.; Oriňaková, R. Recent Developments in the Modelling of Heterogeneous Catalysts for CO<sub>2</sub> Conversion to Chemicals. *ChemCatChem* **2020**, *12* (7), 1802–1825. <https://doi.org/10.1002/cctc.201901879>.
- (51) Ma, Y.; Liu, J.; Chu, M.; Yue, J.; Cui, Y.; Xu, G. Cooperation Between Active Metal and Basic Support in Ni-Based Catalyst for Low-Temperature CO<sub>2</sub> Methanation. *Catal. Letters* **2020**, *150* (5), 1418–1426. <https://doi.org/10.1007/s10562-019-03033-w>.
- (52) Jomjaree, T.; Sintuya, P.; Srifa, A.; Koo-amornpattana, W.; Kiatphuengporn, S.; Assabumrungrat, S.; Sudoh, M.; Watanabe, R.; Fukuhara, C.; Ratchahat, S. Catalytic Performance of Ni Catalysts Supported on CeO<sub>2</sub> with Different Morphologies for Low-Temperature CO<sub>2</sub> Methanation. *Catal. Today* **2021**, *375* (November 2019), 234–244. <https://doi.org/10.1016/j.cattod.2020.08.010>.
- (53) Rui, N.; Zhang, X.; Zhang, F.; Liu, Z.; Cao, X.; Xie, Z.; Zou, R.; Senanayake, S. D.; Yang, Y.; Rodriguez, J. A.; Liu, C. J. Highly Active Ni/CeO<sub>2</sub> Catalyst for CO<sub>2</sub> Methanation: Preparation and Characterization. *Appl. Catal. B Environ.* **2021**, *282* (September 2020). <https://doi.org/10.1016/j.apcatb.2020.119581>.
- (54) Lv, C.; Xu, L.; Chen, M.; Cui, Y.; Wen, X.; Li, Y.; Wu, C. E.; Yang, B.; Miao, Z.; Hu, X.; Shou, Q. Recent Progresses in Constructing the Highly Efficient Ni Based Catalysts With Advanced Low-Temperature Activity Toward CO<sub>2</sub> Methanation. *Front. Chem.* **2020**, *8* (April), 1–32. <https://doi.org/10.3389/fchem.2020.00269>.
- (55) Shen, L.; Xu, J.; Zhu, M.; Han, Y. F. Essential Role of the Support for Nickel-Based CO<sub>2</sub> Methanation Catalysts. *ACS Catal.* **2020**, *10* (24), 14581–14591. <https://doi.org/10.1021/acscatal.0c03471>.
- (56) Alcalde-Santiago, V.; Davó-Quñonero, A.; Lozano-Castelló, D.; Quindimil, A.; De-La-Torre,

- U.; Pereda-Ayo, B.; González-Marcos, J. A.; González-Velasco, J. R.; Bueno-López, A. Ni/LnOx Catalysts (Ln=La, Ce or Pr) for CO<sub>2</sub> Methanation. *ChemCatChem* **2019**, *11* (2), 810–819. <https://doi.org/10.1002/cctc.201801585>.
- (57) Siakavelas, G. I.; Charisiou, N. D.; AlKhoori, S.; AlKhoori, A. A.; Sebastian, V.; Hinder, S. J.; Baker, M. A.; Yentekakis, I. V.; Polychronopoulou, K.; Goula, M. A. Highly Selective and Stable Nickel Catalysts Supported on Ceria Promoted with Sm<sub>2</sub>O<sub>3</sub>, Pr<sub>2</sub>O<sub>3</sub> and MgO for the CO<sub>2</sub> Methanation Reaction. *Appl. Catal. B Environ.* **2021**, *282* (September 2020), 119562. <https://doi.org/10.1016/j.apcatb.2020.119562>.
- (58) Gac, W.; Zawadzki, W.; Rotko, M.; Greluk, M.; Słowik, G.; Kolb, G. Effects of Support Composition on the Performance of Nickel Catalysts in CO<sub>2</sub> Methanation Reaction. *Catal. Today* **2020**, *357* (December 2018), 468–482. <https://doi.org/10.1016/j.cattod.2019.07.026>.
- (59) Le, T. A.; Kim, M. S.; Lee, S. H.; Kim, T. W.; Park, E. D. CO and CO<sub>2</sub> Methanation over Supported Ni Catalysts. *Catal. Today* **2017**, *293–294*, 89–96. <https://doi.org/10.1016/j.cattod.2016.12.036>.
- (60) Italiano, C.; Llorca, J.; Pino, L.; Ferraro, M.; Antonucci, V.; Vita, A. CO and CO<sub>2</sub> Methanation over Ni Catalysts Supported on CeO<sub>2</sub>, Al<sub>2</sub>O<sub>3</sub> and Y<sub>2</sub>O<sub>3</sub> Oxides. *Appl. Catal. B Environ.* **2020**, *264* (September 2019), 118494. <https://doi.org/10.1016/j.apcatb.2019.118494>.
- (61) Muroyama, H.; Tsuda, Y.; Asakoshi, T.; Masitah, H.; Okanishi, T.; Matsui, T.; Eguchi, K. Carbon Dioxide Methanation over Ni Catalysts Supported on Various Metal Oxides. *J. Catal.* **2016**, *343*, 178–184. <https://doi.org/10.1016/j.jcat.2016.07.018>.
- (62) Ashok, J.; Ang, M. L.; Kawi, S. Enhanced Activity of CO<sub>2</sub> Methanation over Ni/CeO<sub>2</sub>-ZrO<sub>2</sub> Catalysts: Influence of Preparation Methods. *Catal. Today* **2017**, *281*, 304–311. <https://doi.org/10.1016/j.cattod.2016.07.020>.
- (63) Kokka, A.; Ramantani, T.; Petala, A.; Panagiotopoulou, P. Effect of the Nature of the Support, Operating and Pretreatment Conditions on the Catalytic Performance of Supported Ni Catalysts for the Selective Methanation of CO. *Catal. Today* **2020**, *355* (March 2019), 832–843. <https://doi.org/10.1016/j.cattod.2019.04.015>.
- (64) Ocampo, F.; Louis, B.; Kiennemann, A.; Roger, A. C. CO<sub>2</sub> Methanation over Ni-Ceria-Zirconia Catalysts: Effect of Preparation and Operating Conditions. *IOP Conf. Ser. Mater. Sci. Eng.* **2011**, *19* (1). <https://doi.org/10.1088/1757-899X/19/1/012007>.

- (65) Bacariza, M. C.; Graça, I.; Westermann, A.; Ribeiro, M. F.; Lopes, J. M.; Henriques, C. CO<sub>2</sub> Hydrogenation over Ni-Based Zeolites: Effect of Catalysts Preparation and Pre-Reduction Conditions on Methanation Performance. *Top. Catal.* **2016**, *59* (2–4), 314–325. <https://doi.org/10.1007/s11244-015-0435-4>.
- (66) Liang, C.; Ye, Z.; Dong, D.; Zhang, S.; Liu, Q.; Chen, G.; Li, C.; Wang, Y.; Hu, X. Methanation of CO<sub>2</sub>: Impacts of Modifying Nickel Catalysts with Variable-Valence Additives on Reaction Mechanism. *Fuel* **2019**, *254* (June), 115654. <https://doi.org/10.1016/j.fuel.2019.115654>.
- (67) Yan, Y.; Dai, Y.; He, H.; Yu, Y.; Yang, Y. A Novel W-Doped Ni-Mg Mixed Oxide Catalyst for CO<sub>2</sub> Methanation. *Appl. Catal. B Environ.* **2016**, *196*, 108–116. <https://doi.org/10.1016/j.apcatb.2016.05.016>.
- (68) Valinejad Moghaddam, S.; Rezaei, M.; Meshkani, F.; Daroughegi, R. Carbon Dioxide Methanation over Ni-M/Al<sub>2</sub>O<sub>3</sub> (M: Fe, Co, Zr, La and Cu) Catalysts Synthesized Using the One-Pot Sol-Gel Synthesis Method. *Int. J. Hydrogen Energy* **2018**, *43* (34), 16522–16533. <https://doi.org/10.1016/j.ijhydene.2018.07.013>.
- (69) Ren, J.; Qin, X.; Yang, J. Z.; Qin, Z. F.; Guo, H. L.; Lin, J. Y.; Li, Z. Methanation of Carbon Dioxide over Ni-M/ZrO<sub>2</sub> (M = Fe, Co, Cu) Catalysts: Effect of Addition of a Second Metal. *Fuel Process. Technol.* **2015**, *137*, 204–211. <https://doi.org/10.1016/j.fuproc.2015.04.022>.
- (70) Vrijburg, W. L.; Moioli, E.; Chen, W.; Zhang, M.; Terlingen, B. J. P.; Zijlstra, B.; Pilot, I. A. W.; Züttel, A.; Pidko, E. A.; Hensen, E. J. M. Efficient Base-Metal NiMn/TiO<sub>2</sub> Catalyst for CO<sub>2</sub> Methanation. *ACS Catal.* **2019**, *9* (9), 7823–7839. <https://doi.org/10.1021/acscatal.9b01968>.
- (71) Wu, Y.; Lin, J.; Xu, Y.; Ma, G.; Wang, J.; Ding, M. Transition Metals Modified Ni–M (M=Fe, Co, Cr and Mn) Catalysts Supported on Al<sub>2</sub>O<sub>3</sub>–ZrO<sub>2</sub> for Low-Temperature CO<sub>2</sub> Methanation. *ChemCatChem* **2020**, *12* (13), 3553–3559. <https://doi.org/10.1002/cctc.202000399>.
- (72) Tsiotsias, A. I.; Charisiou, N. D.; Yentekakis, I. V.; Goula, M. A. Bimetallic Ni-Based Catalysts for CO<sub>2</sub> Methanation: A Review. *Nanomaterials* **2021**, *11* (1), 1–34. <https://doi.org/10.3390/nano11010028>.
- (73) Zhang, Z.; Tian, Y.; Zhang, L.; Hu, S.; Xiang, J.; Wang, Y.; Xu, L.; Liu, Q.; Zhang, S.; Hu, X.

Impacts of Nickel Loading on Properties, Catalytic Behaviors of Ni/ $\Gamma$ -Al<sub>2</sub>O<sub>3</sub> Catalysts and the Reaction Intermediates Formed in Methanation of CO<sub>2</sub>. *Int. J. Hydrogen Energy* **2019**, *44* (18), 9291–9306. <https://doi.org/10.1016/j.ijhydene.2019.02.129>.

- (74) Alarcón, A.; Guilera, J.; Díaz, J. A.; Andreu, T. Optimization of Nickel and Ceria Catalyst Content for Synthetic Natural Gas Production through CO<sub>2</sub> Methanation. *Fuel Process. Technol.* **2019**, *193* (May), 114–122. <https://doi.org/10.1016/j.fuproc.2019.05.008>.
- (75) Quindimil, A.; De-La-Torre, U.; Pereda-Ayo, B.; Davó-Quñonero, A.; Bailón-García, E.; Lozano-Castelló, D.; González-Marcos, J. A.; Bueno-López, A.; González-Velasco, J. R. Effect of Metal Loading on the CO<sub>2</sub> Methanation: A Comparison between Alumina Supported Ni and Ru Catalysts. *Catal. Today* **2020**, *356* (June 2019), 419–432. <https://doi.org/10.1016/j.cattod.2019.06.027>.
- (76) Zhang, B.; Li, D.; Wang, X. Catalytic Performance of La-Ce-O Mixed Oxide for Combustion of Methane. *Catal. Today* **2010**, *158* (3–4), 348–353. <https://doi.org/10.1016/j.cattod.2010.04.019>.
- (77) Lin, F.; Delmelle, R.; Vinodkumar, T.; Reddy, B. M.; Wokaun, A.; Alxneit, I. Correlation between the Structural Characteristics, Oxygen Storage Capacities and Catalytic Activities of Dual-Phase Zn-Modified Ceria Nanocrystals. *Catal. Sci. Technol.* **2015**, *5* (7), 3556–3567. <https://doi.org/10.1039/c5cy00351b>.
- (78) Zhong, S. L.; Zhang, L. F.; Wang, L.; Huang, W. X.; Fan, C. M.; Xu, A. W. Uniform and Porous Ce<sub>1-x</sub>Zn<sub>x</sub>O<sub>2-δ</sub> Solid Solution Nanodisks: Preparation and Their CO Oxidation Activity. *J. Phys. Chem. C* **2012**, *116* (24), 13127–13132. <https://doi.org/10.1021/jp3017826>.
- (79) Faber, J.; Geoffroy, C.; Roux, A.; Sylvestre, A.; Abélard, P. A Systematic Investigation of the Dc Electrical Conductivity of Rare-Earth Doped Ceria. *Appl. Phys. A Solids Surfaces* **1989**, *49* (3), 225–232. <https://doi.org/10.1007/BF00616848>.
- (80) Dholabhai, P. P.; Anwar, S.; Adams, J. B.; Crozier, P.; Sharma, R. Kinetic Lattice Monte Carlo Model for Oxygen Vacancy Diffusion in Praseodymium Doped Ceria: Applications to Materials Design. *J. Solid State Chem.* **2011**, *184* (4), 811–817. <https://doi.org/10.1016/j.jssc.2011.02.004>.
- (81) Charisiou, N. D.; Siakavelas, G.; Papageridis, K. N.; Baklavaridis, A.; Tzounis, L.; Polychronopoulou, K.; Goula, M. A. Hydrogen Production via the Glycerol Steam Reforming

- Reaction over Nickel Supported on Alumina and Lanthana-Alumina Catalysts. *Int. J. Hydrogen Energy* **2017**, *42* (18), 13039–13060. <https://doi.org/10.1016/j.ijhydene.2017.04.048>.
- (82) Ahlers, S. J.; Pohl, M. M.; Radnik, J.; Linke, D.; Kondratenko, E. V. Catalytic Role and Location of Cs Promoter in Cs-Au/TiO<sub>2</sub> Catalysts for Propanol Synthesis from CO<sub>2</sub>, C<sub>2</sub>H<sub>4</sub> and H<sub>2</sub>. *Appl. Catal. B Environ.* **2015**, *176–177*, 570–577. <https://doi.org/10.1016/j.apcatb.2015.04.034>.
- (83) Telkar, M. M.; Rode, C. V.; Rane, V. H.; Chaudhari, R. V. Influence of Alkali Metal Doping on Selectivity Behaviour of Platinum Catalysts for Hydrogenation of 2-Butyne-1,4-Diol. *Catal. Commun.* **2005**, *6* (11), 725–730. <https://doi.org/10.1016/j.catcom.2005.07.009>.
- (84) Sayed, M.; Xu, F.; Kuang, P.; Low, J.; Wang, S.; Zhang, L.; Yu, J. Sustained CO<sub>2</sub>-Photoreduction Activity and High Selectivity over Mn, C-Codoped ZnO Core-Triple Shell Hollow Spheres. *Nat. Commun.* **2021**, *12* (1), 1–10. <https://doi.org/10.1038/s41467-021-25007-6>.
- (85) Chou, C. Y.; Lobo, R. F. Direct Conversion of CO<sub>2</sub> into Methanol over Promoted Indium Oxide-Based Catalysts. *Appl. Catal. A Gen.* **2019**, *583* (July), 117144. <https://doi.org/10.1016/j.apcata.2019.117144>.
- (86) Morse, J. R.; Juneau, M.; Baldwin, J. W.; Porosoff, M. D.; Willauer, H. D. Alkali Promoted Tungsten Carbide as a Selective Catalyst for the Reverse Water Gas Shift Reaction. *J. CO<sub>2</sub> Util.* **2020**, *35* (August 2019), 38–46. <https://doi.org/10.1016/j.jcou.2019.08.024>.
- (87) Zhang, Z.; Zhang, X.; Zhang, L.; Gao, J.; Shao, Y.; Dong, D.; Zhang, S.; Liu, Q.; Xu, L.; Hu, X. Impacts of Alkali or Alkaline Earth Metals Addition on Reaction Intermediates Formed in Methanation of CO<sub>2</sub> over Cobalt Catalysts. *J. Energy Inst.* **2020**, *93* (4), 1581–1596. <https://doi.org/10.1016/j.joei.2020.01.020>.
- (88) Varvoutis, G.; Lykaki, M.; Papista, E.; Carabineiro, S. nia A. C.; Psarras, A. C.; Marnellos, G. E.; Konsolakis, M. Effect of Alkali (Cs) Doping on the Surface Chemistry and CO<sub>2</sub> hydrogenation Performance of CuO/CeO<sub>2</sub> catalysts. *J. CO<sub>2</sub> Util.* **2021**, *44* (October 2020). <https://doi.org/10.1016/j.jcou.2020.101408>.
- (89) Huang, Z.; Yuan, Y.; Song, M.; Hao, Z.; Xiao, J.; Cai, D.; Ibrahim, A. R.; Zhan, G. CO<sub>2</sub> Hydrogenation over Mesoporous Ni-Pt/SiO<sub>2</sub> Nanorod Catalysts: Determining CH<sub>4</sub>/CO

- Selectivity by Surface Ratio of Ni/Pt. *Chem. Eng. Sci.* **2022**, *247*, 117106. <https://doi.org/10.1016/j.ces.2021.117106>.
- (90) Zhang, R.; Wei, A.; Zhu, M.; Wu, X.; Wang, H.; Zhu, X.; Ge, Q. Tuning Reverse Water Gas Shift and Methanation Reactions during CO<sub>2</sub> Reduction on Ni Catalysts via Surface Modification by MoO<sub>x</sub>. *J. CO<sub>2</sub> Util.* **2021**, *52* (August), 101678. <https://doi.org/10.1016/j.jcou.2021.101678>.
- (91) Wang, L. X.; Guan, E.; Wang, Z.; Wang, L.; Gong, Z.; Cui, Y.; Yang, Z.; Wang, C.; Zhang, J.; Meng, X.; Hu, P.; Gong, X. Q.; Gates, B. C.; Xiao, F. S. Dispersed Nickel Boosts Catalysis by Copper in CO<sub>2</sub> hydrogenation. *ACS Catal.* **2020**, *10* (16), 9261–9270. <https://doi.org/10.1021/acscatal.0c00907>.
- (92) Lykaki, M.; Pachatouridou, E.; Carabineiro, S. A. C.; Iliopoulou, E.; Andriopoulou, C.; Kallithrakas-Kontos, N.; Boghosian, S.; Konsolakis, M. Ceria Nanoparticles Shape Effects on the Structural Defects and Surface Chemistry: Implications in CO Oxidation by Cu/CeO<sub>2</sub> catalysts. *Appl. Catal. B Environ.* **2018**, *230* (February), 18–28. <https://doi.org/10.1016/j.apcatb.2018.02.035>.
- (93) Luo, F.; Jia, C.-J.; Song, W.; You, L.-P.; Yan, C.-H. Chelating Ligand-Mediated Crystal Growth of Cerium Orthovanadate. *Cryst. Growth Des.* **2005**, *5* (1), 137–142. <https://doi.org/10.1021/cg049940b>.
- (94) Ren, Z.; Peng, F.; Chen, B.; Mei, D.; Li, J. Science Direct A Combined Experimental and Computational Study of Water-Gas Shift Reaction over Rod-Shaped Catalysts. *Int. J. Hydrogen Energy* **2017**, *42* (51), 30086–30097. <https://doi.org/10.1016/j.ijhydene.2017.10.047>.
- (95) Wang, N.; Qian, W.; Chu, W.; Wei, F. Crystal-Plane Effect of Nanoscale CeO<sub>2</sub> on the Catalytic Performance of Ni/CeO<sub>2</sub> Catalysts for Methane Dry Reforming. *Catal. Sci. Technol.* **2016**, *6* (10), 3594–3605. <https://doi.org/10.1039/C5CY01790D>.
- (96) Liu, S.; Liao, X.; Zhang, Q.; Zhang, Y.; Wang, H.; Zhao, Y. Crystal-Plane and Shape Influences of Nanoscale CeO<sub>2</sub> on the Activity of Ni/CeO<sub>2</sub> Catalysts for Maleic Anhydride Hydrogenation. *Nanomaterials* **2022**, *12* (5), 762. <https://doi.org/10.3390/nano12050762>.
- (97) Li, D.; Li, K.; Xu, R.; Wang, H.; Tian, D.; Wei, Y.; Zhu, X.; Zeng, C.; Zeng, L. Ce<sub>1-x</sub>Fe<sub>x</sub>O<sub>2-Δ</sub> Catalysts for Catalytic Methane Combustion: Role of Oxygen Vacancy and Structural

- Dependence. *Catal. Today* **2018**, *318* (November 2017), 73–85. <https://doi.org/10.1016/j.cattod.2017.12.015>.
- (98) Sudarsanam, P.; Hillary, B.; Amin, M. H.; Rockstroh, N.; Bentrup, U.; Brückner, A.; Bhargava, S. K. Heterostructured Copper-Ceria and Iron-Ceria Nanorods: Role of Morphology, Redox, and Acid Properties in Catalytic Diesel Soot Combustion. *Langmuir* **2018**, *34* (8), 2663–2673. <https://doi.org/10.1021/acs.langmuir.7b03998>.
- (99) Bayram, B.; Soykal, I. I.; Von Deak, D.; Miller, J. T.; Ozkan, U. S. Ethanol Steam Reforming over Co-Based Catalysts: Investigation of Cobalt Coordination Environment under Reaction Conditions. *J. Catal.* **2011**, *284* (1), 77–89. <https://doi.org/10.1016/j.jcat.2011.09.001>.
- (100) Guo, X.; Zhou, R. A New Insight into the Morphology Effect of Ceria on CuO/CeO<sub>2</sub> Catalysts for CO Selective Oxidation in Hydrogen-Rich Gas. *Catal. Sci. Technol.* **2016**, *6* (11), 3862–3871. <https://doi.org/10.1039/c5cy01816a>.
- (101) Aboukaïs, A.; Skaf, M.; Hany, S.; Cousin, R.; Aouad, S.; Labaki, M.; Abi-Aad, E. A Comparative Study of Cu, Ag and Au Doped CeO<sub>2</sub> in the Total Oxidation of Volatile Organic Compounds (VOCs). *Mater. Chem. Phys.* **2016**, *177*, 570–576. <https://doi.org/10.1016/j.matchemphys.2016.04.072>.
- (102) Zhao, P.; Qin, F.; Huang, Z.; Sun, C.; Shen, W.; Xu, H. Morphology-Dependent Oxygen Vacancies and Synergistic Effects of Ni/CeO<sub>2</sub> Catalysts for N<sub>2</sub>O Decomposition. *Catal. Sci. Technol.* **2018**, *8* (1), 276–288. <https://doi.org/10.1039/c7cy02301d>.
- (103) Löfberg, A.; Guerrero-Caballero, J.; Kane, T.; Rubbens, A.; Jalowiecki-Duhamel, L. Ni/CeO<sub>2</sub> Based Catalysts as Oxygen Vectors for the Chemical Looping Dry Reforming of Methane for Syngas Production. *Appl. Catal. B Environ.* **2017**, *212*, 159–174. <https://doi.org/10.1016/j.apcatb.2017.04.048>.
- (104) Barrio, L.; Kubacka, A.; Zhou, G.; Estrella, M.; Martínez-Arias, A.; Hanson, J. C.; Fernández-García, M.; Rodríguez, J. A. Unusual Physical and Chemical Properties of Ni in Ce<sub>1-x</sub>Ni<sub>x</sub>O<sub>2-y</sub> Oxides: Structural Characterization and Catalytic Activity for the Water Gas Shift Reaction. *J. Phys. Chem. C* **2010**, *114* (29), 12689–12697. <https://doi.org/10.1021/jp103958u>.
- (105) Hashimoto, N.; Mori, K.; Asahara, K.; Shibata, S.; Jida, H.; Kuwahara, Y.; Yamashita, H. How the Morphology of NiO<sub>x</sub>-Decorated CeO<sub>2</sub> Nanostructures Affects Catalytic Properties in CO<sub>2</sub> Methanation. *Langmuir* **2021**, *37* (17), 5376–5384.

<https://doi.org/10.1021/acs.langmuir.1c00546>.

- (106) Pantaleo, G.; Parola, V. La; Deganello, F.; Singha, R. K.; Bal, R.; Venezia, A. M. Ni/CeO<sub>2</sub> Catalysts for Methane Partial Oxidation: Synthesis Driven Structural and Catalytic Effects. *Appl. Catal. B Environ.* **2016**, *189*, 233–241. <https://doi.org/10.1016/j.apcatb.2016.02.064>.
- (107) Hu, Z.; Qiu, S.; You, Y.; Guo, Y.; Guo, Y.; Wang, L.; Zhan, W.; Lu, G. Hydrothermal Synthesis of NiCeO<sub>x</sub> Nanosheets and Its Application to the Total Oxidation of Propane. *Appl. Catal. B Environ.* **2018**, *225* (June 2017), 110–120. <https://doi.org/10.1016/j.apcatb.2017.08.068>.
- (108) Iglesias, I.; Baronetti, G.; Mariño, F. Ceria and Ce<sub>0.95</sub>M<sub>0.05</sub>O<sub>2-δ</sub> Mixed Oxides (M = La, Pr, Zr): Vacancies and Reducibility Study. *Solid State Ionics* **2017**, *309* (June), 123–129. <https://doi.org/10.1016/j.ssi.2017.07.008>.
- (109) Zou, W.; Ge, C.; Lu, M.; Wu, S.; Wang, Y.; Sun, J.; Pu, Y.; Tang, C.; Gao, F.; Dong, L. Engineering the NiO/CeO<sub>2</sub> Interface to Enhance the Catalytic Performance for CO Oxidation. *RSC Adv.* **2015**, *5* (119), 98335–98343. <https://doi.org/10.1039/c5ra20466f>.
- (110) Hao, Z.; Shen, J.; Lin, S.; Han, X.; Chang, X.; Liu, J.; Li, M.; Ma, X. Decoupling the Effect of Ni Particle Size and Surface Oxygen Deficiencies in CO<sub>2</sub> Methanation over Ceria Supported Ni. *Appl. Catal. B Environ.* **2021**, *286* (November 2020), 119922. <https://doi.org/10.1016/j.apcatb.2021.119922>.
- (111) Atzori, L.; Cutrufello, M. G.; Meloni, D.; Onida, B.; Gazzoli, D.; Ardu, A.; Monaci, R.; Sini, M. F.; Rombi, E. Characterization and Catalytic Activity of Soft-Templated NiO-CeO<sub>2</sub> Mixed Oxides for CO and CO<sub>2</sub> Co-Methanation. *Front. Chem. Sci. Eng.* **2021**, *15* (2), 251–268. <https://doi.org/10.1007/s11705-020-1951-8>.
- (112) Pal, P.; Singha, R. K.; Saha, A.; Bal, R.; Panda, A. B. Defect-Induced Efficient Partial Oxidation of Methane over Nonstoichiometric Ni/CeO<sub>2</sub> Nanocrystals. *J. Phys. Chem. C* **2015**, *119* (24), 13610–13618. <https://doi.org/10.1021/acs.jpcc.5b01724>.
- (113) Zhang, X.; You, R.; Li, D.; Cao, T.; Huang, W. Reaction Sensitivity of Ceria Morphology Effect on Ni/CeO<sub>2</sub> Catalysis in Propane Oxidation Reactions. *ACS Appl. Mater. Interfaces* **2017**, *9* (41), 35897–35907. <https://doi.org/10.1021/acsami.7b11536>.
- (114) Du, Y.; Qin, C.; Xu, Y.; Xu, D.; Bai, J.; Ma, G.; Ding, M. Ni Nanoparticles Dispersed on Oxygen Vacancies-Rich CeO<sub>2</sub> Nanoplates for Enhanced Low-Temperature CO<sub>2</sub> Methanation

- Performance. *Chem. Eng. J.* **2021**, *418* (January). <https://doi.org/10.1016/j.cej.2021.129402>.
- (115) Mustard, D. G.; Bartholomew, C. H. Determination of Metal Crystallite Size and Morphology in Supported Nickel Catalysts. *J. Catal.* **1981**, *67* (1), 186–206. [https://doi.org/10.1016/0021-9517\(81\)90271-2](https://doi.org/10.1016/0021-9517(81)90271-2).
- (116) Le, T. A.; Kim, T. W.; Lee, S. H.; Park, E. D. Effects of Na Content in Na/Ni/SiO<sub>2</sub> and Na/Ni/CeO<sub>2</sub> Catalysts for CO and CO<sub>2</sub> Methanation. *Catal. Today* **2018**, *303* (September 2017), 159–167. <https://doi.org/10.1016/j.cattod.2017.09.031>.
- (117) Zhou, G.; Liu, H.; Cui, K.; Xie, H.; Jiao, Z.; Zhang, G.; Xiong, K.; Zheng, X. Methanation of Carbon Dioxide over Ni/CeO<sub>2</sub> Catalysts: Effects of Support CeO<sub>2</sub> Structure. *Int. J. Hydrogen Energy* **2017**, *42* (25), 16108–16117. <https://doi.org/10.1016/j.ijhydene.2017.05.154>.
- (118) Lv, Z.; Zhong, Q.; Ou, M. Utilizing Peroxide as Precursor for the Synthesis of CeO<sub>2</sub>/ZnO Composite Oxide with Enhanced Photocatalytic Activity. *Appl. Surf. Sci.* **2016**, *376*, 91–96. <https://doi.org/10.1016/j.apsusc.2016.01.280>.
- (119) Xie, Q.; Zhao, Y.; Guo, H.; Lu, A.; Zhang, X.; Wang, L.; Chen, M.-S.; Peng, D. Facile Preparation of Well-Dispersed CeO<sub>2</sub>–ZnO Composite Hollow Microspheres with Enhanced Catalytic Activity for CO Oxidation. *ACS Appl. Mater. Interfaces* **2014**, *6* (1), 421–428. <https://doi.org/10.1021/am404487b>.
- (120) Golovanova, V.; Spadaro, M. C.; Arbiol, J.; Golovanov, V.; Rantala, T. T.; Andreu, T.; Morante, J. R. Effects of Solar Irradiation on Thermally Driven CO<sub>2</sub> Methanation Using Ni/CeO<sub>2</sub>-Based Catalyst. *Appl. Catal. B Environ.* **2021**, *291* (February). <https://doi.org/10.1016/j.apcatb.2021.120038>.
- (121) Li, S.; Liu, G.; Zhang, S.; An, K.; Ma, Z.; Wang, L.; Liu, Y. Cerium-Modified Ni-La<sub>2</sub>O<sub>3</sub>/ZrO<sub>2</sub> for CO<sub>2</sub> Methanation. *J. Energy Chem.* **2020**, *43*, 155–164. <https://doi.org/10.1016/j.jechem.2019.08.024>.
- (122) Guo, X.; Traitangwong, A.; Hu, M.; Zuo, C.; Meeyoo, V.; Peng, Z.; Li, C. Carbon Dioxide Methanation over Nickel-Based Catalysts Supported on Various Mesoporous Material. *Energy and Fuels* **2018**, *32* (3), 3681–3689. <https://doi.org/10.1021/acs.energyfuels.7b03826>.
- (123) Kostić, R.; Aškračić, S.; Dohčević-Mitrović, Z.; Popović, Z. V. Low-Frequency Raman Scattering from CeO<sub>2</sub> Nanoparticles. *Appl. Phys. A Mater. Sci. Process.* **2008**, *90* (4), 679–683. <https://doi.org/10.1007/s00339-007-4345-6>.

- (124) Wu, Z.; Li, M.; Howe, J.; Meyer, H. M.; Overbury, S. H. Probing Defect Sites on CeO<sub>2</sub> Nanocrystals with Well-Defined Surface Planes by Raman Spectroscopy and O<sub>2</sub> Adsorption. *Langmuir* **2010**, *26* (21), 16595–16606. <https://doi.org/10.1021/la101723w>.
- (125) Huang, S. H.; Chen, Z.; Shen, X. C.; Zhu, Z. Q.; Yu, K. Raman Scattering of Single Tetrapod-like ZnO Nanostructure Synthesized by Catalyst-Free Rapid Evaporation. *Solid State Commun.* **2008**, *145* (7–8), 418–422. <https://doi.org/10.1016/j.ssc.2007.11.014>.
- (126) Rajkumar, T.; Sápi, A.; Ábel, M.; Kiss, J.; Szenti, I.; Baán, K.; Gómez-Pérez, J. F.; Kukovecz, Á.; Kónya, Z. Surface Engineering of CeO<sub>2</sub> Catalysts: Differences Between Solid Solution Based and Interfacially Designed Ce<sub>1-x</sub>M<sub>x</sub>O<sub>2</sub> and MO/CeO<sub>2</sub> (M = Zn, Mn) in CO<sub>2</sub> Hydrogenation Reaction. *Catal. Letters* **2021**, *151* (12), 3477–3491. <https://doi.org/10.1007/s10562-021-03591-y>.
- (127) Gurbani, A.; Ayastuy, J. L.; González-Marcos, M. P.; Gutiérrez-Ortiz, M. A. CuO-CeO<sub>2</sub> Catalysts Synthesized by Various Methods: Comparative Study of Redox Properties. *Int. J. Hydrogen Energy* **2010**, *35* (20), 11582–11590. <https://doi.org/10.1016/j.ijhydene.2010.04.045>.
- (128) Elias, K. F. M.; Bednarczuk, L.; Assaf, E. M.; Ramírez de la Piscina, P.; Homs, N. Study of Ni/CeO<sub>2</sub>-ZnO Catalysts in the Production of H<sub>2</sub> from Acetone Steam Reforming. *Int. J. Hydrogen Energy* **2019**, *44* (25), 12628–12635. <https://doi.org/10.1016/j.ijhydene.2018.10.191>.
- (129) Hao, Z.; Shen, J.; Lin, S.; Han, X.; Chang, X.; Liu, J.; Li, M.; Ma, X. Decoupling the Effect of Ni Particle Size and Surface Oxygen Deficiencies in CO<sub>2</sub> Methanation over Ceria Supported Ni. *Appl. Catal. B Environ.* **2021**, *286* (January), 119922. <https://doi.org/10.1016/j.apcatb.2021.119922>.
- (130) Trogadas, P.; Parrondo, J.; Ramani, V. CeO<sub>2</sub> Surface Oxygen Vacancy Concentration Governs in Situ Free Radical Scavenging Efficacy in Polymer Electrolytes. *ACS Appl. Mater. Interfaces* **2012**, *4* (10), 5098–5102. <https://doi.org/10.1021/am3016069>.
- (131) Mahammadunnisa, S.; Manoj Kumar Reddy, P.; Lingaiah, N.; Subrahmanyam, C. NiO/Ce<sub>1-x</sub>Ni<sub>x</sub>O<sub>2-δ</sub> as an Alternative to Noble Metal Catalysts for CO Oxidation. *Catal. Sci. Technol.* **2013**, *3* (3), 730–736. <https://doi.org/10.1039/c2cy20641b>.
- (132) Sreeremya, T. S.; Krishnan, A.; Remani, K. C.; Patil, K. R.; Brougham, D. F.; Ghosh, S.

- Shape-Selective Oriented Cerium Oxide Nanocrystals Permit Assessment of the Effect of the Exposed Facets on Catalytic Activity and Oxygen Storage Capacity. *ACS Appl. Mater. Interfaces* **2015**, 7 (16), 8545–8555. <https://doi.org/10.1021/acsami.5b00298>.
- (133) Tang, R.; Ullah, N.; Hui, Y.; Li, X.; Li, Z. Enhanced CO<sub>2</sub> Methanation Activity over Ni/CeO<sub>2</sub> Catalyst by One-Pot Method. *Mol. Catal.* **2021**, 508 (May), 111602. <https://doi.org/10.1016/j.mcat.2021.111602>.
- (134) Luo, S.; Fu, P.; Sun, F.; Wang, B.; Zhang, A.; Wang, J.; Sun, Q. Catalytic Steam Reforming of Bio-Oil-Derived Acetic Acid over CeO<sub>2</sub>-ZnO Supported Ni Nanoparticle Catalysts. *ACS Omega* **2020**, 5 (31), 19727–19736. <https://doi.org/10.1021/acsomega.0c02487>.
- (135) Wang, W.; Li, X.; Zhang, Y.; Zhang, R.; Ge, H.; Bi, J.; Tang, M. Strong Metal-Support Interactions between Ni and ZnO Particles and Their Effect on the Methanation Performance of Ni/ZnO. *Catal. Sci. Technol.* **2017**, 7 (19), 4413–4421. <https://doi.org/10.1039/c7cy01119a>.
- (136) Huang, L.; Yan, L.; Tang, M.; Wang, G.; Qin, Z.; Ge, H. Effect of Pretreatment on the Adsorption Performance of Ni/ZnO Adsorbent for Dibenzothiophene Desulfurization. *ACS Omega* **2018**, 3 (12), 18967–18975. <https://doi.org/10.1021/acsomega.8b02843>.
- (137) Johnson, M. F. L.; Mooi, J. Cerium Dioxide Crystallite Sizes by Temperature-Programmed Reduction. *J. Catal.* **1987**, 103 (2), 502–505. [https://doi.org/10.1016/0021-9517\(87\)90142-4](https://doi.org/10.1016/0021-9517(87)90142-4).
- (138) Ye, R. P.; Li, Q.; Gong, W.; Wang, T.; Razink, J. J.; Lin, L.; Qin, Y. Y.; Zhou, Z.; Adidharma, H.; Tang, J.; Russell, A. G.; Fan, M.; Yao, Y. G. High-Performance of Nanostructured Ni/CeO<sub>2</sub> Catalyst on CO<sub>2</sub> Methanation. *Appl. Catal. B Environ.* **2020**, 268 (November 2019), 118474. <https://doi.org/10.1016/j.apcatb.2019.118474>.
- (139) Li, M.; van Veen, A. C. Tuning the Catalytic Performance of Ni-Catalysed Dry Reforming of Methane and Carbon Deposition via Ni-CeO<sub>2-x</sub> Interaction. *Appl. Catal. B Environ.* **2018**, 237 (April), 641–648. <https://doi.org/10.1016/j.apcatb.2018.06.032>.
- (140) Bian, Z.; Chan, Y. M.; Yu, Y.; Kawi, S. Morphology Dependence of Catalytic Properties of Ni/CeO<sub>2</sub> for CO<sub>2</sub> Methanation: A Kinetic and Mechanism Study. *Catal. Today* **2020**, 347 (January 2018), 31–38. <https://doi.org/10.1016/j.cattod.2018.04.067>.
- (141) Lykaki, M.; Pachatouridou, E.; Iliopoulou, E.; Carabineiro, S. A. C.; Konsolakis, M. Impact of the Synthesis Parameters on the Solid State Properties and the CO Oxidation Performance of Ceria Nanoparticles. *RSC Adv.* **2017**, 7 (10), 6160–6169.

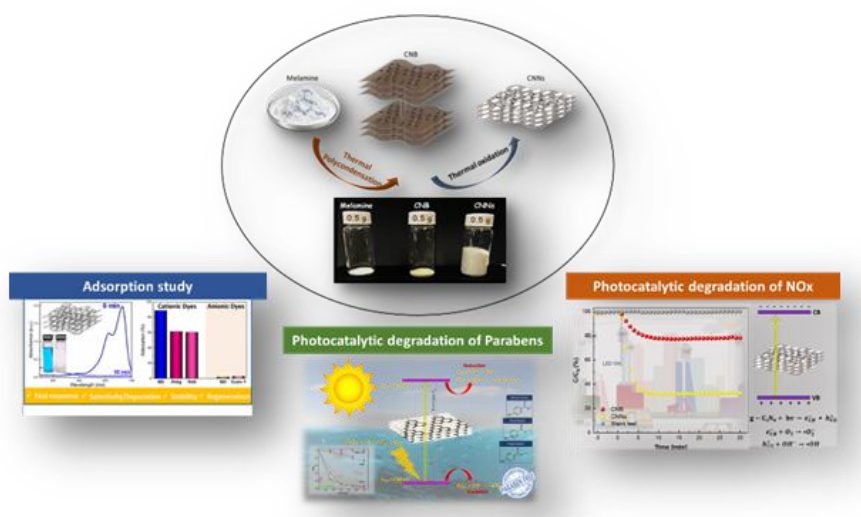
<https://doi.org/10.1039/C6RA26712B>.

- (142) Weatherbee, G. D.; Bartholomew, C. H. Hydrogenation of CO<sub>2</sub> on Group VIII Metals. II. Kinetics and Mechanism of CO<sub>2</sub> Hydrogenation on Nickel. *J. Catal.* **1982**, *77* (2), 460–472. [https://doi.org/10.1016/0021-9517\(82\)90186-5](https://doi.org/10.1016/0021-9517(82)90186-5).
- (143) Zhen, W.; Li, B.; Lu, G.; Ma, J. Enhancing Catalytic Activity and Stability for CO<sub>2</sub> Methanation on Ni@MOF-5 via Control of Active Species Dispersion. *Chem. Commun.* **2015**, *51* (9), 1728–1731. <https://doi.org/10.1039/c4cc08733j>.
- (144) Zhou, G.; Liu, H.; Xing, Y.; Xu, S.; Xie, H.; Xiong, K. CO<sub>2</sub> Hydrogenation to Methane over Mesoporous Co/SiO<sub>2</sub> Catalysts: Effect of Structure. *J. CO<sub>2</sub> Util.* **2018**, *26* (May), 221–229. <https://doi.org/10.1016/j.jcou.2018.04.023>.
- (145) Ginés, M. J. L.; Marchi, A. J.; Apesteguía, C. R. Kinetic Study of the Reverse Water-Gas Shift Reaction over CuO/ZnO/Al<sub>2</sub>O<sub>3</sub> Catalysts. *Appl. Catal. A Gen.* **1997**, *154* (1–2), 155–171. [https://doi.org/10.1016/S0926-860X\(96\)00369-9](https://doi.org/10.1016/S0926-860X(96)00369-9).
- (146) Chen, C. S.; Cheng, W. H. Study on the Mechanism of CO Formation in Reverse Water Gas Shift Reaction over Cu/SiO<sub>2</sub> Catalyst by Pulse Reaction, TPD and TPR. *Catal. Letters* **2002**, *83* (3–4), 121–126. <https://doi.org/10.1023/A:1021006718974>.
- (147) Lin, J.; Ma, C.; Wang, Q.; Xu, Y.; Ma, G.; Wang, J.; Wang, H.; Dong, C.; Zhang, C.; Ding, M. Enhanced Low-Temperature Performance of CO<sub>2</sub> Methanation over Mesoporous Ni/Al<sub>2</sub>O<sub>3</sub>-ZrO<sub>2</sub> Catalysts. *Appl. Catal. B Environ.* **2019**, *243* (July 2018), 262–272. <https://doi.org/10.1016/j.apcatb.2018.10.059>.

# Chapter 5

## Highly Porous Thin-Layer g-C<sub>3</sub>N<sub>4</sub> Nanosheets with Enhanced Adsorption Capacity and Photocatalytic Performance

Chapter 5 presents a comprehensive comparative study of the photocatalytic activity and adsorption capacity of bulk g-C<sub>3</sub>N<sub>4</sub> (CNB) and g-C<sub>3</sub>N<sub>4</sub> nanosheets (CNNs). The synthesis of well-structured porous CNNs through thermal exfoliation of melamine was successfully



achieved. A detailed characterization study was performed to understand the impact of thermal exfoliation on the physicochemical characteristics of both materials. The chapter initially describes the investigation of the adsorption capacity and separation ability of both materials for dyes with different charges and sizes under various experimental conditions. Experimental and theoretical investigations reveal that CNNs exhibit superior adsorption and separation capacity compared to CNB. Subsequently, the photocatalytic performance of CNB and CNNs was comparatively assessed for the degradation of paraben. Several experimental parameters were explored, such as catalyst concentration, initial concentration of parabens, irradiation type, and scavenger addition. The highly porous CNNs exhibited excellent photocatalytic activity and stability under simulated solar irradiation, outperforming CNB. Additionally, the potential of g-C<sub>3</sub>N<sub>4</sub> as a supporting carrier for the transition metal active phase in the photocatalytic degradation of methylparaben was explored. In the context of gas-phase photocatalysis, the photocatalytic efficiency for NO<sub>x</sub> removal was evaluated for both CNB and CNNs under visible LED light illumination. The porous CNNs demonstrated a significant enhancement in photocatalytic activity, along with excellent stability and repeatability.

## Introduction

In recent times, the consequences of long-term industrial and agricultural activities have become increasingly evident, manifesting in significant air and water pollution issues. This alarming situation poses a considerable threat to the delicate ecological balance and the overall well-being of humanity. Urgent action is needed to address and mitigate these environmental challenges before they further exacerbate and adversely affect our ecosystems and health.

Water pollution has emerged as a significant concern among the scientific community, primarily due to the alarming increase in hazardous organic compounds present in wastewater. Among the major contributors to aqueous pollution is the contamination caused by dyes in wastewater<sup>1</sup>. Various industries, such as textile dyeing, papermaking, food processing, paints, and cosmetics, release their dye-contaminated effluents into the environment, resulting in the presence of dye-contaminated wastewater<sup>2</sup>. This issue is further exacerbated by the staggering global production of approximately one million tons of dyes annually, with more than 15% of these dyes being released as pollutants in industrial effluents<sup>2</sup>. The dyes discharged in wastewater pose serious health and ecological risks as they are highly toxic, carcinogenic, and xenobiotic to living organisms. The presence of these dyes in wastewater profoundly impacts the aqueous ecosystem, as the intense color imparted by the dyes hinders the penetration of sunlight into the water body<sup>2,3</sup>.

Another category of widespread contaminants contributing to water pollution is pharmaceuticals and personal care products (PPCPs)<sup>4,5</sup>. Among these, parabens stand out as a significant concern. Parabens are commonly used as preservatives and antimicrobials in cosmetics, pharmaceuticals, processed foods, and various industrial products<sup>6</sup>. However, they have been classified as endocrine disruptors and are acknowledged as emerging contaminants due to their continuous release in aquatic environments, being detected at ng/L to µg/L levels<sup>7</sup>. Parabens exhibit ecotoxicity to various microorganisms and have mild estrogenic properties<sup>8,9</sup>. Although parabens are effective against fungi and gram-positive bacteria, their safety in products remains a subject of substantial debate<sup>6</sup>. Recent concerns have highlighted potential risks to water quality, human health, and the ecosystem. Direct exposure to parabens occurs during the use of PPCPs, leading to their detection in human tissues and urine samples<sup>10,11</sup>. Numerous studies have reported the estrogenic and carcinogenic effects of parabens, underscoring the urgent need to eliminate these contaminants from wastewater and other aqueous effluents<sup>6,12</sup>.

There are various methods available for the removal of organic pollutants from wastewater, with two prominent approaches being oxidation and adsorption processes<sup>4,6,12-15</sup>. Adsorption is highly regarded for its simplicity, efficiency, and economic viability, and it offers the advantage of not

producing any by-products<sup>16–19</sup>. One widely used adsorbent for this purpose is activated carbon, particularly effective in adsorbing and separating dyes<sup>20–22</sup>. However, the activation process of this material involves the use of activation agents and is both complex and time-consuming, limiting its widespread application<sup>23,24</sup>. Another promising technology for effectively eliminating organic pollutants from wastewater is heterogeneous photocatalysis. This technique is known for its affordability, simplicity, and non-toxic nature<sup>4</sup>. Heterogeneous photocatalysis has shown high efficiency in degrading a wide range of pollutants, even under ambient temperature and pressure conditions<sup>25</sup>. Nevertheless, its efficiency is still considered relatively low and requires further investigation. Recent studies have primarily focused on two key areas to enhance photocatalysis. Firstly, researchers have been working on developing solar light-responsive photocatalysts to increase their efficiency and applicability<sup>13,26–32</sup>. Secondly, they are actively optimizing experimental conditions to enhance the photocatalytic performance and stability of these catalysts<sup>28–30</sup>.

In the realm of air pollution, nitrogen oxides (NO<sub>x</sub>) stand out as a major concern due to their significant impact on both human health and the environment. Exposure to NO<sub>x</sub> can trigger and exacerbate asthma symptoms while also contributing to the development of asthma over prolonged periods<sup>33</sup>. NO<sub>x</sub> comprises NO and NO<sub>2</sub> gases, which arise from natural processes like lightning and volcanic activity. However, the most substantial sources of NO<sub>x</sub> stem from the reaction between nitrogen and oxygen during fuel combustion, especially in car engines operating at high temperatures<sup>34</sup>. In densely populated urban areas with heavy motor vehicle traffic, nitrogen oxide emissions can significantly alter the urban atmosphere's chemistry, particularly affecting ozone generation. Motor vehicle engines, being a primary source, are the leading contributors to NO<sub>x</sub> emissions<sup>35</sup>. Recognizing the critical nature of NO<sub>x</sub> emissions, it becomes imperative to implement effective methods for reducing them and safeguarding the environment. As a response, various strategies have been deployed, including primary methods like NO<sub>x</sub> emission controls and secondary approaches involving the conversion of NO<sub>x</sub> into N<sub>2</sub> or HNO<sub>3</sub><sup>34</sup>. Among these secondary methods, heterogeneous photocatalysis stands out as a particularly promising technology for air purification. This method utilizes eco-friendly, cost-effective, adaptable, and high-performance materials, making it well-suited for large-scale applications<sup>36,37</sup>. As a result, the scientific community has extensively examined numerous photocatalysts for their efficacy in removing NO<sub>x</sub> pollutants.

Graphitic carbon nitride (g-C<sub>3</sub>N<sub>4</sub>) has emerged as a highly promising metal-free semiconductor material for various energy and environmental applications, including photocatalytic hydrogen evolution, photocatalytic degradation of pollutants, sensors, and adsorbents<sup>15,19,38–42</sup>. Recent research has focused on synthesizing mesoporous g-C<sub>3</sub>N<sub>4</sub>, and related advances have been reviewed, encompassing the synthesis methods, growth mechanism, modification strategies, and current

applications<sup>43</sup>. Notably, g-C<sub>3</sub>N<sub>4</sub> composed of non-metal, earth-abundant elements (carbon and nitrogen), is characterized as the most stable allotrope among various carbon nitrides under ambient conditions<sup>44</sup>. Typically, bulk g-C<sub>3</sub>N<sub>4</sub> can be easily obtained through traditional thermal condensation of low-cost carbon and nitrogen-based precursors, such as urea, thiourea, melamine, cyanamide, and dicyandiamide, at temperatures ranging from 500–650 °C<sup>45–49</sup>. However, bulk g-C<sub>3</sub>N<sub>4</sub> does suffer from certain drawbacks, including low specific surface area and large particle size resulting from layer stacking, leading to diminished activity and performance<sup>43</sup>. To address these limitations, various methods have been employed to separate the stacked layers and achieve exfoliation into thin-layer g-C<sub>3</sub>N<sub>4</sub> nanosheets. This exfoliation process is crucial to enhance specific surface area and significantly reduce particle size<sup>50–54</sup>. Multiple techniques, such as chemical exfoliation<sup>53,55–57</sup>, thermal exfoliation<sup>42,54,57–60</sup>, liquid ultrasonic exfoliation<sup>61–63</sup>, and chemical blowing<sup>64,65</sup>, have been explored for this purpose. Among them, thermal exfoliation has garnered significant attention for its cost-effectiveness and ease of producing high-quality thin-layered g-C<sub>3</sub>N<sub>4</sub> on a large scale.

In the case of the photocatalytic degradation of parabens, various semiconductors have been explored<sup>28,66–68</sup>, but g-C<sub>3</sub>N<sub>4</sub> has received relatively less attention. Notably, Arvaniti et al.<sup>69</sup> investigated the use of g-C<sub>3</sub>N<sub>4</sub> as a photocatalyst for the degradation of methylparaben under solar irradiation. They reported complete degradation of methylparaben after just 90 minutes of irradiation, even at the lowest initial concentration. Additionally, Fernandes et al.<sup>70</sup> focused on the photocatalytic degradation of multiple parabens, including methyl-, ethyl-, and propylparaben, using exfoliated g-C<sub>3</sub>N<sub>4</sub> under visible irradiation. They achieved complete degradation of each paraben after only 20 minutes of irradiation, highlighting the effectiveness of g-C<sub>3</sub>N<sub>4</sub> as a photocatalyst for paraben removal. Moreover, Kumar et al.<sup>71</sup> took a different approach by synthesizing nano-hybrids of magnetic biochar supported g-C<sub>3</sub>N<sub>4</sub>/FeVO<sub>4</sub> for methylparaben degradation. Their study incorporated adsorption, photocatalysis, and photo-ozonation, ultimately achieving 98.4% degradation of methylparaben after 90 minutes of solar light irradiation.

In the context of photocatalytic oxidation of NO, g-C<sub>3</sub>N<sub>4</sub> has recently garnered significant interest as a potential solution to improve indoor air quality, particularly in cases where conventional photocatalysts may not be effective. Wu et al.<sup>72</sup> successfully synthesized g-C<sub>3</sub>N<sub>4</sub> with a high surface area through repeated post-calcination, resulting in enhanced visible photocatalytic activity for NO oxidation. Similarly, Huang et al.<sup>73</sup> used a hydrothermal pre-treatment-based method to prepare high-quality thin-layered g-C<sub>3</sub>N<sub>4</sub>, which exhibited a significantly increased visible-light photocatalytic performance for NO removal, achieving 5.5 times higher efficiency compared to bulk g-C<sub>3</sub>N<sub>4</sub>. Nie et al.<sup>74</sup> followed an alkaline hydrothermal treatment approach to synthesize g-C<sub>3</sub>N<sub>4</sub> with an increased BET surface area and extended absorption into the visible region, leading to improved

NO removal efficiency. Likewise, Liu et al.<sup>75</sup> employed co-pyrolysis of melamine and  $\text{NH}_4\text{HCO}_3$  to synthesize porous g- $\text{C}_3\text{N}_4$  with an enhanced specific surface area, resulting in a remarkably improved photocatalytic performance for NO removal.

Despite the extensive research on g- $\text{C}_3\text{N}_4$  in the photocatalytic field, there has been limited focus on enhancing its textural and structural characteristics, as well as its adsorption capacity for various organic pollutants<sup>76–78</sup>. The adsorption capability of g- $\text{C}_3\text{N}_4$  is significantly influenced by factors like interactions between the p-conjugated systems of g- $\text{C}_3\text{N}_4$  and the adsorbates, hydrogen bonding, and electrostatic interactions<sup>15,19</sup>. Recognizing the importance of improving g- $\text{C}_3\text{N}_4$ 's adsorption capacity, researchers have recently explored various strategies<sup>16,19,79,80</sup>. One approach involves carbon doping to modify its properties, leading to enhanced adsorption performance<sup>19</sup>. Additionally, increasing the functional groups on the surface of g- $\text{C}_3\text{N}_4$  has been considered in order to boost its adsorption capabilities<sup>15</sup>. Moreover, efforts have been directed towards increasing the specific surface area of g- $\text{C}_3\text{N}_4$ , a critical factor influencing its adsorption efficiency, among other methods.

In light of the above aspects, this chapter focuses on a comprehensive comparative study of the photocatalytic activity and adsorption capacity of bulk g- $\text{C}_3\text{N}_4$  (CNB) and g- $\text{C}_3\text{N}_4$  nanosheets (CNNs). To achieve this, well-structured porous CNNs were successfully synthesized via direct thermal polycondensation of melamine, followed by thermal exfoliation. A range of characterization techniques including TGA, BET, XRD, FTIR, SEM, TEM, AFM, UV-Vis diffuse reflectance, and PL spectroscopy were employed to gain insights into the effect of thermal exfoliation on the physicochemical characteristics of both materials. Initially, the adsorption capacity and separation ability of graphitic carbon nitrides for dyes with different charges and sizes were extensively studied under various experimental conditions. Through experimental and theoretical investigations, the superiority of exfoliated g- $\text{C}_3\text{N}_4$  in terms of adsorption and separation capacity was established. Subsequently, the photocatalytic performance of both CNB and CNNs was comparatively assessed for the degradation of methyl-, ethyl-, and propylparaben, as well as their mixture in liquid-phase photocatalysis. The study explored several experimental parameters such as catalyst concentration, initial concentration of parabens, irradiation type, and the addition of different scavengers. Remarkably, the highly porous CNNs demonstrated excellent photocatalytic activity and stability under simulated solar irradiation, outperforming CNB. Additionally, a preliminary study was conducted, exploring the potential of g- $\text{C}_3\text{N}_4$  as supporting carriers for the transition metal active phase in the photocatalytic degradation of methylparaben. In the context of gas-phase photocatalysis, the photocatalytic efficiency for  $\text{NO}_x$  removal was evaluated for both CNB and CNNs under visible LED light illumination. Encouragingly, the porous CNNs exhibited a significant enhancement in photocatalytic activity, along with excellent stability and repeatability.

## 5.1. Experimental

### 5.1.1. Materials Synthesis

All the chemical compounds used in this chapter were of analytical grade.

Melamine (purity  $\geq$  99%, Sigma-Aldrich),  $\text{Ti}(\text{OCH}(\text{CH}_3)_2)_4$  (purity  $\geq$  97%, Alfa Aesar), VOTP (purity  $\geq$  98%, Sigma-Aldrich),  $\text{Cr}_3(\text{OH})_2(\text{OOCCH}_3)_7$  (purity  $\geq$  24%, Alfa Aesar),  $\text{CH}_3\text{COO})_2\text{Mn}\cdot 4\text{H}_2\text{O}$  (purity  $\geq$  99%, Sigma-Aldrich),  $\text{Fe}(\text{NO}_3)_3\cdot 9\text{H}_2\text{O}$  (purity  $\geq$  98%, Sigma-Aldrich),  $\text{CH}_3\text{COO})_2\text{Co}\cdot 4\text{H}_2\text{O}$  (purity  $\geq$  98%, Alfa Aesar),  $\text{Ni}(\text{OCOCH}_3)_2\cdot 4\text{H}_2\text{O}$  (purity  $\geq$  98%, Sigma-Aldrich),  $\text{Cu}(\text{CO}_2\text{CH}_3)_2\cdot x\text{H}_2\text{O}$  (purity  $\geq$  98%, Sigma-Aldrich) and  $\text{Zn}(\text{CH}_3\text{COO})_2\cdot 2\text{H}_2\text{O}$  (purity  $\geq$  99%, Sigma-Aldrich) were employed as precursors for the synthesis of g- $\text{C}_3\text{N}_4$  as well as of g- $\text{C}_3\text{N}_4$ -based transition metal catalysts (M/g- $\text{C}_3\text{N}_4$ , M: Ti, V, Cr, Mn, Fe, Co, Ni, Cu, Zn).

Methylene blue (MB), rhodamine 6G (Rh6G), rhodamine B (RB), methyl orange (MO), and eosin Y were obtained from Sigma-Aldrich (Sigma-Aldrich, St. Louis, MO, USA) and were utilized for the adsorption experiments. Methyl-paraben (MP), ethyl-paraben (EP), propyl-paraben (PP), disodium ethylenediaminetetraacetate dihydrate ( $\text{EDTA}\cdot\text{Na}_2$ ), and isopropyl alcohol (IPA) were of analytical grade and purchased from Sigma-Aldrich (Sigma-Aldrich, St. Louis, MO, USA) and were used during the liquid-phase photocatalysis. For the preparation of all solutions and in all experiments, methanol ( $\geq$  99.8%, Honeywell Fluka) and distilled water were used.

The catalysts prepared in this chapter (CNB, CNNs, M/CNB) were synthesized by the methods described in Chapter 2 in Section 2.1 (Materials Synthesis). Also, Table 2.1 in Chapter 2 presents all the materials developed in this study.

### 5.1.2. Materials Characterization

Thermal analysis of as-prepared catalysts was carried out by TGA. The textural characteristics of the investigated samples were assessed by  $\text{N}_2$  adsorption-desorption isotherms at  $-196$  °C. The structural properties were determined by XRD. The morphological characteristics of the samples were investigated by SEM and TEM. A more detailed topographic examination was performed with AFM. The chemical structure of CNB and CNNs samples was confirmed by FTIR spectroscopy. Zeta potential was measured to determine the zero point of charge. The characterization techniques are fully described in Chapter 2 in section 2.2 (Characterization Techniques).

## 5.2. Computational Study

The g- $\text{C}_3\text{N}_4$  structural model used for the computations is based on the tri-s-triazine building block. In this model, g- $\text{C}_3\text{N}_4$  adopts a wave-like pattern that has been previously found to be thermodynamically more favorable than other proposed allotropes<sup>81-83</sup>. The adsorption of methylene blue cation and methyl orange anion was studied on a single g- $\text{C}_3\text{N}_4$  sheet considering a variety of

configurations of the adsorbates concerning the wave-like nature of the surface. The choice of a single-layer rather than a multi-layer model is supported by previous findings<sup>83</sup> as there is no difference in the adsorption geometry or energy of water for more than a single layer of g-C<sub>3</sub>N<sub>4</sub>. The size of the supercell used in periodic Self-Consistent Charge Density Functional Tight Binding (SCC-DFTB) calculations was  $a = 27.7 \text{ \AA}$ ,  $b = 24.25 \text{ \AA}$ ,  $c = 22.92 \text{ \AA}$ , and  $\alpha = \beta = \gamma = 90^\circ$ . Initially, the atomic coordinates and the lattice parameters of the supercell of the periodic single layer of g-C<sub>3</sub>N<sub>4</sub> were relaxed, while for the calculations, including the adsorbates, the lattice parameter corresponding to the axis vertical to the sheet was scaled to avoid any interactions with the neighboring periodic images. For the adsorption calculations, only the atomic coordinates were allowed to relax. Due to the large size of the supercell, SCC-DFTB calculations were performed to calculate the adsorption geometries and the corresponding energies. The calculations were performed with the DFTB+58 program<sup>84</sup> (version 22.1) along with the mio-1-1 Slater-Koster set<sup>85</sup>. Dispersion corrections were included in the calculations by adopting the implementation of the D4 model developed by Grimme et. al.<sup>86</sup>. The Brillouin zone was sampled only at the  $\Gamma$  and the convergence criteria for structure optimization and SCC tolerance were set to  $10^{-4}$  and  $10^{-7}$  au respectively.

### 5.3. Characterization studies of g-C<sub>3</sub>N<sub>4</sub>

#### 5.3.1. Formation Mechanism of porous g-C<sub>3</sub>N<sub>4</sub> nanosheets

The thermal exfoliation process of g-C<sub>3</sub>N<sub>4</sub> is illustrated schematically in Figure 5.1 (a). The CNNs obtained from the same weight of material exhibit a significantly larger volume than that of CNB, indicating the presence of a porous structure in the as-prepared composite. Specifically, the polymeric melon units' hydrogen-bond cohered strands within the layers of CNB are susceptible to oxidation in the presence of air. This process gradually reduces the thickness of CNB, ultimately reaching the nanoscale through a layer-by-layer thermal oxidation process<sup>59,87</sup>. Furthermore, Figure 5.1 (a) shows that CNB has a dark yellow color, which transitions to a pale yellow after thermal exfoliation. This observation suggests that the CNNs possess a narrower visible light absorption range, and the slight color loss can be attributed to the quantum confinement effect<sup>59,87</sup>.

Thermogravimetric analysis (TGA) was employed to assess the thermal stability of melamine and CNB, as depicted in Figure 5.1 (b). Upon pyrolysis of melamine, a notable weight loss process occurred when the temperature reached 370 °C (~95%). At this point, melamine underwent rearrangement to form tri-s-triazine, and the structural units polycondensed into layered aggregated C<sub>3</sub>N<sub>4</sub> at around 550 °C<sup>48</sup>. As for CNB, a gradual weight loss was observed at temperatures higher than 600 °C, attributed to the loss of tri-s-triazine-based units or other advanced condensates, respectively. When the temperature reached 650 °C, complete decomposition of the CNB sample in

the air took place <sup>50,52</sup>. Notably, the thermal exfoliation process was conducted over a range of temperatures (530–580 °C) to carefully control the exfoliation of g-C<sub>3</sub>N<sub>4</sub>.

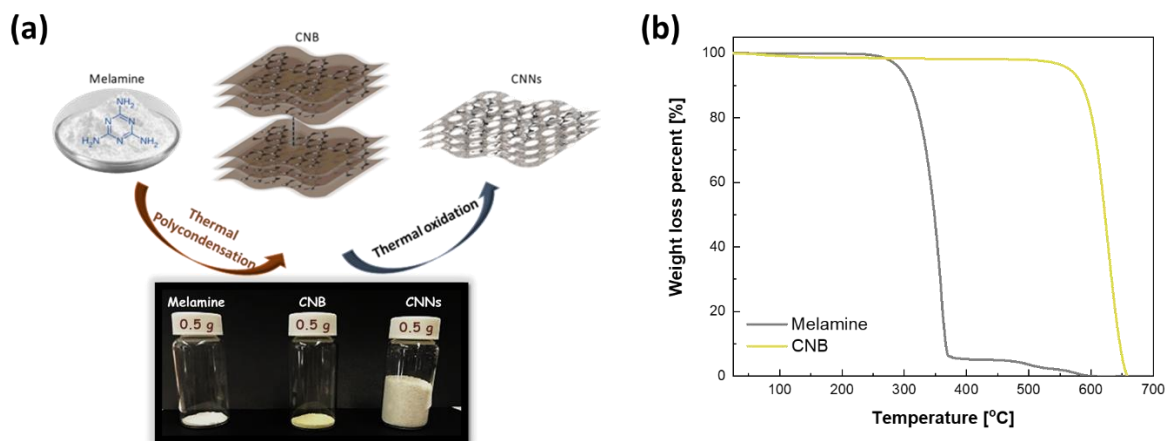


**Figure 5.1.** (a) The preparation process of porous g-C<sub>3</sub>N<sub>4</sub> nanosheets; (b) TG curves of melamine and CNB samples. Adapted from Reference <sup>88</sup>.

### 5.3.2. Textural/Structural Characterization

The porosity of both CNB and CNNs was assessed through N<sub>2</sub> physisorption experiments. Figure 5.2 illustrates the adsorption-desorption isotherms and the Barrett-Joyner-Halenda (BJH) desorption pore size distribution of CNB and CNNs samples. The isotherms displayed typical type IV characteristics with a small H3 hysteresis loop, indicating mesoporous structures with slit-shaped pores, as per the IUPAC classification <sup>50,59</sup>.

A summary of the main textural and structural characteristics of CNB and CNNs samples is presented in Table 5.1. To examine the textural properties, such as surface area, pore volume, and pore size, nitrogen adsorption-desorption (BET) analysis was performed before and after exfoliation of g-C<sub>3</sub>N<sub>4</sub>. The results revealed that CNB exhibited the lowest BET surface area (10 m<sup>2</sup> g<sup>-1</sup>) and pore volume (0.12 cm<sup>3</sup>/g). In contrast, CNNs displayed a significantly increased BET surface area of 212 m<sup>2</sup> g<sup>-1</sup>, approximately 20 times larger than that of CNB. Additionally, the total pore volume increased after exfoliation (CNNs) up to 10 times, evident in the CNNs compared to CNB (Table 5.1). The pore size distribution (Figure 5.2 (b)) for CNNs showcased maxima at a pore diameter of more than 10 nm, indicating the presence of mesopores. These findings highlight the substantial improvement in porosity and textural properties achieved through thermal exfoliation, demonstrating the enhanced mesoporous structure of the CNNs compared to the CNB.

**Table 5.1.** Textural/morphological/optical properties of CNB and CNNs samples.

Sample	BET Analysis		XRD Analysis		AFM Analysis		DRS Analysis	
	BET Surface Area (m <sup>2</sup> /g)	Pore Volume (cm <sup>3</sup> /g)	Pore Size (nm)	(002) peak	d (nm)	Thickness (nm)	Roughness (nm)	E <sub>g</sub> (eV)
CNB	10	0.12	-	27.6	0.323	200 - 300	30 ± 5	2.74
CNNs	212	1.07	16.1	27.85	0.320	15 - 30	10 ± 1	2.91

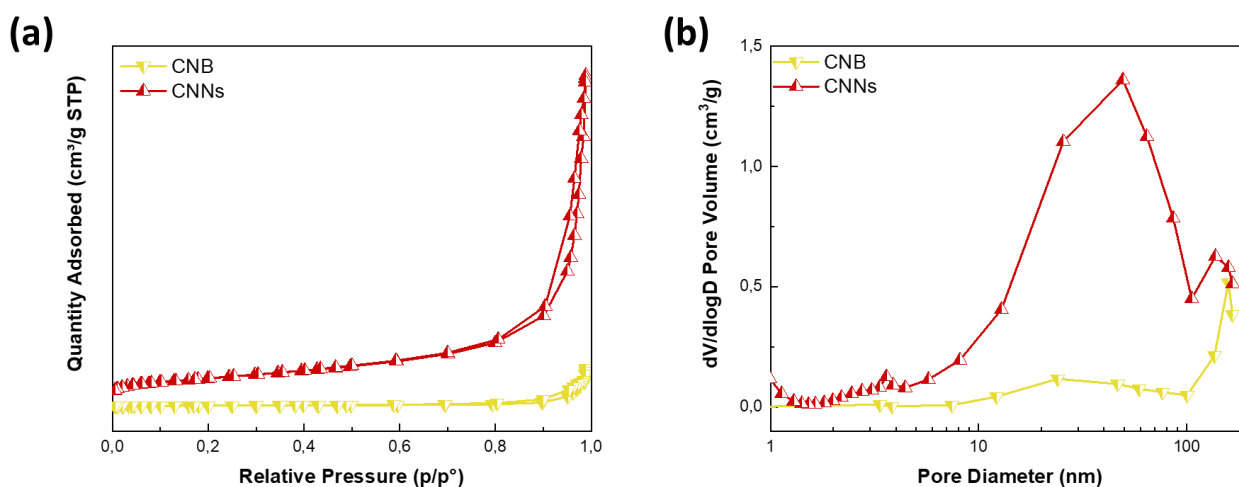
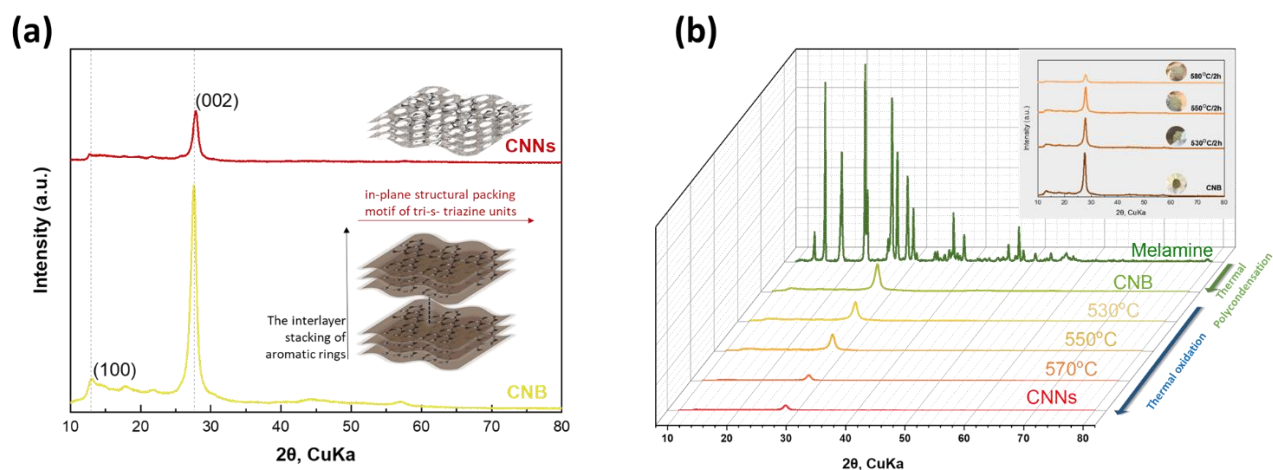
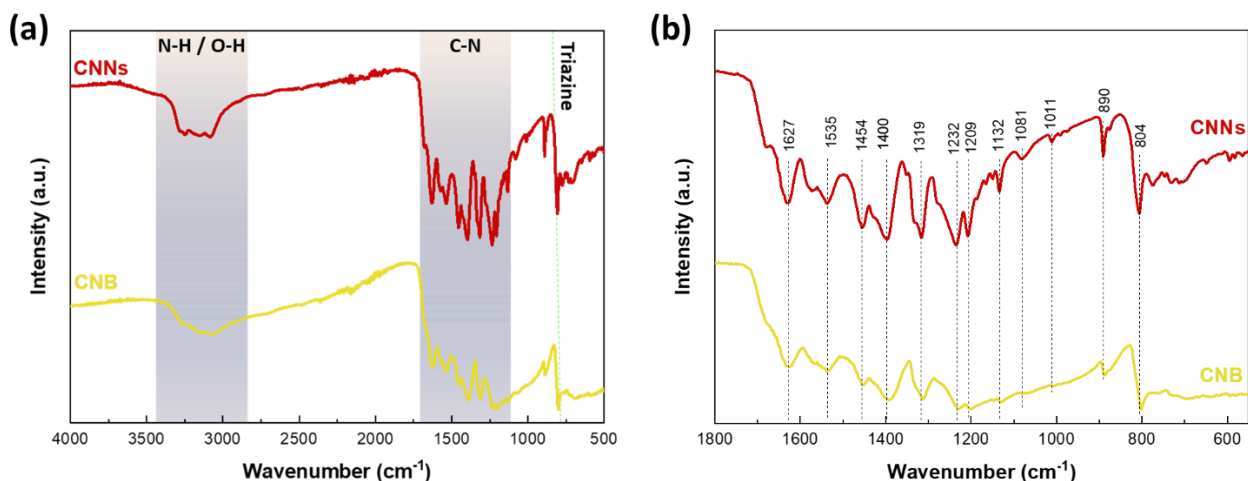
**Figure 5.2.** (a) Adsorption–desorption isotherms; (b) BJH desorption pore size distribution (PSD) for the CNB and CNNs samples.

Figure 5.3 (a) illustrates the XRD patterns of CNB and CNNs samples. For the bulk material, two characteristic diffraction peaks appear at  $2\theta = 13.1$  and  $27.6^\circ$ , corresponding to the (100) and (002) planes, respectively. The weak peak at  $13.1^\circ$ , with an interplanar distance of 0.675 nm, is attributed to the in-plane structural packing motif, while the strong peak at  $27.6^\circ$ , with an interplanar distance of 0.323 nm, arises from the interlayer stacking of the conjugated aromatic systems. In contrast, CNNs show significantly reduced intensity of the (100) and (002) peaks, confirming the successful exfoliation of CNB<sup>50,51,75,87</sup>. This reduction in peak intensity is a consequence of the decrease in the size of the layers achieved through thermal exfoliation. Furthermore, a slight shift of the (002) peak from  $27.6^\circ$  for the CNB sample to  $27.9^\circ$  for the CNNs sample is observed, indicating the formation of a denser packing of g-C<sub>3</sub>N<sub>4</sub> during the thermal oxidation process<sup>59,72,87,89</sup>. Consequently, there is a small decrease in the interlayer distance, reaching a value of 0.320 nm for the CNNs sample. The evolution of XRD patterns during the thermal exfoliation process from CNB to CNNs formation is depicted in Figure 5.3 (b), highlighting the structural changes that occur during the exfoliation process.



**Figure 5.3.** XRD patterns of (a) CNB and CNNs and (b) g-C<sub>3</sub>N<sub>4</sub> at different exfoliation temperatures. Adapted from Reference <sup>88</sup>.

The chemical structure of both CNB and CNNs samples was verified through FTIR spectroscopy. As depicted in Figure 5.4 (a), both samples exhibit similar peak features, indicating that the exfoliated nanosheets maintain the same chemical structure as their parent bulk material. The broad peaks in the range of 3500 to 3000 cm<sup>-1</sup> arise from adsorbed H<sub>2</sub>O and stretching vibrations of N–H bonds, while the absorption peak at 884 cm<sup>-1</sup> is attributed to the cross-linking N–H deformation mode from these groups. Additionally, the strong peaks in the 1700–800 cm<sup>-1</sup> region can be attributed to the characteristic stretching mode of aromatic CN heterocycles. Comparatively, the FTIR spectrum of CNNs in the range of 1700–800 cm<sup>-1</sup> (Figure 5.4 (b)) exhibits highly resolved peaks, a characteristic typically associated with highly ordered carbon-based materials compared to CNB. More specifically, the sharp spectral band at 804 cm<sup>-1</sup> corresponds to the breathing mode of triazine units, while the region from 1132 to 1627 cm<sup>-1</sup> corresponds to the C–N and C=N stretching modes of aromatics <sup>59,87,90</sup>. Furthermore, the region from 1132 to 970 cm<sup>-1</sup> is associated with oxygen-containing groups, and the intensities of 1132, 1081, and 1011 cm<sup>-1</sup> peaks increase after exfoliation, indicating the oxidation of g-C<sub>3</sub>N<sub>4</sub> during the thermal process <sup>51,59,87</sup>.



**Figure 5.4.** (a) FTIR spectra of CNB and CNNs samples; (b) FTIR spectra of CNB and CNNs samples in the spectral region of 1700–800  $\text{cm}^{-1}$ . Adapted from Reference <sup>88</sup>.

### 5.3.3. Morphological Characterization

The morphological characteristics of bulk  $\text{g-C}_3\text{N}_4$  before and after exfoliation were thoroughly investigated using SEM and TEM analyses. Figure 5.5 (a) shows that CNB is composed of solid agglomerates, maintaining a compact bulk structure. However, after the exfoliation process, as depicted in Figure 5.5 (b), the bulk structure is transformed into thin, curved layers, indicating successful exfoliation of the material. In Figure 5.5 (c) and (d), TEM images further corroborate these findings. Specifically, CNB exhibits stacked bulks, consistent with the SEM observations. On the other hand, CNNs display very thin sheets, providing direct evidence for the successful exfoliation of the bulk material.

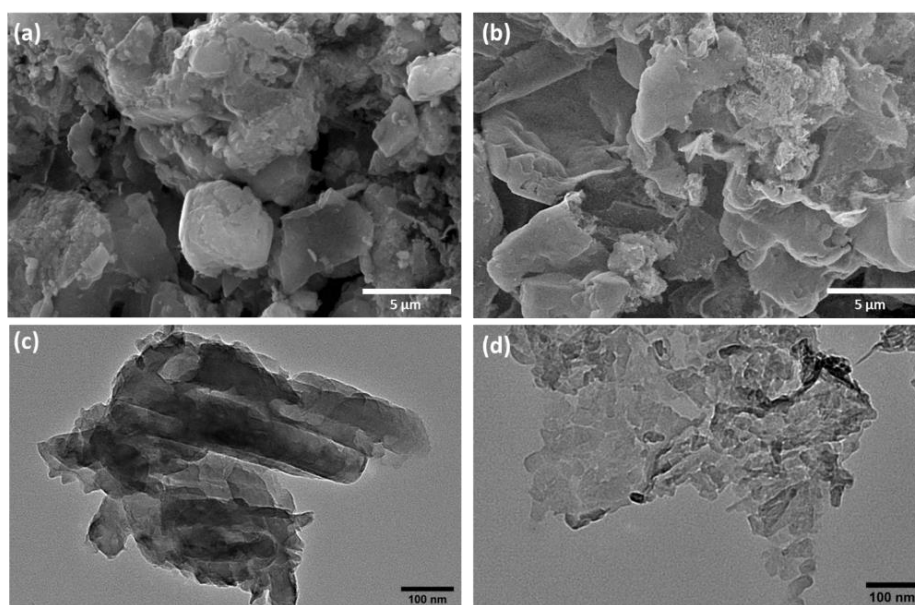


**Figure 5.5.** SEM images of (a) CNB and (b) CNNs and TEM images of (c) CNB and (d) CNNs.

A more detailed topographic examination was performed using AFM. Figure 5.6 presents the AFM images of CNB and CNNs, showcasing their characteristic topography. The synthesis of the bulk material resulted in stacked flakes with lateral dimensions of approximately 40  $\mu\text{m}$ . However, due to the inhomogeneous layer distribution, the thickness of these flakes ranged from 100 to 300 nm, even within the same sheet. In contrast, CNNs were produced through a rigorous thermal exfoliation process, which led to their formation with non-uniform layer thicknesses across the width of the flake, measuring between 5–10  $\mu\text{m}$ . The individual layers of CNNs range from 15 to 30 nm in thickness. These variations in layer thickness within CNNs are clearly demonstrated by the representative topographies and height analysis in Figure 5.6 (g) and (h).

Upon closer examination of the surface of each material, their distinctive porous nanostructures were revealed. The roughness of the bulk flakes was higher, measuring  $30 \pm 5$  nm, primarily due to the presence of increased layers and randomly distributed thickness on the examined area (Table 5.1). In contrast, the exfoliation procedure substantially reduced the number of layers, exposing a structure with enhanced porosity, as clearly shown in the magnified view of its surface (Figure 5.6 (e)). The roughness of the exfoliated nanosheets was found to be  $10 \pm 1$  nm, primarily attributed to the porous structure, with the thickness of the layers having less of an effect (Table 5.1).

Furthermore, the theoretical monolayer thickness value of g-C<sub>3</sub>N<sub>4</sub> is known to be approximately 0.33 nm due to its interlayer distance<sup>91</sup>. However, AFM experimental values can be influenced by various parameters such as surface chemistry and surface roughness<sup>92</sup>, leading to measured values for monolayers closer to 0.6–1 nm<sup>93</sup>. Previous reports on g-C<sub>3</sub>N<sub>4</sub> resulting from melamine polycondensation have indicated ultrathin nanosheets in the range of 3–5 nm<sup>94</sup>. Additionally, our thermal exfoliation process results in the production of highly porous nanosheets, significantly increasing their roughness to approximately 10 nm (Table 5.1). This contributes additively to the thickness of our samples, making it challenging to clearly distinguish between monolayer and multilayer structures. Taking into consideration all these factors along with our results, we deduce that our thin nanosheets likely consist of 5–15 layers, while the CNB is composed of up to 200 layers (Table 5.1).

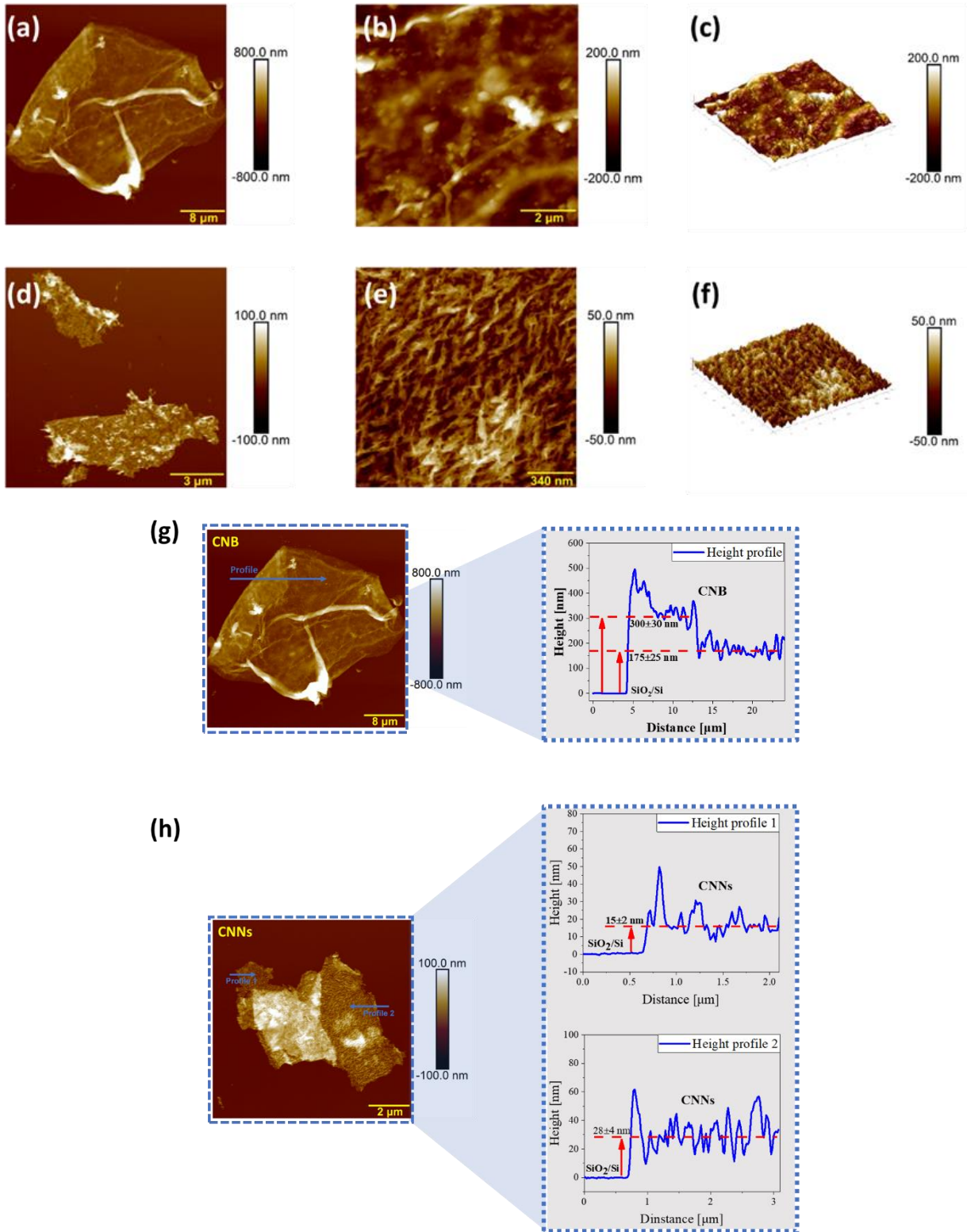


**Figure 5.6.** Topography of a representative (a) CNB and (d) CNNs; Magnified view of (b) CNB and (e) CNNs surface; 3D topography of the magnified surface of (c) CNB and (f) CNNs; Representative topographies of (g) CNB and (h) CNNs along with corresponding height profiles. Adapted from Reference <sup>88</sup>.

### 5.3.4. Optical properties

The optical properties of the as-prepared samples were evaluated using UV-Visible absorption spectroscopy (UV-Vis DRS). As depicted in Figure 5.7 (a), both the CNB and CNNs samples displayed an absorption edge in the visible region. Notably, the absorption edge of the CNNs exhibited a slight blue shift compared to CNB, consistent with the observed color change. The band gap values of the samples were determined using the Kubelka-Munk function and are presented in Table 5.1 and Figure 5.7 (a). The band gap energy ( $E_g$ ) increased from 2.74 to 2.91 eV after the exfoliation process<sup>95–97</sup>. This increase in the band gap energy can be attributed to the quantum confinement effect (QCE) resulting from the reduction in the thickness and size of the g- $C_3N_4$  layers<sup>38,42,59,72</sup>.

The band edge potentials of CNB and CNNs were determined using the following Eq. (1) and (2):

$$E_{VB} = \chi - E^e + 0.5E_g \quad (1)$$

$$E_{CB} = E_{VB} - E_g \quad (2)$$

where  $E_{VB}$  and  $E_{CB}$  represent the potential energy (eV) of the Valence Band (VB) and Conduction Band (CB) respectively.  $\chi$  is the geometric mean of the electronegativity of the constituent atoms of a semiconductor, calculated to be 4.73 eV for g- $C_3N_4$ .  $E^e$  is the energy of free electrons in a standard hydrogen electrode, approximately ~4.5 eV vs NHE<sup>98,99</sup>.  $E_g$  is the experimentally determined band gap energy of the sample. As depicted in Figure 5.7. (b), the  $E_{CB}$  values of both CNB and CNNs are approximately -1.14 and -1.23 eV, respectively, while the  $E_{VB}$  values are estimated to be 1.60 and 1.69 eV, respectively. These values align well with those reported in the literature<sup>98–101</sup>.

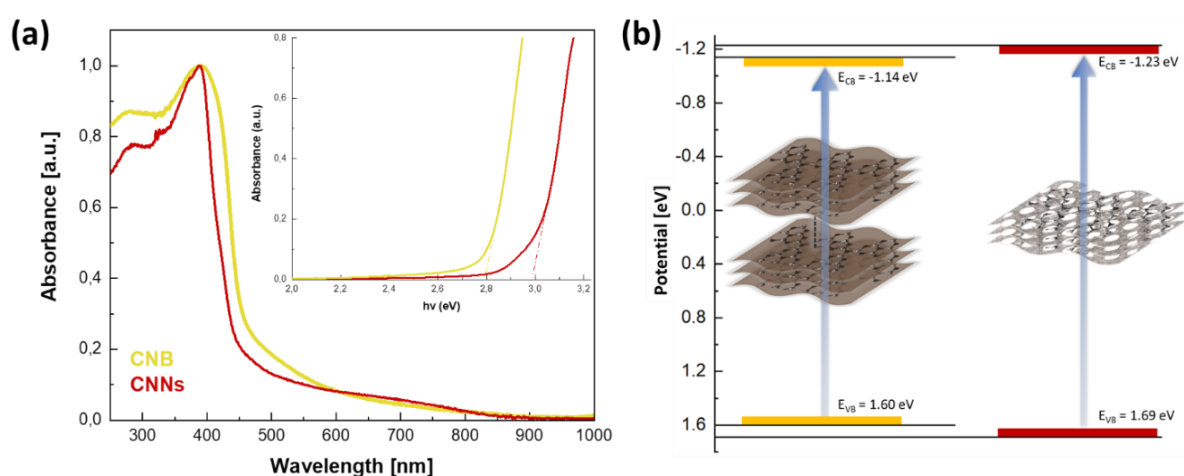


**Figure 5.7.** (a) UV–Vis diffuse reflectance spectra and band gaps obtained from Kubelka-Munk function of CNB and CNNs; (b) schematic illustration of morphology evolution of g- $C_3N_4$  after exfoliation, along with their corresponding band structure.

To investigate the emission and exciton recombination dynamics of CNB and CNNs, room-temperature photoluminescence (PL) spectra were acquired using a 325 nm excitation wavelength. As commonly observed in reduced thickness of 2D semiconductors<sup>102,103</sup>, the PL intensity of CNNs was found to be higher than that of the bulk counterpart, as illustrated in Figure 5.8 (a). This enhancement is attributed to the higher crystallinity and more compact packing of the exfoliated samples, resulting in a reduced number of structural defects<sup>59</sup>. After performing Gaussian fitting of the spectra, three distinct emission peaks were identified from the recombination of electron-hole pairs (Figure 5.8 (b), (c)). The bandgap states of g-C<sub>3</sub>N<sub>4</sub> consist of a sp<sup>3</sup> C–N  $\sigma$  band, sp<sup>2</sup> C–N  $\pi$  band, and the lone pair (LP) state of the bridge nitride atom. P1, P2, and P3 correspond to the pathways of transitions:  $\pi^*-\pi$ ,  $\sigma^*-\text{LP}$ , and  $\pi^*-\text{LP}$ , respectively<sup>104</sup>. The P1 peak was observed at 434 nm and 430 nm for CNB and CNNs, respectively, denoting the band-to-band transition. The blue shift of the P1 emission peak is in agreement with previous findings and is attributed to the quantum confinement effect induced by thin/small nanosheets and the gradual transition from an indirect to a direct band gap. Since most of the exfoliated flakes are thicker than a monolayer, the indirect regime is still predominant, leading to the appearance of the P2 exciton peak. The P2 peak, located at 452 nm for both materials, is attributed to indirect band-to-band transitions. The P3 broad peak, found at 483 nm and 470 nm for CNB and CNNs, respectively, is associated with the recombination of electron-hole pairs due to structural defects still present in the materials. Notably, CNNs exhibit an increased density of defects even after the exfoliation process.

To comprehend this behavior, it is essential to consider the role of surface and bulk defects. Generally, the defect density on the surface is higher than in the bulk<sup>105</sup>. However, it is crucial to acknowledge that the penetration depth of the excitation wavelength (325 nm) limits the ability of PL to probe the entire range of bulk defects<sup>106</sup>. Consequently, the defect density of CNNs compared to CNB appears to be higher.

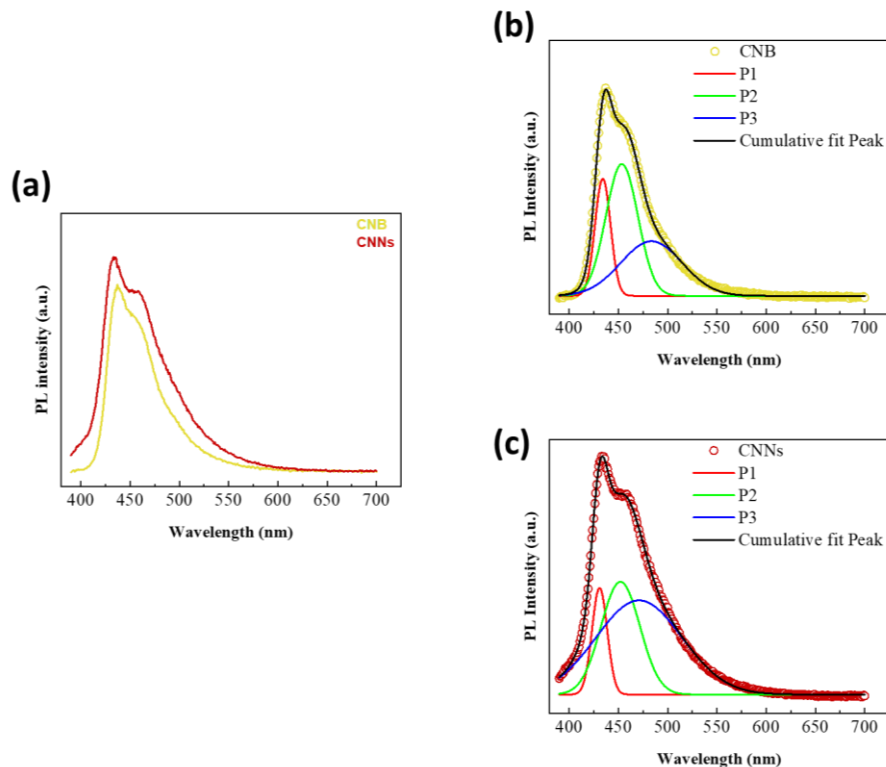


**Figure 5.8.** (a) PL spectra of CNB and CNNs at room temperature at a 325 nm excitation wavelength; Gaussian fitting of the (b) CNB and (c) CNNs (P1, P2, and P3 exciton peaks).

## 5.4. Characterization Studies of g-C<sub>3</sub>N<sub>4</sub>-Based Transition Metal Catalysts

### 5.4.1. Structural Characterization

To investigate the crystal structure of pristine and transition metal-doped (Ti, V, Cr, Mn, Fe, Co, Ni, Cu, and Zn) g-C<sub>3</sub>N<sub>4</sub>, X-ray diffraction was employed. Figure 5.9 displays the recorded diffraction patterns for each sample. In the pristine g-C<sub>3</sub>N<sub>4</sub>, two distinct diffraction peaks were observed at diffraction angles of 13.1° and 27.3°, corresponding to the (100) and (002) planes, respectively, of g-C<sub>3</sub>N<sub>4</sub>. The peak at 13.1° represents the unit of tri-s-triazine connecting to trigonal nitrogen, while the strongest peak at 27.3° indicates the presence of aromatic conjugated structures for long-range interplanar stacking<sup>87,107,108</sup>. Upon doping with transition metals, the diffraction peaks corresponding to the (002) plane of the metal-doped g-C<sub>3</sub>N<sub>4</sub> exhibited a reduction in intensity compared to the undoped sample. This decrease in peak intensity can be attributed to the thinner nature of the doped g-C<sub>3</sub>N<sub>4</sub> successive layers in contrast to CNB. Additionally, a slight shift was observed in the diffraction peaks of the metal-doped samples towards lower diffraction angles when compared to CNB (Table 5.2). This shift indicates an increase in the interatomic spacing within the doped g-C<sub>3</sub>N<sub>4</sub> structure, leading to an enhanced distance between successive layers of the material, as illustrated in Figure 5.9 (b). Remarkably, upon doping with transition metals, the (100) diffraction peak was found

to disappear in most cases, strongly indicating that the metal species were effectively embedded within the in-plane structure of g-C<sub>3</sub>N<sub>4</sub>. This intriguing observation aligns with findings reported in the literature for other metal-doped g-C<sub>3</sub>N<sub>4</sub> materials<sup>107,109</sup>.

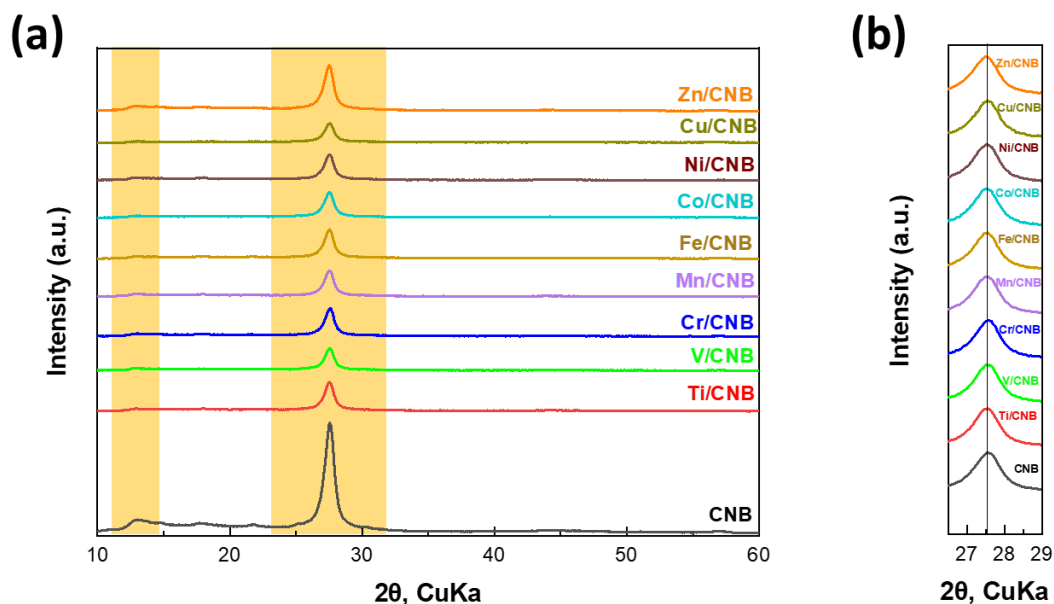


**Figure 5.9.** (a) XRD patterns of CNB and M/CNB (M: Ti, V, Cr, Mn, Fe, Co, Ni, Cu, Zn) samples; (b) the (002) diffraction peak of CNB.

**Table 5.2.** Structural/optical properties of CNB and M/CNB (M: Ti, V, Cr, Mn, Fe, Co, Ni, Cu, Zn) samples.

Sample	XRD Analysis		E <sub>g</sub> (eV)
	(002) peak	d (nm)	
CNB	27.534	0.3237	2.74
Ti/CNB	27.506	0.3240	2.76
V/CNB	27.528	0.3238	2.42
Cr/CNB	27.536	0.3237	2.67
Mn/CNB	27.499	0.3241	2.72
Fe/CNB	27.495	0.3242	2.63
Co/CNB	27.495	0.3242	2.66
Ni/CNB	27.500	0.3241	2.73
Cu/CNB	27.523	0.3239	2.71
Zn/CNB	27.474	0.3244	2.73

### 5.4.2 Morphological Characterization

The morphological characteristics of CNB, Fe/CNB, V/CNB, and Cr/CNB were examined using TEM analysis. In Figure 5.10 (a), it is evident that CNB is composed of solid agglomerates, exhibiting a compact bulk structure. However, upon metal doping, the obtained Fe/CNB, V/CNB, and Cr/CNB samples display distinct features. Notably, the graphitic stacking structures remain intact in the doped-g-C<sub>3</sub>N<sub>4</sub> products, but there is a noticeable change compared to CNB, with the presence of smaller sheets and increased porosity in the doped-g-C<sub>3</sub>N<sub>4</sub>. Furthermore, after the addition of metal, the bulk structure transforms into thin layers, indicating the exfoliation process. This observation aligns with the XRD data. Notably, the Fe/CNB and Cr/CNB samples show a uniform distribution of black spots on the g-C<sub>3</sub>N<sub>4</sub> surface, accompanied by very small particles, indicating excellent dispersion of the metal within the material.

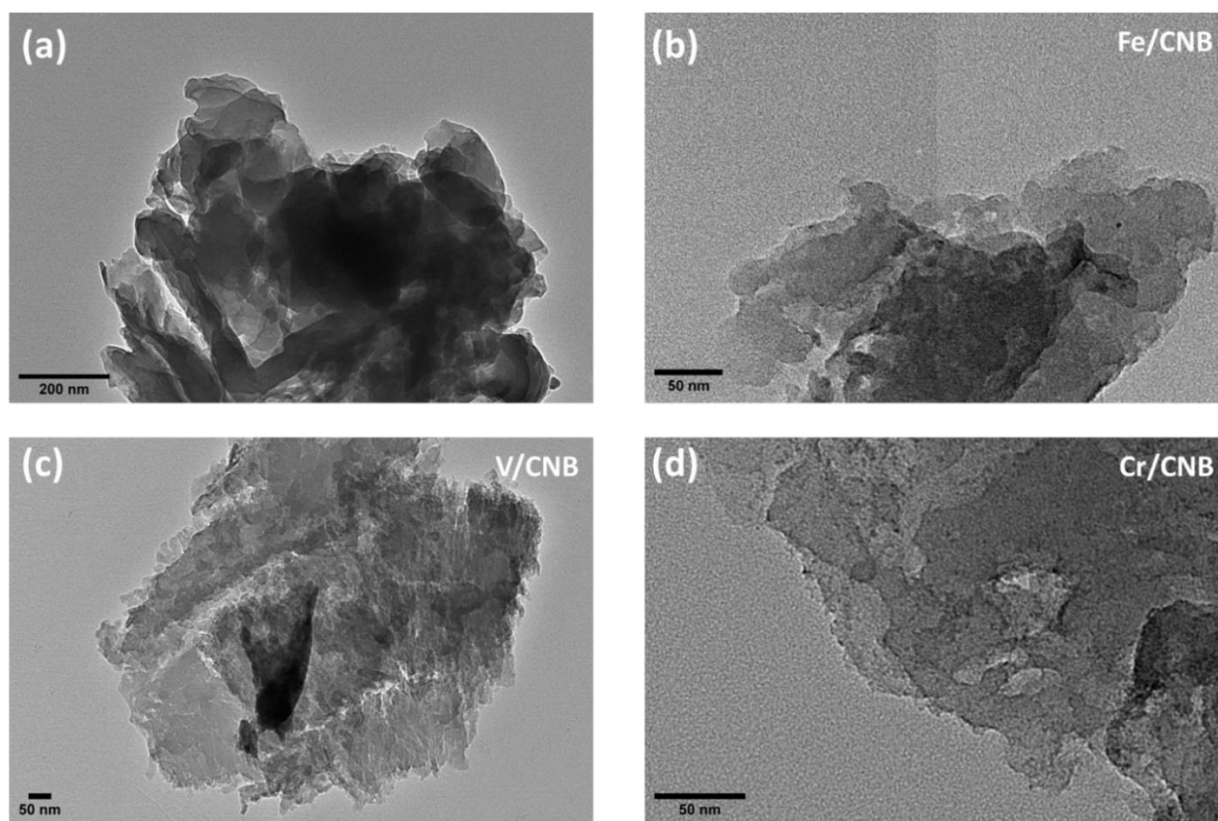


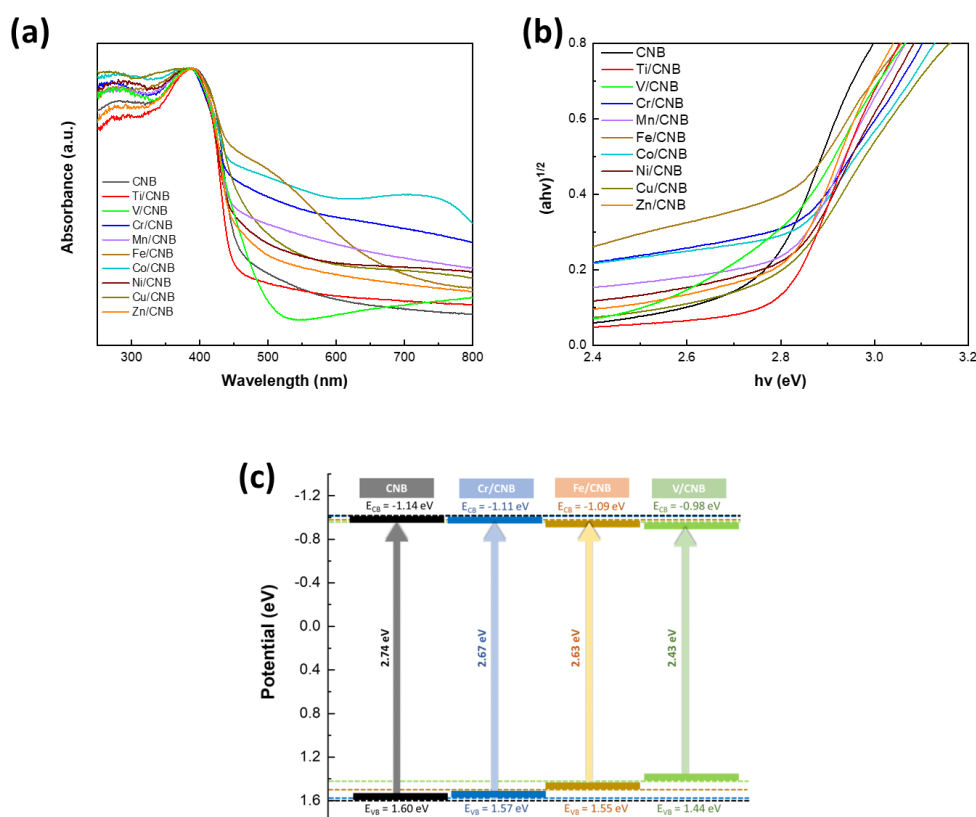
**Figure 5.10.** TEM images of (a) CNB, (b) Fe/CNB, (c) V/CNB, and (d) Cr/CNB samples.

### 5.4.3. Optical properties

The optical properties of pristine CNB and transitional metal-doped CNB were comprehensively assessed using UV-Visible absorption spectroscopy (UV-Vis DRS). Figure 5.11 (a) illustrates that all samples exhibited absorption edges in the visible region. Remarkably, the introduction of Iron, Chromium, Vanadium, and Cobalt dopants resulted in enhanced absorption compared to the pristine

CNB. This enhancement in absorption indicates a narrowing of the bandgap energy, as depicted in Table 5.2 and Figure 5.11 (b). Specifically, the bandgap energy of CNB was measured to be 2.74 eV, while Cr/CNB, Fe/CNB, and V/CNB exhibited bandgap energies of 2.67 eV, 2.63 eV, and 2.42 eV, respectively. The narrowing of the bandgap in the metal-doped  $g\text{-C}_3\text{N}_4$  structures suggests an improved capacity for solar energy absorption, which is a crucial factor in enhancing photocatalytic efficiency, as described in section 5.6 (sub-section 5.6.1.7).

The band edge potentials of CNB, Cr/CNB, Fe/CNB, and V/CNB were determined using Eqs. (1) and (2). The valence band edges of these materials were found to be located at potential energies of 1.60 eV, 1.57 eV, 1.55 eV, and 1.44 eV, respectively. Similarly, the conduction band edges were positioned at potential energies of -1.14 eV, -1.11 eV, -1.09 eV, and -0.98 eV, respectively, as illustrated in Figure 5.11 (c). These results indicate that the introduction of metal dopants significantly alters the energy band structure of  $g\text{-C}_3\text{N}_4$ . Notably, the shifting of band edge positions suggests an enhanced potential for photocatalytic performances in the metal-doped samples.

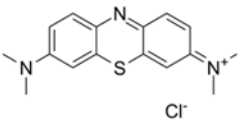
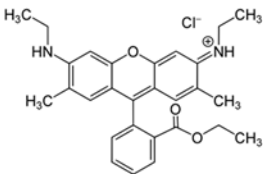
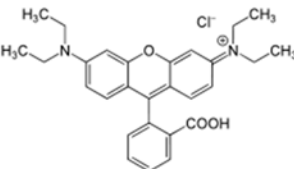
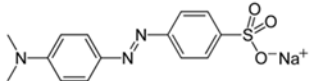
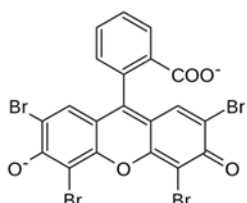


**Figure 5.11.** (a) UV–Vis diffuse reflectance spectra (b) band gaps obtained from Kubelka-Munk function of CNB and M/CNB (M: Ti, V, Cr, Mn, Fe, Co, Ni, Cu, Zn) samples and (c) valence and conduction band potential energy positions for CNB, Fe/CNB, V/CNB, and Cr/CNB samples.

## 5.5. Adsorption Studies

To examine the adsorption behavior of CNB and CNNs, a series of adsorption experiments were conducted using both cationic dyes (MB, Rh6G, and RB) and anionic dyes (MO, eosin Y), as well as mixtures of these dyes. The chemical structure of the investigated dyes is available in Table 5.3. The study comprehensively explored various parameters, including the influence of pH, initial dye concentration, temperature, contact time, selective adsorption, regeneration, and reusability. Additionally, a kinetic analysis was performed to gain deeper insights into the adsorption process.

**Table 5.3.** Chemical structure of the investigated cationic and anionic dyes.  
Adapted from Reference <sup>88</sup>.

Dye	Chemical structure	$\lambda_{\max}$ (nm)
Methylene Blue (MB)		664
Rhodamine 6G (Rh6G)		526
Rhodamine B (RhB)		554
Methyl Orange (MO)		463
Eosin Y		517

### 5.5.1. Effect of solution pH

The pH of the solution significantly impacts both the surface charges of the adsorbent and the degree of ionization of acidic and basic compounds. Changes in pH play a crucial role in influencing the adsorptive process, leading to shifts in equilibrium characteristics. To interpret the effect of pH, the zero point of charge ( $\text{pH}_{\text{ZPC}}$ ) is a key parameter to consider. The  $\text{pH}_{\text{ZPC}}$  is the point at which the net charge of the adsorbent becomes zero, and it plays a vital role in determining the adsorption behavior. It is well-established<sup>110,111</sup> that the adsorption of cations is more favorable at  $\text{pH} > \text{pH}_{\text{ZPC}}$ , whereas for anions, the favorable adsorption condition occurs at  $\text{pH} < \text{pH}_{\text{ZPC}}$ . To decipher the adsorption mechanism, the zero-point charge ( $\text{pH}_{\text{ZPC}}$ ) of the adsorbent was measured, and the results are presented in Figure 5.12. Specifically, the zero point of charge for CNNs and CNB was found to be 3.2 and 4.1, respectively.

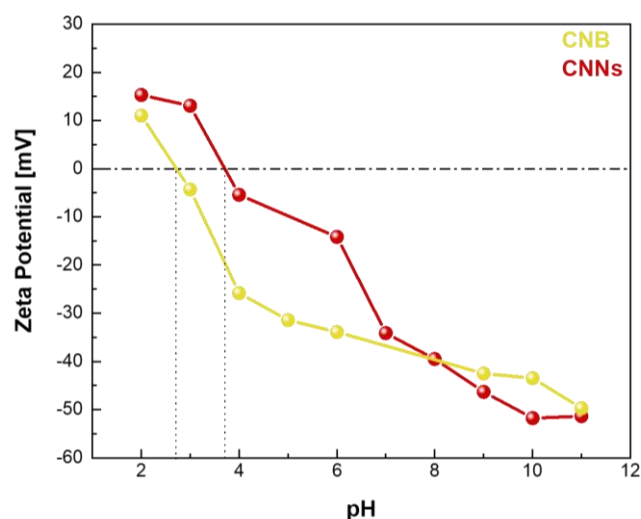


**Figure 5.12.** Zeta potentials of CNNs and CNB as functions of the pH value of the suspensions. Adapted from Reference<sup>88</sup>.

In Figure 5.13 (a), the percentage of MB adsorption on CNB and CNNs is illustrated for a pH range of 3 to 11, using 100 ppm of dye, 25 mg of adsorbent dose, and a 24 h contact time. It is evident that a slight variation in the percentage of removal occurs when the pH is increased from 3 to 8. However, a remarkable enhancement in the adsorption process is observed as the pH is further increased from 9 to 11. Figure 5.13 (b) demonstrates the relationship between the amount of MB adsorbed per unit mass of adsorbents and their final concentrations in the aqueous solution at two distinct pH values: pH 6 (initial) and pH 11. Specifically, at pH 6 (initial pH), CNB exhibits negligible adsorption capacity, while at pH 11, a significant increase in their adsorption capacity is displayed, reaching 38.1 mg/g. For the CNNs, the maximum adsorption capacity increases from 12.5

mg/g at pH 6 (initial pH) to an impressive 76.8 mg/g at pH 11. This behavior can be rationalized by considering the underlying mechanism of dye adsorption on the adsorbent, which involves, among other factors, the electrostatic interaction between the positively charged dye molecules and the negatively charged surface of CNNs ( $\text{pH} > \text{pH}_{\text{ZPC}}$ ).

It is important to highlight that in numerous studies on carbon-based materials, surface area has been identified as a crucial factor influencing adsorption capacity<sup>79,80</sup>. However, intriguingly, our findings, as presented in Table 5.1 and Figure 5.2, reveal a contrasting result. The as-synthesized CNNs exhibit nearly double the adsorption capacity compared to CNB, despite CNB having a surface area 20 times larger and a pore volume 10 times higher than CNNs. This observation leads to the deduction that surface area alone may not be the exclusive determinant of adsorption capacity, as further discussed below.

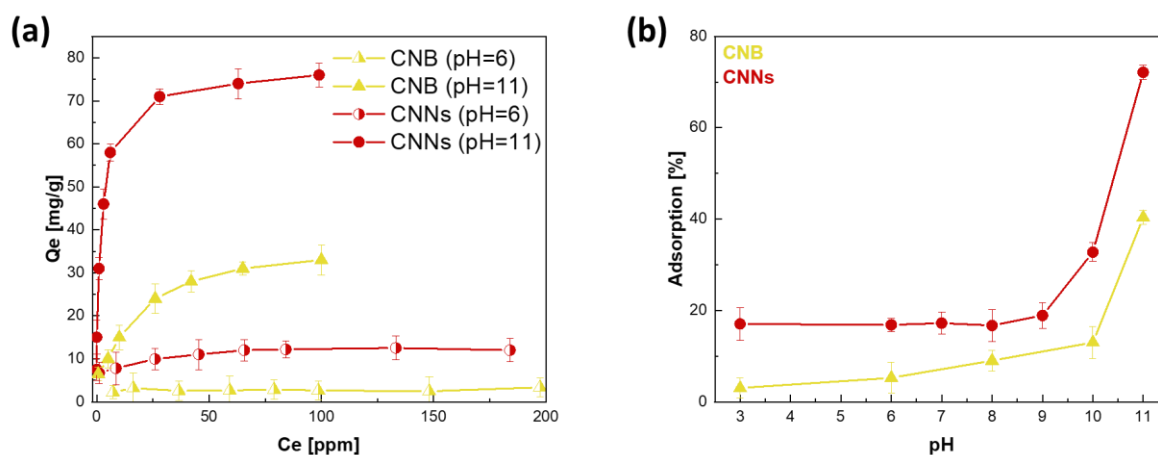


**Figure 5.13.** (a) Effect of the solution pH on the removal efficiency of adsorbents using cationic MB. (Experimental conditions: pH: 3-11, 100 ppm of MB, 25 mg of adsorbent dose, contact time: 24h); (b) The relationship between the amount of MB adsorbed per unit mass of adsorbents and their final concentration in the aqueous solution (Experimental conditions: pH: 6 and 11, 10-200 ppm of MB, 25 mg of adsorbent dose, contact time: 24h). Adapted from Reference<sup>88</sup>.

### 5.5.2. Effect of various adsorption parameters

In addition to studying the effect of pH, we also investigated the influence of the initial dye concentration, temperature, and contact time on the uptake capacity of CNNs using the cationic dye MB as the adsorbate. The results of these investigations are depicted in Figure 5.14. Figure 5.14 (a) illustrates the impact of the initial MB concentration on the percentage of adsorption using CNNs as the adsorbent. It is evident that the MB removal efficiency decreases from 99.9% to 72.1% with an increase in MB concentration from 40 to 100 ppm. This decrease can be attributed to the saturation of active adsorption sites on the adsorbent. Furthermore, Figure 5.14 (c) presents the effect of

temperature on the percentage of adsorption on CNNs. The results indicate that the percentage of adsorption is not significantly influenced by temperature. Regarding the adsorption experiments with different contact times, Figure 5.14 (d) shows that CNNs exhibit a rapid removal rate during the initial 5 minutes and can reach equilibrium within just 10 minutes. This indicates the high efficiency of CNNs as an adsorbent. To further investigate the effect of contact time for both CNB and CNNs, adsorption experiments were performed at 10 min and 24 h of contact time using 10 ppm of dye and 25 mg of adsorbent dose.

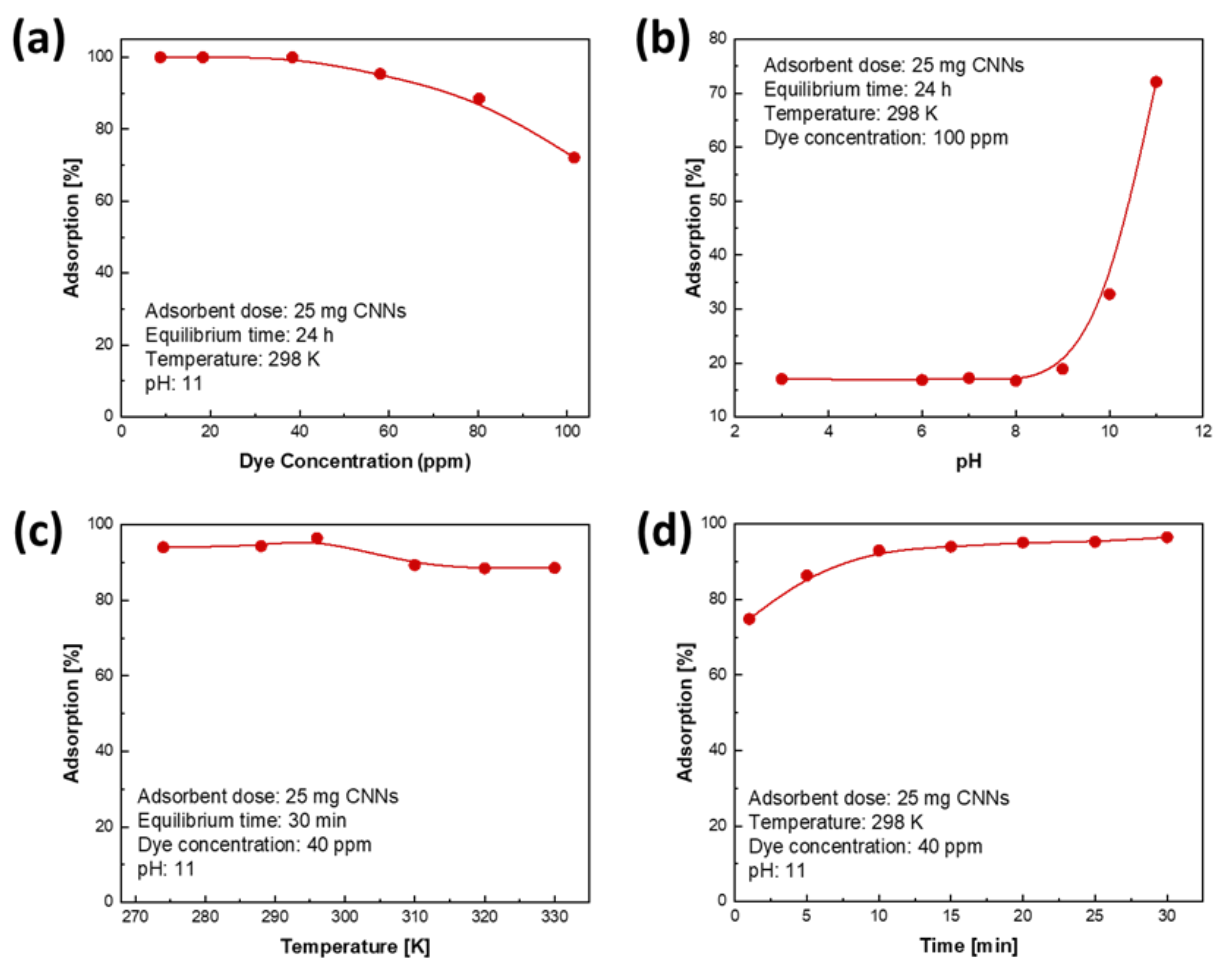


**Figure 5.14.** Effect of (a) initial dye concentration, (b) pH, (c) temperature, and (d) contact time on the removal efficiency of CNNs using cationic MB. Adapted from Reference <sup>88</sup>.

The UV-Vis spectra of the MB cationic dye for both CNB (Figure 5.15 (a)) and CNNs (Figure 5.15 (b)) before and after adsorption are depicted in Figure 5.15. For CNNs, the results revealed complete adsorption of MB within 10 minutes, demonstrating their superior adsorption efficiency. In contrast, CNB exhibited lower adsorption at 10 min compared to that obtained after 24 h of stirring.

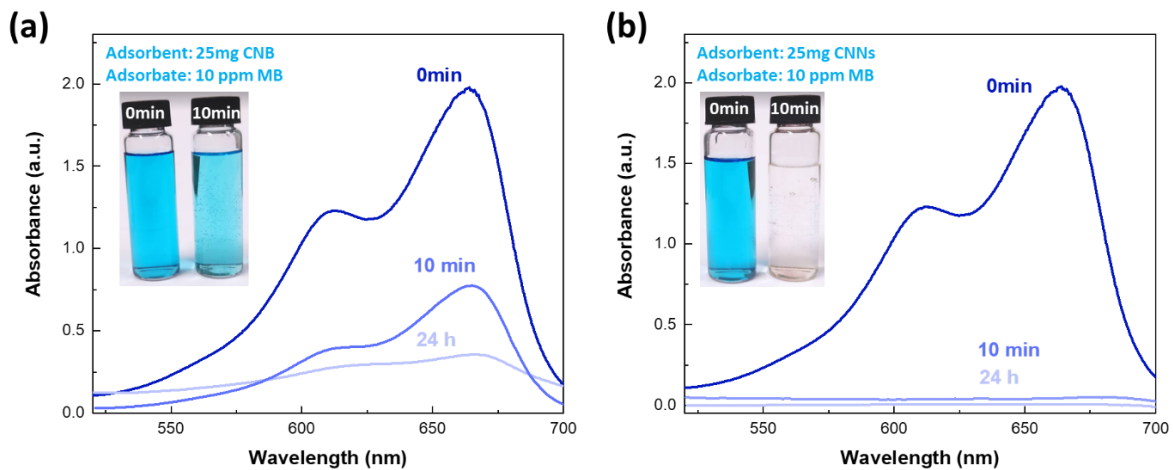


**Figure 5.15.** Effect of contact time using 10 ppm of MB and 25 mg of (a) CNB and (b) CNNs (Experimental conditions: pH = 11, 10 ppm of MB, 25 mg of adsorbent, contact time: 10 min, 24h). Adapted from Reference <sup>88</sup>.

### 5.5.3. Adsorption kinetics and equilibrium modeling

The rate of dye adsorption is strongly influenced by the contact time between the adsorbent and dye solution, as well as diffusion processes. To investigate the adsorption kinetics and mechanism, we examined two kinetic models: pseudo-first-order and pseudo-second-order (see Chapter 2 in Section 2.3). The experimental data were fitted using both models (Figure 5.16), revealing that the pseudo-second-order model exhibited a higher  $R^2$  value compared to the pseudo-first-order model. Moreover, the calculated  $Q_e$  value (30.47 mg/g) closely matched the experimental  $Q_e$  value (30.12 mg/g). These findings conclusively support the description of adsorption kinetics as a pseudo-second-order model (Figure 5.16 (b)).

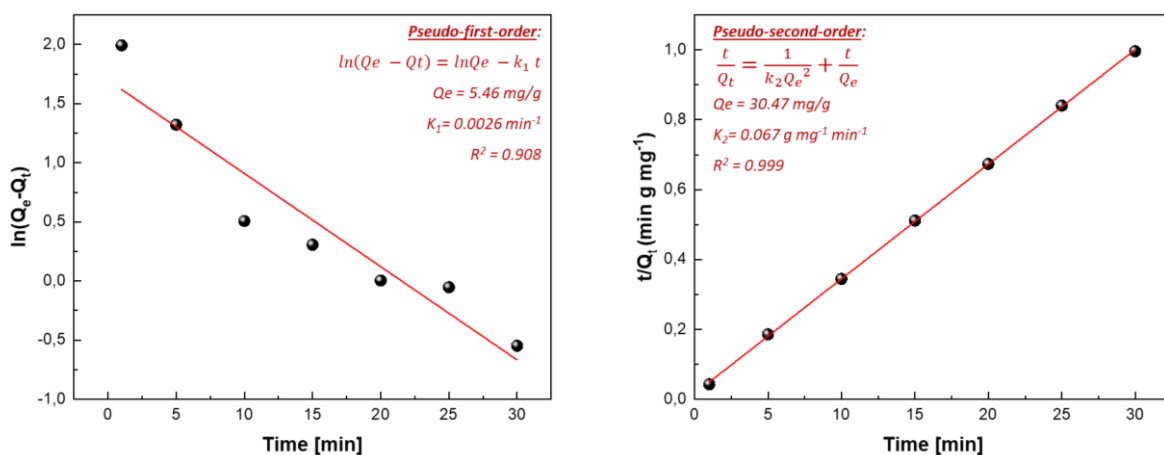


**Figure 5.16.** (a) Plots of  $\ln(Q_e - Q_t)$  against  $t$  based on the pseudo-first-order kinetic model and (b) Plots of  $t/Q_t$  against  $t$  based on the pseudo-second-order kinetic model for adsorption of MB on CNNs. Adapted from Reference <sup>88</sup>.

To gain valuable insights into the adsorption performance of the CNNs and CNB samples, establishing the most appropriate correlation for equilibrium curves is of paramount importance (see Chapter 2 in Section 2.3). As depicted in Figure 5.17, the equilibrium adsorption data were fitted to the Langmuir and Freundlich isotherm equations, with the corresponding coefficients summarized in Table 5.4. Both models displayed a good fit to the experimental data, as indicated by the closely similar  $R^2$  values (Table 5.4). Specifically, Figure 5.17 (a) illustrates the adsorption isotherms of MB on CNNs at pH values of 6 (initial) and 11, while Figure 5.17 (b) showcases the adsorption isotherms of MB on both CNNs and CNB samples at pH = 11.

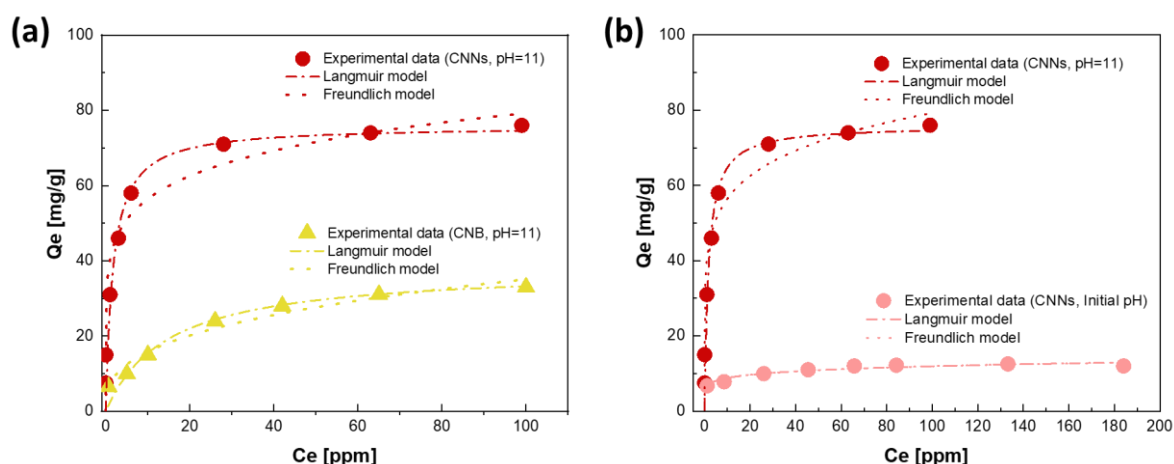


**Figure 5.17.** (a) Adsorption isotherms of MB on CNNs at pH values equal to 6 (initial) and 11 (Experimental conditions: pH: 6 and 11, 100 ppm of MB, 25 mg of CNNs, contact time: 24h); (b) Adsorption isotherms of MB on CNNs and CNB at pH=11 (Experimental conditions: pH: 11, 100 ppm of MB, 25 mg of adsorbent dose, contact time: 24h). Adapted from Reference <sup>88</sup>.

**Table 5.4.** Langmuir and Freundlich isotherm constants for CNB and CNNs samples.

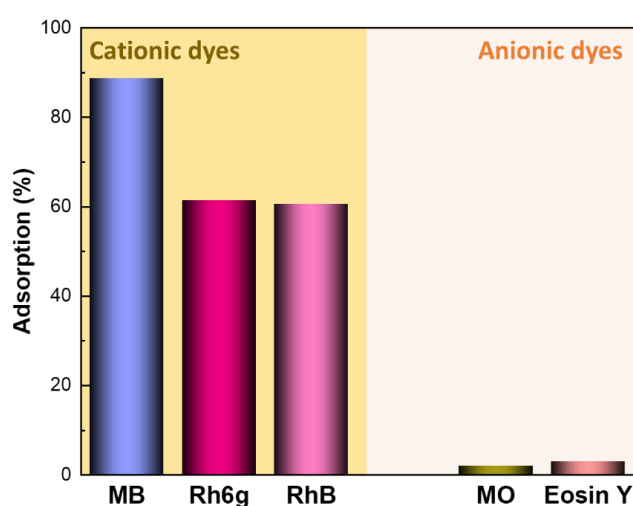
Dye	Sample	pH	Adsorption (%) $C_0:100\text{ppm}$	Langmuir model				Freundlich model		
				$q_m$ (mg/g)	$K_L$ (L/mg)	$R_L$	$R^2$	$K_f$ $((\text{mg/g})(\text{L/mg})^{1/n})$	$1/n$	$R^2$
MB	CNB	6	5.3	-	-	-	-	-	-	-
		11	40.4	38.1	0.068	0.28	0.978	7.20	0.15	0.970
	CNNs	6	16.6	11.6	0.91	0.087	0.674	6.52	0.13	0.926
		11	72.1	75.8	0.58	0.022	0.941	40.2	0.34	0.951

The adsorption process can be described by two different models: the Freundlich model and the Langmuir model. The Freundlich model suggests that adsorption occurs on a heterogeneous surface, and a heterogeneity factor ( $1/n$ ) below 1 indicates a normal Freundlich isotherm, while a factor above 1 indicates cooperative adsorption <sup>110–113</sup>. On the other hand, the Langmuir model assumes a

homogeneous surface with equivalent adsorption sites. It proposes monolayer adsorption with no interactions between adsorbed species<sup>110–113</sup>. To evaluate the adsorption process favorability, we calculated the separation factor  $R_L$ , which is a characteristic of the Langmuir isotherm. As shown in Table 5.4, the  $R_L$  values for both samples were less than 1, indicating that the adsorption process is favorable. The Langmuir equation was used to fit the equilibrium data for MB adsorption, revealing a maximum monolayer adsorption capacity of 75.8 mg/g for exfoliated g-C<sub>3</sub>N<sub>4</sub> and 40.4 mg/g for the bulk material at pH = 11. Interestingly, the CNNs sample exhibited approximately 2 times higher adsorption capacity compared to CNB. Furthermore, using the Langmuir model, the adsorption capacity for CNNs at the initial pH (pH = 6) of the MB solution was calculated to be 11.6 mg/g, significantly lower than the adsorption capacity at pH = 11.

#### 5.5.4. Selective adsorption and separation of dyes

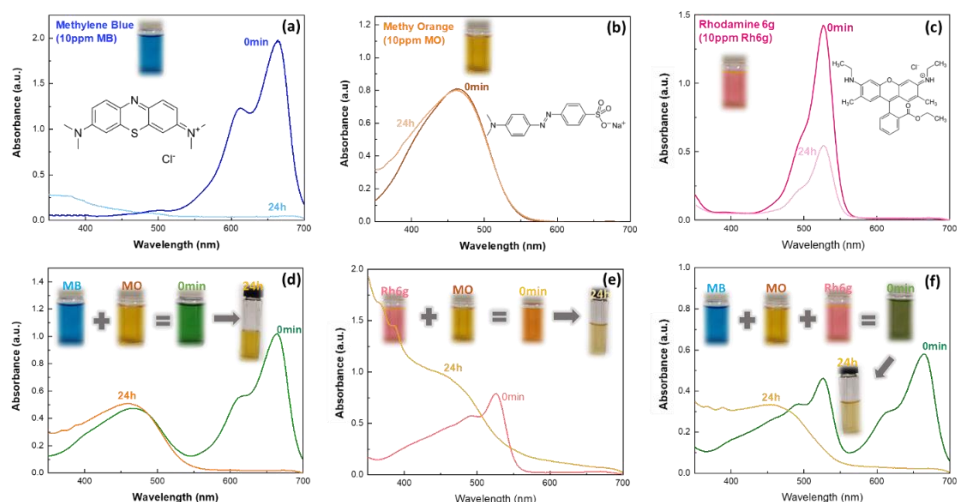
Compared to dye adsorption, the selective adsorption and separation of dyes are particularly appealing. To gain insights into the selective adsorption capacity of CNNs and their ability to separate various dyes, two different types of organic dyes were employed: positively charged dyes such as MB and Rh6G, and negatively charged dyes like MO and Eosin Y, which were used as adsorbates. The adsorption percentages of these dyes onto CNNs are depicted in Figure 5.18. The adsorption experiments were conducted under specific conditions, maintaining a pH value of 6 (initial) using 10 ppm of dye, 25 mg of CNNs, and a 24 h contact time. The results clearly demonstrated the selective adsorption of CNNs towards cationic dyes.



**Figure 5.18.** Adsorption percentages of CNNs using a variety of anionic and cationic dyes (Experimental conditions: pH = 6 (initial), 10 ppm of dye, 25 mg of CNNs, 24 h contact time). Adapted from Reference<sup>88</sup>.

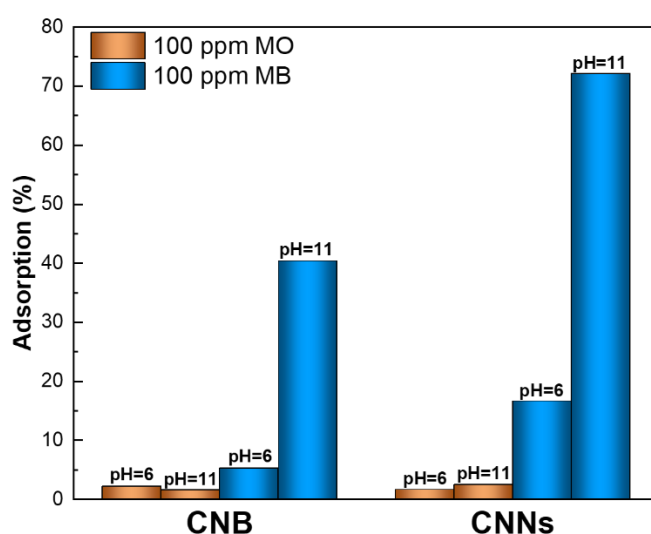
Based on this observation, the UV-Vis spectra of MB, Rh6G (both cationic dyes), and MO (anionic dye), each possessing opposite charges but similar sizes, were recorded before and after the adsorption process, as depicted in Figure 5.19. Specifically, in Figure 5.19 (a), it is evident that the absorbance maximum of the cationic dye MB (at 664 nm) was significantly reduced after the adsorption onto CNNs, further confirming the strong adsorption capability of CNNs towards MB, as mentioned above in Figure 5.13 and 5.17. The rapid decolorization of the aqueous solution of MB within the first 10 minutes of the adsorption process indicated the highly effective removal of almost all dye molecules from the solution (Figure 5.15). Moving on to Figure 5.19 (c), the absorbance maximum of the cationic dye Rh6G (at 530 nm) showed a substantial decrease ( $> 60\%$ ) after the adsorption process, signifying the maximum adsorption capacity of CNNs for Rh6G (10 ppm) under the given conditions. In contrast, when the anionic dye MO was employed as the adsorbate (Figure 5.19 (b)), the adsorption capacity of CNNs for MO was found to be negligible.

Figure 5.19 (d) illustrates the complete and selective adsorption of the cationic dye MB on the CNNs in an MB/MO mixture, while the anionic dye MO remained in the solution with minimal reduction ( $< 1\%$ ). Consequently, the green aqueous solution transformed to orange, reflecting the color of MO. To further assess the selective adsorption and separation capabilities of CNNs for dyes with various charges, adsorption experiments were conducted using two groups of dye mixtures (Rh6G/MO and MB/Rh6G/MO) as adsorbates. The UV-Vis absorption spectra of Rh6G/MO and MB/Rh6G/MO before and after the adsorption are presented in Figure 5.19 (e) and (f). In these experiments, CNNs were mixed into separate aqueous solutions containing two or three types of dyes, namely, Rh6G/MO and MB/Rh6G/MO, each at the same total dye concentration (10 ppm). The results in Figure 5.19 (e) and (f) clearly demonstrate that the cationic dyes (MB and Rh6G) were completely adsorbed on the CNNs, while the anionic dye MO remained in the solution with minimal reduction ( $< 1\%$ ). This finding once again highlights the excellent selective adsorption capacity of CNNs for different charged dyes.



**Figure 5.19.** The UV-Vis absorption spectra of (a) cationic MB, (b) anionic MO, (c) cationic Rh6g, (d) mixture of MB and MO, (e) mixture of Rh6g and MO, (f) mixture of Rh6g, MB, and MO before and after the adsorption (Experimental conditions: pH = 6 (initial), 10 ppm of dye, 25 mg of CNNs, 24 h contact time). Adapted from Reference <sup>88</sup>.

Furthermore, to compare the adsorption performance of CNB, adsorption experiments were carried out using CNB as the adsorbent and 100 ppm of both MB and MO as adsorbates at pH 6 and 11. The corresponding adsorption percentages are presented in Table 5.4. Specifically, CNB exhibited improved adsorption of the cationic dye, resulting in a remarkable 40.4% reduction at pH 11. However, in the case of the anionic dye, CNB showed minimal adsorption, with less than 5% reduction observed in both cases. These findings are further corroborated by Figure 5.20, where the adsorption behavior of CNB towards cationic and anionic dyes is clearly depicted.



**Figure 5.20.** Comparison of CNB and CNNs adsorption percentages at different pH values using anionic MO and cationic MB dyes (Experimental conditions: pH = 6 (initial), 11, 10 ppm of dye, 25 mg of adsorbent, 24 h contact time). Adapted from Reference <sup>88</sup>.

### 5.5.5. Regeneration and reusability of CNNs

The regeneration and reusability of an adsorbent are crucial factors for practical applications. To assess this, regeneration experiments were conducted with CNNs, and XRD measurements were performed before and after the adsorption process, as presented in Figure 5.21 (a). The XRD patterns of CNNs before and after the adsorption process clearly indicate that the crystal structure of CNNs remains unchanged, demonstrating its excellent phase stability. This finding is significant as it ensures the structural integrity of the adsorbent even after multiple adsorption cycles. To further evaluate the reusability of CNNs, the adsorption process was repeated four times. As illustrated in Figure 5.21 (b), the adsorption percentages of CNNs showed only a slight decrease after each cycle, indicating good stability and reusability for MB treatment.

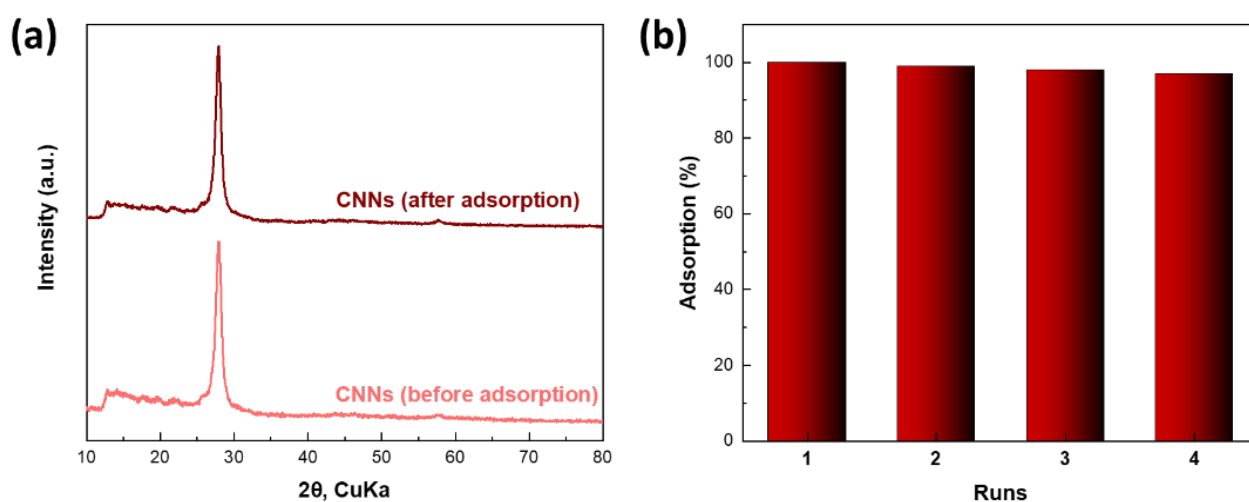


**Figure 5.21.** (a) XRD patterns before and after the adsorption process; (b) MB removal efficiency of CNNs for four adsorption-regeneration cycles. Adapted from Reference <sup>88</sup>.

The impressive MB adsorption capacity of the  $g\text{-C}_3\text{N}_4$  nanosheets prepared in this study is best evaluated through a comparison with state-of-the-art carbon-based materials, as presented in Table 5.5. The data clearly illustrates that CNNs exhibit superior or at least comparable performance compared to a wide range of related systems. Notably, CNNs not only demonstrate excellent adsorption capacity but also require a significantly shorter time for MB removal compared to previously reported materials. These findings highlight the remarkable potential of CNNs as efficient adsorbents. Their facile preparation route, coupled with their high and rapid adsorption capability, makes them highly promising candidates for practical applications. The combination of superior adsorption capacity and faster kinetics makes CNNs stand out among various carbon-based materials.

**Table 5.5.** Comparison of the maximum adsorption capacity (mg/g) and the corresponding equilibrium time for MB on various adsorbents.

Adsorbent	$q_m$ (mg/g)	Eq. time	Reference
g-C <sub>3</sub> N <sub>4</sub> (melamine)	1.6		
g-C <sub>3</sub> N <sub>4</sub> (thiourea)	1.9	1 h	90
g-C <sub>3</sub> N <sub>4</sub> (urea)	2.5		
g-C <sub>3</sub> N <sub>4</sub>	34.0		
g-C <sub>3</sub> N <sub>4</sub> -oxidized at RT	72.0	24 h	15
g-C <sub>3</sub> N <sub>4</sub> -oxidized at 60 °C	98.0		
porous g-C <sub>3</sub> N <sub>4</sub>	72.2	45 min	114
Carbon-doped g-C <sub>3</sub> N <sub>4</sub>	57.9	20 min	19
Activated carbon	36.7	130 min	115
Activated carbon nanofiber	72.5	60 min	116
Multi-walled carbon nanotubes	65.8	30 min	117
Chitosan modified zeolite	37.0	24 h	118
GO/iron oxide	39.0	30 min	119
CMT-g-PAM/Silica nanocomposite	43.8	120 min	120
bulk g-C <sub>3</sub> N <sub>4</sub>	40.4	10 min	this work
g-C <sub>3</sub> N <sub>4</sub> Nanosheets	75.8		

#### 5.5.6. Structure - adsorption relationships

In the case of graphene, the adsorption phenomenon predominantly relies on  $\pi$ - $\pi$  interactions between the  $\pi$ -conjugated systems of graphene and the adsorbate. However, in the case of g-C<sub>3</sub>N<sub>4</sub>, the adsorption mechanism is more diverse, offering a range of possible interactions<sup>15</sup>. Apart from the  $\pi$ - $\pi$  interactions between the  $\pi$ -conjugated systems of g-C<sub>3</sub>N<sub>4</sub> and the adsorbates, the adsorption of organic pollutants on g-C<sub>3</sub>N<sub>4</sub> can also be influenced by electrostatic interactions and hydrogen bonding<sup>15,19</sup>.

In this study, CNNs have demonstrated an outstanding selective adsorption preference for cationic dyes while showing limited interaction with anionic dyes. This behavior can be partially attributed to the electrostatic attraction between the positive charge of cationic dyes and the negative charge on the surface of CNNs. As depicted in Figure 5.12, the negative charges on the surface of CNNs increase with rising pH values. This phenomenon is primarily due to the  $pH_{ZPC}$  of CNNs, which occurs at approximately pH 3.2. Beyond this pH, the surface of CNNs carries a negative charge. Consequently, the electrostatic interactions between CNNs and cationic dyes become more

pronounced at higher pH values. Additionally,  $\pi$ - $\pi$  conjugate interactions play a significant role in cationic dyes adsorption onto g-C<sub>3</sub>N<sub>4</sub>. The unique  $\pi$ -conjugated structure of g-C<sub>3</sub>N<sub>4</sub> facilitates favorable interactions with cationic dye molecules, further enhancing their adsorption onto CNNs. Moreover, AFM topographic measurements and BET results have revealed that the surface of the exfoliated nanosheets possesses a sponge-like morphology, exhibiting a high degree of porosity. This unique structural feature plays a crucial role in facilitating the attachment of pollutant molecules and contributes to the high adsorption capacity observed for CNNs. On the contrary, CNB exhibited a lower adsorption capacity, which can be attributed to its higher roughness and lower porosity compared to that of CNNs.

To further validate our findings, we conducted periodic SCC-DFTB calculations to explore the adsorption behavior of methylene blue cation and methyl orange anion on the planar surface of a single graphitic s-triazine layer. Initially, a 2x2x1 supercell containing sixteen triazine units was constructed and fully optimized. The selected method successfully retained the thermodynamically most favorable wave-like structure, as previously predicted. Subsequently, we obtained optimized geometries for the adsorption of methylene blue and methyl orange, considering various initial orientations of the molecules on the surface, taking into account the wave-like landscape and the relative positions of the triazine units. Figure 5.22 illustrates the lowest energy orientation for both methylene blue and methyl orange, as identified through our calculations. The calculated interaction energies for methylene blue cation and methyl orange anion were found to be  $-53.8$  and  $-45.4$  kcal·mol<sup>-1</sup>, respectively, indicating that methylene blue exhibits a stronger interaction with the surface of the single g-C<sub>3</sub>N<sub>4</sub> sheet compared to methyl orange. Regarding the preferred orientation of both adsorbates, we observed that their long axes align parallel to the grooves formed in the sheet due to the wave-like pattern, as depicted in Figure 5.22. In the case of the methylene blue cation, the central ring is positioned almost on top of the hole formed by the triazine units, and the configuration is further stabilized by the interaction of the methyl H atoms with the lone pairs of the N atoms of the triazine units.

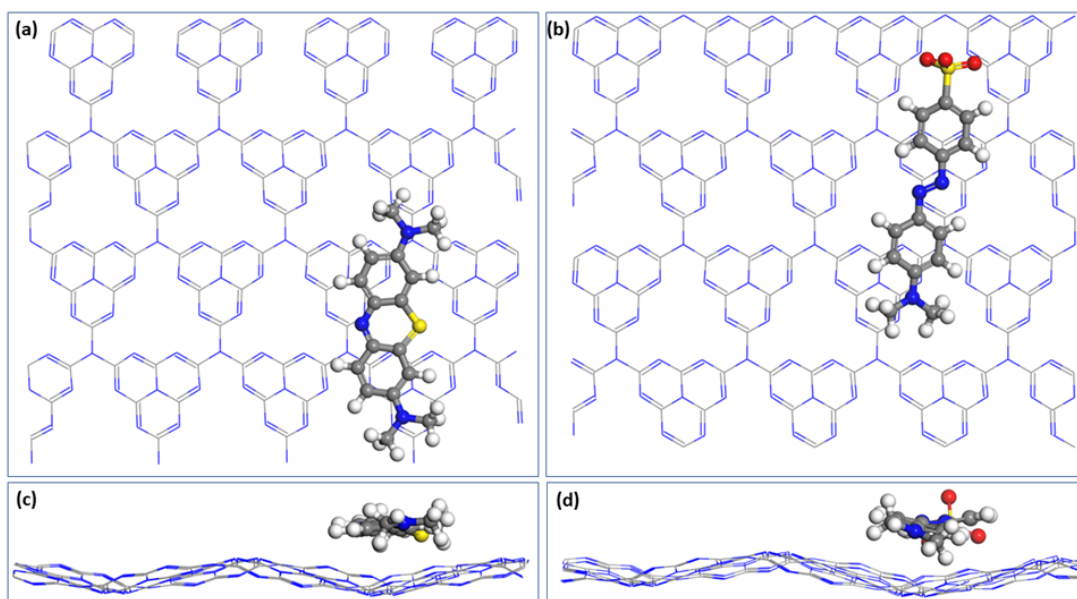


**Figure 5.22.** Top (a), (b) and side (c), (d) views of the optimized geometries corresponding to the adsorption of methylene blue cation and methyl orange anion on the surface of g-C<sub>3</sub>N<sub>4</sub> sheet. Adapted from Reference <sup>88</sup>.

## 5.6. Implication in Catalysis

### 5.6.1. Heterogeneous Catalysis - CO<sub>2</sub> hydrogenation reaction

In the present thesis, a series of g-C<sub>3</sub>N<sub>4</sub>-based catalysts were initially synthesized and evaluated in the context of CO<sub>2</sub> hydrogenation reaction. More specifically, we prepared heterostructures, such as CeO<sub>2</sub>/CNB, CeO<sub>2</sub>/CNNs, and Cu<sub>2</sub>O/CNNs, by utilizing CeO<sub>2</sub> nanorods and Cu<sub>2</sub>O nanocubes. Additionally, we incorporated Ni and Cu onto the CNNs-supported catalysts (Ni/CNNs and Cu/CNNs). The catalytic performance of these samples was investigated across a temperature range spanning 200 to 500°C. Figure 5.23 (a) presents a comparison of the CO<sub>2</sub> conversion rates for all samples with the thermodynamic equilibrium CO<sub>2</sub> conversion profiles for reverse water-gas shift (rWGS) reactions. Notably, Cu<sub>2</sub>O/CNNs and Ni/CNNs samples exhibited increased CO<sub>2</sub> conversion, whereas the remaining samples were nearly inactive. Regarding their selectivity, it is worth noting that the Cu<sub>2</sub>O/CNNs and Ni/CNNs samples demonstrate low and unstable selectivity towards methane, as shown in Figure 5.23 (b). Hence, despite the excellent physicochemical properties of CNB and CNNs, the catalytic activity of these samples does not appear promising. Taking advantage of their excellent properties, CNB and CNNs were subsequently used in photocatalysis, as discussed in the following section.

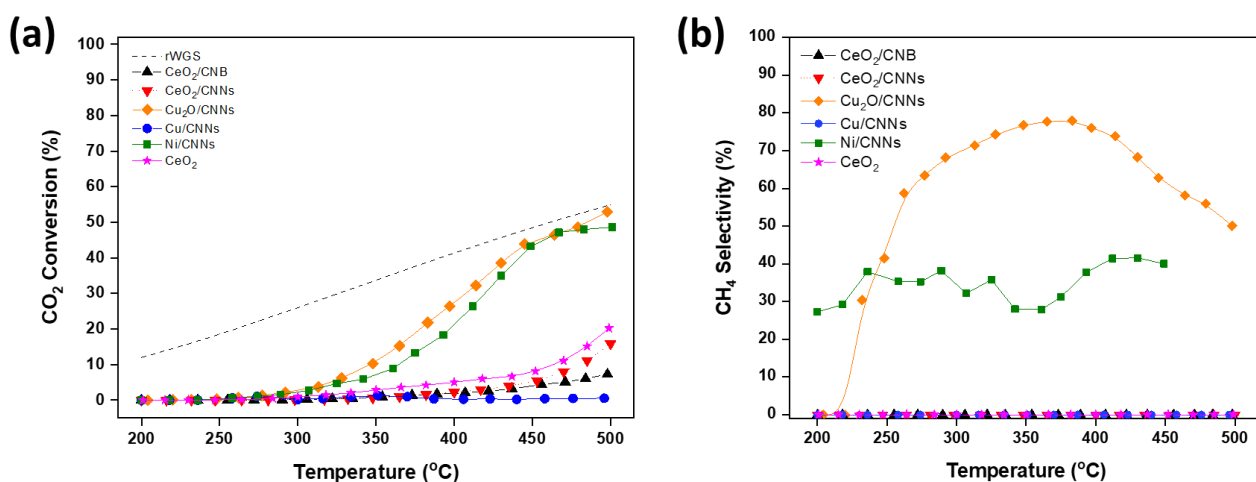


**Figure 5.23.** Catalytic evaluation of g-C<sub>3</sub>N<sub>4</sub>-based catalysts. (a) CO<sub>2</sub> conversion, (b) CH<sub>4</sub> selectivity. Reaction conditions: WHSV = 30 L·g<sup>-1</sup>·h<sup>-1</sup>, H<sub>2</sub>:CO<sub>2</sub> = 4, P = 1 atm.

## 5.6.2. Liquid-phase photocatalysis – Photocatalytic degradation of parabens

### 5.6.2.1. Evaluation of catalyst activity

The photocatalytic performance of CNB and CNNs towards the degradation of methyl-, ethyl-, and propyl-parabens, as well as their mixtures (denoted as MP, EP, PP, and Mixed parabens respectively) under solar irradiation, was thoroughly investigated. Initially, control experiments were conducted without the use of any catalyst, and no significant change in the concentration of MP, EP, and PP was observed (blank test). To ensure an adsorption-desorption equilibrium, the suspension was stirred in the dark for 30 minutes before each sample was exposed to solar irradiation. This step caused only a minor reduction in pollutant concentration, approximately below 15%. However, upon initiating solar irradiation, a remarkable decrease in the concentration of pollutants was observed when using CNNs as the catalyst. Figure 5.24 (a) illustrates the variations in the concentration of the different parabens (MP, EP, PP, and Mixed parabens) over degradation time in the presence of the catalysts under solar irradiation. CNNs demonstrated superior photocatalytic performance, achieving degradation efficiencies of 94.5%, 95.4%, 91.4%, and 92.4% for MP, EP, PP, and mixed parabens, respectively, after 120 minutes of solar light exposure. In contrast, CNB exhibited much lower photocatalytic efficiency, with only 26.8%, 24.7%, 17.2%, and 31.3% degradation for MP, EP, PP, and Mixed parabens, respectively. To better illustrate the disparity in photocatalytic activity, these results have been summarized in Table 5.6 and graphically depicted in Figure 5.24 (b). The data unequivocally demonstrate the significantly superior photocatalytic activity of CNNs compared to CNB for the degradation of the investigated parabens.

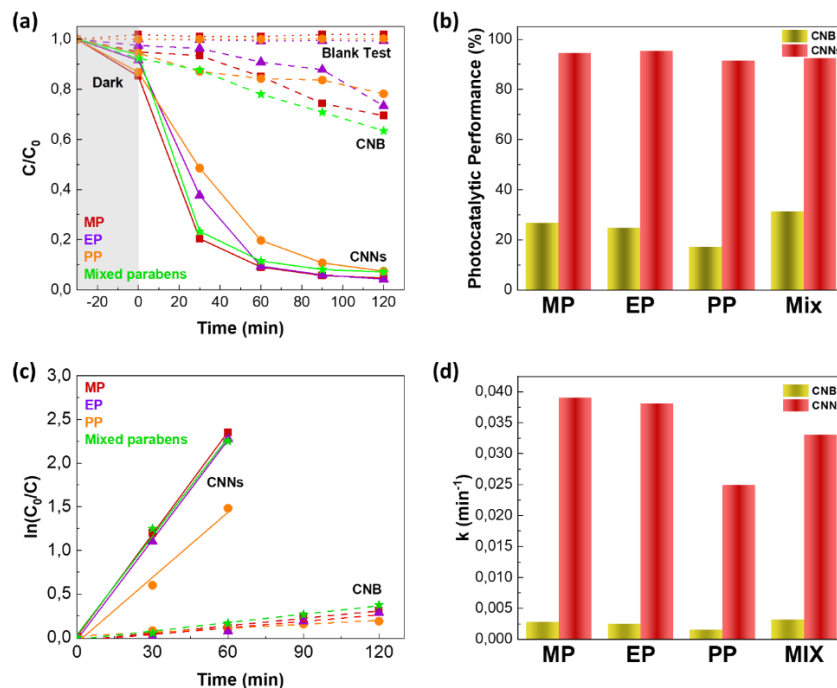


**Figure 5.24.** (a) Photocatalytic degradation of MP, EP, and PP over CNB and CNNs, (b) the comparison of the photocatalytic performance of CNB and CNNs for the removal of MP, EP, and PP, (c) the linear plots of  $\ln(C_0/C)$  versus degradation time, (d) degradation rate constant  $k$  values of CNB and CNNs (initial conditions: 0.01 g/L parabens, 0.5 g/L photocatalyst, solar light irradiation).

**Table 5.6.** The reaction rate constant  $k$  and photocatalytic degradation (%) of MP, EP, PP, and mixed parabens in the presence of CNB and CNNs (initial conditions: 0.01 g/L parabens, 0.5 g/L catalyst, solar light irradiation).

Sample	Pollutant	$k$ ( $\text{min}^{-1}$ )	Photocatalytic degradation (%)
CNB	MP	0.0028	26.8
	EP	0.0025	24.7
	PP	0.0015	17.2
	Mixed parabens	0.0032	31.3
CNNs	MP	0.0394	94.5
	EP	0.0381	95.4
	PP	0.0249	91.4
	Mixed parabens	0.0377	92.4

Additionally, a comprehensive literature comparison with relevant studies is provided in Table 5.7, confirming the outstanding photocatalytic performance of the as-synthesized CNNs in the simultaneous removal of MP, EP, PP, and mixed parabens under solar light irradiation. It is worth noting that the preparation of CNNs involves a facile method, and their composition is relatively simple compared to most studies that utilize multifunctional composites with complex compositions (as shown in Table 5.7).

**Table 5.7.** Literature comparison with relevant studies on the photocatalytic degradation of parabens.

Photocatalysts	S <sub>BET</sub> (m <sup>2</sup> /g)	Parabens	Reaction conditions	Degradation efficiency (%)	Refs.
g-C <sub>3</sub> N <sub>4</sub> nanosheets	212	MP, EP, PP, MIX	0.5 g/L photocatalyst; 0.01 g/L of each paraben in 100ml solution; 120 min; solar irradiation.	94.5 (MP), 95.4 (EP), 91.4 (PP), 92.4 (MIX)	This work
urea-based g-C <sub>3</sub> N <sub>4</sub>	82.5	MP, EP, PP, MIX	200 mg/L photocatalyst; 1 mg/L of each paraben; 180 min; solar irradiation.	92 of each paraben	121
g-C <sub>3</sub> N <sub>4</sub>	33	MP	500 mg/L photocatalyst; 500 µg/L MP in 120ml solution; 90 min; solar irradiation.	100	69
g-C <sub>3</sub> N <sub>4</sub>	111	MP, EP, PP, MIX	1 g/L photocatalyst; 0.08 mM of each paraben in 50ml solution; 20 min; visible irradiation.	100 of each paraben	70
g-C <sub>3</sub> N <sub>4</sub> /FeVO <sub>4</sub> /Fe@NH <sub>2</sub> -Biochar	192.5	EP	90 mg photocatalyst; 20 mg/L EP in 100ml solution; 90 min; solar irradiation.	98.4	71
I-doped Bi <sub>4</sub> O <sub>5</sub> Br <sub>2</sub>	37.3	MP, EP, PP, MIX	50 mg photocatalyst; 10 mg/L MP in 500ml solution; 60 min; visible irradiation.	95 (MP), 98 (EP), 95 (PP)	68
Ag/AgBr@m-WO <sub>3</sub>	16	MP	25 mg photocatalyst; 10 mg/L MP in 25ml solution; 180 min; visible irradiation.	85	122
rGO/AgNPs	-	MP	50 mg photocatalyst; 5 mg/L MP in 100ml solution; 240 min; visible irradiation.	97.6	123

The photocatalytic degradation of the investigated parabens was analyzed using pseudo-first-order kinetics, and the resulting linear plots of  $\ln(C_0/C)$  versus irradiation time for both CNB and CNNs are presented in Figure 5.23 (c). By comparing the degradation rate constants ( $k$  values), as shown in Figure 5.23 (d) and summarized in Table 5.6, the clear superiority of CNNs becomes evident. This underscores the significant impact of the exfoliation process in obtaining nanostructured g-C<sub>3</sub>N<sub>4</sub> with a substantially higher surface area, which in turn is reflected in the photocatalytic performance. The remarkable enhancement in photocatalytic activity can be attributed to the increased surface area of CNNs, which facilitates better adsorption of the target pollutants, resulting in improved degradation rates.

#### 5.6.2.2. Effect of operating conditions

**Effect of catalyst concentration:** The impact of varying the catalyst concentration in the range of 0.1-0.75 g/L on the degradation of MP is illustrated in Figure 5.25 (a). It is evident that the highest photocatalytic performance of CNNs was achieved at a catalyst concentration of 0.5 g/L after 120 minutes of solar light irradiation, resulting in a degradation efficiency of 94.5%. The subsequent concentrations of 0.75 g/L (91.5%), 0.25 g/L (89.8%), and 0.1 g/L (86.2%) also exhibited considerable degradation efficiencies, as detailed in Table 5.8. The observed relationship between catalyst concentration and photocatalytic degradation efficiency can be attributed to the interplay between the population and reactivity of photocatalytic sites in conjunction with the reactant concentration. The findings from this study highlight that an optimal catalyst concentration of 0.5 g/L is crucial for achieving the highest photocatalytic efficiency. Similar trends have been reported in various studies, where no further increase in degradation rate was observed beyond a certain threshold loading of the catalyst. This behavior is primarily ascribed to scattering and screening phenomena, which may result in non-uniform light intensity distribution<sup>124</sup>.

**Effect of initial concentration:** Figure 5.25 (b) illustrates the influence of the initial MP concentration (ranging from 0.001 to 0.02 g/L) on its degradation using CNNs as the photocatalyst. The reaction rate constant ( $k$ ) for MP degradation and the photodegradation efficiency of CNNs remained relatively stable after 120 min of photocatalytic reaction at all concentration levels tested for MP. The data obtained from the experiment showed the following order, in terms of both reaction rate constant ( $k$ ) and photodegradation efficiency: 0.01 g/L > 0.005 g/L > 0.001 g/L > 0.02 g/L, as summarized in Table 5.8. Notably, CNNs achieved the highest degradation of MP at a concentration of 0.01 g/L, resulting in an impressive 94.5% degradation efficiency.

**Effect of irradiation type:** In addition to studying the impact of catalyst and initial paraben concentration, the influence of different types of irradiations was also investigated. Specifically, the

photocatalytic degradation of 0.01 g/L MP using 0.5 g/L CNNs was assessed under solar and visible light irradiation, as depicted in Figure 5.25 (c). The results revealed that the photocatalytic activity of CNNs was significantly higher under solar irradiation, achieving a degradation efficiency of 94.8%, compared to 78.6% under visible light irradiation. To verify that the degradation of MP is indeed due to interactions between photons and the catalyst's surface, an additional experiment was conducted without using any catalyst. The results clearly demonstrated almost zero removal of MP after 120 minutes of solar irradiation, highlighting the essential role of CNNs as a photocatalyst in driving the degradation process. Further analysis of the data showed that the reaction rate constant ( $k$ ) under solar irradiation was approximately three times greater than that under visible light irradiation, indicating the substantial influence of the irradiation type on the photocatalytic activity of CNNs (as presented in Table 5.8).

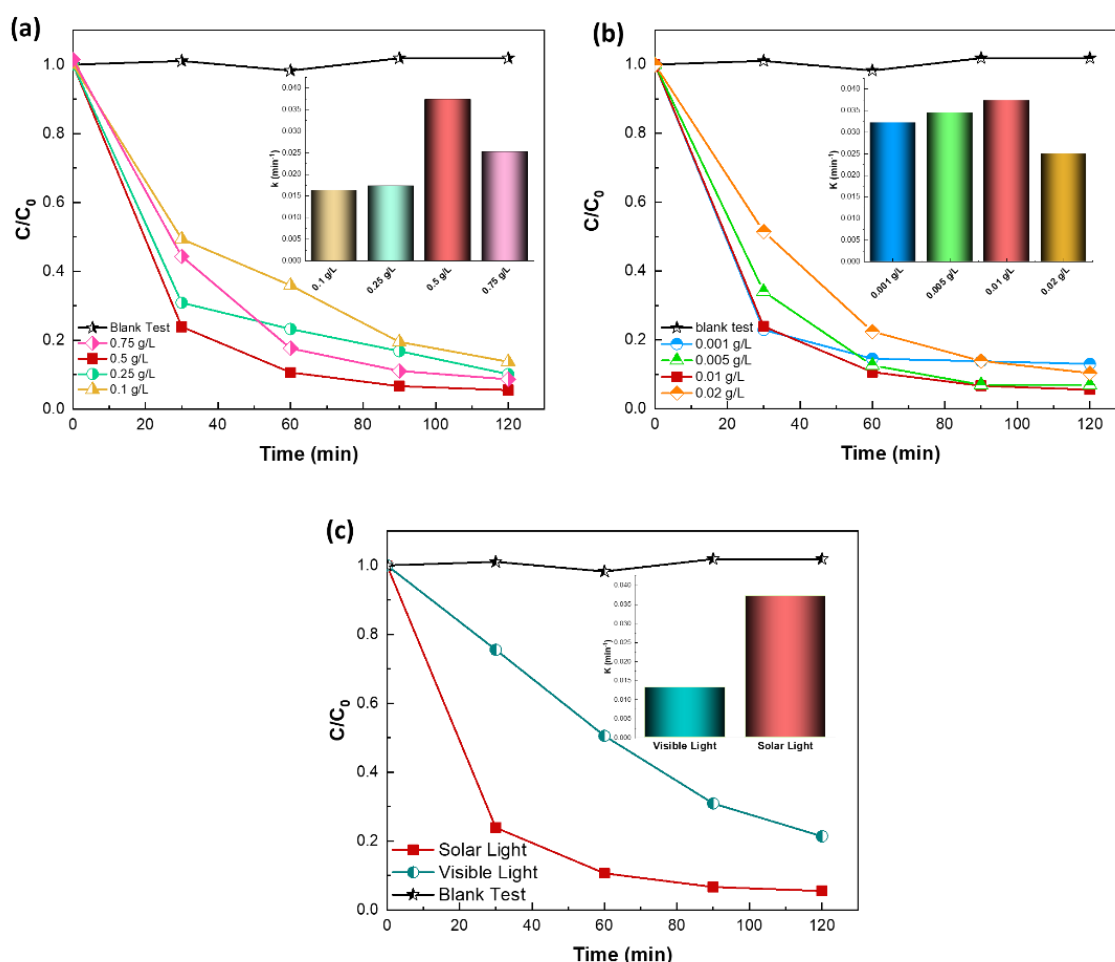


**Figure 5.25.** (a) Effect of the catalyst concentration (initial conditions: 0.01 g/L MP, solar light irradiation); (b) Effect of initial concentration of MP (initial conditions: 0.5 g/L CNNs, solar light irradiation); (c) Photocatalytic degradation of MP under visible or solar irradiation with CNNs (initial conditions: 0.5 g/L CNNs, 0.01 g/L MP).

**Table 5.8.** Effects of the catalyst concentration, initial concentration, and irradiation type on the reaction rate constant  $k$  of MP degradation and photodegradation efficiency of CNNs.

<b>Effect of the catalyst concentration</b>			
Catalyst concentration (g/L)	Initial conditions	$k$ (min <sup>-1</sup> )	Photodegradation efficiency (%)
0.1	0.01 g/L MP, solar light irradiation	0.0173	86.2
0.25		0.0207	89.8
0.5		0.0394	94.5
0.75		0.0261	91.5
<b>Effect of initial MP concentration</b>			
Initial concentration of MP (g/L)	Initial conditions	$k$ (min <sup>-1</sup> )	Photodegradation efficiency (%)
0.001	0.5 g/L CNNs, solar light irradiation	0.03554	87.0
0.005		0.03479	93.1
0.01		0.03941	94.5
0.02		0.02436	89.7
<b>Effect of irradiation type</b>			
Irradiation type	Initial conditions	$k$ (min <sup>-1</sup> )	Photodegradation efficiency (%)
Visible light	0.5 g/L CNNs,	0.0133	78.6
Solar light	0.01 g/L MP	0.0381	94.5

### 5.6.2.3. CNNs reusability and stability

The stability and reusability of a photocatalyst are crucial factors in determining its practical application for water treatment. To assess the stability of CNNs as a photocatalyst for MP degradation, three consecutive photocatalytic cycles were performed under solar light irradiation, with the photocatalyst being collected and reused for each cycle. The results of the photocatalytic stability experiments are depicted in Figure 5.26 (a), which clearly demonstrate that no significant loss of activity occurred in CNNs after three cycles. Remarkably, over 90% of MP degradation was still achieved even after multiple cycles, highlighting the high stability CNNs as an efficient photocatalyst.

To further verify the excellent long-term stability of CNNs, X-ray diffraction (XRD) analysis was conducted on the photocatalyst after repeated reaction cycles. As shown in Figure 5.26 (b), the XRD patterns of both fresh and CNNs used in the three reaction cycles exhibited no noticeable differences, indicating their outstanding phase stability. This further confirms that the crystal structure of CNNs remains unchanged even after repeated use, further validating their durability and reusability.

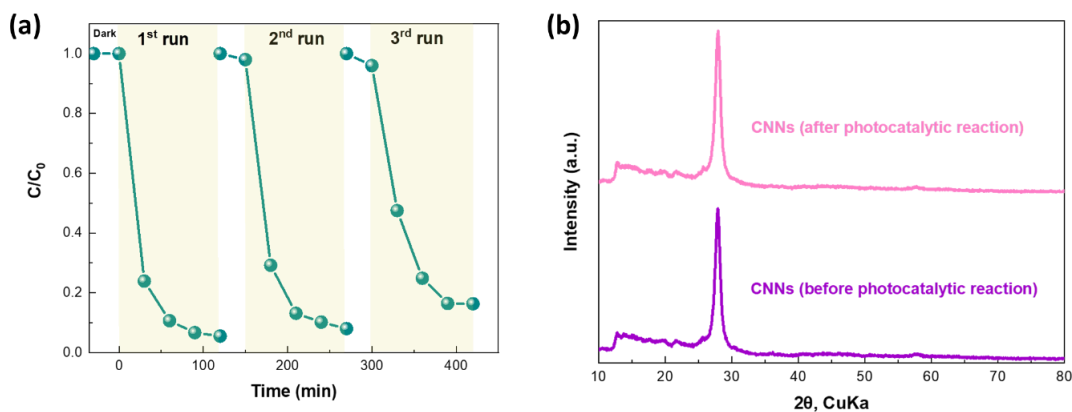


**Figure 5.26.** (a) Stability and reusability of CNNs for the degradation of MP (initial conditions: 0.5 g/L CNNs, 0.01 g/L MP, solar light irradiation); (b) XRD pattern of CNNs after three reaction runs.

#### 5.6.2.4. Mechanism of parabens degradation over CNNs

The photocatalytic performance is strongly influenced by its textural/structural and redox/electronic properties. The former is associated with the abundance and distribution of active sites, while the latter is related to the separation and recombination of photogenerated electron-hole pairs, often linked to interfacial charge transfer phenomena. In the case of CNNs, their superior textural characteristics, as evidenced by a high BET surface area of 212 m<sup>2</sup>/g, provide a greater number of active sites for redox reactions, making the photocatalytic process more efficient. Beyond textural properties, the semiconductor photoexcitation of CNNs is significantly influenced by their photo-absorption ability and band gap. In this study, the band gap values for CNB and CNNs were determined to be 2.74 and 2.91 eV, respectively (as shown in Table 5.1). The increase in the band gap of g-C<sub>3</sub>N<sub>4</sub> induced by the thermal exfoliation process can be attributed to the quantum confinement effect (QCE). According to this, the bandgap can increase due to the opposite shift between the valence and conduction band edges. Consequently, CNNs could provide more powerful photogenerated electron-hole pairs, decreasing the recombination rate of the photogenerated electrons and holes. Additionally, the migration distance of charges from the bulk to the surface was significantly decreased after the delamination, thus reducing the probability of recombination during migration.

To gain deeper insights into the underlying mechanism of the photocatalytic degradation of parabens on CNNs, various scavengers were employed to selectively capture specific reactive species. Isopropyl alcohol (IPA) and disodium ethylenediaminetetraacetate dihydrate (EDTA-Na<sub>2</sub>) were utilized as scavengers for •OH radicals and h<sup>+</sup> holes, respectively. To investigate the role of •O<sub>2</sub><sup>-</sup> superoxide radicals, a photocatalytic test was conducted under a nitrogen atmosphere to remove •O<sub>2</sub><sup>-</sup>. Figure 5.27 presents the results of these scavenger experiments. In the absence of any scavenger, the

photocatalytic degradation of MP over CNNs was 93.3% after 90 minutes of solar irradiation. When IPA was added as a  $\bullet\text{OH}$  radical scavenger, there was only a slight decrease in photocatalytic degradation, indicating that  $\bullet\text{OH}$  radicals have a negligible role in the degradation process. However, when the system was degassed with  $\text{N}_2$  to remove  $\bullet\text{O}_2^-$  superoxide radicals, the photocatalytic activity of CNNs was significantly decreased. An intermediate effect was observed when  $\text{EDTA-Na}_2$  was added as a scavenger. Based on these results, the following order of importance for the various scavengers was obtained: no scavenger (93.3%) > IPA (88.6%) >  $\text{EDTA-Na}_2$  (77.4%) >  $\text{N}_2$  (35.5%) for 90 minutes of solar irradiation. The reaction rate constant ( $k$ ) calculated for each case exhibited the same trend as the photodegradation efficiency of CNNs, as shown in Table 5.9. From these findings, it can be argued that superoxide radicals ( $\bullet\text{O}_2^-$ ) play a vital role in the photodegradation reaction, followed by holes ( $\text{h}^+$ ), while the contribution of hydroxyl radicals ( $\bullet\text{OH}$ ) is relatively minor. This suggests that the photocatalytic degradation of parabens on CNNs is mainly driven by the generation of  $\bullet\text{O}_2^-$  radicals and subsequent charge separation, leading to the efficient degradation of pollutants.

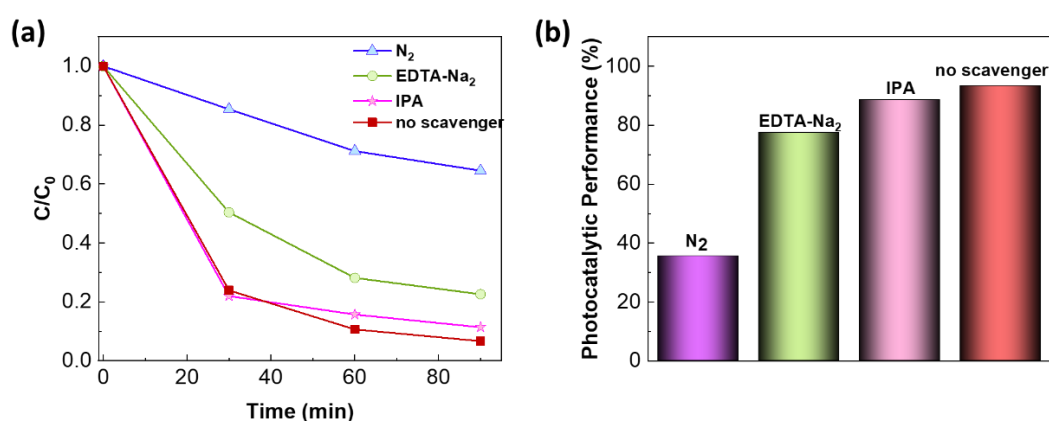


**Figure 5.27.** (a) Photocatalytic degradation of MP over CNNs and (b) the photocatalytic performance of CNNs, in the presence of various scavengers (initial conditions: 0.5 g/L CNNs, 0.01 g/L MP, solar light irradiation).

**Table 5.9.** Effects of the addition of various scavengers on the reaction rate constant  $k$  of MP degradation and photodegradation efficiency of CNNs.

Scavengers	Initial conditions	$k$ ( $\text{min}^{-1}$ )	Photodegradation efficiency (%)
$\text{EDTA-Na}_2$	0.5 g/L CNNs,	0.0211	77.4
IPA	0.01 g/L MP,	0.0309	88.6
$\text{N}_2$	after 90 min of	0.0057	35.5
no scavenger	solar light irradiation	0.0381	93.3

Considering the above-discussed aspects, the photocatalytic degradation mechanism of CNNs under solar irradiation can be elucidated and schematically illustrated in Figure 5.28. The energy levels at the bottom of the conduction band (CB) represent the photoelectrons' reduction potential, while the energy levels at the top of the valence band (VB) determine the oxidizing ability of the generated holes (as shown in Figure 5.7 (b)). These energy levels are critical in driving reduction and oxidation processes, respectively, during the photocatalytic reaction. When CNNs are exposed to solar irradiation, photogenerated electrons ( $e^-$ ) are promoted to higher energy states, while corresponding holes ( $h^+$ ) are generated in the valence band. These photogenerated electrons can reduce adsorbed molecular oxygen, leading to the formation of superoxide radicals ( $\bullet O_2^-$ ). Simultaneously, the generated holes can react with water molecules, producing highly reactive hydroxyl radicals ( $\bullet OH$ ). Based on the scavenger experiments conducted to trap active species, the photocatalytic degradation of MP over CNNs can be primarily attributed to the presence of  $\bullet O_2^-$  radicals and  $h^+$  with strong oxidative potential. These active species efficiently interact with the organic pollutant, facilitating its degradation into harmless byproducts such as  $CO_2$  and  $H_2O$ .

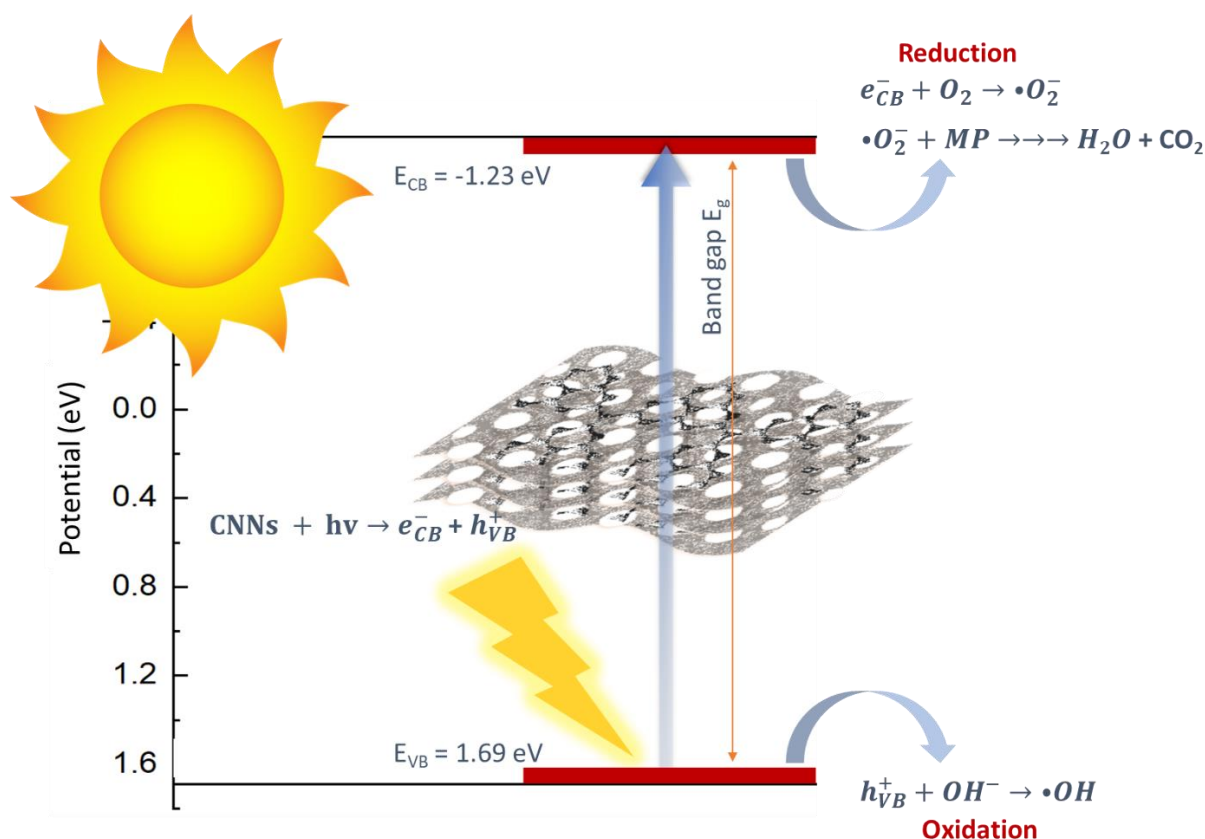


**Figure 5.28.** Schematic diagrams of the photocatalytic mechanism of CNNs under solar light irradiation.

### 5.6.2.5. Preliminary photocatalytic results of g-C<sub>3</sub>N<sub>4</sub>-Based Transition Metal Catalysts

The photocatalytic performances of pristine CNB and transitional metal-doped CNB were evaluated through the degradation of methylparaben (MP) under solar irradiation, as depicted in Figure 5.29 (a). The photodegradation efficiency followed the order: Fe/CNB (83%) > Cr/CNB (79%) > V/CNB (76%) > Ti/CNB (56%) > CNB (41%) > Ni/CNB (36%) > Zn/CNB (25%) > Co/CNB (17%) > Mn/CNB (7%) > Cu/CNB (2%). Notably, Fe/CNB, Cr/CNB, and V/CNB samples demonstrated superior photocatalytic activity for the degradation of MP compared to the pristine CNB. These results highlight that metal doping significantly enhances the photocatalytic degradation performances of g-C<sub>3</sub>N<sub>4</sub>. The photocatalytic degradation of MP was further analyzed using pseudo-first-order kinetics, and the corresponding linear plots of  $\ln(C_0/C)$  versus irradiation time for all samples are presented in Figure 5.29 (b). Interestingly, the degradation rate constants (*k* values) exhibited a similar trend to the photodegradation efficiency, corroborating the influence of metal doping on enhancing photocatalytic activity.

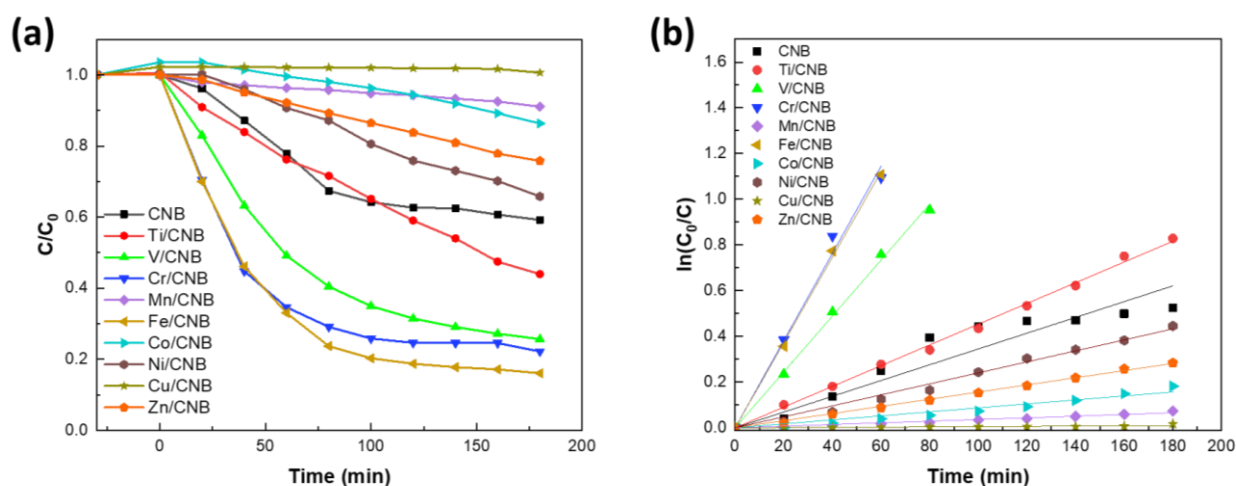


**Figure 5.29.** (a) Photocatalytic degradation of MP over CNB and M/CNB (M: Ti, V, Cr, Mn, Fe, Co, Ni, Cu, Zn) samples, (b) the linear plots of  $\ln(C_0/C)$  versus degradation time (initial conditions: 0.01 g/L MP, 0.5 g/L photocatalyst, solar light irradiation).

### 5.6.3. Gas-phase photocatalysis – Photocatalytic degradation of NO

#### 5.6.3.1. Evaluation of catalyst activity

To demonstrate the potential ability of g-C<sub>3</sub>N<sub>4</sub> samples for air purification, we investigated the photocatalytic removal of NO in the air under visible LED irradiation. Our results, as presented in Figure 5.30 (a), show that the concentration of NO remains unchanged when the reactor was irradiated without any photocatalyst, indicating the necessity of the photocatalyst for effective NO removal (blank test). In the presence of two different photocatalysts, CNB, and CNNs, the NO

concentration decreases rapidly for both samples within just 5 minutes of irradiation. However, the performance of CNNs stands out significantly, achieving a remarkable NO removal percentage of 68% after 5 min, which is approximately 3.6 times higher than that achieved by CNB (19%), as shown in Figure 5.30 (b). Furthermore, the rate constant of CNNs is  $0.28 \text{ min}^{-1}$ , an impressive ca. 17.5 times higher than that of CNB ( $0.016 \text{ min}^{-1}$ ), as presented in Figure 5.29 (b) and summarized in Table 5.10. The superior performance of CNNs samples can be attributed to several factors, including their enhanced textural characteristics, such as a high surface area. Additionally, the prolonged lifetime of charge carriers and the enhanced redox potential caused by the enlarged band gap contribute to their improved photocatalytic activity<sup>59,125</sup>. To quantify the effectiveness of photocatalytic oxidation, we determined the reaction rate of NO removal, which directly represents the number of moles of NO that can be photocatalytically oxidized over  $1 \text{ m}^2$  of irradiated photocatalytic surface area in 1 h. The results for CNNs revealed a photocatalytic oxidation rate of  $7.97 \text{ mg/m}^2\text{s}$ , approximately 2.8 times higher than that of Bulk ( $2.85 \text{ mg/m}^2\text{s}$ ) as shown in Table 5.10.

**Table 5.10.** NO removal, rate constant, and photocatalytic oxidation rate.

Sample	NO removal (%)	k ( $\text{min}^{-1}$ )	r ( $\text{mg/m}^2 \text{ s}$ )
CNB	19.0	0.017	2.85
CNNs	68.0	0.280	7.97

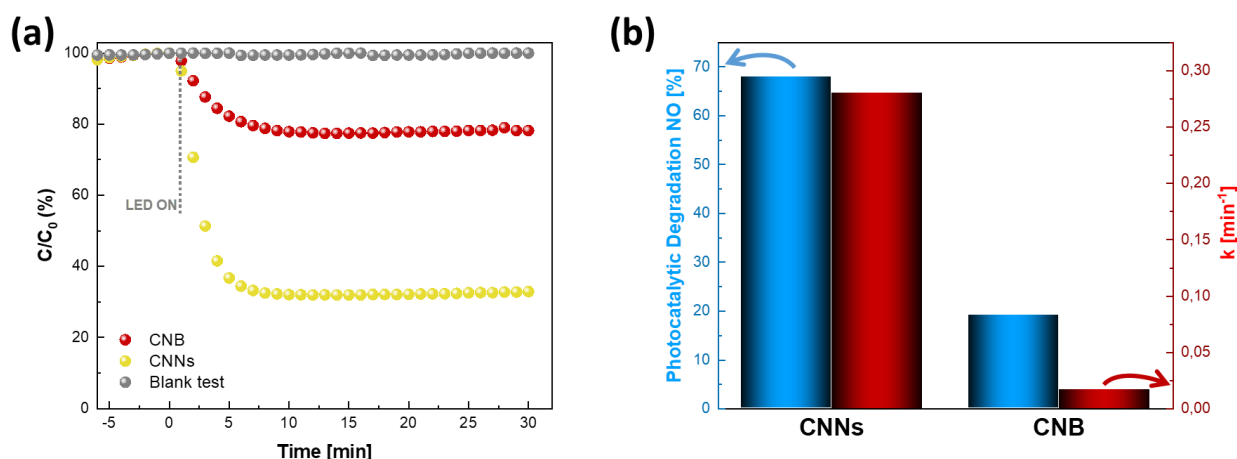


**Figure 5.30.** (a) LED Visible-light photocatalytic performance of CNB and CNNs for the NO removal; (b) NOx removal and Arrhenius rate constants of CNB and CNNs (NO concentration: 600 ppb).

One key advantage of CNNs over bulk material is their large surface area, which provides abundant active sites for redox reactions, resulting in enhanced photocatalytic activity. The higher surface area of Ns facilitates more efficient photocatalytic processes, allowing for greater pollutant removal. In addition to the surface area, the separation and recombination rate of photogenerated electrons and holes significantly influence photocatalytic efficiency. This is closely related to the photo-absorption ability and band gap of the photocatalyst. Our investigation revealed that the band gap of the CNB was 2.74 eV, while that of CNNs was increased to 2.91 eV after exfoliation, as shown in Figure 5.31 (a). This increase in band gap is attributed to the quantum confinement effect (QCE), which shifts the valence and conduction band edges oppositely, resulting in a more substantial intrinsic band gap. The QCE plays a vital role in generating powerful photogenerated holes and electrons, thereby suppressing recombination. Consequently, the separation of photogenerated charge carriers is enhanced, leading to higher photocatalytic activity. Moreover, the delamination process also contributed to reduced charge migration distance from the bulk to the surface. This reduced migration distance further minimized the possibility of charge carrier recombination during migration, promoting photocatalytic efficiency. Furthermore, the surface energy levels of different facets of g-C<sub>3</sub>N<sub>4</sub> play a key role in the movement of photogenerated electrons and holes. The photogenerated electrons tend to move towards the (100) facet, while the holes preferentially migrate towards the (002) facet. This preferential movement reduces the chance of carrier recombination, thus increasing the overall photoreactivity of the g-C<sub>3</sub>N<sub>4</sub> photocatalyst<sup>72</sup>.

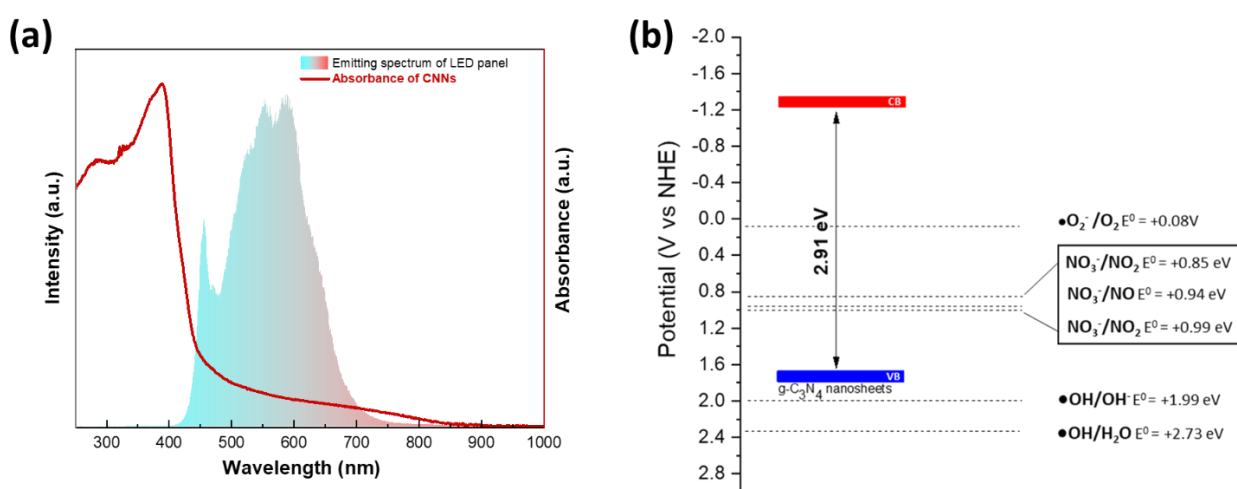


**Figure 5.31.** (a) UV-Vis diffuse reflectance spectra of CNNs and emitting spectrum of LED illumination; (b) Schematic illustration of CNNs band structure.

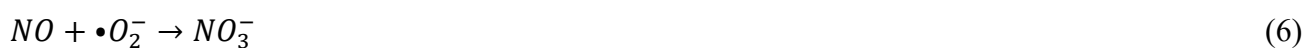
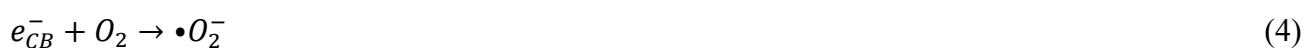
Furthermore, we assessed the photocatalytic performance of CNNs by comparing them with data from the existing literature, as presented in Table 5.11. Impressively, CNNs exhibited outstanding

activity in the removal of NO. Notably, CNNs demonstrated remarkable photocatalytic efficiency due to their well-suited bandgap of 2.91 eV that can be easily excited by visible light which results in the generation of electron-hole pairs in the semiconductor structure.

**Table 5.11.** The photocatalytic performance of CNNs compared with literature data.

Photocatalyst	SSA (m <sup>2</sup> /g)	initial NO concentration	Light source	NO removal time (min)	NO removal ratio (%)	Ref.
CNNs	212	600 ppb	visible LED panel	30	68.0	This work
g-C <sub>3</sub> N <sub>4</sub> (gCN-NSs)	61	600 ppb	visible LED lamp	30	35.8	72
g-C <sub>3</sub> N <sub>4</sub> (CN1)	44	600 ppb	tungsten halogen lamp (λ > 420 nm)	30	17.5	73
g-C <sub>3</sub> N <sub>4</sub> (CN-550)	151	600 ppb	tungsten halogen lamp (λ > 420 nm)	60	33.5	59
g-C <sub>3</sub> N <sub>4</sub> (0.12CN)	65	400 ppb	Xe-lamp (λ > 420 nm)	150	40.4	74
g-C <sub>3</sub> N <sub>4</sub> (CN-240)	71	600 ppb	tungsten halogen lamp (λ > 420 nm)	45	32.3	125
g-C <sub>3</sub> N <sub>4</sub> (CN-E)	33	500 ppb	tungsten halogen lamp (λ > 420 nm)	30	48.3	126

The energy levels at the bottom of the conduction band (CB) and the top of the valence band (VB) play a critical role in determining the reduction potential of photoelectrons and the oxidizing ability of photogenerated holes, respectively. Upon photoexcitation, CNNs generate electron-hole pairs within their semiconductor structure. The photogenerated holes and electrons play a key role in initiating redox reactions, primarily producing oxidizing species such as superoxide anions ( $\bullet O_2^-$ ) and hydroxyl radicals ( $\bullet OH$ ). These reactive species serve as potent initiators of the removal process for NO through a series of reactions (3) - (9):





Previous studies have indeed provided evidence supporting the utilization of electrons carried by the superoxide radicals ( $\bullet O_2^-$ ) in the formation of hydrogen peroxide ( $H_2O_2$ )<sup>127</sup>. This hydrogen peroxide, being a potent oxidizing agent itself, can undergo subsequent oxidation reactions, leading to the generation of highly reactive  $\bullet OH$  through a series of reactions (10) - (11):



In general, the photocatalytic removal of NO involves the utilization of photoinduced charge carriers in redox reactions. These charge carriers play a vital role in generating oxidizing species such as  $\bullet O_2^-$  and  $\bullet OH$ , which serve as initiators for the photocatalytic reaction. Figure 5.31 (b) shows that the catalyst's valence band (VB) potential is lower than the threshold required for the formation of hydroxyl radicals, indicating that the photogenerated holes lack the necessary capacity for reduction to generate  $\bullet OH$  radicals. However, as reported in the literature, the electrons of the  $\bullet O_2^-$  can likely be utilized to facilitate the formation of  $H_2O_2$ . Subsequently, this hydrogen peroxide can undergo further oxidation reactions, leading to the generation of hydroxyl radicals ( $\bullet OH$ )<sup>127</sup>. Therefore, it can be inferred that the primary active species responsible for the oxidation of NO<sub>x</sub> is likely to be superoxide ions ( $\bullet O_2^-$ ).

Furthermore, the photocatalytic oxidation of NO was also tested in N<sub>2</sub> atmosphere instead of air atmosphere to understand the effect of oxygen. As observed in Figure 5.32, the NO removal percentage for the CNNs is less than 10% after 5 min of irradiation under N<sub>2</sub> atmosphere. From this, we can conclude that superoxide radicals ( $\bullet O_2^-$ ) play a crucial role as the main active species in this photocatalytic reaction, driving the oxidation of NO and leading to the formation of nitric oxide (NO<sub>2</sub>) and nitrate ions (NO<sub>3</sub><sup>-</sup>).

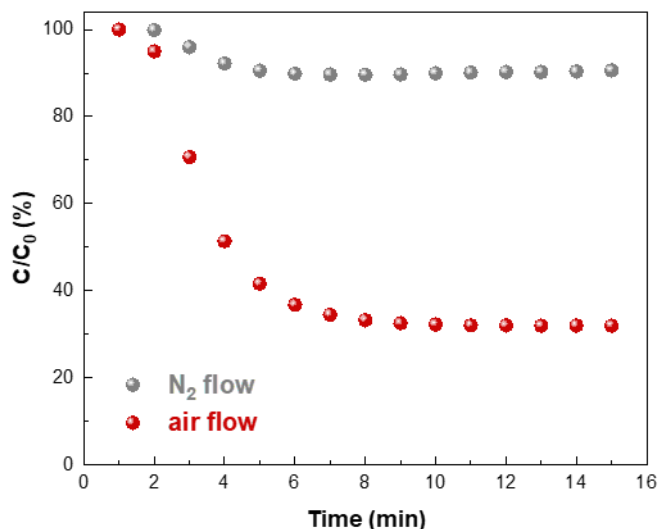


**Figure 5.32.** Photocatalytic oxidation of NO under air and N<sub>2</sub> atmosphere.

### 5.6.3.2. CNNs reusability and stability

To assess the stability of CNNs in NO photocatalytic oxidation, reusability tests were conducted over five consecutive cycles. Figure 5.33 (a) demonstrates that the enhanced photocatalytic activity of CNNs is consistently maintained without noticeable deactivation throughout the five cycles, highlighting their excellent long-term stability in this application. Further confirmation of the stability was obtained through FTIR spectra and XRD pattern analysis before and after repeated reaction runs (Figure 5.33 (b), (c)). In Figure 5.33 (b), the FTIR spectra of both samples show identical absorption bands. The prominent absorption peaks in the 1600-1200 cm<sup>-1</sup> range are attributed to the characteristic aromatic CN heterocycles, while the band at 804 cm<sup>-1</sup> corresponds to the breathing mode of triazine units. Additionally, the absorption band in the range of 3500 - 3000 cm<sup>-1</sup> indicates H<sub>2</sub>O absorption and stretching vibrations of N-H. Notably, after photocatalytic NO removal, two vibration bands appeared at 1278 and 1212 cm<sup>-1</sup>, indicating the stretching of NO<sub>3</sub><sup>-</sup>. This suggests that NO was effectively oxidized to NO<sub>3</sub><sup>-</sup> during the photocatalytic process. The XRD patterns in Figure 5.33 (c) further confirm the outstanding phase stability of CNNs as their crystal structure remained unchanged after five reaction cycles. In addition to the five-cycle stability test, a photocatalytic assessment was conducted after one year, using the previously used sample of CNNs under the same reaction conditions (Figure 5.33 (d)). Surprisingly, the results revealed that the photocatalytic activity remained nearly unchanged even after one year, indicating the superior and long-lasting stability of CNNs.

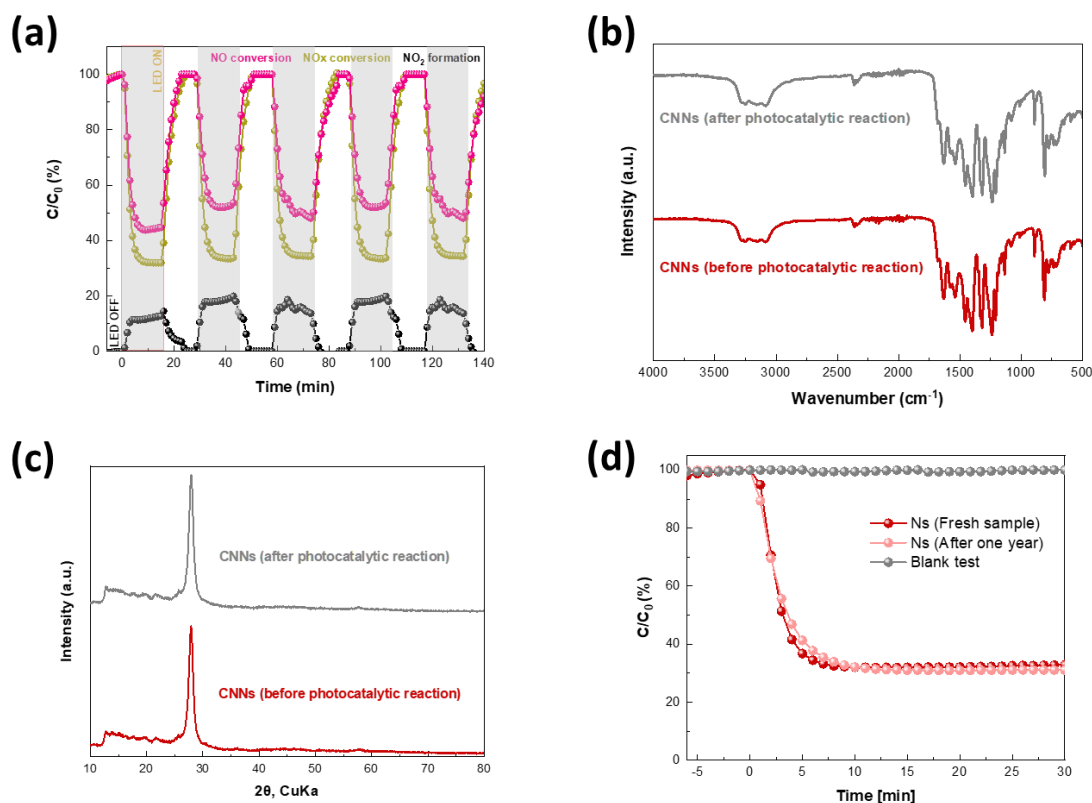


**Figure 5.33.** (a) Five photocatalytic reaction cycles of CNNs, (continuous reactor, NO concentration: 600 ppb); (b) FTIR spectra and (c) XRD pattern of CNNs before and after five reaction runs; (d) Stability photocatalytic test after one year (continuous reactor, NO concentration: 600 ppb).

### 5.6.3.3. Effect of humidity on photocatalytic activity of CNNs

Humidity plays a crucial role in the photocatalytic removal of NO due to the formation of several intermediate radicals induced by water molecules, which significantly influence the overall photocatalytic reaction cycle<sup>128,129</sup>. The interaction of water molecules with the catalyst's surfaces has been extensively studied in the past<sup>130,131</sup>, resulting in different interpretations regarding how adsorbed water molecules or their breakdown products (such as protons, hydroxyl radicals, or hydroxide species) either boost or hinder the catalytic reactivity. For example, in the case of TiO<sub>2</sub> surfaces, it has been observed that the absorption of photons and the generation of electron-hole (e<sup>-</sup>-h<sup>+</sup>) pairs lead to two distinct photocatalytic degradation pathways of NO. One pathway involves hole-mediated steps, resulting in the formation of •OH<sub>ads</sub> and H<sup>+</sup> species, while the other pathway involves electron-mediated steps leading to the generation of superoxide (O<sub>2</sub><sup>-•</sup>)<sup>132</sup>.

Moreover, at high relative humidities, nitrites and/or nitrates can undergo dissociation into NO<sub>2</sub> through two distinct reaction pathways. In the first pathway, NO<sub>2</sub> interacts with water molecules physisorbed on the catalyst's surface, leading to the non-photocatalytic dissociation of nitrite/nitrate and producing NO. This process reduces the overall conversion of NO and negatively impacts the

photocatalytic efficiency. The second reaction pathway involves the dimerization of  $\bullet\text{OH}$  radicals. With high water surface coverages, the concentration of  $\bullet\text{OH}$  radicals increases substantially, promoting their recombination to form hydrogen peroxide, which further dissociates into  $\text{O}_2$  and  $\text{H}_2\text{O}$ . Consequently, the reduction in NO conversion becomes inevitable due to the consumption of  $\bullet\text{OH}$  radicals in these reactions<sup>132,133</sup>. Considering these important factors, Figure 5.34 (a) presents the photocatalytic NO removal ratio at various humidity levels using CNNs as the photocatalyst. Notably, it is evident that the NO removal ratio decreases with increasing relative humidity, clearly illustrating the adverse effect of high relative humidities on the photocatalytic degradation of NO using CNNs as a photocatalyst.

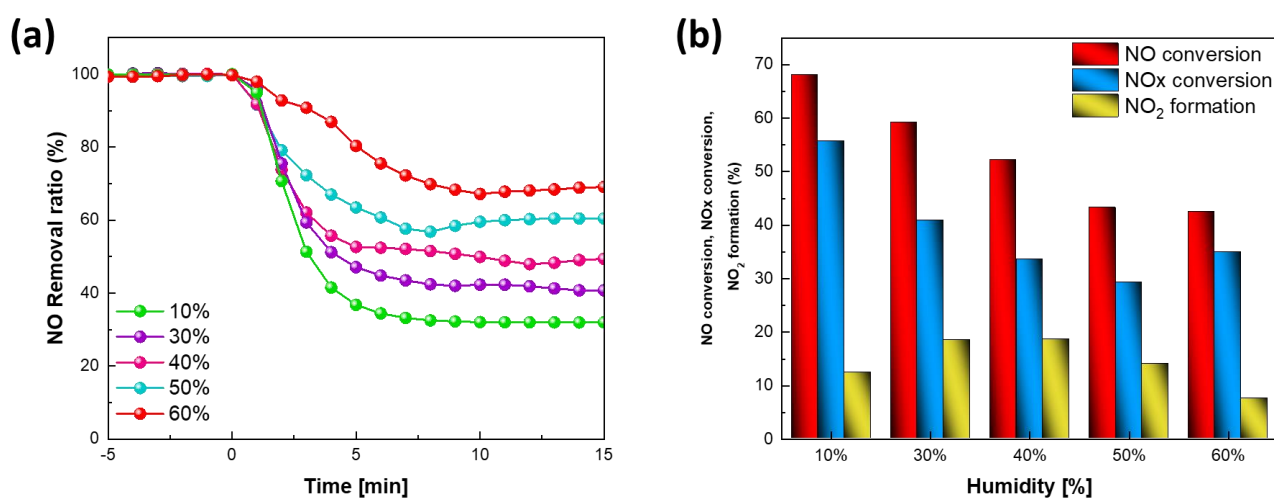


**Figure 5.34.** (a) Photocatalytic NO removal at various humidity levels; (b) NO conversion, NOx conversion, and NO<sub>2</sub> formation (%) for CNNs at various humidity levels.

Furthermore, Table 5.12 summarizes the NO removal (%) and corresponding reaction rate constant ( $k$ ) at various humidity levels. Notably, the reaction rate constant ( $k$ ) experiences a significant decrease with increasing relative humidity, consistent with previous research findings<sup>35,134,135</sup>. This decline in the NO removal rates at higher relative humidities can be attributed to two main factors. Firstly, water molecules may absorb and reflect photon energy, reducing the efficiency of the photocatalytic process. Secondly, an excess of water molecules on the photocatalyst's surface could lead to a light-blocking effect. As a consequence of increased relative humidity, water accumulates on the sample surface, resulting in lower NO and NOx conversion ratios, and NO<sub>2</sub> product formation, as depicted in Figure 5.34 (b). Moreover, the impact of humidity is also influenced by the initial concentration of NO<sup>132</sup>. For low NO concentrations (< 1 ppm), the NO photo-oxidation rate decreases as relative humidity increases. Conversely, at high NO concentrations (5-147 ppm), the NO conversion rate either increases or remains constant with an increase in relative humidity.

Notably, in our study, the use of low initial NO concentrations (600 ppb) led to a negative effect on the photocatalytic degradation of NO when relative humidity was elevated. Further insights from Figure 5.34 (b) reveal that at low humidity levels, an increase in water concentration only slightly enhances NO<sub>2</sub> formation. However, at humidity levels above 40%, the NO<sub>2</sub> formation decreases with increasing water concentration. These observations suggest that water molecules actively participate in the degradation reaction mechanism of NO on the photocatalytic surface under low humidity conditions. However, at humidity levels above 40%, water molecules hinder both NO degradation and NO<sub>2</sub> formation. This hindrance could be attributed to the occupation of more active sites on the photocatalyst's surface or the blocking of light from reaching the photocatalytic surface<sup>128</sup>. A similar relationship between  $\gamma_0$  (to be defined in the following section) and humidity levels has been observed.

**Table 5.12.** Effect of humidity on the photocatalytic removal of NO, reaction rate constant  $k$ , and uptake coefficients  $\gamma_{0,\text{geo}}$  and  $\gamma_{0,\text{BET}}$ .

Sample	Experimental conditions	Humidity (%)	NO removal (%)	$k$ (min <sup>-1</sup> )	$\gamma_{0,\text{geo}}$ ( $\times 10^{-6}$ )	$\gamma_{0,\text{BET}}$ ( $\times 10^{-9}$ )
CNNs	10 W visible LED, 600 ppb NO, 1.5 L/min	10	68.0	0.28	10.4	1.6
		30	59.2	0.24	9.2	1.4
		40	52.1	0.2	8.0	1.2
		50	43.2	0.12	4.2	0.6
		60	32.8	0.063	3.3	0.5

#### 5.6.3.4. Determination of uptake coefficients

To comprehensively understand the uptake process and reaction kinetics in the heterogeneous interaction of NO with g-C<sub>3</sub>N<sub>4</sub> surfaces, it is essential to accurately determine the uptake coefficients ( $\gamma$ )<sup>136</sup>. These coefficients play a crucial role in describing the probability of gas molecules being adsorbed and potentially reacting on the surface. The uptake coefficient ( $\gamma$ ) is defined as the ratio of the number of gas molecules taken up by the surface to the total number of gas-surface collisions<sup>137</sup>. In this study, we focused on determining the initial uptake coefficient ( $\gamma_0$ ) of NO. This coefficient was measured during the initial stage of the experiments on fresh surfaces, and we assumed first-order kinetics<sup>137</sup>. The Eq. (12) used to calculate the initial uptake coefficient ( $\gamma_0$ ) is as follows:

$$\gamma_0 = \frac{4[d(\text{NO})/dt]}{cA_s[\text{NO}]} \quad (12)$$

where  $d(\text{NO})/dt$  is the number of NO molecules taken up and reacted on the surface per unit time (molecules  $\text{s}^{-1}$ ),  $[\text{NO}]$  is the gas-phase concentration of NO (molecules  $\text{cm}^{-3}$ ),  $c$  is the mean molecular speed of NO ( $\text{cm s}^{-1}$ ), and  $A_s$  is the effective surface area of the sample.  $A_s$  is the BET surface area times the mass of the g-C<sub>3</sub>N<sub>4</sub> sample and  $A_{\text{geo}} = 64 \text{ cm}^2$ .

In our experiments, we conducted a thorough investigation of the adsorption kinetics of NO on g-C<sub>3</sub>N<sub>4</sub> surfaces. The rate of NO molecules adsorbed on the surface per unit of time was estimated to be  $1.13 \times 10^{14}$  molecules/s for CNNs and  $3.13 \times 10^{13}$  molecules/s for CNB. To determine the uptake coefficients, we considered the geometric surface area ( $A_{\text{geo}}$ ) and the BET surface area ( $A_s$ ). For the CNNs surface, with  $c = 4.58 \times 10^4 \text{ cm/s}$ ,  $A_s = 4.24 \times 10^5 \text{ cm}^2$ , and  $[\text{NO}] = 1.47 \times 10^{13} \text{ molecules/cm}^3$ , the calculated uptake coefficients were found to be  $\gamma_{0,\text{geo}} = 10.4 \times 10^{-6}$  and  $\gamma_{0,\text{BET}} = 1.6 \times 10^{-9}$ , respectively. The ratio of  $\gamma_{0,\text{geo}}/\gamma_{0,\text{BET}}$  was determined to be  $6.6 \times 10^3$ . Similarly, for CNB surface, with  $c = 4.58 \times 10^4 \text{ cm/s}$ ,  $A_s = 2 \times 10^4 \text{ cm}^2$ , and  $[\text{NO}] = 1.47 \times 10^{13} \text{ molecules/cm}^3$ , the corresponding uptake coefficients were calculated to be  $\gamma_{0,\text{geo}} = 2.88 \times 10^{-6}$  and  $\gamma_{0,\text{BET}} = 0.93 \times 10^{-8}$ , respectively. The  $\gamma_{0,\text{geo}}/\gamma_{0,\text{BET}}$  ratio for CNB was found to be  $3.1 \times 10^2$ . The comparison between  $\gamma_{0,\text{geo}}$  and  $\gamma_{0,\text{BET}}$  reveals that the uptake coefficients based on the geometric surface area ( $\gamma_{0,\text{geo}}$ ) are consistently 2-4 orders of magnitude higher than those based on the BET surface area ( $\gamma_{0,\text{BET}}$ ) for both CNNs and CNB samples. This observation suggests that the photocatalytic activity primarily occurs on the surface of the photocatalyst rather than in the bulk, where the exposure to light is less intense.

Furthermore, to provide a broader context for our findings, we compared the derived  $\gamma$  values from our experiments with those reported in previous studies<sup>73,126</sup> that investigated the visible photocatalytic degradation of NO molecules over g-C<sub>3</sub>N<sub>4</sub> samples. Zhang et al.<sup>126</sup> reported  $\gamma_{0,\text{geo}}$  values for different g-C<sub>3</sub>N<sub>4</sub> samples in the range of  $(0.4 - 5.8) \times 10^{-6}$ , and  $\gamma_{0,\text{BET}}$  values in the range of  $(8 - 12.8) \times 10^{-9}$ . Similarly, Huang et al.<sup>73</sup> reported a  $\gamma_{0,\text{geo}}$  value of  $1.4 \times 10^{-6}$ . In summary, the initial uptake coefficients ( $\gamma_{0,\text{geo}}$  and  $\gamma_{0,\text{BET}}$ ) for the photocatalytic degradation of NO molecules on g-C<sub>3</sub>N<sub>4</sub> surfaces were found to vary within the range of  $(1 - 10) \times 10^{-6}$  and  $(1 - 10) \times 10^{-9}$ , respectively, based on the comparison with the results of other studies<sup>73,126</sup>.

The impact of humidity on the uptake coefficient of NO molecules on g-C<sub>3</sub>N<sub>4</sub> samples was a crucial aspect of our investigation. We determined the values of  $\gamma_{0,\text{geo}}$  and  $\gamma_{0,\text{BET}}$  at various humidity levels in the reactor to gain insights into the photocatalytic NO removal at corresponding humidity conditions. The results of  $\gamma_{0,\text{geo}}$  and  $\gamma_{0,\text{BET}}$  at different humidity levels are presented in Table 5.12, and Figure 5.35 illustrates the trend of these coefficients with increasing humidity. We observed that both  $\gamma_{0,\text{geo}}$

and  $\gamma_{0,BET}$  decrease as the humidity level rises, particularly above 30-40%. This decrease is mainly attributed to the substantial coverage of the catalyst surface area by water molecules at higher humidities<sup>138</sup>. As water molecules accumulate on the surface, they compete with NO molecules for adsorption sites, leading to a reduction in NO degradation rates. Additionally, the extensive water coverage on the surface may hinder the LED light from effectively reaching the photocatalyst surface, resulting in lower NO degradation rates<sup>128</sup>. This humidity effect is consistent with previous findings in the photocatalytic heterogeneous interaction of NO<sub>x</sub> on various solid substrates<sup>129,132,133</sup>.

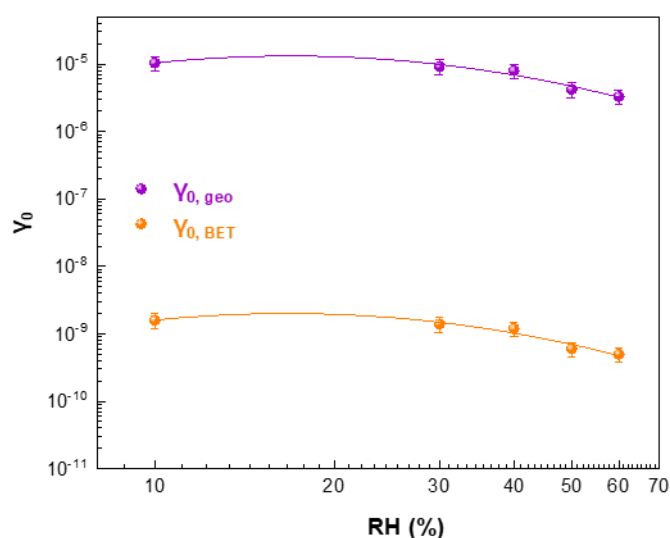


**Figure 5.35.** Initial uptake coefficients  $\gamma_{0,geo}$  and  $\gamma_{0,BET}$  of NO on CNNs versus RH levels (10 - 60%), with initial NO concentration  $1.47 \times 10^{13}$  molecules  $\text{cm}^{-3}$ .

## 5.7. Conclusions

This chapter presents a comprehensive comparative study focusing on the photocatalytic activity and adsorption capacity of two g-C<sub>3</sub>N<sub>4</sub> materials: bulk g-C<sub>3</sub>N<sub>4</sub> (CNB) and g-C<sub>3</sub>N<sub>4</sub> nanosheets (CNNs).

To conduct this investigation, well-structured porous CNNs through a two-step process involving direct thermal polycondensation of melamine, followed by thermal exfoliation were successfully synthesized. The physicochemical characteristics of both materials were thoroughly investigated using a range of characterization techniques, including TGA, BET, XRD, FTIR, SEM, TEM, AFM, UV-Vis diffuse reflectance, and PL spectroscopy. These analyses provided valuable insights into the effect of thermal exfoliation on the properties of CNB and CNNs.

Initially, extensive studies were conducted to explore the adsorption capacity and separation ability of graphitic carbon nitrides for dyes with varying charges and sizes, employing different experimental conditions. The adsorption experiments, involving both anionic and cationic dyes, provided significant insights into the behavior of CNNs. Notably, CNNs exhibited a rapid adsorption

rate towards dye molecules, and they demonstrated a remarkable selective adsorption ability for cationic dyes present in wastewater. Within just 10 minutes, CNNs could completely adsorb Methylene Blue (MB), showcasing their efficiency in capturing cationic dye molecules even when mixed with anionic dyes of similar size. These outcomes can be attributed to the improved textural and structural properties of CNNs, as well as the interactions between the various dyes and the surface of CNNs, including electrostatic interactions. Furthermore, computational studies reinforced the proposed adsorption mechanism, revealing a stronger interaction of cationic dyes with the surface of a single graphitic g-C<sub>3</sub>N<sub>4</sub> sheet.

Subsequently, a comparative study was conducted to assess the photocatalytic performance of CNB and CNNs in degrading methyl-, ethyl-, and propyl-parabens, as well as their mixture. Through comprehensive physicochemical characterization using various techniques, the clear advantage of CNNs in terms of textural properties (surface area of 212 m<sup>2</sup>/g) and optical properties (wide band gap of 2.91 eV) was revealed. This superiority in material characteristics is reflected in excellent photocatalytic efficiency for CNNs under solar light irradiation, achieving over 95% degradation for all types of parabens. In contrast, CNB exhibited a significantly inferior performance, with less than 30% degradation. Moreover, CNNs demonstrated remarkable stability, maintaining high photocatalytic efficiency even after three consecutive photocatalytic cycles. Through radical scavenging experiments, it is revealed that superoxide radicals ( $\bullet\text{O}_2^-$ ) and holes ( $\text{h}^+$ ) played a crucial role in the degradation process, while hydroxyl radicals ( $\bullet\text{OH}$ ) had a less significant impact. Additionally, a preliminary study was conducted, exploring the potential of g-C<sub>3</sub>N<sub>4</sub> as supporting carriers for the transition metal active phase in the photocatalytic degradation of methylparaben.

In the context of gas-phase photocatalysis, a remarkable improvement in the photocatalytic activity of CNNs, along with excellent repeatability over 5 cycles and impressive stability even after 1 year was observed. CNNs demonstrated a notable NO removal efficiency of 68.0% after just 30 minutes of visible irradiation, which was approximately 3.6 times higher than that achieved using bulk material. This superior performance can be attributed to the improved textural characteristics of CNNs, coupled with their unique electronic structure that facilitates efficient charge separation. The initial uptake coefficients  $\gamma_{0,\text{geo}}$  and  $\gamma_{0,\text{BET}}$  for NO on CNNs were found to be  $10.4 \times 10^{-6}$  and  $1.6 \times 10^{-9}$ , respectively, indicating that the photocatalytic conversion of NO primarily occurs on the photocatalyst's surface. Additionally, our tests at different humidity levels revealed a strong effect of humidity on photocatalytic NO removal. This effect can be attributed to the competitive adsorption of water and NO molecules on the active sites of the photocatalyst. It was also observed that both  $\gamma_{0,\text{geo}}$  and  $\gamma_{0,\text{BET}}$  decrease with increasing humidity, particularly above 30-40%, showing similar behavior to the trends observed in NO removal rates.

## References

- (1) Calimli, M. H.; Nas, M. S.; Burhan, H.; Mustafov, S. D.; Demirbas, Ö.; Sen, F. Preparation, Characterization and Adsorption Kinetics of Methylene Blue Dye in Reduced-Graphene Oxide Supported Nano-adsorbents. *J. Mol. Liq.* **2020**, *309*, 113171. <https://doi.org/10.1016/j.molliq.2020.113171>.
- (2) Saeed, M.; Muneer, M.; Haq, A. ul; Akram, N. Photocatalysis: An Effective Tool for Photodegradation of Dyes—a Review. *Environ. Sci. Pollut. Res.* **2022**, *29* (1), 293–311. <https://doi.org/10.1007/s11356-021-16389-7>.
- (3) Cheng, T.; Sun, X.; Xian, T.; Yi, Z.; Li, R.; Wang, X.; Yang, H. Tert-Butylamine/Oleic Acid-Assisted Morphology Tailoring of Hierarchical Bi<sub>4</sub>Ti<sub>3</sub>O<sub>12</sub> Architectures and Their Application for Photodegradation of Simulated Dye Wastewater. *Opt. Mater. (Amst)*. **2021**, *112* (December 2020), 110781. <https://doi.org/10.1016/j.optmat.2020.110781>.
- (4) Ajiboye, T. O.; Oyewo, O. A.; Onwudiwe, D. C. Simultaneous Removal of Organics and Heavy Metals from Industrial Wastewater: A Review. *Chemosphere* **2021**, *262*, 128379. <https://doi.org/10.1016/j.chemosphere.2020.128379>.
- (5) Xia, G.; Zheng, Y.; Sun, Z.; Xia, S.; Ni, Z.; Yao, J. Fabrication of ZnAl-LDH Mixed Metal-Oxide Composites for Photocatalytic Degradation of 4-Chlorophenol. *Environ. Sci. Pollut. Res.* **2022**, *29* (26), 39441–39450. <https://doi.org/10.1007/s11356-022-18989-3>.
- (6) Nguyen, V.-H.; Phan Thi, L.-A.; Chandana, P. S.; Do, H.-T.; Pham, T.-H.; Lee, T.; Nguyen, T. D.; Le Phuoc, C.; Huong, P. T. The Degradation of Paraben Preservatives: Recent Progress and Sustainable Approaches toward Photocatalysis. *Chemosphere* **2021**, *276*, 130163. <https://doi.org/10.1016/j.chemosphere.2021.130163>.
- (7) Gao, Y.; Ji, Y.; Li, G.; An, T. Theoretical Investigation on the Kinetics and Mechanisms of Hydroxyl Radical-Induced Transformation of Parabens and Its Consequences for Toxicity: Influence of Alkyl-Chain Length. *Water Res.* **2016**, *91*, 77–85. <https://doi.org/10.1016/j.watres.2015.12.056>.
- (8) Gmurek, M.; Bizukojć, M.; Mosinger, J.; Ledakowicz, S. Application of Photoactive Electrospun Nanofiber Materials with Immobilized Meso-Tetraphenylporphyrin for Parabens Photodegradation. *Catal. Today* **2015**, *240* (PA), 160–167. <https://doi.org/10.1016/j.cattod.2014.06.015>.

- (9) Papadopoulos, C.; Frontistis, Z.; Antonopoulou, M.; Venieri, D.; Konstantinou, I.; Mantzavinos, D. Sonochemical Degradation of Ethyl Paraben in Environmental Samples: Statistically Important Parameters Determining Kinetics, by-Products and Pathways. *Ultrason. Sonochem.* **2016**, *31*, 62–70. <https://doi.org/10.1016/j.ultsonch.2015.12.002>.
- (10) Hines, E. P.; Mendola, P.; von Ehrenstein, O. S.; Ye, X.; Calafat, A. M.; Fenton, S. E. Concentrations of Environmental Phenols and Parabens in Milk, Urine and Serum of Lactating North Carolina Women. *Reprod. Toxicol.* **2015**, *54*, 120–128. <https://doi.org/10.1016/j.reprotox.2014.11.006>.
- (11) Barr, L.; Metaxas, G.; Harbach, C. A. J.; Savoy, L. A.; Darbre, P. D. Measurement of Paraben Concentrations in Human Breast Tissue at Serial Locations across the Breast from Axilla to Sternum. *J. Appl. Toxicol.* **2012**, *32* (3), 219–232. <https://doi.org/10.1002/jat.1786>.
- (12) Ajiboye, T. O.; Oyewo, O. A.; Onwudiwe, D. C. Photocatalytic Removal of Parabens and Halogenated Products in Wastewater: A Review. *Environ. Chem. Lett.* **2021**, *19* (5), 3789–3819. <https://doi.org/10.1007/s10311-021-01263-2>.
- (13) Ding, C.; Zhu, Q.; Yang, B.; Petropoulos, E.; Xue, L.; Feng, Y.; He, S.; Yang, L. Efficient Photocatalysis of Tetracycline Hydrochloride (TC-HCl) from Pharmaceutical Wastewater Using AgCl/ZnO/g-C<sub>3</sub>N<sub>4</sub> Composite under Visible Light: Process and Mechanisms. *J. Environ. Sci. (China)* **2023**, *126*, 249–262. <https://doi.org/10.1016/j.jes.2022.02.032>.
- (14) Khataee, A.; Kalderis, D.; Motlagh, P. Y.; Binas, V.; Stefa, S.; Konsolakis, M. Synthesis of Copper (I, II) Oxides/Hydrochar Nanocomposites for the Efficient Sonocatalytic Degradation of Organic Contaminants. *J. Ind. Eng. Chem.* **2021**, *95*, 73–82. <https://doi.org/10.1016/j.jiec.2020.12.006>.
- (15) Yousefi, M.; Villar-Rodil, S.; Paredes, J. I.; Moshfegh, A. Z. Oxidized Graphitic Carbon Nitride Nanosheets as an Effective Adsorbent for Organic Dyes and Tetracycline for Water Remediation. *J. Alloys Compd.* **2019**, *809*, 151783. <https://doi.org/10.1016/j.jallcom.2019.151783>.
- (16) Yan, T.; Chen, H.; Jiang, F.; Wang, X. Adsorption of Perfluorooctane Sulfonate and Perfluorooctanoic Acid on Magnetic Mesoporous Carbon Nitride. *J. Chem. Eng. Data* **2014**, *59* (2), 508–515. <https://doi.org/10.1021/je400974z>.
- (17) Zeng, S.; Long, J.; Sun, J.; Wang, G.; Zhou, L. A Review on Peach Gum Polysaccharide:

- Hydrolysis, Structure, Properties and Applications. *Carbohydr. Polym.* **2022**, 279 (October 2021), 119015. <https://doi.org/10.1016/j.carbpol.2021.119015>.
- (18) Binas, V.; Philippidis, A.; Zachopoulos, A.; Kiriakidis, G. Highly Selective Adsorbent and Photocatalytic Material for Industrial Wastewater Treatment. *Adv. Eng. Mater.* **2017**, 19 (8), 1600661. <https://doi.org/10.1002/adem.201600661>.
- (19) Ren, B.; Xu, Y.; Zhang, L.; Liu, Z. Carbon-Doped Graphitic Carbon Nitride as Environment-Benign Adsorbent for Methylene Blue Adsorption: Kinetics, Isotherm and Thermodynamics Study. *J. Taiwan Inst. Chem. Eng.* **2018**, 88, 114–120. <https://doi.org/10.1016/j.jtice.2018.03.041>.
- (20) Ma, J.; Yu, F.; Zhou, L.; Jin, L.; Yang, M.; Luan, J.; Tang, Y.; Fan, H.; Yuan, Z.; Chen, J. Enhanced Adsorptive Removal of Methyl Orange and Methylene Blue from Aqueous Solution by Alkali-Activated Multiwalled Carbon Nanotubes. *ACS Appl. Mater. Interfaces* **2012**, 4 (11), 5749–5760. <https://doi.org/10.1021/am301053m>.
- (21) Song, Y.; Tan, J.; Wang, G.; Zhou, L. Superior Amine-Rich Gel Adsorbent from Peach Gum Polysaccharide for Highly Efficient Removal of Anionic Dyes. *Carbohydr. Polym.* **2018**, 199 (July), 178–185. <https://doi.org/10.1016/j.carbpol.2018.07.010>.
- (22) Zeng, S.; Tan, J.; Xu, X.; Huang, X.; Zhou, L. Facile Synthesis of Amphiphilic Peach Gum Polysaccharide as a Robust Host for Efficient Encapsulation of Methylene Blue and Methyl Orange Dyes from Water. *Int. J. Biol. Macromol.* **2020**, 154, 974–980. <https://doi.org/10.1016/j.ijbiomac.2020.03.151>.
- (23) Medhat, A.; El-Maghrabi, H. H.; Abdelghany, A.; Abdel Menem, N. M.; Raynaud, P.; Moustafa, Y. M.; Elsayed, M. A.; Nada, A. A. Efficiently Activated Carbons from Corn Cob for Methylene Blue Adsorption. *Appl. Surf. Sci. Adv.* **2021**, 3 (December 2020), 100037. <https://doi.org/10.1016/j.apsadv.2020.100037>.
- (24) Mukherjee, A.; Okolie, J. A.; Niu, C.; Dalai, A. K. Techno – Economic Analysis of Activated Carbon Production from Spent Coffee Grounds: Comparative Evaluation of Different Production Routes. *Energy Convers. Manag. X* **2022**, 14 (March), 100218. <https://doi.org/10.1016/j.ecmx.2022.100218>.
- (25) Liang, Y.; Li, J.; Xue, Y.; Tan, T.; Jiang, Z.; He, Y.; Shangguan, W.; Yang, J.; Pan, Y. Benzene Decomposition by Non-Thermal Plasma: A Detailed Mechanism Study by

Synchrotron Radiation Photoionization Mass Spectrometry and Theoretical Calculations. *J. Hazard. Mater.* **2021**, *420* (April), 126584. <https://doi.org/10.1016/j.jhazmat.2021.126584>.

- (26) Ahmad, M.; Qureshi, M. T.; Rehman, W.; Alotaibi, N. H.; Gul, A.; Abdel Hameed, R. S.; Elaimi, M. Al; Abd el-kader, M. F. H.; Nawaz, M.; Ullah, R. Enhanced Photocatalytic Degradation of RhB Dye from Aqueous Solution by Biogenic Catalyst Ag@ZnO. *J. Alloys Compd.* **2022**, *895*, 162636. <https://doi.org/10.1016/j.jallcom.2021.162636>.
- (27) Feng, Z.; Zeng, L.; Zhang, Q.; Ge, S.; Zhao, X.; Lin, H.; He, Y. In Situ Preparation of G-C<sub>3</sub>N<sub>4</sub>/Bi<sub>4</sub>O<sub>5</sub>I<sub>2</sub> Complex and Its Elevated Photoactivity in Methyl Orange Degradation under Visible Light. *J. Environ. Sci. (China)* **2020**, *87* (1972), 149–162. <https://doi.org/10.1016/j.jes.2019.05.032>.
- (28) Frontistis, Z.; Antonopoulou, M.; Venieri, D.; Dailianis, S.; Konstantinou, I.; Mantzavinos, D. Solar Photocatalytic Decomposition of Ethyl Paraben in Zinc Oxide Suspensions. *Catal. Today* **2017**, *280*, 139–148. <https://doi.org/10.1016/j.cattod.2016.06.008>.
- (29) Kotzamanidi, S.; Frontistis, Z.; Binas, V.; Kiriakidis, G.; Mantzavinos, D. Solar Photocatalytic Degradation of Propyl Paraben in Al-Doped TiO<sub>2</sub> Suspensions. *Catal. Today* **2018**, *313* (December 2017), 148–154. <https://doi.org/10.1016/j.cattod.2017.12.006>.
- (30) Moschogiannaki, M.; Frontistis, Z.; Kiriakidis, G.; Mantzavinos, D.; Binas, V. Porous Co<sub>x</sub>Ni<sub>1-x</sub>TiO<sub>3</sub> Nanorods for Solar Photocatalytic Degradation of Ethyl Paraben. *J. Mater.* **2020**, *6* (4), 788–799. <https://doi.org/10.1016/j.jmat.2020.05.006>.
- (31) Xu, P.; Ding, C.; Li, Z.; Yu, R.; Cui, H.; Gao, S. Photocatalytic Degradation of Air Pollutant by Modified Nano Titanium Oxide (TiO<sub>2</sub>) in a Fluidized Bed Photoreactor: Optimizing and Kinetic Modeling. *Chemosphere* **2023**, *319* (December 2022). <https://doi.org/10.1016/j.chemosphere.2023.137995>.
- (32) Ya, Z.; Wang, Q.; Cai, J.; Wang, P.; Jiang, X.; Cai, Z.; Xiang, S.; Wang, T.; Cai, D. An Ultra-Porous g-C<sub>3</sub>N<sub>4</sub> Micro-Tube Coupled with MXene (Ti<sub>3</sub>C<sub>2</sub>T<sub>x</sub>) Nanosheets for Efficient Degradation of Organics under Natural Sunlight. *J. Environ. Sci.* **2022**, *137*, 258–270. <https://doi.org/10.1016/j.jes.2022.10.049>.
- (33) Ajmal, Z.; Haq, M. ul; Naciri, Y.; Djellabi, R.; Hassan, N.; Zaman, S.; Murtaza, A.; Kumar, A.; Al-Sehemi, A. G.; Algarni, H.; Al-Hartomy, O. A.; Dong, R.; Hayat, A.; Qadeer, A. Recent Advancement in Conjugated Polymers Based Photocatalytic Technology for Air

Pollutants Abatement: Cases of CO<sub>2</sub>, NO<sub>x</sub>, and VOCs. *Chemosphere* **2022**, 308 (P2), 136358. <https://doi.org/10.1016/j.chemosphere.2022.136358>.

- (34) Lasek, J.; Yu, Y. H.; Wu, J. C. S. Removal of NO<sub>x</sub> by Photocatalytic Processes. *J. Photochem. Photobiol. C Photochem. Rev.* **2013**, 14 (1), 29–52. <https://doi.org/10.1016/j.jphotochemrev.2012.08.002>.
- (35) Si, H.; Zhou, M.; Fang, Y.; He, J.; Yang, L.; Wang, F. Photocatalytic Concrete for NO<sub>x</sub> Degradation: Influence Factors and Durability. *Constr. Build. Mater.* **2021**, 298, 123835. <https://doi.org/10.1016/j.conbuildmat.2021.123835>.
- (36) Binas, V.; Venieri, D.; Kotzias, D.; Kiriakidis, G. Modified TiO<sub>2</sub> Based Photocatalysts for Improved Air and Health Quality. *J. Mater.* **2017**, 3 (1), 3–16. <https://doi.org/10.1016/j.jmat.2016.11.002>.
- (37) Nguyen, V.-H.; Nguyen, B.-S.; Huang, C.-W.; Le, T.-T.; Nguyen, C. C.; Nhi Le, T. T.; Heo, D.; Ly, Q. V.; Trinh, Q. T.; Shokouhimehr, M.; Xia, C.; Lam, S. S.; Vo, D.-V. N.; Kim, S. Y.; Le, Q. Van. Photocatalytic NO<sub>x</sub> Abatement: Recent Advances and Emerging Trends in the Development of Photocatalysts. *J. Clean. Prod.* **2020**, 270 (x), 121912. <https://doi.org/10.1016/j.jclepro.2020.121912>.
- (38) Liang, Q.; Li, Z.; Huang, Z.-H.; Kang, F.; Yang, Q.-H. Holey Graphitic Carbon Nitride Nanosheets with Carbon Vacancies for Highly Improved Photocatalytic Hydrogen Production. *Adv. Funct. Mater.* **2015**, 25 (44), 6885–6892. <https://doi.org/10.1002/adfm.201503221>.
- (39) Wu, S. Z.; Yu, Y. X.; Zhang, W. De. Processing Graphitic Carbon Nitride for Improved Photocatalytic Activity. *Mater. Sci. Semicond. Process.* **2014**, 24 (1), 15–20. <https://doi.org/10.1016/j.mssp.2014.02.049>.
- (40) Subhan, F.; Khan, I.; Hong, J. Two-Dimensional Graphitic Carbon Nitride (g-C<sub>4</sub>N<sub>3</sub>) for Superior Selectivity of Multiple Toxic Gases (CO, NO<sub>2</sub>, and NH<sub>3</sub>). *Nanotechnology* **2020**, 31 (14), 145501. <https://doi.org/10.1088/1361-6528/ab61d2>.
- (41) Chen, L.; Song, J. Tailored Graphitic Carbon Nitride Nanostructures: Synthesis, Modification, and Sensing Applications. *Adv. Funct. Mater.* **2017**, 27 (39), 1702695. <https://doi.org/10.1002/adfm.201702695>.
- (42) Li, Y.; Wang, M.-Q.; Bao, S.-J.; Lu, S.; Xu, M.; Long, D.; Pu, S. Tuning and Thermal Exfoliation Graphene-like Carbon Nitride Nanosheets for Superior Photocatalytic Activity.

- Ceram. Int.* **2016**, *42* (16), 18521–18528. <https://doi.org/10.1016/j.ceramint.2016.08.190>.
- (43) Sun, S.; Liang, S. Recent Advances in Functional Mesoporous Graphitic Carbon Nitride (Mpg-C<sub>3</sub>N<sub>4</sub>) Polymers. *Nanoscale* **2017**, *9* (30), 10544–10578. <https://doi.org/10.1039/c7nr03656f>.
- (44) Wang, X.; Blechert, S.; Antonietti, M. Polymeric Graphitic Carbon Nitride for Heterogeneous Photocatalysis. *ACS Catal.* **2012**, *2* (8), 1596–1606. <https://doi.org/10.1021/cs300240x>.
- (45) Fu, J.; Yu, J.; Jiang, C.; Cheng, B. G-C<sub>3</sub>N<sub>4</sub>-Based Heterostructured Photocatalysts. *Adv. Energy Mater.* **2018**, *8* (3), 1701503. <https://doi.org/10.1002/aenm.201701503>.
- (46) Cao, S.; Low, J.; Yu, J.; Jaroniec, M. Polymeric Photocatalysts Based on Graphitic Carbon Nitride. *Adv. Mater.* **2015**, *27* (13), 2150–2176. <https://doi.org/10.1002/adma.201500033>.
- (47) Wen, J.; Xie, J.; Chen, X.; Li, X. A Review on G-C<sub>3</sub>N<sub>4</sub> -Based Photocatalysts. *Appl. Surf. Sci.* **2017**, *391*, 72–123. <https://doi.org/10.1016/j.apsusc.2016.07.030>.
- (48) Zhao, Z.; Ma, Y.; Fan, J.; Xue, Y.; Chang, H.; Masubuchi, Y.; Yin, S. Synthesis of Graphitic Carbon Nitride from Different Precursors by Fractional Thermal Polymerization Method and Their Visible Light Induced Photocatalytic Activities. *J. Alloys Compd.* **2018**, *735*, 1297–1305. <https://doi.org/10.1016/j.jallcom.2017.11.033>.
- (49) Zhao, Z.; Sun, Y.; Dong, F. Graphitic Carbon Nitride Based Nanocomposites: A Review. *Nanoscale* **2015**, *7* (1), 15–37. <https://doi.org/10.1039/C4NR03008G>.
- (50) Li, Y.; Wang, M. Q.; Bao, S. J.; Lu, S.; Xu, M.; Long, D.; Pu, S. Tuning and Thermal Exfoliation Graphene-like Carbon Nitride Nanosheets for Superior Photocatalytic Activity. *Ceram. Int.* **2016**, *42* (16), 18521–18528. <https://doi.org/10.1016/j.ceramint.2016.08.190>.
- (51) Papailias, I.; Todorova, N.; Giannakopoulou, T.; Ioannidis, N.; Boukos, N.; Athanasekou, C. P.; Dimotikali, D.; Trapalis, C. Chemical vs Thermal Exfoliation of G-C<sub>3</sub>N<sub>4</sub> for NO<sub>x</sub> Removal under Visible Light Irradiation. *Appl. Catal. B Environ.* **2018**, *239* (May), 16–26. <https://doi.org/10.1016/j.apcatb.2018.07.078>.
- (52) Praus, P.; Smýkalová, A.; Foniok, K.; Matějka, V.; Kormunda, M.; Smetana, B.; Cvejn, D. The Presence and Effect of Oxygen in Graphitic Carbon Nitride Synthesized in Air and Nitrogen Atmosphere. *Appl. Surf. Sci.* **2020**, *529* (May). <https://doi.org/10.1016/j.apsusc.2020.147086>.

- (53) Zhang, X.; Liao, H.; Liu, X.; Shang, R.; Zhou, Y.; Zhou, Y. Graphitic Carbon Nitride Nanosheets Made by Different Methods as Electrode Material for Supercapacitors. *Ionics (Kiel)*. **2020**, *26* (7), 3599–3607. <https://doi.org/10.1007/s11581-020-03458-z>.
- (54) Meng, N.; Ren, J.; Liu, Y.; Huang, Y.; Petit, T.; Zhang, B. Engineering Oxygen-Containing and Amino Groups into Two-Dimensional Atomically-Thin Porous Polymeric Carbon Nitrogen for Enhanced Photocatalytic Hydrogen Production. *Energy Environ. Sci.* **2018**, *11* (3), 566–571. <https://doi.org/10.1039/C7EE03592F>.
- (55) Xu, J.; Zhang, L.; Shi, R.; Zhu, Y. Chemical Exfoliation of Graphitic Carbon Nitride for Efficient Heterogeneous Photocatalysis. *J. Mater. Chem. A* **2013**, *1* (46), 14766. <https://doi.org/10.1039/c3ta13188b>.
- (56) Li, H.-J.; Sun, B.-W.; Sui, L.; Qian, D.-J.; Chen, M. Preparation of Water-Dispersible Porous g-C<sub>3</sub>N<sub>4</sub> with Improved Photocatalytic Activity by Chemical Oxidation. *Phys. Chem. Chem. Phys.* **2015**, *17* (5), 3309–3315. <https://doi.org/10.1039/C4CP05020G>.
- (57) Papailias, I.; Todorova, N.; Giannakopoulou, T.; Ioannidis, N.; Boukos, N.; Athanasekou, C. P.; Dimotikali, D.; Trapalis, C. Chemical vs Thermal Exfoliation of G-C<sub>3</sub>N<sub>4</sub> for NO<sub>x</sub> Removal under Visible Light Irradiation. *Appl. Catal. B Environ.* **2018**, *239* (May), 16–26. <https://doi.org/10.1016/j.apcatb.2018.07.078>.
- (58) Qiu, P.; Chen, H.; Xu, C.; Zhou, N.; Jiang, F.; Wang, X.; Fu, Y. Fabrication of an Exfoliated Graphitic Carbon Nitride as a Highly Active Visible Light Photocatalyst. *J. Mater. Chem. A* **2015**, *3* (48), 24237–24244. <https://doi.org/10.1039/C5TA08406G>.
- (59) Dong, F.; Li, Y.; Wang, Z.; Ho, W.-K. Enhanced Visible Light Photocatalytic Activity and Oxidation Ability of Porous Graphene-like g-C<sub>3</sub>N<sub>4</sub> Nanosheets via Thermal Exfoliation. *Appl. Surf. Sci.* **2015**, *358*, 393–403. <https://doi.org/10.1016/j.apsusc.2015.04.034>.
- (60) Niu, P.; Zhang, L.; Liu, G.; Cheng, H.-M. Graphene-Like Carbon Nitride Nanosheets for Improved Photocatalytic Activities. *Adv. Funct. Mater.* **2012**, *22* (22), 4763–4770. <https://doi.org/10.1002/adfm.201200922>.
- (61) Hatamie, A.; Jalilian, P.; Rezvani, E.; Kakavand, A.; Simchi, A. Fast and Ultra-Sensitive Voltammetric Detection of Lead Ions by Two-Dimensional Graphitic Carbon Nitride (g-C<sub>3</sub>N<sub>4</sub>) Nanolayers as Glassy Carbon Electrode Modifier. *Measurement* **2019**, *134*, 679–687. <https://doi.org/10.1016/j.measurement.2018.10.082>.

- (62) Wang, S. G-C<sub>3</sub>N<sub>4</sub> Nanosheets as “on-off-on” Selective Fluorescence Biosensor to Detect Ascorbic Acid via Redox Reaction. *J. Alloys Compd.* **2019**, *770*, 952–958. <https://doi.org/10.1016/j.jallcom.2018.08.182>.
- (63) Yuan, Y.-J.; Shen, Z.; Wu, S.; Su, Y.; Pei, L.; Ji, Z.; Ding, M.; Bai, W.; Chen, Y.; Yu, Z.-T.; Zou, Z. Liquid Exfoliation of G-C<sub>3</sub>N<sub>4</sub> Nanosheets to Construct 2D-2D MoS<sub>2</sub>/g-C<sub>3</sub>N<sub>4</sub> Photocatalyst for Enhanced Photocatalytic H<sub>2</sub> Production Activity. *Appl. Catal. B Environ.* **2019**, *246* (November 2018), 120–128. <https://doi.org/10.1016/j.apcatb.2019.01.043>.
- (64) Ye, B.; Han, X.; Yan, M.; Zhang, H.; Xi, F.; Dong, X.; Liu, J. Fabrication of Metal-Free Two Dimensional/Two Dimensional Homo Junction Photocatalyst Using Various Carbon Nitride Nanosheets as Building Blocks. *J. Colloid Interface Sci.* **2017**, *507*, 209–216. <https://doi.org/10.1016/j.jcis.2017.08.002>.
- (65) Yan, J.; Han, X.; Zheng, X.; Qian, J.; Liu, J.; Dong, X.; Xi, F. One-Step Template/Chemical Blowing Route to Synthesize Flake-like Porous Carbon Nitride Photocatalyst. *Mater. Res. Bull.* **2017**, *94*, 423–427. <https://doi.org/10.1016/j.materresbull.2017.06.022>.
- (66) Frontistis, Z.; Antonopoulou, M.; Petala, A.; Venieri, D.; Konstantinou, I.; Kondarides, D. I.; Mantzavinos, D. Photodegradation of Ethyl Paraben Using Simulated Solar Radiation and Ag<sub>3</sub>PO<sub>4</sub> Photocatalyst. *J. Hazard. Mater.* **2017**, *323*, 478–488. <https://doi.org/10.1016/j.jhazmat.2016.04.017>.
- (67) Frontistis, Z.; Antonopoulou, M.; Yazirdagi, M.; Kilinc, Z.; Konstantinou, I.; Katsaounis, A.; Mantzavinos, D. Boron-Doped Diamond Electrooxidation of Ethyl Paraben: The Effect of Electrolyte on by-Products Distribution and Mechanisms. *J. Environ. Manage.* **2017**, *195*, 148–156. <https://doi.org/10.1016/j.jenvman.2016.06.044>.
- (68) Xiao, X.; Lu, M.; Nan, J.; Zuo, X.; Zhang, W.; Liu, S.; Wang, S. Rapid Microwave Synthesis of I-Doped Bi<sub>4</sub>O<sub>5</sub>Br<sub>2</sub> with Significantly Enhanced Visible-Light Photocatalysis for Degradation of Multiple Parabens. *Appl. Catal. B Environ.* **2017**, *218*, 398–408. <https://doi.org/10.1016/j.apcatb.2017.06.074>.
- (69) Arvaniti, O. S.; Petala, A.; Zalaora, A. A.; Mantzavinos, D.; Frontistis, Z. Solar Light-Induced Photocatalytic Degradation of Methylparaben by g-C<sub>3</sub>N<sub>4</sub> in Different Water Matrices. *J. Chem. Technol. Biotechnol.* **2020**, *95* (11), 2811–2821. <https://doi.org/10.1002/jctb.6564>.
- (70) Fernandes, R. A.; Sampaio, M. J.; Dražić, G.; Faria, J. L.; Silva, C. G. Efficient Removal of

Parabens from Real Water Matrices by a Metal-Free Carbon Nitride Photocatalyst. *Sci. Total Environ.* **2020**, *716*. <https://doi.org/10.1016/j.scitotenv.2019.135346>.

- (71) Kumar, A.; Kumar, A.; Sharma, G.; Naushad, M.; Stadler, F. J.; Ghfar, A. A.; Dhiman, P.; Saini, R. V. Sustainable Nano-Hybrids of Magnetic Biochar Supported g-C<sub>3</sub>N<sub>4</sub>/FeVO<sub>4</sub> for Solar Powered Degradation of Noxious Pollutants- Synergism of Adsorption, Photocatalysis & Photo-Ozonation. *J. Clean. Prod.* **2017**, *165*, 431–451. <https://doi.org/10.1016/j.jclepro.2017.07.117>.
- (72) Wu, X.; Cheng, J.; Li, X.; Li, Y.; Lv, K. Enhanced Visible Photocatalytic Oxidation of NO by Repeated Calcination of G-C<sub>3</sub>N<sub>4</sub>. *Appl. Surf. Sci.* **2019**, *465* (June 2018), 1037–1046. <https://doi.org/10.1016/j.apsusc.2018.09.165>.
- (73) Huang, H.; Xiao, K.; Tian, N.; Dong, F.; Zhang, T.; Du, X.; Zhang, Y. Template-Free Precursor-Surface-Etching Route to Porous, Thin g-C<sub>3</sub>N<sub>4</sub> Nanosheets for Enhancing Photocatalytic Reduction and Oxidation Activity. *J. Mater. Chem. A* **2017**, *5* (33), 17452–17463. <https://doi.org/10.1039/C7TA04639A>.
- (74) Nie, H.; Ou, M.; Zhong, Q.; Zhang, S.; Yu, L. Efficient Visible-Light Photocatalytic Oxidation of Gaseous NO with Graphitic Carbon Nitride (g-C<sub>3</sub>N<sub>4</sub>) Activated by the Alkaline Hydrothermal Treatment and Mechanism Analysis. *J. Hazard. Mater.* **2015**, *300*, 598–606. <https://doi.org/10.1016/j.jhazmat.2015.07.066>.
- (75) Liu, C.; Zhang, Y.; Dong, F.; Du, X.; Huang, H. Easily and Synchronously Ameliorating Charge Separation and Band Energy Level in Porous G-C<sub>3</sub>N<sub>4</sub> for Boosting Photooxidation and Photoreduction Ability. *J. Phys. Chem. C* **2016**, *120* (19), 10381–10389. <https://doi.org/10.1021/acs.jpcc.6b01705>.
- (76) Xu, J.; Wang, Z.; Zhu, Y. Enhanced Visible-Light-Driven Photocatalytic Disinfection Performance and Organic Pollutant Degradation Activity of Porous g-C<sub>3</sub>N<sub>4</sub> Nanosheets. *ACS Appl. Mater. Interfaces* **2017**, *9* (33), 27727–27735. <https://doi.org/10.1021/acsami.7b07657>.
- (77) Feng, J.; Chen, T.; Liu, S.; Zhou, Q.; Ren, Y.; Lv, Y.; Fan, Z. Improvement of G-C<sub>3</sub>N<sub>4</sub> Photocatalytic Properties Using the Hummers Method. *J. Colloid Interface Sci.* **2016**, *479*, 1–6. <https://doi.org/10.1016/j.jcis.2016.06.040>.
- (78) Zou, L.-R.; Huang, G.-F.; Li, D.-F.; Liu, J.-H.; Pan, A.-L.; Huang, W.-Q. A Facile and Rapid Route for Synthesis of G-C<sub>3</sub>N<sub>4</sub> Nanosheets with High Adsorption Capacity and Photocatalytic

Activity. *RSC Adv.* **2016**, *6* (89), 86688–86694. <https://doi.org/10.1039/C6RA20514C>.

- (79) Haque, E.; Jun, J. W.; Talapaneni, S. N.; Vinu, A.; Jhung, S. H. Superior Adsorption Capacity of Mesoporous Carbon Nitride with Basic CN Framework for Phenol. *J. Mater. Chem.* **2010**, *20* (48), 10801. <https://doi.org/10.1039/c0jm02974b>.
- (80) Yan, T.; Chen, H.; Wang, X.; Jiang, F. Adsorption of Perfluorooctane Sulfonate (PFOS) on Mesoporous Carbon Nitride. *RSC Adv.* **2013**, *3* (44), 22480. <https://doi.org/10.1039/c3ra43312a>.
- (81) Gracia, J.; Kroll, P. Corrugated Layered Heptazine-Based Carbon Nitride: The Lowest Energy Modifications of  $C_3N_4$  Ground State. *J. Mater. Chem.* **2009**, *19* (19), 3013. <https://doi.org/10.1039/b821568e>.
- (82) Deifallah, M.; McMillan, P. F.; Corà, F. Electronic and Structural Properties of Two-Dimensional Carbon Nitride Graphenes. *J. Phys. Chem. C* **2008**, *112* (14), 5447–5453. <https://doi.org/10.1021/jp711483t>.
- (83) Wirth, J.; Neumann, R.; Antonietti, M.; Saalfrank, P. Adsorption and Photocatalytic Splitting of Water on Graphitic Carbon Nitride: A Combined First Principles and Semiempirical Study. *Phys. Chem. Chem. Phys.* **2014**, *16* (30), 15917–15926. <https://doi.org/10.1039/c4cp02021a>.
- (84) Hourahine, B.; Aradi, B.; Blum, V.; Bonafé, F.; Buccheri, A.; Camacho, C.; Cevallos, C.; Deshayé, M. Y.; Dumitrică, T.; Dominguez, A.; Ehlert, S.; Elstner, M.; van der Heide, T.; Hermann, J.; Irle, S.; Kranz, J. J.; Köhler, C.; Kowalczyk, T.; Kubař, T.; Lee, I. S.; Lutsker, V.; Maurer, R. J.; Min, S. K.; Mitchell, I.; Negre, C.; Niehaus, T. A.; Niklasson, A. M. N.; Page, A. J.; Pecchia, A.; Penazzi, G.; Persson, M. P.; Řezáč, J.; Sánchez, C. G.; Sternberg, M.; Stöhr, M.; Stuckenberg, F.; Tkatchenko, A.; Yu, V. W. Z.; Frauenheim, T. DFTB+, a Software Package for Efficient Approximate Density Functional Theory Based Atomistic Simulations. *J. Chem. Phys.* **2020**, *152* (12). <https://doi.org/10.1063/1.5143190>.
- (85) Elstner, M.; Porezag, D.; Jungnickel, G.; Elsner, J.; Haugk, M.; Frauenheim, T.; Suhai, S.; Seifert, G. Self-Consistent-Charge Density-Functional Tight-Binding Method for Simulations of Complex Materials Properties. *Phys. Rev. B* **1998**, *58* (11), 7260–7268. <https://doi.org/10.1103/PhysRevB.58.7260>.
- (86) Caldeweyher, E.; Ehlert, S.; Hansen, A.; Neugebauer, H.; Spicher, S.; Bannwarth, C.; Grimme, S. A Generally Applicable Atomic-Charge Dependent London Dispersion

Correction. *J. Chem. Phys.* **2019**, *150* (15), 154122. <https://doi.org/10.1063/1.5090222>.

- (87) Niu, P.; Zhang, L.; Liu, G.; Cheng, H. M. Graphene-like Carbon Nitride Nanosheets for Improved Photocatalytic Activities. *Adv. Funct. Mater.* **2012**, *22* (22), 4763–4770. <https://doi.org/10.1002/adfm.201200922>.
- (88) Stefa, S.; Griniezi, M.; Dimitropoulos, M.; Paterakis, G.; Galiotis, C.; Kiriakidis, G.; Klontzas, E.; Konsolakis, M.; Binas, V. Highly Porous Thin-Layer g-C<sub>3</sub>N<sub>4</sub> Nanosheets with Enhanced Adsorption Capacity. *ACS Appl. Nano Mater.* **2023**, *6* (3), 1732–1743. <https://doi.org/10.1021/acsanm.2c04632>.
- (89) Dong, F.; Wang, Z.; Sun, Y.; Ho, W.-K.; Zhang, H. Engineering the Nanoarchitecture and Texture of Polymeric Carbon Nitride Semiconductor for Enhanced Visible Light Photocatalytic Activity. *J. Colloid Interface Sci.* **2013**, *401*, 70–79. <https://doi.org/10.1016/j.jcis.2013.03.034>.
- (90) Zhu, B.; Xia, P.; Ho, W.; Yu, J. Isoelectric Point and Adsorption Activity of Porous G-C<sub>3</sub>N<sub>4</sub>. *Appl. Surf. Sci.* **2015**, *344*, 188–195. <https://doi.org/10.1016/j.apsusc.2015.03.086>.
- (91) Wang, H.; Yuan, X.; Wu, Y.; Zeng, G.; Chen, X.; Leng, L.; Li, H. Synthesis and Applications of Novel Graphitic Carbon Nitride/Metal-Organic Frameworks Mesoporous Photocatalyst for Dyes Removal. *Appl. Catal. B Environ.* **2015**, *174–175*, 445–454. <https://doi.org/10.1016/j.apcatb.2015.03.037>.
- (92) Shearer, C. J.; Slattery, A. D.; Stapleton, A. J.; Shapter, J. G.; Gibson, C. T. Accurate Thickness Measurement of Graphene. *Nanotechnology* **2016**, *27* (12). <https://doi.org/10.1088/0957-4484/27/12/125704>.
- (93) Xu, J.; Zhang, L.; Shi, R.; Zhu, Y. Chemical Exfoliation of Graphitic Carbon Nitride for Efficient Heterogeneous Photocatalysis. *J. Mater. Chem. A* **2013**, *1* (46), 14766–14772. <https://doi.org/10.1039/c3ta13188b>.
- (94) Wu, X.; Wang, X.; Wang, F.; Yu, H. Soluble G-C<sub>3</sub>N<sub>4</sub> Nanosheets: Facile Synthesis and Application in Photocatalytic Hydrogen Evolution. *Appl. Catal. B Environ.* **2019**, *247* (January), 70–77. <https://doi.org/10.1016/j.apcatb.2019.01.088>.
- (95) Saleem, M.; Ullah, F.; Qureshi, M. T.; Abdel Hameed, R. S.; Abdallah, M.; Farghaly, O.; Othman, M.; Atta, A. DFT and Experimental Investigations on CdTe<sub>1-x</sub>Sex for Thermoelectric and Optoelectronic Applications. *J. Alloys Compd.* **2022**, *921*, 1–9.

<https://doi.org/10.1016/j.jallcom.2022.166175>.

- (96) Zeeshan, T.; Qureshi, M. T.; Kayani, Z. N.; Arshad, A.; Ullah, F.; Hameed, R. A.; Ragab, H.; Alam, N.; Rehman, W.; Saleem, M. A Comparative Computational and Experimental Study of Al-ZrO<sub>2</sub> Thin Films for Optoelectronic Applications. *Solid State Commun.* **2022**, *358* (November), 115006. <https://doi.org/10.1016/j.ssc.2022.115006>.
- (97) Ullah, N.; Qureshi, M. T.; Toufiq, A. M.; Ullah, F.; Al Elaimi, M.; Hameed, R. S. A.; Khan, A.; Ragab, H. M. E. Effect of Cobalt Doping on the Structural, Optical and Antibacterial Properties of  $\alpha$ -MnO<sub>2</sub> Nanorods. *Appl. Phys. A Mater. Sci. Process.* **2021**, *127* (10), 1–7. <https://doi.org/10.1007/s00339-021-04926-7>.
- (98) Panneri, S.; Ganguly, P.; Mohan, M.; Nair, B. N.; Mohamed, A. A. P.; Warriar, K. G.; Hareesh, U. S. Photoregenerable, Bifunctional Granules of Carbon-Doped g-C<sub>3</sub>N<sub>4</sub> as Adsorptive Photocatalyst for the Efficient Removal of Tetracycline Antibiotic. *ACS Sustain. Chem. Eng.* **2017**, *5* (2), 1610–1618. <https://doi.org/10.1021/acssuschemeng.6b02383>.
- (99) Thurston, J. H.; Hunter, N. M.; Cornell, K. A. Preparation and Characterization of Photoactive Antimicrobial Graphitic Carbon Nitride (g-C<sub>3</sub>N<sub>4</sub>) Films. *RSC Adv.* **2016**, *6* (48), 42240–42248. <https://doi.org/10.1039/C6RA05613J>.
- (100) Yan, T.; Yan, Q.; Wang, X.; Liu, H.; Li, M.; Lu, S.; Xu, W.; Sun, M. Facile Fabrication of Heterostructured G-C<sub>3</sub>N<sub>4</sub>/Bi<sub>2</sub>MoO<sub>6</sub> Microspheres with Highly Efficient Activity under Visible Light Irradiation. *Dalt. Trans.* **2015**, *44* (4), 1601–1611. <https://doi.org/10.1039/C4DT02127D>.
- (101) Zhang, W.; Zhang, Z.; Kwon, S.; Zhang, F.; Stephen, B.; Kim, K. K.; Jung, R.; Kwon, S.; Chung, K. B.; Yang, W. Photocatalytic Improvement of Mn-Adsorbed g-C<sub>3</sub>N<sub>4</sub>. *Appl. Catal. B Environ.* **2017**, *206* (November), 271–281. <https://doi.org/10.1016/j.apcatb.2017.01.034>.
- (102) Mak, K. F.; Lee, C.; Hone, J.; Shan, J.; Heinz, T. F. Atomically Thin MoS<sub>2</sub>: A New Direct-Gap Semiconductor. *Phys. Rev. Lett.* **2010**, *105* (13), 136805. <https://doi.org/10.1103/PhysRevLett.105.136805>.
- (103) Splendiani, A.; Sun, L.; Zhang, Y.; Li, T.; Kim, J.; Chim, C.-Y.; Galli, G.; Wang, F. Emerging Photoluminescence in Monolayer MoS<sub>2</sub>. *Nano Lett.* **2010**, *10* (4), 1271–1275. <https://doi.org/10.1021/nl903868w>.
- (104) Yuan, Y.; Zhang, L.; Xing, J.; Utama, M. I. B.; Lu, X.; Du, K.; Li, Y.; Hu, X.; Wang, S.;

- Genç, A.; Dunin-Borkowski, R.; Arbiol, J.; Xiong, Q. High-Yield Synthesis and Optical Properties of g-C<sub>3</sub>N<sub>4</sub>. *Nanoscale* **2015**, *7* (29), 12343–12350. <https://doi.org/10.1039/c5nr02905h>.
- (105) Ruan, D.; Kim, S.; Fujitsuka, M.; Majima, T. Defects Rich G-C<sub>3</sub>N<sub>4</sub> with Mesoporous Structure for Efficient Photocatalytic H<sub>2</sub> Production under Visible Light Irradiation. *Appl. Catal. B Environ.* **2018**, *238*, 638–646. <https://doi.org/10.1016/j.apcatb.2018.07.028>.
- (106) Aggelopoulos, C. A.; Dimitropoulos, M.; Govatsi, A.; Sygellou, L.; Tsakiroglou, C. D.; Yannopoulos, S. N. Influence of the Surface-to-Bulk Defects Ratio of ZnO and TiO<sub>2</sub> on Their UV-Mediated Photocatalytic Activity. *Appl. Catal. B Environ.* **2017**, *205*, 292–301. <https://doi.org/10.1016/j.apcatb.2016.12.023>.
- (107) Gao, J.; Wang, Y.; Zhou, S.; Lin, W.; Kong, Y. A Facile One-Step Synthesis of Fe-Doped g-C<sub>3</sub>N<sub>4</sub> Nanosheets and Their Improved Visible-Light Photocatalytic Performance. *ChemCatChem* **2017**, *9* (9), 1708–1715. <https://doi.org/10.1002/cctc.201700492>.
- (108) Hussain, A.; Maqsood, S.; Ji, R.; Zhang, Q.; Farooq, M. U.; Boota, M.; Umer, M.; Hashim, M.; Naeem, H.; Toor, Z. S.; Ali, A.; Hou, J.; Xue, Y.; Wang, X. Investigation of Transition Metal-Doped Graphitic Carbon Nitride for MO Dye Degradation. *Diam. Relat. Mater.* **2023**, *132* (December 2022), 109648. <https://doi.org/10.1016/j.diamond.2022.109648>.
- (109) Gao, J.; Wang, J.; Qian, X.; Dong, Y.; Xu, H.; Song, R.; Yan, C.; Zhu, H.; Zhong, Q.; Qian, G.; Yao, J. One-Pot Synthesis of Copper-Doped Graphitic Carbon Nitride Nanosheet by Heating Cu–Melamine Supramolecular Network and Its Enhanced Visible-Light-Driven Photocatalysis. *J. Solid State Chem.* **2015**, *228*, 60–64. <https://doi.org/10.1016/j.jssc.2015.04.027>.
- (110) El Qada, E. N.; Allen, S. J.; Walker, G. M. Adsorption of Methylene Blue onto Activated Carbon Produced from Steam Activated Bituminous Coal: A Study of Equilibrium Adsorption Isotherm. *Chem. Eng. J.* **2006**, *124* (1–3), 103–110. <https://doi.org/10.1016/j.cej.2006.08.015>.
- (111) Ghorai, S.; Sarkar, A.; Raoufi, M.; Panda, A. B.; Schönherr, H.; Pal, S. Enhanced Removal of Methylene Blue and Methyl Violet Dyes from Aqueous Solution Using a Nanocomposite of Hydrolyzed Polyacrylamide Grafted Xanthan Gum and Incorporated Nanosilica. *ACS Appl. Mater. Interfaces* **2014**, *6* (7), 4766–4777. <https://doi.org/10.1021/am4055657>.
- (112) Cheung, W. H.; Szeto, Y. S.; McKay, G. Enhancing the Adsorption Capacities of Acid Dyes

- by Chitosan Nano Particles. *Bioresour. Technol.* **2009**, *100* (3), 1143–1148. <https://doi.org/10.1016/j.biortech.2008.07.071>.
- (113) Spagnoli, A. A.; Giannakoudakis, D. A.; Bashkova, S. Adsorption of Methylene Blue on Cashew Nut Shell Based Carbons Activated with Zinc Chloride: The Role of Surface and Structural Parameters. *J. Mol. Liq.* **2017**, *229*, 465–471. <https://doi.org/10.1016/j.molliq.2016.12.106>.
- (114) Li, D.-F.; Huang, W.-Q.; Zou, L.-R.; Pan, A.; Huang, G.-F. Mesoporous G-C<sub>3</sub>N<sub>4</sub> Nanosheets: Synthesis, Superior Adsorption Capacity and Photocatalytic Activity. *J. Nanosci. Nanotechnol.* **2018**, *18* (8), 5502–5510. <https://doi.org/10.1166/jnn.2018.15441>.
- (115) Djilani, C.; Zaghdoudi, R.; Djazi, F.; Bouchekima, B.; Lallam, A.; Modarressi, A.; Rogalski, M. Adsorption of Dyes on Activated Carbon Prepared from Apricot Stones and Commercial Activated Carbon. *J. Taiwan Inst. Chem. Eng.* **2015**, *53* (March), 112–121. <https://doi.org/10.1016/j.jtice.2015.02.025>.
- (116) Ibupoto, A. S.; Qureshi, U. A.; Ahmed, F.; Khatri, Z.; Khatri, M.; Maqsood, M.; Brohi, R. Z.; Kim, I. S. Reusable Carbon Nanofibers for Efficient Removal of Methylene Blue from Aqueous Solution. *Chem. Eng. Res. Des.* **2018**, *136* (July), 744–752. <https://doi.org/10.1016/j.cherd.2018.06.035>.
- (117) Wang, P.; Cao, M.; Wang, C.; Ao, Y.; Hou, J.; Qian, J. Kinetics and Thermodynamics of Adsorption of Methylene Blue by a Magnetic Graphene-Carbon Nanotube Composite. *Appl. Surf. Sci.* **2014**, *290*, 116–124. <https://doi.org/10.1016/j.apsusc.2013.11.010>.
- (118) Xie, J.; Li, C.; Chi, L.; Wu, D. Chitosan Modified Zeolite as a Versatile Adsorbent for the Removal of Different Pollutants from Water. *Fuel* **2013**, *103*, 480–485. <https://doi.org/10.1016/j.fuel.2012.05.036>.
- (119) Sharif, F.; Gagnon, L. R.; Mulmi, S.; Roberts, E. P. L. Electrochemical Regeneration of a Reduced Graphene Oxide/Magnetite Composite Adsorbent Loaded with Methylene Blue. *Water Res.* **2017**, *114*, 237–245. <https://doi.org/10.1016/j.watres.2017.02.042>.
- (120) Pal, S.; Ghorai, S.; Das, C.; Samrat, S.; Ghosh, A.; Panda, A. B. Carboxymethyl Tamarind-g-Poly(Acrylamide)/Silica: A High Performance Hybrid Nanocomposite for Adsorption of Methylene Blue Dye. *Ind. Eng. Chem. Res.* **2012**, *51* (48), 15546–15556. <https://doi.org/10.1021/ie301134a>.

- (121) Fernandes, E.; Mazierski, P.; Klimeczuk, T.; Zaleska-Medynska, A.; Martins, R. C.; Gomes, J. G-C<sub>3</sub>N<sub>4</sub> for Photocatalytic Degradation of Parabens: Precursors Influence, the Radiation Source and Simultaneous Ozonation Evaluation. *Catalysts* **2023**, *13* (5), 789. <https://doi.org/10.3390/catal13050789>.
- (122) Suliman, M. A.; Gondal, M. A.; Dastageer, M. A.; Chuah, G. K.; Basheer, C. Method for Visible Light-Induced Photocatalytic Degradation of Methylparaben in Water Using Nanostructured Ag/AgBr@m-WO<sub>3</sub>. *Photochem. Photobiol.* **2019**, *95* (6), 1485–1494. <https://doi.org/10.1111/php.13118>.
- (123) Khan, S. A.; Jain, M.; Pant, K. K.; Ziora, Z. M.; Blaskovich, M. A. T. Photocatalytic Degradation of Methylparaben Using Green Nanosilver Supported on Reduced Graphene Oxide. *Ind. Eng. Chem. Res.* **2023**, *62* (17), 6646–6659. <https://doi.org/10.1021/acs.iecr.3c00146>.
- (124) Velegraki, T.; Hapeshi, E.; Fatta-Kassinos, D.; Poulios, I. Solar-Induced Heterogeneous Photocatalytic Degradation of Methyl-Paraben. *Appl. Catal. B Environ.* **2015**, *178*, 2–11. <https://doi.org/10.1016/j.apcatb.2014.11.022>.
- (125) Dong, F.; Ou, M.; Jiang, Y.; Guo, S.; Wu, Z. Efficient and Durable Visible Light Photocatalytic Performance of Porous Carbon Nitride Nanosheets for Air Purification. *Ind. Eng. Chem. Res.* **2014**, *53* (6), 2318–2330. <https://doi.org/10.1021/ie4038104>.
- (126) Zhang, W.; Zhao, Z.; Dong, F.; Zhang, Y. Solvent-Assisted Synthesis of Porous g-C<sub>3</sub>N<sub>4</sub> with Efficient Visible-Light Photocatalytic Performance for NO Removal. *Chinese J. Catal.* **2017**, *38* (2), 372–378. [https://doi.org/10.1016/S1872-2067\(16\)62585-8](https://doi.org/10.1016/S1872-2067(16)62585-8).
- (127) Duan, L.; Li, G.; Zhang, S.; Wang, H.; Zhao, Y.; Zhang, Y. Preparation of S-Doped g-C<sub>3</sub>N<sub>4</sub> with C Vacancies Using the Desulfurized Waste Liquid Extracting Salt and Its Application for NO<sub>x</sub> Removal. *Chem. Eng. J.* **2021**, *411* (October 2020), 128551. <https://doi.org/10.1016/j.cej.2021.128551>.
- (128) Guo, M.-Z.; Ling, T.-C.; Poon, C. S. Photocatalytic NO<sub>x</sub> Degradation of Concrete Surface Layers Intermixed and Spray-Coated with Nano-TiO<sub>2</sub>: Influence of Experimental Factors. *Cem. Concr. Compos.* **2017**, *83* (x), 279–289. <https://doi.org/10.1016/j.cemconcomp.2017.07.022>.
- (129) Liu, G.; Xia, H.; Zhang, W.; Song, L.; Chen, Q.; Niu, Y. Improvement Mechanism of NO

Photocatalytic Degradation Performance of Self-Cleaning Synergistic Photocatalytic Coating under High Humidity. *J. Hazard. Mater.* **2021**, *418* (April), 126337. <https://doi.org/10.1016/j.jhazmat.2021.126337>.

- (130) Thiel, P. A.; Madey, T. E. The Interaction of Water with Solid Surfaces: Fundamental Aspects. *Surf. Sci. Rep.* **1987**, *7* (6–8), 211–385. [https://doi.org/10.1016/0167-5729\(87\)90001-X](https://doi.org/10.1016/0167-5729(87)90001-X).
- (131) Madey, T. The Interaction of Water with Solid Surfaces: Fundamental Aspects. *Vacuum* **1990**, *40* (1–2), 224. [https://doi.org/10.1016/0042-207X\(90\)90169-Y](https://doi.org/10.1016/0042-207X(90)90169-Y).
- (132) Çağlayan, M.; Irfan, M.; Ercan, K. E.; Kocak, Y.; Ozensoy, E. Enhancement of Photocatalytic NO<sub>x</sub> Abatement on Titania via Additional Metal Oxide NO<sub>x</sub>-Storage Domains: Interplay between Surface Acidity, Specific Surface Area, and Humidity. *Appl. Catal. B Environ.* **2020**, *263* (x), 118227. <https://doi.org/10.1016/j.apcatb.2019.118227>.
- (133) Yang, L.; Hakki, A.; Zheng, L.; Jones, M. R.; Wang, F.; Macphee, D. E. Photocatalytic Concrete for NO<sub>x</sub> Abatement: Supported TiO<sub>2</sub> Efficiencies and Impacts. *Cem. Concr. Res.* **2019**, *116* (May 2018), 57–64. <https://doi.org/10.1016/j.cemconres.2018.11.002>.
- (134) Jin, H.; Lee, T. M.; Choi, H.; Kim, K.-S. Effects of Process Variables for NO Conversion by Double-Layered Photocatalytic Mortar with TiO<sub>2</sub> Nanoparticles. *J. Ind. Eng. Chem.* **2022**, *117* (2), 461–472. <https://doi.org/10.1016/j.jiec.2022.10.034>.
- (135) Seo, D.; Yun, T. S. NO<sub>x</sub> Removal Rate of Photocatalytic Cementitious Materials with TiO<sub>2</sub> in Wet Condition. *Build. Environ.* **2017**, *112*, 233–240. <https://doi.org/10.1016/j.buildenv.2016.11.037>.
- (136) Ravishankara, A. R. Heterogeneous and Multiphase Chemistry in the Troposphere. *Science* (80-. ). **1997**, *276* (5315), 1058–1065. <https://doi.org/10.1126/science.276.5315.1058>.
- (137) Crowley, J. N.; Ammann, M.; Cox, R. A.; Hynes, R. G.; Jenkin, M. E.; Mellouki, A.; Rossi, M. J.; Troe, J.; Wallington, T. J. Evaluated Kinetic and Photochemical Data for Atmospheric Chemistry: Volume V – Heterogeneous Reactions on Solid Substrates. *Atmos. Chem. Phys.* **2010**, *10* (18), 9059–9223. <https://doi.org/10.5194/acp-10-9059-2010>.
- (138) Ma, Q.; He, H.; Liu, Y. In Situ DRIFTS Study of Hygroscopic Behavior of Mineral Aerosol. *J. Environ. Sci.* **2010**, *22* (4), 555–560. [https://doi.org/10.1016/S1001-0742\(09\)60145-5](https://doi.org/10.1016/S1001-0742(09)60145-5).

# Chapter 6

## General Conclusions & Future Research Outlook

**Chapter 6** represents the culmination of this thesis, presenting a comprehensive set of conclusions drawn from the research findings. Moreover, this chapter lays the groundwork for future research endeavors by offering insightful guidelines and perspectives.



## General Conclusions

In this thesis, a series of bare  $\text{CeO}_2$ ,  $g\text{-C}_3\text{N}_4$ , and their respective composites were synthesized, comprehensively characterized using various techniques, and evaluated in various catalytic reactions. These reactions include CO oxidation,  $\text{CO}_2$  hydrogenation to CO and  $\text{CH}_4$ , as well as photocatalysis. As highlighted in the Abstract, the primary aim of this thesis is the development of innovative compositions and architectures of noble metal-free nanostructured ceria-based transition metal catalysts ( $\text{M}_x\text{Ce}_{1-x}\text{O}_8$ , M: Ti, V, Cr, Mn, Fe, Co, Ni, Cu). These catalysts are appropriately modified by aliovalent dopants (e.g.,  $\text{TiO}_2$ , ZnO,  $g\text{-C}_3\text{N}_4$ ), which are characterized by low cost. To elaborate further, the surface chemistry of the as-prepared catalysts and their catalytic activity was attempted to be enhanced (fine-tuning) appropriately through:

- (a) **Advanced Synthetic Methods:** Employing advanced synthetic techniques (such as hydrothermal, precipitation, wet impregnation, and Stöber methods) to develop nanomaterials with predefined morphology.
- (b) **Catalyst Promotion:** Appropriate adjustment of the intrinsic properties of catalysts through surface and/or structural promotion.
- (c) **Metal-Support Interactions Modification:** Utilization of promoting/reducing agents, such as  $g\text{-C}_3\text{N}_4$ , to modify interactions between the metal phase and the support matrix.

On the basis of the above objectives and the progress achieved in the framework of the present thesis, the following conclusions can be drawn:

- ✓ In the context of developing cost-efficient and highly active catalytic materials,  $\text{CeO}_2/\text{TiO}_2$  and  $\text{CeO}_2/\text{ZnO}$  mixed oxides for the CO oxidation reaction were prepared. Specifically, the influence of the synthesis method of  $\text{CeO}_2/\text{TiO}_2$  mixed oxides on their physicochemical properties and catalytic activity was investigated. Four different synthesis methods were employed: hydrothermal one-step and two-step methods, precipitation, and the Stöber method. Among these, the catalyst prepared using the Stöber method exhibited optimal catalytic activity, which can be attributed to its enhanced reducing capability. Additionally,  $\text{CeO}_2/\text{ZnO}$  mixed oxides were synthesized, and the effect of different Zn/Ce ratios on their physicochemical properties and catalytic activity was investigated. Using the hydrothermal method, a series of bare  $\text{CeO}_2$  and ZnO oxides, as well as  $\text{CeO}_2/\text{ZnO}$  mixed oxides with varying Zn/Ce atomic ratios (0.2, 0.4, 0.6), were prepared. The catalytic results demonstrate the improved performance of the mixed oxides compared to the bare catalysts, revealing synergistic interactions between  $\text{CeO}_2$  and ZnO.
- ✓ In the case of  $\text{CO}_2$  hydrogenation, the effect of the active phase nature on the physicochemical properties and catalytic activity of ceria-based transition metal catalysts,  $\text{M}/\text{CeO}_2$  (M: Ti, V, Cr,

Mn, Fe, Co, Ni, Cu), was investigated. It was found that the CO<sub>2</sub> conversion follows the order: Ni/CeO<sub>2</sub> > Co/CeO<sub>2</sub> > Cu/CeO<sub>2</sub> > Fe/CeO<sub>2</sub> > CeO<sub>2</sub> > Cr/CeO<sub>2</sub> > Mn/CeO<sub>2</sub> > Ti/CeO<sub>2</sub> > V/CeO<sub>2</sub>. Based on the selectivity results, it was observed that bare ceria, Cu/CeO<sub>2</sub>, Fe/CeO<sub>2</sub>, Cr/CeO<sub>2</sub>, Mn/CeO<sub>2</sub>, Ti/CeO<sub>2</sub>, and V/CeO<sub>2</sub>, are selective towards CO production, while Co/CeO<sub>2</sub> and Ni/CeO<sub>2</sub> catalysts are particularly selective towards methane (CH<sub>4</sub>). Specifically, the combination of nickel with ceria significantly favors the CO<sub>2</sub> methanation reaction. Furthermore, the role of Ni particle size and the phenomenon of promotion using ZnO was studied. CeO<sub>2</sub>/ZnO mixed oxides as supporting carriers of Ni active phase were prepared. In contrast to the catalytic activity of Ni/CeO<sub>2</sub>, Ni/ZnO and Ni/CeO<sub>2</sub>-ZnO catalysts are selective towards CO production, suppressing the CO<sub>2</sub> methanation to a large extent, revealing the role of ZnO promoter in determining the reaction mechanism.

- ✓ In the framework of rational design, graphitic carbon nitride (g-C<sub>3</sub>N<sub>4</sub>) was synthesized, characterized, and evaluated in liquid- and gas-phase photocatalysis. Specifically, a comparative study was conducted on the physicochemical properties and adsorption capacity of bulk g-C<sub>3</sub>N<sub>4</sub> and g-C<sub>3</sub>N<sub>4</sub> nanosheets. The results revealed significantly improved physicochemical characteristics for the nanosheets, as well as enhanced adsorption capacity compared to the bulk structure of g-C<sub>3</sub>N<sub>4</sub>. Furthermore, both bulk g-C<sub>3</sub>N<sub>4</sub> and g-C<sub>3</sub>N<sub>4</sub> nanosheets were evaluated for their photocatalytic degradation of gaseous and liquid pollutants, and the g-C<sub>3</sub>N<sub>4</sub> nanosheets exhibited exceptional photocatalytic performance.

## Future Research Outlook

The primary aim of this thesis was the development of cost-effective noble metal-free catalytic systems that possess remarkable activity, stability, and selectivity, with applicability extending to practical applications. The present thesis demonstrates that rational design involving adjustments of size, shape, and chemical/electronic environment can yield materials of exceptional catalytic efficiency. Specifically, these factors can have significant influence over the reactivity of metal sites and interfacial activity, through both geometric and electronic synergistic interactions. These interactions pave the way for the development of noble metal-free composite materials that are not only highly active but also exceptionally selective for energy and environmental applications.

In the context of ceria-based catalysts, beyond the fine-tuning of various parameters such as the active phase nature, particle size, shape, and structure promotion, the addition of carbon-based materials such as graphitic carbon nitride (g-C<sub>3</sub>N<sub>4</sub>), or the employment of metal-organic frameworks (MOFs), emerges as additional functionalization tools. This approach contributes to the modulation

of the electronic environment and oxygen exchange kinetics of metal oxides. An alternate strategy for fine-tuning metal oxides involves the implementation of computational studies, such as Density Functional Theory (DFT) calculations before catalyst synthesis. This proactive approach facilitates acquiring necessary insights guiding the precise adjustment of specific parameters. Additionally, it's noteworthy that reducible oxides, like ceria or titania, can be synergized with bimetallic or carbide-based materials, yielding multifunctional composites with heightened attributes and catalytic efficiency. Furthermore, it should be mentioned that reducible oxides, such as ceria or titania, could be combined with bimetallic or carbide-based materials towards the development of multifunctional composites with enhanced properties and catalytic performance.

In the case of g-C<sub>3</sub>N<sub>4</sub>-based catalysts, in addition to the development of highly porous g-C<sub>3</sub>N<sub>4</sub> nanosheets, there are a variety of g-C<sub>3</sub>N<sub>4</sub> nanosheet-based modification strategies to further optimize their catalytic activity. In particular, the local electron density of the nanosheets can be tuned and the electron structure optimized by introducing intrinsic defects or foreign dopants. To functionalize the surface into nanosheets, functional groups, metal clusters, or molecular catalysts are modified on the surface to enlarge the delocalization range of  $\pi$  electron of nanosheets and increase the reactive center. In addition, 2D semiconductor materials with tunable energy band structure and g-C<sub>3</sub>N<sub>4</sub> nanosheets can be selected to fabricate 2D/2D nanosheet heterojunctions to realize rapid separation and efficient utilization of photogenerated electron-hole pairs. Finally, the g-C<sub>3</sub>N<sub>4</sub>-based single-atom catalyst can be fabricated by anchoring an isolated metal atom to nanosheets, greatly improving the photocatalytic property. Consequently, appropriate modification of g-C<sub>3</sub>N<sub>4</sub> nanosheets in different aspects can significantly enrich their photocatalytic applications more reasonably.

Ultimately, the conclusions drawn from this thesis offer fundamental design principles for the development of catalytic composites that are either noble-free metals or incorporate very low noble metal content. This direction paves the way for replacing or reducing the use of noble metals in energy and environmental applications, where their use is inevitable. In any case, understanding the fundamental relationships between structure and properties is a critical prerequisite, leading to the rational design of efficient and inexpensive catalytic composites.

# Sofia Stefa

## Curriculum Vitae

✉ [sstefa@tuc.gr](mailto:sstefa@tuc.gr)  
**in** [linked.in/ Stefa](https://www.linkedin.com/in/Stefa)  
[research.gate/Stefa](https://www.researchgate.net/profile/Stefa)

### Education

- 2018–present **Doctor of Philosophy**, *School of Production Engineering and Management, Technical University of Crete, Chania, Greece*  
*Thesis: Rational design & development of nanostructured non-precious metal catalysts for energy and environmental applications.*
- 2016–2018 **Master in Physics with major in Energy and Environment**, *University of Patras, Department of Physics, Patras, Greece*
- 2010–2016 **Diploma of Physics**, *University of Patras, Department of Physics, Patras, Greece*

### Research Experience

- May 2022–present **Research during PhD**, *IKY Scholarship*, Technical University of Crete, Chania, Greece
- April 2023–August 2023 **Research during PhD**, *Erasmus Scholarship*, Fraunhofer Institute for Solar Energy Systems ISE, Freiburg, Germany
- May 2020–May 2021 **Research during PhD**, *Research project LIFE VISIONS*, Foundation for Research and Technology Hellas, Heraklion, Greece
- May 2020–May 2021 **Research during PhD**, *Research project LIGBIO-GASOFC*, Technical University of Crete, Chania, Greece
- November 2018–April 2020 **Research during PhD**, *Research project NANOCO2*, Technical University of Crete, Chania, Greece
- October 2016–April 2018 **Master thesis**, Institute of Chemical Engineering Sciences (ICE-HT), Patras, Greece
- October 2015–September 2016 **Research Assistant**, Institute of Chemical Engineering Sciences (ICE-HT), Patras, Greece
- July–September 2015 **Undergraduate Internship**, Institute of Chemical Engineering Sciences (ICE-HT), Patras, Greece

## Teaching Experience

2017-2018 **Undergraduate course in Physics**, University of Patras, Department of Physics  
Teaching assistance during master studies: 2 semesters, 59 teaching hours

## Fellowships & Awards

May 2022-September 2023 16-month Greek scholarship granted by State Scholarships Foundation (IKY).

April 2023-August 2023 3-month Erasmus scholarship.

## Personal skills

### Languages

Greek	Mother tongue	
English	Proficient	C2
German	Basic	A2

*\*level of the Common European Framework of Reference for Languages*

### Computer skills

Microsoft Office Tools (Word, Excel and PowerPoint), OriginPro, ImageJ, Eva, C++/FORTRAN,  $\LaTeX$

### Communication Skills

Team working gained through preparing group projects during undergraduate and postgraduate studies

### Interests

- Travelling - Improving my skills in languages
- Swimming

## Journal Publications

1. **Visible light photocatalytic oxidation of NO using g-C<sub>3</sub>N<sub>4</sub> nanosheets: Stability, kinetics and effect of humidity**, Sofia Stefa, Evangelia Skliri, Emmanouil Gagaoudakis, George Kiriakidis, Dimitrios Kotzias, Panos Papagiannakopoulos, Michalis Konsolakis, Samuel Mao, Vassilios Binas, (2023) (submitted)
2. **High surface area g-C<sub>3</sub>N<sub>4</sub> Nanosheets as superior Solar-Light Photocatalyst for the Degradation of Parabens**, Sofia Stefa, Maria Zografaki, Marinos Dimitropoulos, George Paterakis, Costas Galiotis, Palanivelu Sangeetha, George Kiriakidis, Michalis Konsolakis, Vassilios Binas, Applied Physics A, (2023) (accepted)

3. **The Combined Impact of Ni-Based Catalysts and a Binary Carbonate Salts Mixture on the CO<sub>2</sub> Gasification Performance of Olive Kernel Biomass Fuel**, Athanasios Lampropoulos, Stamatia A Karakoulia, Georgios Varvoutis, Stavros Spyridakos, Vassilios Binas, Leila Zouridi, **Sofia Stefa**, Michalis Konsolakis, George E Marnellos, *Catalysts* **13**, 596 (2023)
4. **Highly Porous Thin Layer g-C<sub>3</sub>N<sub>4</sub> Nanosheets with Enhanced Adsorption Capacity**, **Sofia Stefa**, Maria Griniezaki, Marinos Dimitropoulos, George Paterakis, Costas Galiotis, George Kiriakidis, Emmanuel Klontzas, Michalis Konsolakis, Vassilios Binas, *ACS Applied Nano Materials* **6**, 1732–1743 (2023)
5. **Highly performant nanocomposite cryogels for multicomponent oily wastewater filtration**, Lía Vásquez, Katarzyna Dziza, Siew-Leng Loo, Vassilios Binas, **Sofia Stefa**, George Kiriakidis, Athanassia Athanassiou, Despina Fragouli, *Separation and Purification Technology*, 122252 (2022)
6. **Support-induced modifications on the CO<sub>2</sub> hydrogenation performance of Ni/CeO<sub>2</sub>: The effect of ZnO doping on CeO<sub>2</sub> nanorods**, Georgios Varvoutis, Stamatia A Karakoulia, Maria Lykaki, **Sofia Stefa**, Vassilios Binas, George E Marnellos, Michalis Konsolakis, *Journal of CO<sub>2</sub> Utilization* **61**, 102057 (2022)
7. **Deciphering the role of Ni particle size and nickel-ceria interfacial perimeter in the low-temperature CO<sub>2</sub> methanation reaction over remarkably active Ni/CeO<sub>2</sub> nanorods**, Georgios Varvoutis, Maria Lykaki, **Sofia Stefa**, Vassilios Binas, George E Marnellos, Michalis Konsolakis, *Applied Catalysis B: Environmental* **297**, 120401 (2021)
8. **Shape Effects of Ceria Nanoparticles on the Water–Gas Shift Performance of CuO<sub>x</sub>/CeO<sub>2</sub> Catalysts**, Maria Lykaki, **Sofia Stefa**, Sónia A. C. Carabineiro, MA Soria, LM Madeira, Michalis Konsolakis, *Catalysts* **11**, 753 (2021)
9. **Synthesis of copper (I, II) oxides/hydrochar nanocomposites for the efficient sonocatalytic degradation of organic contaminants**, Alireza Khataee, Dimitrios Kalderis, Parisa Yekan Motlagh, Vassilis Binas, **Sofia Stefa**, Michalis Konsolakis, *Journal of Industrial and Engineering Chemistry* **95**, 73-82 (2020)
10. **Hydrothermal Synthesis of ZnO–doped Ceria Nanorods: Effect of ZnO Content on the Redox Properties and the CO Oxidation Performance**, **Sofia Stefa**, Maria Lykaki, Vassilios Binas, Pavlos K Pandis, Vassilis N Stathopoulos, Michalis Konsolakis, *Applied Sciences* **10**, 7605 (2020)
11. **Effect of the Preparation Method on the Physicochemical Properties and the CO Oxidation Performance of Nanostructured CeO<sub>2</sub>/TiO<sub>2</sub> Oxides**, **Sofia Stefa**, Maria Lykaki, Dimitrios Fragkoulis, Vasileios Binas, Pavlos K Pandis, Vassilis N Stathopoulos, Michalis Konsolakis, *Processes* **8**, 847 (2020)
12. **Remarkable efficiency of Ni supported on hydrothermally synthesized CeO<sub>2</sub> nanorods for low-temperature CO<sub>2</sub> hydrogenation to methane**, Georgios Varvoutis, Maria Lykaki, **Sofia Stefa**, Eleni Papista, Sónia AC Carabineiro, Georgios E Marnellos, Michalis Konsolakis, *Catalysis Communications* **142**, 106036 (2020)

13. **CO<sub>2</sub> Hydrogenation over Nanoceria-Supported Transition Metal Catalysts: Role of Ceria Morphology (Nanorods versus Nanocubes) and Active Phase Nature (Co versus Cu)**, *Michalis Konsolakis, Maria Lykaki, Sofia Stefa, Sónia A. C. Carabineiro, Georgios Varvoutis, Eleni Papista and Georgios E. Marnellos*, *Nanomaterials* **9**, 1739 (2019)
14. **Facet-Dependent Reactivity of Fe<sub>2</sub>O<sub>3</sub>/CeO<sub>2</sub> Nanocomposites: Effect of Ceria Morphology on CO Oxidation**, *Maria Lykaki, Sofia Stefa, Sónia A. C. Carabineiro, Pavlos K. Pandis, Vassilis N. Stathopoulos and Michalis Konsolakis*, *Catalysts* **9**, 371 (2019)

Citations: 252, h-index: 8

---

## Conferences

1. **Study of the Physicochemical Properties and Photocatalytic Activity of Graphitic Carbon Nitride (g-C<sub>3</sub>N<sub>4</sub>) nanosheets**, *Sofia Stefa, Maria Zografaki, Marinos Dimitropoulos, George Paterakis, Costas Galiotis, George Kiriakidis, Michalis Konsolakis, Vasileios Binas*, 16th Panhellenic Symposium of Catalysis, Chania, Greece 20–22 October 2022
2. **Study of the photocatalytic activity of CeO<sub>2</sub>/g-C<sub>3</sub>N<sub>4</sub> heterostructures towards the removal of pharmaceutical substances under visible irradiation**, *Maria Zografaki, Sofia Stefa, George Kiriakidis, Vasileios Binas*, 16th Panhellenic Symposium of Catalysis, Chania, Greece 20–22 October 2022
3. **The role of nanoceria morphology as support of Ni for the dry reforming of methane studied by transient techniques**, *C.M. Damaskinos, M.A. Vasiliades, M. Lykaki, S. Stefa, V. Binas, M. Konsolakis, A.M. Efstathiou*, 16th Panhellenic Symposium of Catalysis, Chania, Greece 20–22 October 2022
4. **Comparative study of the activity of 3d transition metal catalysts supported on CeO<sub>2</sub> nanorods in the CO<sub>2</sub> hydrogenation reaction**, *Georgios Varvoutis, Maria Lykaki, Sofia Stefa, Georgios E. Marnellos, Michalis Konsolakis*, 16th Panhellenic Symposium of Catalysis, Chania, Greece 20–22 October 2022
5. **Highly Porous g-C<sub>3</sub>N<sub>4</sub> Nanosheets as Solar-Light Photocatalyst for the Degradation of Hazardous Organic Micropollutants**, *Sofia Stefa, Maria Zografaki, Marinos Dimitropoulos, George Paterakis, Costas Galiotis, George Kiriakidis, Michalis Konsolakis, Vasileios Binas*, 8th International Symposium on Transparent Conductive Materials (TCM), Heraklion, Greece 16–21 October 2022
6. **Design of Visible Light Active Photocatalytic Nanomaterials: From Lab To Real Environmental Applications**, *Maria Zografaki, Evangelia Skliri, Sofia Stefa, Emmanouil Gagaoudakis, George Kiriakidis, Kostas Theodorou, Panagiotis Panagopoulos, Thomas Maggos, Vasileios Binas*, 8th International Symposium on Transparent Conductive Materials (TCM), Heraklion, Greece 16–21 October 2022

7. **Highly Porous g-C<sub>3</sub>N<sub>4</sub> Nanosheets as Superior Solar-Light Photocatalyst for the Degradation of Hazardous Organic Micropollutants**, Sofia Stefa, Maria Zografaki, Marinos Dimitropoulos, George Paterakis, Costas Galiotis, George Kiriakidis, Michalis Konsolakis, Vasileios Binas, 11th European Conference on Solar Chemistry and Photocatalysis: Environmental Applications (SPEA), Turin, Italy  
6–10 June 2022
8. **Enhanced visible light photocatalytic activity of porous g-C<sub>3</sub>N<sub>4</sub> nanosheets for nitrogen oxides (NO<sub>x</sub>) abatement**, Sofia Stefa, Evangelia Skliri, Emmanouil Gagaoudakis, George Kiriakidis, Michalis Konsolakis, Samuel Mao, Shaohua Shen, Vasileios Binas, 11th European Conference on Solar Chemistry and Photocatalysis: Environmental Applications (SPEA), Turin, Italy  
6–10 June 2022
9. **Design of Visible Light Active Photocatalytic Nanomaterials: From Lab to Real Environmental Applications**, Maria Zografaki, Evangelia Skliri, Thomas Maggos, Sofia Stefa, Emmanouil Gagaoudakis, George Kiriakidis, Vasileios Binas, 11th European Conference on Solar Chemistry and Photocatalysis: Environmental Applications (SPEA), Turin, Italy  
6–10 June 2022
10. **Physicochemical study of highly porous g-C<sub>3</sub>N<sub>4</sub> nanosheets with superior adsorption capacity**, Sofia Stefa, Maria Griniezaki, Marinos Dimitropoulos, George Paterakis, Costas Galiotis, George Kiriakidis, Michalis Konsolakis, Vasileios Binas, 13th Panhellenic Symposium in Chemical Engineering, Patras, Greece  
2–4 June 2022
11. **Support-induced effects on the CO<sub>2</sub> Hydrogenation performance of Ni/Ce<sub>1-x</sub>Zn<sub>x</sub>O catalysts**, Georgios Varvoutis, Maria Lykaki, Sofia Stefa, Stamatia A Karakoulia, Georgios E. Marnellos, Michalis Konsolakis, 13th Panhellenic Symposium in Chemical Engineering, Patras, Greece  
2–4 June 2022
12. **Effect of thermal exfoliation of g-C<sub>3</sub>N<sub>4</sub> on the physicochemical properties, adsorption capacity and NO<sub>x</sub> removal under indoor LED irradiation**, Sofia Stefa, Maria Griniezaki, Evangelia Skliri, Emmanouil Gagaoudakis, George Kiriakidis, Michalis Konsolakis, Vasileios Binas, XXXV Panhellenic Conference on Solid State Physics and Materials Science, Athens, Greece  
26–29 September 2021
13. **Study of the physicochemical properties and photocatalytic activity of graphitic carbon nitride (g-C<sub>3</sub>N<sub>4</sub>)**, 1st Online Symposium of Young Scientists Mineral Resources-Environment-Chemical Engineering, Sofia Stefa, Maria Lykaki, Vasileios Binas, Michalis Konsolakis, 26–28 February 2021
14. **Catalytic hydrogenation of CO<sub>2</sub> to methane over transition metals (Ni, Co) supported on nano-ceria**, Michalis Konsolakis, Maria Lykaki, Sofia Stefa, Sónia A. C. Carabineiro, Georgios Varvoutis, Georgios E. Marnellos, 2nd Webinar on Material Science and Nanotechnology  
18–19 November 2020

15. **CO<sub>2</sub> hydrogenation over alkali-promoted CuO/CeO<sub>2</sub> catalysts**, *Georgios Varvoutis, Maria Lykaki, Sofia Stefa, Evridiki Mandela, Georgios E. Marnellos, Michalis Konsolakis*, 2nd Webinar on Material Science and Nanotechnology  
18–19 November 2020
16. **Turning CO<sub>2</sub> emissions to CH<sub>4</sub> by means of green H<sub>2</sub> and novel catalytic materials**, *Michalis Konsolakis, Spiros Papaefthimiou, Dimitris Ipsakis, Maria Lykaki, Sofia Stefa, Georgios Varvoutis, Georgios E. Marnellos*, 5th HAAE Energy Transition Symposium, Athens, Greece  
30 September–2 October 2020
17. **Rational design of ceria-based nanocatalysts for CO<sub>2</sub> hydrogenation to value-added products**, *Michalis Konsolakis, Maria Lykaki, Sofia Stefa, Sónia A. C. Carabineiro, Georgios Varvoutis, Eleni Papista, Georgios E. Marnellos*, International Conference on Materials and Nanomaterials, Paris, France  
17–19 July 2019
18. **Effect of synthesis procedure on the physicochemical properties of nanostructured CeO<sub>2</sub>-TiO<sub>2</sub> mixed oxides**, *Sofia Stefa, Maria Lykaki, Vasileios Binas, Pavlos K Pandis, Vassilis N Stathopoulos, Michalis Konsolakis*, 12th Panhellenic Symposium in Chemical Engineering, Athens, Greece  
29–31 May 2019
19. **Effect of CeO<sub>2</sub> morphology on the physicochemical and catalytic characteristics of supported transition metals MO<sub>x</sub>/CeO<sub>2</sub> (M: Ni, Co, Fe)**, *Maria Lykaki, Sofia Stefa, Vasileios Binas, Sónia A. C. Carabineiro, Pavlos K Pandis, Vassilis N Stathopoulos, Michalis Konsolakis*, 12th Panhellenic Symposium in Chemical Engineering, Athens, Greece  
29–31 May 2019
20. **CO<sub>2</sub> Hydrogenation Reaction on CeO<sub>2</sub>-Supported Transition Metal Catalysts: Effect of CeO<sub>2</sub> Morphology**, *Georgios Varvoutis, Eleni Papista, Nicolaos Kaklidis, Georgios E. Marnellos, Sónia A. C. Carabineiro, Maria Lykaki, Sofia Stefa, Michalis Konsolakis*, 12th Panhellenic Symposium in Chemical Engineering, Athens, Greece  
29–31 May 2019
21. **Effect of support nanostructure on the physicochemical and catalytic properties of Fe<sub>2</sub>O<sub>3</sub>/CeO<sub>2</sub> mixed oxides**, *Maria Lykaki, Sofia Stefa, Sónia A. C. Carabineiro, Pavlos K. Pandis, Vassilis N. Stathopoulos and Michalis Konsolakis*, 15th Panhellenic Symposium of Catalysis, Ioannina, Greece  
18–20 October 2018
22. **Solution based synthesis of Ag<sub>3</sub>PO<sub>4</sub>/Fe<sub>2</sub>TiO<sub>5</sub> nanocomposites for photodegradation of organic pollutants**, *Natalia Andrigiannaki, Sofia Stefa, Marilena Moschogiannaki, George Kiriakidis, Vasileios Binas*, 7th International Symposium on Transparent Conductive Materials & 4th EMRS & MRS-J Bilateral Symposium on Advanced Oxides and Wide Bandgap Semiconductors, Chania, Crete, Greece  
14–19 October 2018

23. **Parameters affecting the sensitization of ZnO nanowires for Dye Sensitized Solar Cells**, **Sofia Stefa**, *George Syrokostas, George Leftheriotis and Spyros N. Yannopoulos*, 3rd Workshop of Graduates and Post-Docs in Chemical Engineering Sciences (CES-WGP3), Patras, Greece  
4 October 2017